

ISSN 1983-4195



**IBRACON**

**IBRACON Structures and Materials Journal**  
Revista IBRACON de Estruturas e Materiais

---

**Volume 14, Number 3**  
June 2021



# IBRACON Structures and Materials Journal

## Revista IBRACON de Estruturas e Materiais

### Contents

- Evaluation of production quality and mechanical behavior of low-cost shear connectors manufactured with perforated GFRP plates.....* 14301  
J. K. F. SILVA, R. R. RIBEIRO and R. M. LAMEIRAS
- Towards improving the seismic hazard map and the response spectrum for the state of RN/Brazil.....* 14302  
P. G. B. NOBREGA, B. R. S. SOUZA and S. H. S. NOBREGA
- Effect of filler nature on mechanical performance and drying shrinkage of self-leveling mortars.....* 14303  
T. P. SCOLARO AND J. C. ROCHA
- Size effect on the methodology with cylinder specimens for FRP-to-concrete debonding analysis.....* 14304  
L. F. BORGES and A. C. SANTOS
- Design and verification of reinforced concrete shell elements.....* 14305  
M. V. CRAVEIRO, T. N. BITTENCOURT and J. C. D. BELLA
- Bending reinforced concrete beams with glass fiber reinforced polymer bars: an experimental analysis.....* 14306  
T. V. FERNANDES, A. R. PALIGA and C. M. PALIGA
- Shear in sand-lightweight and conventional high strength concrete through the push-off test.....* 14307  
P. S. FIGUEIREDO, T. A. SOARES, S. L. G. GARCIA, A. C. S. PEREIRA and J. C. TRINDADE
- Alkali-silica reaction (ASR) - Investigation of crystallographic parameters of natural sands by backscattered electron diffraction.....* 14308  
K. F. PORTELLA, L. E. LAGOEIRO, J. L. BRONHOLO, D. C. MIRANDA, M. D. G. P. BRAGANÇA, B. G. DIAS, N. P. HASPARYK and S. C. KUPERMAN
- Reaction mechanisms of alkali-activated materials.....* 14309  
M. T. MARVILA, A. R. G. AZEVEDO and C. M. F. VIEIRA
- Numerical modeling and design of precast prestressed UHPFRC I beams.....* 14310  
G. M. S. GIDRÃO, P. A. KRAHL and R. CARRAZEDO
- Residual Strength of Reinforced Concrete Stub Columns Subject to Moderate Temperatures.....* 14311  
E. H. B. LIMA and D. C. T. CARDOSO
- Strain, natural frequency, damping coefficient and elastic modulus of mortar beams determined by fiber Bragg grating (FBG) sensors.....* 14312  
G. MACIOSKI, V. OLIVEIRA and M. H. F. MEDEIROS
- Behavior of CFA and H-section steel piles in lateral loading: experimental and numerical analysis.....* 14313  
A. M. D. SOUSA, Y. D. J. COSTA, A. G. D. ARAUJO and C. M. L. COSTA
- Influence of hydraulic jiggling of construction and demolition waste recycled aggregate on hardened concrete properties.....* 14314  
I. L. SANTOS, L. V. FRANTZ and A. B. MASUERO
- Seismic analysis of reinforced concrete buildings with participating masonry infills.....* 14315  
G. M. S. ALVA, A. O. RIGÃO, J. KAMINSKI and M. A. S. PINHEIRO



Cover: Parametric Tower

Courtesy: Marcela Noronha P. de O. e Sousa



**IBRACON**

IBRACON Structures and Materials Journal is published bimonthly (February, April, June, August, October, and December) by IBRACON.

**IBRACON**  
Instituto Brasileiro do Concreto Founded in 1972

Av. Queiroz Filho, nº 1700 — sala 407/408  
Torre D — Villa Lobos Office Park  
CEP 05319-000 — São Paulo, SP — Brazil  
Phone: +55 11 3735-0202  
Fax: +55 11 3733-2190  
E-mail: [riem@ibracon.org.br](mailto:riem@ibracon.org.br)  
Website: <http://www.ibracon.org.br>

Cover design & Layout: Editora Cubo  
[www.editoracubo.com.br](http://www.editoracubo.com.br)

---

## Aims and Scope

### Aims and Scope

The IBRACON Structures and Materials Journal (in Portuguese: Revista IBRACON de Estruturas e Materiais) is a technical and scientific divulgation vehicle of IBRACON (Brazilian Concrete Institute), published every two months. Each issue has 12 to 15 articles and, possibly, a technical note and/or a technical discussion regarding a previously published paper. All contributions are reviewed and approved by professionals with recognized scientific competence in the area. The IBRACON Structures and Materials Journal is an open access Journal, free of charges for authors and readers.

### Objectives

The IBRACON Structures and Materials Journal's main objectives are:

- Present current developments and advances in concrete structures and materials.
- Make possible the better understanding of structural concrete behavior, supplying subsidies for a continuous interaction among researchers, producers, and users.
- Stimulate the development of scientific and technological research in the areas of concrete structures and materials, through papers peer-reviewed by a qualified Editorial Board.
- Promote the interaction among researchers, constructors and users of concrete structures and materials and the development of Civil Construction.
- Provide a vehicle of communication of high technical level for researchers and designers in the areas of concrete structures and materials.

### Submission Procedure

The procedure to submit and revise the contributions, as well as the formats, are detailed in the Journal Website ([ismj.org](http://ismj.org)).

The papers and the technical notes are revised by at least two reviewers indicated by the editors. Discussions and replies are accepted for publication after a review by the editors and at least one member of the Editorial Board. In case of disagreement between the reviewer and the authors, the contribution will be sent to a specialist in the area, not necessarily linked to the Editorial Board. Conflict of interests is carefully handled by the Editors.

### Contribution Types

The Journal will publish original papers, short technical notes, and paper discussions. Original papers will be accepted if they are in accordance with the objectives of the Journal and present quality of information and presentation. A technical note is a brief manuscript. It may present a new feature of research, development, or technological application in the areas of Concrete Structures and Materials, and Civil Construction. This is an opportunity to be used by industries, companies, universities, institutions of research, researchers, and professionals willing to promote their works and products under development.

A discussion is received no later than 3 months after the publication of the paper or technical note. The discussion must be limited to the topic addressed in the published paper and must not be offensive. The right of reply is granted to the Authors. The discussions and the replies are published in the subsequent issues of the Journal.

The submission file should be in accordance with the paper template available at the Journal Website. It is recommended that the length of the papers does not exceed 25 pages. Where available, URLs for the references should be provided.

The IBRACON Structures and Materials Journal will conduct the review process for manuscripts submitted in English. Titles, abstracts, and keywords are presented in English, and in Portuguese or Spanish. Articles and technical notes are peer-reviewed and only published after approval of the reviewers and the Editorial Board.

Once accepted, an article is typeset according to the journal layout. The author will be required to review and approve the galleys before publishing. At this stage only typesetting errors will be considered.

### Internet Access

The IBRACON Structures and Materials Journal Webpage is available at <http://ismj.org>.

### Sponsors

The funds for the maintenance of the Journal are currently obtained from the IBRACON. The Journal is not supposed to be maintained with funds from private sponsorship, which could diminish the credit of the publications.

### Photocopying

Photocopying in Brazil. Brazilian Copyright Law is applicable to users in Brazil. IBRACON holds the copyright of contributions in the journal unless stated otherwise at the bottom of the first page of any contribution. Where IBRACON holds the copyright, authorization to photocopy items for internal or personal use, or the internal or personal use of specific clients, is granted for libraries and other users registered at IBRACON.

### Copyright

All rights, including translation, reserved. Under the Brazilian Copyright Law No. 9610 of 19th February, 1998, apart from any fair dealing for the purpose of research or private study, or criticism or review, no part of this publication may be reproduced, stored in a retrieval system, or transmitted in any form or by any means, electronic, mechanical, photocopying, recording or otherwise, without the prior written permission of IBRACON. Requests should be directed to IBRACON:

### IBRACON

Av. Queiroz Filho, 1700 – sala 407/408 – Torre D  
Villa Lobos Office Park  
05319-000 – Vila Hamburguesa  
São Paulo – SP  
Phone: +55 (11) 3735-0202  
E-mail: [riem@ibracon.org.br](mailto:riem@ibracon.org.br)

### Disclaimer

Papers and other contributions and the statements made or opinions expressed therein are published on the understanding that the authors of the contribution are the only responsible for the opinions expressed in them and that their publication does not necessarily reflect the views of IBRACON or of the Journal Editorial Board.

---

## Editorial Board

### Editor-in-chief emeritus

José Luiz Antunes de Oliveira e Sousa, Universidade Estadual de Campinas - UNICAMP, Campinas, SP, Brazil, jls@fec.unicamp.br

### Editor-in-chief

Guilherme Aris Parsekian, Universidade Federal de São Carlos – UFSCAR, São Carlos, SP, Brazil, parsekian@ufscar.br

### Associate Editors

Antônio Carlos dos Santos, Universidade Federal de Uberlândia – UFU, Uberlândia, MG, Brazil  
Bernardo Horowitz, Universidade Federal de Pernambuco - UFPE, Recife, PE, Brazil  
Bernardo Tutikian, Universidade do Vale do Rio dos Sinos – UNISINOS, São Leopoldo, RS, Brazil  
Bruno Briseghella, Fuzhou University, Fujian, China  
David Oliveira, Jacobs Engineering, Sydney, Australia  
Edgar Bacarji, Universidade Federal de Goiás - UFG, Goiânia, GO, Brazil  
Edna Possan, Universidade Federal da Integração Latino Americana – UNILA, Foz do Iguaçu, PR, Brazil  
Fernando Pelisser, Universidade Federal de Santa Catarina – UFSC, Florianópolis, SC, Brazil  
Fernando Soares Fonseca, Brigham Young University – BYU, Provo, UT, USA  
José Marcio Fonseca Calixto, Universidade Federal de Minas Gerais – UFMG, Belo Horizonte, MG, Brazil  
José Tadeu Balbo Universidade de São -Paulo, São Paulo, SP, Brazil  
Leandro Mouta Trautwein, Universidade Estadual de Campinas - UNICAMP, Campinas, SP, Brazil  
Leandro F. M. Sanchez, University of Ottawa, Ottawa, Canada  
Lia Lorena Pimentel, Pontifícia Universidade Católica de Campinas – PUCCAMP, Campinas, SP, Brazil  
Luís Oliveira Santos, Laboratório Nacional de Engenharia Civil, Lisboa, Portugal  
Mark G Alexander, University of Cape Town, Cape Town, South Africa  
Marco Di Prisco, Politecnico di Milano, Milan, Italy  
Mário Jorge de Seixas Pimentel, Universidade do Porto - FEUP, Porto, Portugal  
Maurício de Pina Ferreira, Universidade Federal do Pará - UFPA, Belém, PA, Brazil  
Mauro de Vasconcellos Real, Universidade Federal do Rio Grande – FURG, Rio Grande, RS, Brazil  
Nigel G. Shrive, University of Calgary, Calgary, Canada  
Osvaldo Luís Manzoli, Universidade Estadual Paulista “Júlio de Mesquita Filho” - UNESP, Bauru, SP, Brazil  
Rebecca Gravina, RMIT University, Melbourne, Australia  
Ricardo Carrazedo, Universidade de São Paulo - USP, São Carlos, SP, Brazil  
Samir Maghous, Universidade Federal do Rio Grande do Sul - UFRGS, Porto Alegre, RS, Brazil  
Sérgio Hampshire de Carvalho Santos, Universidade Federal do Rio de Janeiro - UFRJ, Rio de Janeiro, RJ, Brazil  
Túlio Nogueira Bittencourt, Universidade de São -Paulo, São Paulo, SP, Brazil  
Vladimir Guilherme Haach, Universidade de São Paulo - USP, São Carlos, SP, Brazil  
Yury Villagrán Zaccardi, Universidad Tecnológica Nacional Facultad Regional La Plata, Buenos Aires, Argentina

### Editorial Comission

Antônio Carlos R. Laranjeiras, ACR Laranjeiras, Salvador, BA, Brazil  
Emil de Souza Sánchez Filho, Universidade Federal Fluminense, UFF, Rio de Janeiro, RJ, Brazil  
Geraldo Cechella Isaia, Universidade Federal de Santa Maria, UFSM, Santa Maria, RS, Brazil  
Gonzalo Ruiz, Universidad de Castilla-La Mancha - UCLM, Ciudad Real, Spain  
Ivo José Padaratz, Universidade Federal de Santa Catarina - UFSC, Florianópolis, SC, Brazil  
Joaquim de Azevedo Figueiras, Faculdade de Engenharia da Universidade do Porto - FEUP, Porto, Portugal  
Paulo Monteiro, University of California Berkeley, Berkeley, CA, USA  
Pedro Castro Borges, CINVESTAV, Mérida, Yuc., México  
Vladimir Antônio Paulon, Universidade Estadual de Campinas - UNICAMP, Campinas, SP, Brazil

### Former Editors

Américo Campos Filho, Universidade Federal do Rio Grande do Sul - UFRGS, Porto Alegre, RS, Brazil  
Denise C. C. Dal Molin Universidade Federal do Rio Grande do Sul - UFRGS, Porto Alegre, RS, Brazil  
Eduardo Nuno Brito Santos Júlio, Instituto Superior Técnico - IST, Lisboa, Portugal  
Guilherme Sales Melo, Universidade de Brasília, UnB, Brasília, DF, Brazil  
Luiz Carlos Pinto da Silva Filho, Universidade Federal do Rio Grande do Sul - UFRGS, Porto Alegre, RS, Brazil  
Mounir Khalil El Debs, Universidade de São Paulo - USP, São Carlos, SP, Brazil  
Nicole Pagan Hasparyk, Eletrobras Furnas, Aparecida de Goiânia, GO, Brazil  
Paulo Helene, Universidade de São Paulo - USP, São Paulo, SP, Brazil  
Roberto Caldas de Andrade Pinto, Universidade Federal de Santa Catarina - UFSC, Florianópolis, SC, Brazil  
Ronaldo Barros Gomes, Universidade Federal de Goiás - UFG, Goiânia, GO, Brazil  
Romilde Almeida de Oliveira, Universidade Católica de Pernambuco - UNICAP, Recife, PE, Brazil  
Romildo Dias Toledo Filho, Universidade Federal do Rio de Janeiro - UFRJ, Rio de Janeiro, RJ, Brazil  
Rubens Machado Bittencourt, Eletrobras Furnas, Aparecida de Goiânia, GO, Brazil



## **Board of Direction 2019/2021 Biennium**

### **President**

Paulo Helene

### **1<sup>st</sup> Vice-President Director**

Júlio Timerman

### **2<sup>nd</sup> Vice-President Director**

Enio José Pazini Figueiredo

### **Presidency Advisors**

Antônio Domingues de Figueiredo

Iria Lícia Oliva Doniak

Jairo Abud

Jorge Batlouni Neto

Luís Aurélio Fortes da Silva

Mario William Esper

Maurice Antoine Traboulsi

Paula Baillot

Simão Priskulnik

### **1<sup>st</sup> Director-Secretary**

Cláudio Sbrighi Neto

### **2<sup>nd</sup> Director-Secretary**

Carlos José Massucato

### **1<sup>st</sup> Treasurer Director**

Júlio Timerman

### **2<sup>nd</sup> Treasurer Director**

Hugo S. Armelin

### **Marketing Director**

Jéssika Pacheco

### **Marketing Director Advisor**

Guilherme Covas

### **Publications Director**

Guilherme Parsekian

### **Publications Director Advisor**

Túlio Nogueira Bittencourt

### **Event Director**

Rafael Timerman

### **Event Director Advisor**

Luis César De Luca

### **Technical Director**

José Tadeu Balbo

### **Technical Director Advisor**

Selmo Chapira Kuperman

### **Institutional Relations Director**

César Henrique Daher

### **Institutional Relations Director Advisor**

José Vanderley de Abreu

### **Course Director**

Leandro Moura Trautwein

### **Course Director Advisor**

Antônio Carlos dos Santos

### **Student Activities Director**

Jéssica Andrade Dantas

### **Student Activities Director Advisor**

Sandra Regina Bertocini

### **Personnel Certification Director**

Adriano Damásio Soterio

### **Personnel Certification Director Advisor**

Gilberto Antônio Giuzio

### **Research and Development Director**

Bernardo Tutikian

### **Research and Development Director Advisor**

Roberto Christ

## **Council 2019/2021 Biennium**

### **Individual Members**

Antônio Carlos dos Santos

Antônio Domingues de Figueiredo

Arnaldo Forti Battagin

Bernardo Fonseca Tutikian

Carlos José Massucato

César Henrique Sato Daher

Cláudio Sbrighi Neto

Enio José Pazini Figueiredo

Hugo da Costa Rodrigues Filho

Inês Laranjeira da Silva Battagin

Iria Lícia Oliva Doniak

Jéssika Mariana Pacheco

José Tadeu Balbo

Leandro Moura Trautwein

Luiz Carlos de Almeida

Luiz Prado Vieira Júnior

Mário William Esper

Maurice Antoine Traboulsi

Rafael Timerman

Vladimir Antônio Paulon

### **Past President Members**

Eduardo Antônio Serrano

José Marques Filho

Júlio Timerman

Paulo Helene

Ronaldo Tartuce

Rubens Machado Bittencourt

Selmo Chapira Kuperman

Simão Priskulnik

Túlio Nogueira Bittencourt

### **Corporate Members**

ABCIC - Associação Brasileira da  
Construção Industrializada de Concreto –  
Iria Lícia Oliva Doniak

ABCP - Associação Brasileira de Cimento  
Portland – Paulo Camilo Penna

ABECE - Associação Brasileira de  
Engenharia e Consultoria Estrutural –  
João Alberto de Abreu Vendramini

ABESC - Associação Brasileira das  
Empresas de Serviços de Concretagem –  
Jairo Abud

EPUSP - Escola Politécnica da  
Universidade de São Paulo – Túlio  
Nogueira Bittencourt

FURNAS Centrais Elétricas S/A – Flávio  
de Lima Vieira

IPT - Instituto de Pesquisas Tecnológicas  
do Estado de São Paulo – José Maria de  
Camargo Barros

L. A. FALCÃO BAUER Centro  
Tecnológico – Patrícia Bauer

PhD Engenharia Ltda – Douglas de  
Andreza Couto

TQS Informática Ltda – Nelson Covas

VOTORANTIM Cimentos S/A –

Maurício Bianchini



## ORIGINAL ARTICLE

# Evaluation of production quality and mechanical behavior of low-cost shear connectors manufactured with perforated GFRP plates

*Avaliação da qualidade de produção e do comportamento mecânico de conectores de cisalhamento de baixo custo fabricados com placas perfuradas de PRFV*

John Kennedy Fonsêca Silva<sup>a</sup>

Renan Rocha Ribeiro<sup>a</sup>

Rodrigo de Melo Lameiras<sup>a</sup>

<sup>a</sup>Universidade de Brasília – UnB, Faculdade de Tecnologia, Brasília, DF, Brasil

Received 09 March 2020

Accepted 17 July 2020

**Abstract:** Insulated pre-cast concrete wall panels, also called sandwich panels, consist in two external concrete layers, in which an internal layer of thermal insulation material is inserted between, aiming better acoustic and thermal performance. One of the main concerns regarding the performance of these panels refers to the elimination of thermal bridges caused by metallic connectors, which jeopardize the panels' thermal efficiency. One of the proposals to solve this problem consists in the use of PERFOFRP connectors, which are plane plates with perforated holes through its thickness, which are embedded into the concrete plates, creating anchorage pins that enhance the shear strength and the layers' debonding resistance. This research had the objective of evaluating the production quality of this type of connector, produced with a low-cost and easy-to-use vacuum assisted resin infusion system; considering the effects of: (a) resin plate homogeneity, by taking samples from various locations on the plate; (b) fabrication repeatability; and (c) raw production materials' origin; on the results of: (I) ultimate tensile stress, (II) modulus of elasticity, and (III) volume fraction of fibre. Also, 18 specimens in the form of representative models of the shear connector in insulated pre-cast concrete wall panels, with six different hole configurations achieved by varying the holes' diameter and spacing, were subjected to push-out tests, to assess the holes' diameter and spacing effects on the mechanical performance of the connection in terms of ultimate load capacity and stiffness. The results indicated a production quality with a satisfactory level of characteristics variation, considering: the variability in different parts of a single composite plate, the variability between composite plates from different infusion process, and the variability between different production batches. Furthermore, the push-out tests demonstrated that the perforated connectors presented, when compared to non-perforated connectors: a gain in shear strength from 8% to 25%, lower relative displacements, and higher levels of stiffness. It was also observed that connectors with 25.40 mm diameter holes presented better performance than connectors with 31.75 mm diameter holes; and that the reducing the hole spacing from 2.00 to 1.75, for the 25.40 mm diameter specimens, caused a decrease in the load capacity of the connector. Thus, it was verified that variations on the hole's diameter and spacing influenced the load carrying capacity of the connection.

**Keywords:** composite structures, sandwich panels, shear connectors, PERFOFRP connectors, fibre reinforced polymers.

**Resumo:** Paredes de concreto pré-moldado com isolamento incorporado, também chamadas de painéis sanduíche, consistem em duas camadas externas de concreto, entre as quais uma camada interna de material isolante é inserida, visando melhorar os desempenhos acústico e térmico. Uma das principais preocupações em relação ao desempenho desses painéis refere-se à eliminação de pontes térmicas causadas por conectores metálicos, que comprometem a eficiência térmica dos painéis. Uma das propostas para resolver esse problema consiste no uso de conectores PERFOFRP, que consistem em placas planas perfuradas, embebidas em ambas as camadas externas de concreto, que criam pinos de ancoragem que aumentam a resistência ao cisalhamento dos painéis e à separação das camadas de concreto. Esta pesquisa objetivou avaliar a qualidade de produção

Corresponding author: John Kennedy Fonsêca Silva. E-mail: kennedy1317@gmail.com

Financial support: Conselho Nacional de Desenvolvimento Científico e Tecnológico – CNPq; Universidade de Brasília – UnB.

Conflict of interest: Nothing to declare.



This is an Open Access article distributed under the terms of the Creative Commons Attribution License, which permits unrestricted use, distribution, and reproduction in any medium, provided the original work is properly cited.

desse tipo de conector, produzido com um sistema de infusão por resina à vácuo de baixo custo e de fácil uso; considerando os efeitos da: (a) homogeneidade da placa de PRFV; (b) repetibilidade de fabricação; e (c) origem das matérias-primas; sobre os resultados de: (I) tensão última à tração, (II) módulo de elasticidade, e (III) fração volumétrica de fibras. Além disso, 18 espécimes na forma de modelos representativos do conector de cisalhamento em painéis sanduíche, com seis configurações diferentes de perfuração obtidas por meio da variação do diâmetro e do espaçamento entre os furos, foram submetidos à ensaios *push-out*, para avaliar o efeito que essas variações produzem no desempenho mecânico da conexão em termos de capacidade de carga final e de rigidez. Os resultados indicaram uma qualidade de produção com um nível satisfatório de variação das características, considerando: a variabilidade em diferentes pontos de uma única placa, a variabilidade entre placas compostas por diferentes processos de infusão e a variabilidade entre diferentes lotes de produção. Além disso, os testes *push-out* demonstraram que os conectores perfurados apresentaram, quando comparados com conectores não perfurados: um ganho na resistência ao cisalhamento variando entre 8% e 25%, deslocamentos relativos mais baixos e níveis mais elevados de rigidez. Observou-se também que os conectores com furos de 25.40 mm de diâmetro apresentaram melhor desempenho do que os conectores com furos de 31.75 mm de diâmetro; e que a redução do espaçamento entre furos de 2.00 para 1.75, para as amostras de 25.40 mm de diâmetro, causou uma diminuição na capacidade de carga do conector. Assim, verificou-se que as variações no diâmetro e no espaçamento do furo influenciaram a capacidade de carga da conexão.

**Palavras-chave:** estruturas compostas, painéis sanduíche, conectores de cisalhamento, conectores PERFOFRP, polímeros reforçados com fibras.

---

**How to cite:** J. K. F. Silva, R. R. Ribeiro, and R. M. Lameiras, "Evaluation of production quality and mechanical behavior of low-cost shear connectors manufactured with perforated GFRP plates," *Rev. IBRACON Estrut. Mater.*, vol. 14, no. 3, e14301, 2021, <https://doi.org/10.1590/S1983-41952021000300001>

## 1 INTRODUCTION

Insulated pre-cast concrete wall panels, also called sandwich panels, consist in two external concrete layers, in which an internal layer of thermal insulation material is inserted between, aiming better acoustic and thermal performance. To maintain the panel's integrity during the stages of lifting and transport, and throughout the building's lifespan, the use of connectors, which can either be shear-type or non-composites, is required. These connectors are anchored in both external concrete layers, passing through the inner layer of insulation material. The external layers are, usually, made of reinforced concrete and the inner layer of expanded polystyrene (EPS).

Sandwich panels can be classified as: (a) non-composites, in which the concrete layers behave mechanically independently, and, usually, one of them is a thick structural layer and the other is a thin non-structural layer; (b) composites, in which both concrete layers act as a single composite layer to sustain applied loads, such as bending; (c) partially composites, in which shear connectors connect the concrete layers but can only guarantee a moderate composite action [1]. The degree of composite action depends mainly on the stiffness, strength and connector's location along the panel [2].

Some advantages of the sandwich panels are: durability; economy; fire resistance; possibility of use in large spans; superior energetic performance and moisture protection when compared to other conventional building systems; resistance to impacts, thefts and vandalism; and easy surface finishing [1]. The sandwich panel is a significant development in the concept of sustainable architecture and a great advantage in the process of sustainable building certification. With new normative requirements for energetic performance, the industry has been adopting sandwich panels to improve building's thermal performance, while still taking advantage of the fast construction provided by concrete panels [3].

According to the PCI Committee Report [1], connectors for insulated pre-cast concrete panels have a variety of functions, among which it can be cited: sustaining the stress produced by the weight of the non-structural layer, supporting any horizontal load caused by winds or seismic actions; resisting the horizontal shearing due to panel bending. These connectors can be divided in two categories: (a) shear connectors, that are used mainly to transfer the in-plane shear forces between the two concrete layers; (b) non-composite connectors, that are designed only to hold the concrete layers connected.

Solid regions of concrete and steel trusses were the first type of connectors used in sandwich panels [4]–[6]. Even though panels with these types of connectors present a high degree of composite action when subjected to bending, a thermal bridge between the internal and external layer is created due to the high thermal conductivity of the steel and concrete, which, consequentially, compromises the thermal performance of the panel. According to MacCall [7], the use of steel-pin connectors, which also have such thermal issue, in an amount representing 0.08% of the sandwich panel area, may reduce the panel's thermal performance by up to 38%. Being the thermal insulation one of the main requirements for this type of construction system, this is a relevant research topic.

In order to solve this problem, fibre reinforced polymers (FRP) connectors have been developed, having the advantage of a reasonable mechanical strength and a considerably low thermal conductivity [8]. Nowadays, the most common FRP connectors are: glass-fibre reinforced polymer (GFRP) grids [9]; carbon-fibre reinforced polymer (CFRP) grids [10]–[12]; corrugated GFRP [13]; and shell GFRP [14]. Concerning the mechanical strength of FRP connectors, several tests have been conducted in order to assess the mechanical performance and composite action degree of this type of connector, such as: Naito et al. [3], that used double-shear tests to evaluate the performance of 14 types of commercial connectors, including FRP connectors, and developed a simplified tri-linear model of force versus relative displacement for use in structural performance analysis of sandwich panels; Hodicky et al. [15], that analysed the effect of connector spacing and insulation thickness in the strength of a CFRP grid connector, observing that an increase in insulation thickness leads to a decrease in the connector strength; and Tomlinson et al. [16], that tested connectors composed by angled bars of basalt-fibre reinforced polymer (BFRP) and analysed the effects of varying the bar diameter, inclination angle, and orientation of the diagonal connector relative to loading in tension and compression cases, in the bond between concrete and insulation layers and the overall performance of the connector.

In this sense, the PERFOFRP connectors were developed aiming both better mechanical and thermal insulation performance. This type of connector for sandwich panels was originally proposed by Lameiras et al. [17], [18].

The PERFOFRP connectors are made of GFRP, which provides an excellent thermal insulation performance due to its low thermal conductivity (0.04 W/mK) when compared to steel (50.2 W/mK) and concrete (0.8 W/mK) [19]. The connector is fabricated as a plane plate with perforated holes through the thickness, which are embedded into the concrete plates, creating anchorage pins that enhance the shear strength and the layers' debonding resistance. The PERFOFRP connectors can also be easily standardized for mass production or customized for a specific application and require neither large nor expensive industrial facilities for fabrication.

The PERFOFRP was further studied by Lameiras et al. [20], [21], in studies performed at University of Minho, in which push-out tests were conducted aiming the assessment of the connector's resistance capacity. Chen et al. [22] and Norris and Chen [23], at Iowa State University, analysed the flexural behaviour of similar connectors. Recently, Huang and Dai [2] conducted, at Hong Kong Polytechnic University, a series of direct shear tests of this type of connector, assessing the effect of the connector's thickness and height in its shear resistance.

The aforementioned researches attested the viability of the PERFOFRP and demonstrated a satisfactory degree of composite action, in terms of strength and stiffness, in sandwich panels produced with this connector. However, they indicate that there is limited information regarding this type of connector since the relation between the connector's geometric parameters and performance is still unknown. Thus, the next logical step is the study of the properties and factors that affect the connector's performance, aiming the development of design guidance.

This research has two main objectives: (a) assess the production quality of a low-cost fabrication system of shear connectors for sandwich panels, produced from plane perforated plates of GFRP according to the PERFOFRP proposal; (b) assess the mechanical behaviour of the produced connectors, by means of double-shear push-out tests on representative models of the shear connector in insulated pre-cast concrete wall panels, with hole of various diameter and spacing.

## 2 MATERIALS AND EXPERIMENTAL PROGRAM

The experimental program was divided in two main stages: (a) production and evaluation of production quality of the GFRP composite plates used in the shear connectors fabrication, by means of ultimate tensile stress, modulus of elasticity and volume fraction of fibre test results; (b) fabrication and testing of the shear connectors, by means of double-shear push-out tests of representative models of the shear connector in insulated pre-cast concrete wall panels, with six different hole configurations achieved by varying the holes' diameter and spacing.

### 2.1 Production and evaluation of production quality of GFRP composite plates

GFRP composite plates were produced aiming the fabrication of shear connectors for insulated pre-cast concrete wall panels, according to connectors previously studied by Lameiras et al. [17], [18], [20], [21] and Huang and Dai [2]. A total of 27 GFRP composite plates of 25 cm width, 70 cm length and approximately 2.30 mm thickness was produced during the experimental program, used for both production quality evaluation and mechanical tests in the representative models. The plate production was divided in three batches, denominated Group 01, 02 and 03, each composed by, respectively, 6, 10 and 11 plates. Each group/batch was produced with resin, catalyst, and fibres from the same origin/manufacturer's batch. All composites were composed by five layers of fibre glass of 450 g/m<sup>2</sup>, embedded in polyester resin.



A vacuum assisted resin infusion process, performed with an in-house developed system, was used to produce the composites. This in-house developed system is one of the original contributions of this work, since it used low-cost and easy-to-use materials, that can be acquired and used at, virtually, any place and ambient. Figure 1 presents the main stages of the composites fabrication process, which will be further detailed in the topics 2.1.1, 2.1.2, 2.1.3, e 2.1.4. The production size of the composite plates was defined by the available vacuum level, and the viscosity and working time of the resin.

Aiming the evaluation of the production quality of the produced composite plates, samples were extracted from random regions of the plate to allow tests for ultimate tensile strength and volume fraction of fibre determination.

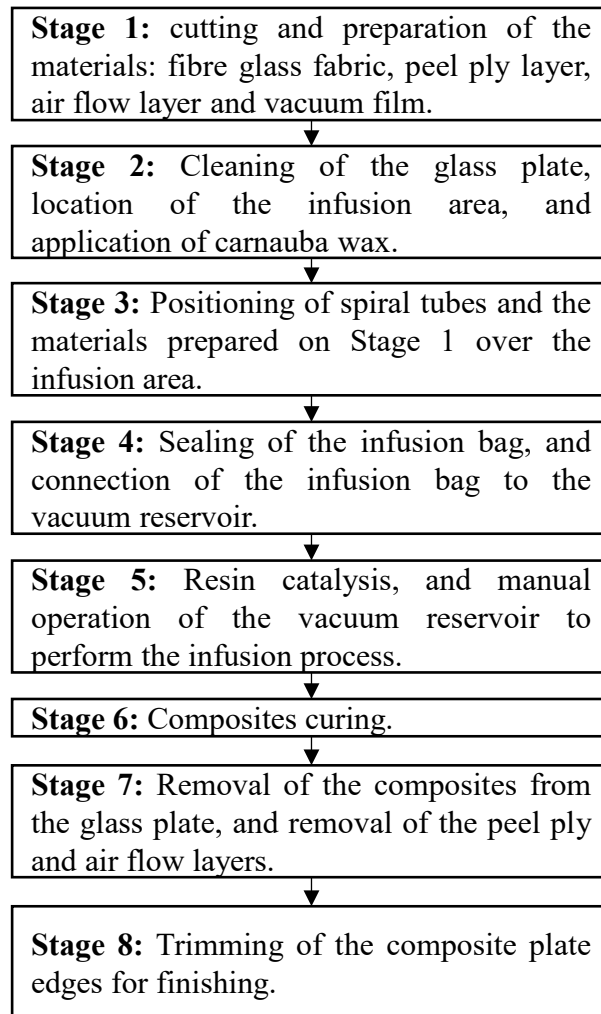


Figure 1. Stages of the composites fabrication process.

### 2.1.1 In-house developed system for vacuum assisted resin infusion

The vacuum assisted resin infusion system, that was developed in-house for this work, is composed by four main components, with the following functions:

- a) Resin reservoir: a reservoir produced from polyvinyl chloride (PVC) in which the catalysed resin is deposited and is left ready to be suctioned during the infusion process;
- b) Infusion bag: an air-tight bag into which the resin flows, being composed by the following sequential layers, from top to bottom: one glass plate; one peel ply; five fibre glass fabrics; one peel ply; one air flow layer; one vacuum film. The purpose of each layer is described in 2.1.2. The vacuum film, which is the last layer in the system, is sealed in its external perimeter with a silicon bead that guarantees its adhesion to the glass plate. Inside the infusion

bag, just before positioning the vacuum film, two 70 cm spiral tube lines were placed in opposite longitudinal sides, and denominated vacuum and infusion lines. The vacuum line is used to apply vacuum in the system, being positioned 5 cm from the border of the glass fibre fabrics. The infusion line is used to infuse the resin in the system, being positioned close to the glass fibre fabrics. In both lines, a T-shaped connection is fixed in the central region, which allows access to the infusion bag by the other parts of the system;

- c) Vacuum reservoir: a system of interconnected hydraulic components with 100 mm diameter, composed by pipes, cap, and T- and L-shaped connections. The vacuum reservoir works with an inner pressure isolated from the atmosphere, which promotes the stabilization and vacuum reserve of the system. It has four ends composed by caps, to which three gate valves of 0.5 in (denominated vacuum, infusion and scape) and an analogic vacuum gauge (with 0.0 to -1.0 atm measuring range) are connected, in order to allow measurement of the negative pressure inside the infusion system. Furthermore, the vacuum reservoir guarantees the safety functioning for the vacuum pump, acting as a drain to prevent that excess of resin reach the pump;
- d) Vacuum pump: a device responsible for the application of vacuum inside the system. In the present work, an air compressor, working in inverse mode, was used (i.e., the air suction socket) usually used as supply for the compressor pressure vessel, was employed as the suction socket in the infusion system, allowing the application of vacuum.

All four main components of the vacuum assisted resin infusion system were interconnected by reinforced transparent plastic hoses, of 0.5 in diameter, in the following order: resin reservoir, infusion bag, vacuum reservoir, and vacuum pump. A valve for opening and closing the resin flow into the system, denominated as resin valve, was placed in the hose connecting the resin reservoir to the infusion bag.

### 2.1.2 Assembly of the vacuum assisted resin infusion system

The composite plates production was initiated by the assembly of the production system. The assembly process initiated with the cut of the glass fibre fabric, peel ply and air flow layers, in 25 cm by 70 cm, and vacuum film in 90 cm by 120 cm, rectangles (Figure 2a). Next, the glass plate was cleaned to eliminate any contamination source in the composite production (Figure 2b).

Then, the vacuum bag assembly was initiated, by locating the infusion area with use of white adhesive tapes over the glass plate (Figure 2c). In this area, three layers of carnauba wax with demoulding agent were applied in intervals of 30 min. After the drying of the last wax layer, the infusion bag layers and the spiral tubes were positioned over the glass plate, according to the order described in 2.1.1, over the already located and waxed infusion area (Figure 2d).

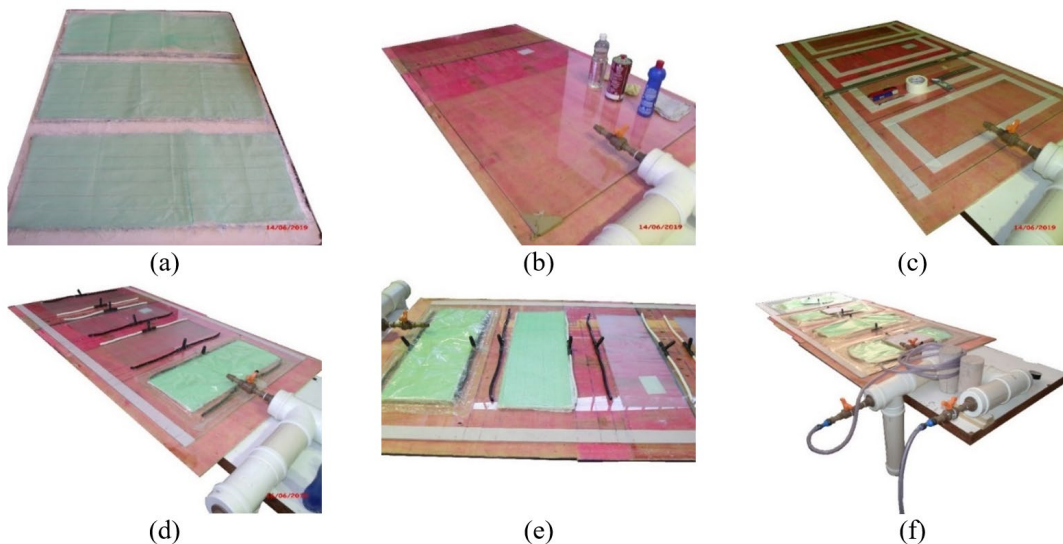


**Figure 2.** GFRP composite fabrication process: (a) curing and preparation of the materials; (b) cleaning of the glass plate; (c) location of the infusion area and application of carnauba wax; (d) positioning of the pipes, spiral tubes and materials over the glass plate; (e) lateral view of the positioning of the pipes, spiral tubes and materials over the glass plate; (f) resin infusion system ready for use, requiring only the positioning of the last pipes.

The peel ply layer has the purpose of guaranteeing the demoulding, since it does not present post-infusion adhesiveness to the glass plate and to the GFRP composite, being easily removed after the partial cure of the composite (12 h). The air flow layer, by its turn, has the purpose of guaranteeing a certain free space between the peel ply and the vacuum film layer, to allow the passage of resin and guarantee an air exit.

With the infusion bag assembled, the reinforced plastic hoses, connecting the resin reservoir and the vacuum pump to the T-shaped connections of the spiral tubes inside the infusion bag, were connected. This concluded the assembly of the vacuum assisted resin infusion system (Figure 2e and Figure 2f).

### 2.1.3 Production of GFRP composite plates

For each produced plate of 25 cm by 70 cm, it was used approximately 550 g of polyester unsaturated resin, obtained by the condensation of carboxylic diacids and glycols, in a solution of styrene monomer ( $C_8H_8$ ), catalysed with 1.0%, in mass, of methyl ethyl ketone peroxide ( $C_4H_{10}O_4$ ), according to the information provided by the resin manufacturer.

Previously to the resin application, the infusion bag and the vacuum reservoir were tested to verify whether leakage points existed. Following, the inner negative pressure was elevated to a 0.80 atm value and stabilized at this level. The infusion initiated with the addition of the catalyst to the resin, in quantities and proportions already mentioned. Then, by manual setting of the valves, the catalysed resin was suctioned from the resin reservoir to the infusion bag and, slowly, all the layers inside the infusion bag were impregnated with resin. This stage was performed in approximately 10 min, with minor variation depending on the temperature and the viscosity of the resin in the moment of infusion of each GFRP composite plate.

Once the suction stage was finished, the resin valve was closed. After 15 min of the beginning of the catalysis, the resin started to present a gel-like aspect, with high viscosity and a low workability that hindered any suction process impossible. After this period, the vacuum pump was kept on for more 30 min, aiming the removal of any air excess impregnated in the composite. In the end of this 30 min period, the resin passed to a rigid state and, since this made impossible any air entrance into the composite plate, the vacuum pump was turned off (Figure 3a).

After 12h of the start of the resin catalyztion, the GFRP composite plates were under partial cure state and could be removed from the glass plate, allowing the production of the next plate. After 24 h of the start of the resin catalyztion, the composite plates reached a complete cure state, with virtually full resin stiffness, and could have its borders trimmed with the aid of a circular table saw. Lastly, the peel ply and air flow layers were removed, and the plates were ready for use (Figure 3b).

At this point, the composite is at full cure and can be mechanically loaded. All the produced plates followed the proceedings described, with small and specific adjustments in the disposition, and geometry, of the pipelines and other components of the infusion system.

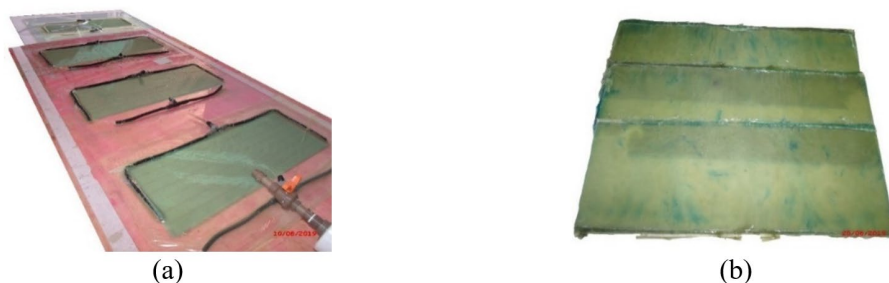


**Figure 3.** GFRP composite plates production process: (a) aspect of the plates immediately after partial curing, still inside the infusion bag; (b) aspect of the composite plates after the removal of vacuum, and the air flow and peel ply layers.

### 2.1.4 Evaluation of the production quality of the GFRP composites plates

The evaluation of the production quality of the GFRP composite plates encompassed three characterization procedures: (a) a dimensional homogeneity analysis, by measurement of the plate thickness ( $\epsilon$ ), which refers to geometric conformity; (b) the mechanical characterization of the main properties of interest (i.e., ultimate tensile stress ( $\sigma_{pt,u}$ ), longitudinal ( $E_{pt,l}$ ) and transversal tensile modulus of elasticity ( $E_{pt,t}$ ), and Poisson's ratio ( $\nu$ )), which refer to composite strength conformity; (c) the determination of the volume fraction of fibre ( $V_f$ ), which refer to

the material composition conformity. The characterization procedures provided not only parameters for the evaluation of the production quality, but also for the overall characterization of the composites produced and used in this work. All characterization procedures were performed in at least two samples per plate taken from random regions.

The evaluation of production quality of the GFRP composite plates was performed by using three parameters: ultimate tensile stress, volume fraction of fibres, and modulus of elasticity, as shown on Figure 4. These three parameters were assessed in three different levels:

- a) Along the extension of each plate, aiming the assessment of variations that may have occurred in the infusion processes;
- b) Among different plates belonging to the same group/batch, aiming the assessment of variations that may have occurred between different infusion processes;
- c) Among different groups/batches, aiming the assessment of the reproducibility of the composites characteristics when produced with materials from different sources/manufacturer's batch.

Up to three statistical tests were applied to the data, as shown on Figure 4: analysis of the magnitude of the coefficient of variation; variance analysis; and a normality test. The choice of which tests were to be applied to each dataset depended on the minimum amount of data required by a given test and the amount of available data on the dataset.

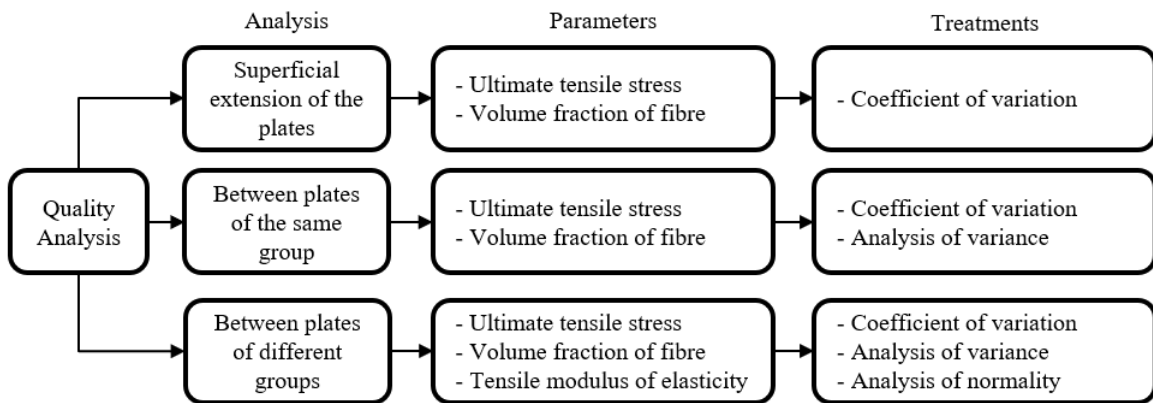


Figure 4. Evaluated parameters, with the respective statistical treatments, in each of the three analyzes level considered.

Samples in the form of 25 cm by 2.50 cm rectangles, with approximately 2.30 mm thickness, were used to perform the ultimate tensile stress and modulus of elasticity tests (Figure 5). The tests were performed in a universal testing machine with load capacity of 300 kN and displacement control. The ultimate tensile stress was determined in a total of 59 specimens, which were also used in the thickness measurement. The tests were conducted according to ASTM D3039 [24], which specifies parameters such as sample geometry and testing machine's displacement velocity. The specimens were clamped, at the inferior and superior extremities, by a compressed air pressure system, and tensioned from the inferior extremity with a constant velocity of 2 mm/min. At the extremity of each specimen, two GFRP plates of 25 mm by 25 mm were fixed, aiming a better distribution of the stress applied by the clamping claws of the testing machine (Figure 6). The load readings were performed with the software and the data-acquisition system of the testing machine. The strain measurement, required for the modulus of elasticity determination, was performed in 14 specimens, of which at 12 the longitudinal strains were measured and at 2 the transversal strains were measured, to provide longitudinal and transversal modulus of elasticity estimates, respectively. The strain gauges were positioned in the central portion of the specimens, and connected to a data-acquisition system.

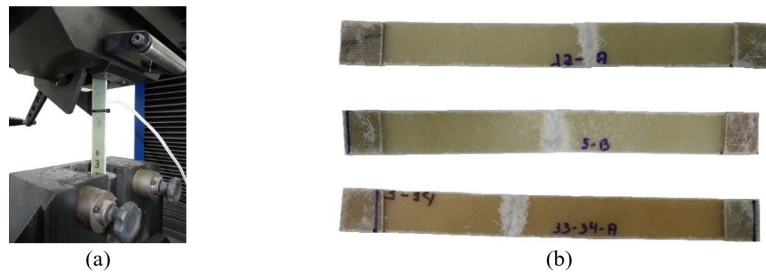


Figure 5. Ultimate tensile stress test: (a) test execution; (b) specimens after failure.

Samples in the form of 25 mm by 25 mm specimen were used for the volume fraction of fibre determination ( $V_f$ ), in a total of 53 specimens. The procedure consisted in submitting these specimens to a 565 °C temperature, during 6 h, according to ASTM D2584 [25]. The mass of the specimens was measured before and after this heating process. The mass loss, caused by the volatilization of the resin, allows the computation of the volume fraction of fibre.

## 2.2 Push-out tests

### 2.2.1 Fabrication of connectors and push-out test specimens

Representative models of the shear connector in insulated pre-cast concrete wall panels, to allow double-shear push-out tests, in the form of concrete primers, were moulded following the geometries suggested by Huang and Dai [2], but with connectors' holes close to that presented by Lameiras et al. [17], [18], [20], [21]. However, the size of the connectors differed from both works. The connector's geometry was defined aiming the maximum possible size considering the model geometry used in the push-out test, but allowing a minimum concrete confinement of 50 mm in the connector's superior and inferior parts, besides a minimum cover of 25 mm. The Figure 7 presents the test specimen.

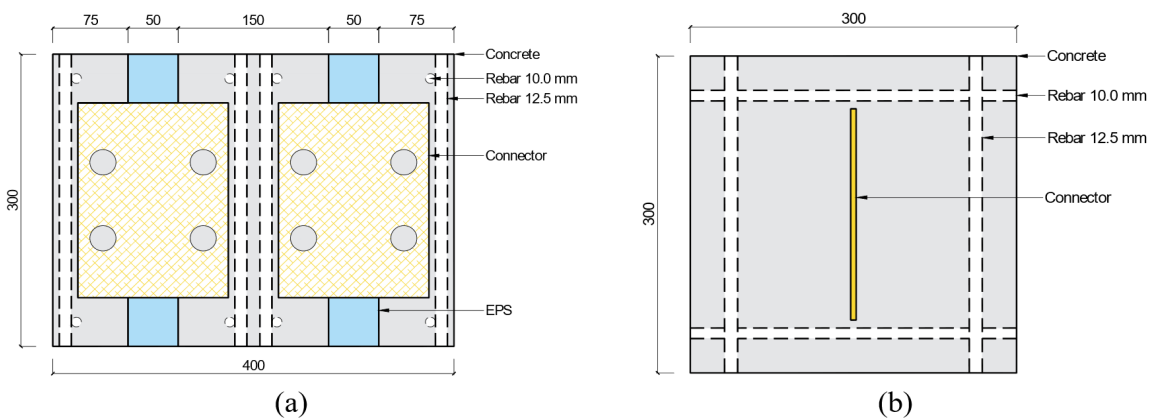


Figure 6. Test specimen: (a) front view; (b) side view.

For the fabrication of the connectors, the GFRP composite plates were saw into dimensions of 15 cm by 20 cm, which was the final size of the connectors tested in this work. These plates were randomly obtained from the Groups 01, 02 and 03, and sorted before the perforation, aiming a better homogeneity of the tested connectors' mechanical characteristics. The sawing was performed in a circular table saw. Next, the perforation of the connectors was performed with a set of hole saws and a bench drill press. The adopted holes had diameters of 25.40 mm and 31.75 mm, and were spaced by 1.75, 2.00 and 3.00 times the hole's diameters, with such spacing taken from the centre of the holes. The PERFOFRP connectors were centralized in the specimen, passing through the insulating material, before the concrete moulding. After the moulding, the connector was embedded in both concrete layers adjacent to the insulating material, i.e. two PERFOFRP connectors were symmetrically positioned in each push-out test specimen. To assess the efficiency

of the perforated connectors, control specimens were produced containing a non-perforated GFRP connector. Three replicate specimens of each connector type were tested. In these tests, the analysed parameters were the hole’s diameter and spacing, aiming the assessment of the effect of such variables in the ultimate load capacity and connection stiffness

The identification of test specimens followed the nomenclature format “SP-X-Y-R (n)”, in which: SP abbreviates the term specimen; X encodes the connector’s hole diameter, in millimetres; Y encodes the hole spacing, in number hole’s diameters; r indicates the replicate, either A, B or C; and n encodes a unique identifier associated to the specimen type, from 1 to 6, for concise reference. For the control specimen, that contained a connector without holes, the “X-Y-r” identifiers were substituted by “CTL”, abbreviating the term control. Table 1 presents the connector’s main characteristics of each specimen tested. The Figure 7 illustrates the hole configuration of the connectors tested.

**Table 1.** Specimens’ identification and their main connector’s characteristics.

Specimen	Amount of tested specimen	Diameter	Spacing
		[mm]	[-]
SP-25.40-1.75	3	25.40	1.75
SP-25.40-2.00	3	25.40	2.00
SP-25.40-3.00	3	25.40	3.00
SP-31.75-2.00	3	31.75	2.00
SP-31.75-3.00	3	31.75	3.00
SP-CTL	3	-	-

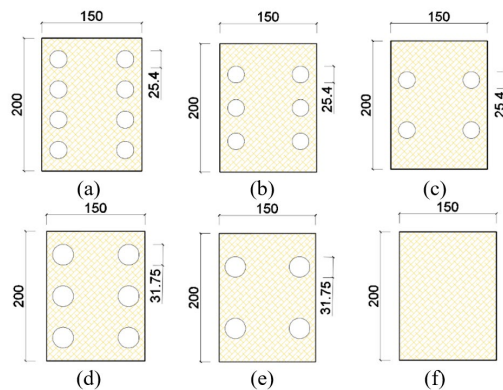


**Figure 7.** Hole configuration of the connectors tested: (a) SP-25.40-1.75; (b) SP-25.40-2.00; (c) SP-25.40-3.00; (d) SP-31.75-2.00; (e) SP-31.75-3.00; (f) SP-CTL.

The holes were aligned to be centralized to the region that would be embedded in concrete. The number of holes was calculated based on the hole diameter and spacing, considering that the most external holes had to be in a distance of, at least, half of the hole spacing. After computing the number of holes, the set was centralized to the connector’s geometric centroid. A perforation template was employed to aid in the dimensional precision of the drilling.

The preparing for the moulding of specimens for the push-out test involved the following stages: formwork fabrication; rebar placement, with 12.5 mm diameter bars for the longitudinal steel, and 10.0 mm bars for the transversal steel; cut of EPS plates to emulate the insulation layer; fixation of the connectors through the insulation layer; and final assembly of the prism. Lastly, the moulding of the prisms was performed with a ready-mix concrete, with consistency of  $10 \pm 2$  cm in the slump test. The concrete’s mechanical parameters values were compressive strength of 37.5 MPa, tensile strength of 4.5 MPa, and modulus of elasticity of 31.0 GPa, evaluated at 28 days in cylindrical specimens of 10 cm by 20 cm size, cured under the same ambient of the prisms.

### 2.2.2 Push-out test execution

The push-out tests were performed according to the test setup shown in the Figure 8. The test consists in inserting, inside the reaction frame, these parts in the following order: prism supports; steel plate supports; a ball-and-socket joint for load direction adjustment; the load cell, with a load capacity of 500 kN produced by HBM Test and Measurement; and the hydraulic actuator, with load capacity of 500 kN produced by Enerpac. The execution of the push-out test consisted in, basically, supporting the external concrete layers and applying a loading to the central concrete layer. This induced a shearing force in the GFRP connectors inside the EPS insulation layer.

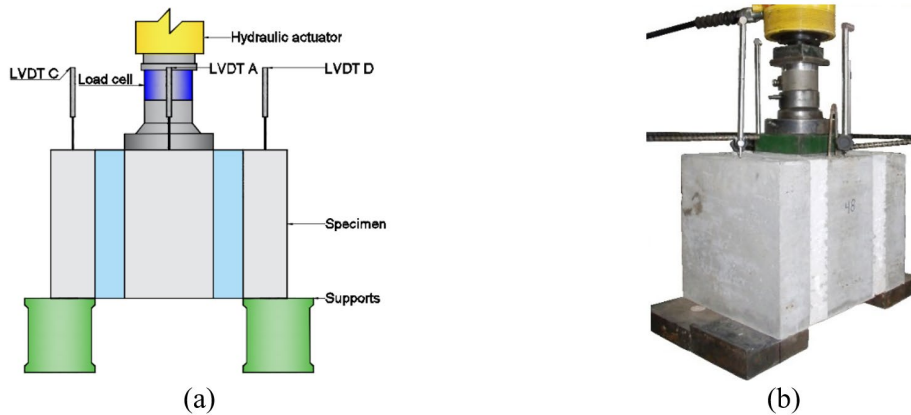


Figure 8: Push-out test: (a) schematic illustration; (b) test execution.

The displacements were measured with a deflector of the linear variable differential transducer (LVDT) type, with a total path of 50 mm produced by HBM Test and Measurement. A single LVDT was positioned in each external concrete layer, denominated C and D, and two LVDTs were positioned in the internal concrete layer, denominated A and B. The relative displacement was calculated computing the difference between the average of the LVDTs A and B, which represent the total displacement of the connectors, and the average of the LVDTs C and D, which represent the settlement at the supports and imply a rigid body motion of the entire prism. This procedure allowed the determination of the relative displacement of the connectors.

Rubber plates were placed in the contact areas between the supports and the external concrete layers, and between the ball-and-socket joint and the internal concrete layer, aiming to allow better accommodation of surface imperfections. The data was sampled at a frequency of 1.0 Hz, with a Spider 8 data-acquisition system, controlled by the software Catman 4.5.

The testing procedure consisted in manually controlling a hydraulic pump, produced by Enerpac, that, by its turn, controlled the loading applied by the hydraulic actuator. The loading rate was approximately constant at a value of 8.1 kN/min. The loading was applied until the detection of the connector's failure, which was verified by a sudden drop in the load cell readings. From this point onwards, the loading rate was kept constant until approximately 50% of the ultimate load. After testing, the connectors were removed from inside the prisms, for failure mode analysis.

## 3 RESULTS AND DISCUSSIONS

### 3.1 Production cost analysis of the in-house developed infusion system

A cost analysis of the production was performed aiming to compare the cost of the produced composites to the prices of composites commercially found on Brazil. Considering only the costs of raw materials (i.e. not including machinery and labour costs) the composites produced in this work costed 107.34 \$/m<sup>2</sup>, or 546.38 R\$/m<sup>2</sup> with the current exchange rate. Currently, composites could be found on the market with prices of the order of 1,091.46 \$/m<sup>2</sup>, or 5,555.56 R\$/m<sup>2</sup> with the current exchange rate, which is 1,016.79% higher than the production costs with the method described in this work.

### 3.2 Composite characterization

The Table 2 shows the results obtained in the measurement of thickness ( $\varepsilon$ ), ultimate tensile stress ( $\sigma_{pl.u}$ ), and volume fraction of fibre ( $V_f$ ), and the respective coefficients of variation (CoV) and number of samples tested.

**Table 2.** Thickness, ultimate tensile stress and volume fraction of fibre of the GFRP plates

GFRP plate	Thickness			Ultimate tensile stress			Volume fraction of fibre		
	Sample	Avg.	CoV	Sample	Avg.	CoV	Sample	Avg.	CoV
	size	[mm]	[%]	size	[MPa]	[%]	size	[%]	[%]
01	2	2.20	3.33	2	180.77	9.10	2	45.92	1.05
02	2	2.29	1.68	2	196.14	4.85	2	38.45	0.60
03	2	2.30	1.81	2	212.56	2.17	2	43.24	1.88
04	2	2.53	0.40	2	181.17	17.47	2	37.21	1.51
05	2	2.25	0.81	2	154.33	6.69	2	38.06	3.67
06	2	2.60	1.93	2	126.66	9.81	1	37.80	-
11	2	2.54	12.60	2	161.41	2.69	2	35.79	3.38
12	2	2.53	4.42	2	178.50	1.66	2	33.81	2.29
13	2	2.27	0.22	2	162.93	2.80	2	38.59	1.48
14	2	2.41	11.14	2	155.24	12.35	1	36.15	-
15	2	2.55	1.24	2	168.98	0.46	2	36.86	0.02
16	3	2.11	7.01	3	172.79	15.13	3	44.06	2.49
17	3	2.58	5.60	3	139.66	10.61	3	39.19	1.97
18	2	2.11	8.00	2	165.05	7.32	2	41.16	3.04
19	3	2.25	1.98	3	165.15	10.64	2	35.86	0.05
20	2	1.97	2.03	2	184.62	5.31	2	40.84	1.20
31	2	2.27	4.77	2	162.25	1.27	1	36.48	-
32	2	2.42	1.52	2	134.50	5.15	1	37.03	-
33	3	2.39	4.04	3	156.46	17.45	3	39.34	0.10
34	2	2.36	0.28	2	160.96	10.49	2	39.13	2.08
35	2	2.27	1.10	2	124.76	19.82	2	39.38	0.09
36	2	2.19	1.82	2	172.55	7.30	2	40.38	2.95
37	2	2.32	0.36	2	147.54	11.26	2	37.65	1.85
38	3	2.28	0.66	3	175.26	1.09	2	40.26	0.00
39	2	2.24	9.29	2	170.09	8.59	2	38.38	3.54
40	2	2.16	0.54	2	160.31	9.52	2	41.74	1.02
41	2	2.20	5.84	2	163.82	1.81	2	41.24	2.49
Avg.		2.32	3.50		164.24	7.88		39.04	1.69

The Figures 9a, 9b, and 9c present the stress-strain curves obtained in the longitudinal modulus of elasticity determination tests under tensile stress of the composites. The curves presented comprise approximately half of the test, up to the moment in which the maximum displacement of the strain gauges used was reached. In other words, the complete stress-strain curves could not be obtained in these tests due to a technical limitation of the type of strain gauges used, since their maximum measurable strain is lower than the maximum strain the composites can sustain. It could be observed, by visual inspection, that the composites presented a remarkably fragile behaviour during the tensile stress tests. The same fragile behaviour was observed during the push-out tests with the PERFOFRP connectors.

The Figure 9d presents the stress-strain curve obtained in the transversal modulus of elasticity determination tests under tensile stress, in which the curve encompasses the entire test due to the lower magnitude of strains produced. For both modulus of elasticity tests, strong linear correlations were observed, with a  $R^2$  coefficient of 0.997 and 0.992 for the longitudinal and transversal modulus, respectively.



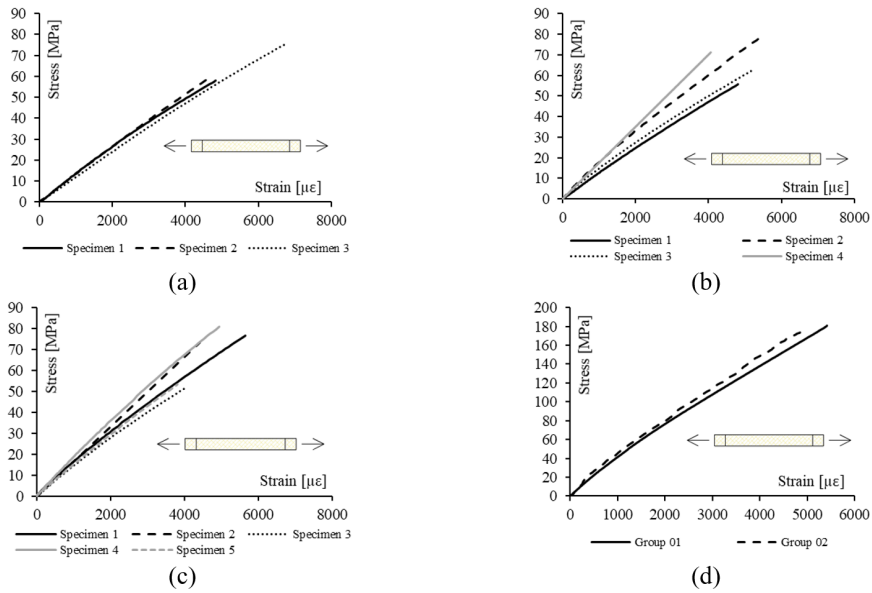


**Figure 9.** Experimental stress-strain curves: (a) longitudinal tensile modulus of elasticity for Group 01; (b) longitudinal tensile modulus of elasticity for Group 02; (c) longitudinal tensile modulus of elasticity for Group 03; (d) transversal tensile modulus of elasticity for Groups 01 and 02.

From the data presented in the Figures 9a, 9b, and 9c, a linear model was adjusted to obtain the value of the longitudinal modulus of elasticity for the composite. An average value of 13.35 GPa was obtained, as shown on Table 3.

**Table 3.** Longitudinal tensile modulus of elasticity for GFRP plates

Group	Longitudinal tensile modulus of elasticity		
	Sample size	Avg. [GPa]	CoV. [%]
01	3	12.46	4.39
02	4	13.28	8.82
03	5	14.30	11.31
Avg.		13.35	8.17

From the data presented in the Figure 9d, a linear model was adjusted to obtain the value of the transversal modulus of elasticity for the composite, being found an average value of 36.36 GPa. Then, by taking the quotient between the longitudinal and transversal modulus of elasticity, the average Poisson’s ratio value was computed as 0.35, as shown on Table 4.

**Table 4.** Transversal modulus of elasticity and Poisson’s ratio for GFRP plates

Group	Transversal modulus of elasticity			Poisson's ratio		
	Value [GPa]	Avg. [GPa]	CoV. [%]	Value	Avg.	CoV. [%]
01	4.591	4.753	3.41	0.357	0.35	0.76
02	4.915			0.351		

The average experimental values for the properties evaluated in this composite characterization were  $\epsilon = 2.32$  mm,  $\sigma_{pt,u} = 164.2$  MPa,  $V_f = 39.0\%$ ,  $E_{pt,l} = 13.35$  GPa, and  $E_{pt,t} = 4.75$  GPa. They were similar to the expected values obtained by previous works [17], [18], [20], [21] that employed similar materials and fabrication process, which presented average properties values of  $\epsilon = 2.00$  mm,  $\sigma_{pt,u} = 199.5$  MPa,  $V_f = 40.8\%$ ,  $E_{pt,l} = 12.65$  GPa, e  $E_{pt,t} = 5.41$  GPa.

### 3.3 Evaluation of production quality of the GFRP composites plates

#### 3.3.1 Superficial extension of the plates

The statistics used in this evaluation (i.e., the coefficient of variation) is an indicative of the precision of the production. Following to Pimentel-Gomes [26], a classification for the coefficients of variation, based on their magnitude, was adopted: Low, when inferior to 10%; Average, when between 10% and 20%; High, when between 20% and 30%; and Very High, when higher than 30%. The classes Low and Average are considered to indicate a satisfactory production quality condition.

By analysing the Table 2, it can be observed that, considering the ultimate tensile stress coefficients of variation, 18 samples can be classified as Low and 9 as Average. For the volume fraction of fibres, all samples can be classified as Low. This allowed to conclude that, considering the parameters evaluated, the plates presented satisfactory homogenous characteristics along their extension (i.e., the infusion process did not cause significant variations that could have compromised the homogeneity of the plates). This homogeneity was more evident in the volume fraction of fibres than in the ultimate tensile stress.

#### 3.3.2 Reproducibility of the infusion process employing materials of same origin

The Figures 10 and 11 show the average values, and the respective dispersions, of the results obtained in the ultimate tensile stress and volume fraction of fibre. Each column represents a single plate result. For the ultimate tensile stress (Figure 10), a higher dispersion was observed in the Group 01 (Figure 10b) when compared to the other groups (Figure 10c and Figure 10d). For the volume fraction of fibre (Figure 11), a higher dispersion was observed in the Groups 01 and 02 (Figure 11b and Figure 11c) when compared to the Group 03 (Figure 11d).

The Table 5 presents the group’s coefficients of variation that were calculated from the average results obtained in each GFRP composite plate in the ultimate tensile stress and volume fraction of fibre tests. It was observed that all results presented coefficients of variation classified as Low, according to the aforementioned criteria by Pimentel-Gomes [26], with the exception of the ultimate tensile stress obtained in the Group 01, that presented an Average coefficient of variation. These results confirm the trend observed in the Figures 10 and 11, which consists in a higher dispersion in the ultimate tensile stress for the Group 01, and a lower dispersion for the volume fraction of fibre for the Group 03.

Aiming the validation of such trends, an Analysis of Variance (ANOVA) was performed with the data for each of the three groups, with results presented in the Table 6. A p-value of 0.05 was adopted, which implied a confidence interval of 95%.

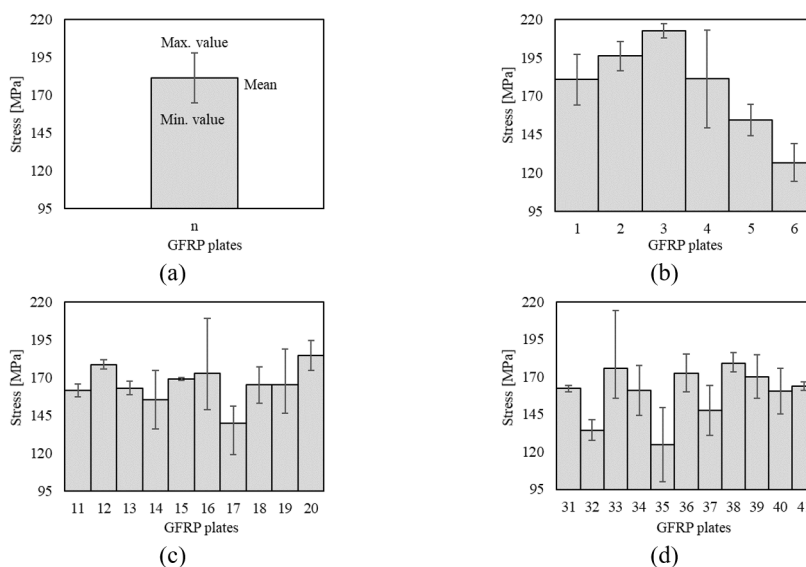


**Figure 10.** Ultimate tensile stress: (a) description of the constituent parts of the graphics; (b) Group 01; (c) Group 02; (d) Group 03.

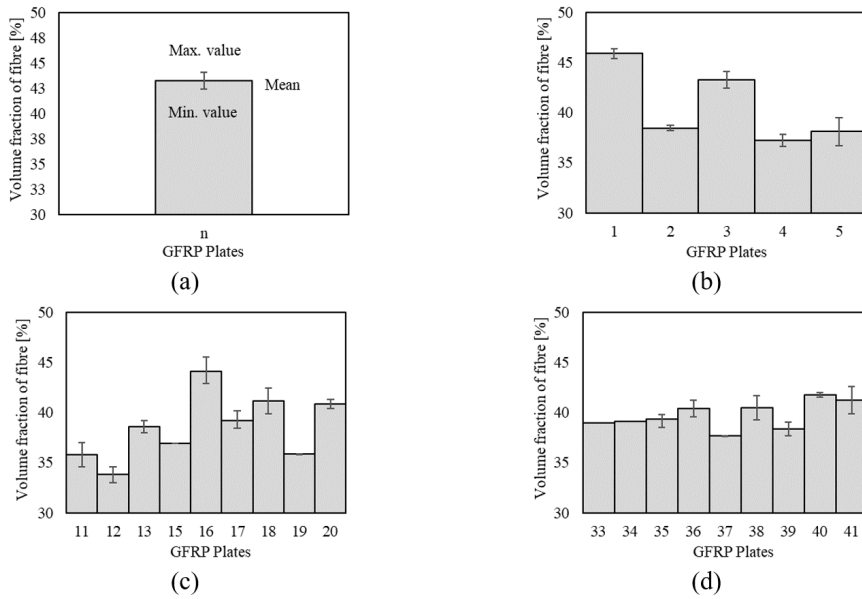


**Figure 11.** Volume fraction of fibre: (a) description of the constituent parts of the graphics; (b) Group 01; (c) Group 02; (d) Group 03.

**Table 5.** Coefficient of variation for Groups 01, 02 and 03: ultimate tensile stress and volume fraction of fibre.

Group	Ultimate tensile stress		Volume fraction of fibre	
		[%]		[%]
01		15.96		8.16
02		7.14		7.75
03		9.56		4.10

Both the coefficients of variation and ANOVA suggest a satisfactory homogeneity in the results obtained for the ultimate tensile stress in all groups. This allows to infer that differences in the production process, due to minor variations in sequential infusion process, did not compromise the precision/repeatability of the production process, as far as the ultimate tensile stress is concerned.

**Table 6.** ANOVA results for Groups 01, 02 e 03

Group	Analysis	Ultimate tensile stress		Volume fraction of fibre	
		Value	Significant comparisons	Value	Significant comparisons
01	DF	5		4	
	MS	1876.77	no	28.9043	yes
	F ratio	3.418		22.40	
	p normal	0.0833		0.002163	
DF	9	8			
02	MS	388.21	no	24.4804	yes
	F ratio	1.020		19.53	
	p normal	0.4724		0.000018	
03	DF	10	no	8	no
	MS	646.72		3.73156	
	F ratio	1.401		3.012	
	p normal	0.2797		0.052920	

The volume fraction of fibre, however, presented results with statistically significant differences between the plates from Group 01 and 02, suggesting that the variations occurred between the production process of these groups resulted in different fibre content in these groups. In the Group 03, these statistically significant differences were not observed. These results suggest that there was a progressive improvement in the fabrication process, since Groups 01 and 02 were produced before Group 03. Nonetheless, even though the differences observed in the Groups 01 and 02 can be considered an indicative of some error in the production quality of the composites, such error did not appear in the ultimate tensile stress property, which, as mentioned before, is the main characteristic of interest. The overall homogeneity of the plate composites of the same production group was, therefore, considered satisfactory. Moreover, the fact that all coefficients of variation obtained in the test results for the volume fraction of fibres were considered Low also supports this conclusion.

### 3.3.3 Reproducibility of the infusion process employing materials of different origins

The variability of properties between composite plates of different production groups was analysed to assess the reproducibility of the composites' properties when produced with materials from different origins/manufacturer's batch. The Figures 12 and 13 present the histograms generated from the frequency distribution of results obtained in the ultimate tensile stress and volume fraction of fibres, respectively. Normal distribution curves were fitted to each histogram.

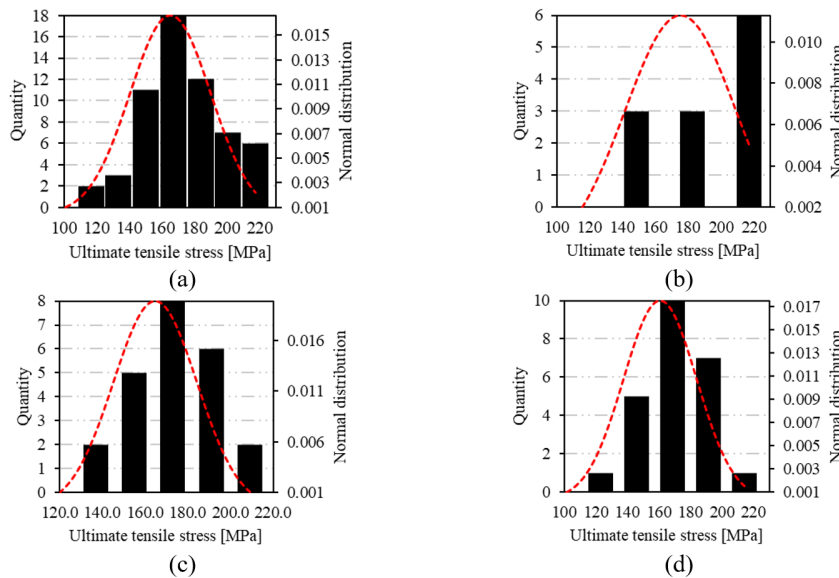


**Figure 12.** Histograms and normal distribution curves of ultimate tensile stress test results for: (a) all specimens; (b) group A; (c) group B; (d) group C.

Even though the Figures 12b and 13b, both corresponding to the Group 01, and the Figure 12d, which corresponds to the Group 03, do not visually seem to present a good adherence between the fitted curve and the histogram, this adherence was verified for all histograms with a confidence level of 95%, i.e. with p-values higher than 0.05, by using the Shapiro-Wilk test.

The Figure 14 presents the box diagrams for the test results of ultimate tensile stress (Figure 14b), volume fraction of fibres (Figure 14c) and longitudinal tensile modulus of elasticity (Figure 14d), for the Groups 01, 02 and 03. The visual analysis of the diagrams suggests a satisfactory dispersion for all results.

To statistically support the analysis of the box diagrams, an ANOVA test was conducted on the data. The results are presented on Table 7. A p-value of 0.05 was adopted, implying a confidence level of 95%. The p-values obtained suggest that the data did not present statistically significant differences. This indicates that the variation on material's origin/manufacturer's batch did not cause significant differences in the characteristics of the composite plates produced.

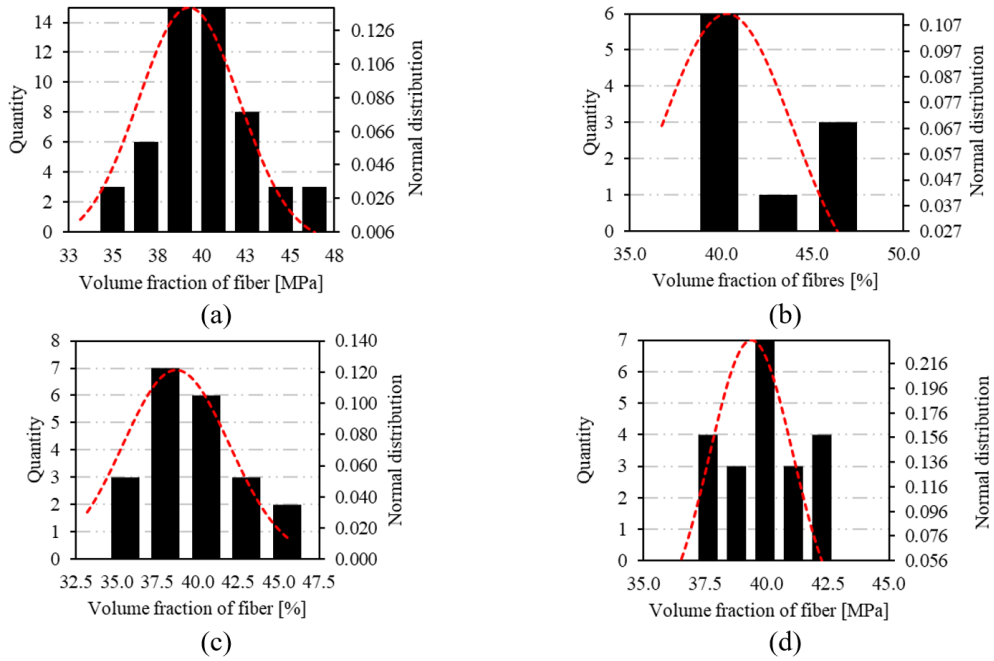


**Figure 13.** Histograms and normal distribution curves of volume fraction of fibre test results for: (a) all specimens; (b) group A; (c) group B; (d) group C.

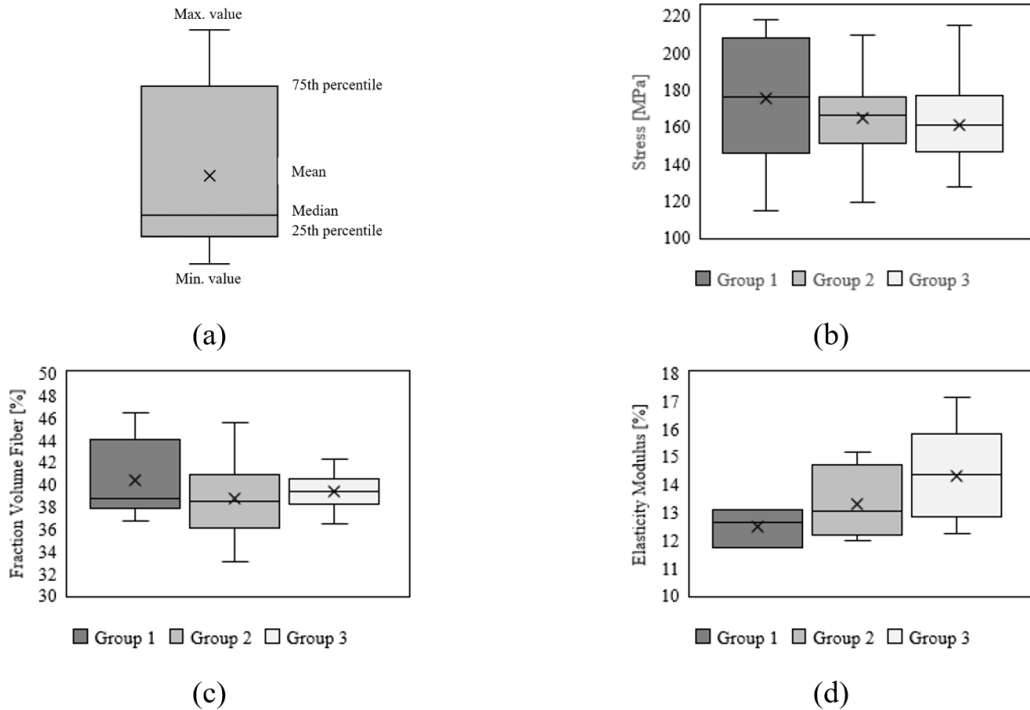


**Figure 14.** Box diagrams: (a) graphics legend; (b) ultimate tensile stress; (c) volume fraction of fibres; (d) longitudinal modulus of elasticity.

### 3.4 Push-out tests

The Figure 15 presents the failure modes of the tested connectors. In all the figures, the right-hand side represents the portion of the connector embedded in the internal concrete layer, while the left-hand side represents the portion

embedded in the external concrete layer. The rupture planes did not present a very well clear trend, although a general tendency of 45° inclined planes, starting from the superior external surface to the inferior internal surface, can be identified. Other works have presented clearer failure modes [2] due to the utilization of fibre oriented composites.

**Table 7.** ANOVA for evaluation of statistically significant differences in the characteristics of the composite plates from different production groups.

Group	Analysis	Ultimate tensile stress		Volume fraction of fibre		Longitudinal tensile modulus of elasticity	
		Value	Significant comparisons	Value	Significant comparisons	Value	Significant comparisons
All	DF	2	no	2	no	2	no
	MS	851.285		10.234		3.325	
	F ratio	1.419		1.270		1.537	
	p normal	0.25004		0.28998		0.26650	

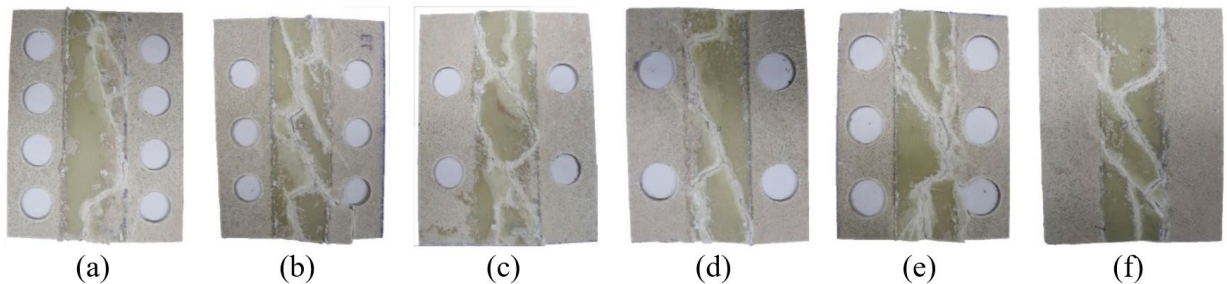


**Figure 15.** Failure modes of the tested connectors: (a) SP-25.4-1.75; (b) 25.4-2.00; (c) SP-25.4-3.00; (d) SP-31.75-2.00; (e) SP-31.75-3.00; (f) SP-CTL.

The Figure 16 presents the load-relative displacement curve for each of the tested specimens. Three curves were plotted in each graphic of Figure 16, corresponding to the three replicates of the same connector. The load refers to the load acquired during the test divided by two, to account for the double-shear of the two connectors inside the tested specimen, assuming an equivalent distribution of internal forces.

During the test execution, it was not observed visible concrete cracks close to the connector’s region. The connector’s behaviour was, in general, very stiff until failure. After failure, a very erratic behaviour was observed, with some connectors presenting a well-defined yielding plateau, while others presented a sudden load reduction.

The Table 8 summarizes the push-out test results, presenting, for each group of replicates: the average maximum peak load; the average relative displacement associated to the maximum peak load of each replicate ( $Q_{lo,u}$ ); and the average connector’s stiffness ( $K_f$ ), calculated, for each specimen, as the ratio between the maximum peak load and the associated relative displacement ( $S_{lo,u}$ ). The  $K_f$  parameter was calculated similar to previous works [2], assuming the simplification of a linear behaviour up to the peak loading, which, in fact, does not occur. This simplified analysis was performed due to the high variation observed in the  $S_{lo,u}$  results and provided a measurement of the general trend of the results. Currently, there are no standard recommendations for the stiffness evaluation of sandwich panels connectors.

Bar chart, presenting the average, minimum and maximum values of each parameter evaluated in the push-out test, are presented in the Figure 17. The observed magnitude of the error bars suggests, in general, a high variability in all specimens’ results. This is supported by the average coefficients of variation, presented on Table 8, with values of 7.66%, 35.58% and 35.44% for the maximum loading, relative displacement and stiffness, respectively.

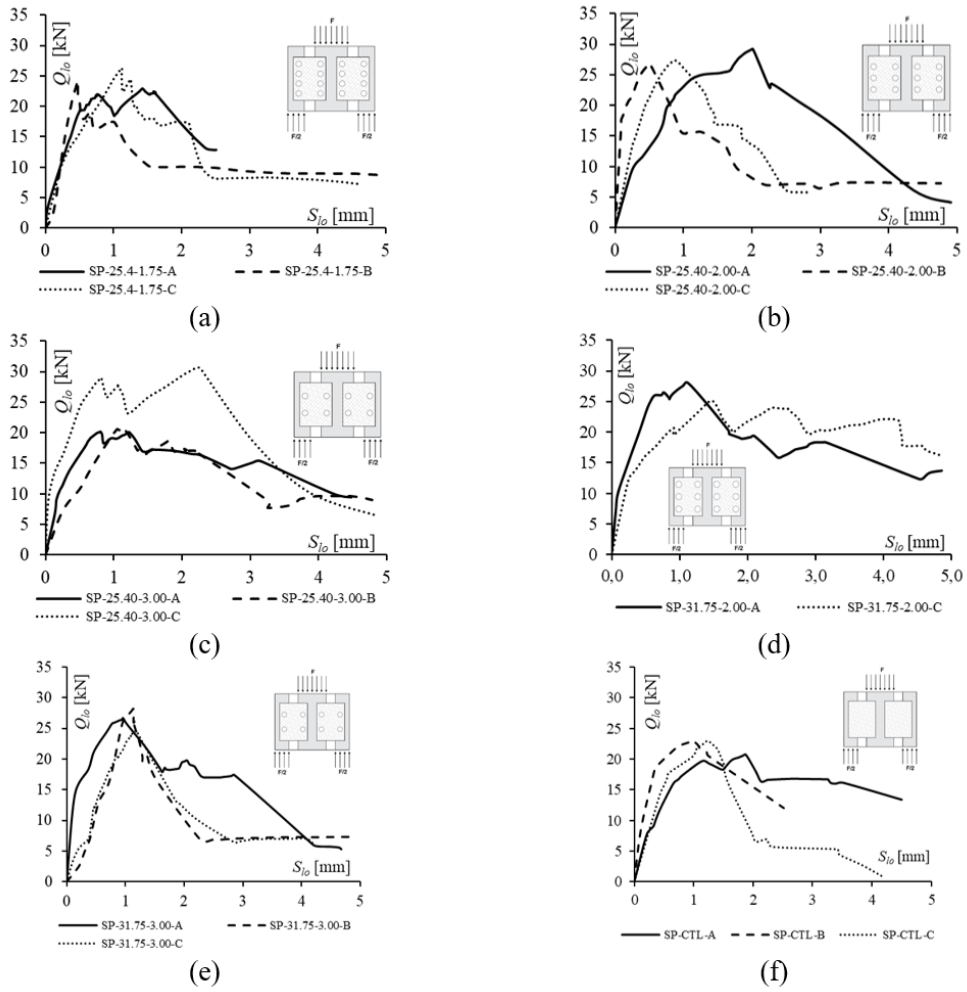


Figure 16. Load-relative displacement curves for: (a) SP-25.40-1.75; (b) SP-25.40-2.00; (c) SP-25.40-3.00; (d) SP-25.40-3.00 C; (e) SP-31.75-3.00; (f) SP-25.40-2.00.

Table 8. Push-out test results.

Specimen	Sample size	Ultimate load		Relative slip		Stiffness	
		Avg. [kN]	CoV. [%]	Avg. [mm]	CoV. [%]	Avg. [kN/mm]	CoV. [%]
SP-25.40-1.75 (1)	3	24.50	5.77	1.01	39.43	30.15	49.79
SP-25.40-2.00 (2)	3	27.85	3.56	1.13	56.80	33.02	47.92
SP-25.40-3.00 (3)	3	23.94	20.14	1.39	44.19	19.09	23.93
SP-31.75-2.00 (4)	3	25.89	6.20	1.29	13.40	21.20	18.89
SP-31.75-3.00 (5)	3	26.51	5.54	0.94*	32.25	32.71*	42.44
SP-CTL (6)	3	22.21	4.77	1.37	27.44	17.57	29.66
Average			7.66		35.58		35.44

\*: The relative displacement and stiffness of the SP-31.75-3.00 specimen were computed with just two samples.

Despite the elevated coefficients of variation, some trends can be observed. In the case of maximum load, it was observed that all groups presented values higher than the control specimen. Furthermore, only the SP-25.40-3.00 specimen presented a relative displacement equivalent to that of the control specimen, while all the others presented lower displacements. For the stiffness, only the SP-25.40-3.00 presented values close to the control specimen, with all

the others presenting higher values. Therefore, it was inferred that the perforated connectors tend to present higher ultimate load values, lower relative displacements and higher stiffness.

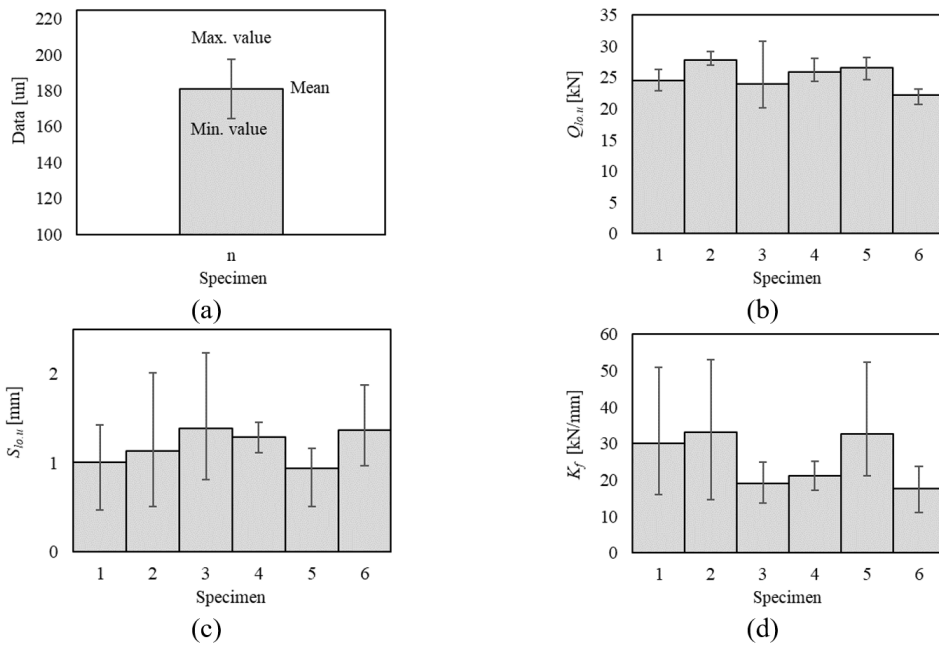


**Figure 17.** Bar chart of push-out test results: (a) graphics legend; (b) ultimate load; (c) relative displacement; (d) stiffness.

It is also interesting to compare these results to steel pin connectors results found on the literature, to evaluate the performance of the produced PERFOFRP connectors in comparison to a currently widely used connector. In a comprehensive study, it was found that a bending angle of  $45^\circ$  resulted in the best performance for 5.8 mm diameter steel pin connectors [16]. For this specific connector, it was found that the average ultimate load and stiffness were, respectively: 22.3 kN and 15.0 kN/mm, under tensile load until yielding; 18.1 kN and 16.5 kN/mm, under compressive load until buckling [16]. Comparing these results to the specimen SP-25.40-2.00, which was the specimen with the best performance in the present study, it can be observed a gain in ultimate load of 24.7% and 54.3%, considering the tensile and compressive behaviour, respectively. Furthermore, the SP-25.40-2.00 presented a stiffness 219.8% and 199.6% higher than those obtained for the steel pin connector under tension and compression, respectively.

The Figure 18a presents the ultimate load of the connectors in terms of the total area of holes. The number indicated at the side of each symbol corresponds to the hole spacing. One of the objectives of the push-out tests was to determine the hole spacing that leads to the maximum ultimate load, considering each hole diameter studied. This optimization could be performed by finding the maxima of a function correlating the ultimate load to the hole spacing, for each hole diameter, or, alternatively, to another parameter that is dependent on the hole spacing, such as the total area of holes, which is dependent on hole spacing accordingly to the rules explained in the item 2.2.1. The simplest function to be fitted to the experimental data, to allow such optimization, would be a parabola. From this, a visual inspection of the Figure 18a suggested that, for connectors with 25.40 mm holes, the optimization most likely occurs for spacings around 2.00 times the hole diameter, while for connectors with 31.75 mm holes, the optimization apparently occurs for spacings between 3.00 and 2.00.

The Figure 18b presents the ultimate load values ( $Q_{lo,u}$ ) of each specimen type, sorted in ascending order, as well as the ultimate load gain, in percentage, in relation to the control specimen's ultimate load. It also presents the total area of holes ( $A_f$ ), in the secondary vertical axis. The gains ranged from 8% to 25% in relation to the control group, and the highest ultimate load was that of specimen SP-25.40-2.00, encoded by the group code 2 in the graph, even though its total area of holes is not the smallest. This illustrates that the ultimate load is also sensitive to the hole configuration, with both parameters analysed (diameter and spacing) inducing visible influences in the connector's performance.



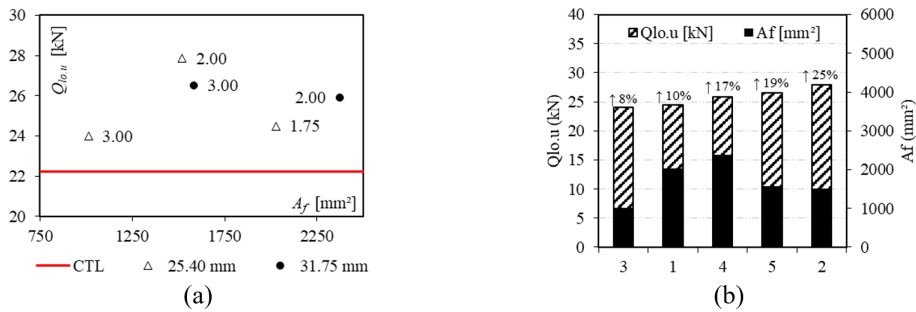


**Figure 18.** Relation between (a) the ultimate load by the total area of holes, for each hole diameter; (b) ultimate load increase for each specimen type, and the total area of holes, in relation to the control group.

#### 4 CONCLUSIONS

This work presented the evaluation of production quality and the mechanical behaviour of shear connectors manufactured with perforated GFRP plates for insulated pre-cast concrete wall panels (sandwich panels), produced with an in-house developed low-cost vacuum assisted resin infusion system. A complete explanation of the low-cost production system and process was also presented. Moreover, the mechanical behaviour of the shear connectors was assessed by 18 specimens, produced as representative models of the shear connector in insulated pre-cast concrete wall panels, subjected to double-shear push-out tests. The main conclusions were:

- The in-house developed low-cost vacuum assisted resin infusion process used to produce the GFRP composite plates is an original contribution of this work, with a high potential use in industry and research, since the low-cost (the required investment for the acquisition of raw materials was around 1/10 of the cost of commercially available connectors) and easy-access materials required to build it can be acquired and used at, virtually, any place and ambient.
- The average properties of the GFRP composite plates produced with the low-cost production systems were: 2.32 mm thickness; 164.24 MPa ultimate tensile stress; 39.04% volume fraction of fibre; 13.35 GPa longitudinal modulus of elasticity; 4.753 GPa transversal elastic modulus; and 0.35 Poisson's ratio. These values were remarkably close to those obtained in previous research that employed similar materials and production process.
- The production quality of the plates, assessed by statistical analysis of the ultimate tensile stress and volume fraction of fibre of samples taken from the plates, was considered satisfactory, validating the production process employed in this work. This analysis was performed in different levels: samples from the same plate; samples from plates from the same production group (i.e., plates produced with materials from the same origin); samples from plates with different origin.
- The push-out tests demonstrated that the perforated connectors presented, when compared to non-perforated connectors, a strength gain ranging from 8% to 25% (depending on the hole diameter and spacing used), lower relative displacements, and higher stiffness levels. It was also observed that a hole spacing of 2.00 times the hole diameter induced the best performance (i.e., the highest ultimate load value), for the hole diameter of 25.40 mm, while this optimum point, for the hole diameter of 31.75 mm, is probably reached with a hole spacing between 2.00 and 3.00.

#### ACKNOWLEDGEMENTS

The authors would like to thank the financial support provided by Brazilian Coordination of Superior Level Staff Improvement (CAPES) and Brazilian National Council for Scientific and Technological Development (CNPq).

#### CITATIONS

- PCI Committee on Precast Sandwich Wall Panels, "PCI Committee Report: state of the art of precast/prestressed concrete sandwich wall panels," *PCI J.*, vol. 56, no. 2, pp. 131–176, 2011.
- J. Q. Huang and J. G. Dai, "Direct shear tests of glass fiber reinforced polymer connectors for use in precast concrete sandwich panels," *Compos. Struct.*, vol. 207, pp. 136–147, 2019.
- C. Naito, J. Hoemann, M. Beacraft, and B. Bewick, "Performance and characterization of shear ties for use in insulated precast concrete sandwich wall panels," *J. Struct. Eng.*, vol. 138, no. 1, pp. 52–61, 2012.

- [4] A. Benayoune, A. A. A. Samad, D. N. Trikha, A. A. A. Ali, and S. H. M. Ellinna, "Flexural behaviour of pre-cast concrete sandwich composite panel: experimental and theoretical investigations," *Constr. Build. Mater.*, vol. 22, no. 4, pp. 580–592, 2008.
- [5] T. D. Bush and G. L. Stine, "Flexural behavior of composite precast concrete sandwich panels with continuous truss connectors," *PCI J.*, vol. 39, no. 2, pp. 112–121, 1994.
- [6] T. D. Bush and Z. Wu, "Flexural analysis of prestressed concrete sandwich panels with truss connectors," *PCI J.*, vol. 43, no. 5, pp. 76–86, 1998.
- [7] W. C. MacCall, "Thermal properties of sandwich panels," *Concr. Int. Des. Constr.*, vol. 7, pp. 34–41, 1985.
- [8] D. Salmon, A. Einea, M. K. Tadros, and T. D. Culp, "Full scale testing of precast concrete sandwich panels," *ACI Struct. J.*, vol. 94, no. 4, pp. 354–362, 1997.
- [9] J. H. Kim and Y. C. You, "Composite behavior of a novel insulated concrete sandwich wall panel reinforced with GFRP shear grids: effects of insulation types," *Materials*, vol. 8, no. 3, pp. 899–913, 2015.
- [10] T. K. Hassan and S. H. Rizkalla, "Analysis and design guidelines of precast, prestressed concrete, composite load-bearing sandwich wall panels reinforced with CFRP grid," *PCI J.*, vol. 55, no. 2, pp. 147–162, 2010.
- [11] B. A. Frankl, G. W. Lucier, T. K. Hassan, and S. H. Rizkalla, "Behavior of precast, prestressed concrete sandwich wall panels reinforced with CFRP shear grid," *PCI J.*, vol. 56, no. 2, pp. 42–54, 2011.
- [12] H. Gleich, "New carbon fiber reinforcement advances sandwich wall panels," *Prod. Watch*, pp. 61–63, 2007.
- [13] K.-B. Choi, W.-C. Choi, L. Feo, S.-J. Jang, and H.-D. Yun, "In-plane shear behavior of insulated precast concrete sandwich panels reinforced with corrugated GFRP shear connectors," *Compos., Part B Eng.*, vol. 79, pp. 419–429, 2015.
- [14] C. P. Pantelides, R. Surapaneni, and L. D. Reaveley, "Structural performance of hybrid GFRP/steel concrete sandwich panels," *J. Compos. Constr.*, vol. 12, no. 5, pp. 570–576, 2008.
- [15] K. Hodicky, G. Sopal, S. Rizkalla, T. Hulin, and H. Stang, "Analytical model for CFRP-strengthened prestressed concrete girders subject to cyclic loading," *J. Compos. Constr.*, vol. 19, no. 5, 2015.
- [16] D. G. Tomlinson, N. Teixeira, and A. Fam, "New shear connector design for insulated concrete sandwich panels using basalt fiber-reinforced polymer bars," *J. Compos. Constr.*, vol. 20, no. 4, pp. 1–13, 2016.
- [17] R. Lameiras, J. Barros, M. Azenha, and I. B. Valente, "Development of sandwich panels combining fibre reinforced concrete layers and fibre reinforced polymer connectors. Part II: evaluation of mechanical behaviour," *Compos. Struct.*, vol. 105, pp. 460–470, 2013.
- [18] R. Lameiras, J. Barros, I. B. Valente, and M. Azenha, "Development of sandwich panels combining fibre reinforced concrete layers and fibre reinforced polymer connectors. Part I: conception and pull-out tests," *Compos. Struct.*, vol. 105, pp. 446–459, 2013.
- [19] H. D. Young and R. A. Freedman, *Física I*, 12th ed. São Paulo: Addison Wesley, 2008.
- [20] R. Lameiras, J. A. O. Barros, I. B. Valente, J. Xavier, and M. Azenha, "Pull-out behaviour of glass-fibre reinforced polymer perforated plate connectors embedded in concrete. Part II: prediction of load carrying capacity," *Constr. Build. Mater.*, vol. 169, pp. 142–164, Apr 2018.
- [21] R. Lameiras, I. B. Valente, J. A. O. Barros, M. Azenha, and C. Gonçalves, "Pull-out behaviour of Glass-Fibre Reinforced Polymer perforated plate connectors embedded in concrete. Part I: experimental program," *Constr. Build. Mater.*, vol. 162, pp. 155–169, Feb 2018.
- [22] A. Chen, T. G. Norris, P. M. Hopkins, and M. Yossef, "Experimental investigation and finite element analysis of flexural behavior of insulated concrete sandwich panels with FRP plate shear connectors," *Eng. Struct.*, vol. 98, pp. 95–108, 2015.
- [23] T. G. Norris and A. Chen, "Development of insulated FRP-confined Precast Concrete Sandwich panel with side and top confining plates and dry bond," *Compos. Struct.*, vol. 152, pp. 444–454, 2016.
- [24] American Society for Testing and Materials, *Standard Test Method for Tensile Properties of Polymer Matrix Composite Materials*, ASTM D3039/D3039M, 2017, pp. 1–13.
- [25] American Society for Testing and Materials, *Standard Test Method for Ignition Loss of Cured Reinforced Resin*, ASTM D2584, 2018.
- [26] F. Pimentel-Gomes, *Experimental Statistics Course*, 15th ed. Piracicaba: FEALQ, 2009.

---

**Author contributions:** JKFS and RRR.: conceptualization, formal analysis, writing, methodology. RML: supervision, proofreading.

**Editors:** Vladimir Guilherme Haach, Guilherme Aris Parsekian.



ORIGINAL ARTICLE

# Towards improving the seismic hazard map and the response spectrum for the state of RN/Brazil

*Em busca da melhoria do mapa de perigo sísmico e do espectro de resposta do estado do RN/Brasil*

Petrus Gorgônio Bulhões da Nóbrega<sup>a</sup>

Bruno Rammon Silva Souza<sup>a</sup>

Selma Hissae Shimura da Nóbrega<sup>a</sup>

<sup>a</sup>Universidade Federal do Rio Grande do Norte – UFRN, Centro de Tecnologia, Campus Universitário Lagoa Nova, Natal, RN, Brasil

Received 18 July 2020

Accepted 28 October 2020

**Abstract:** Although Brazilian seismic activity is defined as low to moderate, it is known that intraplate earthquakes can also be associated to high intensities. In Brazil, the state of Rio Grande do Norte (RN) is one of the most seismically active areas, but there is no specific study to evaluate the seismic hazard in this region. This paper presents analyses towards improving the seismic hazard map, the peak ground acceleration value and the response spectrum of RN. The methodology is based on Probabilistic Seismic Hazard Analysis, comparing the results to the design criteria defined in the Brazilian code NBR 15421:2006 (Design of seismic resistant structures – Procedure). The analyses show that, in general, the code sets conservative values for the peak ground acceleration and for the design response spectrum; however, related to this last one, the shape is quite different.

**Keywords:** seismic design, seismic hazard, response spectra, PSHA.

**Resumo:** Embora a atividade sísmica no Brasil seja definida como baixa a moderada, sabe-se que os terremotos intraplaca também podem produzir grandes intensidades. No Brasil, o estado do Rio Grande do Norte (RN) é uma das áreas sísmicas mais ativas, em relação ao qual inexistem qualquer estudo de avaliação do perigo sísmico. Este artigo apresenta análises em busca da melhoria do mapa de perigo sísmico, do valor da aceleração de pico, e do espectro de resposta do RN. A metodologia é baseada na Análise Probabilística de Perigo Sísmico, comparando os resultados com os critérios de projeto estabelecidos na norma Brasileira NBR 15421:2006 (Projeto de estruturas resistentes a sismo – Procedimento). As análises comprovam, em geral, que a norma define valores conservadores para a aceleração de pico e para o espectro de resposta de projeto, em relação ao qual o formato é muito diferente.

**Palavras-chave:** projeto sísmico, perigo sísmico, espectro de resposta, PSHA.

**How to cite:** P. G. B. Nóbrega, B. R. S. Souza, and S. H. S. Nóbrega, “Towards improving the seismic hazard map and the response spectrum for the state of RN/Brazil,” *IBRACON Struct. Mater. J.*, vol. 14, no. 3, e14302, 2021, <https://doi.org/10.1590/S1983-41952021000300002>

## 1 INTRODUCTION

The expression “hazard”, in common words, means the situation or agent that can cause harm, damage or an adverse effect to humans, properties, or the environment. The hazard is real, if it occurs here and now, or potential, when it may happen in short, medium or long term, depending on the nature of its causes. In this context, the seismic hazard analysis, which is associated to the evaluation of the potential earthquake consequences, is important and proposed as the main theme of this paper, focusing the Rio Grande do Norte (RN), a state of the Brazilian Northeast region.

However, is there a real seismic hazard in Brazil, a country often considered free of earthquakes? Indeed, its geology and geographic position, in the middle of an extensive tectonic plate, contributes to a greater seismic stability than that

Corresponding author: Petrus Gorgônio Bulhões da Nóbrega. E-mail: [petrus@ufrn.edu.br](mailto:petrus@ufrn.edu.br)

Financial support: None.

Conflict of interest: Nothing to declare.



This is an Open Access article distributed under the terms of the Creative Commons Attribution License, which permits unrestricted use, distribution, and reproduction in any medium, provided the original work is properly cited.

presented by nearby countries as Chile, Peru, Ecuador and Colombia, which are along the South America plate borders. As stated by Talwani [1], the plate borders are the genesis location of more than 95% of the global seismic energy release and about 5% are developed intraplate.

It is obvious the earthquakes do occur in Brazil, and there are many historical and experimental data registered (Berrocal *et al.* [2], Bianchi *et al.* [3]). Lopes and Nunes [4] pointed out that in Brazil there is an average occurrence of less than two earthquakes greater than M4 per year (M means magnitude and the number is the numerical value correlated), one earthquake greater than M5 every six years (Assumpção *et al.* [5] indicates that events with M5 or above occur over four-year period, a slightly shorter term), and one M6 earthquake every forty-five years. Assumpção [6] complements this statistic indicating that M7 earthquakes are extremely rare, perhaps one every five hundred years, and M8 are “practically impossible”.

Although Brazilian seismic activity is defined as low to moderate (Borges *et al.* [7], Talwani [1]), it is known that intraplate earthquakes can also be associated to high intensities (Talwani [8], Agurto-Detzel *et al.* [9]), especially if they are not deep, which is a general feature in Brazil, particularly in RN. Besides this first characteristic, a low attenuation in intraplate settings, such occurs in Brazil (Borges *et al.* [7]), makes greater intensities possible. The neotectonic activity in Brazilian Platform were described by Saadi [10] and Saadi *et al.* [11], and the possible correlations with geological and geophysical properties were detailed by Assumpção *et al.* [5] and Agurto-Detzel *et al.* [9].

According to Assumpção [6], one of the great difficulties in dealing with rare events is that the little known about the past does not ensure a set pattern in the future. For Seismic Engineering, the past is only a reference and the future is a probability, being the seismic hazard analysis the most appropriate way to deal with rare events and their possible consequences. At this point, it is important to carefully observe the two warnings made by Hough [12, pp. 304]: “Quantifying probabilistic seismic hazard remains a vexing problem in intraplate regions throughout the world” and “in intraplate regions, estimation of long-term earthquake rates is far more challenging”.

After a hazard analysis, a seismic risk evaluation may be performed. Although the terms “hazard” and “risk” are often used interchangeably in usual sense, they are distinct terms used to the risk assessment. If the hazard is something that can cause harm, the risk is the chance or probability, high or low, that a person will be harmed or experience an adverse health effect if exposed to a hazard. This concept of risk may also be applied to property or equipment losses, or harmful effects on the environment (Pitilakis *et al.* [13], FEMA P-58-1 [14]). Obviously, there is no risk if there is no exposure to the hazard.

The exposure can be associated (or not) to another definition: the vulnerability, which can be generally described as the potential for loss. In fact, the vulnerability may cover the exposure (population and value exposed) and the various susceptibilities (physical, social, environmental, economic, among others). From this discussion, the following qualitative expression of the problem results:

$$\text{Risk} = \text{Hazard} \times \text{Vulnerability} \times (\text{Exposure})$$

Seismic vulnerability of a structure can be described as its susceptibility to damage by ground shaking of a given intensity, and the aim of a vulnerability assessment, due to an earthquake scenario, is to obtain the probability of a certain level of damage related to a given building type. It depends on the building typology, structural system, age, contents and use, plane and elevation regularity, design and detailing of the structural elements, materials employed, construction practices and ground conditions. A state-of-the-art review of the seismic vulnerability assessment methodologies was done by Kassem *et al.* [15].

A comparison between two real examples illustrates the vulnerability influence, although they do not reflect the Brazilian seismic hazard reality. On 12 January 2010, a 7.0  $M_w$  earthquake hits Haiti ( $M_w$  is the moment magnitude scale based on the seismic moment, a measure of the work done by the earthquake, considered the most reliable magnitude scale for ranking earthquakes because it is more directly related to the energy of an earthquake than the other scales). This country, unprepared for this type of phenomenon, registered the chaos and more than 200,000 deaths (7% of the capital's population and 2.2% of the country's population). A few days later, on 27 February 2010, a much larger earthquake occurred in Chile with a 8.8  $M_w$  (which means, approximately, an earthquake 80 times greater with 800 times more energy released), resulting in 521 deaths, a corresponding number to 1/380 of the total victims in Haiti.

Paultre *et al.* [16] noted that Haitian tragedy happened because the earthquake occurred in a heavily populated region of a very poor country with substandard building practices, in a city that had not, in any way, been prepared for such an eventuality. The mitigation and preparedness efforts were minimal, and the earthquake threat was not accounted for in construction, land-use planning, or emergency procedures. The authors estimated that approximately 90% of

houses and buildings are built without the intervention of an architect or engineer, and a large portion of them are found in slums constructed on the mountainside terrain of Port-au-Prince and Pétionville cities.

If it is not possible to reduce the seismic hazard (a natural and uncontrollable characteristic), the alternative is to minimize the vulnerability in order to have an acceptable risk, with an economic and a social admissible cost. This is an aspect that must be considered by skeptics who neglect the seismic risk in Brazil. Although, in fact, the seismic hazard is not critical, compared to other countries, the people exposure and the buildings vulnerability of the large urban centers, especially the slums, tend to maximize the risk in case of a seismic event.

This paper focus on one variable of the Risk expression: Hazard. It presents an overview about the probabilistic seismic hazard analysis and the results of several analyses carried out for the state of RN, one of the most seismically active areas located in Brazil. The obtained results, expressed as exceedance probabilities of the horizontal peak ground acceleration values and acceleration response spectra, will be compared to the design parameters defined by NBR 15421 (ABNT [17]), the Brazilian code for the design of seismic resistant civil structures. The conclusions may serve as subsidies data for the NBR 15421 code discussion, which might be under revision process in the future.

## 2 BRIEF DESCRIPTION OF THE SEISMIC CONTEXT IN RN STATE

Figure 1 illustrates the most recent earthquake distribution maps for Brazil. Figure 1a refers to the general seismic catalog (1720 to 2019), where only earthquakes greater than M2.5 are plotted, also including historical events, not registered by instruments but indirectly inferred from reports and news (Berrocal *et al.* [2]). Figure 1b refers to the uniform catalog (1939 to 2019), where the earthquakes greater than M3.5 are shown. This catalog is filtered according to the event's detectability, that is, only the most recent earthquakes with an equal chance of being detected anywhere in Brazil are plotted, and the different colors represent the major tectonic provinces of the South American stable continental region.

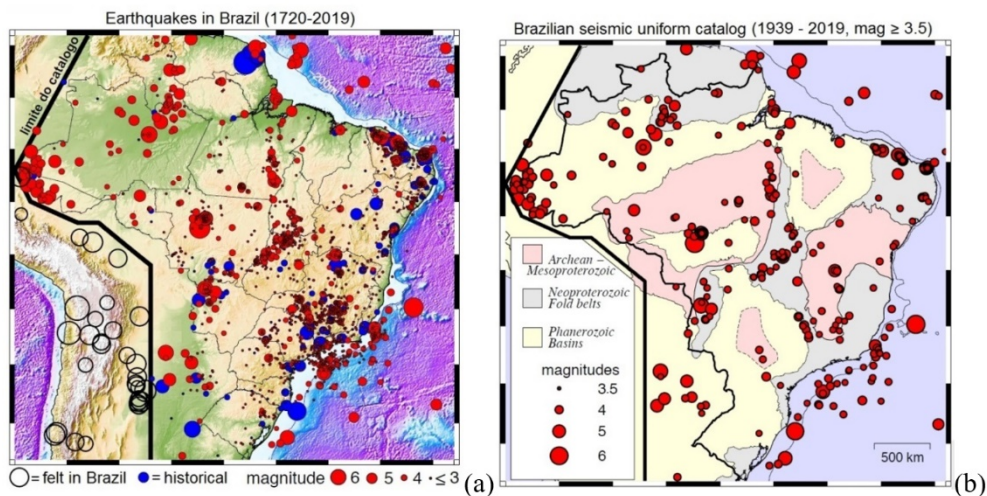
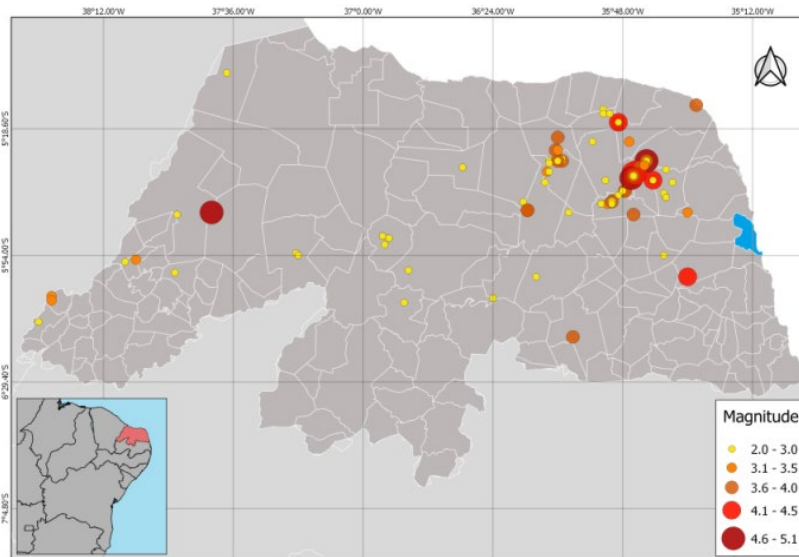


**Figure 1.** Brazilian seismic and uniform catalogs maps (adapted from M. S. Assumpção 2020, personal communication, 8 July).

It can be seen in Figure 1 that some areas present no relevant seismic activity and others are quite active. The earthquakes in the North region have greater magnitude but associated to few events. Probably this is due to underestimation generated by the low distribution of the Brazilian seismographic network, mainly in the North region, where the stations are about 500 km away from each other (Bianchi *et al.* [9]).

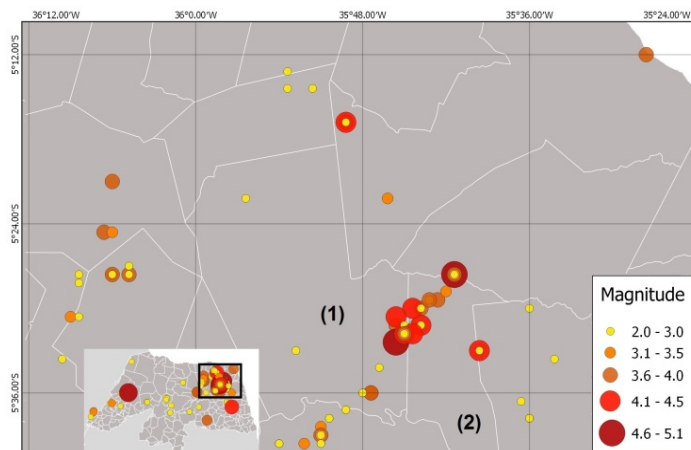
The state of RN, the focus of this study, is one of the most important seismic areas in Brazil (Ferreira *et al.* [18]). From the database, two events in the 1980s with magnitude  $\geq 5.0$   $m_R$  should be highlighted ( $m_R$  is the regional magnitude scale, formulated for the attenuation conditions of the seismic waves in the Brazilian lithosphere) and several others with magnitude greater than 4.0  $m_R$ . RN represents 0.6% of the country's total area, but is approximately associated to 15% of the earthquakes. This aspect makes it one of Brazilian states with the highest seismic activity (the neighboring state Ceará, CE, presents about 17% of earthquakes with three times the area).

Figure 2 shows the earthquakes distribution in RN and the area highlighted in blue refers to its capital, the city of Natal. The scale of the map does not allow a clear visualization of the strong seismic activity because almost 300 events are plotted in a small area causing overlapping points. In addition, there are hundreds of earthquakes less than M2 that have not been considered in this map. A review about the seismicity in RN and a description about the active faults with many geophysical details can be found in Ferreira *et al.* [18], Bezerra *et al.* [19] and Reis *et al.* [20].



**Figure 2.** Seismic activity in RN (magnitude  $\geq 2.0$ ).

The most important seismic source is the “Samambaia fault” (Figure 3), which forms a main alignment about 27 km long crossing the areas of the cities João Câmara (1) and Poço Branco (2), with ramifications to other cities. The depth of the seismic events is extremely low, ranging from 1 km to 9 km (Bezerra *et al.* [21]). Next to this fault, there is the “Poço Branco fault”, which also contributes to the occurrence of earthquakes in the region.



**Figure 3.** Seismic activity around “Samambaia fault”.

### 3. THE PSHA AND THE ACCELERATION MAP OF THE NBR 15421 CODE

Seismic hazard can be represented in several ways, but this is usually done based on the distribution of acceleration (or velocity or displacement) of the ground surface. This happens because the destructive effects of an earthquake are

related to the ground motion induced by the seismic waves. The seismic hazard analysis can be deterministic (DSHA, “Deterministic Seismic Hazard Analysis”) or probabilistic (PSHA, “Probabilistic Seismic Hazard Analysis”), the latter being the most used methodology. A detailed review on PSHA is given by Reiter [22], McGuire [23] and Baker [24].

The PSHA process, as expressed by McGuire [23], incorporates several uncertainties in the probabilities calculation of the event occurrence, classified as “epistemic or knowledge uncertainties” (for example, seismic sources definition, election of the ground motion prediction equations, and maximum magnitude) and as “aleatory or random uncertainties” (for example, earthquake depth and variability of ground properties). Baker [24] states that if on one side the incorporation of uncertainties adds some complexity to the procedure, on the other side the resulting calculations are more defensible for use in engineering decision-making for reducing risks.

Recently, some researchers have studied the seismic hazard for some specific areas of Brazil performing PSHA: Almeida *et al.* [25] analyzed an area of the Southeast region, site of a nuclear power plant, and Borges *et al.* [7] studied the continental margin of Southeastern region. Besides them, Santos *et al.* [26] studied the seismic hazard for the Brazilian Northeastern region.

The technical resource that best guides the structural engineer is the seismic hazard map, which will show the ground movement levels in a given area for a certain occurrence probability, or for its exceedance, which means the probability of this value being exceeded.

The most common in maps is to present the maximum acceleration, or “Peak Ground Acceleration” (PGA), related to a probability of occurrence/exceedance during an exposure time, which implies (by statistical concept) in a “mean return period”. Several different seismic hazard maps, indicated in sequence, can be found in technical literature or in international codes. Earthquakes with these characteristics are consistent with the ground-shaking levels: (a) likely, (b) possible, and (c) rare (Petersen *et al.* [27]), and it is easy to realize that they are in an increasing magnitude:

- a) PGA with 50% probability of exceedance in 50 years, which corresponds to a mean return period of 72 years (*e.g.* ASCE [28]);
- b) PGA with 10% probability of exceedance in 50 years, which corresponds to a mean return period of 475 years (*e.g.* CEN [29]);
- c) PGA with 2% probability of exceedance in 50 years, which corresponds to a mean return period of 2475 years (*e.g.* ASCE [30]).

In addition to these traditional alternatives, there are other standards such as the seismic action with 10% probability of exceedance in 10 years, which corresponds to a mean return period of 95 years (*e.g.* CEN [29]); or the action with 20% probability of exceedance in 10 years, which corresponds to a mean return period of 45 years (*e.g.* ASCE [28]).

The NBR 15421 – Design of seismic resistant structures – Procedure (ABNT [17]) is the Brazilian code that sets methods, parameters and requirements to the consideration of seismic effects in civil building design. Among all these information, there are two fundamental criteria: (1) the characteristic horizontal seismic acceleration map (Figure 4a), which is exactly a PGA map with 10% probability of exceedance in 50 years, which corresponds to a mean return period of 475 years; and (2) the design response spectrum (Figure 4b).

For example, for a structure built in RN (Zone 1), the characteristic horizontal acceleration is 0.05 g (5% g), considering rock soil type (according to NBR 15421, Class “B”, the standard characteristic for this map). Based on the real soil and on the zone type (site) of the building, the design response spectrum is established, adopting a damping ratio of 5%.

It has been 14 years since NBR 15421 was published and it should be under review process in the future. A detailed discussion of the acceleration map, its origin, criticisms and some new proposals can be found in Nóbrega *et al.* [31]. Santos and Lima [32] conclude that seismological studies in Brazil should be developed, evaluating the NBR 15421 code and pointing out the necessary modifications.

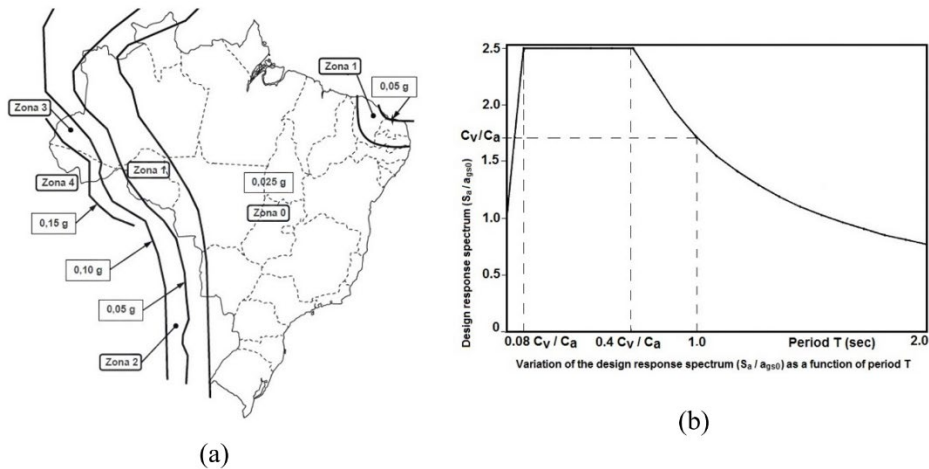


Figure 4. Characteristic seismic acceleration map and design response spectrum (adapted from ABNT [17]).

#### 4. THE PSHA METHODOLOGY APPLIED TO THE ANALYSIS OF RN STATE

The PSHA methodology, didactically divided into four steps according to Table 1, is briefly discussed in sequence. In parallel with it, the analysis of RN is presented.

Table 1. PSHA steps.

Step	Description
1	Identification of the seismic sources from historical, tectonic and geological surveys (Figure 5a)
2	Characterization of the seismic sources: maximum and minimum magnitudes determination, and definition of the seismic recurrence law (Figure 5b)
3	Prediction of the resulting distribution of ground motion intensity as a function of earthquake magnitude, distance, etc., by ground models (Figure 5c)
4	Calculation of the exceedance probability and return period for a given ground motion intensity as a combination of previous information (Figure 5d)

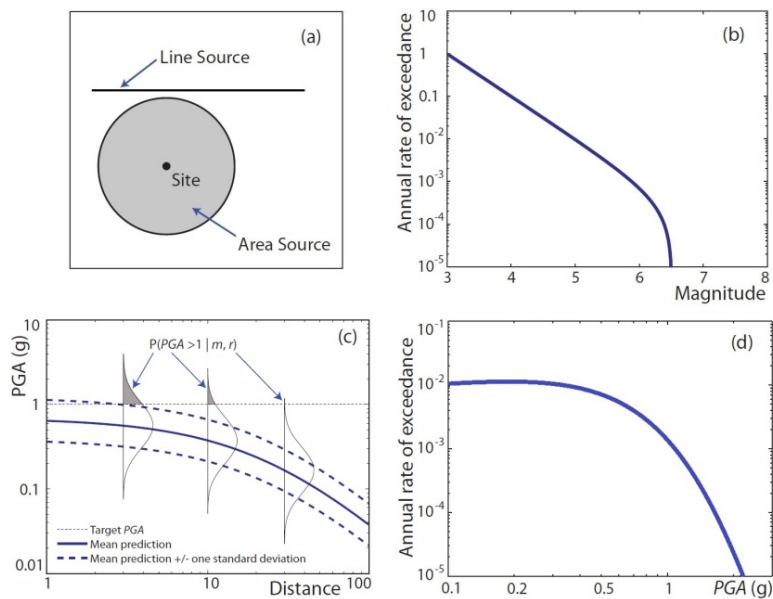


Figure 5. PSHA steps (adapted from Baker [24]).



#### 4.1 Seismic source identification

Seismic sources are sites that have relative uniform seismic characteristics and are distinct from the nearby ones. First, it is necessary to determine all the sources capable of producing some energy that generate soil vibration at the analysis location.

Budnitz *et al.* [33] indicate that seismic sources can be categorized into four basic types: (a) geological faults, represented as lines or planes (Figure 6a); (b) areas enclosing concentrated zones of seismicity (Figure 6b); (c) regional areas (Figure 6c); and (d) background areas (Figure 6d) with diffuse seismicity (note the scale in Figure 6d).

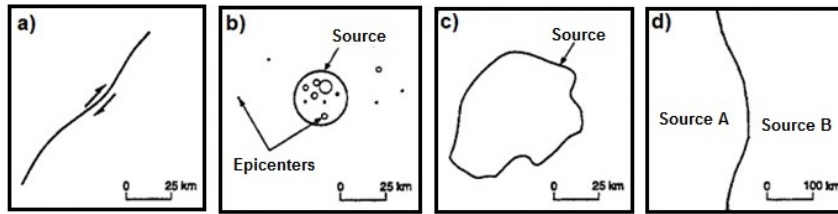


Figure 6. Seismic source types (adapted from Budnitz *et al.* [33]).

In intraplate regions, the seismic source identification can be complex and, according to Almeida [34], its characterization is extremely dependent on the tectonic environment considered, which makes it a difficult task for regions with low seismicity. This occurs because there is no clear correlation between seismicity and the known tectonic structures or surface geology.

Although in RN the main seismic source is the “Samambaia fault” (presented in section 2), in this study the seismic source was not defined as a line, but as an area with uniform seismicity. This is a simplification, which tends to be suitable for regions with low seismicity, such as RN. It is important to highlight that such procedure do not cause a seismic hazard amplification, since in the characterization of this source (discussed in the next subsection), only the events that actually occurred in the target area are considered.

#### 4.2 Seismic source characterization

For the seismic source identification and characterization phases, according to Pirchiner [35], all the available geological knowledge must be considered to define: (a) the spatial geometry of the geological feature and the probable seismic source; and (b) the number of earthquakes related to the energy released by each one (ratio number of events versus magnitude). Budnitz *et al.* [33] establish three key elements for the source characterization:

- (a) Seismic source locations/geometries. The seismic sources are defined in locations within the earth's crust that have relatively uniform seismicity characteristics;
- (b) Maximum earthquake magnitude. It is the upper-bound magnitude to the earthquake recurrence (frequency-magnitude) curve. Baker [24, pp. 44] complements this key element, explaining about the minimum earthquake magnitude: “For practical reasons, not all earthquake magnitudes are considered in PSHA calculations. Typically, only earthquakes with magnitudes greater than approximately 4.5 or 5 are considered. This is chosen as a conservative value, for which the omitted small-magnitude earthquakes are not believed to be capable of damaging structures, and thus not relevant for seismic risk calculations. This also reduces the size of the calculations. The exact magnitude at which an earthquake is no longer damaging is not obvious, however, and unfortunately the choice of cutoff magnitude can significantly affect some PSHA results”.
- (c) Earthquake recurrence. This is the frequency of the several earthquake occurrences (magnitude variable). Recurrence relationships or curves are developed for each seismic source and reflect the frequency of occurrence (usually expressed on an annual basis) of magnitudes up to the maximum. This earthquake recurrence, which is an essential information, is usually associated with a relationship known as Gutenberg-Richter law (Equation 1):

$$\log \lambda_m = a - b m \tag{1}$$

Where:

$m$  = magnitude value of reference;

$\lambda_m$  = the earthquake rate (or the number of events per year, also represented by  $\sum N$ ) with magnitudes greater than or equal to a minimum “ $m$ ”;

“ $a$ ” and “ $b$ ” = coefficients that depend on the characteristics of each location and are determined from statistical analysis of historical observations, obtained through catalogs produced by institutions devoted to earthquake records.

Related to Brazil, Almeida *et al.* [25] and Borges *et al.* [7] adopted the maximum of M7.0 for the continental area, what is commonly used for stable continental regions worldwide, except for very special areas. According to Almeida [34], for locations classified as source areas, the maximum magnitude is determined by earthquake’s historical data in the region. Thus, it is common to add half a unit to the maximum historical magnitude to represent the possible maximum one from that source.

It is acceptable that the largest earthquakes in RN may be considered between the values M5.5 and M6, according to what is observed from the seismological and geological data. The absence of events greater than M6 in the past 180 years may indicate a possible recurrence of earthquakes with this magnitude. Therefore, it would be reasonable to adopt M6.5 as maximum, like Dourado [36] did when studied the states of CE and RN. For the minimum magnitude, M4.5 was considered, similar to the value used by Almeida *et al.* [25] and Borges *et al.* [7].

Regarding the law of recurrence, it should be emphasized that the precise determination of the parameters for the RN or a detailed discussion about its methodology are beyond the objectives of this study. Thus, some relationships already defined for the region and available in the literature will be used. Ideally, it should be as up-to-date as possible, in order to reflect numerically the real situation. So, according Equation 1, Marza *et al.* [37] studied the state of CE, defining the values  $a = 2.92$  and  $b = 1.01$ ; Almeida [34] refers to the entire Northeast, using the expression with the values  $a = 3.10$  and  $b = 0.93$ ; and Dourado [36] considered CE and RN, adopting  $a = 3.1131$  and  $b = 0.96$ . In short:

$$\log \lambda_m = 2.92 - 1.01 m \text{ (Marza's law)} \tag{2}$$

$$\log \lambda_m = 3.10 - 0.93 m \text{ (Almeida's law)} \tag{3}$$

$$\log \lambda_m = 3.1131 - 0.96 m \text{ (Dourado's law)} \tag{4}$$

However, as these laws cover a larger area than the considered in this study, it is necessary to correct the parameter "a" of the Equation 1 to "a<sub>1</sub>", according to the Equation 5. The logic is to maintain the "seismic density" as constant.

$$a_1 = a - \log_{10} \left( \frac{A_0}{A_1} \right) \tag{5}$$

Where:

$A_0$  = original area related to the recurrence law (Marza’s or Almeida’s or Dourado’s law);

$A_1$  = new area related to the present study (illustrated in section 5.1, in sequence);

Finally, the recurrence laws become (the expressions below were used in analysis):

$$\log \lambda_m = 2.356 - 1.01 m \text{ (modified Marza's law)} \tag{6}$$

$$\log \lambda_m = 1.785 - 0.93 m \text{ (modified Almeida's law)} \tag{7}$$

$$\log \lambda_m = 2.267 - 0.96 m \text{ (modified Dourado's law)} \tag{8}$$

Although the three equations are numerically similar, the seismic hazard calculation is very sensitive to these coefficients and any variation causes significant changes in the results, especially due to the influence of the higher magnitudes. The ideal procedure, obviously, is to deduce a specific recurrence law for the state of RN.

#### 4.3 Prediction of the resulting distribution of ground motion intensity

Now it is important to define models, which adequately describe the seismic ground movement from earthquake epicenter to the desired location, considering its magnitude, distance, attenuation, and other parameters. These models

are named as Ground Motion Prediction Equations (GMPE) or Ground Motion Prediction Models (GMPM). Douglas [38] presents an extensive collection with 452 GMPE developed and studied between 1964 and 2018 around the world.

Usually, the acceleration is considered as the ground motion parameter, assuming that it is a random variable, with dispersion around the mean (standard deviation). The graph shown in Figure 5c illustrates a central continuous trace that represents the mean values of PGA, given by a GMPE, for which a magnitude value is set. It is observed that this curve has a decreasing trend, that is, the greater the distance from the earthquake, the smaller the accelerations caused by the event.

Unfortunately, there is no study defining a specific GMPE for any region of Brazil. In such cases, McGuire [23] suggests the use of a GMPE from similar sites. Bommer *et al.* [39] affirm that it is not necessary to choose a mathematical model from the same analyzed area, and it is possible to adopt models of places with similar seismic conditions, even though these have been developed in very distant regions.

In fact, there is a specific GMPE for RN (Dantas [40]), but limited to magnitudes lower than M3.0, which is not feasible for a seismic hazard analysis. Truly, this model is a simplification of Toro *et al.* [41] GMPE, originally formulated for the Central and the Eastern area of the USA, which has been widely used by Brazilian researchers for its geological similarities (*e.g.* Borges *et al.* [7]; Almeida *et al.* [25]; Santos *et al.* [26]; and Dourado [36]).

Toro *et al.* [41], Atkinson and Boore [42], and Atkinson [43] GMPE were used in this study. The last two models were related to the Eastern USA, applicable to a stable continental type tectonic region. From this point on, the GMPE will be referred as “Toro”, “Atk. & Boore”, and “Atkinson”. It is important to highlight that all these GMPE were set to hard rock soil type (NBR 15421, Class “A”).

#### 4.4 Calculation of the exceedance probability and the return period

The PSHA’s main result is the acceleration hazard curve, obtained by repeating the calculation for many different levels of acceleration. The curve shows the relation between this parameter and its exceedance probability, or its annual rate of exceedance ( $\lambda$ ), as can be seen by a single example in Figure 7. In other words, this curve represents the probabilities of the acceleration values being exceeded, and this probability decreases as its level increases.

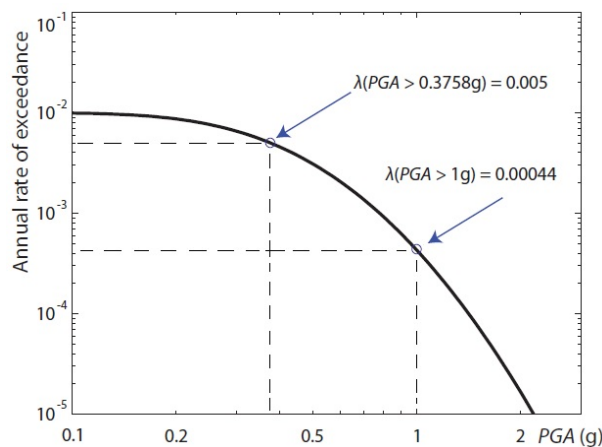


Figure 7. Example of a PGA hazard curve (adapted from Baker [24]).

Some important observations about the PGA hazard curve:

- (a) Usually, one or both axes of the graph are plotted in log scale because they often cover several orders of magnitude, and the vertical-axis contains very small values;
- (b) On the horizontal-axis, there are the values of the spectral acceleration (accelerations associated with any period, or frequency) resulting from spectral analysis. Figure 7 also indicates the PGA, when the period is equal to zero;
- (c) the curve is drawn for a specific point in the studied area, while a seismic hazard map is valid for a certain region, that is, several points (in this case, the probability is fixed);
- (d) The variable called “return period” (T) is very important and is defined as the inverse of the “annual rate of occurrence”. For example, if a given ground motion has a 0.02 annual rate of occurrence, then the return period is

equal to  $1/0.02 = 50$  years. However, as this does not imply that the ground motion will be exceeded exactly once every 50 years, the term is more precisely defined as the “mean return period” because 50 years is the average time between exceedances.

(e) For a given “probability of exceedance” (PE), it is possible to compute the “occurrence rate of events” ( $\gamma$ ) related to a given ground motion, associated to “t” years of exposure. The inverse calculation is obviously possible. As the ground motion occurrences follow a Poisson distribution, by hypothesis, Equations 9 and 10 express:

$$\gamma = -[\ln(1 - PE)] / t \tag{9}$$

$$PE = 1 - e^{-\gamma t} \tag{10}$$

For example, if a given ground motion has a probability of exceedance  $PE = 10\% = 0.10$ , considering a period of time  $t = 50$  years, the occurrence rate  $\gamma = 0.0021072$  per year, which is associated to one event each 475 years ( $475 = 1 / 0.0021072$ ). This value corresponds to the “mean return period” (T).

Equation 10 can also be formulated considering T directly, resulting in:

$$PE = 1 - \left(1 - \frac{1}{T}\right)^t \tag{11}$$

For example, if a given ground motion has a probability of exceedance  $PE = 2\% = 0.02$ , considering a period of time  $t = 50$  years, the mean return period  $T = 2475$  years. The same may be applied to obtain different return periods, indicated in section 3 for some codes.

## 5 RESULTS AND COMMENTS

### 5.1 Introduction

The purpose of the analyses is to evaluate if the design criteria presented by NBR 15421 are consistent with the RN reality, whether in terms of the maximum acceleration values, or in the form and values of the design response spectrum. All simulations considered the mean return period of 475 years (like NBR 15421).

The proper software should perform calculation based on probabilities (not a deterministic process) and in this study the R-CRISIS v20.1 was the chosen one. Dourado [36] and Borges *et al.* [7] also used it, although in previous versions. Details on the capacity and evolution of the software were presented by Aguilar-Meléndez *et al.* [44].

R-CRISIS software provides the seismic acceleration map for the studied area with a color gradient. In Figure 8, there is an example for RN. The acceleration value is constant and equal to the maximum at the center of the seismic source area (red plots), decreasing in the points far from it. The PGA expressed in the results is the acceleration maximum value. The quadrilateral area in Figure 8 is the new area related to the present study and to the Equation 5.

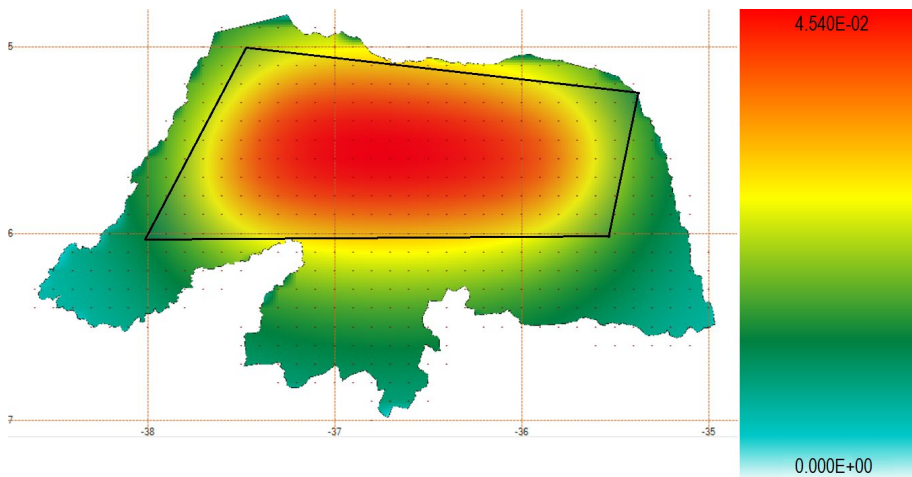


**Figure 8.** Example of a hazard map for RN obtained from R-CRISIS 20.1.

At last, it should be highlighted that, usually in order to reduce the uncertainties in the hazard analysis, it is common to adopt a logic tree, what it was not considered in this paper. Logic tree is an approach to capture and to quantify the uncertainties associated with the parameters required to perform the analysis (Bommer *et al.* [45]), as those mentioned in section 3. So, the practice is the use of multiple input options considering different seismic zone models, seismic activity parameters, scale factors, among others.

### 5.2 Analysis varying the recurrence laws

Initially, the modified recurrence laws (section 4.2) were evaluated by adopting, separately, each one of the three GMPE (section 4.3). The results are shown in Table 2 and Figure 9. In this figure, and others, the design response spectrum of NBR 15421 will always be plotted together with the result curves to better illustrate the differences between it and the numerical simulations. The X-axis is the natural period (s) and the Y-axis is the acceleration (fraction of “g”).

It can be observed that all the curves are beneath the code spectrum, for the three GMPE. Dourado’s law always is related to the highest values and Atkinson is the most conservative GMPE. About the PGA, Table 2 shows that the NBR 15421 value (reference) is superior to the results of the numerical simulations, except for Atkinson in two situations.

Note that the characteristic horizontal acceleration value for RN is 0.05 g, illustrated in Figure 3a, considering a rock type soil (Class B). Because the GMPE used in this paper were formulated for a hard rock type soil (Class A), it is necessary to convert the acceleration basis for Class A. The NBR 15421 conversion coefficient is 0.8. So, this value corresponds a 0.04 g (4% g) and all the results exposed in sequence are referenced to a hard rock type soil (Class A).

**Table 2.** PGA value (% g) considering different recurrence laws.

GMPE	Almeida’s law	Dourado’s law	Marza’s law	NBR 15421 [17]
Toro	1.00%	2.77%	1.84%	4.00%
Atkinson	2.86%	6.00%	4.54%	4.00%
Atk & Boore	0.50%	1.36%	0.90%	4.00%

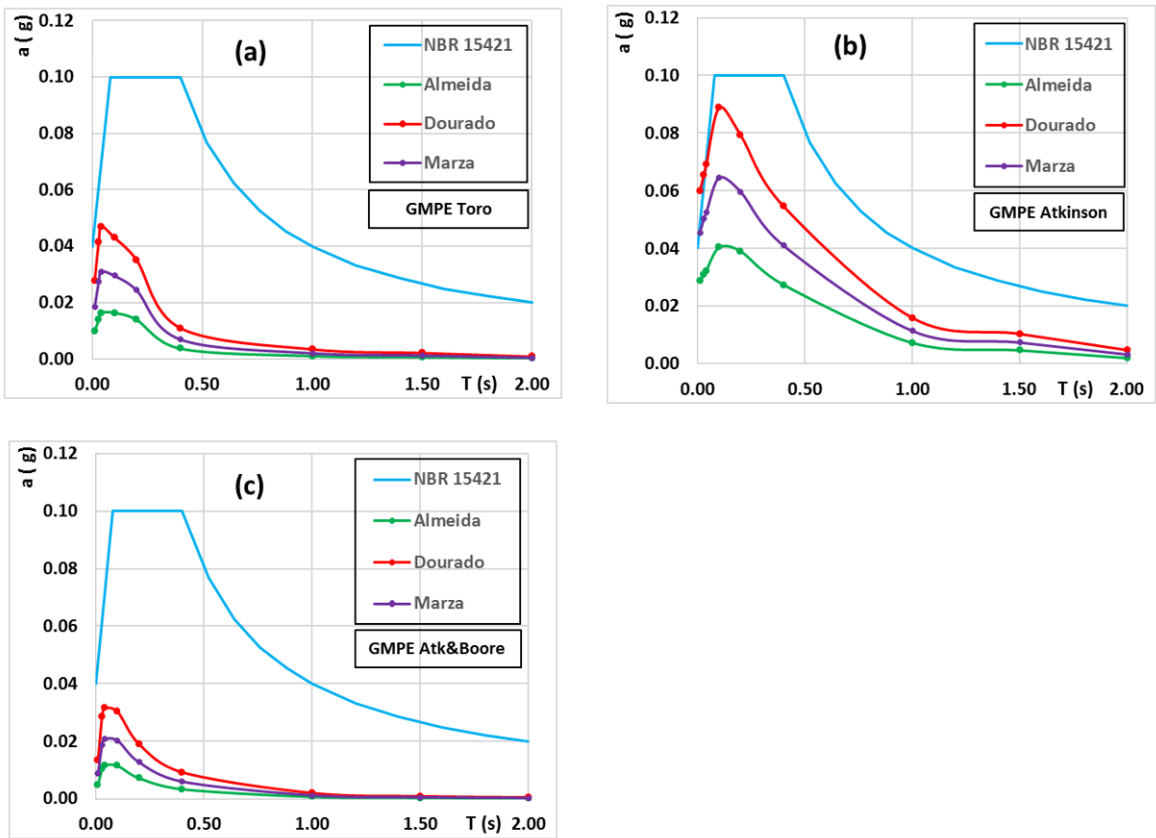


Figure 9. Response spectra for different recurrence laws.

### 5.3 Analysis varying the GMPE

It can be seen from Figure 9 that Dourado’s law is the most conservative one and as it is the most recent publication, it will be taken as reference in the next analyses. Figure 10 illustrates, for better visualization, the three GMPE curves together using the modified Dourado’s law. As already seen in Figure 9, the Atkinson model is the closest to the NBR 15421 design response spectrum (but still lower, except for the PGA value).

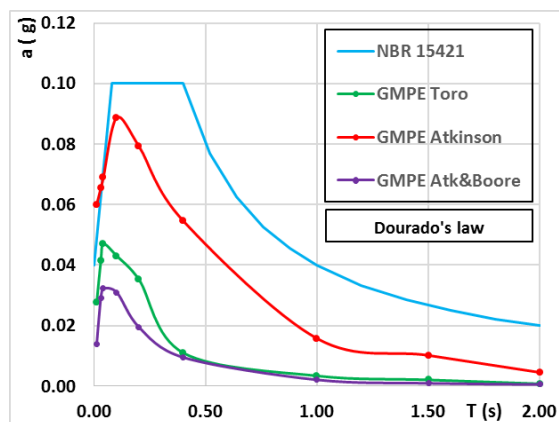


Figure 10. Response spectra for different GMPE.

### 5.4 Analysis varying the mean return period

One of the most important definitions in the PSHA is the mean return period, as discussed in section 3. Several codes, as NBR 15421, consider 475 years (PGA with PE = 10% in 50 years). Other codes, however, have increased the rigor of the criterion, changing this value to 2475 years (PGA with PE = 2% in 50 years). McGuire [23] notes that the period of time  $t = 50$  years is associated to the usual nominal lifetime of major civil structures, and the difference between the two criteria, of course, is only the probability of exceedance. This discussion has not yet been carried out in Brazil.

So, Table 3 and Figure 11 aims to make a simple comparison and encourage discussion about the engineering judgment of changing this mean return period. Figure 11 shows the response spectra for Dourado’s law and the three GMPE. Table 3 shows that the PGA values for a return period of 2475 years are the double or triple the NBR 15421 PGA (return period of 475 years), for any GMPE. The difference is significant, but this comparison cannot be made directly because the mean return periods are not the same.

**Table 3.** PGA value (% g) considering different mean return periods.

Main return period	Toro	Atkinson	Atk and Boore	NBR 15421 [17]
475 years	2.77%	6.00%	1.36%	4.00%
2475 years	11.00%	12.60%	7.11%	-

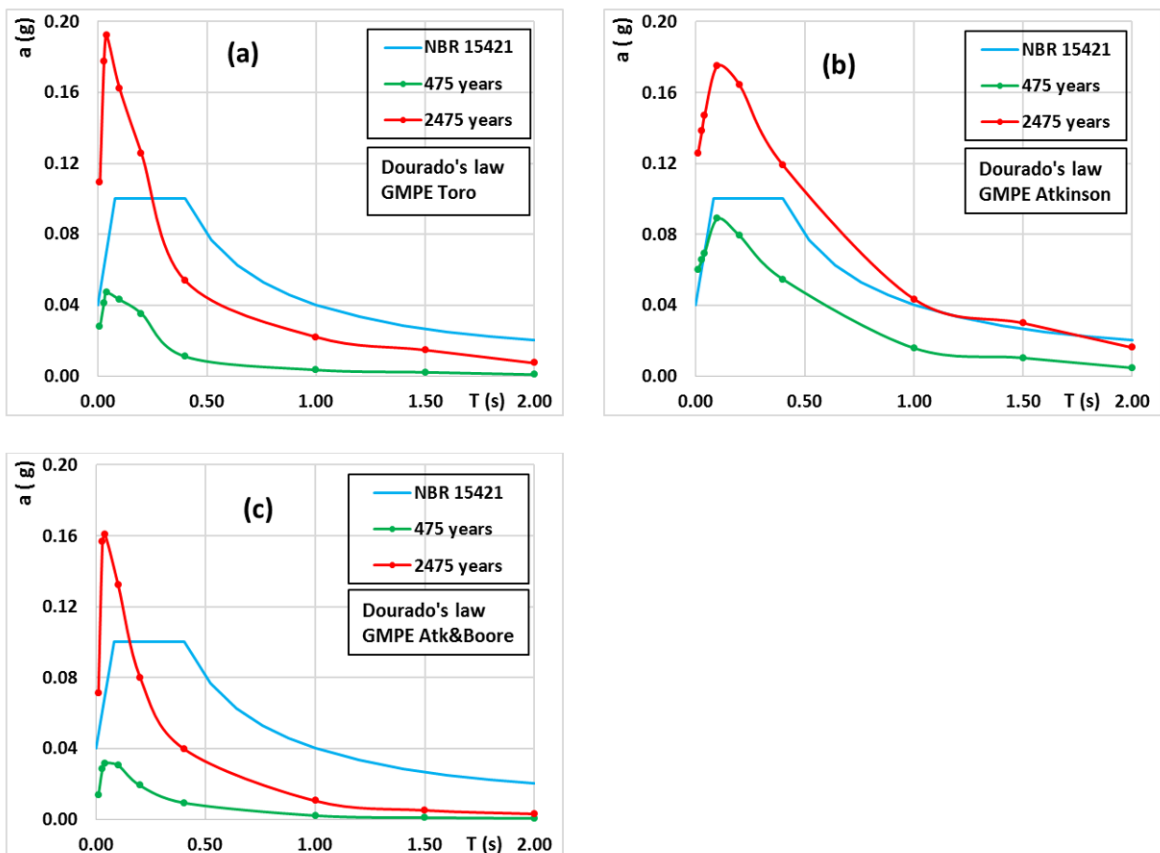


**Figure 11.** Response spectra for different mean return periods.

## 5.5 Design response spectrum shape

It should be highlighted that the shape of the response spectra derived from the analyses differs from the design spectrum presented in the NBR 15421 code. They present a higher peak and decrease with a higher ratio (the constant horizontal line is almost nonexistent).

FIB [46, pp. 91] describes that the author Free, in 1996,

[...] observed that ground motions from intraplate earthquakes have response spectral amplitudes that are appreciably higher than those from interplate earthquakes for high frequencies (greater than 10 Hz); although for lower frequencies the amplitude are similar.

Frequencies greater than 10 Hz is equivalent to periods lower than 0.1 s, and lower frequencies mean higher periods. This seems to be exactly what is illustrated in the previous figures.

FIB [46, pp. 91] still alerts that “[...] there is very significant scatter in the attenuation relationships and there are also important differences from one stable continental region to another [...]”. For last, this reference notes that the differences between strong-motion characteristics in intraplate and interplate regions are usually attributed to source and path effects. In terms of the path effects, inelastic attenuation is generally assumed to be greater in the more fragmented interplane regions. Despite these observations, a more accurate study should be conducted in order to analyze if the Brazilian standard design response spectrum should be improved considering different spectra curves (shapes) according the building site.

## 6 CONCLUSIONS

Brazil is not free of earthquakes, despite an evident relatively low seismic activity, in general. The correct technique must be used in order to assess the seismic hazard level in areas where the engineering judgment considers necessary, and the probabilistic seismic hazard analysis (PSHA) is an adequate methodology for this objective.

This paper presents analyses considering PSHA approach towards improving the hazard map, the peak ground acceleration value and the response spectrum of the state of Rio Grande do Norte, one of the most seismically active areas in Brazil, considering different recurrence laws and different ground motion prediction equations.

It was verified that the peak ground acceleration values and the response spectra obtained from the analyses are usually lower when compared to the design criteria defined by the Brazilian code NBR 15421. So, the code establishes conservative and adequate parameters.

A next stage of this work should be the adoption of a logic tree approach, in order to reduce the uncertainties in the hazard calculations. A second discussion, which might be faced, is the modification of the design mean return period, like what has already been done in other international codes. Evidently, this change will lead to more conservative results and should be developed based on specific studies.

## ACKNOWLEDGEMENTS

The authors are grateful to Prof. Marcelo S. de Assumpção (IAG/USP) for providing the updated Brazilian seismic maps and to Prof. Sergio Hampshire de C. Santos (UFRJ) for clarifying some aspects of the methodology.

## REFERENCES

- [1] P. Talwani Introduction. in *Intraplate Earthquakes*, P. Talwani, Ed., Cambridge, U.K.: Cambridge University Press, 2014, pp. 1–7. <http://doi.org/10.1017/CBO9781139628921.002>.
- [2] J. Berrocal et al., *Sismicidade do Brasil*. São Paulo: IAG-USP/CNEN, 1984.
- [3] M. B. Bianchi et al., "The Brazilian seismographic network (RSBR): improving seismic monitoring in Brazil," *Seismol. Res. Lett.*, vol. 89, no. 2A, pp. 452–457, 2018, <http://dx.doi.org/10.1785/0220170227>.
- [4] A. E. V. Lopes, and L. C. Nunes. "Intensidades sísmicas de terremotos: formulação de cenários sísmicos no Brasil," *Rev USP*, no. 91, pp. 90-103, Nov. 2011, <https://doi.org/10.11606/issn.2316-9036.v0i91p90-103>.
- [5] M. Assumpção et al. "Intraplate seismicity in Brazil," in *Intraplate Earthquakes*, P. Talwani, Ed., Cambridge, U.K.: Cambridge University Press, 2014, pp. 50-71. <https://doi.org/10.1017/CBO9781139628921.004>
- [6] M. S. Assumpção, "Terremotos e a convivência com as incertezas da natureza," *Rev USP*, no. 91, pp. 76-89, Nov. 2011. <https://doi.org/10.11606/issn.2316-9036.v0i91p76-89>.



- [7] R. G. Borges, M. S. Assumpção et al. "Seismicity and seismic hazard in the continental margin of southeastern Brazil," *J. Seismol.*, vol. 24, pp. 1205–1224, 2020, <http://dx.doi.org/10.1007/s10950-020-09941-4>.
- [8] P. Talwani, Ed., *Intraplate Earthquakes*. Cambridge, U.K.: Cambridge University Press, 2014. <https://doi.org/10.1017/CBO9781139628921>.
- [9] H. Agurto-Detzel et al., "Intraplate seismicity in mid-plate South America: correlations with geophysical lithospheric parameters," in *Seismicity, Fault Rupture and Earthquake Hazards in Slowly Deforming Regions*, A. Landgraf et al., London, U.K.: Geological Society, 2017. Special Publications. <https://doi.org/10.1144/SP432.5>.
- [10] A. Saadi, "Neotectônica da plataforma brasileira: esboço e interpretação preliminares," *Rev. Geonomos*, vol. 1, no. 1, pp. 1–15, Feb 1993, <http://dx.doi.org/10.18285/geonomos.v1i1e2.233>.
- [11] A. Saadi et al., *Map and Database of Quaternary Faults and Lineaments in Brazil*. USA: USGS, 2003. U. S. Geological Survey Open-File Report 02-230. <https://doi.org/10.3133/ofr02230>.
- [12] S. E. Hough Intraplate seismic hazard: Evidence for distributed strain and implications for seismic hazard. in *Intraplate Earthquakes*, P. Talwani (Ed.), Cambridge: Cambridge University Press, 2014, pp. 303–327. <https://doi.org/10.1017/CBO9781139628921.013>.
- [13] K. Pitilakis et al., *Systemic Seismic Vulnerability and Risk Analysis for Buildings, Lifeline Networks and Infrastructures Safety Gain*. Luxembourg: Publications Office of the European Union, 2013. <https://doi.org/10.2788/23242>.
- [14] Federal Emergency Management Agency, *FEMA P-58-1 – Seismic Performance Assessment of Buildings, vol. 1, Methodology*, 2nd ed. Washington, D.C.: FEMA, 2018. Accessed: Jul 18, 2020. [Online]. Available: <https://www.fema.gov/media-library/assets/documents/90380>
- [15] M. M. Kassem, F. M. Nazri, and E. N. Farsangi, "The seismic vulnerability assessment methodologies: A state-of-the-art review," *Ain Shams Eng. J.*, vol. 11, no. 4, pp. 849–864, 2020. <https://doi.org/10.1016/j.asej.2020.04.001>.
- [16] P. Paultre et al., "Damage to engineered structures during the 12 January 2010, Haiti (Léogâne) earthquake," *Can. J. Civ. Eng.*, vol. 40, no. 8, pp. 777–790, 2013, <http://dx.doi.org/10.1139/cjce-2012-0247>.
- [17] Associação Brasileira de Normas Técnicas. *Projeto de Estruturas Resistentes a Sismos – Procedimento*, NBR 15241:2006, 2006.
- [18] J. M. Ferreira et al., "Superposition of local and regional stresses in northeast Brazil: evidence from focal mechanisms around the Potiguar marginal basin," *Geophys. J. Int.*, vol. 134, no. 2, pp. 341–355, Aug 1998., <http://dx.doi.org/10.1046/j.1365-246x.1998.00563.x>.
- [19] F. H. R. Bezerra et al., "Review of active faults in the Borborema Province, Intraplate South America – Integration of seismological and paleoseismological data," *Tectonophysics*, vol. 510, no. 3–4, pp. 269–290, Oct 2011, <http://dx.doi.org/10.1016/j.tecto.2011.08.005>.
- [20] Á. F. C. Reis et al., "Stress magnitude and orientation in the Potiguar Basin, Brazil: Implications on faulting style and reactivation," *J. Geophys. Res. Solid Earth*, vol. 118, pp. 5550–5563, 2013., <http://dx.doi.org/10.1002/2012JB009953>.
- [21] F. H. R. Bezerra et al., "Coseismic reactivation of the Samambaia fault, Brazil," *Tectonophysics*, vol. 430, no. 1–4, pp. 27–39, Feb 2007, <http://dx.doi.org/10.1016/j.tecto.2006.10.007>.
- [22] L. Reiter, *Earthquake Hazard Analysis: Issues and Insights*. New York: Columbia University Press, 1990.
- [23] R. K. McGuire, *Seismic Hazard and Risk Analysis*. EEEI, 2004.
- [24] J. W. Baker, *Introduction to Probabilistic Seismic Hazard Analysis*, 2013. White Paper Version.
- [25] A. A. D. Almeida et al., "Probabilistic seismic hazard analysis for a nuclear power plant site in southeast Brazil," *J. Seismol.*, vol. 23, pp. 1–23, 2018, <http://dx.doi.org/10.1007/s10950-018-9755-8>.
- [26] S. H. C. Santos, S. S. Lima, and F. C. M. Silva, Seismic Hazard for Brazilian Northeastern Region. *IBRACON Struct. Mater. J.*, vol. 3, n. 3, p. 374–389, Sep. 2010. Accessed: Jul 18, 2020. [Online]. Available: [http://www.ibracon.org.br/publicacoes/revistas\\_ibracon/riem/volume3\\_n3.asp](http://www.ibracon.org.br/publicacoes/revistas_ibracon/riem/volume3_n3.asp)
- [27] M. D. Petersen et al., "Seismic hazard, risk, and design for south america," *Bull. Seismol. Soc. Am.*, vol. 108, no. 2, pp. 781–800, Jan 2018, <http://dx.doi.org/10.1785/0120170002>.
- [28] American Society of Civil Engineers, *Seismic Evaluation and Retrofit of Existing Buildings*, ASCE/SEI 41-17. 2017. <https://doi.org/10.1061/9780784414859>.
- [29] Comité Européen De Normalisation, *Eurocode 8: Design of structures for earthquake resistance - Part 1: General rules, seismic actions and rules for buildings*, EN 1998-1:2004:E, 1998.
- [30] American Society of Civil Engineers, *Minimum Design Loads and Associated Criteria for Buildings and Other Structures*, ASCE/SEI 7-16, 2016. <https://doi.org/10.1061/9780784414248>.
- [31] P. G. B. Nóbrega et al., "Sobre os mapas de perigo sísmico para o projeto de estruturas," in *Cong. Brasileiro do Concreto*, Vol. 61, Fortaleza, 2019. Available: <https://www.researchgate.net/publication/336672092>
- [32] S. H. C. Santos and S. S. Lima, Base sismológica para a zonificação sísmica da ABNT NBR 15421. *Concr. Constr.*, vol. 92, p. 72–77, Out-Dez. 2018. Accessed: Jul 18, 2020. [Online]. Available: [http://ibracon.org.br/Site\\_revista/Concreto\\_Construcoes/pdfs/revista92.pdf](http://ibracon.org.br/Site_revista/Concreto_Construcoes/pdfs/revista92.pdf)

- [33] R. J. Budnitz et al., *Recommendations for Probabilistic Seismic Hazard Analysis: Guidance on Uncertainty and Use for Experts*. Vol. 1. Livermore: Lawrence Livermore National Laboratory, 1997. NUREG/CR-6372. Accessed: Jul 18, 2020. [Online]. Available: <https://www.nrc.gov/reading-rm/doc-collections/nuregs/contract/cr6372/vol1/index.html>
- [34] A. A. D. Almeida, "Análise Probabilística de Segurança Sísmica de Sistemas e Componentes Estruturais," PhD thesis, Univ. Fed. Rio Jan., Rio de Janeiro, 2002. <https://doi.org/10.17771/PUCRio.acad.2667>.
- [35] M. Pirchiner, "Técnicas de suavização aplicadas à caracterização de fontes sísmicas e à análise probabilística de ameaça sísmica," MSc thesis, Esc. Matem. Apl., Fund. Get. Vargas, Rio de Janeiro, 2014. [Online]. Available: <http://hdl.handle.net/10438/14010>
- [36] J. C. Dourado, "Mapa de ameaça sísmica do Brasil," in *Anais Cong. Bras. Geol.*, Vol. 47, Salvador, 2014.
- [37] V. I. Marza, et al., *Breve Caracterização da Sismicidade no Ceará*. Brasília: Observatório Sismológico, Universidade de Brasília, [20--?].
- [38] J. Douglas *Ground Motion Prediction Equations 1964-2018*. Glasgow: Department of Civil and Environmental Engineering, University of Strathclyde, 2019. Accessed: Jul 18, 2020. [Online]. Available: <http://www.gmpe.org.uk/gmpereport2014.pdf>
- [39] J. J. Bommer et al., "On the selection of ground-motion prediction equations for seismic hazard analysis," *Seismol. Res. Lett.*, vol. 81, no. 5, pp. 783–793, Aug 2010, <http://dx.doi.org/10.1785/gssrl.81.5.783>.
- [40] R. R. S. Dantas, "Decaimento da aceleração de ondas sísmicas dos terremotos na borda da Bacia Potiguar," Bacharel, Univ. Fed. Rio Gde Norte, Natal, 2012.
- [41] G. R. Toro, N. A. Abrahamson, and J. F. Schneider, "Model of strong ground motions from earthquakes in central and eastern north america: best estimates and uncertainties," *Seismol. Res. Lett.*, vol. 68, no. 1, pp. 41–57, Jan 1997, <http://dx.doi.org/10.1785/gssrl.68.1.41>.
- [42] G. M. Atkinson and D. M. Boore, "Earthquake ground-motion prediction equations for eastern north america," *Bull. Seismol. Soc. Am.*, vol. 96, no. 6, pp. 1304–1318, Jun 2008, <http://dx.doi.org/10.1785/0120050245>.
- [43] G. M. Atkinson, "Ground-motion prediction equations for eastern north america from a referenced empirical approach: implications for epistemic uncertainty," *Bull. Seismol. Soc. Am.*, vol. 96, no. 3, pp. 2181–2205, Dec 2006, <http://dx.doi.org/10.1785/0120070199>.
- [44] A. Aguilar-Meléndez et al., "Development and validation of software CRISIS to perform probabilistic seismic hazard assessment with emphasis on the recent CRISIS2015," *Comput. Syst.*, vol. 21, no. 1, pp. 67–90, 2017, <http://dx.doi.org/10.13053/cys-21-1-2578>.
- [45] J. J. Bommer et al., "On the use of logic trees for ground-motion prediction equations in seismic-hazard analysis," *Bull. Seismol. Soc. Am.*, vol. 95, no. 2, pp. 377–389, 2005, <http://dx.doi.org/10.1785/0120040073>.
- [46] Fédération Internationale Du Béton, "Displacement-based seismic design of reinforced concrete buildings," *fib CEB- FIP*, no. 25, 2003, <http://dx.doi.org/10.35789/fib.BULL.0025>.

---

**Authors contributions:** PGBN: conceptualization, methodology, analysis, writing – original draft, supervision; BRSS: investigation, formal analysis, writing – review; SHSN: writing – review and editing, supervision.

**Editors:** Sergio Hampshire C. Santos, Guilherme Aris Parsekian.



## ORIGINAL ARTICLE

## Effect of filler nature on mechanical performance and drying shrinkage of self-leveling mortars

### *Efeito de fillers minerais no desempenho mecânico e na retração de argamassas autonivelantes*

Taylana Piccinini Scolaro<sup>a</sup> Janaíde Cavalcante Rocha<sup>a</sup> <sup>a</sup>Universidade Federal de Santa Catarina – UFSC, Departamento de Engenharia Civil, Florianópolis, SC, Brasil

Received 22 July 2020

Accepted 28 October 2020

**Abstract:** Self-leveling mortars (SLM) have a high filler content in their composition to achieve fluidity, without component separation. These mortars are mainly used in floor systems and have a large area exposed to the external environment, which facilitates water loss and increases the risk of cracking due to drying shrinkage. This study, in order to verify the influence of filler on the production of SLMs, used for comparative effect, quartz filler (QF) and crushed basalt filler (BF), in addition to limestone filler (LF), in contents of 5%, 10% and 20% of the mass of total solid. For that purpose, the tests of spreading in the fresh state and flexural strength, compressive strength, dynamic modulus of elasticity, drying shrinkage and desorption isotherm in the hardened state were carried out. SLMs microstructure was evaluated through isothermal calorimetry. The results show that the use of LF provides higher compressive strengths (up to 18% and 14% higher than QF and BF, respectively, in the first ages, and up to 13% and 22% higher than QF and BF, respectively, at 28 days), probably due to the better physical effect of this filler. In formulations with 20% of filler, LF and QF SLMs showed lower shrinkage when compared to BF SLMs (shrinkage 44% higher than LF mixture and 64% higher than QF mixture). It is concluded that the ideal content of filler to be used in SLMs must be between 10% and 20% of the mass of total solid and varies according to the filler.

**Keywords:** self-leveling mortar, filler, mechanical behavior, hygroscopic, drying shrinkage.

**Resumo:** As argamassas autonivelantes apresentam elevado teor de fillers em sua composição para o alcance da fluidez, sem separação dos componentes. Essas argamassas são utilizadas principalmente em sistemas de pisos e apresentam uma grande área exposta ao ambiente externo, o que facilita a perda de água e aumenta o risco de fissuração devido a retração por secagem. O presente estudo, com o intuito de verificar a influência do filler no comportamento mecânico e na retração por secagem de argamassas autonivelantes, utilizou para efeito comparativo, os fillers quartzoso (QF) e de britagem basáltico (BF), além do filler calcário (LF), em teores que correspondem a 5%, 10% e 20% em massa. Para tanto, foram realizados os ensaios de espalhamento no estado fresco e resistência à tração na flexão, resistência à compressão, módulo de elasticidade dinâmico, retração por secagem e isoterma de dessorção no estado endurecido. A microestrutura das argamassas foi avaliada por meio de calorimetria isotérmica. Os resultados obtidos mostram que a utilização do LF proporciona resistências à compressão superiores (até 18% e 14% maior que QF e BF, respectivamente, nas primeiras idades, e até 13% e 22% maior que QF e BF, respectivamente, aos 28 dias), provavelmente devido ao melhor efeito físico desse filler. Em formulações com 20% de fino, argamassas de LF e QF apresentaram menor retração, se comparadas com argamassas de BF (retração 44% maior que a formulação com LF e 64% maior que a com QF). Conclui-se que o teor ideal de filler a ser empregado nessas argamassas deve estar entre 10% e 20% da massa de sólidos e varia conforme o filler.

**Palavras-chave:** argamassa autonivelante, filler, comportamento mecânico, higroscopia, retração por secagem.

**How to cite:** T. P. Scolaro and J. C. Rocha, "Effect of filler nature on mechanical performance and drying shrinkage of self-leveling mortars," *Rev. IBRACON Estrut. Mater.*, vol. 14, no. 3, e14303, 2021, <https://doi.org/10.1590/S1983-41952021000300003>

Corresponding author: Taylana Piccinini Scolaro. E-mail: [taylanaps@hotmail.com](mailto:taylanaps@hotmail.com)

Financial support: None.

Conflict of interest: Nothing to declare.



This is an Open Access article distributed under the terms of the Creative Commons Attribution License, which permits unrestricted use, distribution, and reproduction in any medium, provided the original work is properly cited.

## 1 INTRODUCTION

Self-leveling mortar, commonly used in flooring systems, is characterized by a smooth and regular surface, high fluidity, high early strength and volumetric stability [1]. To achieve the necessary fluidity without component segregation, high levels of cement and fillers ( $<125\mu\text{m}$ ), usually limestone filler, are added. The limestone filler has been widely used in cementitious materials, including self-leveling mortars, due to economic factors, its physical [2], [3] and chemical effects [4] and its good performance in mechanical strength [5].

Currently, in Portland cement compounds, the effect of different types of fillers has been compared [6], [7], [2], [3], [8]. The literature reports that the effect of limestone filler is more effective than quartz filler in accelerating the C3S hydration. According to Berodier and Scrivener [2], this is due to the dissolution of this phase and may be related to the fact that the limestone has a favorable surface structure to the C-S-H nucleation (in the end of the induction period, the limestone surface is completely covered with nuclei, which is not observed on the quartz surface at the same age). Kumar et al. [3] states that the limestone filler accelerates initial hydration due to its ability to induce ion exchange reactions with C-S-H, which increases the driving force of C-S-H growth.

The basaltic filler seems to act as inert material at early ages and later its reactivity is increased due to pozzolanic reaction. In a comparative study, Nam and Chuong [6] reported that the addition of limestone filler in mortars benefits the initial strength development, while the use of basaltic filler contributes more prominently to later age strength, due to the slowness of the pozzolanic reaction. According to the study of Saraya [7], even in early ages, pastes with basalt showed better mechanical properties than those containing limestone as filler, as a result of the better packing caused by basalt, forming a more dense matrix, and a better dispersion of cement grains. The use of basaltic filler improves the strength of the concrete, mainly due to the better packing of particles. In addition, the particles act as nucleation sites for the precipitation of hydration products, accelerating the hydration of the cement grains and contributing to the increase of early age strength. Also, chemical interactions may occur on the surface of the basalt particles, through a gradual local exchange of ions between minerals on the basalt surface and C-S-H phase. Calcium ions diffuse from the pore solution and exchange magnesium, while magnesium ions diffuse into C-S-H phase. This local transformation of the minerals leads to enhancement of the interfacial transition zone [9].

Moreover, according to Liu et al. [10], the supplementary cementitious materials (SCMs) affect the compressive strength of pastes through three main effects: characteristics inherent to SCM, particle size refinement of the SCM and hydration of the SCM. The inherent characteristic effect of SCM is related with surface texture, charge properties, elastic modulus and others. The particle size refinement effect influences the paste compressive strength due to the increase of the interface area between SCM particles and hydration products, while the interface distributes more homogeneously (this effect account for 1% - 10% of the total compressive strength). The hydration effect of SCM leads to a densification of interface between SCM particles and the matrix, through the formation of hydration products and, consequently, mechanical properties of the interface can be improved. The high activity of fine particles is of great importance to early strength, while the 28 days compressive strength is significantly influenced by the activity of SCM.

However, it is still unclear whether the use of different types of filler influences the mechanical behavior and dimensional stability of SLMs. The role of limestone filler in the dimensional stability of cementitious systems has been studied and research shows that its incorporation may not change significantly [11] and in some cases may reduce drying shrinkage [12]. According to Itim et al. [12], the replacement of cement by this filler up to 15% may reduce drying shrinkage, because it provides a less porous structure, forming more refined pores, preventing desiccation. Benachour et al. [11] reported that the addition of up to 35% limestone filler (sand replacement) does not cause increases in drying shrinkage, despite inducing a finer pore size population. The higher specific surface of the filler, compared to sand, increases the water demand due to the adsorption phenomenon. On the other hand, filler particles fill the voids and the water has less pore space available.

However, the information available in the literature about the influence of mineral additions on drying shrinkage is still contradictory. Some authors claim that the use of these additions reduces drying shrinkage, possibly due to the matrix densification, preventing the evaporation of internal moisture, or because of the restriction to shrinkage deformation [12], [13]. Differently, other studies report that mixtures with incorporation of mineral additions show greater drying shrinkage. This could be due to the formation of smaller capillary voids. The shrinkage occurs mainly due to the loss of water from smaller voids [14]. Moreover, it is known that the drying shrinkage generally increases with the increase in the paste volume, since only the paste shrinks due to drying [15].

Self-leveling mortars have a large area exposed to the external environment, which facilitates water loss and increases the risk of cracking. Therefore, it is necessary to understand the impact of the filler nature on the mechanical properties and on the drying shrinkage of these mixtures to obtain durable products. This research used for comparative effect, in addition to limestone filler (LF), quartz filler (QF) and crushed basalt filler (BF) in contents of 5%, 10% and

20% of the mass of total solid in the production of these mortars. The study aimed to identify the impact of these fillers on the resulting mortar and the filler content that may be added to them without loss of performance.

## 2 MATERIALS AND METHODS

### 2.1 Materials

Portland cement CPV - ARI was used as a binder, according to NBR 16697 [16] (equivalent to Type III Portland cement specified by ASTM C150 [17]). This cement was chosen due to the low admixture content and because it presents a high initial mechanical strength, suitable for self-levelling systems. Three different fillers were evaluated: limestone (LF), quartz (QF) and crushed basalt (BF). The properties of cement and fillers are given in Table 1 and their particle size distributions are given in Figure 1. The LF is the filler that has the smallest particle size. The particle size distribution of QF and BF were similar, although the range of particle size distribution of BF is narrower. A quartz sand with fineness of 2.09, specific mass of 2.52g/cm<sup>3</sup> and 6.5% of powdery material was used as fine aggregate. A polycarboxylate superplasticizer with specific mass between 1.080 - 1.120g/cm<sup>3</sup>, pH between 4,5 - 6,5 and solid content of 51%, was used.

**Table 1.** Chemical and physical properties of cement and fillers.

Composition (%)	Cement	Limestone filler	Quartz filler	Crushed basalt filler
SiO <sub>2</sub>	17.297	3.210	99.457	68.599
Al <sub>2</sub> O <sub>3</sub>	-	-	-	12.775
Fe <sub>2</sub> O <sub>3</sub>	3.027	0.754	0.043	5.887
CaO	66.096	62.037	0.034	5.174
K <sub>2</sub> O	1.376	0.202	0.031	3.781
SO <sub>3</sub>	4.632	-	0.092	-
CO <sub>2</sub>	6.930	33.550	0.280	2.670
Specific mass (g/cm <sup>3</sup> )	3.16	2.85	2.74	2.52
Blaine specific surface (cm <sup>2</sup> /g)	5,416.44	2,558.78	2,944.42	2,804.63

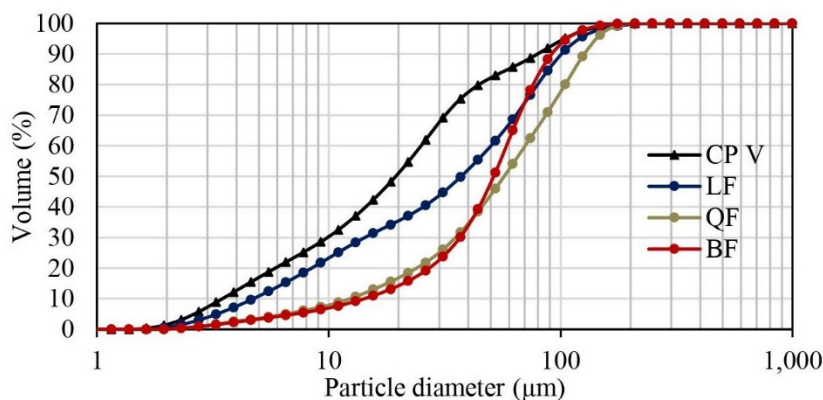


**Figure 1.** Particle size distributions of cement and fillers.

Figure 2 shows images of limestone, quartz and crushed basalt filler. It is possible to observe that the limestone and the crushed basalt filler surfaces are rougher than that of the quartz filler. The three fillers have particles with angular shape.

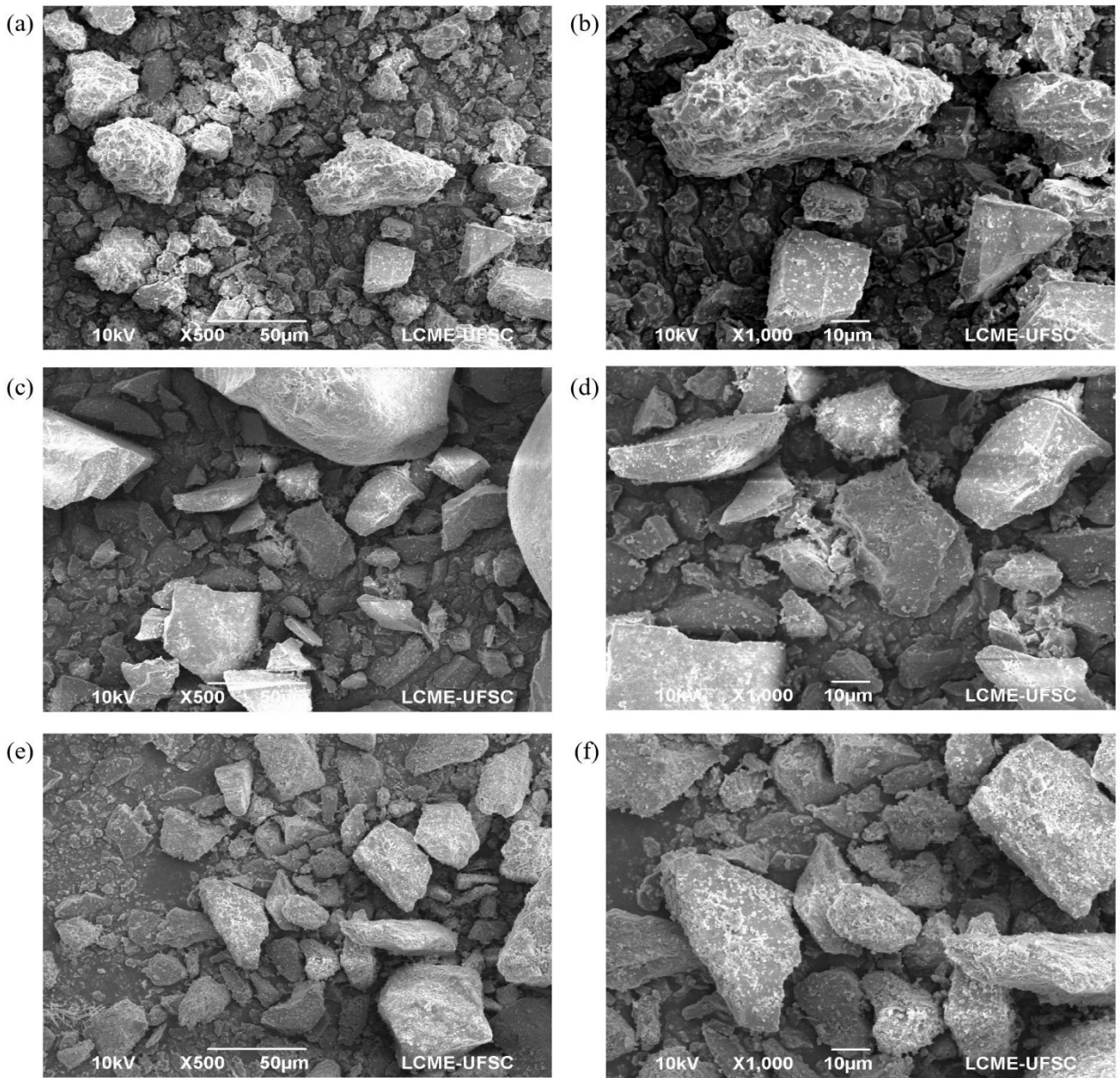


**Figure 2.** SEM micrographs of (a) limestone with 500x and (b) 1000x magnification, (c) quartz with 500x and (d) 1000x magnification and (e) crushed basalt filler with 500x and (f) 1000x magnification.

## 2.2 Mixture proportion and test program

In this study, SLMs were produced considering an agglomerate: aggregate (cement: filler + sand) ratio of 1:2 (mass) and water/cement ratio (w/c) of 0.5 (wt%). The mixture proportions were defined based on preliminary studies, aiming to verify the ability to incorporate aggregates in SLMs. These studies involved some visual analysis: leveling, edge quality, risks of segregation and bleeding. For mortars with a 1:2 ratio, the following requirements in the fresh state were: self-leveling, regular edges and absence of signs of segregation or bleeding. The limestone filler was used as a reference, due to its traditional use in self-leveling and self-compacting mortars [18]–[20] and it was used in contents of 5%, 10% and 20% of the mass of total solid. Limestone filler replacements by other fillers (quartz and crushed basalt) were performed with specific mass correction. Thus, the volume of filler used in each mixture with the same filler content was not changed.

Due to the correction of the specific mass of the fillers in relation to the LF in each filler contents, the percentage of mass of QF and BF show a small difference from the percentages initially defined (5%, 10% and 20%). However,

to facilitate the designation of the samples, the nomenclatures QF5, QF10, QF20, BF5, BF10 and BF20 were maintained. The mixtures were prepared adding different amounts of superplasticizer in order to achieve spreading values between 25 and 30cm, values recommended by Barluenga and Hernández-Olivares [21] for SLMs, which need large flow ability. In view to ensure a practical application, the required dosage of superplasticizer was established to ensure a spreading diameter of  $27,5 \pm 2,5$  cm, as listed in Table 2.

The mixing procedure was done according to NBR 16541 [22]: 1) mixing of anhydrous materials at low speed for 60s, 2) mixing at low speed for 30s with the addition of 75% of water in the initial 10s, 3) mixing at high speed for 60s, 4) stop the mixer for 90s for scraping the bowl and paddle, 5) mixing at low speed for 60s with the addition of the remaining 25% of water and superplasticizer in the initial 10s.

Table 2 provides the detailed composition of the SLMs.

**Table 2.** Mixture proportion of SLMs.

Mixture	Binder (kg/m <sup>3</sup> )		Aggregate (kg/m <sup>3</sup> )			Water (kg/m <sup>3</sup> )	%SP <sup>1</sup>	Paste volume (%) <sup>2</sup>	Spreading (cm)
	Cement	Limestone filler	Quartz filler	Crushed basalt filler	Sand				
LF5	621.33	93.21	-	-	1149.63	310.66	0.45	54.38	28.5
LF10	624.00	187.22	-	-	1060.97	312.00	0.45	57.90	28.0
LF20	629.41	377.69	-	-	881.33	314.71	0.40	65.03	30.0
QF5	621.33	-	89.61	-	1149.63	310.66	0.40	54.38	25.0
QF10	624.00	-	179.99	-	1060.97	312.00	0.45	57.90	28.5
QF20	629.41	-	363.11	-	881.33	314.71	0.43	65.03	25.0
BF5	621.33	-	-	82.42	1149.63	310.66	0.45	54.38	28.5
BF10	624.00	-	-	165.54	1060.97	312.00	0.60	57.90	26.0
BF20	629.41	-	-	333.95	881.33	314.71	0.70	65.03	29.3

<sup>1</sup> By cement mass. <sup>2</sup> Paste = cement, filler and water.

### 2.2.1 Workability

Workability was measured by means of the spreading diameter of SLMs. For this purpose, a cone trunk was placed at the center of a glass plate and filled with mortar. After, the truncated cone was lifted and the mortar spreads. The average of two perpendicular measurements of diameter was taken. The cone trunk used has the following dimensions:  $\phi_{sup} = 70\text{mm}$ ,  $\phi_{inf} = 100\text{mm}$  and  $h = 50\text{mm}$ . The spreading diameter of SLMs was carried out to determine the content of superplasticizer needed for each mixture to reach a spreading flow between 25 and 30 cm.

### 2.2.2 Flexural and compressive strength

Flexural strength was evaluated in three 40x40x160mm prismatic specimens and compressive strength was determined in each of the halves of the specimens resulting from flexural test, according to NBR 13279 [23]. Mixtures were poured into molds without any vibration and compaction. Specimens were demolded 24h after casting and were covered with plastic film until demolding. Specimens were tested at 1 and 28 days.

### 2.2.3 Dynamic modulus of elasticity

Dynamic modulus of elasticity of SLMs was determined in three 40x40x160mm prismatic specimens, at 28 days of age, according to NBR 15630 [24]. The test was carried out in a room with  $60 \pm 5\%$  RH and the specimens remained until the 28th day in the same room. Specimens were demolded 24h after casting and were covered with plastic film until demolding.

### 2.2.4 Desorption isotherm

Water vapor isotherm test was conducted in accordance with C 1498-01 [25] in specimens with 10% e 20% of filler, obtained from the specimens that were evaluated for shrinkage up to 28 days. After shrinkage test, the specimens were sawn into pieces of approximately 5mm thick and section 25x25mm. Afterwards, specimens were dried at 50°C for 48 hours. Later drying, the samples were placed in airtight containers with decreasing relative humidity to check the mass moisture content in each relative humidity (RH).

The different relative humidity of the environments were provided by six salts: potassium sulfate ( $K_2SO_4$ ), sodium chloride (NaCl), sodium nitrite ( $NaNO_2$ ), magnesium chloride ( $MgCl_2 \cdot 6H_2O$ ), potassium acetate ( $KCH_3CO_2$ ) and hydroxide potassium (KOH), which provided the relative humidity (RH) of, respectively, 96%, 75%, 65%, 31%, 20% and 6% at 50°C. The mass moisture content was calculated according to Equation 1.

$$W = \frac{m - m_0}{m_0} \times 100 \quad (1)$$

where  $W$  = mass moisture content (%);  $m$  = mass of the equilibrium specimen (g) and  $m_0$  = mass of the dry specimen (g).

The GAB method was used to obtain the adjustment of the experimental points using the nonlinear least squares method. The specific surface of SLMs (SGAB) was calculated according to Equation 2.

$$S = \frac{W_m \times a_m \times N_{avg}}{M} \quad (2)$$

where  $S$  = specific area of the material ( $m^2/g$ );  $W_m$  = monolayer moisture content (g/g);  $a_m$  = area occupied by one water molecule ( $10\text{\AA}^2$  or  $10 \times 10^{-20}m^2$ );  $N_{avg}$  = Avogadro's number ( $mol^{-1}$ ) and  $M$  = molecular mass of water (g/mol).

### 2.2.5 Drying shrinkage

Drying shrinkage was measured in two 25x25x285mm prismatic specimens. According to C 1708 [26], specimens were demolded after 24 hours and then the initial length reading was done (with 1 day). The other readings were taken at 3, 7, 14 and 28 days from the moment of mixing the materials. Specimens were covered with plastic film in the first 24h and after demolding they were stored in an environment with  $65 \pm 10\%$  RH. Shrinkage was calculated according to Equation 3.

$$\varepsilon_i = (L_i - L_0) / 250 \times 100\% \quad (3)$$

where  $\varepsilon_i$  = value of shrinkage at age "i" (%);  $L_i$  = length at certain age (mm);  $L_0$  = length after demolding (mm);  $i$  = age of measurement and 250 = effective length of mortar specimen (mm).

Mass loss was calculated according to Equation 4.

$$\Delta m = (m_i - m_0) / m_0 \times 100\% \quad (4)$$

where  $\Delta m$  = mass loss (%);  $m_i$  = mass at certain age (g) and  $m_0$  = mass after demolding (g).

### 2.2.6 Hydration kinetics by isothermal calorimetry

The test was carried out on pastes considering the same proportion between Portland cement and filler used in LF20, QF20 and BF20 SLMs and in a reference paste (REF) containing only cement. The ratio water/binder = 0.5 was used and, in this case, the fillers were considered as part of the binder. The cement mass was kept constant in all pastes and therefore the fillers were used as an addition to the pastes.

The hydration kinetics of the pastes were evaluated by isothermal calorimetry in a Thermometric AB calorimeter from TAM Air from TA Instruments. The powdered materials were previously homogenized for 1 minute. Then, water



was added and, after manual external mixing for a period of 2 minutes, the samples were inserted into the calorimeter. The heat released was recorded at a temperature of 23°C.

### 3 RESULTS AND DISCUSSIONS

#### 3.1 Workability

In Table 2 it is possible to observe that, in general, with the increase in filler content, there is an increase of superplasticizer content to obtain the target spreading, since the w/c ratio was kept constant. The increase in the filler content requires a greater amount of water to wet the surface of the particles, due to the greater specific surface area [18].

Higher contents of superplasticizer were necessary for formulations with BF. Although this material has the specific surface slightly smaller than the specific surface of QF, the values are quite similar between these fillers. However, the BF particles have a rougher texture, which may result in a decrease in the mixture fluidity and an increase in the superplasticizer demand for the same spreading [19], [27].

All mixtures showed spreading between 25 and 30cm and without segregation or bleeding.

#### 3.2 Flexural and compressive strength

Figure 3a shows the results of flexural strength and Figure 3b, the results of compressive strength of SLMs, at 1 and 28 days.

The flexural strength at 1 day increased with the increase in filler content. However, at 28 days, there was no noticeable influence of the use of different types and contents of filler. About compressive strength, the use of filler up to 20% resulted in higher early strength for all fillers. At 28 days, the compressive strength increased significantly with the increase of LF up to 10%, however, the use of QF and BF in 5%, 10% and 20% resulted in equivalent compressive strength.

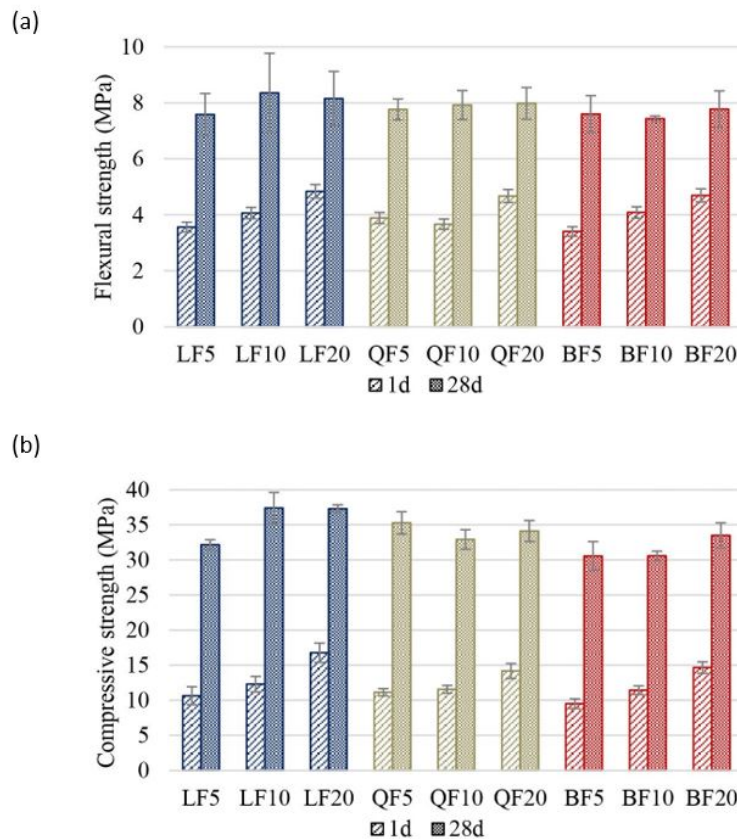


Figure 3. (a) Flexural and (b) compressive strength of self-leveling mortars at 1 and 28 days.

With the use of filler, the solid matrix may have been reinforced due to a more homogeneous distribution of smaller C-S-H crystals [11] and due to the filling of voids between the cement paste and the fine sand particles [18]. Filler acts mainly on the first day of hydration, when the microstructure is developing rapidly. Hydrates, such as C-S-H, form connections between cement grains, explaining the compressive strength increase at 1 day as the filler content increases [2].

Regarding the type of filler, it was observed that at 1 day, only SLMs with 20% of filler showed differences in the results of compressive strength. No influence of the filler nature in SLMs with 5% and 10% of filler was verified. SLMs containing LF showed higher early compressive strengths, LF20 showed compressive strength 18% and 14.4% greater than QF20 and BF20, respectively. At 28 days, in general, compressive strengths were also greater for formulations with LF, up to 13% and 22% greater than QF and BF, respectively.

It was observed that the limestone filler was more favorable to the development of compressive strength compared to quartz and crushed basalt filler. Assuming that limestone filler is an inert material, mixtures with LF show better compressive strength, probably due to the more effective behavior of LF in relation to the physical effects when compared to QF and BF. As the w/c ratio was fixed for all SLMs and the amount of cement was constant in formulations with the same filler content, it was excluded the possibility of dilution effect on the mixtures. So, the higher compressive strength values of SLMs mixes with LF are probably result of the inherent characteristic effect (such as surface texture, charge properties and elastic modulus) and the particle size refinement effect of LF (LF  $d_{50}=37\mu\text{m}$ , QF  $d_{50}=57\mu\text{m}$  and BF  $d_{50}=51\mu\text{m}$ ). A hypothesis is that the inherent characteristic may have affected the heterogeneous nucleation of C-S-H on the filler surface and the particle size may have reduced the distance between particles, due to a more homogeneous particle distribution in the cement paste, besides having contributed with nucleation.

From a practical purpose, the compressive strength at early ages may be a motivation for the use of LF, since early compressive strength is important in self-leveling systems. Moreover, similarly to the early strength, the use of LF influenced the compressive strength at 28 days.

In the SLMs of this study, sand was replaced by fillers in mass, which resulted in slight changes in cement consumption between the mixtures. Figure 4 shows the relationship between cement consumption and the compressive strengths achieved by mortars at 1 and 28 days.

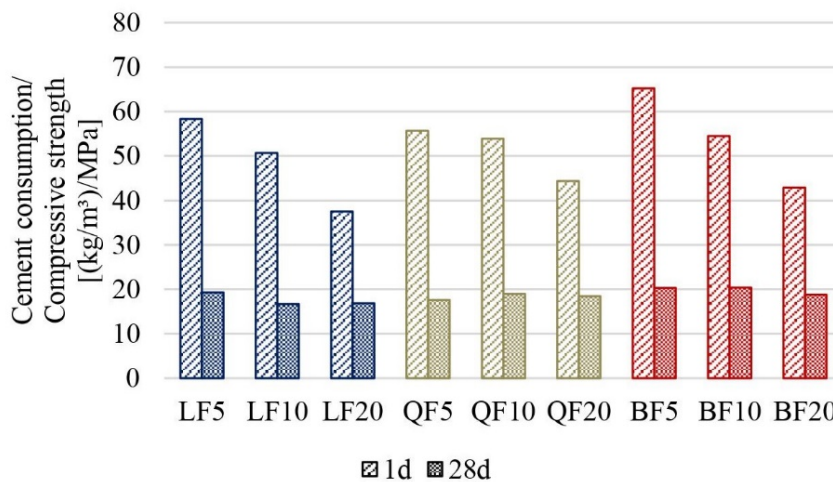


**Figure 4.** Relation between cement consumption and compressive strength of self-leveling mortars at 1 and 28 days.

It is possible to observe that, at the age of 1 day, the relationship between cement consumption and compressive strength is lower in SLMs with higher filler content. That is, for equivalent cement consumption, the results of compressive strength are higher in mortars with higher filler content, motivating the increase of filler content in these SLMs. At 28 days, the relationship between cement consumption and compressive strength was similar between the mixtures.

### 3.3 Dynamic modulus of elasticity

The dynamic modulus of elasticity values are reported in Figure 5.

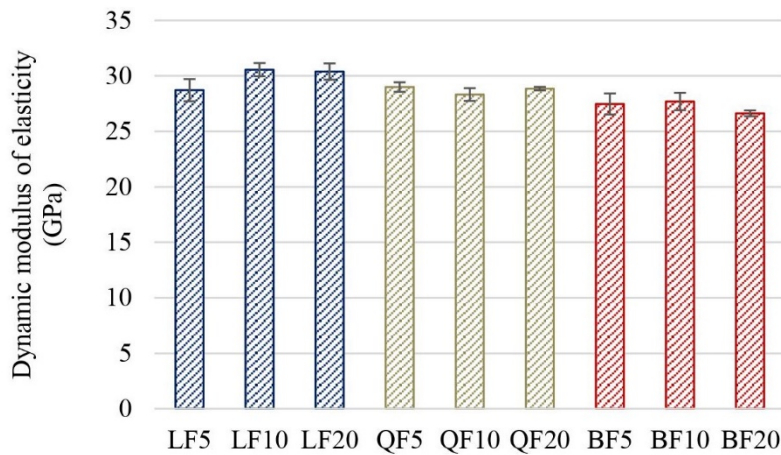


Figure 5. Dynamic modulus of elasticity of self-leveling mortars.

All the mixtures showed similar values. However, it is possible to observe that SLMs with LF showed dynamic modulus of elasticity slightly higher than other SLMs. This may be related to the higher compressive strengths of mixtures containing limestone filler.

### 3.4 Desorption isotherm

The desorption isotherms were developed for mortars with 10% and 20% of filler, since these mixtures showed better mechanical performance at early ages and allow higher incorporation of filler in the SLMs. Figure 6 shows the desorption isotherms of SLMs, where the points represent the points obtained experimentally and the lines represent the mathematical adjustment based on the GAB model.

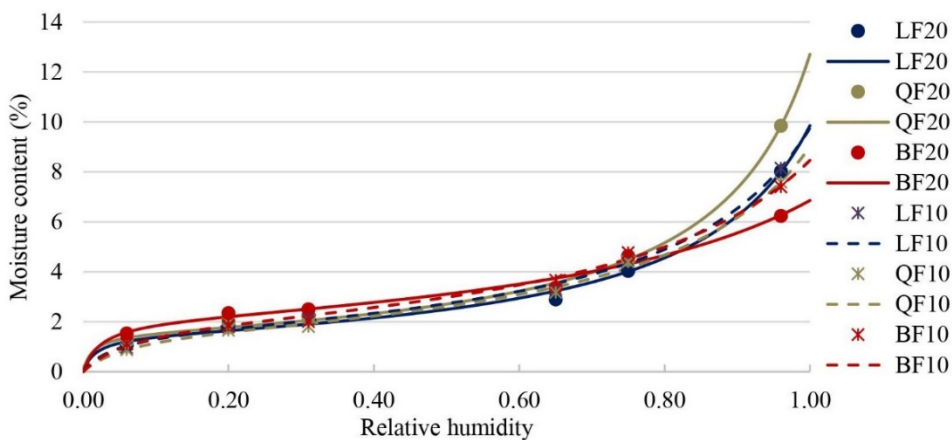


Figure 6. Desorption isotherms of self-leveling mortars with 10% and 20% of filler.

Figure 6 shows that the shape of the desorption curves was quite similar for all SLMs. The BF20 mixture showed higher moisture content in RH < 65%, which may be seen by the curve shifted upwards in relation to the others. Table

3 shows the specific surface of the SLMs calculated from the GAB adjustment. It can be observed that the specific surface increases with the use of BF, with the sample BF20 having the highest SGAB.

**Table 3.** Monolayer moisture content ( $W_m$ ) and specific surface area ( $S_{GAB}$ ) calculated from the GAB model of self-leveling mortars with 10% and 20% of filler.

Mixture	$W_m$ (%)	$S_{GAB}$ (m <sup>2</sup> /g)
LF20	1.46	48.85
QF20	1.54	51.46
BF20	2.09	69.77
LF10	1.68	56.18
QF10	1.66	55.49
BF10	1.98	66.19

According to Jennings et al. [28], water isotherms may be used to estimate the amount of water contained and removed from gel pores and capillary pores. In desorption, the size and quantity of the pores may be assessed by calculating the water lost in established RH intervals. At each interval, pores of a certain size are emptied and the amount of water lost represents the amount of pores of such dimension.

This is a simplified qualitative analysis to avoid calculating pore size distributions, which may be complicated and uncertain - the results vary depending on the assumed function for the thickness of the adsorbed layer (if the adsorption curve is used) and are underestimated due to the pore ink-bottle effect (desorption) [29], [30]. Based on Jennings et al. [28] and in Saeidpour and Wadsö [30], the amount of water desorbed (calculated from the mass moisture content measured) was divided into four intervals:

- i. Between 100 and 85% RH, where capillary pores (width between ~8nm and ~10µm) are emptied;
- ii. Between 85 and 50% RH, where large gel pores are emptied (~4nm);
- iii. Between 50 and 25% RH, where small gel pores are emptied (~2nm);
- iv. Between 25 and 0% RH, where the interlayer water is removed (spaces ≤ 2nm).

Figure 7 shows the amount of water desorbed in each described interval.

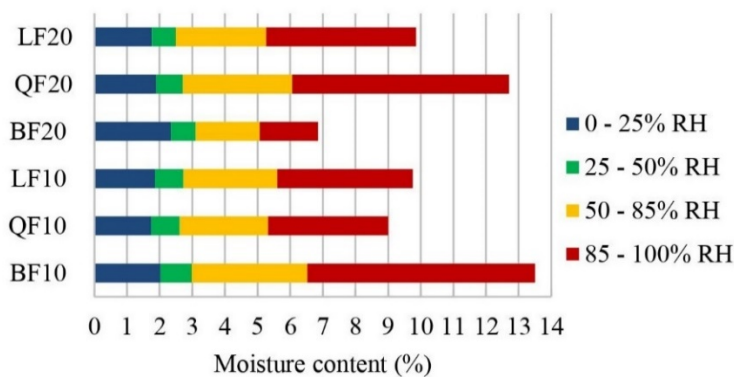


**Figure 7.** Amount of water desorbed in each RH interval for self-leveling mortars with 10% and 20% of filler.

At lower humidity intervals (50 - 25% RH and 25 - 0% RH), desorption occurs in the small gel pores (~2nm) and in the interlayer spaces of C-S-H (≤ 2nm). Based on Figure 7, it can be observed that between 50% and 0% RH mixtures containing BF have higher moisture content, when compared to mixtures with LF and QF, especially BF20. Therefore, these SLMs probably have a larger amount of smaller pores - small gel pores and interlayer spaces - consistent with the larger specific surfaces showed by these formulations.

The amount of large gel pores (85 - 50% RH) is greater in BF10 and QF20 mixtures. The amount of capillary pores is only an estimative (85 - 100% RH), since the complete filling of larger pores occurs only under conditions of

immersion in water and immersion or saturation under vacuum and the larger pores are only covered by thin adsorbed layers [28]. However, it was observed that the BF20 mortar had significantly lower moisture content in this relative humidity range.

### 3.5 Drying shrinkage

The results of drying shrinkage and mass loss of SLMs at 3, 7, 14 and 28 days are shown in Figure 8. The shrinkage and mass loss values increased until 28 days and the increases were more evident in the first 14 days. There was no correlation between the mass loss and the drying shrinkage values. Shrinkage not only occurs due to the water loss to the external environment, but also depends on the size and type of voids that lose water (difficulty in removing water) and the mechanical properties of the material.

In SLMs developed with LF, the one with 10% of filler showed the lowest shrinkage value. In mixtures with QF, there is a decrease in shrinkage with increase of filler content up to 20%. Concerning mixtures with BF, the shrinkage decreases as the filler content increase up to 10%.

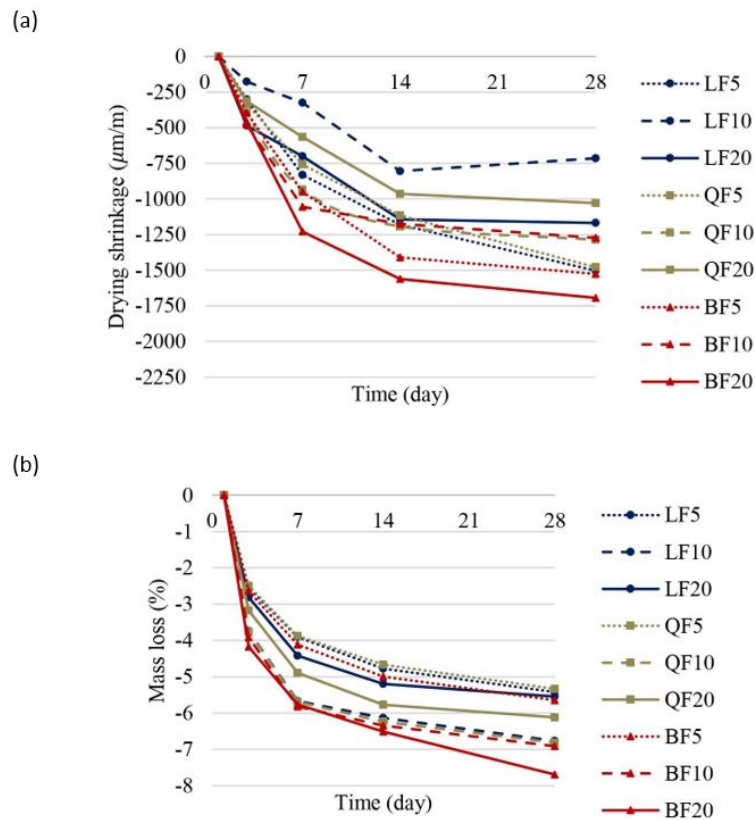


**Figure 8.** (a) Drying shrinkage and (b) mass loss of self-leveling mortars.

With the increase in filler content in the mixtures studied, the paste content (cement, filler and water) increases and the volume of sand decreases. However, the fillers seem to contribute to filling pores [12], being able to reduce the shrinkage of mortars, when used up to a certain content, which varies according to the filler. In addition, the decrease in shrinkage may also be due to the restraint in paste level provided by the fillers [13].

Regarding the type of filler, in mixtures developed with 5 and 10% of filler, there is no notable trend in the results. In general, the differences in shrinkage values of SLMs with the different fillers in these filler contents are not so prominent. In SLMs with 20% of filler, mixtures with BF showed greater shrinkage at 28 days (44% greater than LF and 64% greater than QF). Mixtures with the same filler content were developed with the same initial paste volume.

Therefore, the differences between shrinkage values may be related to the differences on the porous structure formed, to the deformation linked with filler nature and to the differences in the superplasticizer content.

Mortars with greater porosity tend to shrink more than those with less porosity, as long as they present similar pore size distributions. When the porosity is similar, the pore size distribution may still influence the shrinkage [13]. For drying above 50% RH, capillary stresses are the primary driving force for shrinkage [31]. Besides the lower moisture content verified in the capillary pores of BF20 mortar, compared to LF20 and QF20 (item 3.4), it showed the higher water loss. Moreover, it was found that the BF20 mortar (highest shrinkage) showed a lower mass loss/ drying shrinkage ratio at 28 days. This ratio was 47.5, 59.5 and 45.4, for LF20, QF20 and BF20, respectively. The lower this ratio, the higher the shrinkage for the same water loss, possibly due to the difficulty in removing water from the pores.

In addition, drying shrinkage may be related to the elastic deformation of the mortar (affected by the modulus of elasticity of the aggregates). In this context, mixtures produced with aggregate with low modulus of elasticity, result in higher shrinkage. Furthermore, it is believed that the higher shrinkage values observed when 20% of BF is used may also be associated with the higher superplasticizer content used (about twice the amount of SLMs with 20% of LF or QF). According to Ma et al. [32], the increase in polycarboxylate-based superplasticizer content may increase drying shrinkage of mortars. This occurs possible due to the increase in fine capillary pores.

### 3.6 Hydration kinetics by isothermal calorimetry

Figure 9a shows the heat flow curves and Figure 9b shows the cumulative heat curves during the first hours of pastes hydration, obtained from isothermal calorimetry. The peak of heat shown in Figure 9a occurs after the period of induction and corresponds to the period of acceleration, controlled by nucleation and the growth of hydration products.

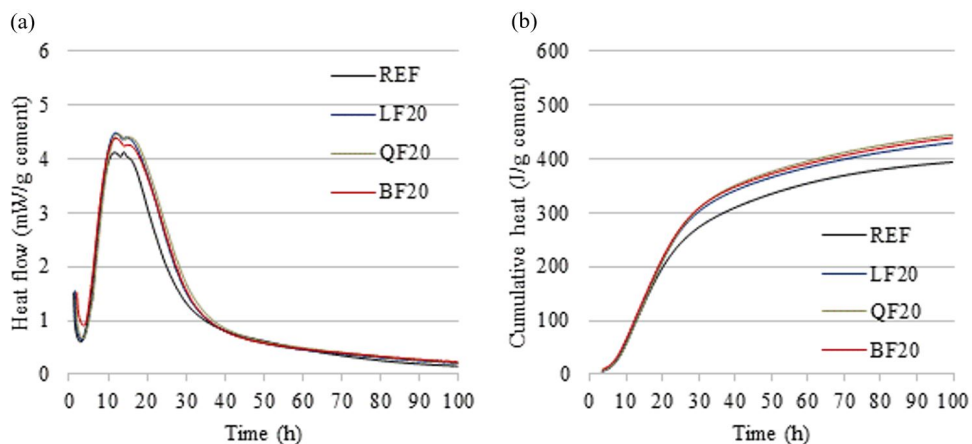


**Figure 9.** (a) Heat flow and (b) cumulative heat of LF20, QF20 and BF20 pastes.

From Figure 9a, it is possible to notice that pastes with filler show an increase in the heat flow when compared with pure cement paste (REF), probably by facilitating hydration reactions due to nucleation. In the LF paste was verified a slight increase in the maximum value of this peak, when compared with the QF and BF pastes. However, the curves of LF20, QF20 and BF20 pastes showed very close maximum values of heat flow, 4.48, 4.46 and 4.38mW/g cement, respectively. In addition, comparing the stretch that leads to the main peak between REF paste and the pastes with filler, there were no differences in the slope intensity, which indicates that there was no chemical effect of the fillers [33].

Figure 9b shows that the LF20, QF20 and BF20 pastes presented greater cumulative heat compared to the REF paste. At the end of the analyzed period, it is observed that the amount of heat released by the LF20 paste was lower than the QF20 and BF20 pastes (despite the greater peak presented by LF20, verified in Figure 5a). Thus, there is a decrease in the hydration kinetics of the paste with LF. However, pastes with filler did not show noticeable variations between them with relation to cumulative heat. After a hundred hours, the cumulative heat was 429.74, 444.42 and 439.07J/g cement for LF20, QF20 and BF20 pastes, respectively.

It is believed that the LF used may be considered as an inert filler [10]. Hence, it is assumed that the use of LF contributed to the development of the early strength due to its better physical effect caused by its inherent

characteristics, providing stiffness to the mixture, and its particle size distribution in the mixture [34]. When the filler particle size decreases, filler particles are distributed more homogeneously in the cement paste and the whole mix tend to be more homogeneous, resulting in higher compressive strength [10].

## 5 CONCLUSIONS

Based on the results obtained, the following conclusions can be drawn:

- It is possible to incorporate up to 20% of limestone, quartz or crushed basalt filler in SLMs, achieving the desired fluidity;
- The use of limestone filler provided better mechanical performance at early ages and better response of dimensional stability when a maximum amount of 10% is added to SLM;
- Regarding SLMs produced with quartz filler, the compressive strength values were similar to those showed by SLMs containing limestone filler. Moreover, SLMs with quartz filler promoted the lowest shrinkage values when used 20% of filler;
- In SLMs with crushed basalt filler, it was verified a higher superplasticizer demand to achieve the target fluidity, especially when used 20% of filler. Despite of this, it was possible to achieve strength levels similar to those of SLMs with limestone and quartz filler. However, mortars containing crushed basalt filler exhibited the highest shrinkage values (at 20%) and this can indicate a limitation of its use in practice;
- It was verified that limestone, quartz and basalt filler have potential for use in the development of self-leveling mortars and, in general, perform better when used in contents of 20%, 20% e 10%, respectively.

## ACKNOWLEDGEMENTS

The authors acknowledgment the Central Laboratory of Electronic Microscopy (LCME) for technical support. They would also like to acknowledgment CAPES for the financial support and CNPq for research founds.

## REFERENCES

- [1] S. Seifert, J. Neubauer, and F. Goetz-Neunhoeffler, "Spatially resolved quantitative in-situ phase analysis of a self-leveling compound," *Cement Concr. Res.*, vol. 42, no. 7, pp. 919–927, 2012, <http://dx.doi.org/10.1016/j.cemconres.2012.03.012>.
- [2] E. Berodier and K. Scrivener, "Understanding the filler effect on the nucleation and growth of C-S-H," *J. Am. Ceram. Soc.*, vol. 97, no. 12, pp. 3764–3773, 2014, <http://dx.doi.org/10.1111/jace.13177>.
- [3] A. Kumar et al., "The filler effect: The influence of filler content and type on the hydration rate of tricalcium silicate," *J. Am. Ceram. Soc.*, vol. 100, no. 7, pp. 3316–3328, 2017, <http://dx.doi.org/10.1111/jace.14859>.
- [4] K. De Weerd, M. B. Haha, G. Le Saout, K. O. Kjellsen, H. Justnes, and B. Lothenbach, "Hydration mechanisms of ternary Portland cements containing limestone powder and fly ash," *Cement Concr. Res.*, vol. 41, no. 3, pp. 279–291, 2011, <http://dx.doi.org/10.1016/j.cemconres.2010.11.014>.
- [5] H. Fanghui, W. Qiang, L. Mutian, and M. Yingjun, "Early hydration properties of composite binder containing limestone powder with different finenesses," *J. Therm. Anal. Calorim.*, vol. 123, no. 2, pp. 1141–1151, 2016, <http://dx.doi.org/10.1007/s10973-015-5088-9>.
- [6] V. H. Nam and T. H. Chuong, "Influence of limestone powder and quang ngai basalt on strength of blended Portland cement," in *Proc. 3<sup>rd</sup> ACF Int. Conf. ACF/VCA*, 2008.
- [7] M. E.-S. I. Saraya, "Study physico-chemical properties of blended cements containing fixed amount of silica fume, blast furnace slag, basalt and limestone, a comparative study," *Constr. Build. Mater.*, vol. 72, pp. 104–112, 2014, <http://dx.doi.org/10.1016/j.conbuildmat.2014.08.071>.
- [8] S.-H. Kang, Y. Jeong, K. H. Tan, and J. Moon, "The use of limestone to replace physical filler of quartz powder in UHPFRC," *Cement Concr. Compos.*, vol. 94, pp. 238–247, 2018, <http://dx.doi.org/10.1016/j.cemconcomp.2018.09.013>.
- [9] M. Dobiszewska, A. K. Schindler, and W. Pichór, "Mechanical properties and interfacial transition zone microstructure of concrete with waste basalt powder addition," *Constr. Build. Mater.*, vol. 177, pp. 222–229, 2018, <http://dx.doi.org/10.1016/j.conbuildmat.2018.05.133>.
- [10] S. Liu, T. Zhang, Y. Guo, J. Wei, and Q. Yu, "Effects of SCMs particles on the compressive strength of micro-structurally designed cement paste: Inherent characteristic effect, particle size refinement effect, and hydration effect," *Powder Technol.*, vol. 330, pp. 1–11, 2018, <http://dx.doi.org/10.1016/j.powtec.2018.01.087>.
- [11] Y. Benachour, C. A. Davy, F. Skoczylas, and H. Houari, "Effect of a high calcite filler addition upon microstructural, mechanical, shrinkage and transport properties of a mortar," *Cement Concr. Res.*, vol. 38, no. 6, pp. 727–736, 2008, <http://dx.doi.org/10.1016/j.cemconres.2008.02.007>.

- [12] A. Itim, K. Ezziane, and E.-H. Kadri, "Compressive strength and shrinkage of mortar containing various amounts of mineral additions," *Constr. Build. Mater.*, vol. 25, no. 8, pp. 3603–3609, 2011, <http://dx.doi.org/10.1016/j.conbuildmat.2011.03.055>.
- [13] G. Egan, A. Kumar, N. Neithalath, and G. Sant, "Re-examining the influence of the inclusion characteristics on the drying shrinkage of cementitious composites," *Constr. Build. Mater.*, vol. 146, pp. 713–722, 2017, <http://dx.doi.org/10.1016/j.conbuildmat.2017.04.048>.
- [14] D. W. Mokarem, R. E. Weyers, and D. S. Lane, "Development of a shrinkage performance specifications and prediction model analysis for supplemental cementitious material concrete mixtures," *Cement Concr. Res.*, vol. 35, no. 5, pp. 918–925, 2005, <http://dx.doi.org/10.1016/j.cemconres.2004.09.013>.
- [15] E. Rozière, S. Granger, P. Turcry, and A. Loukili, "Influence of paste volume on shrinkage cracking and fracture properties of self-compacting concrete," *Cement Concr. Compos.*, vol. 29, no. 8, pp. 626–636, 2007, <http://dx.doi.org/10.1016/j.cemconcomp.2007.03.010>.
- [16] Associação Brasileira de Normas Técnicas, *Cimento Portland – Requisitos*, NBR 16697, 2018.
- [17] American Society for Testing and Materials, *Standard Specification for Portland Cement*, ASTM C150, 2020.
- [18] B. Benabed, E.-H. Kadri, L. Azzouz, and S. Kenai, "Properties of self-compacting mortar made with various types of sand," *Cement Concr. Compos.*, vol. 34, no. 10, pp. 1167–1173, 2012, <http://dx.doi.org/10.1016/j.cemconcomp.2012.07.007>.
- [19] S. A. Rizwan and T. A. Bier, "Blends of limestone powder and fly-ash enhance the response of self-compacting mortars," *Constr. Build. Mater.*, vol. 27, no. 1, pp. 398–403, 2012, <http://dx.doi.org/10.1016/j.conbuildmat.2011.07.030>.
- [20] M. A. S. Anjos, T. R. Araújo, R. L. S. Ferreira, E. C. Farias, and A. E. Martinelli, "Properties of self-leveling mortars incorporating a high-volume of sugar cane bagasse ash as partial Portland cement replacement," *J. Build. Eng.*, vol. 32, pp. 101694, 2020, <http://dx.doi.org/10.1016/j.job.2020.101694>.
- [21] G. Barluenga and F. Hernández-Olivares, "Self-levelling cement mortar containing grounded slate from quarrying waste," *Constr. Build. Mater.*, vol. 24, no. 9, pp. 1601–1607, 2010, <http://dx.doi.org/10.1016/j.conbuildmat.2010.02.033>.
- [22] Associação Brasileira de Normas Técnicas, *Argamassa para Assentamento e Revestimento de Paredes e Tetos – Preparo da Mistura para a Realização de Ensaio*, NBR 16541, 2016.
- [23] Associação Brasileira de Normas Técnicas, *Argamassa para Assentamento e Revestimento de Paredes e Tetos – Determinação da Resistência à Tração na Flexão e à Compressão*, NBR 13279, 2005.
- [24] Associação Brasileira de Normas Técnicas, *Argamassa para Assentamento e Revestimento de Paredes e Tetos – Determinação do Módulo de Elasticidade Dinâmico Através da Propagação de Onda Ultrassônica*, NBR 15630, 2009.
- [25] American Society for Testing and Materials, *Standard Test Method for Hygroscopic Sorption Isotherms of Building Materials*, ASTM C 1498-01, 2001.
- [26] American Society for Testing and Materials, *Standard Test Methods for Self-Leveling Mortars Containing Hydraulic Cements*, ASTM C 1708, 2016.
- [27] I. Mehdipour, M. S. Razzaghi, K. Amini, and M. Shekarchi, "Effect of mineral admixtures on fluidity and stability of self-consolidating mortar subjected to prolonged mixing time," *Constr. Build. Mater.*, vol. 40, pp. 1029–1037, 2013, <http://dx.doi.org/10.1016/j.conbuildmat.2012.11.108>.
- [28] H. M. Jennings, A. Kumar, and G. Sant, "Quantitative discrimination of the nano-pore-structure of cement paste during drying: new insights from water sorption isotherms," *Cement Concr. Res.*, vol. 76, pp. 27–36, 2015, <http://dx.doi.org/10.1016/j.cemconres.2015.05.006>.
- [29] R. M. Espinosa and L. Franke, "Inkbottle Pore-Method: prediction of hygroscopic water content in hardened cement paste at variable climatic conditions," *Cement Concr. Res.*, vol. 36, no. 10, pp. 1954–1968, 2006, <http://dx.doi.org/10.1016/j.cemconres.2006.06.011>.
- [30] M. Saeidpour and L. Wadsö, "Moisture equilibrium of cement based materials containing slag or silica fume and exposed to repeated sorption cycles," *Cement Concr. Res.*, vol. 69, pp. 88–95, 2015, <http://dx.doi.org/10.1016/j.cemconres.2014.12.005>.
- [31] I. Vlahinić, H. M. Jennings, and J. J. Thomas, "A constitutive model for drying of a partially saturated porous material," *Mech. Mater.*, vol. 41, no. 3, pp. 319–328, 2009, <http://dx.doi.org/10.1016/j.mechmat.2008.10.011>.
- [32] B. Ma, X. Wang, W. Liang, X. Li, and Z. He, "Study on early-age cracking of cement-based materials with superplasticizers," *Constr. Build. Mater.*, vol. 21, no. 11, pp. 2017–2022, 2007, <http://dx.doi.org/10.1016/j.conbuildmat.2006.04.012>.
- [33] B. Lothenbach, K. Scrivener, and R. D. Hooton, "Supplementary cementitious materials," *Cement Concr. Res.*, vol. 41, no. 12, pp. 1244–1256, 2011, <http://dx.doi.org/10.1016/j.cemconres.2010.12.001>.
- [34] P. Lawrence, M. Cyr, and E. Ringot, "Mineral admixtures in mortars: effect of inert materials on short-term hydration," *Cement Concr. Res.*, vol. 33, no. 12, pp. 1939–1947, 2003, [http://dx.doi.org/10.1016/S0008-8846\(03\)00183-2](http://dx.doi.org/10.1016/S0008-8846(03)00183-2).

---

**Author contributions:** TPS: conceptualization, data curation, formal analysis, methodology, writing - original draft, writing - review & editing. JCR: conceptualization, supervision, writing - review & editing.

**Editors:** Edna Possan, José Luiz Antunes de Oliveira e Sousa, Guilherme Aris Parsekian.







ORIGINAL ARTICLE

# Size effect on the methodology with cylinder specimens for FRP-to-concrete debonding analysis

*Efeito de escala na metodologia para análise do descolamento entre concreto e PRF com corpos de prova cilíndricos*

Luana Ferreira Borges<sup>a</sup>   
Antonio Carlos dos Santos<sup>b</sup> 

<sup>a</sup>Universidade de Brasília – UnB, Departamento de Engenharia Civil e Ambiental, Programa de Pós-graduação em Estruturas e Construção Civil, Brasília, DF, Brasil

<sup>b</sup>Universidade Federal de Uberlândia – UFU, Faculdade de Engenharia Civil, Programa de Pós-graduação em Engenharia Civil, Uberlândia, MG, Brasil

Received 17 December 2019  
Accepted 05 August 2020

**Abstract:** This is a study about the size effect on the methodology with concrete cylinder specimens for analysis of the debonding phenomenon at the interface between concrete and carbon fiber reinforced polymer (FRP). The influence of the concrete specimen size variation is analyzed by maintaining the same geometry in adhered FRP. Direct tensile experiments were performed with three dimensions of cylindrical concrete specimens (diameter × height) for analysis of size effect: 50 mm × 100 mm, 100 mm × 200 mm, and 150 mm × 300 mm. Ten different geometries of the composite material were tested. Two failure modes were observed in the experiments: debonding between the two materials and tensile failure in concrete specimens. In experiments with interface failure, the size of concrete specimens has no significant influence on maximum force, shear stress to peak, and stiffness in debonding between concrete and FRP. However, the use of smaller specimens for analysis of interface collapse is limited because the concrete reaches its normal stress capacity with a lower tensile force, and therefore, the failure often occurs in the concrete.

**Keywords:** size effect, debonding, FRP, direct tensile experiments.

**Resumo:** Este trabalho apresenta um estudo sobre o efeito de escala na metodologia para análise do fenômeno do colapso de interface entre concreto e polímero reforçado com fibra (PRF) de carbono por meio de corpos de prova cilíndricos. Buscou-se analisar a influência da variação da dimensão do corpo de prova ao manter a mesma geometria de PRF aderida. Para a análise do efeito de escala, foram realizados experimentos de tração direta com três dimensões de corpos de prova cilíndricos (diâmetro × altura): 50 mm × 100 mm, 100 mm × 200 mm, e 150 mm × 300 mm. Dez geometrias diferentes do material compósito foram testadas. Dois modos de falha foram observados nos experimentos: deslizamento entre os dois materiais e falha por tração no concreto. Nos experimentos com falha na interface, não se notou uma influência da dimensão do corpo de prova na força máxima, tensão de cisalhamento até o pico, e rigidez no descolamento entre concreto e PRF. No entanto, o uso de corpos de prova menores é limitado, pois muitas vezes é atingida a tensão normal limite que o concreto resiste, causando sua ruptura.

**Palavras-chave:** efeito de escala, descolamento, PRF, ensaios de tração direta.

**How to cite:** L. F. Borges and A. C. Santos, “Size effect on the methodology with cylinder specimens for FRP-to-concrete debonding analysis,” *Rev. IBRACON Estrut. Mater.*, vol. 14, no. 3, e14304, 2021, <https://doi.org/10.1590/S1983-41952021000300004>

## 1 INTRODUCTION

Fiber reinforced polymer (FRP) is one of the most modern materials for strengthening reinforced concrete structures. FRP application can be made in two ways: it is externally bonded reinforcement (EBR) on structural elements or, it is

Corresponding author: Luana Ferreira Borges. E-mail: [luana\\_f.borges@hotmail.com](mailto:luana_f.borges@hotmail.com)

Financial support: This study was financed in part by the Coordenação de Aperfeiçoamento de Pessoal de Nível Superior – Brasil (CAPES) – Finance Code 001. This study was financed in part by the Fundação de Amparo à Pesquisa do Estado de Minas Gerais – Minas Gerais, Brasil (FAPEMIG) – Finance Code APQ-00367-14.

Conflict of interest: Nothing to declare.



This is an Open Access article distributed under the terms of the Creative Commons Attribution License, which permits unrestricted use, distribution, and reproduction in any medium, provided the original work is properly cited.

near surface mounted (NSM) within grooves on the concrete cover. A great progress occurred in FRP research and studies for structural strengthening of reinforced concrete structures [1], [2] in the last decades. As a result, various standards and design guidelines were published [1]–[3]. FRP is also used for strengthening of metallic structures [4]–[7], masonry [4], [6], [8], [9], and wood structures [6], [10], [11].

Some advantages, compared to the use of other strengthening materials, are that FRP are noncorrosive, they are materials with high strength-to-weight [12], [13], and high stiffness-to-weight [1], [2], [14]–[16] ratios. However, there are some questions about failure modes, in particular the collapse at the interface, which occurs by means of FRP and concrete debonding in regions of high stress concentrations. One of the main failure mechanisms in FRP-strengthening concrete structures is the loss of adhesion between substrates and strengthening. This failure mode was verified in some experiments (e.g. [17]–[20]). Many studies about debonding were conducted, but initiation and the failure mechanism, relationship with local phenomena and influence of materials are not fully understood [21].

Basically, the main tests for analyzing debonding between concrete and FRP include shear experiments (single or double) and beam tests [22]. The single shear test is the most common methodology [22]. In this test, one FRP sheet is adhered to a prismatic concrete sample, and force is applied to the FRP, which is pulled until debonding occurs. In the double shear test, tensile force is applied simultaneously on two FRP sheets [23]. This methodology is preferred over the previous due to symmetry and for better control of induced normal stresses [24]. Bending experiments on beams include three-point bending tests and four-point bending tests. These bending experiments are performed on a beam strengthened with FRP on its bottom face. Bending tests better reproduce the actual interfacial stress state, but such tests are cumbersome to set up [24]. A review of the experimental tests between FRP and concrete can be found in Mukhtar and Faysal [23], which presents the pros and cons of each of the test methods.

Santos et al. [25] proposed a direct tensile test on concrete cylinder specimens (150 mm × 300 mm) for analysis of the bond strength of FRP-to-concrete joints (see Section: Methodology). They tested and corroborated this methodology. The authors demonstrated the reproducibility of the test. The main advantages of this test are the inexistence of large eccentricities, good reproducibility, the use of cylindrical specimens (a very common geometry in civil engineering), and one test allows obtaining three simultaneous interface tests [25]. Its main disadvantage is that the concrete specimens have a circular surface, while structural elements in which the debonding occurs are usually non-circular. However, the shear stress distribution along the length and the width of the FRP sheet has not been much influenced by the sheet curvature [25]. The objective of the present study was to evaluate this methodology with concrete cylinder specimens of different dimensions to analyze the size effect.

One of the main problems associated with the bond analysis is the significant difference between the largest dimension of the set (the length of a beam) and the smallest dimension (the thickness of the FRP strengthening) [26]. The debonding mechanism tend to follow the smallest geometrical dimension (the thickness of FRP), and the stress concentration associated with the debonding are distributed along few millimeters [26]. In this paper, the debonding mechanism is analyzed with direct tensile tests using 150 mm × 300 mm cylinder specimens and with smaller concrete cylinders than proposed by Santos et al. [25] methodology. The effect of the use of smaller concrete specimens is analyzed on the maximum debonding force and the stiffness.

The size effect on mechanical properties of concrete was a topic of interest to several researchers. The size effect is the variation in the strength with size changes in geometrically similar structures [27]. The influence of specimen size was noticed in tensile strength, compressive strength [28]–[32] and other mechanical properties. Del Viso et al. [31] observed the size effect on compressive strength is more noticed in concrete cubic specimens, in comparison with concrete cylinder specimens. Not only the average strength, but also the variability of results decreases as specimens increases [29]. However, increasing size does not result in a reduced strength from a size value. In other words, the strength *versus* characteristic dimensions of the cross-section diagram presents asymptotic trends [33]. In addition, there is a transition from ductile behavior to brittle behavior with the increase in dimensions of concrete specimens [27], [34]. The influence of element dimensions on characteristics is a property of so-called quasi-brittle materials [35], [36], such as concrete. Quasi-brittle materials have a relatively large fracture process zone, compared to cross section of structure [34], [37]. The size effect is most acute and most complex in these materials [37]. Some studies analyze the size effect on the edge debonding between concrete and FRP [38], the interfacial shear stress concentration at the carbon FRP cut-off regions and the failure mode of FRP-strengthened beams as a function of beam size and FRP thickness [39], and a comparison between analysis of full-scale beams and small “laboratory scale” beams in a study focused on the intermediate crack (IC) debonding [26].

### 1.1 Chen and Teng's model (2001)

Various analytical models are available for predicting the force that causes debonding between concrete and FRP. In this study, the experimental results (direct tensile tests) are compared to values predicted using the Chen and Teng's [40] bond strength model. This model is simple, rational and accurate, and it is based on fracture mechanics and experimental observations [40]. Lu et al. [41] compared prediction of 12 models with 253 test results. They concluded that the Chen and Teng's model is accurate, with a low coefficient of variation and a high correlation coefficient [41].

An important aspect of the FRP-to-concrete bond behavior is that there exists a bond length from which its increase will not increase the ultimate load [14], [41]–[45]. The effective length ( $L_e$ ) is a parameter in various analytical models. This value is a characteristic of the adhesively bonded joints [43], and its definition is an important part of all FRP strengthening calculations [44]. Chen and Teng [40] propose Equation 1 to compute the effective bond length.

$$L_e = \sqrt{\frac{E_p t_p}{\sqrt{f_c'}}} \quad (1)$$

where  $L_e$  = effective bond length (mm);  $E_p$  = Young's modulus of the bonded FRP plate (MPa);  $t_p$  = thickness of the bonded FRP plate (mm); and  $f_c'$  = cylinder concrete compressive strength (MPa).

In the Chen and Teng's [40] model, the prediction of maximum transferable load is made by Equation 2, in which the width ratio coefficient ( $\beta_p$ ) and the length ratio coefficient ( $\beta_L$ ) are defined by Equations 3 and 4, respectively.

$$P_u = 0.427 \beta_p \beta_L \sqrt{f_c'} b_p L_e \quad (2)$$

$$\beta_p = \sqrt{\frac{2 - (b_p / b_c)}{1 + (b_p / b_c)}} \quad (3)$$

$$\beta_L = \begin{cases} 1 & \text{if } L \geq L_e \\ \text{sen}\left(\frac{\pi L}{2L_e}\right) & \text{if } L < L_e \end{cases} \quad (4)$$

where  $P_u$  = maximum transferable load (kN);  $\beta_p$  = width ratio coefficient (dimensionless);  $\beta_L$  = length ratio coefficient (dimensionless);  $f_c'$  = cylinder concrete compressive strength (MPa);  $b_c$  = width of concrete member (mm);  $b_p$  = width of bonded FRP plate (mm);  $L_e$  = effective bond length (mm); and  $L$  = bond length (mm).

## 2 MATERIALS AND METHODS

### 2.1 Material properties

The fiber reinforced polymer consists of fibers (the structural component of FRP) with trade name of MBrace 120 in the sheet system and epoxy resin (the polymer component of FRP) with trade name of Viapol Carbon Saturante. The carbon fiber with unidirectional orientation of fibers has 0.117 mm thickness, 3900 MPa ultimate tensile strength, 240 GPa modulus of elasticity, and 1.55% ultimate tensile elongation. The epoxy resin has 29 MPa strength, 68 MPa compressive strength and 1470 MPa compression modulus. These properties are in the suppliers' catalogs.

The concrete is composed of cement containing pozzolanas (CPIV-32 cement), coarse basaltic aggregate (12.5 mm characteristic dimension), fine aggregate (1.18 mm characteristic dimension), water, and a superplasticizer. The proportions of cement, sand, coarse aggregate and water to cement ratio is 1.00: 1.50: 1.99: 0.49 by weight. The superplasticizer with sulphonated naphthalene composition was added in a proportion of 1.5% cement weight. The mechanical properties of concrete were evaluated at 90 days on cylinder specimens (diameter 100 mm, height 200 mm). The mechanical properties of concrete are listed in Table 1.

**Table 1.** Concrete material properties at 90 days.

Mechanical property	Number of experiments	Average value	Sample standard deviation
Compressive strength	20	38.9 MPa	4.7 MPa
Modulus of elasticity	30	36.5 GPa	3.6 GPa
Brazilian splitting test	20	3.41 MPa	0.7 MPa

**2.2 Methodology**

The direct tensile method proposed by Santos et al. [25] was used herein to analyze the bond capacity at the interface between FRP and concrete. In this methodology, two cylindrical concrete specimens are placed end-to-end and three FRP sheets are symmetrically adhered to the specimens (with an angle of 120 degrees between an FRP sheet and another FRP sheet). Each FRP sheet had three regions: upper adhesion region, unbonded region, and lower adhesion region. The length of the lower region is 1.5 times the length of the upper region to induce failure in the upper region. Figure 1 illustrates a scheme of specimen and FRP regions.

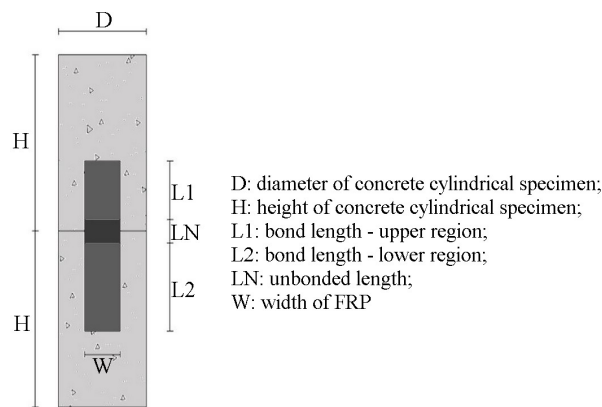


**Figure 1.** Specimen and FRP regions

Single shear test is one of the most performed experiments for analysis of debonding between concrete and FRP. The unbonded zone was adopted in some single shear tests with prismatic concrete specimens, but this region has not been tested in some experiments [41]. In shear experiments, a piece of concrete may be removed from the prism near the loaded end when the unbonded region does not exist or it is small [41]. However, this variation has no significant effect on the overall behavior provided the bond length is not too short [41].

In the static direct tensile test, the lower cylindrical specimen was fixed at its base, and a displacement of 0.12 micrometer per second was applied on the upper cylindrical specimen. Preparation of experiments is shown in the “Preparation of experiment” section. The application of tensile force induces the appearance of shear stresses at the interface between FRP and concrete. Data were acquired at a frequency of 10 Hz. A scheme of the experiment is shown in Figure 2.



**Figure 2.** Aspect of direct tensile test.

### 2.3 Preparation of experiment

All experiments were performed over 90-day-old concrete. At first, the ends of concrete specimens were ground aiming to achieve parallelism between the two ends of the cylinders. The bonded regions and the unbonded regions (see Figure 1) were delimited in the concrete with a permanent marker pen. These regions were sanded with a micro rotary tool in order to partially expose aggregates of concrete and to obtain a small surface irregularity. Water was thrown on the side of specimens to eliminate dust generated in the previous step. After a few hours, silicone was applied in the outside of the bonded and unbonded regions delimiting the perimeter, and inside the unbonded zone. Silicone prevents adhesion between resin and concrete.

The dry carbon fiber and the saturating epoxy resin presented in the “Material properties” section were used in the application of wet lay-up FRP system. A resin layer of 0.4 kilogram per square meter consumption was uniformly applied on the surface of the bonded and unbonded zones with a spatula. The carbon fiber was firmly pressed on the substrate with a metal-groove roller, which is also used to eliminate the entrapped air. After that, another resin layer with the same consumption was applied on the fiber. The experiments were performed after seven days of application of FRP.

A metallic apparatus was produced for direct tensile experiments in cylindrical specimens. This apparatus contains one metal shaft, a load cell of 100 KN, metal parts to allow a simply supported connection at the point of loading, plates, and metal rings. Three pairs of metal rings, with internal diameters of 150 mm, 100 mm, and 50 mm, were produced. In these pairs, each ring is 75 mm high, 50 mm high, and 22 mm high, respectively. The pair of rings with an inner diameter of 50 mm is inserted into the pair of rings with an inner diameter of 100 mm, during experiments with 50 mm × 100 mm specimens. The apparatus is shown in Figures 3, 4 and 5. The set (concrete specimens and FRP sheets) was fixed in the plates and metal rings with screws and epoxy-based adhesive. The experiment was performed three days after application of adhesive.

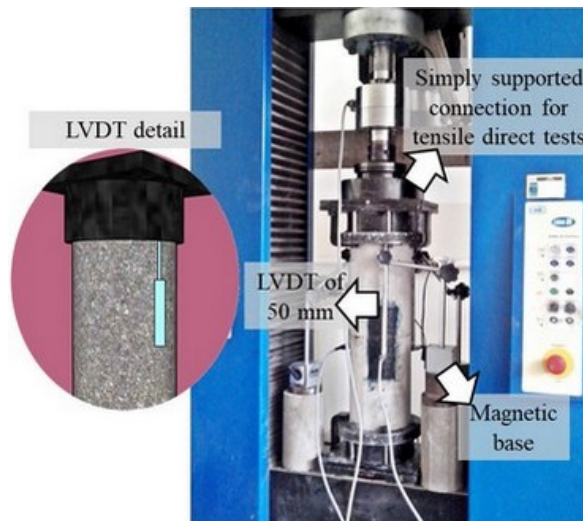


Figure 3. Apparatus with internal diameter of 150 mm for conducting direct tensile tests.

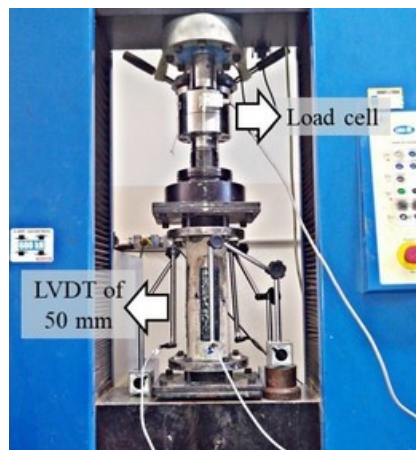
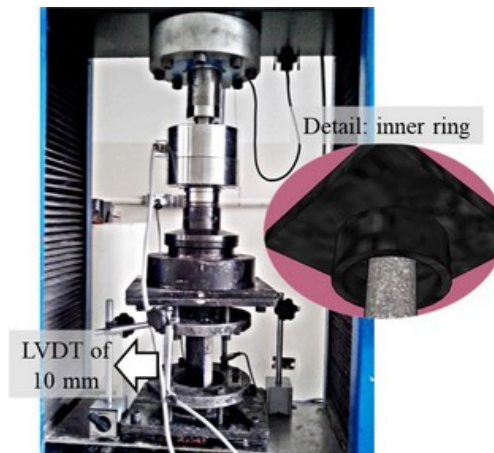


Figure 4. Apparatus with internal diameter of 100 mm for conducting direct tensile tests.



**Figure 5.** Apparatus with internal diameter of 50 mm for conducting direct tensile tests.

Three linear variable differential transformers (LVDT) were used in each experiment to measure of vertical displacement. Each LVDT was placed parallel to the center of an FRP sheet, in the upper part of the metallic apparatus, in the vertical direction. In experiments with 50 mm × 100 mm specimens, each LVDT was placed on the upper metallic plate (see Figure 5). In experiments with 100 mm × 200 mm specimens and 150 mm × 300 mm specimens, each LVDT was placed on the upper metallic ring (see Figures 3 and 4).

#### 2.4 Application of the Chen and Teng’s model (2001)

In this study, some considerations were adopted to compare the experimental results (Santos et al. [25] methodology) to the force values predicted using the Chen and Teng’s model [40], according to Equations 5, 6 and 7.

$$L = LI \tag{5}$$

$$b_c = 2\pi R = \pi D \tag{6}$$

$$b_p = 3W \tag{7}$$

where  $L$  = bond length (mm);  $LI$  = bond length - upper region (mm);  $b_c$  = width of concrete member (mm);  $R$  = cylindrical specimen radius (mm);  $D$  = diameter of concrete cylindrical specimens (mm);  $b_p$  = width of bonded FRP plates (mm); and  $W$  = width of an FRP sheet in the direct tensile test (mm).

### 3 EXPERIMENTAL PROGRAM

Three dimensions of cylindrical specimens (diameter × height) were used for analysis of size effect: 50 mm × 100 mm, 100 mm × 200 mm, and 150 mm × 300 mm, as shown in Figure 6. The influence of specimen size on the debonding between concrete and FRP was evaluated for ten different geometries of FRP. These geometries are listed in Table 2. In all experiments, the length of unbonded zone (LN) was 40 mm: 20 mm on the upper specimen and 20 mm on the lower specimen. Santos et al. [25] defined this length of the unbonded zone by means of two-dimensional and three-dimensional numerical simulations of the stress distribution along the interface.



Figure 6. Variation in specimen dimensions.

Table 2. Experimental program.

Geometry code	FRP geometry	50 mm × 100 mm cylindrical specimen	100 mm × 200 mm cylindrical specimen	150 mm × 300 mm cylindrical specimen
G01	L1 = 33 mm	X	X	X
	L2 = 50 mm			
	W = 10 mm			
G02	L1 = 33 mm	X	X	X
	L2 = 50 mm			
	W = 20 mm			
G03	L1 = 33 mm		X	X
	L2 = 50 mm			
	W = 40 mm			
G04	L1 = 33 mm		X	X
	L2 = 50 mm			
	W = 60 mm			
G05	L1 = 33 mm		X	X
	L2 = 50 mm			
	W = 80 mm			
G06	L1 = 50 mm		X	X
	L2 = 75 mm			
	W = 10 mm			
G07	L1 = 50 mm		X	X
	L2 = 75 mm			
	W = 20 mm			
G08	L1 = 50 mm		X	X
	L2 = 75 mm			
	W = 40 mm			
G09	L1 = 50 mm		X	X
	L2 = 75 mm			
	W = 60 mm			
G10	L1 = 50 mm		X	X
	L2 = 75 mm			
	W = 80 mm			
		2 experiments	10 experiments	10 experiments
		4 specimens	20 specimens	20 specimens

## 4 RESULTS AND DISCUSSIONS

### 4.1 Failure modes

Twenty-two experiments were conducted. Two failure modes were observed in the experiments: failure in concrete specimens and debonding in the interface between FRP and concrete. Figures 7 and 8 illustrate failure modes. Debonding failures were observed in 63.6% of these experiments. Tests with concrete tensile failure are not valid when analyzing the interface between concrete and FRP, and they are presented only for a verification of the maximum stress values. In the experiments with concrete failure, ruptures were very close to the end of the metal ring in which specimen was inserted (see Figure 8). There is probably a stress concentration at this place. For this reason, it is intended to make a stress analysis in future studies. The metallic apparatus produced in this work and the methodology of Santos et al. [25] will be considered in stress analysis.

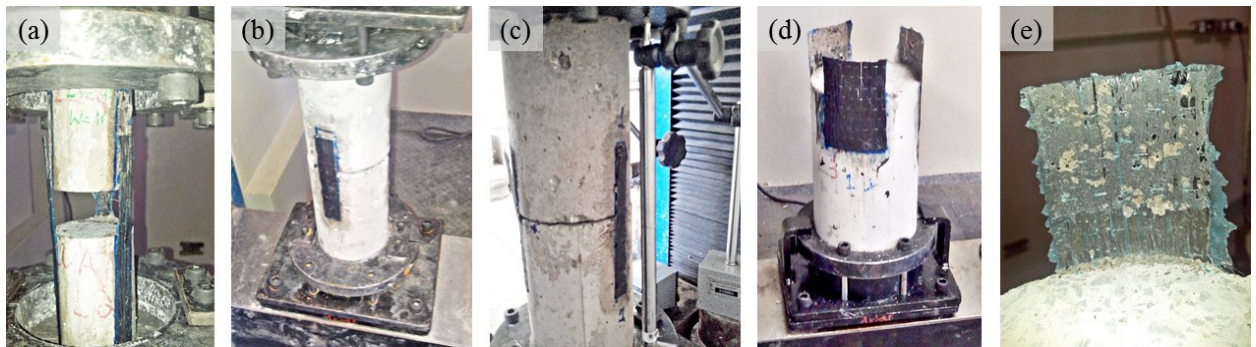


**Figure 7.** Experiments with debonding failure between concrete and FRP: a) FRP geometry G01 and 50 mm × 100 mm specimens; b) FRP geometry G02 and 100 mm × 200 mm specimens; c) FRP geometry G01 and 100 mm × 200 mm specimens; d) FRP geometry G05 and 150 mm × 300 mm specimens; e) FRP geometry G09 and 150 mm × 300 mm specimens.



**Figure 8.** Experiments with concrete failure: a) FRP geometry G02 and 50 mm × 100 mm specimens; b) FRP geometry G05 and 100 mm × 200 mm specimens; c) FRP geometry G08 and 100 mm × 200 mm specimens; d) FRP geometry G10 and 100 mm × 200 mm specimens; e) FRP geometry G10 and 150 mm × 300 mm specimens.

The failure modes in each experiment are listed in Table 3. This table also contains values of maximum tensile force ( $P_{max}$ ) reached in each experiment, values of normal tensile stress ( $\sigma$ ) on the concrete relating to this force, and values of maximum shear stress ( $\tau$ ) at the interface between concrete and FRP. The stress  $\sigma$  is the maximum force divided by the cross-sectional area of concrete specimen, and the stress  $\tau$  is the maximum force divided by the upper adhesion area of the three FRP sheets. In case of interface failures, shear stress refers to stress reached in debonding the first FRP sheet. Figure 9 shows a comparison between the maximum force values in experiments with debonding failure and the force values predicted by Chen and Teng's model, with considerations in the section "Application of the Chen and Teng's model". The experimental results are in good agreement with the model.



**Table 3.** Failure mode, maximum tensile force (Pmax), normal tensile stress on the concrete ( $\sigma$ ), and shear stress at the interface between concrete and FRP ( $\tau$ ).

Geometry code	50 mm × 100 mm cylindrical specimen	100 mm × 200 mm cylindrical specimen	150 mm × 300 mm cylindrical specimen
G01	Debonding	Debonding	Debonding
	Pmax = 4.30 KN	Pmax = 4.60 KN	Pmax = 4.51 KN
	$\sigma = 2.19$ MPa	$\sigma = 0.59$ MPa	$\sigma = 0.25$ MPa
G02	$\tau = 4.35$ MPa	$\tau = 4.65$ MPa	$\tau = 4.55$ MPa
	Concrete failure	Debonding	Debonding
	Pmax = 4.74 KN	Pmax = 9.12 KN	Pmax = 8.90 KN
G03	$\sigma = 2.41$ MPa	$\sigma = 1.16$ MPa	$\sigma = 0.50$ MPa
	$\tau = 2.39$ MPa	$\tau = 4.60$ MPa	$\tau = 4.49$ MPa
	Concrete failure	Concrete failure	Debonding
G04	Pmax = 10.92 KN	Pmax = 17.92 KN	Pmax = 17.92 KN
	$\sigma = 1.39$ MPa	$\sigma = 1.01$ MPa	$\sigma = 1.01$ MPa
	$\tau = 2.76$ MPa	$\tau = 4.52$ MPa	$\tau = 4.52$ MPa
G05	Concrete failure	Concrete failure	Debonding
	Pmax = 11.99 KN	Pmax = 11.75 KN	Pmax = 11.75 KN
	$\sigma = 1.53$ MPa	$\sigma = 0.66$ MPa	$\sigma = 0.66$ MPa
G06	$\tau = 2.02$ MPa	$\tau = 1.98$ MPa	$\tau = 1.98$ MPa
	Concrete failure	Concrete failure	Debonding
	Pmax = 9.21 KN	Pmax = 22.47 KN	Pmax = 22.47 KN
G07	$\sigma = 1.17$ MPa	$\sigma = 1.27$ MPa	$\sigma = 1.27$ MPa
	$\tau = 1.16$ MPa	$\tau = 2.84$ MPa	$\tau = 2.84$ MPa
	Debonding	Debonding	Debonding
G08	Pmax = 6.30 KN	Pmax = 6.15 KN	Pmax = 6.15 KN
	$\sigma = 0.80$ MPa	$\sigma = 0.35$ MPa	$\sigma = 0.35$ MPa
	$\tau = 4.20$ MPa	$\tau = 4.10$ MPa	$\tau = 4.10$ MPa
G09	Debonding	Debonding	Debonding
	Pmax = 8.95 KN	Pmax = 10.47 KN	Pmax = 10.47 KN
	$\sigma = 1.14$ MPa	$\sigma = 0.59$ MPa	$\sigma = 0.59$ MPa
G10	$\tau = 2.98$ MPa	$\tau = 3.49$ MPa	$\tau = 3.49$ MPa
	Concrete failure	Concrete failure	Debonding
	Pmax = 10.61 KN	Pmax = 19.64 KN	Pmax = 19.64 KN
G11	$\sigma = 1.35$ MPa	$\sigma = 1.11$ MPa	$\sigma = 1.11$ MPa
	$\tau = 1.77$ MPa	$\tau = 3.27$ MPa	$\tau = 3.27$ MPa
	Concrete failure	Concrete failure	Debonding
G12	Pmax = 14.84 KN	Pmax = 29.69 KN	Pmax = 29.69 KN
	$\sigma = 1.89$ MPa	$\sigma = 1.68$ MPa	$\sigma = 1.68$ MPa
	$\tau = 1.65$ MPa	$\tau = 3.30$ MPa	$\tau = 3.30$ MPa
G13	Concrete failure	Concrete failure	Concrete failure
	Pmax = 13.60 KN	Pmax = 34.23 KN	Pmax = 34.23 KN
	$\sigma = 1.73$ MPa	$\sigma = 1.94$ MPa	$\sigma = 1.94$ MPa
G14	$\tau = 1.13$ MPa	$\tau = 2.85$ MPa	$\tau = 2.85$ MPa

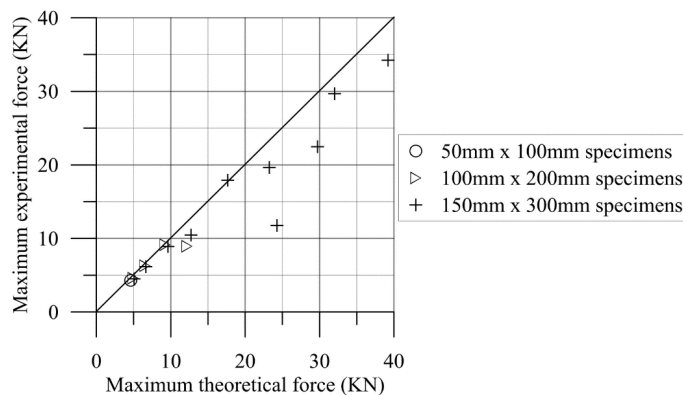


**Figure 9.** Comparison between experimental maximum force and theoretical maximum force.

In Table 3, in some FRP geometries, it can be observed that concrete failure occurred in experiments with smaller specimens (50 mm × 100 mm and 100 mm × 200 mm), while debonding failure was verified in experiments with larger specimens (150 mm × 300 mm). Cross-sectional area of 150 mm × 300 mm cylinders is larger than the cross-sectional area of the smaller specimens, and the concrete of all specimens had the same mixing ratio. Therefore, a higher tensile force can be applied in experiments with 150 mm × 300 mm specimens before reaching the tensile strength of the concrete, compared to experiments with 50 mm × 100 mm and 100 mm × 200 mm concrete specimens. Shear stress required to cause the composite debonding was not reached in experiments with concrete failure because concrete reached first the normal tensile strength.

In general, failure mode has been altered to concrete failure as the strengthening perimeter increased to a same specimen size. Therefore, concrete becomes the “weakest element” of the system as the perimeter of adhered FRP increases significantly, and no longer the interface between concrete and FRP. This shows that FRP strengthening in concrete structure is efficient.

#### 4.2 Considerations on experiments with concrete failure

Some initial excerpts from plot of load *versus* displacement in experiments are presented in this section and in the next section. In experiments with debonding failures, the initial excerpt represents the behavior regarding the debonding of the first FRP sheet. The three LVDT presented very similar behavior in each experiment. For this reason, displacement represented in each graph is the average of the three values obtained in each test.

A stiffness comparison between two experiments with the same FRP geometry and different specimen dimensions is made in Figure 10, in which failure was due to concrete failure. A smaller force was reached in the experiment with 100 mm × 200 mm cylindrical specimens, in comparison with the experiment with 150 mm × 300 mm specimens. However, the slopes of the curves were very similar in the two cases. As a curiosity, two graphs (Figure 11) are presented, in which experiments with the same FRP geometry, different dimensions of specimens, and different failure modes were considered. In these cases, the slopes of graphs were very similar in the two failure modes for the same FRP geometry, especially at the initial excerpt of load *versus* displacement curves. There is a significant reduction in stiffness near the failure in the curve of experiment with concrete rupture, but the initial excerpt of this graph was very similar to the curve of the experiment with debonding failure.

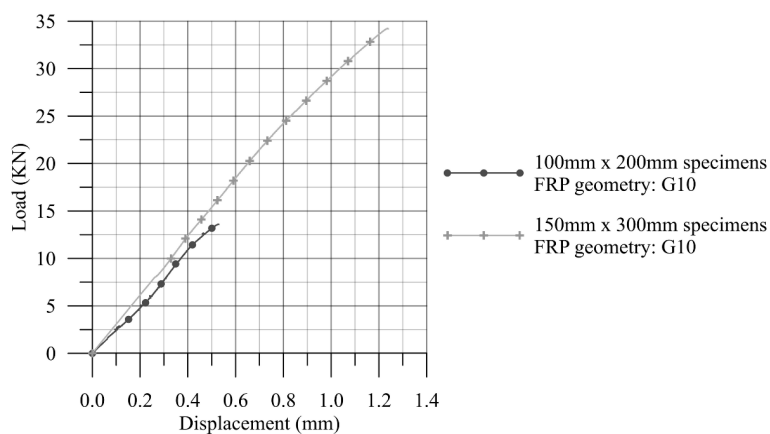


**Figure 10.** Plot of load *versus* displacement to the peak in experiments with the same FRP geometry and concrete failure.

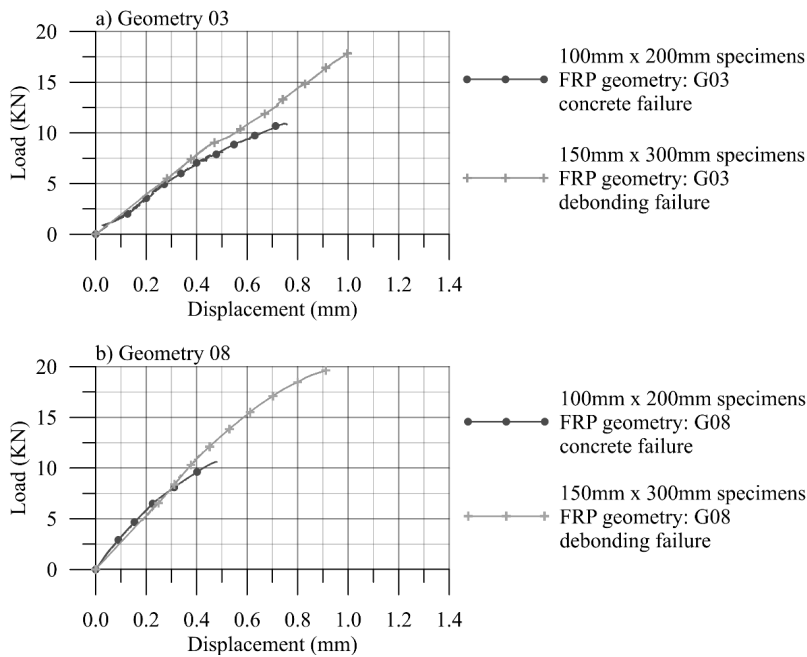


Figure 11. Plot of load versus displacement to the peak in experiments with the same FRP geometry and different failure modes.

### 4.3 Size effect on interface failure between concrete and FRP

In this section, the cases in which debonding failure was observed in experiments with different dimensions of concrete specimens and the same dimensions of FRP sheets are analyzed. Thus, experiments with the FRP geometries G01, G02, G06 and G07 are considered. The maximum shear stress values in these experiments are shown in Figure 12. Table 3 contains the maximum tensile force (Pmax) in these experiments. The values of maximum force and shear stress were very similar in experiments with debonding failure, different dimensions of specimens, and same FRP geometry. The differences in maximum shear strength in relation to the experiments with 150 mm × 300 mm (the specimens proposed in the methodology of Santos et al. [25]) are: 4.40% decrease for 50 mm × 100 mm specimens and G01 geometry, 2.20% increase for 100 mm × 200 mm specimens and G01 geometry, 2.45% increase for 100 mm × 200 mm specimens and G02 geometry, 2.43% increase for 100 mm × 200 mm specimens and G06 geometry, and 14.61% decrease for 100 mm × 200 mm specimens and G07 geometry.

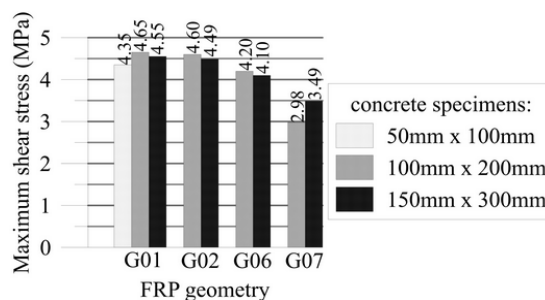


Figure 12. Comparison of the maximum shear stress in the debonding failure in experiments with different specimen dimensions.

The greatest difference in shear stress and maximum force values, in experiments with the same FRP geometry and debonding failure, was registered in the experiments with G07 geometry (14.61% decrease in maximum shear strength for 100 mm × 200 mm specimens compared to the result with 150 mm × 300 mm specimens). In experiments with debonding failure, there is a tendency for a maximum force to increase when the width is the same and bond length augments, as shown in Figure 13. This was verified in experiments with 100 mm × 200 mm and 150 mm × 300 mm specimens. However, while increasing the bond length, the maximum force decreased in the experiments with

100 mm × 200 mm cylinders and width of 20 mm (G02 and G07 geometries). Therefore, according to the tendency of the maximum force values (Figure 13), a greater force should have been reached in the experiment with 100 mm × 200 mm specimens and G07 geometry, and consequently a greater maximum shear strength should have been reached. Some reason may have caused the drop of the maximum force in debonding in the experiment with 100 mm × 200 mm specimens and G07 geometry. The reasons for this reduction may be the use of specimens with a defect, error in preparation of the resin, deficiency in the fiber debonding process (for example, non-application of required pressure), among others. In addition, a readjustment occurred in the position of the parts of the metallic apparatus during this experiment, and this readjustment may have influenced the maximum strength.

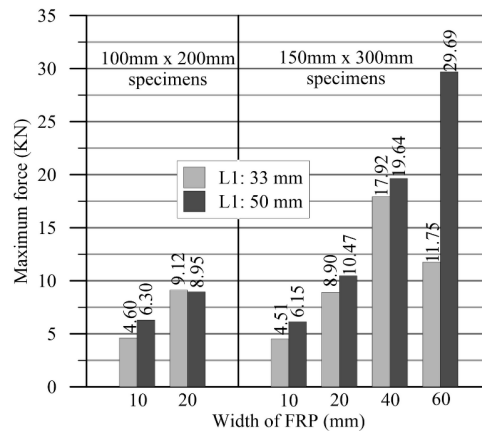


Figure 13. Influence of the bond length on the maximum debonding force.

Finally, the influence of the specimen size on the plot of load versus displacement in experiments with debonding failure is evaluated in Figure 14. Readjustments in the position were observed in some experiments, in parts that were not graphically presented in Figure 14. There is no significant influence on stiffness due to change in the size of concrete specimens.

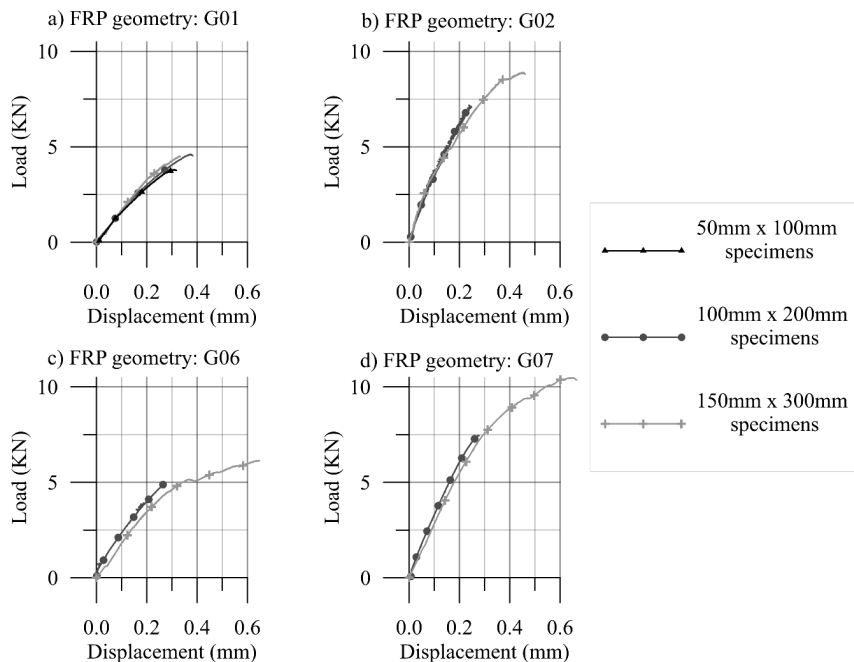


Figure 14. Initial portions of load versus displacement graphs in experiments with different dimensions of concrete specimens, the same FRP geometry, and debonding failure between concrete and FRP.

## 5 CONCLUSIONS

In this study, the test for evaluating the debonding between FRP and concrete by means of direct tensile on concrete cylinders was carried out on specimens of different dimensions for the evaluation of the size effect. Two failure modes were observed in the experiments: debonding between the two materials and failure in concrete specimens (when the concrete's tensile strength was reached). In this methodology, concrete failure is not desirable, because the test is done for evaluate the debonding phenomenon. In experiments with debonding failure, the size of concrete specimens has no significant influence on maximum force ( $P_{max}$ ), shear stress to the peak, and stiffness in debonding between concrete and FRP. The interface collapse was found in experiments with small specimens (50 mm × 100 mm and 100 mm × 200 mm) with results similar to those obtained in experiments with 150 mm × 300 mm specimens. In other words, analysis of the debonding in experiments with small cylindrical concrete specimens also leads to good results. Nevertheless, the use of smaller specimens for interface collapse analysis is limited because the failure often occurs in the concrete (the concrete reaches its normal stress capacity with a lower value of tensile force). Since its cross section is larger, a greater tensile force can be applied to 150 mm × 300 mm specimens, compared to smaller specimens. For the same FRP geometry, small concrete cylinders are more susceptible to concrete failure. Thus, the use of larges specimens of concrete (for example, 150 mm × 300 mm cylinders) is recommended in future studies with the same methodology of this paper.

## ACKNOWLEDGEMENTS

The authors gratefully acknowledge CAPES (Coordenação de Aperfeiçoamento de Pessoal de Nível Superior) and FAPEMIG (Fundação de Amparo à Pesquisa do Estado de Minas Gerais) for financial support.

## REFERENCES

- [1] A. K. El-Sayed and K. Soudki, "Evaluation of shear design equations of concrete beams with FRP reinforcement," *J. Compos. Constr.*, vol. 15, no. 1, pp. 9–20, 2011, [http://dx.doi.org/10.1061/\(ASCE\)CC.1943-5614.0000158](http://dx.doi.org/10.1061/(ASCE)CC.1943-5614.0000158).
- [2] R. H. Haddad, R. Z. Al-Rousan, and B. K. Al-Sedyiri, "Repair of shear-deficient and sulfate-damaged reinforced concrete beams using FRP composites," *Eng. Struct.*, vol. 56, pp. 228–238, 2013, <http://dx.doi.org/10.1016/j.engstruct.2013.05.007>.
- [3] A. Carpinteri, P. Cornetti, G. Lacidogna, and M. Paggi, "Towards a unified approach for the analysis of failure modes in FRP-retrofitted concrete beams," *Adv. Struct. Eng.*, vol. 12, no. 5, pp. 715–729, 2009, <http://dx.doi.org/10.1260/136943309789867863>.
- [4] K. Lang and A. Schumacher, "Strengthening of masonry and metallic structures," in *The International Handbook of FRP Composites in Civil Engineering*, M. Zoghi, Ed., Boca Raton: CRC Press, 2014, ch. 17, pp. 293–312.
- [5] A. Manalo, C. Sirimanna, W. Karunasena, L. McGarva, and P. Falzon, "Pre-impregnated carbon fibre reinforced composite system for patch repair of steel I-beams," *Constr. Build. Mater.*, vol. 105, pp. 365–376, 2016, <http://dx.doi.org/10.1016/j.conbuildmat.2015.12.172>.
- [6] O. Rabinovitch, "Dynamic debonding in concrete beams strengthened with composite materials," *Int. J. Solids Struct.*, vol. 49, no. 26, pp. 3641–3658, 2012, <http://dx.doi.org/10.1016/j.ijsoistr.2012.07.025>.
- [7] T. J. Stratford and J. F. Chen, "Designing for tapers and defects in FRP-strengthened metallic structures," in *Int. Symp. Bond Behav. FRP Struct. BBFS*, 2005, pp. 453–458. [Online]. Available: [http://www.research.ed.ac.uk/portal/files/4127274/c2005\\_1.pdf](http://www.research.ed.ac.uk/portal/files/4127274/c2005_1.pdf)
- [8] V. Gattulli, E. Lofrano, A. Paolone, and G. Pirolli, "Performances of FRP reinforcements on masonry buildings evaluated by fragility curves," *Comput. Struc.*, vol. 190, pp. 150–161, 2017, <http://dx.doi.org/10.1016/j.compstruc.2017.05.012>.
- [9] B. Pantò, F. Cannizzaro, S. Caddemi, I. Calì, C. Chàcara, and P. B. Lourenço, "Nonlinear modelling of curved masonry structures after seismic retrofit through FRP reinforcing," *Buildings*, vol. 7, no. 3, pp. 79, 2017, <http://dx.doi.org/10.3390/buildings7030079>.
- [10] D. Lau, Q. Qiu, A. Zhou, and C. L. Chow, "Long term performance and fire safety aspect of FRP composites used in building structures," *Constr. Build. Mater.*, vol. 126, pp. 573–585, 2016, <http://dx.doi.org/10.1016/j.conbuildmat.2016.09.031>.
- [11] K. U. Schober, A. M. Harte, R. Kliger, R. Jockwer, Q. Xu, and J. F. Chen, "FRP reinforcement of timber structures," *Constr. Build. Mater.*, vol. 97, pp. 106–118, 2015, <http://dx.doi.org/10.1016/j.conbuildmat.2015.06.020>.
- [12] F. Greco, L. Leonetti, and P. Lonetti, "A two-scale failure analysis of composite materials in presence of fiber/matrix crack initiation and propagation," *Compos. Struct.*, vol. 95, pp. 582–597, 2013, <http://dx.doi.org/10.1016/j.compstruct.2012.08.035>.
- [13] H. R. E. Houachine, Z. Sereir, B. Kerboua, and K. Hadjazi, "Combined cohesive-bridging zone model for prediction of the debonding between the FRP and concrete beam interface with effect of adherend shear deformations," *Compos., Part B Eng.*, vol. 45, no. 1, pp. 871–880, 2013, <http://dx.doi.org/10.1016/j.compositesb.2012.08.009>.
- [14] L. Biolzi, C. Ghittoni, R. Fedele, and G. Rosati, "Experimental and theoretical issues in FRP-concrete bonding," *Constr. Build. Mater.*, vol. 41, pp. 182–190, 2013, <http://dx.doi.org/10.1016/j.conbuildmat.2012.11.082>.

- [15] M. M. Fayyadh and H. A. Razak, "Analytical and experimental study on repair effectiveness of CFRP sheets for RC beams," *J. Civ. Eng. Manag.*, vol. 20, no. 1, pp. 21–31, 2013, <http://dx.doi.org/10.3846/13923730.2013.799095>.
- [16] J. G. Teng, J. F. Chen, S. T. Smith, and L. Lam, *FRP Strengthened RC Structures*. Chichester: John Wiley & Sons, 2002.
- [17] M. R. Aram, C. Czaderski, and M. Motavalli, "Debonding failure modes of flexural FRP-strengthened RC beams," *Compos., Part B Eng.*, vol. 39, no. 5, pp. 826–841, 2008, <http://dx.doi.org/10.1016/j.compositesb.2007.10.006>.
- [18] J. A. O. Barros, S. J. E. Dias, and J. L. T. Lima, "Efficacy of CFRP-based techniques for the flexural and shear strengthening of concrete beams," *Cement Concr. Compos.*, vol. 29, no. 3, pp. 203–217, 2007, <http://dx.doi.org/10.1016/j.cemconcomp.2006.09.001>.
- [19] H. C. Biscaia, M. A. G. Silva, and C. Chastre, "An experimental study of GFRP-to-concrete interfaces submitted to humidity cycles," *Compos. Struct.*, vol. 110, no. 1, pp. 354–368, 2014, <http://dx.doi.org/10.1016/j.compstruct.2013.12.014>.
- [20] J. Yao and J. G. Teng, "Plate end debonding in FRP-plated RC beams-I: Experiments," *Eng. Struct.*, vol. 29, no. 10, pp. 2457–2471, 2007, <http://dx.doi.org/10.1016/j.engstruct.2006.11.022>.
- [21] H. Toutanji, M. Han, and E. Ghorbel, "Interfacial bond strength characteristics of FRP and RC substrate," *J. Compos. Constr.*, vol. 16, no. 1, pp. 35–46, 2012, [http://dx.doi.org/10.1061/\(ASCE\)CC.1943-5614.0000236](http://dx.doi.org/10.1061/(ASCE)CC.1943-5614.0000236).
- [22] T. Mohammadi, "Failure mechanisms and key parameters of FRP debonding from cracked beams," Ph.D. dissertation, Marquette Univ., Milwaukee, Wis., 2014.
- [23] F. M. Mukhtar and R. M. Faysal, "A review of test methods for studying the FRP-concrete interfacial bond behavior," *Constr. Build. Mater.*, vol. 169, pp. 877–887, Apr 2018, <http://dx.doi.org/10.1016/j.conbuildmat.2018.02.163>.
- [24] A. Serbescu, M. Guadagnini, and K. Pilakoutas, "Standardised double-shear test for determining bond of FRP to concrete and corresponding model development," *Compos., Part B Eng.*, vol. 55, pp. 277–297, Dec 2013, <http://dx.doi.org/10.1016/j.compositesb.2013.06.019>.
- [25] A. C. Santos, T. N. Bittencourt, and R. Gettu, "Experimental analysis of the interface between CFRP and concrete through use of cylindrical specimens," in *6th Int. Symp. FRP Reinf. Concr. Struct.*, 2003, pp. 173–182. [http://dx.doi.org/10.1142/9789812704863\\_0014](http://dx.doi.org/10.1142/9789812704863_0014).
- [26] E. Ben Dror and O. Rabinovitch, "Size effect in the debonding failure of FRP strengthened beams," *Eng. Fract. Mech.*, vol. 156, pp. 161–181, May 2016, <http://dx.doi.org/10.1016/j.engfracmech.2016.02.007>.
- [27] S. Moallemi, S. Pietruszczak, and Z. Mróz, "Deterministic size effect in concrete structures with account for chemo-mechanical loading," *Comput. Struct.*, vol. 182, pp. 74–86, 2017, <http://dx.doi.org/10.1016/j.compstruc.2016.10.003>.
- [28] G. Muciaccia, G. Rosati, and G. Di Luzio, "Compressive failure and size effect in plain concrete cylindrical specimens," *Constr. Build. Mater.*, vol. 137, pp. 185–194, 2017, <http://dx.doi.org/10.1016/j.conbuildmat.2017.01.057>.
- [29] A. M. Neville, *Properties of Concrete*, 5th ed. Harlow: Pearson, 2011.
- [30] C. Ozyildirim and N. J. Carino, "Concrete strength testing," in *Significance of Tests and Properties of Concrete and Concrete-Making Materials*, J. F. Lamond and J. H. Pielert, Eds., West Conshohocken: ASTM Int., 2006, ch. 13, pp. 125–140, <http://dx.doi.org/10.1520/STP37731S>.
- [31] J. R. Del Viso, J. R. Carmona, and G. Ruiz, "Shape and size effects on the compressive strength of high-strength concrete," *Cement Concr. Res.*, vol. 38, no. 3, pp. 386–395, 2008, <http://dx.doi.org/10.1016/j.cemconres.2007.09.020>.
- [32] Ş. Yazıcı and G. İnan Sezer, "The effect of cylindrical specimen size on the compressive strength of concrete," *Build. Environ.*, vol. 42, no. 6, pp. 2417–2420, 2007, <http://dx.doi.org/10.1016/j.buildenv.2006.06.014>.
- [33] A. Carpinteri, "Scaling laws and renormalization-groups for strength and toughness of disordered materials," *Int. J. Solids Struct.*, vol. 31, no. 3, pp. 291–302, 1994, [http://dx.doi.org/10.1016/0020-7683\(94\)90107-4](http://dx.doi.org/10.1016/0020-7683(94)90107-4).
- [34] Z. P. Bažant and J.-L. Le, *Probabilist Mechanics of Quasibrittle Structures: Strength, Lifetime and Size Effect*. Cambridge: Camb. Univ. Press, 2017. <http://dx.doi.org/10.1017/9781316585146>.
- [35] Z. P. Bažant, "Probability distribution of energetic-statistical size effect in quasibrittle fracture," *Probab. Eng. Mech.*, vol. 19, no. 4, pp. 307–319, 2004, <http://dx.doi.org/10.1016/j.probengmech.2003.09.003>.
- [36] J. Vorel, M. Gattu, and Z. P. Bažant, "Size effect in flexure of prestressed concrete beams failing by compression softening," *J. Struct. Eng.*, vol. 140, no. 10, pp. 1–8, 2014, [http://dx.doi.org/10.1061/\(ASCE\)ST.1943-541X.0000983](http://dx.doi.org/10.1061/(ASCE)ST.1943-541X.0000983).
- [37] Z. P. Bažant, *Scaling of Structural Strength*, 2nd ed. Burlington: Elsevier, 2005.
- [38] A. Carpinteri, P. Cornetti, and N. Pugno, "Edge debonding in FRP strengthened beams: stress versus energy failure criteria," *Eng. Struct.*, vol. 31, no. 10, pp. 2436–2447, Oct 2009, <http://dx.doi.org/10.1016/j.engstruct.2009.05.015>.
- [39] M. Maalej and K. S. Leong, "Effect of beam size and FRP thickness on interfacial shear stress concentration and failure mode of FRP-strengthened beams," *Compos. Sci. Technol.*, vol. 65, no. 7–8, pp. 1148–1158, Jun 2005, <http://dx.doi.org/10.1016/j.compscitech.2004.11.010>.
- [40] J. F. Chen and J. G. Teng, "Anchorage strength Models for FRP and steel plates," *J. Struct. Eng.*, vol. 127, no. 7, pp. 784–791, 2001, [http://dx.doi.org/10.1061/\(ASCE\)0733-9445\(2001\)127:7\(784\)](http://dx.doi.org/10.1061/(ASCE)0733-9445(2001)127:7(784)).

- [41] X. Z. Lu, J. G. Teng, L. P. Ye, and J. J. Jiang, "Bond-slip models for FRP sheets/plates bonded to concrete," *Eng. Struct.*, vol. 27, no. 6, pp. 920–937, 2005, <http://dx.doi.org/10.1016/j.engstruct.2005.01.014>.
- [42] X. Z. Lu, L. P. Ye, J. G. Teng, and J. J. Jiang, "Meso-scale finite element model for FRP sheets/plates bonded to concrete," *Eng. Struct.*, vol. 27, no. 4, pp. 564–575, Mar 2005, <http://dx.doi.org/10.1016/j.engstruct.2004.11.015>.
- [43] S. A. Hadigheh, R. J. Gravina, and S. Setunge, "Identification of the interfacial fracture mechanism in the FRP laminated substrates using a modified single lap shear test set-up," *Eng. Fract. Mech.*, vol. 134, pp. 317–329, Jan 2015, <http://dx.doi.org/10.1016/j.engfracmech.2014.12.001>.
- [44] A. Hosseini and D. Mostofinejad, "Effective bond length of FRP-to-concrete adhesively-bonded joints: Experimental evaluation of existing models," *Int. J. Adhes. Adhes.*, vol. 48, pp. 150–158, 2014, <http://dx.doi.org/10.1016/j.ijadhadh.2013.09.022>.
- [45] H. Yuan, J. G. Teng, R. Seracino, Z. S. Wu, and J. Yao, "Full-range behavior of FRP-to-concrete bonded joints," *Eng. Struct.*, vol. 26, no. 5, pp. 553–565, Apr 2004, <http://dx.doi.org/10.1016/j.engstruct.2003.11.006>.

---

**Author contributions:** LFB: conceptualization, metallic apparatus design, master's scholarship acquisition, experiment design, experimental work, data analysis, data interpretation, conclusions, writing, writing-review and editing. ACDS: conceptualization, supervision, planning of the project, methodology, funding acquisition, metallic apparatus design, experiment design, data analysis, data interpretation, conclusions, writing-review. All authors read and approved the final submitted version of this manuscript.

**Editors:** Ricardo Carrazedo, José Luiz Antunes de Oliveira e Sousa, Guilherme Aris Parsekian.



ORIGINAL ARTICLE

# Design and verification of reinforced concrete shell elements

## *Dimensionamento e verificação de elementos de casca de concreto armado*

Marina Vendl Craveiro<sup>a</sup> Túlio Nogueira Bittencourt<sup>a</sup> João Carlos Della Bella<sup>a</sup> <sup>a</sup>Universidade de São Paulo – USP, Escola Politécnica, Departamento de Engenharia de Estruturas e Geotécnica, São Paulo, SP, Brasil

Received 10 February 2020

Accepted 07 August 2020

**Abstract:** Reinforced concrete shell elements are relevant in several civil and industrial structures. It is important to know the methods for designing and verifying such elements. In this context, the present paper aims at describing the iterative three-layer method proposed by Colombo et al. This method is based on the Model Code/1990, and it can be applied in the design of shell elements. An additional method for verifying reinforced concrete shell elements is also proposed and discussed. This one is based on the multilayer method proposed by Kollegger et al. Formulations as well as numerical examples are presented for both methods. The design proposed by Colombo et al. is verified by using the methodology based on the multilayer method. Although both methods lead to the equilibrium between applied and resistance loads using approximately the same amount of reinforcement, especially for small neutral axes in relation to the element thickness, one may conclude that the three-layer design method has limitations due to not considering strain compatibility along the thickness of the element and due to the impossibility to calculate the compression reinforcement. Although the multilayer method overcomes such limitations, it is a verification method, and more studies about its use in the design of reinforced concrete shell elements are necessary.

**Keywords:** reinforcement, reinforced concrete, design, shell elements, verification.

**Resumo:** Os elementos de casca de concreto armado podem ser aplicados em diversas estruturas civis e industriais, sendo importante conhecer os métodos de dimensionamento e verificação desses elementos. Dentro desse contexto, o presente trabalho tem como objetivo descrever o método iterativo das três chapas proposto por Colombo et al., o qual se baseia nas ideias do Model Code/1990 e é aplicado no dimensionamento dos elementos de casca. Um método adicional para verificação de elementos de casca de concreto armado também é proposto e discutido. Esse último se baseia no método das multicamadas de Kollegger et al. Tanto as formulações quanto exemplos numéricos de aplicação são apresentados para ambos os métodos. O dimensionamento proposto por Colombo et al. é verificado utilizando a metodologia baseada no método das multicamadas. Embora ambos os métodos levem ao equilíbrio entre esforços solicitantes e resistentes com aproximadamente a mesma quantidade de armadura, sobretudo para linhas neutras pequenas em relação à espessura do elemento, pode-se concluir que o método das três chapas possui limitações devido a não consideração da compatibilidade de deformações ao longo da espessura do elemento e à impossibilidade de dimensionar armaduras de compressão. O método das multicamadas supera tais limitações, mas é, a princípio, um método de verificação, havendo necessidade de mais estudos sobre a sua utilização no dimensionamento de elementos de casca de concreto armado.

**Palavras-chave:** armadura, concreto armado, dimensionamento, elementos de casca, verificação.

**How to cite:** M. V. Craveiro, T. N. Bittencourt, and J. C. Della Bella, “Design and verification of reinforced concrete shell elements,” *Rev. IBRACON Estrut. Mater.*, vol. 14, no. 3, e14305, 2021, <https://doi.org/10.1590/S1983-41952021000300005>

Corresponding author: Marina Vendl Craveiro. E-mail: [marina.craveiro@usp.br](mailto:marina.craveiro@usp.br)

Financial support: None.

Conflict of interest: Nothing to declare.



This is an Open Access article distributed under the terms of the Creative Commons Attribution License, which permits unrestricted use, distribution, and reproduction in any medium, provided the original work is properly cited.



## 1 INTRODUCTION

### 1.1 Overview

The behavior of concrete structures can be analyzed through models composed of basic structural elements. Such elements are classified according to the geometry and the loads acting on them. NBR 6118/2014 [1], for example, depending on geometry, separates the structural elements into linear elements and surface elements. The linear elements are those in which the longitudinal dimension is relatively larger than the dimensions of the cross section. They are defined by the longitudinal axis that crosses the centroids of the cross sections and by the dimensions of the cross sections perpendicular to the axis. Surface elements, on the other hand, are those in which one dimension, usually called thickness, is relatively smaller than the other two dimensions. They are defined by the average surface and by the thicknesses perpendicular to it. Within this classification, NBR 6118/2014 [1] also differentiates several types of structural elements according to the loads to which they are subjected. The linear elements are:

- a) beams, in which bending is predominant;
- b) columns, in which compressive axial forces are predominant;
- c) ties, in which tensile axial forces are predominant;
- d) arches, in which compressive axial forces are predominant, with or without bending loads.

The surface elements, in their turn, are:

- a) plates, in which the loads act predominantly normal to their plane;
- b) membranes, in which the loads are predominantly contained in their plane;
- c) shells, which consist in non-flat surface elements;
- d) shear walls, which consist in either flat surface elements or cylindrical shells subjected predominantly to compression and with the smallest dimension of the cross section smaller than 1/5 of the largest dimension.

Regarding the modeling of surface structures, the plate elements can represent flat surfaces subjected to loads normal to their plane and are able to resist such loads by means of bending effects, that is, bending moments in both directions ( $M_x$  and  $M_y$ ), torsional moment ( $M_{xy}$ ) and shear forces in both directions ( $V_x$  and  $V_y$ ), outside the plane of the plate. Figure 1a illustrates the resulting loads in a plate element. The membrane elements, as they are subjected to loads contained in their plane, resist the external loads by means of membrane loads, that is, axial forces in both directions ( $N_x$  and  $N_y$ ) and shear force ( $N_{xy}$ ), contained in the plane of the membrane. Figure 1b illustrates the resulting loads in a membrane element used to model flat structures subjected to loads contained in their plane. The shell elements, in their turn, can be subjected to both loads normal to their plane and loads contained in their plane, resisting such loads by means of bending and membrane loads ([2] and [3]). It is assumed here that any elements under such conditions, flat or non-flat, can be considered shell elements, extending, therefore, the definition of shells given by NBR 6118/2014 [1]. Figure 1c illustrates the resulting loads in a flat shell element. The flat elements are the elements most used in practice to represent shell structures, being also useful for modeling curved structures, since they can be represented by several flat elements. Thus, non-flat shell elements will not be addressed in the present paper. Another point to be commented on is related to the evaluation of the loads illustrated in Figure 1. In general, such loads are obtained in practice from elastic-linear analyses, which must employ appropriate theories according to the relationship between the element thickness and the structure span, taking into account or not shear strains.

The reinforced concrete shells can be used in the design of roofs, silos, offshore platforms, industrial facilities, nuclear power plants, tunnels, dam structures, etc. Figure 2 shows, for example, the bottom discharge of a dam, which is subjected to loads normal to its plane and to loads contained in its plane. It can be modeled with the flat shell elements presented in Figure 1c. Shells consist in a powerful structural system to resist the applied loads, even with large spans and thin sections. The loads to which these structures are subjected can be determined by numerical elastic-linear analysis techniques, such as the finite element method. The difficulty of designing such structures, however, is their detailing, since it must take into account the nonlinear constitutive behavior of concrete and steel to evaluate the structure strength ([4] and [5]). It is noteworthy that the nonlinear analysis of reinforced concrete structures is also possible [6]. However, since the dimensions and the reinforcement should already be pre-defined and the computational cost is significant, such analysis is usually used in more complex structures and in verification and not designing procedures.

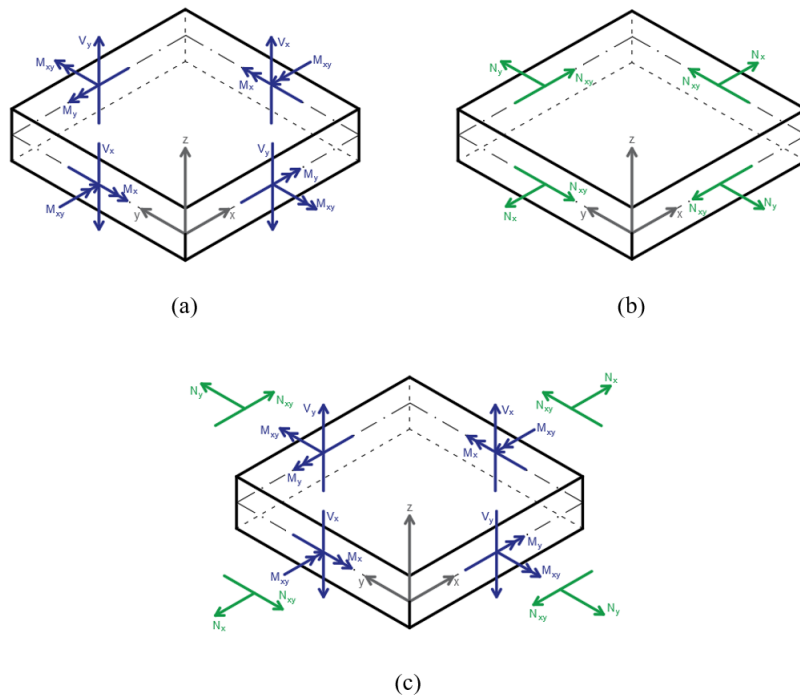


**Figure 1.** Surface element loads. a) Plate element. b) Membrane element. c) Shell element.

Many researchers have studied how to determine the reinforcement of shell elements subjected to  $M_x$ ,  $M_y$ ,  $M_{xy}$ ,  $N_x$ ,  $N_y$  and  $N_{xy}$ , defined per unit length. Among them, it can be mentioned Brandurn-Nielsen [7], Gupta [8] and Lourenço and Figueiras [9]. The basic idea of the authors is to resist such loads by tension in the reinforcement and compression in the concrete. Dividing the reinforced concrete shell element into two outer layers of concrete with reinforcement arranged orthogonally in both directions in each layer, Gupta [8] created an iterative trial-and-error method for the determination of reinforcement based on the equilibrium conditions and on the principle of minimum resistance. Gupta [8] seeks to achieve the smallest possible strength of the element, that is, the smallest resistance loads capable of equilibrating the applied loads, with the maximum use of concrete and steel materials. So, it is assumed that the failure occurs with a unitary relationship between the resistance loads and the applied loads. It is worth mentioning that Gupta [8] studied only the case in which reinforcement is necessary in both concrete layers.

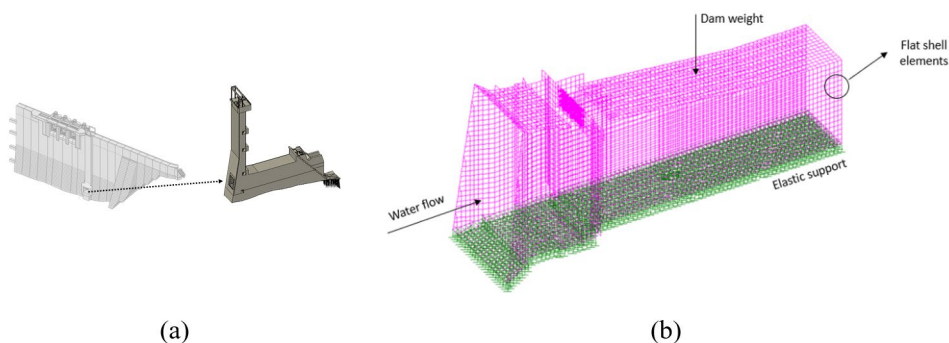


**Figure 2.** Use of flat shell elements to model a bottom discharge of a dam. a) Structure. b) Model.

Lourenço and Figueiras [9] proposed an automated method for calculating the shell reinforcement based on the three-layer method proposed by Model Code/1990 [10], extending the idea of Gupta [8] also for cases in which the reinforcement is not necessary in one or two outer layers. The three-layer method, also present in Model Code/2010 [11], consists in the idealization of the shell element as a superposition of three layers. The two outer layers are responsible for resisting the moments and the membrane forces, and the central layer is responsible for resisting transverse shear. Colombo et al. [12] were also based on this three-layer method to develop an algorithm for reinforced concrete shell design.

Another line of analysis of shell elements consists in that followed by Kollegger et al. [13], which is also indicated in Comité Euro-International du Béton [14]. Such analysis divides the shell element into layers that have uniform stress and strain states. Assuming linear variation of strain along the element thickness, the strain state can be estimated from the element center strains and the curvatures. From the strains, the stresses can be estimated by using suitable constitutive models for concrete and steel. These stresses are used to determine the resistance loads of the element. The determination of the element center strains and the curvatures compatible with the applied loads can be done with the Newton-Raphson nonlinear iterative method, imposing the equilibrium between the resistance and applied loads. This is a method to be used for element verification, but it can also be expanded to design by means of iterative procedures.

### 1.2 Objectives and methodology

Given the great applicability of shells in civil and industrial structures, it is important to compare the existing methods for designing and verifying reinforced concrete shell elements. In this context, the objective of the work is to describe the methodology developed by Colombo et al. [12] for designing reinforced concrete shells and to present a methodology based on the idea proposed by Kollegger et al. [13] for verifying such shells. The work will be developed through the presentation of formulations and numerical examples as well as comparisons between the two methodologies. It is worth noting that the focus of the research is only on the design and verification of shell elements from the point of view of resistance. The work will not address the stability issues of shell elements, which, in practice, also need to be taken into account, especially in the case of thin shells.

## 2 DESIGN BY THE THREE-LAYER METHOD

The formulation proposed by Colombo et al. [12] for designing reinforced concrete shells will be presented below. It can be applied to both thin and thick shells, requiring only that the loads are obtained accordingly. Numerical applications will also be detailed.

### 2.1 Formulation

The three-layer method idealizes the reinforced concrete shell element as a superposition of three layers/membranes (Figure 3a). The outer layers are designed to resist the moments  $M_x$ ,  $M_y$  and  $M_{xy}$  and the membrane forces  $N_x$ ,  $N_y$  and  $N_{xy}$ . The central layer is responsible for resisting the transverse shear. Separating the study of the outer layers from the study of the central layer, the idea is that  $M_x$ ,  $M_y$ ,  $M_{xy}$ ,  $N_x$ ,  $N_y$  and  $N_{xy}$  are resisted by membrane forces in each of the outer layers. The membrane forces of the upper and lower layers may be determined such that the loads applied to the shell element are equilibrated by the membrane forces of both layers. Figure 4 illustrates the proposed equilibrium and Equations 1 to 6 determine the membrane forces in each outer layer by means of the imposition of such equilibrium. The forces  $N_{x(z+)}$ ,  $N_{y(z+)}$  and  $N_{xy(z+)}$  correspond to the membrane forces of the layer of face  $z+$  of the shell element and the forces  $N_{x(z-)}$ ,  $N_{y(z-)}$  and  $N_{xy(z-)}$  correspond to the membrane forces of the layer of face  $z-$  of the shell element. The dimensions  $a_{(z+)}$ ,  $a_{(z-)}$ ,  $h_{(z+)}$ ,  $h_{(z-)}$ ,  $h_{sx(z+)}$ ,  $h_{sx(z-)}$ ,  $h_{sy(z+)}$  and  $h_{sy(z-)}$ , in their turn, are indicated in Figure 3b.

$$\sum M_{center\ of\ the\ layer\ of\ face\ z-} = 0 \rightarrow N_{x(z+)} = \frac{N_x h_{(z-)} + M_x}{(h_{(z+)} + h_{(z-)})} \tag{1}$$

$$\sum M_{center\ of\ the\ layer\ of\ face\ z-} = 0 \rightarrow N_{y(z+)} = \frac{N_y h_{(z-)} + M_y}{(h_{(z+)} + h_{(z-)})} \tag{2}$$

$$\Sigma M_{center\ of\ the\ layer\ of\ face\ z-} = 0 \rightarrow N_{xy(z+)} = \frac{N_{xy}h_{(z-)} + M_{xy}}{(h_{(z+)} + h_{(z-)})} \tag{3}$$

$$M_{center\ of\ the\ layer\ of\ face\ z+} = 0 \rightarrow N_{x(z-)} = \frac{N_x h_{(z+)} - M_x}{(h_{(z+)} + h_{(z-)})} \tag{4}$$

$$\Sigma M_{center\ of\ the\ layer\ of\ face\ z+} = 0 \rightarrow N_{y(z-)} = \frac{N_y h_{(z+)} - M_y}{(h_{(z+)} + h_{(z-)})} \tag{5}$$

$$\Sigma M_{center\ of\ the\ layer\ of\ face\ z+} = 0 \rightarrow N_{xy(z-)} = \frac{N_{xy}h_{(z+)} - M_{xy}}{(h_{(z+)} + h_{(z-)})} \tag{6}$$

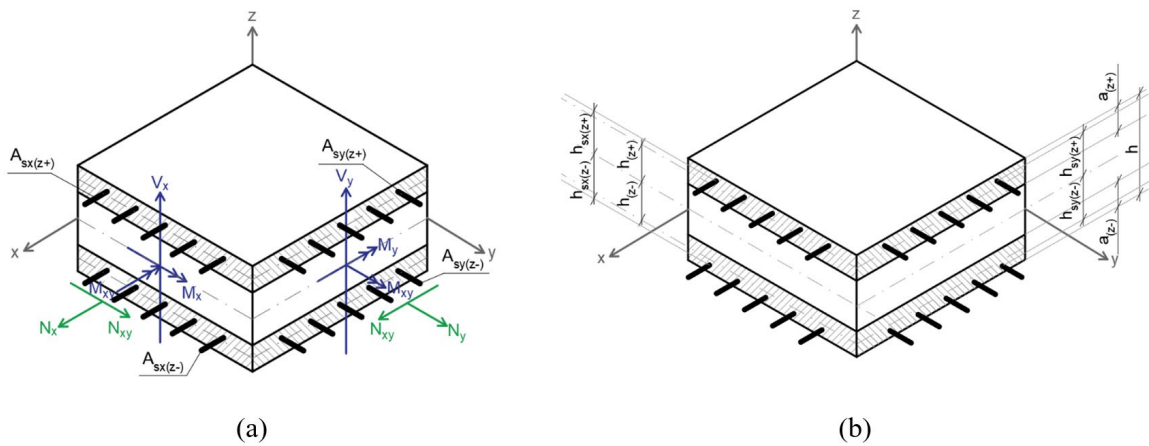


Figure 3. Reinforced concrete shell element idealized by the three-layer method. (a) Loads and reinforcement. (b) Dimensions.

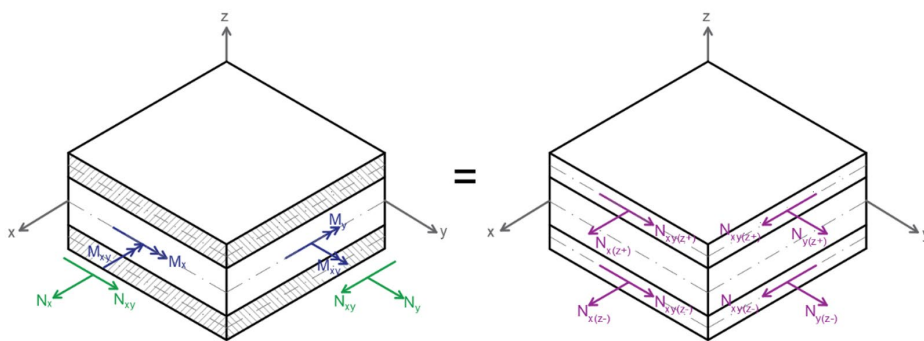
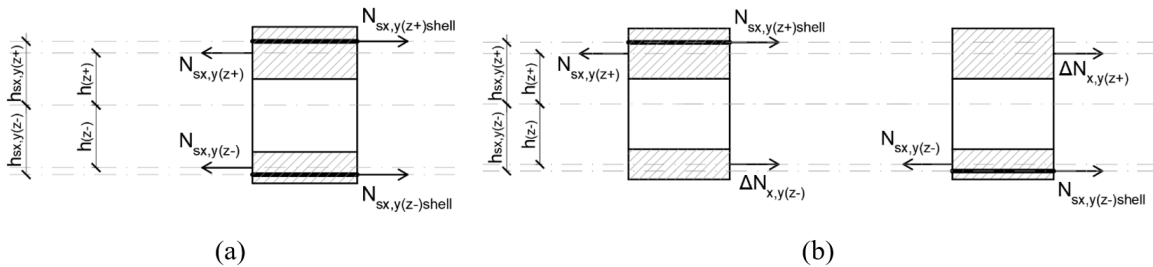


Figure 4. Equilibrium between the loads applied to the shell element and the membrane forces of the outer layers.

Note that in the equations resulting from the equilibrium the membrane forces in each outer layer are in the center of the respective layer. Thus, for the model to be valid, the reinforcement must also be in this position, which may not be true in practice. Then, it is necessary to correct the reinforcement and membrane forces to take into account the real position of the reinforcement in the element. For that, it is possible to impose the equilibrium between the forces in the reinforcement calculated in the center of the layers and the forces that occur in the real positions of the reinforcement.

Such procedure, which is important in the iterative process of determining the reinforcement of shell elements, is illustrated in Figure 5a for the cases in which there is reinforcement in the two outer layers and in Figure 5b for the cases in which the reinforcement is required only in one layer. Equations 7 and 8 calculate the real forces in the reinforcement when there is reinforcement in the two outer layers and Equations 9 to 12 calculate the real forces in the reinforcement when there is reinforcement in only one layer.  $N_{sx,y(z^+)}$  and  $N_{sx,y(z^-)}$  are resistance forces per unit length in the reinforcement x or y of the layers of faces  $z^+$  and  $z^-$ , respectively, calculated in the center of the layers.  $N_{sx,y(z^+)shell}$  and  $N_{sx,y(z^-)shell}$  are resistance forces per unit length in the reinforcement x or y of the layers of faces  $z^+$  and  $z^-$ , respectively, calculated in the real position of the reinforcement.  $\Delta N_{x,y(z^+)}$  and  $\Delta N_{x,y(z^-)}$  are correction forces per unit length in the layers of faces  $z^+$  and  $z^-$ , respectively.



**Figure 5.** Correction of the forces in the reinforcement for cases in which the reinforcement is necessary in: (a) both outer layers. (b) only one outer layer.

$$\sum M_{\text{reinf. } z^-} = 0 \rightarrow N_{sx,y(z^+)shell} = \frac{N_{sx,y(z^+)}(h(z^+) + h_{sx,y(z^-)}) + N_{sx,y(z^-)}(h_{sx,y(z^-)} - h(z^-))}{(h_{sx,y(z^+)} + h_{sx,y(z^-)})} \quad (7)$$

$$N_{sx,y(z^-)shell} = N_{sx,y(z^+)} + N_{sx,y(z^-)} - N_{sx,y(z^+)shell} \quad (8)$$

$$\sum M_{\text{center of the layer of face } z^-} = 0 \rightarrow N_{sx,y(z^+)shell} = \frac{N_{sx,y(z^+)}(h(z^+) + h(z^-))}{(h_{sx,y(z^+)} + h(z^-))} \quad (9)$$

$$\Delta N_{x,y(z^-)} = N_{sx,y(z^+)} - N_{sx,y(z^+)shell} \quad (10)$$

$$\sum M_{\text{center of the layer of face } z^+} = 0 \rightarrow N_{sx,y(z^-)shell} = \frac{N_{sx,y(z^-)}(h(z^+) + h(z^-))}{(h_{sx,y(z^-)} + h(z^+))} \quad (11)$$

$$\Delta N_{x,y(z^+)} = N_{sx,y(z^-)} - N_{sx,y(z^-)shell} \quad (12)$$

Once the membrane forces in each outer layer are found, the problem is to determine the reinforcement in each of such layers. The determination of the reinforcement in membrane elements has been studied by many authors, including Brandurn-Nielsen [7], Baumann [15] and Gupta [16]. The ideas present in Comité Euro-International du Béton [10] are based on the study of such authors. Consider the membrane element illustrated in Figure 6a. The membrane forces per unit length of the element must be equilibrated by the tensile forces per unit length in the reinforcement ( $N_{sx}$  and  $N_{sy}$ ) and by the compressive force per unit length in the concrete in the direction of the cracks ( $N_c$ ). The angle  $\theta$  is that between the x-direction and the principal tensile direction (direction perpendicular to the cracks). The direction of the cracks is coincident with the principal compressive direction, because it is considered that there is no shear stress between the cracks. In addition, some other basic assumptions are made [15]: the cracks are approximately straight and parallel; the concrete tensile strength, the reinforcement dowel action, the aggregate interlock and the tension stiffening

are neglected; perfect bonding is assumed between the concrete and the steel; the directions of principal stresses and principal strains are coincident.

Consider two sections of the membrane element shown in Figure 6a: one parallel to the crack (Figure 6b) and another perpendicular to the crack (Figure 6c), both of unit length. By imposing equilibrium between the membrane forces and the forces in the reinforcement and in the concrete and by applying the principle of the minimum resistance, Equations 13 and 14 are obtained on the basis of Figure 6b and Equation 15 is obtained on the basis of Figure 6c.

$$\Sigma F_x = 0 \rightarrow N_{sx} = N_x + N_{xy} \tan \theta \tag{13}$$

$$\Sigma F_y = 0 \rightarrow N_{sy} = N_y + N_{xy} \cot \theta \tag{14}$$

$$\Sigma F_x = 0 \rightarrow N_c = -\frac{N_{xy}}{\sin \theta \cos \theta} \tag{15}$$

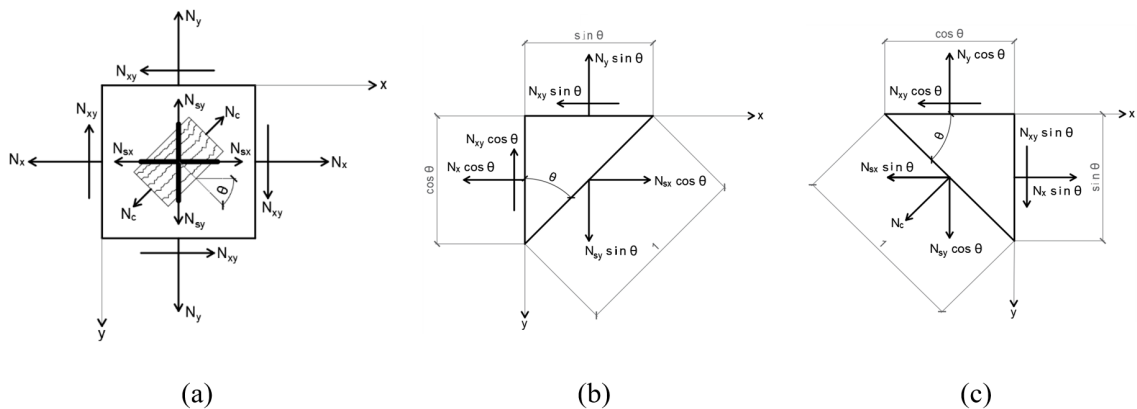


**Figure 6.** Membrane element. a) Membrane forces per unit length. b) Section parallel to the crack. c) Section perpendicular to the crack.

It is possible to see that there are three equations for four unknowns. Thus, if one variable were arbitrated, the other three could be determined. In the case in which the reinforcement is necessary in both directions, called case I in Comité Euro-International du Béton [10], the value of  $\theta$  that provides the smallest reinforcement amount and, therefore, the most economical solution is  $45^\circ$ . For the case I, Equations 13 to 15 can be rewritten in the form of Equations 16 to 18.

$$N_{sx} = N_x + |N_{xy}| \tag{16}$$

$$N_{sy} = N_y + |N_{xy}| \tag{17}$$

$$N_c = -2|N_{xy}| \tag{18}$$

When  $N_{sx}$  is negative, there is no need for reinforcement in the x-direction, leading to the called case II in Comité Euro-International du Béton [10]. Assuming  $N_{sx} = 0$ , Equations 19 to 21 are obtained.

$$\operatorname{tg}\theta = -\frac{N_x}{N_{xy}} \tag{19}$$

$$N_{sy} = N_y - \frac{N_{xy}^2}{N_x} \tag{20}$$

$$N_c = N_x + \frac{N_{xy}^2}{N_x} \tag{21}$$

Similarly, when  $N_{sy}$  is negative, there is no need for reinforcement in the y-direction, leading to the called case III in Comité Euro-International du Béton [10]. Assuming  $N_{sy} = 0$ , Equations 22 to 24 are obtained.

$$\operatorname{tg}\theta = -\frac{N_{xy}}{N_y} \tag{22}$$

$$N_{sx} = N_x - \frac{N_{xy}^2}{N_y} \tag{23}$$

$$N_c = N_y + \frac{N_{xy}^2}{N_y} \tag{24}$$

If Equations 20 and 23 also give negative values for  $N_{sy}$  and  $N_{sx}$ , respectively, no reinforcement is necessary in the membrane, leading to the called case IV in Comité Euro-International du Béton [10]. The value of  $N_c$  is the value of the minimum principal force  $N_{c2}$ . The maximum principal force  $N_{c1}$  must also be compressive. The principal forces are obtained by Equations 25 and 26.

$$N_{c1} = \frac{N_x + N_y}{2} + \sqrt{\left(\frac{N_x - N_y}{2}\right)^2 + N_{xy}^2} \tag{25}$$

$$N_{c2} = \frac{N_x + N_y}{2} - \sqrt{\left(\frac{N_x - N_y}{2}\right)^2 + N_{xy}^2} \tag{26}$$

Once the forces in the reinforcement are obtained, the required area of reinforcement per unit length can be determined by Equations 27 and 28 for x-direction and y-direction, respectively, imposing the yield stress on the reinforcement.

$$A_{sx} = \frac{N_{sx}}{f_{yd}} \tag{27}$$

$$A_{sy} = \frac{N_{sy}}{f_{yd}} \tag{28}$$

In the design process of reinforced concrete shell elements, the thickness of the layer required to resist  $N_c$  must be determined by Equation 29.

$$a = \frac{N_c}{f_c} \tag{29}$$

One possibility for determining  $f_c$  in each outer layer is to consider an uniform compressive strength of the concrete depending on the cracking state to which the concrete is subjected. According to Comité Euro-International du Béton [10], when the concrete is uncracked,  $f_c$  can be given by Equation 30. If the concrete is cracked,  $f_c$  can be given by Equation 31.

$$f_c = f_{cd1} = 0.85 \left( 1 - \frac{f_{ck}}{250} \right) f_{cd} \tag{30}$$

$$f_c = f_{cd2} = 0.60 \left( 1 - \frac{f_{ck}}{250} \right) f_{cd} \tag{31}$$

Colombo et al. [12] propose a model for the concrete that is based on the experimental results obtained by Vecchio and Collins [17]. Such model assumes that the maximum compressive strength  $f_{cmax}$  of the concrete decreases as the maximum tensile strain  $\epsilon_1$  increases. This property can be described by Equation 32, which depends on  $f_{ck}$  and on the shortening strain  $\epsilon_{cp}$  corresponding to the concrete strength peak.

$$f_{cmax} = \frac{f_{ck}}{0.8 - 0.34(\epsilon_1 / \epsilon_{cp})} \tag{32}$$

Colombo et al. [12] consider that for cases I, II and III, in which the concrete is cracked,  $f_c$  can be interpolated between the values of  $f_{cd1}$  and  $f_{cd2}$  through Equation 33. For the case IV, Equation 30 is valid because the concrete is uncracked. In this case, one can further increase the strength of the concrete by a factor  $K$  due to the existing biaxial compression. Such factor depends on the principal stresses  $\sigma_1$  and  $\sigma_2$  and is given by Equation 34.

$$f_c = \frac{f_{cd1}}{0.8 - 0.34(\epsilon_1 / \epsilon_{cp})}, \text{ where } \frac{0.6}{0.85} \leq \frac{I}{0.8 - 0.34(\epsilon_1 / \epsilon_{cp})} \leq 1 \tag{33}$$

$$K = \frac{1 + 3.8(\sigma_1 / \sigma_2)}{(1 + \sigma_1 / \sigma_2)^2} \tag{34}$$

The use of Equation 33 depends on the determination of  $\epsilon_1$ , which can be done by using Equations 35 and 36 proposed by Gupta [16]. For the case I, the strain  $\epsilon_1$  can be determined by assuming  $\epsilon_2$  equal to  $\epsilon_{cp}$ ,  $\epsilon_x$  equal to the steel yield strain  $\epsilon_{yi}$  and  $\theta = 45^\circ$ . Equation 37 can be used for case I. For case II, it is assumed that  $\epsilon_2$  is equal to  $\epsilon_{cp}$  and  $\epsilon_y$  is equal to  $\epsilon_{yi}$ , leading to Equation 38. For case III, in its turn, it is assumed that  $\epsilon_2$  is equal to  $\epsilon_{cp}$  and  $\epsilon_x$  is equal to  $\epsilon_{yi}$ , leading to Equation 39.

$$\epsilon_x = \epsilon_1 \cos^2 \theta + \epsilon_2 \sin^2 \theta \tag{35}$$

$$\epsilon_y = \epsilon_1 \sin^2 \theta + \epsilon_2 \cos^2 \theta \tag{36}$$

$$\epsilon_1 = 2(\epsilon_{yi} - 0.5\epsilon_{cp}) \tag{37}$$



$$\varepsilon_I = \frac{(\varepsilon_{yi} - \varepsilon_{cp} \cos^2 \theta)}{\sin^2 \theta} \tag{38}$$

$$\varepsilon_I = \frac{(\varepsilon_{yi} - \varepsilon_{cp} \sin^2 \theta)}{\cos^2 \theta} \tag{39}$$

From the design expressions for membrane elements, the iterative procedure proposed by Colombo et al. [12] can be used to estimate the reinforcement of the reinforced concrete shell element. For that, the thicknesses  $a_{(z+)}$  and  $a_{(z-)}$  of the outer layers of the idealized shell element are arbitrated. Then, the membrane forces in each of the outer layers are estimated and their design are done. The initial values of the forces in the reinforcement are corrected taking into account the difference between the centers of the layers and the real positions of the reinforcement. With the values of  $N_{c(z+)}$  and  $N_{c(z-)}$ , new values of  $a_{(z+)}$  and  $a_{(z-)}$  are obtained. The procedure is repeated until the thicknesses converge. According to Colombo et al. [12], the mentioned iterative process presents a good convergence and stability since Equation 33 introduces a certain continuity to the behavior of the concrete under compression, that is, there is a gradual transition between the non-cracked state of the concrete and the totally cracked state of the concrete.

### 2.2 Numerical examples

To illustrate the iterative procedure proposed by Colombo et al. [12], four numerical examples of shell elements are presented below. Table 1 presents the geometry and material data as well as the loads to which such elements are subjected. The elements can, for example, be taken from a linear finite element analysis carried out for the bottom discharge of the dam illustrated in Figure 2.

**Table 1.** Shell element data.

Elem.	h	h <sub>sx(z+)</sub>	h <sub>sx(z-)</sub>	h <sub>sy(z+)</sub>	h <sub>sy(z-)</sub>	f <sub>ck</sub>	f <sub>yk</sub>	γ <sub>c</sub>	γ <sub>s</sub>	N <sub>x</sub>	N <sub>y</sub>	N <sub>xy</sub>	M <sub>x</sub>	M <sub>y</sub>	M <sub>xy</sub>
	[m]	[m]	[m]	[m]	[m]	[MPa]	[MPa]			[tf/m]	[tf/m]	[tf/m]	[tf.m/m]	[tf.m/m]	[tf.m/m]
1	1.5	0.55	0.477	0.55	0.477	20	500	1.4	1.15	202.46	-9.31	27.26	-28.79	-36.28	-16.66
2	1.5	0.55	0.477	0.55	0.477	20	500	1.4	1.15	-4.72	124.82	-10.59	-0.38	23.24	4.82
3	1.5	0.55	0.477	0.55	0.477	20	500	1.4	1.15	-175.95	-544.86	-93.69	50.40	303.93	19.62
4	1.5	0.55	0.477	0.55	0.477	20	500	1.4	1.15	-161.52	733.60	-65.28	201.20	968.00	94.40

The first step in the process of determining the reinforcement of a shell element is to estimate the thicknesses  $a_{(z+)}$  and  $a_{(z-)}$  of the upper and lower layers of the idealized element and to determine  $h_{(z+)}$  and  $h_{(z-)}$ . Colombo et al. [12] propose as an initial thickness estimate the value of 0.2 times the total thickness of the element. See Equations 40 and 41.

$$a_{(z+)} = a_{(z-)} = 0.2 \times 1.50 = 0.30 \text{ m} \tag{40}$$

$$h_{(z+)} = h_{(z-)} = \frac{1.50}{2} - \frac{0.30}{2} = 0.60 \text{ m} \tag{41}$$

Next, the values of the membrane forces acting on the upper and lower layers must be estimated by using Equations 1 to 6. Table 2 presents the membrane forces for the upper layers of the four shell elements and Table 3 presents the membrane forces for the lower layers of the four shell elements.

With the membrane forces, it is possible to estimate the principal forces acting on each layer. Table 4 presents such forces for the upper layers and Table 5 presents such forces for the lower layers of the four shell elements.

It is possible to note that for the lower layers of the elements 3 and 4 the values of  $N_{c1}$  are negative; therefore, no reinforcement in the x-direction and y-direction will be required. This is the case of designing IV. For the lower layers of the elements 1 and 2 and for the upper layer of the element 4,  $N_{x(z+)/(-)} > -|N_{xy(z+)/(-)}|$  and  $N_{y(z+)/(-)} > -$

$|N_{xy(z^+)/(z^-)}|$ . Thus, there will be reinforcement in the x-direction and y-direction, leading to the case of designing I. For the upper layer of the element 1,  $N_{x(z^+)} > -|N_{xy(z^+)}|$  and  $N_{y(z^+)} < -|N_{xy(z^+)}|$ , which leads to the case of designing III. Finally, the upper layers of the elements 2 and 3 have  $N_{x(z^+)} < -|N_{xy(z^+)}|$  and  $N_{y(z^+)} > -|N_{xy(z^+)}|$ , which leads to the case of designing II. The design of the upper and lower layers are presented in Table 6 and Table 7, respectively, for the four shell elements.

Since the formulation assumes that the reinforcement is in the center of the outer layers, the forces in the reinforcement and the membrane forces must be corrected to take into account the real position of the reinforcement in the element. Table 8 presents the results of this correction in the x-direction and y-direction for the shell elements 1 and 2. Table 9, in its turn, presents the results of the correction in the x-direction and y-direction for the shell elements 3 and 4.

**Table 2.** Membrane forces for the upper layers.

Element 1			Element 3		
Membrane forces		Equation	Membrane forces		Equation
$N_x(z^+)$ [tf/m]	77.24	(1)	$N_x(z^+)$ [tf/m]	-45.98	(1)
$N_y(z^+)$ [tf/m]	-34.89	(2)	$N_y(z^+)$ [tf/m]	-19.15	(2)
$N_{xy}(z^+)$ [tf/m]	-0.25	(3)	$N_{xy}(z^+)$ [tf/m]	-30.50	(3)
Element 2			Element 4		
Membrane forces		Equation	Membrane forces		Equation
$N_x(z^+)$ [tf/m]	-2.68	(1)	$N_x(z^+)$ [tf/m]	86.91	(1)
$N_y(z^+)$ [tf/m]	81.78	(2)	$N_y(z^+)$ [tf/m]	1173.47	(2)
$N_{xy}(z^+)$ [tf/m]	-1.28	(3)	$N_{xy}(z^+)$ [tf/m]	46.03	(3)

**Table 3.** Membrane forces for the lower layers.

Element 1			Element 3		
Membrane forces		Equation	Membrane forces		Equation
$N_x(z^-)$ [tf/m]	125.22	(4)	$N_x(z^-)$ [tf/m]	-129.98	(4)
$N_y(z^-)$ [tf/m]	25.58	(5)	$N_y(z^-)$ [tf/m]	-525.71	(5)
$N_{xy}(z^-)$ [tf/m]	27.51	(6)	$N_{xy}(z^-)$ [tf/m]	-63.20	(6)
Element 2			Element 4		
Membrane forces		Equation	Membrane forces		Equation
$N_x(z^-)$ [tf/m]	-2.04	(4)	$N_x(z^-)$ [tf/m]	-248.43	(4)
$N_y(z^-)$ [tf/m]	43.04	(5)	$N_y(z^-)$ [tf/m]	-439.87	(5)
$N_{xy}(z^-)$ [tf/m]	-9.31	(6)	$N_{xy}(z^-)$ [tf/m]	-111.31	(6)

**Table 4.** Principal forces for the upper layers.

Element 1			Element 3		
Case of designing III			Case of designing II		
Principal forces		Equation	Principal forces		Equation
$N_{c1}(z^+)$ [tf/m]	77.24	(25)	$N_{c1}(z^+)$ [tf/m]	0.75	(25)
$N_{c2}(z^+)$ [tf/m]	-34.89	(26)	$N_{c2}(z^+)$ [tf/m]	-65.88	(26)
Element 2			Element 4		
Case of designing II			Case of designing I		
Principal forces		Equation	Principal forces		Equation
$N_{c1}(z^+)$ [tf/m]	81.80	(25)	$N_{c1}(z^+)$ [tf/m]	1175.41	(25)
$N_{c2}(z^+)$ [tf/m]	-2.70	(26)	$N_{c2}(z^+)$ [tf/m]	84.96	(26)

**Table 5.** Principal forces for the lower layers.

Element 1		
Case of designing I		
Principal forces		Equation
$N_{c1(z-)} [tf/m]$	132.31	(25)
$N_{c2(z-)} [tf/m]$	18.49	(26)
Element 2		
Case of designing I		
Principal forces		Equation
$N_{c1(z-)} [tf/m]$	44.89	(25)
$N_{c2(z-)} [tf/m]$	-3.89	(26)

Element 3		
Case of designing IV		
Principal forces		Equation
$N_{c1(z-)} [tf/m]$	-120.13	(25)
$N_{c2(z-)} [tf/m]$	-535.55	(26)
Element 4		
Case of designing IV		
Principal forces		Equation
$N_{c1(z-)} [tf/m]$	-197.34	(25)
$N_{c2(z-)} [tf/m]$	-490.95	(26)

**Table 6.** Design of the upper layers.

Element 1		
Case of designing III		
Design parameters		Equation
$NS_x(z+) [tf/m]$	77.24	(23)
$NS_y(z+) [tf/m]$	0.00	-
$N_c(z+) [tf/m]$	-34.89	(24)
$tg \theta$	-0.01	(22)
Element 2		
Case of designing II		
Design parameters		Equation
$NS_x(z+) [tf/m]$	0.00	-
$NS_y(z+) [tf/m]$	82.39	(20)
$N_c(z+) [tf/m]$	-3.29	(21)
$tg \theta$	-2.09	(19)

Element 3		
Case of designing II		
Design parameters		Equation
$NS_x(z+) [tf/m]$	0.00	-
$NS_y(z+) [tf/m]$	1.07	(20)
$N_c(z+) [tf/m]$	-66.20	(21)
$tg \theta$	-1.51	(19)
Element 4		
Case of designing I		
Design parameters		Equation
$NS_x(z+) [tf/m]$	132.93	(16)
$NS_y(z+) [tf/m]$	1219.49	(17)
$N_c(z+) [tf/m]$	-92.05	(18)
$tg \theta$	1.00	-

**Table 7.** Design of the lower layers.

Element 1		
Case of designing I		
Design parameters		Equation
$NS_x(z-) [tf/m]$	152.74	(16)
$NS_y(z-) [tf/m]$	53.09	(17)
$N_c(z-) [tf/m]$	-55.03	(18)
$tg \theta$	1.00	-
Element 2		
Case of designing I		
Design parameters		Equation
$NS_x(z-) [tf/m]$	7.27	(16)
$NS_y(z-) [tf/m]$	52.36	(17)
$N_c(z-) [tf/m]$	-18.62	(18)
$tg \theta$	1.00	-

Element 3		
Case of designing IV		
Design parameters		Equation
$NS_x(z-) [tf/m]$	0.00	-
$NS_y(z-) [tf/m]$	0.00	-
$N_c(z-) [tf/m]$	-535.55	(26)
$tg \theta$	-	-
Element 4		
Case of designing IV		
Design parameters		Equation
$NS_x(z-) [tf/m]$	0.00	-
$NS_y(z-) [tf/m]$	0.00	-
$N_c(z-) [tf/m]$	-490.95	(26)
$tg \theta$	-	-

**Table 8.** Correction of the position of the reinforcement in the x-direction and y-direction for elements 1 and 2.

Element 1 - x-direction		
Correction		Equation
$N_{Sx(z^+)} \text{ shell [tf/m]}$	62.71	(7)
$N_{Sx(z^-)} \text{ shell [tf/m]}$	167.27	(8)

Element 2 - x-direction		
Correction		Equation
$N_{Sx(z^-)} \text{ shell [tf/m]}$	8.10	(11)
$\Delta N_x(z^+) \text{ [tf/m]}$	-0.83	(12)
$N_x(z^+) \text{ [tf/m]}$	-3.51	-
$N_y(z^+) \text{ [tf/m]}$	81.78	-
$N_{xy}(z^+) \text{ [tf/m]}$	-1.28	-
$N_{e1}(z^+) \text{ [tf/m]}$	81.80	(25)
$N_{e2}(z^+) \text{ [tf/m]}$	-3.53	(26)
$N_{Sx}(z^+) \text{ [tf/m]}$	0.00	-
$N_{Sy}(z^+) \text{ [tf/m]}$	82.24	(20)
$N_c(z^+) \text{ [tf/m]}$	-3.97	(21)
$\text{tg } \theta$	-2.74	(19)

Element 1 - y-direction		
Correction		Equation
$N_{Sy(z^-)} \text{ shell [tf/m]}$	59.16	(11)
$\Delta N_y(z^+) \text{ [tf/m]}$	-6.06	(12)
$N_x(z^+) \text{ [tf/m]}$	77.24	-
$N_y(z^+) \text{ [tf/m]}$	-40.95	-
$N_{xy}(z^+) \text{ [tf/m]}$	-0.25	-
$N_{e1}(z^+) \text{ [tf/m]}$	77.24	(25)
$N_{e2}(z^+) \text{ [tf/m]}$	-40.95	(26)
$N_{Sx}(z^+) \text{ [tf/m]}$	77.24	(23)
$N_{Sy}(z^+) \text{ [tf/m]}$	0.00	-
$N_c(z^+) \text{ [tf/m]}$	-40.95	(24)
$\text{tg } \theta$	-0.01	(22)

Element 2 - y-direction		
Correction		Equation
$N_{Sy}(z^+) \text{ shell [tf/m]}$	79.98	(7)
$N_{Sy}(z^-) \text{ shell [tf/m]}$	54.62	(8)

**Table 9.** Correction of the position of the reinforcement in the x-direction and y-direction for elements 3 and 4.

Element 3 - x-direction		
No correction		

Element 4 - x-direction		
Correction		Equation
$N_{Sx}(z^+) \text{ shell [tf/m]}$	138.71	(9)
$\Delta N_x(z^-) \text{ [tf/m]}$	-5.78	(10)
$N_x(z^-) \text{ [tf/m]}$	-254.21	-
$N_y(z^-) \text{ [tf/m]}$	-492.89	-
$N_{xy}(z^-) \text{ [tf/m]}$	-111.31	-
$N_{e1}(z^-) \text{ [tf/m]}$	-210.36	(25)
$N_{e2}(z^-) \text{ [tf/m]}$	-536.74	(26)
$N_{Sx}(z^-) \text{ [tf/m]}$	0.00	-
$N_{Sy}(z^-) \text{ [tf/m]}$	0.00	-
$N_c(z^-) \text{ [tf/m]}$	-536.74	(26)
$\text{tg } \theta$	-	-

Element 3 - y-direction		
Correction		Equation
$N_{Sy}(z^+) \text{ shell [tf/m]}$	1.12	(9)
$\Delta N_y(z^-) \text{ [tf/m]}$	-0.05	(10)
$N_x(z^-) \text{ [tf/m]}$	-129.98	-
$N_y(z^-) \text{ [tf/m]}$	-525.75	-
$N_{xy}(z^-) \text{ [tf/m]}$	-63.20	-
$N_{e1}(z^-) \text{ [tf/m]}$	-120.13	(25)
$N_{e2}(z^-) \text{ [tf/m]}$	-535.60	(26)
$N_{Sx}(z^-) \text{ [tf/m]}$	0.00	-
$N_{Sy}(z^-) \text{ [tf/m]}$	0.00	-
$N_c(z^-) \text{ [tf/m]}$	-535.60	(26)
$\text{tg } \theta$	-	-

Element 4 - y-direction		
Correction		Equation
$N_{Sy}(z^+) \text{ shell [tf/m]}$	1272.51	(9)
$\Delta N_y(z^-) \text{ [tf/m]}$	-53.02	(10)
$N_x(z^-) \text{ [tf/m]}$	-248.43	-
$N_y(z^-) \text{ [tf/m]}$	-492.89	-
$N_{xy}(z^-) \text{ [tf/m]}$	-111.31	-
$N_{e1}(z^-) \text{ [tf/m]}$	-205.34	(25)
$N_{e2}(z^-) \text{ [tf/m]}$	-535.97	(26)
$N_{Sx}(z^-) \text{ [tf/m]}$	0.00	-
$N_{Sy}(z^-) \text{ [tf/m]}$	0.00	-
$N_c(z^-) \text{ [tf/m]}$	-535.97	(26)
$\text{tg } \theta$	-	-

The next step is to calculate the new thicknesses  $a_{(z+)}$  and  $a_{(z-)}$  for the upper and lower layers based on the forces  $N_{c(z+)}$  and  $N_{c(z-)}$ , respectively. For that, the value of  $f_c$  must be found. For the lower layers of the elements 3 and 4, which correspond to the case of designing IV and in which the concrete is under compression and uncracked, Equation 30 shall be used. For the other cases, the layers are cracked and  $f_c$  must be evaluated by using Equation 33. The thicknesses can then be determined from Equation 29. Table 10 presents the calculation of the thicknesses of the upper layers and Table 11 presents the calculation of the thicknesses of the lower layers.

Note that the new values of thickness  $a_{(z+)}$  and  $a_{(z-)}$  do not coincide with the initial values. Thus, the entire procedure should be repeated as many times as necessary so that the final values of thickness coincide with the initial values within a pre-established tolerance. Once the problem has converged, the reinforcement can be determined by Equations 27 and 28. For the shell elements in question, the final values of thickness and reinforcement are indicated in Table 12.

**Table 10.** Thicknesses of the upper layers.

Element 1			Element 3		
Case of designing III			Case of designing II		
Thickness calculation		Equation	Thickness calculation		Equation
$\epsilon_{cp}$	-0.0020	-	$\epsilon_{cp}$	-0.0020	-
$\epsilon_{yi}$	0.00207	-	$\epsilon_{yi}$	0.00207	-
$\epsilon_1$	0.00207	(39)	$\epsilon_1$	0.00386	(38)
$f_c$ [MPa]	9.70	(33)	$f_c$ [MPa]	7.89	(33)
$a_{(z+)}$ [m]	0.042	(29)	$a_{(z+)}$ [m]	0.084	(29)

Element 2			Element 4		
Case of designing II			Case of designing I		
Thickness calculation		Equation	Thickness calculation		Equation
$\epsilon_{cp}$	-0.0020	-	$\epsilon_{cp}$	-0.0020	-
$\epsilon_{yi}$	0.00207	-	$\epsilon_{yi}$	0.00207	-
$\epsilon_1$	0.00261	(38)	$\epsilon_1$	0.00614	(37)
$f_c$ [MPa]	8.98	(33)	$f_c$ [MPa]	7.89	(33)
$a_{(z+)}$ [m]	0.004	(29)	$a_{(z+)}$ [m]	0.117	(29)

**Table 11.** Thicknesses of the lower layers.

Element 1			Element 3		
Case of designing I			Case of designing IV		
Thickness calculation		Equation	Thickness calculation		Equation
$\epsilon_{cp}$	-0.0020	-	$f_c$ [MPa]	11.17	(30)
$\epsilon_{yi}$	0.00207	-	$a_{(z-)}$ [m]	0.479	(29)
$\epsilon_1$	0.00614	(37)			
$f_c$ [MPa]	7.89	(33)			
$a_{(z-)}$ [m]	0.070	(29)			

Element 2			Element 4		
Case of designing I			Case of designing IV		
Thickness calculation		Equation	Thickness calculation		Equation
$\epsilon_{cp}$	-0.0020	-	$f_c$ [MPa]	11.17	(30)
$\epsilon_{yi}$	0.00207	-	$a_{(z-)}$ [m]	0.480	(29)
$\epsilon_1$	0.00614	(37)			
$f_c$ [MPa]	7.89	(33)			
$a_{(z-)}$ [m]	0.024	(29)			

**Table 12.** Final design of the shell elements.

Element 1		Element 2	
Final results		Final results	
a (z+) [m]	0.040160	a (z+) [m]	0.005969
f <sub>c</sub> [MPa]	9.68	f <sub>c</sub> [MPa]	8.40
θ [degrees]	2.97	θ [degrees]	-63.07
a (z-) [m]	0.064037	a (z-) [m]	0.021726
f <sub>c</sub> [MPa]	7.89	f <sub>c</sub> [MPa]	7.89
θ [degrees]	45.00	θ [degrees]	-45.00
A <sub>sx</sub> (z+) [cm <sup>2</sup> /m]	13.85	A <sub>sx</sub> (z+) [cm <sup>2</sup> /m]	0.00
A <sub>sx</sub> (z-) [cm <sup>2</sup> /m]	38.55	A <sub>sx</sub> (z-) [cm <sup>2</sup> /m]	1.80
A <sub>sy</sub> (z+) [cm <sup>2</sup> /m]	0.00	A <sub>sy</sub> (z+) [cm <sup>2</sup> /m]	18.32
A <sub>sy</sub> (z-) [cm <sup>2</sup> /m]	12.59	A <sub>sy</sub> (z-) [cm <sup>2</sup> /m]	12.60

Element 3		Element 4	
Final results		Final results	
a (z+) [m]	0.056171	a (z+) [m]	0.137339
f <sub>c</sub> [MPa]	7.89	f <sub>c</sub> [MPa]	7.89
θ [degrees]	-53.41	θ [degrees]	45.00
a (z-) [m]	0.536420	a (z-) [m]	0.537011
f <sub>c</sub> [MPa]	11.17	f <sub>c</sub> [MPa]	11.17
θ [degrees]	0.00	θ [degrees]	0.00
A <sub>sx</sub> (z+) [cm <sup>2</sup> /m]	0.00	A <sub>sx</sub> (z+) [cm <sup>2</sup> /m]	41.56
A <sub>sx</sub> (z-) [cm <sup>2</sup> /m]	0.00	A <sub>sx</sub> (z-) [cm <sup>2</sup> /m]	0.00
A <sub>sy</sub> (z+) [cm <sup>2</sup> /m]	13.46	A <sub>sy</sub> (z+) [cm <sup>2</sup> /m]	308.64
A <sub>sy</sub> (z-) [cm <sup>2</sup> /m]	0.00	A <sub>sy</sub> (z-) [cm <sup>2</sup> /m]	0.00

### 3 VERIFICATION BY THE MULTILAYER METHOD

One possibility for the verification of shell elements is to use the idea proposed by Kollegger et al. [13] as a basis, which will be described in detail below. It is worth mentioning that the formulation was adapted to incorporate new constitutive models based on NBR 6118/2014 [1] and on experimental results obtained by Vecchio and Collins [17]. Verifications of the examples presented in Section 2.2 will be made based on the new formulation, which can be used for both thin and thick shells.

#### 3.1 Formulation

The idea proposed by Kollegger et al. [13] consists in dividing the reinforced concrete shell element with thickness  $h$  into concrete layers with thickness  $h_i$  and distance  $z_i$  from the center of the element. The author also identifies the reinforcement layers in x-direction and y-direction with areas  $A_{sxi}$  and  $A_{syi}$ , which have distance  $z_{sxi}$  and  $z_{syi}$  from the center of the element, respectively. Figure 7 illustrates the proposed element.

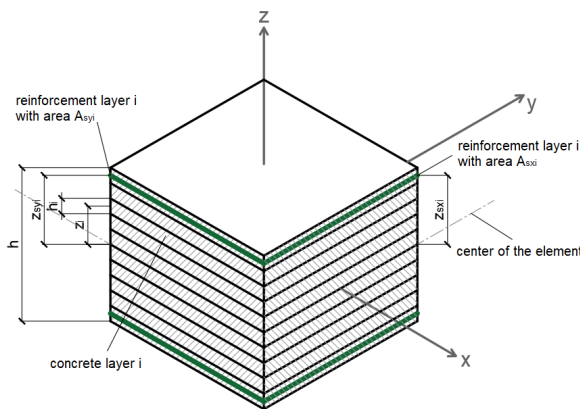


**Figure 7.** Reinforced concrete shell element idealized by Kollegger et al. [13].

It is assumed that the normal strains  $\epsilon_x$  and  $\epsilon_y$  and the tangential strain  $\gamma_{xy}$  vary linearly along the thickness of the shell element. Thus, from the strain values  $\epsilon_{0x}$ ,  $\epsilon_{0y}$  and  $\gamma_{0xy}$  in the center of the element and from the curvatures  $1/r_x$ ,  $1/r_y$  and  $1/r_{xy}$  related to each strain, respectively, it is possible to determine the strains  $\epsilon_{xi}$ ,  $\epsilon_{yi}$  and  $\gamma_{xyi}$  in the center of each concrete layer and the strains  $\epsilon_{sxi}$  and  $\epsilon_{syi}$  in the center of each reinforcement layer, assuming similar strains for concrete and steel. For that, Equations 42 to 46 shall be used.

$$\epsilon_{xi} = \epsilon_{0x} + \frac{1}{r_x} \cdot z_i \tag{42}$$

$$\epsilon_{yi} = \epsilon_{0y} + \frac{1}{r_y} \cdot z_i \tag{43}$$

$$\gamma_{xyi} = \gamma_{0xy} + \frac{1}{r_{xy}} \cdot z_i \tag{44}$$

$$\epsilon_{sxi} = \epsilon_{0x} + \frac{1}{r_x} \cdot z_{sxi} \tag{45}$$

$$\epsilon_{syi} = \epsilon_{0y} + \frac{1}{r_y} \cdot z_{syi} \tag{46}$$

For the concrete, it is necessary to determine the principal strains  $\epsilon_{1i}$  and  $\epsilon_{2i}$  in each layer by Equations 47 and (48). The direction  $\theta_i$  of these principal strains is coincident with the direction of the principal stresses and can be determined by Equation 49.

$$\epsilon_{1i} = \frac{\epsilon_{xi} + \epsilon_{yi}}{2} + \sqrt{\left(\frac{\epsilon_{xi} - \epsilon_{yi}}{2}\right)^2 + \left(\frac{\gamma_{xyi}}{2}\right)^2} \tag{47}$$

$$\epsilon_{2i} = \frac{\epsilon_{xi} + \epsilon_{yi}}{2} - \sqrt{\left(\frac{\epsilon_{xi} - \epsilon_{yi}}{2}\right)^2 + \left(\frac{\gamma_{xyi}}{2}\right)^2} \tag{48}$$

$$-tg\theta_i = \frac{\gamma_{xyi} / 2}{\epsilon_{yi} - \epsilon_{1i}} \tag{49}$$

From the principal strains and by using a suitable constitutive model for the concrete, it is possible to determine the principal stresses in each concrete layer. The model chosen for the present work is the parabola-rectangle diagram of NBR 6118/2014 [1], which is adapted so that the peak stress depends on the biaxial state of concrete stresses, that is, depends on  $\epsilon_{1i}$ , as proposed by Vecchio and Collins [17]. Figure 8a illustrates the proposed model, in which  $\epsilon_{c2}$  is the shortening strain of concrete at the beginning of the plastic branch and  $\epsilon_{cu}$  is the shortening strain of concrete at failure. The parameter  $\beta$  is based on the experimental results obtained by Vecchio and Collins [17] and is given by Equation 50, taking into account whether or not the concrete is cracked. The tensile strength of the concrete is neglected.

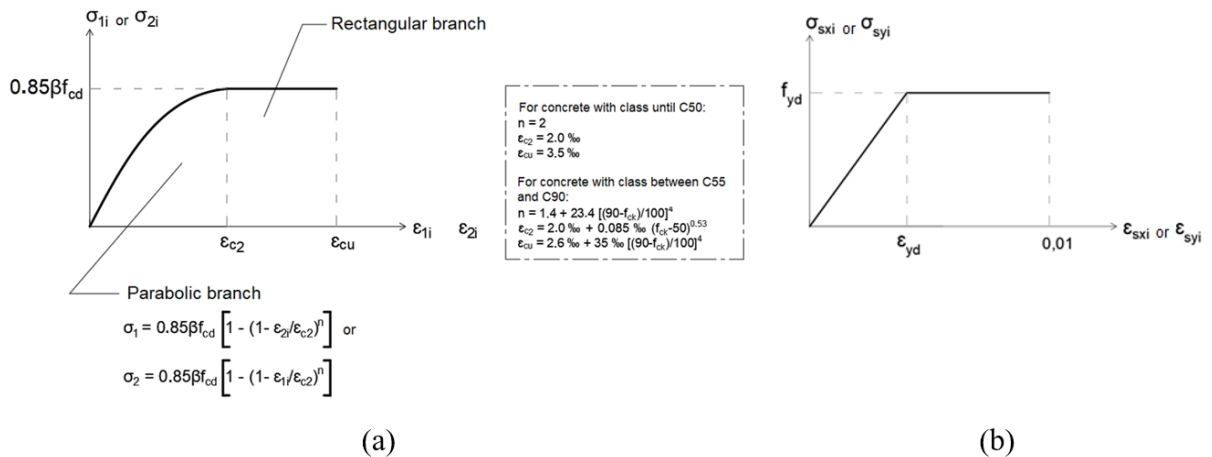


Figure 8. Constitutive models. (a) Concrete. (b) Steel.

$$\beta = \frac{1}{0.8 - 0.34(\epsilon_{1i} / \epsilon_{c2})}, \text{ where } \frac{0.6}{0.85} \leq \beta \leq 1 \tag{50}$$

Once the stresses in each concrete layer are found, it is possible to determine, through the integration of such stresses on the thickness of the element, the concrete resistance loads that partially equilibrate the applied loads; however, as the applied loads are referenced in relation to the x-direction and y-direction, it is first necessary to determine the stresses according to such directions. Equations 51 to 53 calculate  $\sigma_{xi}$ ,  $\sigma_{yi}$  and  $\tau_{xyi}$  for each concrete layer.

$$\sigma_{xi} = \sigma_{2i} \sin^2 \theta_i + \sigma_{1i} \cos^2 \theta_i \tag{51}$$

$$\sigma_{yi} = \sigma_{2i} \cos^2 \theta_i + \sigma_{1i} \sin^2 \theta_i \tag{52}$$

$$\tau_{xyi} = (\sigma_{1i} - \sigma_{2i}) \sin \theta_i \cos \theta_i \tag{53}$$

Since the problem is discretized into layers, the integration of stresses on the thickness of the element can be easily developed for determining the concrete resistance loads  $N_{cx}$ ,  $N_{cy}$ ,  $N_{cxy}$ ,  $M_{cx}$ ,  $M_{cy}$  and  $M_{cxy}$  that partially equilibrate the applied loads  $N_x$ ,  $N_y$ ,  $N_{xy}$ ,  $M_x$ ,  $M_y$  and  $M_{xy}$ . For that, Equations 54 to 59 can be used.

$$N_{cx} = \Sigma(\sigma_{xi} \cdot h_i) \tag{54}$$

$$N_{cy} = \Sigma(\sigma_{yi} \cdot h_i) \tag{55}$$

$$N_{cxy} = \Sigma(\tau_{xyi} \cdot h_i) \tag{56}$$

$$M_{cx} = \Sigma(\sigma_{xi} \cdot h_i \cdot z_i) \tag{57}$$



$$M_{cy} = \Sigma(\sigma_{yi} \cdot h_i \cdot z_i) \tag{58}$$

$$M_{cxy} = \Sigma(\tau_{xyi} \cdot h_i \cdot z_i) \tag{59}$$

The same procedure performed for the concrete, that is, the determination of the stresses from the strains and the subsequent determination of the resistance loads from the integration of the stresses, can be performed for the steel by employing a suitable constitutive model. The model assumed in the present work is that given by NBR6118/2014 [1], which is described in Figure 8b.

Since the reinforcement is not responsible for resisting shear stresses, the analysis of stresses can be performed directly according to the x-direction and y-direction. Once the stress in each reinforcement layer is determined, it is possible to proceed with the integration of such stress on the reinforcement cross section in order to obtain the steel resistance loads  $N_{sx}$ ,  $N_{sy}$ ,  $M_{sx}$  and  $M_{sy}$  that partially equilibrate the applied loads  $N_x$ ,  $N_y$ ,  $M_x$  and  $M_y$ , respectively. The loads resisted by the reinforcement are given by Equations 60 to 63.

$$N_{sx} = \Sigma(\sigma_{sxi} \cdot A_{sxi}) \tag{60}$$

$$N_{sy} = \Sigma(\sigma_{syi} \cdot A_{syi}) \tag{61}$$

$$M_{sx} = \Sigma(\sigma_{sxi} \cdot A_{sxi} \cdot z_{sxi}) \tag{62}$$

$$M_{sy} = \Sigma(\sigma_{syi} \cdot A_{syi} \cdot z_{syi}) \tag{63}$$

To obtain the final resistance loads  $N_{Rx}$ ,  $N_{Ry}$ ,  $N_{Rxy}$ ,  $M_{Rx}$ ,  $M_{Ry}$  and  $M_{Rxy}$ , it is necessary to sum the loads resisted by the concrete and the reinforcement. Such resistance loads must equilibrate the applied loads so that the shell element can be given as verified.

It is clear that the procedure for determining whether or not a reinforced concrete shell element resist the applied loads is quite simple when the strains in the center of the element and the corresponding curvatures are known. But how is it possible to know if there is any set of strains in the center of the shell element and of curvatures that generates internal loads that resist the applied loads? To solve this problem, the Newton-Raphson nonlinear iterative method can be used. The applied loads (**S**) must be equal to the resistance loads (**R**) for equilibrium. It is also known that the resistance loads are function of the strains and curvatures  $\epsilon_{0x}$ ,  $\epsilon_{0y}$ ,  $\gamma_{0xy}$ ,  $1/r_x$ ,  $1/r_y$  and  $1/r_{xy}$ . Thus, one can write Equation 64.

$$\mathbf{f}(\boldsymbol{\epsilon}) = \mathbf{0} \text{ where } \mathbf{f} = \mathbf{R} - \mathbf{S} \text{ and } \boldsymbol{\epsilon} \text{ is the vector of strains and curvatures} \tag{64}$$

By using the Newton-Raphson method, from an estimate  $i$  of strains and curvatures, the values of strains and curvatures of the next iteration  $i + 1$  are obtained by Equation 65.  $\partial \mathbf{f} / \partial \boldsymbol{\epsilon}(\boldsymbol{\epsilon}_i)$  stands for the tangent matrix of the problem, which can be determined analytically or numerically. The use of the Newton-Raphson method implies choosing an initial estimate for  $\epsilon_{0x}$ ,  $\epsilon_{0y}$ ,  $\gamma_{0xy}$ ,  $1/r_x$ ,  $1/r_y$  and  $1/r_{xy}$ . The idea of Kollegger et al. [13] is to use the elastic estimate of strains and curvatures.

$$\left[ \frac{\partial \mathbf{f}}{\partial \boldsymbol{\epsilon}}(\boldsymbol{\epsilon}_i) \right] (\boldsymbol{\epsilon}_{i+1} - \boldsymbol{\epsilon}_i) = -\mathbf{f}(\boldsymbol{\epsilon}_i) \tag{65}$$

The iterative method was computationally implemented and employed to verify the reinforced concrete shell elements of Section 2.2.

### 3.2 Numerical examples

From the results obtained in the design performed in Section 2.2, the shell elements were verified by using the multilayer method described in Section 3.1. By using the Newton-Raphson iterative method, it is concluded that the equilibrium between the resistance loads and the applied loads can be reached with strains within the limits defined by NBR 6118/2014 [1]. Table 13, Table 14 and Table 15 present the strains, stresses and resistance loads calculated for the final equilibrium condition of the shell element 1. The strains in the center of the element and the curvatures found for the equilibrium condition are summarized in Table 16 not only for element 1 but also for elements 2, 3 and 4. The equilibrium is also possible for the elements 2, 3 and 4 with reinforcement approximately equal to that calculated by the three-layer method. For elements 3 and 4, it would even be possible to reduce the reinforcement because the concrete and steel strains are below the limits established by NBR 6118/2014 [1]. It is worth mentioning that the elements 3 and 4 are not over dimensioned in the sense that the increase in the loads would yield the reinforcement before crushing the concrete. Note that differences begin to occur when, in the three-layer method, the thicknesses of the upper and lower concrete layers necessary for the equilibrium increase in relation to the shell thickness, as occurs in elements 3 and 4. As the thicknesses of the layers necessary for the equilibrium were limited to 0.45d in the present paper (d is the effective depth of the section), the differences are still minimal, but the increase in the loads can lead to larger thicknesses and greater differences between the two models. This is because the assumptions of uniformization of the concrete stresses and of strains equal to  $\epsilon_{cp}$  begin to distance from the assumptions of the parabola-rectangle diagram and of the linear variation of concrete strains along the thickness of the element, respectively.

**Table 13.** Multilayer method: input data of shell element 1.

$f_{ck}$ (MPa)	$h$ (m)										
20	1.5										
$\epsilon_{0x}$ (‰)	$\epsilon_{0y}$ (‰)	$\gamma_{0xy}$ (‰)	$1/r_x$ (‰/m)	$1/r_y$ (‰/m)	$1/r_{xy}$ (‰/m)	$N_x$ (tf/m)	$N_y$ (tf/m)	$N_{xy}$ (tf/m)	$M_x$ (tf·m/m)	$M_y$ (tf·m/m)	$M_{xy}$ (tf·m/m)
3.1494	1.0386	2.4179	2.2759	-1.9826	-3.3593	202.46	-9.31	27.26	-28.79	-36.28	-16.66

$i$	$h_i$ (m)	$z_i$ (m)	$A_{sxi}$ (cm <sup>2</sup> )	$z_{sxi}$ (m)	$A_{syi}$ (cm <sup>2</sup> )	$z_{syi}$ (m)	$N_{Rx}$ (tf/m)	$N_{Ry}$ (tf/m)	$N_{Rxy}$ (tf/m)	$M_{Rx}$ (tf·m/m)	$M_{Ry}$ (tf·m/m)	$M_{Rxy}$ (tf·m/m)
1	0.15	0.675	14.00	0.55	0.00	0.55	202.46	-9.31	27.26	-28.79	-36.28	-16.66
2	0.15	0.525	39.70	-0.477	12.70	-0.477						
3	0.15	0.375										
4	0.15	0.225										
5	0.15	0.075										
6	0.15	-0.075										
7	0.15	-0.225										
8	0.15	-0.375										
9	0.15	-0.525										
10	0.15	-0.675										

**Table 14.** Multilayer method: equilibrium of shell element 1 (part 1).

$i$	$\epsilon_{xi}$ (‰)	$\epsilon_{yi}$ (‰)	$\gamma_{xyi}/2$ (‰)	$\epsilon_{1i}$ (‰)	$\epsilon_{2i}$ (‰)	$\theta_i$ (°)	$\epsilon_{sxi}$ (‰)	$\epsilon_{syi}$ (‰)	$\sigma_c, peak$ (tf/m <sup>2</sup> )	$\sigma_{1i}$ (tf/m <sup>2</sup> )	$\sigma_{2i}$ (tf/m <sup>2</sup> )
1	4.6856	-0.2997	0.0752	4.6868	-0.3008	0.8639	4.4011	-0.0519	857.14	0.00	-238.45
2	4.3442	-0.0023	0.3271	4.3687	-0.0268	4.2803	2.0638	1.9842	857.14	0.00	-22.80
3	4.0029	0.2951	0.5791	4.0912	0.2068	8.6736			857.14	0.00	0.00
4	3.6615	0.5925	0.8310	3.8721	0.3819	14.2195			857.14	0.00	0.00
5	3.3201	0.8899	1.0830	3.7327	0.4773	20.8549			857.14	0.00	0.00
6	2.9787	1.1872	1.3349	3.6906	0.4754	28.0695			857.14	0.00	0.00
7	2.6373	1.4846	1.5869	3.7493	0.3727	35.0198			857.14	0.00	0.00
8	2.2959	1.7820	1.8389	3.8957	0.1823	41.0225			857.14	0.00	0.00
9	1.9546	2.0794	2.0908	4.1087	-0.0748	45.8551			857.14	0.00	-62.88
10	1.6132	2.3768	2.3428	4.3686	-0.3787	49.6282			857.14	0.00	-293.86

**Table 15.** Multilayer method: equilibrium of shell element 1 (part 2).

i	N <sub>sxi</sub> (tf/m)	N <sub>syi</sub> (tf/m)	N <sub>cxi</sub> (tf/m)	N <sub>cyi</sub> (tf/m)	N <sub>exyi</sub> (tf/m)	M <sub>sxi</sub> (tf.m/m)	M <sub>syi</sub> (tf.m/m)	M <sub>cxi</sub> (tf.m/m)	M <sub>cyi</sub> (tf.m/m)	M <sub>cxyi</sub> (tf.m/m)
1	60.87	0.00	-0.01	-35.76	0.54	33.48	0.00	-0.01	-24.14	0.36
2	172.06	52.92	-0.02	-3.40	0.25	-82.07	-25.24	-0.01	-1.79	0.13
3	0.00	0.00	0.00	0.00	0.00	0.00	0.00	0.00	0.00	0.00
4	0.00	0.00	0.00	0.00	0.00	0.00	0.00	0.00	0.00	0.00
5	0.00	0.00	0.00	0.00	0.00	0.00	0.00	0.00	0.00	0.00
6	0.00	0.00	0.00	0.00	0.00	0.00	0.00	0.00	0.00	0.00
7	0.00	0.00	0.00	0.00	0.00	0.00	0.00	0.00	0.00	0.00
8	0.00	0.00	0.00	0.00	0.00	0.00	0.00	0.00	0.00	0.00
9	0.00	0.00	-4.86	-4.58	4.71	0.00	0.00	2.55	2.40	-2.47
10	0.00	0.00	-25.58	-18.49	21.75	0.00	0.00	17.27	12.48	-14.68
Σ	232.93	52.92	-30.47	-62.23	27.26	-48.59	-25.24	19.80	-11.04	-16.66

**Table 16.** Strains and curvatures of the shell elements 1, 2, 3 and 4 for the equilibrium condition.

Element 1		Element 2	
ε <sub>0x</sub> [‰]	3.149	ε <sub>0x</sub> [‰]	1.275
ε <sub>0y</sub> [‰]	1.039	ε <sub>0y</sub> [‰]	2.062
γ <sub>0xy</sub> [‰]	2.418	γ <sub>0xy</sub> [‰]	-3.101
1/r <sub>x</sub> [‰/m]	2.276	1/r <sub>x</sub> [‰/m]	-1.380
1/r <sub>y</sub> [‰/m]	-1.983	1/r <sub>y</sub> [‰/m]	0.008
1/r <sub>xy</sub> [‰/m]	-3.359	1/r <sub>xy</sub> [‰/m]	1.996
Element 3		Element 4	
ε <sub>0x</sub> [‰]	-0.062	ε <sub>0x</sub> [‰]	0.491
ε <sub>0y</sub> [‰]	0.100	ε <sub>0y</sub> [‰]	0.229
γ <sub>0xy</sub> [‰]	-0.397	γ <sub>0xy</sub> [‰]	1.233
1/r <sub>x</sub> [‰/m]	0.233	1/r <sub>x</sub> [‰/m]	2.284
1/r <sub>y</sub> [‰/m]	2.819	1/r <sub>y</sub> [‰/m]	3.329
1/r <sub>xy</sub> [‰/m]	-0.411	1/r <sub>xy</sub> [‰/m]	5.032

#### 4 RESULTS AND DISCUSSIONS

Having presented the design of four shell elements by the three-layer method and their verification by the multilayer method, it is valid to discuss some assumptions of both models.

It can be concluded from the results of Sections 2.2 and 3.2 that both formulations lead to the equilibrium between the resistance loads and the applied loads with the same amount of reinforcement, especially when the thicknesses of the concrete layers are not significant in relation to the thickness of the element. The increase in the loads can lead to an increase in the thicknesses of the layers, making the assumption of uniformization of concrete stresses and strains invalid. Therefore, it cannot be said that there is a total similarity between the strains and stresses in both models. In the three-layer method, it is assumed that the contribution of the concrete for the strength is given by means of constant stresses at the thicknesses of the upper and lower layers in the direction of the principal compression. It is used the maximum strength of the concrete reduced by the factor  $(1 - \frac{f_{ck}}{250})$ . The value of the maximum strength of the concrete, in its turn, depends on the state of cracking of the concrete, as it also occurs in the method of verification described. The concrete strain in the direction of the principal compression is assumed to be constant and equal to the strain that occurs at the peak strength of the concrete, and the strain in the reinforcement is always assumed to be equal to the yield strain of the steel. Besides this, the upper and lower layers, although contributing together for the equilibrium of the element, are treated separately in the evaluation of the stresses and strains, not having compatibility along the thickness.

In the multilayer method, unlike the three-layer method, it is possible to describe a more realistic constitutive behavior of the materials, in which the stress depends on the strain in each layer of concrete and reinforcement. The strains, in their turn, are not considered with the maximum values possible, but calculated along the thickness through

the values obtained in the center of the element. See comparisons between the two models in Figure 9 and Figure 10, which are based on the shell element 1 of Section 2.2. There are differences in both stresses and strains. It is worth mentioning that the direction of the principal stresses is not coincident in both methods.

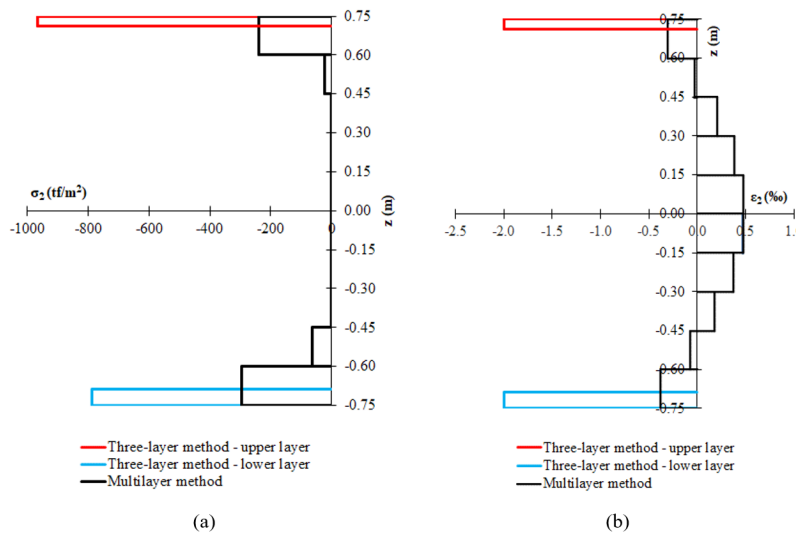


**Figure 9.** Three-layer method versus multilayer method. (a) Comparison of concrete stresses in the principal direction of compression for the shell element 1. (b) Comparison of concrete strains in the principal direction of compression for the shell element 1.

Another limitation of the three-layer method is when compression reinforcement is required. In this case, the iterative process increases the thickness of each layer in order to increase the contribution of the concrete for the equilibrium, but, since the concrete alone is not able to equilibrate the applied compressive loads, the thicknesses of the layers exceed the half of the thickness of the element, with no solution. This is because the method is not able to predict compression reinforcement. The multilayer method, on the other hand, is able to verify elements with compression reinforcement.

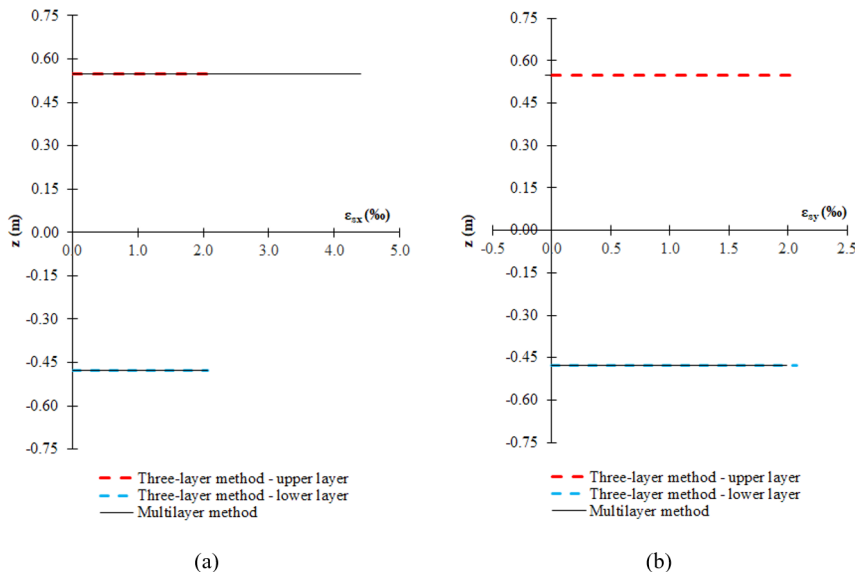


**Figure 10.** Three-layer method versus multilayer method. (a) Comparison of steel strains in the x-direction for the shell element 1. (b) Comparison of steel strains in the y-direction for the shell element 1.

In short, the three-layer method is used to design shell elements, but with limitations regarding the strain compatibility and the determination of compression reinforcement. The multilayer method overcomes such limitations, but at first it is a verification method. So, would it not be possible to adopt the idea of the multilayer method for designing reinforced concrete shell elements? Kollegger et al. [13] points out a procedure for this. The idea is to start from a shell element with minimum reinforcement and to apply the external loads in steps. Thus, with the minimum reinforcement, the loads are increased until there is no more equilibrium. The reinforcement with the largest strain is then incremented as well as the loads. The procedure is repeated as many times as necessary to equilibrate the applied loads with allowable strains and stresses. An alternative to this method would be to start from the maximum reinforcement of the element and to decrease the reinforcement iteratively until the equilibrium is no longer possible or until the strains exceed the values established by the standards. Such procedure consists in the next step of the present research.

## 5 CONCLUSIONS

In practice, it is common to perform elastic-linear structural analyses aiming at obtaining the loads to which the reinforced concrete structures are subjected. The nonlinearity of the problem is taken into account in the models for reinforcement design and for verification of concrete in ultimate and service limit states. This is a simple practice with lower computational cost when compared to the nonlinear analysis, and it does not require prior knowledge of the amount and position of the reinforcement in the structural element. However, it is necessary to have design models that reproduce the behavior of concrete and steel together, calculating the reinforcement and verifying the concrete. In the case of the reinforced concrete shell element, the models are not so straightforward and are rarely described in detail in technical standards.

The present work addressed two formulations for reinforced concrete shell elements. The first formulation consists in the three-layer method, which is intended for designing and is based on the work of Colombo et al. [12], Model Code/1990 [10] and Lourenço and Figueiras [9]. The second one consists in the multilayer method that is based on and adapted from Kollegger et al. [13], which is intended for verification of shell elements. Both methods are compatible from the point of view of reinforcement when the concrete thicknesses required for the equilibrium are not significant. In other words, the design by the three-layer method imposing a limit for the thicknesses of the layers equal to 0.45d was, for the examples presented, satisfactory in the verification by the multilayer method. However, the three-layer method does not consider the evaluation of strains and stresses along the thickness of the element. It becomes a rough approximation when the layer thickness tends to increase in relation to the shell thickness. The three-layer method is also restricted to the determination of tension reinforcement. The multilayer method, in its turn, despite not having the previous limitations, is a verification method and requires the prior knowledge of the reinforcement. Such problem could be overcome through iterative procedures as indicated by Kollegger et al. [13]. Thus, as future developments, it is predicted the implementation of an iterative method that, from initial values of reinforcement, minimum or maximum, finds the tension and compression reinforcement of reinforced concrete shell elements, obeying the constitutive models of the materials and the strain limitations prescribed by standards.

## ACKNOWLEDGEMENTS

The authors thank the Department of Structural and Geotechnical Engineering of University of Sao Paulo.

## REFERENCES

- [1] Associação Brasileira de Normas Técnicas, *Projeto de Estruturas de Concreto – Procedimento*, NBR 6118, 2014.
- [2] S. D. Kumar. "Two vector variable problems (plate and shell theory): finite element analysis." <https://pt.slideshare.net/dharanimech/finite-element-analysis-plate-shell-skew-plate> (accessed Sep. 25, 2020).
- [3] E. Oñate, *Structural Analysis with the Finite Element Method - Linear Statics: Beams, Plates and Shells*, 1st ed. Barcelona: Springer, 2013.
- [4] O. B. Isgor, "Analysis and design of reinforced concrete shell elements," M.S. thesis, Dept. Civ. Environ. Eng., Univ. Ottawa, Ottawa, 1997.
- [5] J. Blaauwendraad, "Reinforcement design using linear analysis," in *Plates and FEM*. Dordrecht: Springer, 2009, pp. 291–318.
- [6] T. D. Hrynyk and F. J. Vecchio, "Capturing out-of-plane shear failures in the analysis of reinforced concrete shells," *J. Struct. Eng.*, vol. 141, no. 12, pp. 1–11, 2015, [http://dx.doi.org/10.1061/\(asce\)st.1943-541x.0001311](http://dx.doi.org/10.1061/(asce)st.1943-541x.0001311).

- [7] T. Brandurn-Nielsen, "Optimization of reinforcement in shells, folded plates, walls and slabs," *ACI J. Proc.*, vol. 82, no. 3, pp. 304–309, 1985.
- [8] A. K. Gupta, "Combined membrane and flexural reinforcement in plates and shells," *J. Struct. Div.*, vol. 112, no. 3, pp. 550–557, 1986.
- [9] P. B. Lourenço and J. A. Figueiras, "Automatic design of reinforcement in concrete plates and shells," *Eng. Comput.*, vol. 10, no. 6, pp. 519–541, 1993.
- [10] Comité Euro-International du Béton, *Model Code 1990*, 1993.
- [11] Comité Euro-International du Béton, *Model Code 2010*, 2013.
- [12] A. B. Colombo, J. C. Della Bella, and T. N. Bittencourt, "An algorithm for the automatic design of concrete shell reinforcement," *IBRACON Struct. Mater. J.*, vol. 7, no. 1, pp. 53–67, 2014.
- [13] J. Kollegger, M. Azevedo, P. Kinzler, and A. Schirp, "Automated design procedure for reinforced concrete plates and shells," in *Proc. Comput. Model. Concr. Struct.*, 1998, pp. 959–967.
- [14] Comité Euro-International du Béton, *Bulletin 45: Practitioners' Guide to Finite Element Modelling of Reinforced Concrete Structures*, 2013.
- [15] T. Baumann, "Zur Frage der Netzbewehrung von Flächentragwerken," *Bauingenieur*, vol. 47, no. 10, pp. 367–377, 1972.
- [16] A. K. Gupta, "Membrane reinforcement in shells," *J. Struct. Div.*, vol. 107, no. 1, pp. 41–56, 1981.
- [17] F. J. Vecchio and M. P. Collins, "The modified compression-field theory for reinforced concrete elements subjected to shear," *ACI J.*, vol. 83, no. 2, pp. 219–231, 1986.

---

**Author contributions:** MVC: literature review, practical examples, discussions, conclusions, writing and translation; TNB and JCDB: advisory and review.

**Editors:** Ricardo Carrazedo, José Luiz Antunes de Oliveira e Sousa, Guilherme Aris Parsekian.



## ORIGINAL ARTICLE

# Bending reinforced concrete beams with glass fiber reinforced polymer bars: an experimental analysis

## *Vigas de concreto armadas à flexão com barras de polímeros reforçados com fibras de vidro: uma análise experimental*

Tales Viebrantz Fernandes<sup>a</sup> Aline Ribeiro Paliga<sup>a</sup> Charlei Marcelo Paliga<sup>b</sup> <sup>a</sup>Univesidade Federal de Pelotas – UFPel, Centro de Engenharias, Pelotas, RS, Brasil<sup>b</sup>Univesidade Federal de Pelotas – UFPel, Faculdade de Arquitetura e Urbanismo, Pelotas, RS, Brasil

Received 15 January 2020

Accepted 07 August 2020

**Abstract:** There is a recurring need to construct in places where environmental aggressiveness is very high, such as tidal-splash sites, chemical industries, etc. In these places, steel bars, commonly used for concrete reinforcement, can suffer deterioration, losing cross-sectional area and consequently the resistant capacity. In this regard, Glass Fiber Reinforced Polymers (GFRP) bars can replace steel because of its high strength to harsh environments, low weight and high tensile strength. Thus, this work aimed to compare reinforced concrete beams with steel bars and GFRP bending bars using the procedures indicated in ABNT:NBR 6118 and ACI 440.1R-15, respectively. Experimental three-point flexural tests were performed on six concrete beams, three reinforced with steel bars and three reinforced with GFRP bars. The beams were designed for centered point loads of 23.5 kN, 37.5 kN and 57 kN, and for each load one beam was reinforced in steel and one in GFRP. As main conclusions, it can be said that the beams reinforced with GFRP bars presented greater transverse displacements due to the low modulus of elasticity of this material. In addition, the beams presented rupture loads close to each design load, showing agreement in the recommendations of the two normative documents. Comparing the maximum loads of steel and GFRP beams, ratios of +9.3%, -3.2% and -3% were obtained for beams designed for 23.5 kN, 37.5 kN and 57 kN, respectively. Also, that variations in design loads cause greater variation in the longitudinal reinforcement rate of GFRP bar-beams compared to steel-bar beams.

**Keywords:** GFRP bars, reinforced concrete beams, bending moment design, bending moment test.

**Resumo:** É recorrente a necessidade da realização de construções em locais onde a agressividade ambiental é muito elevada, como locais propensos a respingos de maré, indústrias químicas, etc. Nesses locais, as barras de aço, comumente utilizadas para a armação do concreto, podem sofrer deterioração, perdendo área da seção transversal e conseqüentemente a capacidade resistente. Nessa questão, as barras de GFRP (Glass Fiber Reinforced Polymers/polímeros reforçados com fibras de vidro) podem substituir o aço por conta de sua alta resistência a ambientes agressivos, baixo peso e elevada resistência à tração. Assim, esse trabalho teve como objetivo comparar vigas de concreto armadas com barras de aço e com barras de GFRP dimensionadas à flexão através dos procedimentos indicados nas normas ABNT:NBR 6118 e ACI 440.1R-15, respectivamente. Foram realizados ensaios experimentais à flexão por três pontos em seis vigas de concreto, sendo três armadas com barras de aço e três armadas com barras de GFRP. As vigas foram dimensionadas para cargas pontuais centradas de 23,5 kN, 37,5 kN e 57 kN, sendo que para cada carga uma viga foi armada em aço e outra em GFRP. Como principais conclusões, pode-se dizer que as vigas armadas com barras de GFRP apresentaram maiores deslocamentos transversais em virtude do baixo módulo de elasticidade desse material. Ademais, as vigas apresentaram cargas de ruptura próximas para cada carga de dimensionamento, mostrando a concordância nas recomendações dos dois documentos normativos. Se comparadas as cargas máximas das vigas armadas com aço e com GFRP, foram obtidas relações de +9,3%, -3,2% e -3%, para as vigas dimensionadas para 23,5 kN, 37,5 kN e 57 kN, respectivamente. Também, que variações nas cargas de

Corresponding author: Charlei Marcelo Paliga. E-mail: charlei.paliga@ufpel.edu.br

Financial support: None.

Conflict of interest: Nothing to declare.



This is an Open Access article distributed under the terms of the Creative Commons Attribution License, which permits unrestricted use, distribution, and reproduction in any medium, provided the original work is properly cited.

dimensionamento provocam maior variação da taxa de armadura longitudinal das vigas armadas com barras de GFRP quando comparadas com vigas armadas com barras de aço.

**Palavras-chave:** barras de GFRP, vigas de concreto armado, dimensionamento à flexão, ensaio à flexão.

---

**How to cite:** T. V. Fernandes, A. R. Paliga, and C. M. Paliga, "Bending reinforced concrete beams with glass fiber reinforced polymer bars: an experimental analysis," *Rev. IBRACON Estrut. Mater.*, vol. 14, no. 3, e14306, 2021, <https://doi.org/10.1590/S1983-41952021000300006>

## 1 INTRODUCTION

Technology is constantly and rapidly advancing, and this can be observed in all industries, where new products and materials are constantly made available. In civil construction, however, this process takes longer. When comparing construction with other industries, it becomes obvious that it is lagging behind, since it has long used concrete, wood and steel as its main materials. Yet, analyzing the concrete throughout history, it has not changed significantly since the 1930s [1]. According to Medeiros and Helene [2], this is because concrete has always been an extremely durable material, with no concern for its performance in terms of service life.

According to Bolina et al. [3], a concern with the principles of durability was what started to constitute studies linked to the science of materials used in construction. Although with some delay, the belief that buildings were "forever" started to dissolve, and a restriction on the indiscriminate use of materials in all circumstances began to gain strength. A concern with not only constructing a usable building, but also ensuring that it was a durable product, began to take place.

In Brazil, the first concerns with this issue, in normative terms, emerged in 2003, with the revision of NBR 6118. Then, the classes of environmental aggressiveness were defined, separating the surrounding environment from the structures into four categories, ranked according to their aggressiveness potential against reinforced concrete structures. NBR 6118 was also revised in 2007 and in 2014 and, on both occasions, it still did not quantify the service life of projects for buildings, and this gap was filled in 2013, when the performance standard, which is so debated and put into question [3], came into force.

Pereira and Helene [4] emphasize that the concept of service life is linked to the structural system of the construction, and that when the service life of the structural system ends, the service life of the building also ends. Because this is so important, studies related to the pathological manifestations of reinforced concrete structures are in evidence today.

According to Zhao et al. [5], in engineering, the problem of corrosion of steel bars has increasingly affected the use of reinforced concrete structures and can be classified as one of the main and most important pathological problems. In the 1960s, in the United States, problems related to corrosion began to emerge in road structures treated with deicing salt in colder climates, and in bridges that came into contact with sea salt. Consequently, the steel used in these structures started to present problems related to corrosion [6]. Furthermore, reinforced concrete with steel bars is the most used structural system in Brazil. Therefore, improvements to this system regarding service life and maintenance cost are necessary, mainly in coastal structures, such as bridges, subways, and slope abutments, which are the most critical cases [1].

In addition to issues related to the durability of traditional materials, the increase in the speed of construction has contributed to the development and use of lighter-weight structural materials, with less need for maintenance and less degradation caused by environmental agents [7]. Thus, composite materials based on synthetic fibers and resins are an effective way to solve the problem of corrosion of steel bars.

Today, there are many varieties of composite materials, including SFRP (Steel Fiber Reinforced Polymer), GFRP (Glass Fiber Reinforced Polymer), CFRP (Carbon Fiber Reinforced Polymer), and AFRP (Aramid Fiber Reinforced Polymer), among which GFRP is the cheapest [5].

Thus, according to ACI 440R-96 [6], the main interest of the construction industry in the use of fiber-reinforced polymer bars as reinforcement is linked to their durability, as they do not present corrosion issues, as occurs with reinforced concrete steel. Furthermore, by replacing steel bars, which are conventionally used, with GFRP bars, there is a 25% reduction in the weight of the bars. This can make structures lighter, reducing the loads needed and optimizing logistics processes and handling of precast concrete parts [8].

Landesmann et al. [9] state that the use of GFRP elements has grown steadily in recent years, as they have become extremely popular in different industries, such as aerospace, automotive, marine, O&G (oil and gas), and construction. In addition, the authors say that GFRP provides very flexible design solutions, due to its extraordinary flexibility of manufacture, high durability, and structural efficiency (high strength-to-weight ratio). Its use also benefits from increasingly lower production and efficiency costs. As a negative of using GFRP bars to replace steel in concrete beams, Silva [10] points out that beams reinforced with steel bars have greater stiffness, which has been proven through the



analysis of load x deflection curves, when compared to beams reinforced with fiber-reinforced polymer bars. This need for improvement justifies studies on the use of these materials in the construction industry.

Although fiber-reinforced polymer bars show high potential for use, currently there is no specific Brazilian standard that regulates the use of this material. Due to this, structural designers have to resort to international standards or practical recommendations from manufacturers. Thus, studies on the use of these bars as reinforcement elements in concrete structures are needed to establish guidelines for their use, which need an abundant number of analyses, studies, and tests. Studies are necessary to obtain a document that can assist projects that aim to use a very promising material.

To better understand a specific use of this material, the present work had the general objective of analyzing the bending behavior of concrete beams reinforced with GFRP bars and comparing them with steel-reinforced beams. To achieve the general objective, some specific objectives were formulated, such as verifying the influence of different design methods (NBR 6118 and ACI 440.1R-15) for bending reinforcement, for the same load levels; analyzing changes in bending behavior of beams when using different standards and different materials, for the same load level; and analyzing the effect of different design loads on the behavior of beams reinforced with steel bars and with GFRP bars in relation to rupture loads and flexural stiffness.

## 2 MATERIALS AND EXPERIMENTAL PROGRAM

Six reinforced concrete beams were designed and tested for different load magnitudes. The point loads applied to the center chosen to perform the flexural design were 23.5 kN, 37.5 kN, and 57 kN, in addition to the beam's self-weight. Thus, two beams were designed for each of these loads, one reinforced with steel bars, designed according to NBR 6118 [11], and the other with GFRP bars, designed according to American standard ACI 440.1R-15 [12]. The dimensions of the beams for all situations were set at 14 x 20 x 105 cm (width x height x length), and their details followed the recommendations of each standard. Figure 1 presents the schematic drawing of how the experimental tests and the application of the loads were carried out.

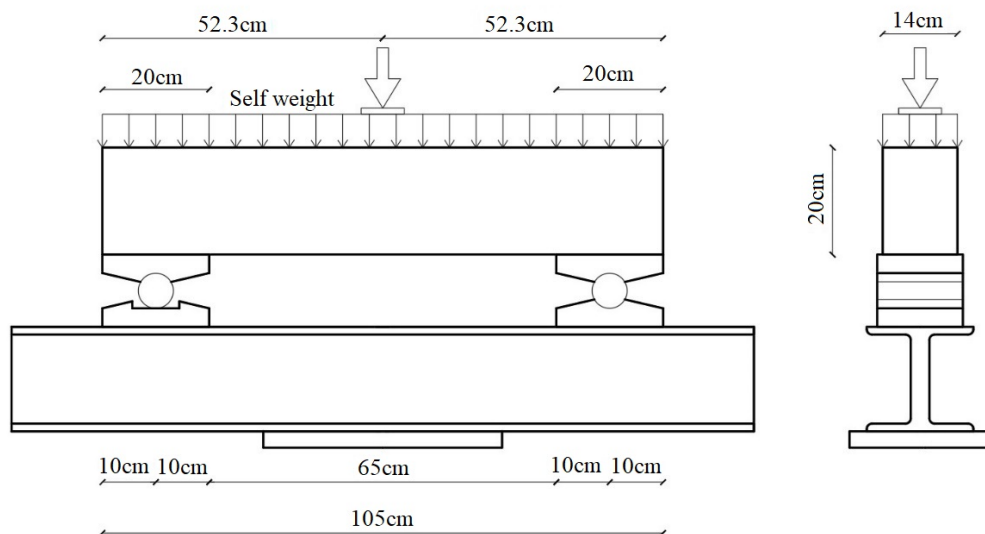


Figure 1. Diagram of the loads of the beams.

The shear design of the beams was determined according to NBR 6118 [11]. Thus, the stirrups on all beams were made of metallic material, CA-60 steel. Since the goal of this work is to analyze flexural behavior, it was ensured, through transverse reinforcement, that the rupture in the beams would occur as desired, that is, due to the normal stress applied to the cross section. Furthermore, since the design of the longitudinal reinforcements resulted in simple reinforcement (only the tensile reinforcement was designed), the upper bars were only used for the assembly of the stirrups. Thus, they were made of steel bars in all six beams.

Table 1 shows the nomenclatures of the beams, which will be used from now on in the text, as well as the design load for each one, and a brief description of their characteristics.

**Table 1.** Characteristics of the beams.

Abbreviation	Characteristic	Design load (kN)
VA23		23.5
VA37	Beam reinforced with steel bars	37.5
VA57		57
VV23		23.5
VV37	Beam reinforced with GFRP bars	37.5
VV57		57

## 2.1 Materials

For the construction of the six beams, a conventional concrete was produced in the laboratory with characteristic strength to compression,  $f_{ck}$ , of 25 MPa, since this is the minimum strength for use in urban environments, and widespread in the construction market, for parts used for structural purposes. To achieve this strength, the dosage method of the Brazilian Portland Cement Association (ABCP) was used. The value of 31.6 MPa was calculated for the average dosage strength, with 4.0 MPa standard deviation. The slump test was 80 to 100 mm, and the water/cement ratio was determined using the dosing methodology (Abrams curve) with a value of 0.51. At the end, a mass unitary trace was reached, with the following proportions: 1 kg of cement: 1.98 kg of sand: 2.31 kg of gravel, and 0.51 kg of water.

The aggregate characteristics were determined according to NBR NM 248 [13], NBR NM 53 [14], NBR NM 45 [15], and NBR NM 52 [16], and the results are shown in Table 2. The cement used was CP IV-32 RS, with a specific mass of 2810 kg/m<sup>3</sup>, purchased in direct contact with the manufacturer. The water used was supplied by the local water company.

**Table 2.** Material properties.

	Maximum characteristic diameter (mm)	Fineness modulus	Unit mass (kg/m <sup>3</sup> )	Specific mass (kg/m <sup>3</sup> )
Gravel of granitic origin	19	4.29	1348	2655
Quartz sand	2.36	2.59	-	2430

To guarantee the technological control of the concrete produced, 18 (three for each beam) 10x20cm (diameter x height) cylindrical specimens were cast. They were tested by compression at 28 days, with an average strength value of 31.13 MPa, which is close to the average dosage strength of 31.6 MPa. This value demonstrates the good quality of the concrete.

## 2.2 Design and reinforcement of the beams

The material of the longitudinal reinforcement of beams reinforced against tension with steel bars, VA23, VA37 and VA57, was CA-50 steel. The design and detailing were carried out according to NBR 6118 [11]. The nominal coverage of the reinforcement was 25 mm, going from the face of the beam to the face of the reinforcement. Plastic spacers were used to ensure this coverage.

The flexural design and detailing of the beams reinforced with GFRP bars, VV23, VV37, and VV57, was carried out according to the American standard ACI 440.1R-15 [12] – Guide for the Design and Construction of Concrete Reinforced with FRP Bars. The properties of the GFRP bars were provided by the manufacturer and can be seen in Table 3. Figure 2 shows the GFRP bars, with diameters of 6 mm, 12 mm and 25 mm.

**Table 3.** Commercial diameters of the GFRP bars, and their properties.

Properties		Standard diameters (mm)							
		6	9	12	14	18	20	25	32
Nominal tensile strength	MPa	1070	1047	989	953	903	876	831	727
Tensile force	kN	24.53	53.96	91.23	119.68	187.37	224.65	333.54	420.85
Poisson's ratio	-	0.25	0.21	0.26	0.25	0.25	0.25	0.28	0.26
Young's modulus	GPa	48	48	48	48	47	47	46	46
Nominal compressive stress	MPa	553	541	494	483	514	516	505	493
Elongation	%	2.12	2.11	2.05	2.03	2.08	2.1	2.07	2.15
Nominal shear stress	MPa	210	210	210	210	204	204	200	200



**Figure 2.** Ribbed GFRP bars.

Table 4 presents the areas of steel and GFRP calculated to absorb the tensile stress caused by the bending of the beams, and Figure 3 brings the details of the beams. Figure 4 shows the completed reinforcement of beams VV37 and VA37. After concreting the beams, they were left in an appropriate place in the laboratory, with wet curing by sprinkling water during the first days, and then they were ruptured after 28 days.

**Table 4.** Reinforcement area found in the design stage.

Abbreviation	Point load (kN)	Designed area (cm <sup>2</sup> )	Adopted solution	Existing area (cm <sup>2</sup> )
VA23	23.5	1.04	2ø8	1.01
VV23		0.84	3ø6	0.85
VA37	37.5	1.87	2ø10 + 1ø6.3	1.88
VV37		2.25	2ø12	2.26
VA57	57	2.87	2ø12.5 + 1ø8	2.95
VV57		9.48	2ø25	9.82

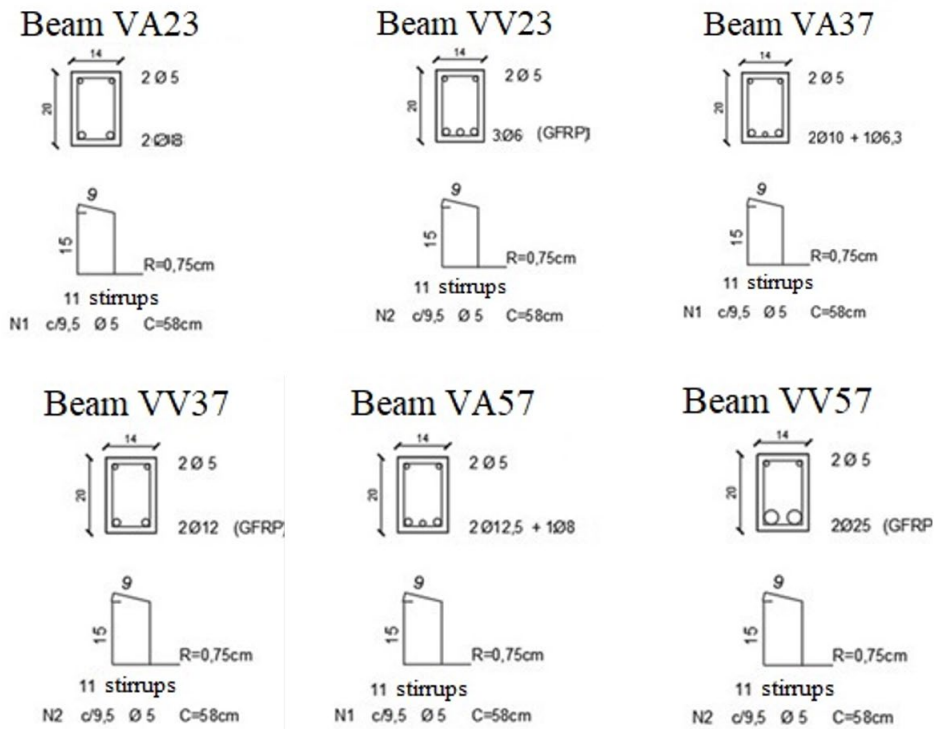


Figure 3. Transversal detailing of the tested beams.



Figure 4. Reinforcement of beams VV37 and VA37.

### 3 RESULTS AND DISCUSSION

This section presents the results obtained for the beams during the experimental tests performed at 28 days.

#### 3.1 Beams designed for 23.5 kN (VA23 and VV23)

The load x displacement curves obtained in the tests of beams VA23 and VV23 are shown in Figure 5. With a load of approximately 20 kN, beam VA23 began to crack, after that, appeared the next two cracks with loads of 30 kN and 45 kN, caused by bending. After that, the cracking increased until the reinforcement began to yield, with a load of approximately 60 kN. The maximum load supported by this beam was 76.32 kN, and the corresponding displacement was 8.62 mm. This rupture happened smoothly, since steel was in plastic regime.

For beam VV23, cracks began to appear with a load of 24.5 kN, as can be clearly seen in Figure 5. The cracks were limited to the lower part of the beam, in the direction of the neutral line, presenting a more visible opening close to the bottom endpoint. Flexural cracks can be seen in Figure 6. As the load increased, the beam ruptured abruptly, which is consistent with the brittle linear behavior of the GFRP bars. The mode of failure of the concrete beam occurred due to the tensile rupture of the GFRP bars, as expected, and according to the calculation for this beam, in which the bars were designed considering their tensile strength. This mode of failure of the concrete beam is the one that uses the GFRP bars to their maximum, however, it is the form that requires the greatest care, due to the brittle form of rupture. The maximum load supported by the beam was 69.8 kN for an 11.3 mm deflection. At that moment, there was a rupture of one of the GFRP bars, shown in the graph in Figure 5 by the abrupt drop in the load to maintain the displacement rate constant. In addition, it is possible to observe the rupture of the other two bars in the displacements around 13.2 mm and 14 mm. Figure 7 shows the ruptured bars, through the crack that caused the beam to break.

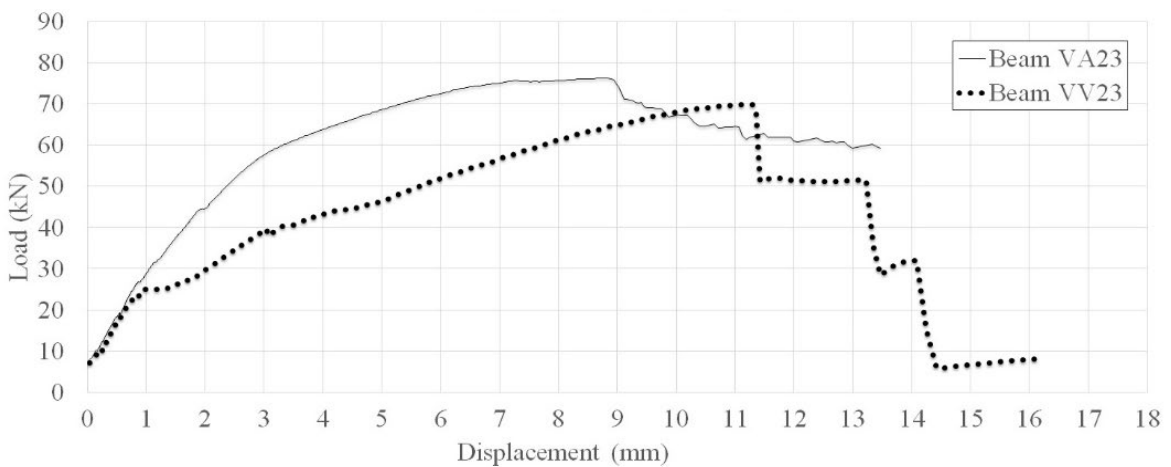


Figure 5. Load vs displacement curves of the 23.5 kN beams.



Figure 6. Cracks observed in the VV23 beam.



Figure 7. Rupture of the GFRP bars of the VV23.

Analyzing the graphs presented in Figure 5, the steel-reinforced beam presented a greater maximum load and displacement corresponding to the smaller load when compared to the beam reinforced with GFRP. In percentage terms, beam VA23 supported a load 9.3% higher than beam VV23, that is, 76.32 kN and 69.8 kN, respectively. In addition, the GFRP beam had a displacement 26% greater than the beam reinforced with steel against tension, at its maximum load. Also, it should be noted that until they started to crack, the two beams presented the same stiffness. This behavior can be explained by the fact that the tensile stress is absorbed by the concrete, with the collaboration of the tension reinforcement starting after the cracking. After that, for the same load level, beam VV23 showed greater displacements, a fact that can be easily explained by the lower longitudinal elastic modulus of the GFRP bars when compared to the same property in steel, 48 GPa and 210 GPa, respectively. In addition, after cracking, the behavior of the GFRP-reinforced beam is practically linear until it reaches its maximum load. This behavior is given by the linearity of the stress x strain curve of the bars made of composite materials.

Another extremely important fact that should be noted regarding the different behaviors of the beams reinforced with metallic material or with material based on fiber-reinforced polymer is that after reaching its maximum load capacity, beams with metallic material still managed to withstand a quite considerable load level, which was not observed for the GFRP beams. This difference in behavior can be explained by one material being ductile (steel) and the other brittle (GFRP).

### 3.2 Beams designed for 37.5 kN (VA37 and VV37)

The load x displacement curves obtained during the tests with beams VA37 and VV37 are shown in Figure 8.

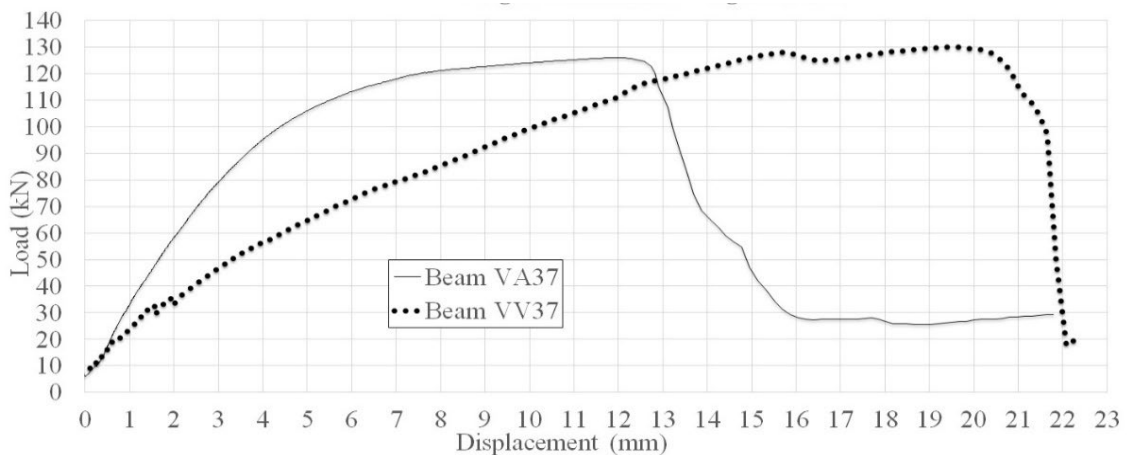
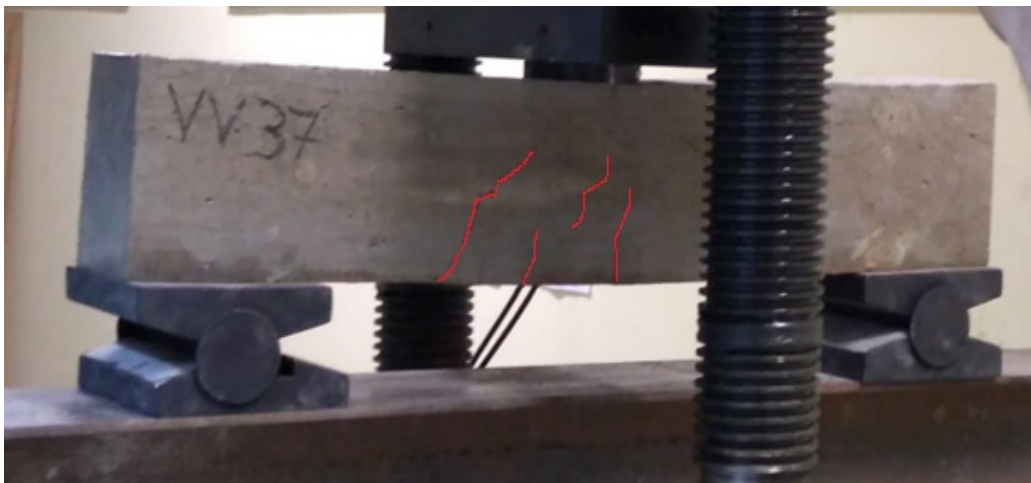


Figure 8. Load vs displacement curves of the 37.5 kN beams.

The maximum load supported by the VA37 was 126 kN, for a corresponding deflection of 11.8 mm. The cracks started to be visible with a load of approximately 52 kN. However, at a load close to 20 kN, there was a change in the slope of the load x displacement curve shown in Figure 8, possibly indicating the opening of the first crack within the beam. The rupture occurred smoothly, with steel in the plastic regime, as expected.

The maximum load supported by beam VV37 was 130.13 kN, with a corresponding deflection of 19.6 mm. Figure 9 shows the cracks that appeared during the test, the first of which appeared with a load of approximately 20 kN, as can be seen in Figure 8 through the disturbance in the load so the press could adjust and apply the displacement at a constant rate again. Other cracks occur near 35 kN, when the GFRP bars become more important in absorbing the tensile stress generated by the bending of the beam. It should be noted that up to a load of approximately 130 kN, the beam's behavior was almost linear, suggesting the actual collaboration of the bars for the absorption of stress. The rupture occurred abruptly, indicated by the drop in load applied to the beam for a displacement of about of 21 mm. Before the rupture, there was "crackling" due to concrete crushing; it is believed that the concrete reached its compression limit when the beam displacements were between 16 and 20 mm, approximately.



**Figure 9.** Cracks observed in beam VV37.

The failure of the beam reinforced with GFRP bars occurred by concrete crushing, without the bars breaking due to tension. It is noteworthy that this was the mode of failure obtained when designing the cross-sectional area of the GFRP bars, corroborating the results observed in the test, with concrete crushing without reaching the ultimate tensile strength of the bars.

When analyzing Figure 8, which shows the overlapped curves of the steel-reinforced beam, VA37, and the GFRP-reinforced beam, VV37, it can be observed that the GFRP beam presented a higher load, about 3% greater. Also, the deflection found was 64% higher for the maximum load of the GFRP beam, when compared to the displacement of the maximum load of the steel beam. The same behavior was obtained for the 23.5 kN beams, due to the elastic modulus of the GFRP bars being lower than that of steel bars.

Again, these tests showed that the two beams behave similarly until the concrete begins to crack. After this, the tensile reinforcement starts to collaborate effectively for the absorption of stress, affecting and differentiating the behavior of the two beams according to the different behaviors of the steel bars and the GFRP bars.

### **3.3 Beams designed for 57 kN (VA57 and VV57)**

The VA57 beam supported a load of 143.8 kN, with a corresponding deflection of 18.6 mm. Figure 10 shows the cracks that caused the beam to rupture, which occurred due to flexural stresses. Figure 11 presents the load x displacement curves of the beams designed for the 57 kN load.



Figure 10. Rupture of beam VA57.

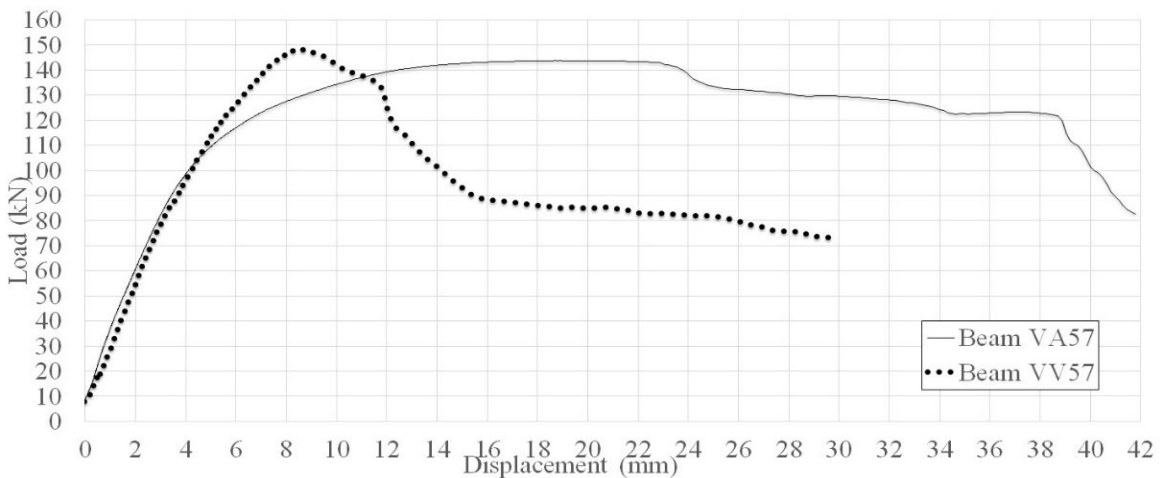


Figure 11. Load vs displacement curves of the 57 kN beams.

An analysis of the VA57 beam shows that it behaved linearly up to a load of approximately 100 kN, indicating the effective collaboration of the tensile reinforcement, possibly working in the elastic regime. After this load level, it is believed that the steel entered its plastic phase, that is, it yielded, absorbing stresses up to a displacement level of 23 mm, when it is believed that concrete crushing began. It is noteworthy that this beam was designed with a position relative to the neutral line close to 0.45 (domain 3), which indicates failure of the element with concrete crushing and steel in the plastic regime. Failure said to be ductile with intense cracking and compressed concrete reaching its resistant capacity, which meets the rupture mode found in the test.

The VV57 beam supported a maximum load of 148.3 kN for an 8.5 mm deflection. The graph in Figure 11 shows the actual collaboration of the GFRP bars for beam strength, due to the linear behavior of the load x displacement curve of VV57 until the maximum load (148.3 kN). This behavior is typical of fiber-reinforced polymer bars. After the maximum load, the press was forced to decrease the load applied to the beam so that it could maintain a constant displacement rate, due to the loss of stiffness caused by the start of concrete crushing, going up to a displacement of about 16 mm.

As an important information, it should be said that the GFRP area for the 57 kN load was designed by predicting beam failure by concrete crushing with underutilization of the resistant capacity of the bars, which can be seen in Figure 12, which translates the behavior expected in the test. The same Figure 12a shows how the excess compression deformed the upper reinforcement, while the lower reinforcement, shown in Figure 12b, did not reach its maximum capacity.





**Figure 12.** a Crushed concrete. b. Intact GFRP bars.

The load supported by beam VV57 is about 3% higher than beam VA57. Still, its vertical displacement was much lower than the displacement of the steel beam, about 119%, when compared to the displacements in the maximum loads supported by the beams. This behavior is different from the other results presented here. This was due to the reinforcement rate of the GFRP beam (9.82 cm<sup>2</sup>) being much higher than that of the steel beam (2.95 cm<sup>2</sup>), thus compensating for the lower elastic modulus of the fiber-reinforced polymer bars. In addition, as shown in the graphs in Figure 11, the two beams behaved very similarly until a load level close to 100 kN. This is explained by the high GFRP reinforcement rate in relation to the steel rate, approximately 3.3 times higher, which made these beams behave differently than the other four beams. After this load, the beams start to behave differently, because the steel yields, providing greater ductility to the beam, unlike the GFRP bars, which have elastic-linear behavior. Through these curves, it becomes clear how the properties of the materials (steel/GFRP) interfere in the behavior of the beams, giving them more or less ductility.

### 3.4 Comparison between steel and GFRP bars

Table 5 shows the tensile reinforcement area used in each of the beams. Most of the beams designed with GFRP had a larger cross-sectional area when compared to the corresponding steel beams. This was expected, due to the elastic modulus of the GFRP bars being lower than the longitudinal elastic modulus of the steel bars. However, it should be noted that the bars were not ruptured in beams VV37 and VV57, thus, their resistant capacity was not reached. In beam VV23, however, failure occurred due to the rupture of the GFRP bars due to tensile strength, with the three failure modes obtained in the tests following those used in the design.

**Table 5.** Comparison between flexural reinforcement areas.

Abbreviation	Flexural reinforcement area (cm <sup>2</sup> )	Ratio between the VV/VA areas (%)	Ratio between Design load/Reinforcement area (kN/cm <sup>2</sup> )
VA23	1.01	84%	23.27
VV23	0.85		27.65
VA37	1.88	120%	19.95
VV37	2.26		16.59
VA57	2.95	333%	19.32
VV57	9.82		5.80

Beam VV57 presented an area 3.33 times greater when compared with the corresponding steel beam, VA57. However, it did not present a much higher ultimate load, only 1.06 times greater, because the final strength in these

beams was limited by the compressive strength of the concrete, with underutilization of the resistant capacity of the bars.

In addition, the beam that presented the best design load/reinforcement area ratio, that is, the most efficient design, was VV23, which was designed for the tensile rupture of the GFRP bars, and reached what was expected, with the total use of its resistant capacity. However, it should be noted that these results have to do with the ultimate flexural limit when the resistant capacity of the element is exhausted.

Regarding issues related to deformations, which must be sufficiently small when in service loads, under penalty of causing problems for the use of the buildings, VV23 had a worse performance than VA23 after moving to stage II. For a load of 30 kN, the steel-reinforced beams presented a displacement of 1.05 mm, while the GFRP-reinforced beams had a 94% greater displacement, of 2.04 mm. After a load increase, this loss of performance became more pronounced, with displacements 101% and 138% greater than the steel-reinforced beam for loads of 40 kN and 50 kN, respectively. Thus, the lower post-cracking stiffness presented by the VV23 beam in comparison to the corresponding steel-reinforced beam should be noted. This is due to the longitudinal elastic modulus of the GFRP being approximately 23% of the longitudinal elastic modulus of steel, which is a negative point of using this material. This issue can be compensated with a larger cross section, for example.

The beams reinforced against tension with steel bars did not present great differences between design load/reinforcement area ratio, with an average ratio of 20.85 kN/cm<sup>2</sup>, standard deviation of 2.12 kN/cm<sup>2</sup>, and coefficient of variation related to these values of 10.2%. The GFRP-reinforced beams, on the other hand, had an average ratio of 16.68 kN/cm<sup>2</sup>, standard deviation of 10.93 kN/cm<sup>2</sup>, and coefficient of variation of 65.5%. Thus, variations in design loads induce more significant variations in the reinforcement areas of GFRP bars than in steel bars.

### 3.5 Steel-reinforced beams

Figure 13 shows the load x displacement curves of the beams that used steel to resist the tensile stresses caused by the bending moment. All beams had curves with a very similar shape, with changes in the strength and also the stiffness scales, mainly for beam VA23 when compared to beams VA37 and VA57. This is the expected behavior for beams designed to have good ductility, as recommended by standards for design. In addition, there is a change in stiffness of the beams when they enter stage III (reinforcement yield), especially beams VA37 and VA57 (load greater than 110 kN), where VA57 had less deformation compared to VA37 due to higher reinforcement rate.

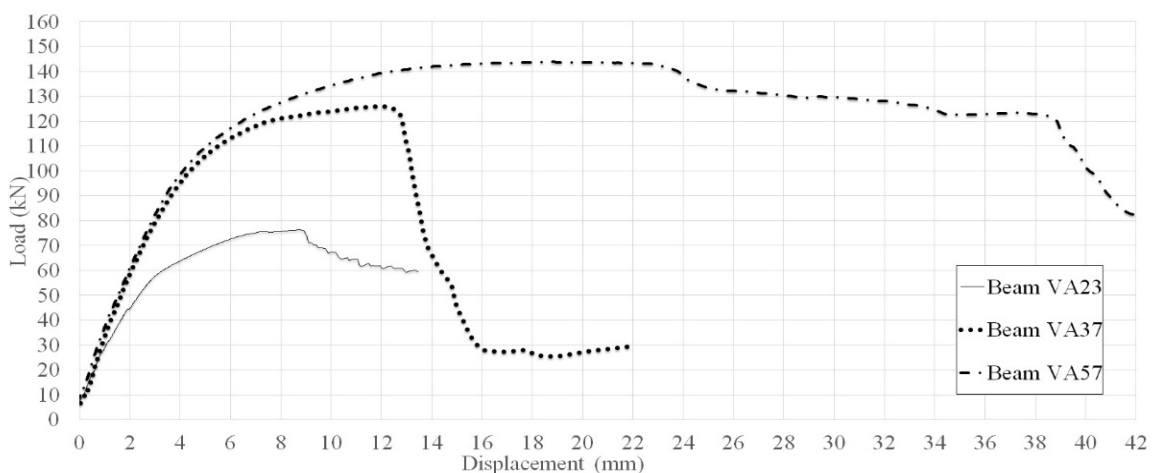


Figure 13. Load vs displacement curves - Beams reinforced with steel.

Also, there was no major increase in strength between beams VA37 and VA57, in which the latter had a reinforcement rate 57% higher, with load capacity only 14% higher than VA37. In these cases, the strengths of the beams were limited by the compressive strength of the concrete. Thus, the bars that resisted bending, at the bottom of the beams, did not significantly increase their final strengths. For that, it would be necessary to increase the compressive strength of the concrete or the cross section of the beam.

### 3.6 GFRP-reinforced beams

Figure 14 shows that the GFRP beams had a sudden drop in strength after reaching their maximum load. This was due to the brittle behavior of the concrete and GFRP that were used. Beams VV23 and VV37 completely lost their load capacities after reaching their maximum load, even though they have different modes of failure, with the first, for beam VV23, caused by the tensile rupture of the bars, and the second, for beam VV37, by concrete crushing. It is important to note that the modes of failure obtained with the tests faithfully followed the modes of failure detailed in the design process.

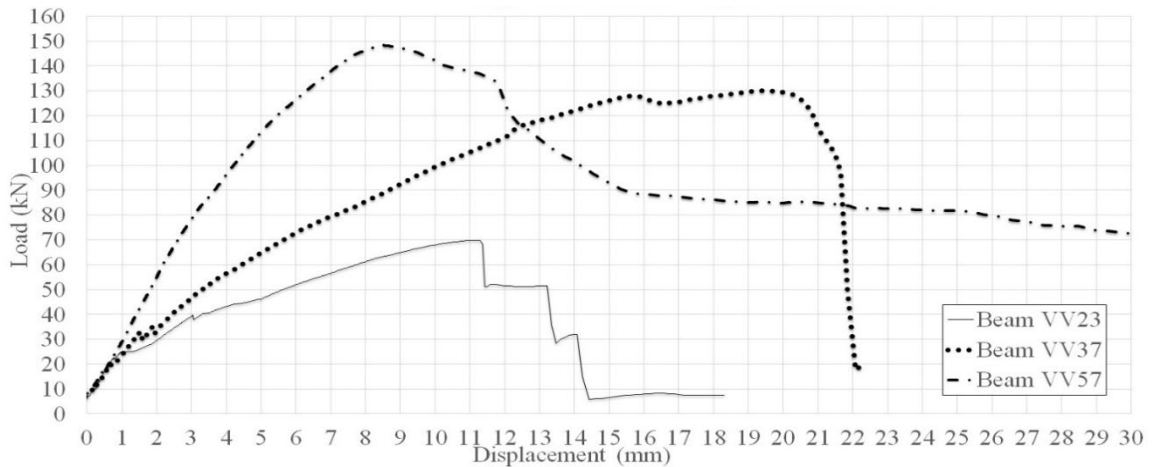


Figure 14. Load vs displacement curves - Beams reinforced with GFRP.

The behavior of beam VV57 was not compatible with the two other GFRP-reinforced beams. This was because the VV57 beam had a much higher tensile reinforcement area than the others. While beam VV57 had a tensile reinforcement area 4.35 times greater than that of VV37, this difference was even greater compared to VV23, where it was 11.55 times greater. Thus, even after the concrete crushing, the beam still retained a rate of load capacity. However, this higher reinforcement rate did not mean differences of the same magnitude in relation to rupture loads, with the maximum load of VV57 being 2.12 times higher than the load of VV23, and 1.14 times higher than the maximum load of VV37. This increase in area by 4.35 times, but only 1.14 times of maximum load, when compared to beams VV37 and VV57, is a clear indication that their mode of failure was given by the limitation of concrete compressive strength.

### 3.7 Beams reinforced with steel and GFRP bars

Figure 15 shows that beam VV57 behaved similarly to the beams reinforced with steel bars, VA37 and VA57, mainly until the steel bars yielded. After that, VV57 presented greater stiffness in relation to the other two beams until reaching its maximum load capacity. This is due to the reinforcement area of this beam being much higher than the reinforcement of beams VA37 and VA57, that is, 5.22 and 3.33 times higher, respectively, thus compensating for its low longitudinal elastic modulus. However, beam VV57 had significantly lower deflection than beams reinforced with steel bars when comparing the maximum loads, which is a negative factor, due to the greater fragility of this material.

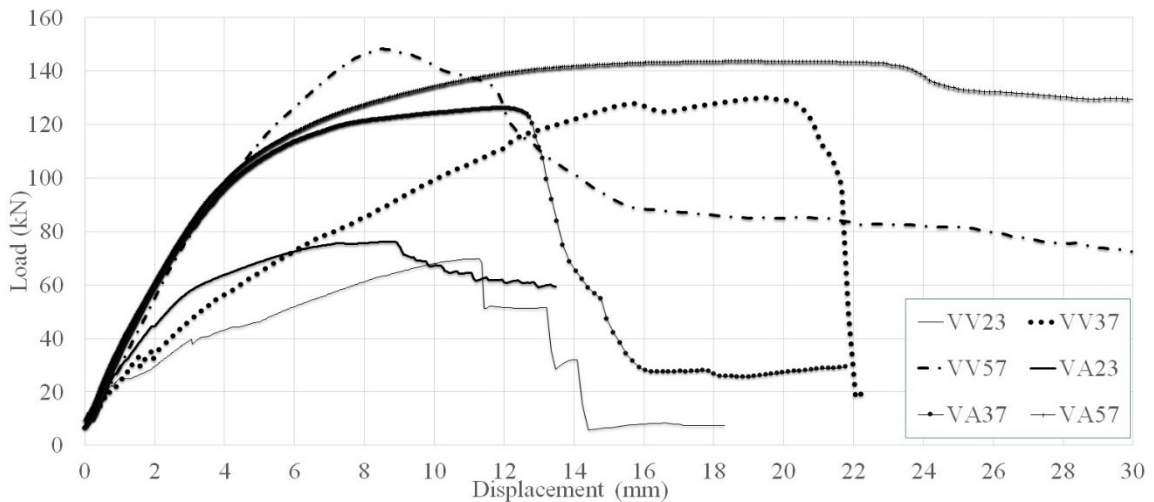


Figure 15. Load vs displacement curves for all beams.

#### 4 CONCLUSIONS

The present work aimed to compare beams reinforced with GFRP and reinforced with steel, which followed different standards documents and had different load levels. After reaching and presenting the results of this experimental research, some conclusions can be drawn.

The beams reinforced with GFRP bars had greater displacements when compared to those reinforced with steel, due to the elastic modulus of this material being almost 80% lower. Although the rupture occurs abruptly, which is characteristic of brittle materials, the displacement of the beam is excessive before failure. This displacement can serve as a warning for possible design flaws before the collapse, because after the beam reaches its maximum load, its strength drops abruptly, leading to its collapse. However, it is important to highlight here that the beams were designed only for the limit state of depletion of the resistant capacity of the materials, both in terms of bending and shear. Thus, for a confirmation of what was said above, an analysis must be carried out during the project regarding the service limit state related to excessive deformations.

Although the deformations of the GFRP beams were quite high, due to the low elastic modulus of this material, this behavior can be mitigated by a higher flexural reinforcement rate. The results of beam VV57 can be used as an example. This beam had a higher maximum load (about 3%), and the displacement related to the maximum load was about 50% lower when compared to VA57. However, this behavior can make the production of the piece quite expensive due to the high cost of GFRP bars, when compared to steel. Also, care must be taken when designing a concrete element with low displacement in the ultimate limit state, since displacement is an early warning for failure.

The final strength of the beam is sensitive to the concrete compressive strength and its cross-sectional dimensions, because of the modes of failure linked to concrete crushing. For the safer design of beams reinforced with GFRP bars, it is important to pay greater attention to the form of failure and seek to ensure the greatest possible ductility. This situation occurs when there is a high deformation at the compressed edge at the moment of the rupture simultaneously with a high tensile deformation in the bars, resulting in a large curvature.

The American standard allows that both the form of rupture dominated by tensile and compression can occur, although it recommends that the concrete crushing occurs before the FRP rupture, this being the failure mode of the VV37, with concrete crushing and possible great deformation in the GFRP bars, even if its strength has not been reached. In the VV57 case, there was a failure of the beam by concrete crushing before mobilizing a significant tensile deformation in the GFRP bars, indicated by the low ductility of the beam compared to the respective beam reinforced with steel. It is noteworthy that this was the only beam reinforced with GFRP that presented a lower displacement than its respective reinforced steel beam when the maximum load was reached.

However, this form of design may not be the most efficient. An example of this is beam VV23, in which there was tensile rupture of the GFRP bars, indicating they had reached their limits of use. Furthermore, the rate of flexural reinforcement was lower in the beams reinforced with GFRP bars compared to the beams reinforced with steel bars (VA23). Also, there were no significant differences in the maximum loads between these two beams, with a maximum load/design load ratio of 3.25 and 2.97 for beams VA23 and VV23, respectively.

Regarding the standards for design used in this work with steel bars (NBR 6118) or GFRP bars (ACI 440.1R-15), it can be said that the different guidelines did not lead to significant differences in terms of the beams' resistant capacity. When comparing the maximum loads of beams reinforced with steel and with GFRP, ratios of +9.3%, -3.2%, and -3% were obtained, for beams designed for 23.5 kN, 37.5 kN, and 57 kN, respectively. These results indicate good design practices in the two standards.

Also, the results suggest the beam designs had good levels of safety, with maximum load/design load ratios for beams VA23, VA37 and VA57 of 3.25, 3.36 and 2.52, respectively. For beams VV23, VV37 and VV57, the ratios were 2.97, 3.47 and 2.60, respectively.

## ACKNOWLEDGEMENTS

The authors would like to thank the company STRATUS Compostos Estruturais Ltda. for donating the GFRP bars, and the Laboratory of Materials and Construction Techniques (LabMat) of the Federal University of Pelotas for making space and equipment available for the tests.

## REFERENCES

- [1] D. H. Tavares, "Análise teórica e experimental de vigas de concreto armadas com barras não metálicas de GFRP," M.S. thesis, Dept. Eng. Estrut., Univ. São Paulo, 2006.
- [2] M. H. F. Medeiros and P. R. L. Helene, *Durabilidade e Proteção do Concreto Armado*. São Paulo: Téchne, 2009.
- [3] F. L. Bolina, B. F. Tutikian, and P. R. L. Helene, *Patologia de Estruturas*. São Paulo: Oficina de Textos, 2019.
- [4] F. Pereira and P. R. L. Helene, "Guía para el diagnóstico y la intervención correctiva," in *Rehabilitación y Mantenimiento de Estructuras de Concreto*. Bogotá: SIKA, 2007.
- [5] X. Zhao, X. J. He, and Y. C. Yang, "Numerical simulation of GFRP reinforced concrete beams," *Adv. Mater. Sci. Eng.*, vol. 2017, pp. 1–10, 2017.
- [6] American Concrete Institute, *State-of-the-Art Report on Fiber Reinforced Plastic (FRP) Reinforcement for Concrete Structures*, ACI 440R-96, 2002.
- [7] J. R. Correia, J. Ferreira, and F. Branco, "Utilização de perfis pultrudidos de fibra de vidro (GFRP) na construção," in *An. 2º Congr. Nac. Constr. – Repensar a Construção*, 2004.
- [8] J. Farmer Junior, M. Aurich and R. Girardi, "Estudo comparativo entre vigas de concreto armado convencional e vigas armadas com barras de fibra de vidro," in *An. 60º Congr. Bras. Conc.*, 2018.
- [9] A. Landesmann, C. A. Seruti, and E. M. Batista, "Mechanical properties of glass fiber reinforced polymers members for structural applications," *Mater. Res.*, vol. 18, no. 6, pp. 1372–1383, 2015.
- [10] R. C. B. Silva, "Comportamento de vigas de concreto armadas com barras de CFRP e GFRP para infraestrutura de transportes," M.S. thesis, Inst. Mil. Eng., Rio de Janeiro, 2014.
- [11] Associação Brasileira de Normas Técnicas, *Projeto de Estruturas de Concreto – Procedimento*, NBR 6118, 2014.
- [12] American Concrete Institute, *Guide for the Design and Construction of Concrete Reinforced with FRP Bars*, ACI 440.1R-15, 2015.
- [13] Associação Brasileira de Normas Técnicas, *Agregados – Determinação da Composição Granulométrica*, NBR NM 248, 2003.
- [14] Associação Brasileira de Normas Técnicas, *Agregado Graúdo – Determinação da Massa Específica, Massa Específica Aparente e Absorção de Água*, NBR NM 53, 2009.
- [15] Associação Brasileira de Normas Técnicas, *Agregados – Determinação da Massa Unitária e Volume de Vazios*, NBR NM 45, 2006.
- [16] Associação Brasileira de Normas Técnicas, *Agregado Miúdo – Determinação da Massa Específica Aparente e Absorção de Água*, NBR NM 52, 2009.

---

**Author contributions:** TVF: conceptualization, obtaining the data, writing; ARP: conceptualization, methodology, supervision and CMP: conceptualization, methodology, supervision, formal analysis.

**Editors:** Ricardo Carrazedo, José Luiz Antunes de Oliveira e Sousa, Guilherme Aris Parsekian.



ORIGINAL ARTICLE

# Shear in sand-lightweight and conventional high strength concrete through the push-off test

*Cisalhamento em concreto leve e convencional de alta resistência através do ensaio push-off*

Patricia da Silva Pereira Figueiredo<sup>a</sup> Thais Amaral Soares<sup>a</sup> Sergio Luis González García<sup>a</sup> Allonso Curty da Silva Pereira<sup>a</sup> Juliana Corrêa Trindade<sup>a</sup> <sup>a</sup>Universidade Estadual do Norte Fluminense Darcy Ribeiro – UENF, Laboratório de Engenharia Civil, Campos dos Goytacazes, RJ, Brasil

Received 20 August 2018

Accepted 10 August 2020

**Abstract:** Shear design models in reinforced concrete structures depend on stress transfer through cracks. Such mechanism is influenced by the displacement and roughness of the opposite faces generated during cracking. Shear is reduced when an aggregate particle is fractured leading to a smoother crack as found in lightweight and high strength concrete. This study evaluated the ultimate shear strength of sand-lightweight and conventional high strength concrete as well as the differences in their behavior. Results from Pereira and Soares with 29 push-off test specimens were used. Transverse clamping stress ranged from 4.79 to 12.71 MPa while  $f_{cm}$  was 30 and 50 MPa. The experimental results showed significant differences in the concrete studied. A tri-linear model was proposed to calculate the ultimate shear strength. An overall mean value of  $\tau_{u, exp}/\tau_{u, cal}$  was 0.96.

**Keywords:** shear-friction, lightweight concrete, high-strength concrete.

**Resumo:** Os modelos de dimensionamento ao cisalhamento em estruturas de concreto armado dependem da transferência de esforços através das fissuras, tal mecanismo é influenciado pelo deslocamento e rugosidade das faces opostas geradas durante a fissuração. O cisalhamento é reduzido quando a partícula do agregado se fratura, levando à fissura mais lisa, como ocorre em concretos leve e de alta resistência. O trabalho objetiva avaliar a resistência última de cisalhamento de concretos leve e convencional de alta resistência, mostrando-se as diferenças no comportamento dos mesmos. Para tal, foram utilizados os resultados de Pereira e Soares, com 29 corpos de prova *push-off*, com tensão de confinamento variando de 4,79 a 12,71 MPa e  $f_{cm}$  de 30 e 50 MPa. Os resultados experimentais exibiram diferenças significativas nos concretos estudados. Foi proposto um modelo trilinear para calcular resistência última de cisalhamento, com valor de média geral da relação  $\tau_{u, exp}/\tau_{u, cal}$  de 0,96.

**Palavras-chave:** atrito-cisalhamento, concreto leve, concreto alta resistência.

**How to cite:** P. S. P. Figueiredo, T. A. Soares, S. L. González García, A. C. S. Pereira, and J. C. Trindade, "Shear in sand-lightweight and conventional high strength concrete through the push-off test," *Rev. IBRACON Estrut. Mater.*, vol. 14, no. 3, e14307, 2021, <https://doi.org/10.1590/S1983-41952021000300007>

## 1 INTRODUCTION

Proposed by Birkeland and Birkeland [1] in 1966, the shear-friction theory is an approach that aims to evaluate the transfer of shear forces in concrete-concrete interfaces submitted at the same time by compression and shear stresses. According to the shear-friction theory, these stresses are strengthened exclusively by friction.

Corresponding author: Sergio Luis González García. E-mail: [liluiser@yahoo.com.br](mailto:liluiser@yahoo.com.br)

Financial support: The study was funded in part by the Coordenação de Aperfeiçoamento de Pessoal de Ensino Superior (CAPES) - Funding Code 001.

Conflict of interest: Nothing to declare.



This is an Open Access article distributed under the terms of the Creative Commons Attribution License, which permits unrestricted use, distribution, and reproduction in any medium, provided the original work is properly cited.

According to Hsu et al. [2], the shear transfer mechanism occurs in two different ways: shear transfer through an initially uncracked plane or shear transfer through an initially cracked plane.

In the first shear transfer mechanism, inclined cracks occur to the shear plane, which results in strut and tie-type action. In the second one, initial cracks prevent the development of the truss action. Under shear stress, the concrete element on one side of the crack slides to the other. The sliding is accompanied by an increase in cracks due to the roughness and irregularities along the surface.

This served as a basis for the application of the shear-friction theory that assesses the capacity of a crack to transfer shear forces in structural concrete.

According to González Fonteboa et al. [3], the factors that influence the friction-shear capacity are aggregate interlock, friction, compression force applied perpendicular to interface, the reinforcement across the shear plane and concrete strength.

A model denominated a saw-tooth is commonly used to exemplify the mechanisms involved in this theory. According to Santos and Júlio [4], the model considers the influence of the reinforcement placed crossing the interface and the external forces acting perpendicularly to the shear plane.

In the model, the rough interface is replaced by a series of small teeth. When a horizontal force is applied, one part will slide over the other. Due to the presence of the teeth, the sliding is accompanied by a separation of the surface and this pulls the transverse reinforcement through the interface. To keep a balance, the reinforcement generates compression stresses at the interface and the sliding generates bending and shear forces. Thus, the shear is transmitted due to the aggregates interlock on the cracked surface, friction, and the reinforced shear strengths by dowel action.

The friction and the aggregate interlock are results of the cracked face roughness and are increased by the normal compression force at the interface. The contribution of concrete strength is related to the rupture of the interface, which transmits shear forces and results in loss of contact due to the crushing of the aggregates and the cement matrix. The crushing occurs when the constituents reach their capacity, which is related to the concrete strength.

Concrete can be represented as a system consisting of two phases: the matrix and the particles incorporated into it. The contact area between the two materials is called the interface zone. Generally, the parameters of strength and rigidity of the matrix are lower than those of the particle aggregate. However, the interface zone is the weakest link in this system. Thus, the cracks normally propagate through the matrix, around the aggregates [5].

Considering the shear plane of lightweight concrete, the slip strength is lower than the one in conventional concrete. This occurs because the lightweight aggregate allows the cracks to cross the aggregate instead of moving around it, as in conventional concrete. In other words, cracking is linked to the rupture of aggregate since the strength is comparable to the matrix strength and the “face-smooth crack” results in a less efficient transfer of shear-friction through the aggregate interlock [6].

The High-strength concrete matrix has a higher compressive strength compared to conventional concrete. Thus, the behavior presented by high-strength concrete is similar to lightweight concrete with regard to rupture mode where cracks cross the aggregate.

Few experimental studies have been performed to determine the shear-friction characteristics in concrete with lightweight aggregates [7]–[9]. Some studied the various origins of aggregates [10] and others tried to develop high-efficiency concrete [11], [12].

Push-off test models were used to develop this study. The model has been often used because it requires small-sized specimens, it is cheap and easy to perform and highly specialized test equipment is not needed. The specimens are formed by two L-shaped parts, with two openings that delimit them which allow sliding between them. It has a section reduction in the direction of the shear plane (Figure 1). It also has an auxiliary reinforcement to not allow premature rupture by bending stresses in external phases.

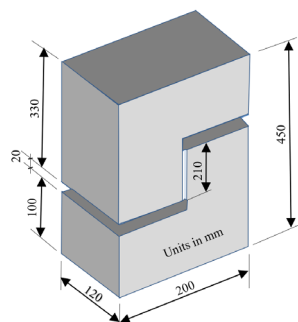


Figure 1. Push-off specimen dimensions.

## 2 JUSTIFICATION

According to Santos and Júlio [13], the friction-shear theory was adopted in most design codes to analyze the concrete-concrete interfaces, and over the past years, it has received several suggestions for improvements to increase accuracy and field application.

Even though it has received many contributions, the ultimate shear capacity has not been fully designed yet for being a complex phenomenon. Currently proposed models and standards to determine ultimate shear capacity present significant differences with respect to experimental values.

We aim to contribute to the development of shear-friction theory and its application in sand-lightweight concrete and conventional high-strength concrete. The main variables studied were clamping stress ( $\rho_v f_{yd}$ ), concrete compressive strength ( $f_{cm}$ ), and coarse aggregate type (lightweight expanded clay aggregate and conventional granite gravel aggregate). We compared the experimental results obtained in these studies with analytical models and prescriptions of ACI 318 [14] and proposed a tri-linear model for the determination of the ultimate shear capacity with greater reliability.

## 3 MATERIALS AND EXPERIMENTAL PROGRAM

This paper analyzed results obtained by Pereira [15] and Soares [16]. Both studies used Mizu® high-initial-strength Portland cement (CP V). Quartz sand from Paraíba do Sul River (Campos dos Goytacazes, Brazil) was used as a fine aggregate. Two types of coarse aggregates were used: CINEXPAN® expanded spherical clay type 1506 with an average diameter of 12.5 mm, and granite type gravel from crushing stones from Campos dos Goytacazes region.

The maximum diameter, the fineness module and the real specific mass of the aggregates were calculated according to ABNT NBR NM 248 [17] and ABNT NBR-NM 45 [18]. The results for granite gravel were 19.00 mm, 5.65 mm and 2.90 kg/dm<sup>3</sup> respectively. The values for expanded clay were 12.5 mm, 3.6 mm and 1.15 kg/dm<sup>3</sup>. Viapol® PLASTOL 5035 was used as the superplasticizer and the water used was supplied by Águas do Paraíba, the company responsible for water supply.

GERDAU CA-50 ribbed bars were used as transverse reinforcement and auxiliary reinforcements. They had nominal diameters of 8 mm and 12.5 mm. For the 8-mm transverse reinforcement, it was obtained a yield strength ( $f_y$ ) of 570 MPa and yield deformation of 2.3%.

Table 1 shows the four concrete compositions produced: one for sand-lightweight concrete and three for high-strength conventional concrete, having  $f_{cm}$  of approximately 30 and 50 MPa, respectively. The slump test value for all compositions was 70 ± 10 mm.

**Table 1.** Composition of concrete used in research (kg/m<sup>3</sup>).

Type of Concrete	Water	Materials					
		Cement	Sand	Gravel	Expanded Clay	W/C	SP (%)
Sand-Lightweight (series A and D)	196.5	517	672.1	-	361.9	0.38	-
Conventional 1 (series B)	205	456	682	1005	-	0.45	-
Conventional 2 (series C)	164.4	478	905.3	860	-	0.34	0.83
Conventional 3 (series E)	225.8	511.6	719.77	905.2	-	0.44	1.47

SP - superplasticizer; W/C - water/cement ratio.

To achieve the proposed objectives, 29 initially cracked push-off specimens from Pereira [15] and Soares [16] were manufactured and tested, under constant monotonous load. The experimental program was divided into five series: A, B and C produced by Pereira [15], and D and E, produced by Soares [16]. The nomenclature adopted for the specimens was: Xn-PO-Y-Z, where X specifies the type of concrete, n specifies the number of concrete (when there is more than one), PO refers to the push-off test, Y is the type of composition and Z was the clamping stress of the transverse reinforcement.

The dimensions of push-off specimens were defined considering ranges used by previous studies, as shown in Pereira [15]. Transverse reinforcements were those commonly used in concrete submitted to this type of stress. The auxiliary reinforcement was defined through stress analysis using SAP 2000® software, allowing the flow of compressive stresses (strut) and tensile stresses (tie) to be found and subsequently sized using the model of connecting strut and tie, by CAST® software, both shown in Figure 2. Details of the push-off specimens are shown in Figure 3.



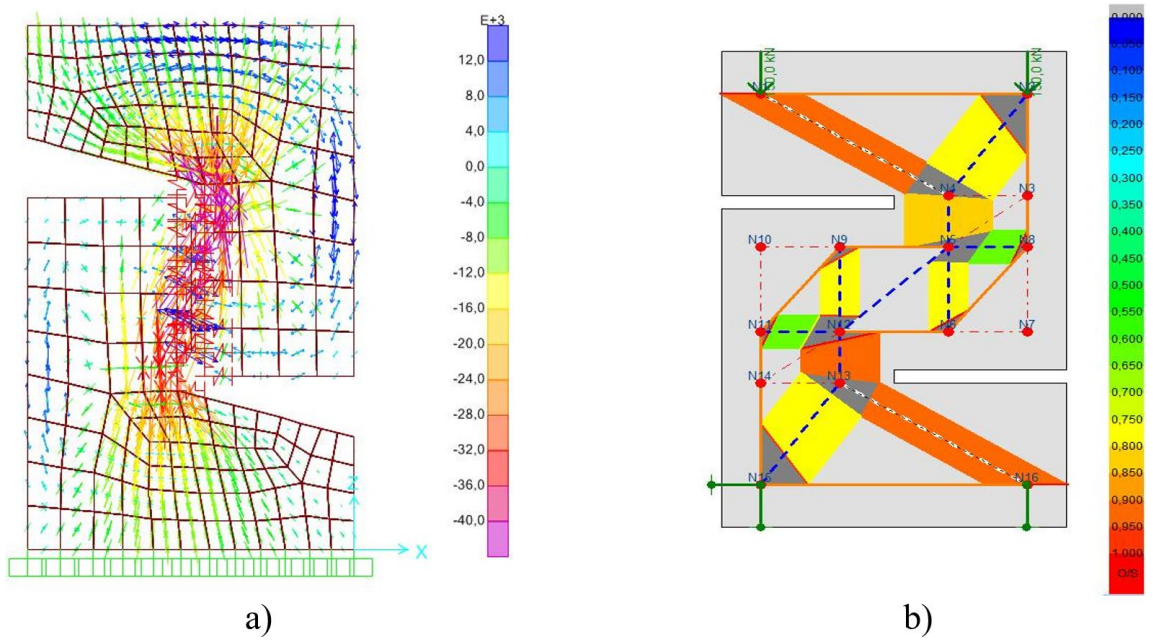


**Figure 2.** Push-off specimen stress analysis: a) main stress distribution using SAP software (2000)<sup>®</sup> and b) strut and tie model using the software CAST<sup>®</sup> [15].

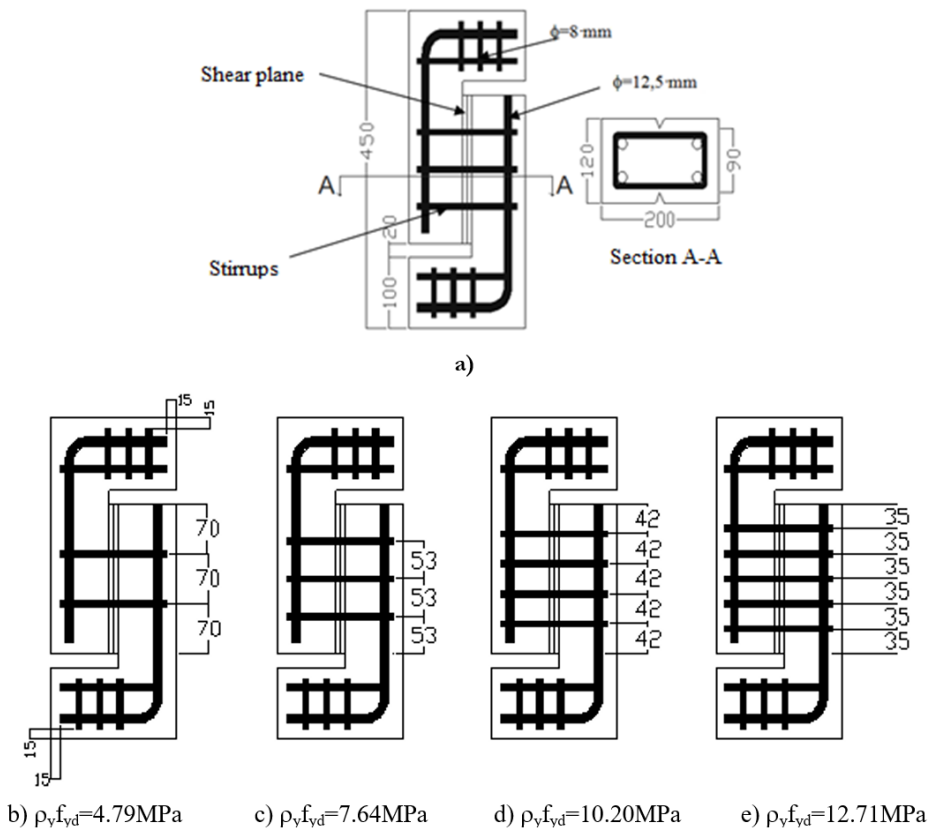


**Figure 3.** Transverse and auxiliary reinforcements on push-off specimens: a) specimen dimensions (mm); b), c) d) series A, B, C, D and E and e) series A, B e C.

To manufacture push-off specimens, metal forms were made as shown in Figure 4. They had a protrusion at the bottom and at the top to delimit the shear plane. Two Styrofoam plates fixed to the form were used for the opening at the ends.

The compressive strength of the concrete was evaluated by rupture cylindrical specimens with dimensions of 100 mm in diameter and 200 mm in height, according to ABNT NBR 5739 [19]. The splitting tensile strength was determined using cylindrical specimens with the same geometrical characteristics and in accordance with the ABNT NBR 7222 [20]. Both results are shown in Table 2.



Figure 4. Metallic form for the production of push-off specimens [15].

The push-off specimens were initially cracked. For this purpose, steel rollers were placed in the shear plane of the specimen in the horizontal position, applying a constant linear load. The tests were performed on an EMIC® test machine with capacity of 2000 kN until the initial point of pre-cracking was detected. The diagram and the pre-cracking test are shown in Figure 5.

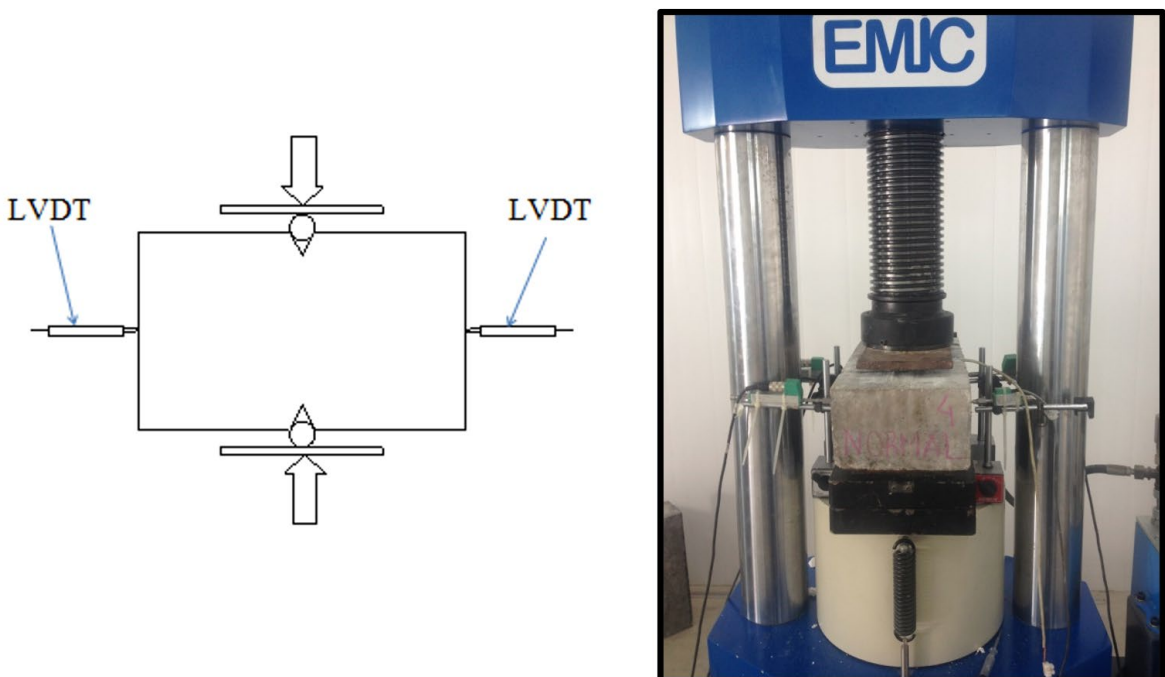


Figure 5. Instrumentation schematic of the push-off pre-cracking test specimens [15].

**Table 2.** Results of compression, splitting tensile and direct shear tests.

Series	Specimens	$f_{cm}$ (MPa)	$f_{ct, sp}$ (MPa)	$\tau_{u, exp}$ (MPa)	$\tau_{u, exp}/f_{cm}$	$\rho_v f_{yd}/f_{cm}$
A	L-PO-1- 4.79	30.9	1.9	4.2	0.14	0.16
	L-PO-1- 7.64			4.3	0.14	0.25
	L-PO-1-10.20			5.6	0.18	0.33
	L-PO-1-12.71			5.7	0.18	0.41
B	N-PO-1- 4.79	52.2	3.2	5.8	0.11	0.09
	N-PO-1- 7.64			8.5	0.16	0.15
	N-PO-1-10.20			10.1	0.19	0.20
	N-PO-1-12.71			7.5	0.14	0.24
C	N-PO-2- 4.79	50.3	3.0	6.4	0.13	0.10
	N-PO-2- 7.64			7.5	0.15	0.15
	N-PO-2-10.20			7.8	0.16	0.20
	N-PO-2-12.71			8.9	0.18	0.25
D	L1-PO-1- 4.79	26.2	2.5	3.9	0.15	0.18
	L2-PO-1- 4.79			5.9	0.22	0.18
	L3-PO-1- 4.79			3.4	0.14	0.19
	L1-PO-1- 7.64			5.1	0.19	0.29
	L2-PO-1- 7.64			5.3	0.19	0.28
	L3-PO-1- 7.64			7.2	0.29	0.30
	L1-PO-1-10.20			4.9	0.19	0.39
	L2-PO-1-10.20			5.5	0.20	0.38
	L3-PO-1-10.20			4.5	0.18	0.41
E	N1-PO-3- 4.79	54.0	4.3	5.2	0.09	0.08
	N2-PO-3- 4.79			5.9	0.12	0.10
	N3-PO-3- 4.79			5.5	0.10	0.09
	N1-PO-3- 7.64			6.6	0.11	0.13
	N2-PO-3- 7.64			5.7	0.11	0.15
	N3-PO-3- 7.64			7.2	0.13	0.14
	N2-PO-3-10.20			6.9	0.14	0.20
	N3-PO-3-10.20			7.2	0.13	0.19

where:  $f_{cm}$  is the compressive strength of concrete.  $f_{ct, sp}$  is the splitting tensile strength,  $\tau_u$  is the ultimate shear strength and  $\rho_v f_{yd}$  is the clamping stress of the transverse reinforcement.

After pre-cracking preparation, the specimens were instrumented by four GEFTRAN® brand variable linear displacement transducers (LVDTs) with a 5 mm stroke and 0.98 calibration constants. Subsequently, they were submitted to direct shear testing as shown in Figure 6.



**Figure 6.** Set of steel plates and rollers for the direct shear test of push-off specimens [15].

Two LVDTs were positioned vertically to measure the slip of one part of the specimen relative to the other and the other two were positioned horizontally to measure the horizontal displacement. The results were recorded by Lynx Technology's AqDados® 7.5.

The push-off specimens were tested using an EMIC® universal testing machine with a capacity of 2000 kN by placing a spherical seat and a set of steel plates and rollers to ensure that the separation of the two halves of the specimen was not restricted by the testing machine as shown in Figure 7. The load application speed was 0.3 mm/s.

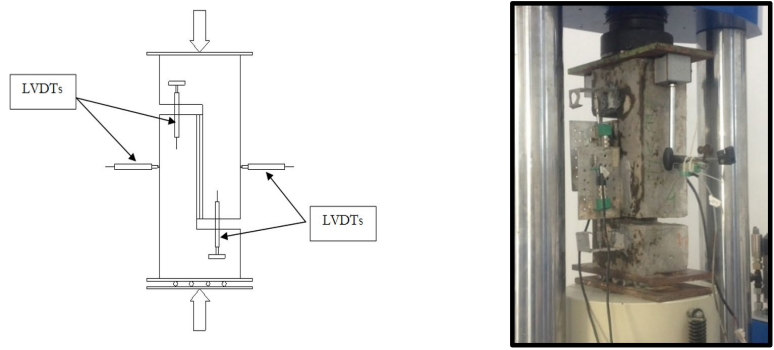


Figure 7. Instrumentation schematic and direct shear testing of push-off specimens [15].

## 4 RESULTS AND DISCUSSIONS

### 4.1 The behavior of push-off specimens

Figure 8a shows the rupture mode of push-off specimens that cracked by shear in the initial cracked plane. L-PO-1-12.71 and N-PO-1-12.71 which ruptured by the combination of bending and shear, as shown in Figure 8b. The flexion occurred on the outer faces as previously reported by Kahn and Mitchell [21], and Shaw and Sneed [22].

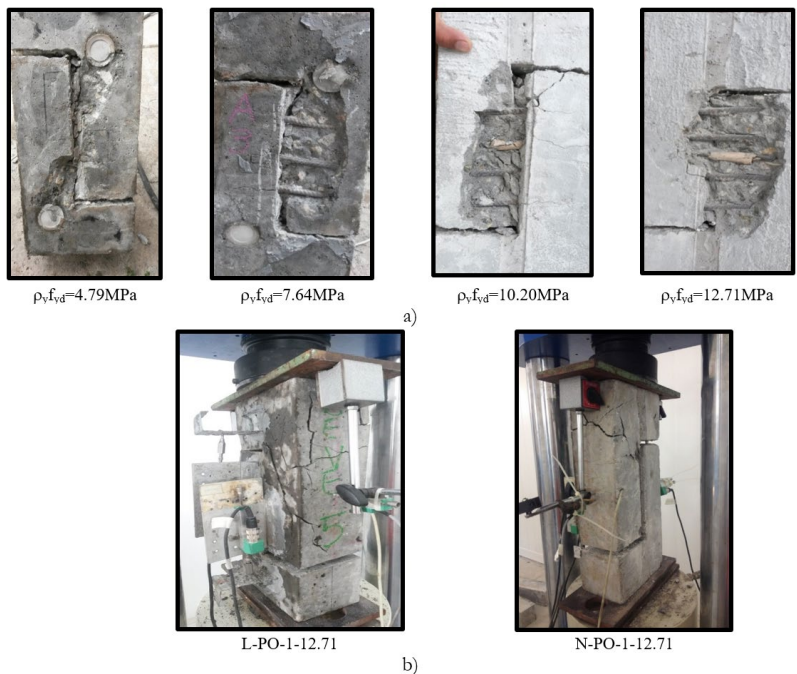


Figure 8. Modes of shear failure of push-off specimens: a) shear plane failure, b) bending and shear combination failure [15].

Figure 9 shows the shear stress variation normalized by  $f_{cm}$  versus slip for sand-lightweight concrete (series A and D) and high-strength conventional concrete (series B, C, and E), respectively, produced by Pereira [15] and Soares [16].

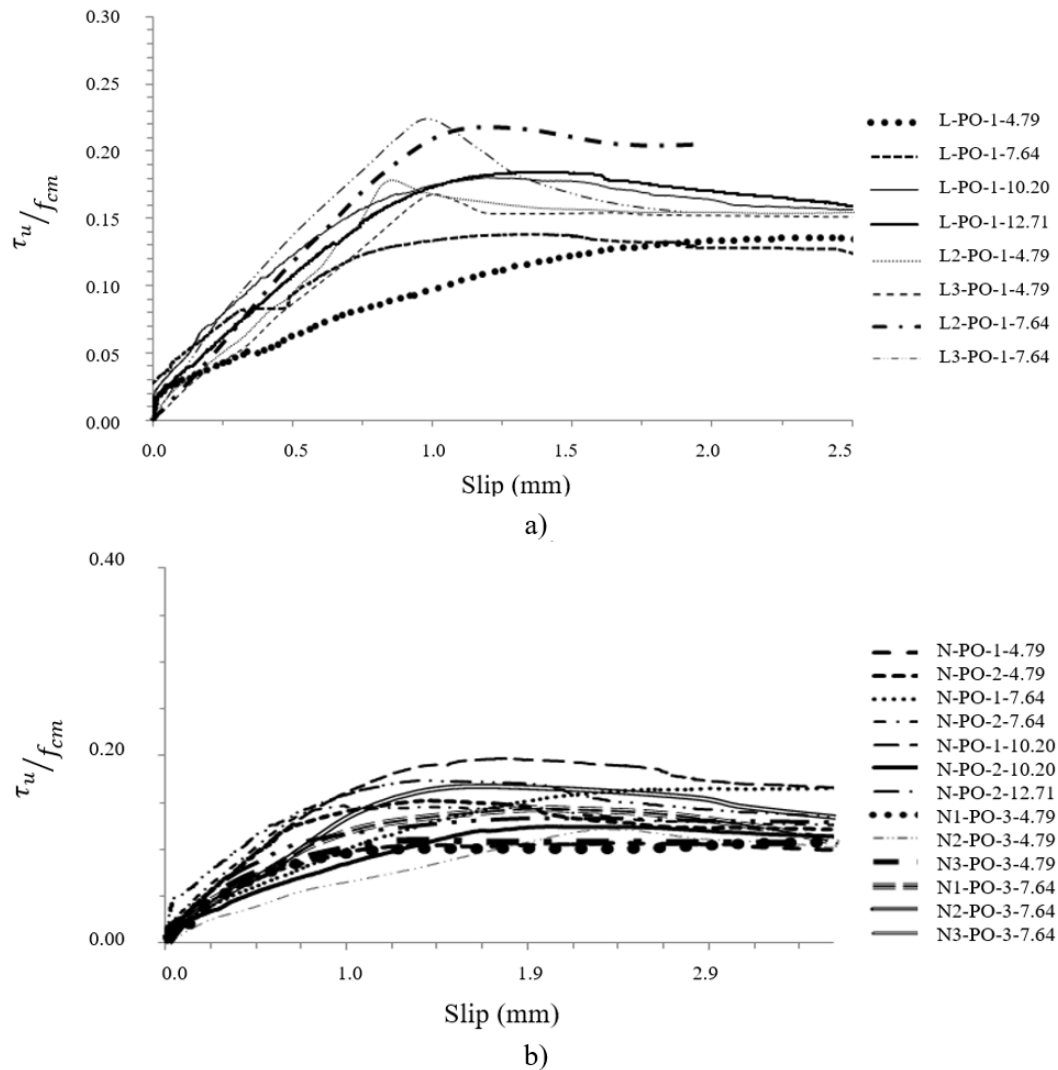
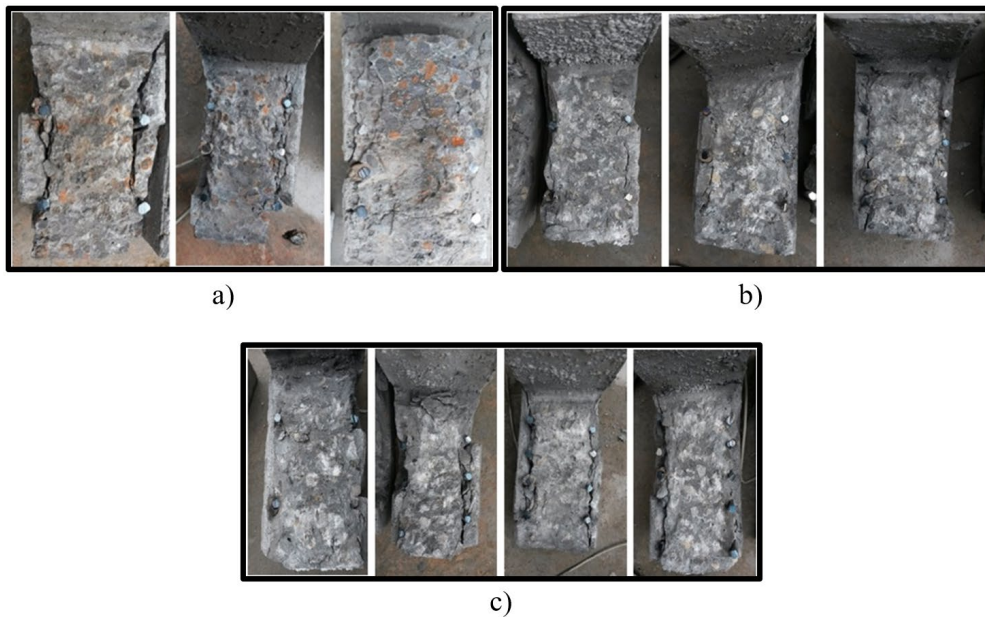


Figure 9. Normalized shear stress vs. slip curves: a) sand-lightweight concrete; b) conventional high-strength concrete.

Similar behavior was noticed for both concrete groups which was an increase in the ultimate shear capacity ( $\tau_u$ ) with an increase in the shear stress ( $\rho_v f_{yd}$ ). The initial stiffness is characterized by the steep rising of the curve at the beginning, which tends to decrease with an increase in load application after reaching the maximum shear strength. Then, there is a gradual reduction in strength and a rise in longitudinal displacement. This behavior is expected for initially cracked push-off specimens as reported by Mansur et al. [23] and Emiko et al. [6].

After performing the push-off tests, the specimens were divided into two parts for a further analysis of the shear place surface. It was found the increase in degree of clamping stress provided by the transverse reinforcement resulted in a smoother surface. For sand-lightweight concrete and conventional high-strength concrete (Figures 10a and 10b), the surface was smoother regardless of the transverse reinforcement rate. For sand-lightweight concrete, there was no rupture of the expanded clay by grinding or shear. However, the rupture was caused by traction rupture. “White points” appeared in the matrix surrounding the expanded clay. For conventional high-strength concrete, there was a growth in these white points (regions?), especially in large aggregate. This was caused by increased interlock between the aggregates in the shear plane. For conventional low-strength concrete, the surface has become rougher (Figure 10c).



**Figure 10.** Rupture surfaces: a) sand-lightweight concrete, b) high-strength concrete and c) low-strength concrete.

#### 4.2 Ultimate shear strength

Table 2 shows the results of the compression tests, splitting tensile strength and last normalized strength. Figure 11 shows the values obtained for the last normalized strength ( $\tau_u/f_{cm}$ ) versus normalized clamping stress by concrete strength ( $\rho_v f_{yd}/f_{cm}$ ) to assess the influence of the clamping stress on the ultimate shear capacity between series. The individual values of each push-off specimen for the series A and D (sand-lightweight concrete) and series B, C, and E (high-strength conventional concrete) are presented in Table 2. It was noticed that concrete produced with expanded clay has lower shear strength when compared to concrete produced with conventional aggregate. Gerritse [24], Mattock et al. [8] and Emiko et al. [6] have previously reported and confirmed cracks go through the light aggregate, differently from what is observed in conventional concrete aggregate where cracks move around the aggregate. It can be inferred that cracking is linked to the aggregate rupture.

It is observed that, in general, an increase in clamping stress leads to an increase in ultimate shear strength.

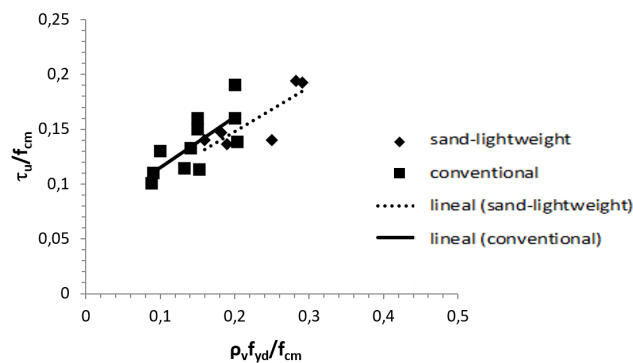
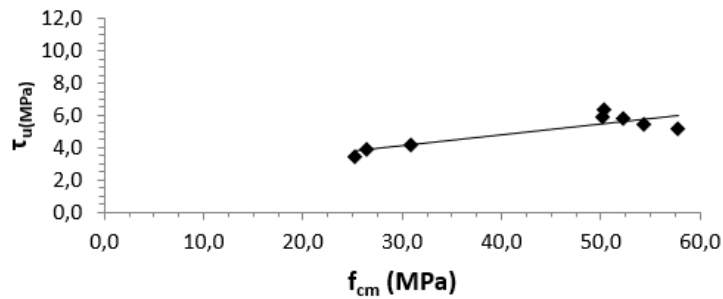


**Figure 11.** Influence of the clamping stress of the transverse reinforcement ( $\rho_v f_{yd} / f_{cm}$ ) in ultimate shear capacity.

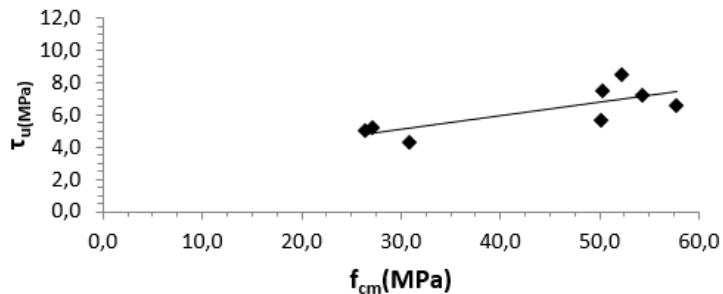
#### 4.3 Influence of concrete compressive strength on ultimate shear capacity

Figure 12 shows the individual values of ultimate shear strength ( $\tau_{u,exp}$ ) versus concrete compressive strength ( $f_{cm}$ ), for all series and the different clamping stress ( $\rho_v f_{yd}$ ) studied. It is observed that the ultimate shear strength becomes greater as concrete compressive strength increases. This is mainly because of aggregate interlock, which the more

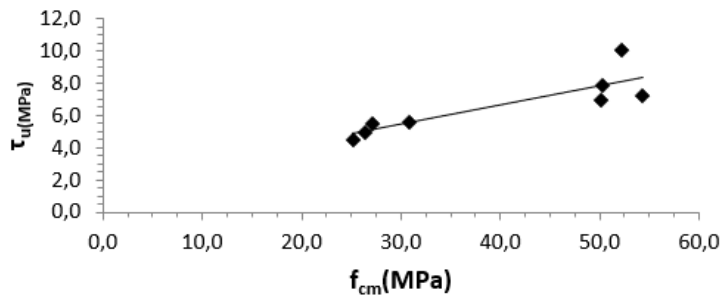
effective it is, the higher the concrete strength value. In concrete with sand-lightweight aggregate, cracks penetrate more easily through the aggregate instead of occurring around the aggregate, as in concrete with normal weight and low strength. The slope (m) of each curve was greater with an increase of ( $\rho_v f_{yd}$ ). The values were 0.0697, 0.0834, 0.1189, at clamping stresses of 4.79, 7.64, 10.20, respectively. It is noticed that for the clamping stress of 12.71 MPa, the slope was 0.1170, being lower when compared with the clamping stress of 10.20 MPa. This was probably due to the few data evaluated, and also, to the ruptured specimens influenced by bending.



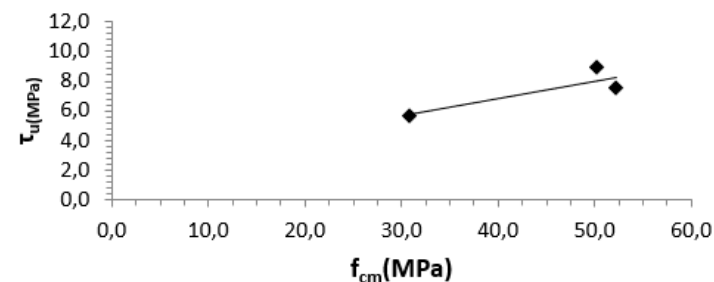
a)  $\rho_v f_{yd} = 4.79$  MPa



b)  $\rho_v f_{yd} = 7.64$  MPa



c)  $\rho_v f_{yd} = 10.20$  MPa



d)  $\rho_v f_{yd} = 12.71$  MPa

**Figure 12.** Influence of concrete compressive strength on the ultimate shear capacity for different clamping stresses.

#### 4.4 Comparison of the ultimate shear strength obtained experimentally with proposed models

Table 3 shows the experimental ultimate shear strength values ( $\tau_{u,exp}$ ) and the calculated values ( $\tau_{u,cal}$ ) obtained by the models proposed by Mattock et al. [8], [25], [6], [26], [23].

Table 4 shows the relationship between the ultimate shear strength ( $\tau_{u,exp}$ ) and the calculated ultimate shear strength ( $\tau_{u,cal}$ ) as prescribed by ACI 318 [14].

The average value and standard deviation of ( $\tau_{u,exp}/\tau_{u,cal}$ ) of series A, B, C, D, and E were 1.20 and 0.35; 1.65 and 0.45; 1.58 and 0.45; 1.42 and 0.47; and 1.54 and 0.37, respectively.

It was noticed that series A having clamping stress of 4.79 MPa showed experimental strength 70% higher than the one calculated by ACI 318 [14]. For clamping stress of 7.64 MPa and 10.20 MPa, the increase was 10%.

In series B, for clamping stress of 4.79 MPa, the experimental strength was 100% higher than calculated ACI 318 [14]. For specimens having clamping stress of 7.64 MPa and 10.20 MPa, this ratio was 90% and 70% higher, respectively.

In series C, the experimental strength was 120% higher for samples having clamping stress of 4.79 MPa compared to those calculated by ACI 318 [14]. For clamping stress of 7.64 MPa, 10.20 MPa, and 12.71 MPa, this ratio was 60%, 30%, and 20% higher, respectively.

**Table 3.** Ultimate shear strength values obtained experimentally and the calculated values of proposed models.

Series	Specimens	$\tau_{u,exp}$ (MPa)			$\tau_{u,calc}$ (MPa)			
		[15], [16]	[8]	[25]	[6]	[26]	[23]	
A	L-PO-1- 4.79	4.20	5.53	5.78	5.35	-	-	
	L-PO-1- 7.64	4.27	7.81	7.31	6.76	-	-	
	L-PO-1-10.20	5.56	9.86	8.44	7.81	-	-	
	L-PO-1-12.71	5.70	11.87	9.42	8.72	-	-	
B	N-PO-1- 4.79	5.84	-	-	-	9.05	8.95	
	N-PO-1- 7.64	8.50	-	-	-	11.33	11.3	
	N-PO-1-10.20	10.13	-	-	-	13.38	13.06	
	N-PO-1-12.71	7.54	-	-	-	15.39	14.58	
C	N-PO-2- 4.79	6.38	-	-	-	8.86	8.78	
	N-PO-2- 7.64	7.52	-	-	-	11.14	11.09	
	N-PO-2-10.20	7.8	-	-	-	13.19	12.82	
	N-PO-2-12.71	8.89	-	-	-	15.2	14.31	
D	L1-PO-1- 4.79	3.86	5.53	5.79	4.71	-	-	
	L2-PO-1- 4.79	5.90	5.53	5.79	4.77	-	-	
	L3-PO-1- 4.79	3.44	5.53	5.79	4.61	-	-	
	L1-PO-1- 7.64	5.06	7.81	7.31	5.65	-	-	
	L2-PO-1- 7.64	5.25	7.81	7.31	5.71	-	-	
	L3-PO-1- 7.64	7.20	7.81	7.31	5.55	-	-	
	L1-PO-1-10.20	4.91	9.86	8.44	6.49	-	-	
	L2-PO-1-10.20	5.51	9.86	8.44	6.56	-	-	
	L3-PO-1-10.20	4.51	9.86	8.44	6.40	-	-	
E	N1-PO-3- 4.79	5.21	-	-	-	8.45	8.55	
	N2-PO-3- 4.79	5.89	-	-	-	7.84	8.06	
	N3-PO-3- 4.79	5.48	-	-	-	8.18	8.33	
	N1-PO-3- 7.64	6.58	-	-	-	10.73	10.12	
	N2-PO-3- 7.64	5.68	-	-	-	10.12	9.62	
	N3-PO-3- 7.64	7.20	-	-	-	10.46	9.90	
	N2-PO-3-10.20	6.92	-	-	-	12.17	11.03	
	N3-PO-3-10.20	7.23	-	-	-	12.51	11.31	



**Table 4.** Relationship between ultimate shear strength ( $\tau_{u, exp}$ ) and calculated ultimate shear strength ( $\tau_{u, cal}$ ) according to the requirements of the ACI 318 [14].

Series	Specimens	$\tau_{u, cal}$ [14]	$\tau_{u, exp}$	$\tau_{u, exp}/\tau_{u, cal}$	Average	SD
A	L-PO-1-4.79	2.4	4.2	1.7	1.20	0.35
	L-PO-1-7.64	3.9	4.3	1.1		
	L-PO-1-10.20	5.2	5.6	1.1		
	L-PO-1-12.71	6.5	5.7	0.9		
B	N-PO-1-4.79	2.9	5.8	2.0	1.65	0.45
	N-PO-1-7.64	4.6	8.5	1.9		
	N-PO-1-10.20	6.1	10.1	1.7		
	N-PO-1-12.71	7.6	7.5	1.0		
C	N-PO-2-4.79	2.9	6.4	2.2	1.58	0.45
	N-PO-2-7.64	4.6	7.5	1.6		
	N-PO-2-10.20	6.1	7.8	1.3		
	N-PO-2-12.71	7.6	8.9	1.2		
D	L1-PO-1-4.79	2.4	3.9	1.6	1.42	0.47
	L2-PO-1-4.79	2.4	5.9	2.4		
	L3-PO-1-4.79	2.4	3.4	1.4		
	L1-PO-1-7.64	3.9	5.1	1.3		
	L2-PO-1-7.64	3.9	5.3	1.4		
	L3-PO-1-7.64	3.9	7.2	1.8		
	L1-PO-1-10.20	5.2	4.9	0.9		
	L2-PO-1-10.20	5.2	5.5	1.1		
	L3-PO-1-10.20	5.2	4.5	0.9		
E	N1-PO-1-4.79	2.9	5.2	1.8	1.54	0.37
	N2-PO-1-4.79	2.9	5.9	2.1		
	N3-PO-1-4.79	2.9	5.5	1.9		
	N1-PO-1-7.64	4.6	6.6	1.4		
	N2-PO-1-7.64	4.6	5.7	1.2		
	N3-PO-1-7.64	4.6	7.2	1.6		
	N2-PO-1-10.20	6.1	6.9	1.1		
	N3-PO-1-10.20	6.1	7.2	1.2		

SD- Standard Deviation

It was observed that the average experimental strength for clamping stress of 4.79 MPa was 80% higher than calculated by ACI 318 [14] for series D. For clamping stress of 7.64 MPa in this series, the percentage was 50% higher than calculated.

For series E, the average experimental strength for clamping stress of 4.79 MPa was 93% higher than calculated by ACI 318 [14]. For 7.64 MPa clamping stress, the percentage was 40% higher.

For specimens having 12.71 MPa of clamping stress from series A and B and the ones having 10.20 MPa of clamping stress from series D and E, the values were lower than those calculated taking into account ACI 318 [14] requirements. This was caused by the influence of bending rupture, which occurred by over-covering, limiting the effect of auxiliary reinforcement on the face of push-offs.

#### 4.5 Tri-linear model proposal for determining the ultimate shear strength

After evaluating the studies conducted by Mansur et al. [23] in which a tri-linear model was proposed to predict the ultimate shear strength of different types of concrete with varying clamping stress and considering the inclusion of new experimental data, it was developed a new tri-linear approach in Soares [16], using the same limits proposed by Mansur et al. [23].

Each equation proposed by Soares [16] was obtained with the best fit curve, as shown in Figure 13a.

The new tri-linear approach is defined by the equations below.

- for values of  $\rho_v f_{yd}/f_{cm} \leq 0.075$ :

$$\frac{\tau_u}{f_{cm}} = 1.4259 \frac{\rho_v f_{yd}}{f_{cm}} + 0.0377 \tag{1}$$

- for values of  $0.075 \leq \rho_v f_{yd}/f_{cm} \leq 0.27$ :

$$\frac{\tau_u}{f_{cm}} = 0.0154 \frac{\rho_v f_{yd}}{f_{cm}} + 0.2491 \tag{2}$$

- for values of  $\rho_v f_{yd}/f_{cm} > 0.27$ :

$$\frac{\tau_u}{f_{cm}} = 0.24 \tag{3}$$

To compare both models, the following relations were plotted in Figures 13b and 13c  $\tau_{u, \text{exp}}/\tau_{u, \text{cal}}$  for data collected from previous research, including that conducted by Pereira [15] and Soares [16].

A horizontal line has been inserted which intersects the axis in  $\tau_{u, \text{exp}}/\tau_{u, \text{cal}}=1$  which is the optimum value where the calculated and experimental values are equivalent. The points closest to the line refer to the values whose experimental and theoretical data are approximate.

Figures 13b and 13c show the values of the relationship ( $\tau_{u, \text{exp}}/\tau_{u, \text{cal}}$ ) by the tri-linear approach developed by Soares [16] and [23], respectively.

Table 5 shows the statistical parameters of the calculated values of the ( $\tau_{u, \text{exp}}/\tau_{u, \text{cal}}$ ) of the model proposed by Mansur et al. [23], and Soares [16].

**Table 5.** Comparison of statistical parameters obtained according to the equations of Mansur et al. [23] and Soares [16].

Research	Average of $\tau_{u, \text{exp}}/\tau_{u, \text{cal}}$		Standard Deviation		Coefficient of variation (%)	
	[23]	[16]	[23]	[16]	[23]	[16]
[8]	0.92	1.17	0.18	0.22	19.57	18.51
[21]	0.87	0.95	0.43	0.39	49.43	40.86
[23]	0.99	1.06	0.36	0.13	36.36	12.51
[6]	0.79	0.96	0.13	0.14	16.46	14.76
[27]	0.81	0.97	0.18	0.14	22.22	14.16
[22]	0.81	0.97	0.15	0.18	18.52	18.23
[28]	0.77	0.96	0.12	0.15	15.58	15.08
[29]	0.82	1.04	0.13	0.16	15.85	15.46
[15]	0.65	0.77	0.10	0.09	15.38	12.12
[16]	0.63	0.77	0.16	0.22	25.40	28.39
<b>General Average</b>	<b>0.81</b>	<b>0.96</b>				

Analyzing the data from Table 5 and Figure 13b, it can be seen the tri-linear model developed by Soares [16] provides theoretical values closer to the corresponding experimental values.

The overall average obtained for the ( $\tau_{u, \text{exp}}/\tau_{u, \text{cal}}$ ) was 0.81 and 0.96 for Mansur et al. [23] and Soares [16], respectively.

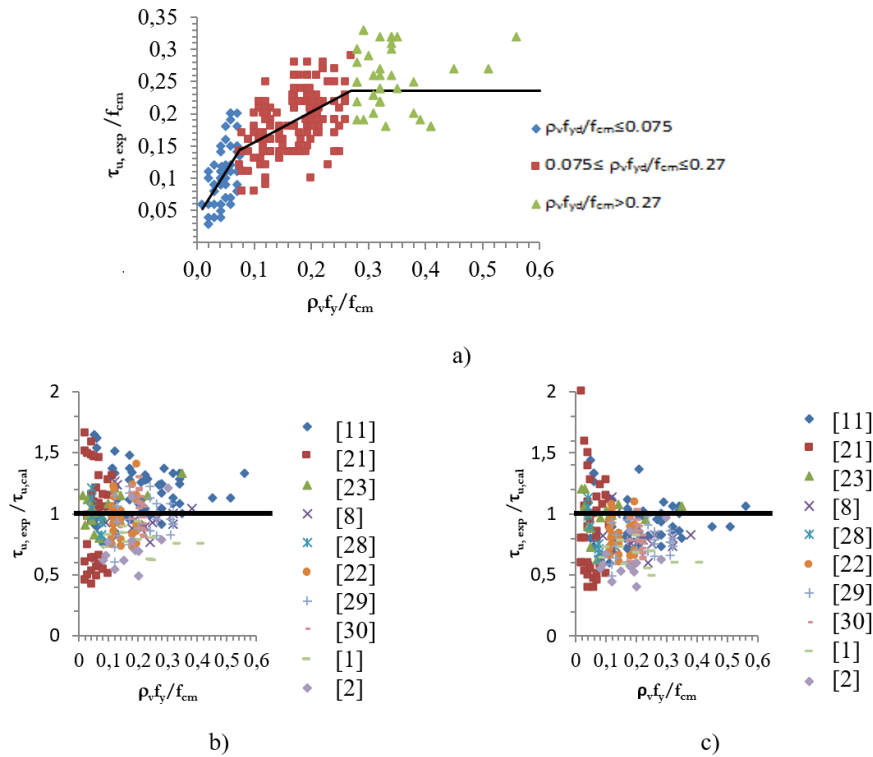


**Figure 13.** Study of tri-linear models to calculate ultimate shear strength: a) model proposed by Soares [16]; b) model results of Soares [16]; c) model results of Mansur et al. [23].

## 5 CONCLUSIONS

This work aimed to analyze shear transfer in sand-lightweight and conventional high-strength concrete. Direct shear tests were performed on push-off specimens for this purpose.

After evaluating the ultimate shear strength results obtained experimentally, comparisons were made with analytical models proposed by previous researchers and the code ACI 318 [14]. It was concluded that:

- the ultimate shear strength increased as the clamping stress increased;
- there was a rise in ultimate shear strength as concrete compression strength increased;
- the code ACI 318 [14] has proven to be conservative, with average values for  $(\tau_{u,exp}/\tau_{u,cal})$  varying from 1.20 (series A) to 1.65 (series B);
- the trilinear model developed by Soares [16] proved to be more effective in the calculation of the ultimate shear capacity, based on the results of the statistical parameters presented, with an overall average of 0.96.

## REFERENCES

- [1] H. W. Birkeland and P. W. Birkeland, "Connections in precast concrete construction," *J. Am. Concr. Inst.*, vol. 63, pp. 345–367, 1966.
- [2] T. T. C. Hsu et al., "Theory of shear transfer strength of reinforced concrete," *ACI Struct. J.*, vol. 84, pp. 149–160, 1987.
- [3] B. González Fonteboa, F. Martínez, D. Carro, and J. Eiras, "Cortante-fricción de los hormigones reciclados Shear friction capacity of recycled concretes," *Mater. Constr.*, vol. 60, no. 299, pp. 53–67, 2010, <http://dx.doi.org/10.3989/mc.2010.49708>.
- [4] P. M. D. Santos and E. N. B. S. Júlio, "A state-of-the-art review on shear-friction," *Eng. Struct.*, vol. 45, pp. 435–448, 2012, <http://dx.doi.org/10.1016/j.engstruct.2012.06.036>.
- [5] J. Wairaven, J. Frenay, and A. Pruijssers, "Influence of concrete strength and load history on the shear friction capacity of concrete members," *PCI J.*, vol. 32, no. 1, pp. 66–84, 1987.
- [6] L. Emiko, V. Thamarakkannan, W. T. Huan, and T. Thangayah, "Shear transfer in lightweight concrete," *Mag. Concr. Res.*, vol. 63, no. 6, pp. 393–400, 2011., <http://dx.doi.org/10.1680/mac.9.00162>.

- [7] A. F. Yang, J.-I. Sim, J.-H. Kang, and A. F. Ashour, "Shear capacity of monolithic concrete joints without transverse reinforcement," *Mag. Concr. Res.*, vol. 64, no. 9, pp. 767–779, 2012., <http://dx.doi.org/10.1680/mac.11.00107>.
- [8] A. H. Mattock, W. K. Li, and T. C. Wang, "Shear transfer in lightweight reinforced concrete," *PCI J.*, vol. 21, no. 1, pp. 20–39, 1976.
- [9] W. C. Tang, T. Y. Lo, and W. K. Chan, "Fracture properties of normal and lightweight high-strength concrete," *Mag. Concr. Res.*, vol. 60, no. 4, pp. 237–244, 2008, <http://dx.doi.org/10.1680/mac.2008.60.4.237>.
- [10] K. H. Yang and K. H. Lee, "Shear friction characteristics and modification factor of concrete prepared using expanded bottom ash and dredged soil granules," *Int. J. Concr. Struct. Mater.*, vol. 13, no. 1, pp. 50, 2019, <http://dx.doi.org/10.1186/s40069-019-0364-x>.
- [11] P. Wu, C. Wu, Z. Liu, and H. Hao, "Investigation of shear performance of UHPC by direct shear tests," *Eng. Struct.*, vol. 183, pp. 780–790, 2019, <http://dx.doi.org/10.1016/j.engstruct.2019.01.055>.
- [12] J. Peng, P. Z. Zhao, S. Wang, S. W. Lee, and S. B. Kang, "Interface shear transfer in reinforced engineered cementitious composites under push-off loads," *Eng. Struct.*, vol. 206, pp. 110013, 2020, <http://dx.doi.org/10.1016/j.engstruct.2019.110013>.
- [13] P. M. D. Santos and E. N. B. S. Júlio, "Interface shear transfer on composite concrete members," *ACI Struct. J.*, vol. 111, no. 1, pp. 113–121, 2014, <http://dx.doi.org/10.14359/51686543>.
- [14] ACI Committee 318, *Building Code Requirements for Structural Concrete*, ACI 318M-14, 2014.
- [15] P. D. S. Pereira, "Avaliação da teoria atrito-cisalhamento em concreto leve e de alta resistência," M.S. thesis, Univ. Est. Norte Fluminense, Campos dos Goytacazes, 2016.
- [16] T. A. Soares, "Teoria atrito-cisalhamento em concretos de diferentes resistências e densidades através do ensaio de *Push-off*," M.S. thesis, Univ. Est. Norte Fluminense, Campos dos Goytacazes, 2018.
- [17] Associação Brasileira de Normas Técnicas, *Análise Granulométrica*, ABNT NBR NM 248, 2003.
- [18] Associação Brasileira de Normas Técnicas, *Agregados – Determinação da Massa Unitária e do Volume de Vazios*, NBR NM 45, 2006.
- [19] Associação Brasileira de Normas Técnicas, *Concreto-Ensaio de Compressão de Corpos-de-prova Cilíndricos*, ABNT NBR 5739, 2007.
- [20] Associação Brasileira de Normas Técnicas, *Argamassa e Concreto – Determinação da Resistência à Tração por Compressão Diametral de Corpos-de-Prova Cilíndricos*, ABNT NBR 7222, 2011.
- [21] L. F. Kahn and A. D. Mitchell, "Shear friction tests with high-strength concrete," *Struct. J.*, vol. 99, no. 1, pp. 98–103, 2002.
- [22] L. H. Shaw and L. H. Sneed, "Interface shear transfer of lightweight-aggregate concretes cast at different times," *PCI J.*, vol. 53, no. 3, pp. 130–144, 2014.
- [23] M. A. Mansur, T. Vinayagam, and K.-H. Tan, "Shear transfer across a crack in reinforced high-strength concrete," *J. Mater. Civ. Eng.*, vol. 20, no. 4, pp. 294–302, 2008, [http://dx.doi.org/10.1061/\(ASCE\)0899-1561\(2008\)20:4\(294\)](http://dx.doi.org/10.1061/(ASCE)0899-1561(2008)20:4(294)).
- [24] A. Gerritse, "Design considerations for reinforced lightweight concrete," *Int. J. Cement Compos. Lightweight Concr.*, vol. 3, no. 1, pp. 57–69, 1981, [http://dx.doi.org/10.1016/0262-5075\(81\)90031-2](http://dx.doi.org/10.1016/0262-5075(81)90031-2).
- [25] C. H. Raths, "Design proposals for reinforced concrete corbels," *PCI J.*, vol. 21, no. 3, pp. 18–42, 1977.
- [26] A. H. Mattock, "Shear friction and high-strength concrete," *ACI Struct. J.*, vol. 98, no. 1, pp. 50–59, 2001, <http://dx.doi.org/10.14359/10146>.
- [27] K. A. Harries, G. Zeno, and B. Shahrooz, "Toward an improved understanding of shear-friction behavior," *ACI Struct. J.*, vol. 109, no. 6, pp. 835–844, 2012, <http://dx.doi.org/10.14359/51684127>.
- [28] S. L. Wermager, "Shear-friction of sand-lightweight clay and slate aggregate concretes with varied reinforcement ratios," M.S. thesis, Missouri Univ. Sci. Technol., Rolla, MO, 2015.
- [29] K. Krc, "An investigation of shear-friction of lightweight aggregate concretes," M.S. thesis, Missouri Univ. Sci. Technol., Rolla, MO, 2015.

---

**Authors contributions:** PSPF, TAS: Fund acquisition, production, data acquisition and analysis; SLGG: conceptualization, supervision and writing; ACSP: writing; JCT: methodology

**Editors:** Leandro Mouta Trautwein, José Luiz Antunes de Oliveira e Sousa, Guilherme Aris Parsekian.



ORIGINAL ARTICLE

# Alkali-silica reaction (ASR) - Investigation of crystallographic parameters of natural sands by backscattered electron diffraction

*Reação álcali-sílica (RAS) - Investigação de parâmetros cristalográficos de areias naturais, por difração de elétrons retroespalhados*

Kleber Franke Portella<sup>a</sup>   
Leonardo Evangelista Lagoeiro<sup>b</sup>   
Jeferson Luiz Bronholo<sup>a</sup>   
Dayane de Cristo Miranda<sup>a</sup>   
Mariana D'Orey Gaivão Portella Bragança<sup>a</sup>   
Bruna Gomes Dias<sup>a</sup>   
Nicole Pagan Hasparyk<sup>c</sup>   
Selmo Chapira Kuperman<sup>d</sup> 

<sup>a</sup>LACTEC, Estruturas Cívicas, Curitiba, PR, Brasil

<sup>b</sup>Universidade Federal do Paraná – UFPR, Departamento de Geologia, Curitiba, PR, Brasil

<sup>c</sup>FURNAS Centrais Elétricas S. A., Gerência de Serviços e Suporte Tecnológico, Goiânia, GO, Brasil

<sup>d</sup>DESEK, São Paulo, SP, Brasil

Received 02 June 2020  
Accepted 13 August 2020

**Abstract:** This study involved analyzing several natural sands to ascertain the possible causes for distress due to ASR. The analyses were performed using the following techniques: X-ray diffractometry, accelerated mortar bar tests (AMBT), electron backscattering diffraction and elementary chemistry analyses, by FEG-SEM/EBSD/EDS. These experiments allowed identifying the presence of several mineral composites (such as microcline, anorthite, among others), as well as the microstructural-crystallographic planes of quartz (such as the Dauphiné type). From the results it could be inferred that the multiple techniques used, especially the FEG-SEM / EBSD, proved to be promising in the analysis of the ASR potential of sands for use in Portland cement mortars and concretes.

**Keywords:** ASR, EBSD, natural sand, microstructural-crystallographic quartz planes, potential reactivity.

**Resumo:** Este estudo envolveu a análise de várias areias naturais para verificar as possíveis causas de manifestações patológicas pela ASR. As análises foram realizadas utilizando as seguintes técnicas: difratometria de raios X, testes acelerados de barra de argamassa (AMBT), a difração de elétrons retroespalhados e as análises químicas elementares, por FEG-SEM / EBSD / EDS. Esses experimentos permitiram identificar a presença de vários compostos minerais (como microclina, anortita, entre outros), bem como os planos microestruturais-cristalográficos de quartzo (como o tipo Dauphiné). Dos resultados se pode inferir que as múltiplas técnicas utilizadas, especialmente a FEG-SEM/EBSD, mostraram ser promissoras na análise da reatividade potencial de areias para uso em argamassas e concretos de cimento Portland.

**Palavras-chave:** RAS, EBSD, areia natural, planos microestruturais e cristalográfico do quartzo, reatividade potencial.

**How to cite:** K. F. Portella et al., “Alkali-silica reaction (ASR) - Investigation of crystallographic parameters of natural sands by backscattered electron diffraction” *Rev. IBRACON Estrut. Mater.*, vol. 14, no. 3, e14308, 2021, <https://doi.org/10.1590/S1983-41952021000300008>

Corresponding author: Kleber Franke Portella. E-mail: portella@lactec.org.br

Financial support: None.

Conflict of interest: Nothing to declare.



This is an Open Access article distributed under the terms of the Creative Commons Attribution License, which permits unrestricted use, distribution, and reproduction in any medium, provided the original work is properly cited.

## 1 INTRODUCTION

The alkali-aggregate reaction, AAR, which is mostly represented by the alkali-silica reaction, ASR, is autogenous, inhomogeneous and occurs in certain regions of a concrete structure containing Portland cement. The result from ASR is usually an expansive gel (alkaline-calcium silica gel) that can cause damage to concrete structures and occurs in the presence of progressive and map-shaped micro-cracks. The lifetime of a civil structure depends on environmental conditions, the concrete mix design, among other factors. The presence of ASR has been detected as early as 1 year after construction completion, such as reported at the Parker dam, in California, in 1939 [1], [2].

The initial conditions for ASR to develop are associated with the presence of reactive aggregates, such as varieties of crystalline or amorphous silica and alkalis, mainly released from the cement paste. Other factors include environmental conditions, such as temperature, pressure and high moisture contents. According to the literature, the reaction mechanism involves two processes, that lead to the decomposition of the mineral structure by the formation of a sodium or potassium silica-alkaline gel [3].

The damage caused by ASR is the result of a series of sequential reactions involving the silica and alkalis present in the alkaline concrete. The damage occurs by hydration or dissolution of the solid silica contained in the reactive aggregate, generating a nano-colloidal silica (silica sol) and the transformation of silica sol to gel. Afterwards, the presence of water causes the silica gel to expand. However, as reported by Rajabipour et al. [4], the expansion mechanism depends on humidity and on how easy the transport of the solution is throughout the concrete (continuous pores, microcracks and voids).

During the reaction of the compounds, in the presence of silica and alkaline hydroxides for the formation of the gel, a difference in chemical potential arises between the gel and the substances contained in the pores of the concrete, inducing greater water adsorption and allowing its expansion [1], [5].

The kinetics of ASR also depends on the type of silica available, such as the shape in which the silica crystallized as well as the density and the surface area of the grains, since the mechanism is a result of alkali attack on the substrate. Thus, crystalline quartz aggregates with a low density of structural defects are less susceptible to the reaction with ASR, contrasting with a cryptocrystalline structure or one with a high degree of crystalline defects (deformation). Figueira et al. [1], inferred that four conditions for the occurrence of ASR have to be satisfied, which are: i) reactive silica in a critical concentration range (the source may be igneous, metamorphic and sedimentary rocks), depending on its geological origin, its composition and microstructure (such as opal, tridymite, cristobalite, volcanic acid glass); ii) a high concentration of alkalis or  $\text{OH}^-$  in the solution inside the concrete pore; iii) a source of calcium ions such as portlandite (reaction inducer) to react with  $\text{SiO}_2$  sol and form the deleterious gel and, finally; iv) an optimum moisture condition to promote gel adsorption and expansion. As for the grain size, the authors inferred that the coarser particles of reactive silica (from 630  $\mu\text{m}$  to 1,250  $\mu\text{m}$ ) were the ones that resulted in greater expansions, in contrast to the smaller ones (with particle size distribution between 50 and 160  $\mu\text{m}$ ). With respect to the reaction rate, it was concluded that sodium hydroxides were more reactive than potassium hydroxides, for the same environment. Furthermore, an increase in the ratios of  $\text{Na}/\text{Si}$  and  $\text{K}/\text{Si}$  in the gel corresponds to an increase in both expansion and water absorption coefficient. Therefore, the accelerated tests are performed with immersion in a  $\text{NaOH}$  aqueous solution. However, for the  $\text{Ca}/\text{Si}$  ratio, this is not a direct relationship between the increase of that ratio and the water expansions and absorptions. In this case, there was no direct relation, so for a ratio between 0.05 and 0.18 the water absorption coefficient was observed to be lower than for a range between 0.18 to 0.40, in which the largest water expansions and absorptions coefficients were found [1], [5], [6].

According to Broekmans [7], in deformed quartz crystals, containing low-angle grain boundaries or subgrains, internal stresses or defects can be generated and accommodate foreign ions in their lattices (usually alkalis,  $\text{Na}^+$  and  $\text{K}^+$ ), causing the rupture of local silica bonds. As a result, there is an increase in its solubility to alkalis in solution, when compared to a non-deformed quartz structure. An example of this occurrence was found in AMBT results with Norwegian mylonites, where the author identified a higher potential reactivity in these deformed rocks. However, the relationship between potential reactivity and the deformational features, such as the formation of subgrains, distortions in the crystalline lattice and Dauphiné twinning, are not always observed. This is particularly the case as structures need specific techniques rather than OM to be determined, such as scanning electron microscopy (SEM) with backscattered electron diffraction (EBSD) and elementary chemical analysis by dispersion of X-rays (EDS).

According to Tiecher et al. [8], although the angle of undulatory extinction in quartz is an essentially subjective parameter, which is difficult to measure in common thin sections of petrographic microscopes, this may be an indication of its potential reactivity in minerals. This parameter was used for the qualification of the reactive potential of some Brazilian rocks [9], [10].

Hasdemir et al. [9], studied the potential reactivity of natural sands, applying the AMBT (ASTM C 1260 [11]), petrographic analysis, scanning electron microscopy and EDS, among other techniques, concluding that the presence of reactive silica and mineral silicates from metamorphic and volcanic rock particles makes the samples potentially reactive to ASR. The authors observed that the potential damage to natural sands came from the release of silica from quartz and its polymorphs, in addition to different amounts of aluminum, calcium, potassium, sodium and magnesium from feldspars, biotite, illite and volcanic rocks. They observed that the potential reactivity of the samples was caused by their microstructural, mineralogical and chemical characteristics, with high proportions of silica (95 to 98%) and

others chemical constituents of equal potential reactivity, resulting from quartz polymorphs with lower proportions of mineral silicates. Most of the analyzed sands were identified by means of X-ray diffractometry and mineralogical composition (quartz, feldspar, calcite, muscovite, illite, chert/chalcedony, dolomite, epidote, and kaolinite).

In order to assess the possible causes for pathological manifestations by ASR, this study involved the analysis of some natural sand samples, by X-ray diffractometry, the accelerated test of potential reactivity, electron backscattering diffraction and elementary chemistry analyses, by FEG-SEM/EBSD/EDS. The experiments aimed the identification of the presence of several mineral composites, the evaluation of the microstructural-crystallographic planes and the establishment of their relationship with the ASR, intending a better comprehension of the mechanisms that can take place in concrete and mortars structures.

## 2 MATERIALS AND EXPERIMENTAL PROGRAM

**Physicochemical and geotechnical characterization of the sands.** A set of 11 samples of natural sand products of weathering of sedimentary rocks from Paraná Basin, Brazil, were collected along riverbanks and caves, according to normative procedures and general macroscopic characterizations.

**Sand expansion tests.** Three mortar bars of dimensions (25 x 25 x 285) mm were prepared and analyzed for each sample, with proportions of cement to aggregate of 1: 2.25 and a water/cement of 0.47 (by mass) by the accelerated method and other standard tests [11]–[20]. After being molded, the bars were cured for 24 h in a humid chamber and were maintained immersed in water for 24 h at 80 °C. After curing, they were subjected to a solution of sodium hydroxide (NaOH) at 1 N, at a temperature of 80 °C, with expansion being measured daily for 30 days.

To determine the potential reactivity of the sands in relation to expansion by ASR, 5 samples were selected from the characterized lots ranging from the largest to the smallest expansion values. To characterize the mineralogy, X-ray diffraction and field emission scanning electron microscopy (FEG-SEM), equipped with an energy dispersive X-ray spectrometer (EDS) and a detector of electron backscatter diffraction (EBSD), were applied. Among the samples considered, the two largest and smallest expansion by ASR results were also analyzed by optical polarized microscopy, OM, to compare both techniques.

The X-ray diffractometer, by polycrystalline powder's method, was done at Bruker equipment, model D8 Advance, with a Cu X-ray tube,  $\lambda = 1.54060 \text{ \AA}$ , operating at a current of 25 mA and a voltage of 40 kV; 0.02 s step, 0.1 s time per step; with  $\Theta/2\Theta$  scanning between 5 and 70°. The samples were analyzed after passing through a 0.075 mm mesh sieve.

**Microstructures, mineralogy, and chemical and phase compositions of the samples.** Initially all the samples were observed in a Leitz polarized light microscope model Ortholux 2 Pol-BK. The light microscope allows a comprehensive analysis of microstructures and mineralogy of the sample. However, most of the observations done in the optical microscope (OM) were qualitative and fine-sized minerals were almost impossible to identify. To overcome the limitations of the OM, X-ray diffraction and FEG-SEM/EBSD were applied, by Kernel average misorientation (KAM) and Grain Reference Orientation Deviation (GROD) maps methods.

The FEG-SEM used for this analysis was a TESCAN, model MIRA 3 LM, with an EDS and EBSD from Oxford Instruments. A set of applications integrated to the Oxford Aztec 3.3/Channel 5 platform was used for the acquisition and processing of EDS and EBSD data. In addition, the following analysis parameters were used: acceleration voltage of 15 kV; beam current intensity of 18 nA, working distance between 15 and 21 mm and scanning depth mode.

The aggregates were mounted in epoxy resin. The mounted samples were ground with 240, 600 and 1000 grit sandpaper to remove the excess of resin. The samples were then polished in an automated polishing machine Buehler Metaserv 250, with diamond crystalline suspension with particle sizes of 9, 6, 3, 1, 0.25  $\mu\text{m}$  for 30 minutes in each size. The final polishing was carried out in an alumina solution of 0.05  $\mu\text{m}$  for 60 min followed by chemical mechanical polishing in an aqueous solution of colloidal silica, 20 nm, for 60 min in Buehler Minimet Polisher. The surface quality images, or zero solutions of each one was kept close to 15%. All samples were grounded with conductive paint and taped to prevent the samples from charging.

**The application of the FEG-SEM/EBSD.** The Channel 5 bundled software was used for FEG-SEM/EBSD analyses. The representation of the data was done by generating maps that included phase distribution, grain boundaries and average misorientations. The later provide a picture of the deformation of the samples by distributions of the local geometric necessary dislocations (GND) as the average misorientation angles and axes in different parts of the grain. The modal distribution of minerals in percentage of area occupied by a specific phase was quantified as well as the size distribution from the EBSD analyses. The misorientation angles, defined by the rotation necessary to bring together two crystal lattices, were the base for representing the maps of intracrystalline deformation of sand grains.

**The approaches of using FEG-SEM/EBSD in an ASR investigation.** The plasticity of crystalline materials usually results in a local rotation in the crystal, for which the EBSD is the appropriate instrument for measuring. Typical resolution values for the disorientations that can be measured in the EBSD are in the order of 0.5° [21], [22]. EBSD grain edges or contours are determined as locations where the difference between orientations of adjacent pixels is of

some critical value. In this work, low-angle grain edges were plotted with misorientation angles between 1° and 10°. Misorientation higher than 10° was marked on the map as high angle grain boundaries. There are special boundaries for quartz grains where two neighboring lattices are disorientated by 60°. This is a typical relationship between quartz crystals defined as Dauphiné Twinning where the angle around which the twinned crystals are rotated is parallel to the [0001] crystal axis. It can be caused by quartz symmetry transformation as well as by deformation. Another approach in the evaluation of intracrystalline deformation was made from the analysis of local misorientation. Local misorientation was characterized by a change in orientation caused by geometrically necessary dislocations (GND).

The local misorientation or kernel average misorientation (group of pixels), KAM, was plotted onto a map, which revealed areas of contrast in dislocation densities in a scale of colors. The average values of these misorientations, after scanning a certain area of the grain, reflected the history of its deformation. Through this technique it is also possible to quantify and map the average misorientation around a measured point in relation to a group of previously established neighboring points, that is, a group of pixels or kernels, these being larger in deformed grains due to the higher density of dislocations.

An additional way of evaluating the internal deformation of the grain and substructures (subgrains), is the analysis of the grain reference orientation deviation (GROD) angle. This is a map component where the average orientation is determined for each grain based on the user-defined grain detection. The deviation angle from this mean orientation is plotted for each pixel belonging to a grain. The GROD parameter is often used in quantifying the recrystallization process to separate deformed and recrystallized grain populations. This is due to recrystallized strain-free grains having lower GROD value.

### 3 RESULTS AND DISCUSSIONS

**General characteristics of natural sands.** In Table 1, the mesoscopic characteristics of natural sands are presented. Grains showed a wide range of sizes and are basically composed by quartz grains, fragments of sandstones and lesser proportions of granitic rocks (quartz and feldspars).

**Table 1.** Geotechnical characteristics of the sands collected and analyzed for ASR potential reactivity [23]–[27].

Samples	Origins and geological units	Technical features
624.18	River: alluvial deposits; migmatite gneissic complex	Sub-angular grains; rounded grains with an opaque and irregular surface; and heterogeneous particle size distribution.
030.18	Cave: alluvial deposits; Campo Mourão formation, Itararé group	Angular to sub-angular grains; sharp edges; irregular surface; concave and convex faces; heterogeneous particle size distribution
025.18	Cave: alluvial deposits: Campo Mourão formation, Itararé group	Angular to sub-angular grains; sharp edges; irregular surface; concave and convex faces; heterogeneous particle size distribution
100.18	River: Ponta Grossa formation	Rounded grains; opaque surface; some angular grains; heterogeneous granulometric composition, with millimeter to submillimeter grains.
024.18	Cave: alluvial deposits: Campo Mourão formation, Itararé group	Angular to sub-angular grains; sharp edges; irregular surface; concave and convex faces; grains of mafic minerals are present.
029.18	River: alluvial deposits; Campo Mourão formation, Itararé group	Angular to sub-angular grains; sharp edges; irregular surface; concave and convex faces; heterogeneous particle size distribution
718.18	River: alluvial deposits; Caiuá formation	Rounded grains; polished and shiny surfaces which suggest transport in water; homogeneous granulometric distribution.
716.18	River: alluvial deposits; Caiuá formation	Rounded grains; polished and brilliant surfaces
032.18	River: Ponta Grossa formation	Sub-angular grains; polished surface, vitreous shine and subordinate round grains with an opaque aspect; homogeneous granulometric distribution.
101.18	Cave: Ponta Grossa formation	Rounded to sub-rounded grains; angular edges; some with an opaque surface; millimeter to submillimeter; heterogeneous granulometry.
031.18	River: Ponta Grossa formation	Rounded grains predominant to sub-rounded; matte appearance.

The samples came from caves and rivers in alluvial deposits and rock formations, such as: (i) the Caiuá type is represented mainly by purple sandstones, in an area corresponding to approximately 30,000 km<sup>2</sup> [23]; ii) the Ponta Grossa formation is composed by dark fossiliferous shales and clay of marine origin [24]; iii) in Campo Mourão, samples came from Itararé Group is represented by shale, diamictite, sandstone and, conglomerate [25]; and iv) a fourth type of samples were collected in the migmatite gneiss complex, represented by banded, mylonitized gneisses [26]. More details of these geologic area are reported by Miranda et al. [27].

Optical microscopy images of natural sands examples from migmatite gneissic complex, Campo Mourão, Ponta Grossa and Cauá formations, were shown in Figure 1.



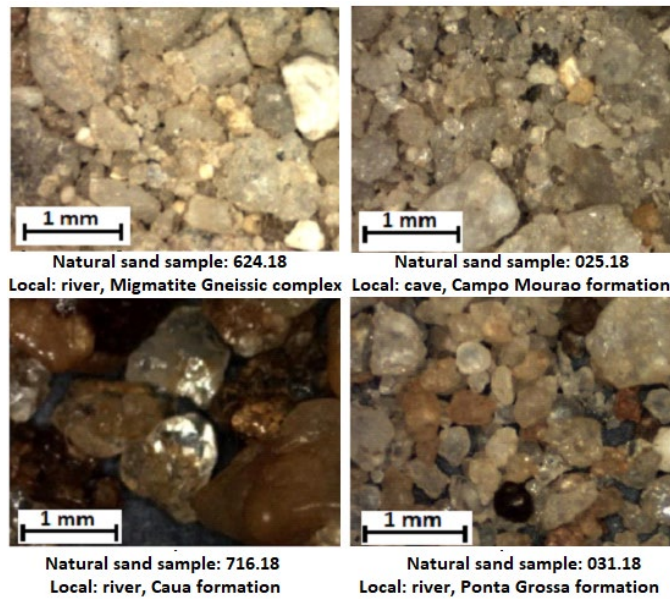


Figure 1. Images, by optical microscopy, of some natural sands from the rock formations highlighted in Table 1.

**Physicochemical characterizations of sands.** The physical and chemical properties measured are shown in Table 2. The fineness modulus and the powdery material content were  $(2.84 \pm 0.01)$  and  $(3.10 \pm 0.02)\%$ , respectively, for sample 624.18, and for sample 031.18 of  $(1.82 \pm 0.01)$  to  $(0.20 \pm 0.01)\%$ , respectively. The samples had the highest and lowest percentage of expansion, respectively.

**Potential reactivity and mineral phases by XRD.** Table 2 shows the results of the ASR potential of 11 sand samples which 73% of them presented ASR potential, with average expansions above the standard limit of 0.19%, in 30 days [12].

The following samples were chosen in a decrescent order of expansion: 624.18, with 0.36% expansion; 025.18, with 0.30%; 716.18, with 0.21%; 032.18 with 0.15%; and 031.18, with 0.09%. They represent natural sands according to the microstructural and crystallographic characteristics of the quartz grains as well as with respect to the proportions of powdery fraction of the samples.

Table 2. Results of the physicochemical and expansion tests of the 11 sand samples evaluated applying the standards [11]–[20].

Properties	Sand samples										
	624.18	030.18	100.18	025.18	024.18	029.18	718.18	716.18	032.18	101.18	031.18
Fineness modulus	2.84	3.29	2.39	3.32	2.38	3.11	2.00	2.89	2.60	1.90	1.82
Clay content, %	0.20	0.50	1.80	0.40	0.20	0.40	-	0	0	0.10	-
Powdery material, %	3.10	0.40	1.40	1.90	3.00	0.20	0.10	0	0.40	1.90	0.20
Expansion, %	0.36	0.31	0.30	0.30	0.29	0.28	0.24	0.21	0.15	0.12	0.09

Figure 2 shows the expansion curves for samples 624.18, 024.18 and 716.18, which presented values above the standard limit of expansion by NBR 15577 [12], but similar method of preparation of ASTM C1260 [11]. Samples 032.18 and 031.18 presented lowest expansion percentage.

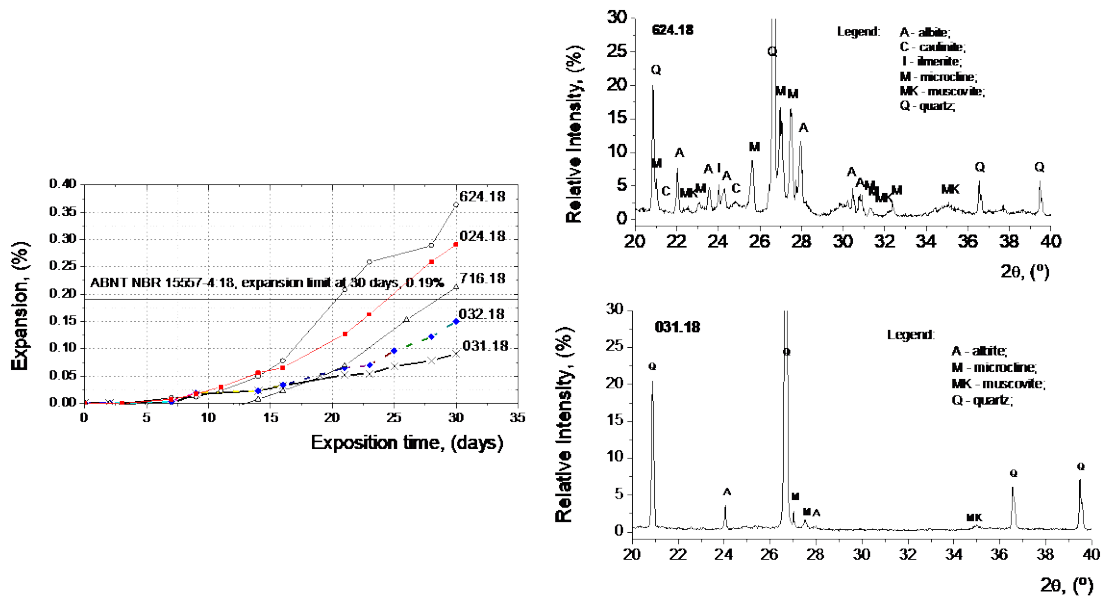


**Figure 2.** ASR potential reactivity for sand samples on the left. On the right, the XDR results for samples with the highest (624.18) and lowest (031.18) expansion rates.

When analyzing the mineral composition of samples 624.18 and 031.18 by XRD (20 to 40°, in 2θ, and from 0 to 30% in relative intensity), with the highest and lowest expansion results, at least two variables were considered. The first and more straightforward one was the high amount of reactive minerals, such as feldspars, found in samples with high expansion rates, as seen in Table 3. Secondly, the microstructures and crystallographic aspect of the samples were considered, as discussed by Bauer et al. [28], where the silica with a very low state of crystallization is very reactive in an alkaline solution. The sample 624.18, for example, had the highest potential reactivity (0.36%), and contains the lowest quartz content (44.90%) compared to the other samples. On the other hand, the sample 031.18 had the highest amount of quartz (62.27%) and the lowest expansion rate of just 0.09%. In addition, the proportion of feldspar minerals in sample 624.18 was considerably high and may also play an important role in increasing the potential reactivity of ASR in this sample. However, the analysis of sample 716.18 showed that its quartz content was like that of sample 031.18. Therefore, the mineral composition as well as grain size (fineness), which were similar in both samples, could not be the only factors that contributed to the potential reactivity of ASR. Thus, microstructures and crystallographic aspects of the grains and aggregates were considered. The importance of this study corroborates the research carried out by Monteiro et al. [29], that concluded from the studies with mortars prepared with granodiorite, mylonite, phyllonite, and ultramylonite from the Santa Rosa mylonite zone in southern California, that the resulting ASR expansions were dependent on the degree of deformation of the analyzed rocks and their granulometric distributions.

**Table 3.** Semiquantitative proportions of mineralogical phases, by FEG-SEM/EBSD, in natural sands.

Sand sample	Type and content of mineral phases in natural sands, %					
	Quartz	Anorthite	Albite	Microcline	Biotite	Muscovite
624.18	44.90	12.01	8.33	22.82	6.02	5.92
030.18	66.73	7.58	6.21	9.06	5.47	4.96
100.18	72.11	6.59	4.96	7.81	4.04	4.50
025.18	65.74	7.46	6.49	11.00	4.48	4.83
024.18	48.46	11.27	9.80	16.10	7.10	7.27
029.18	60.00	8.64	8.04	11.12	6.87	5.33
718.18	61.03	9.24	7.67	11.04	4.95	6.07
716.18	63.00	8.35	7.36	10.32	5.11	5.85
032.18	62.14	9.42	6.73	10.06	5.50	6.15
101.18	65.95	8.01	6.62	8.28	5.44	5.71
031.18	62.27	8.34	7.31	8.74	7.51	5.83

**Semi-quantitative investigation of mineral phases.** In Figure 3, the mineral composition was represented as a phase map obtained by simultaneous analyses of EDS (elemental chemical composition) and EBSD (crystallographic symmetry). The mineralogy was shown in colors and modal proportions could be calculated by the area occupied by each phase on the map. Quartz was the main mineral found in all samples with proportions varying from 44.9 to 65.77%. K, Na and Ca feldspars were the second major constituents with a wide range of proportions. Grain size distributions were polymodal and had similar distribution throughout the samples and could be an important metric when the reactivity of the sample was being analyzed. But just considering one example, looking at the most and least reactive samples in the whole spectrum, 624.18 and 031.18, both were samples with smaller grain sizes. Therefore, the grain size alone could not be accountable for the reactivity of the samples.

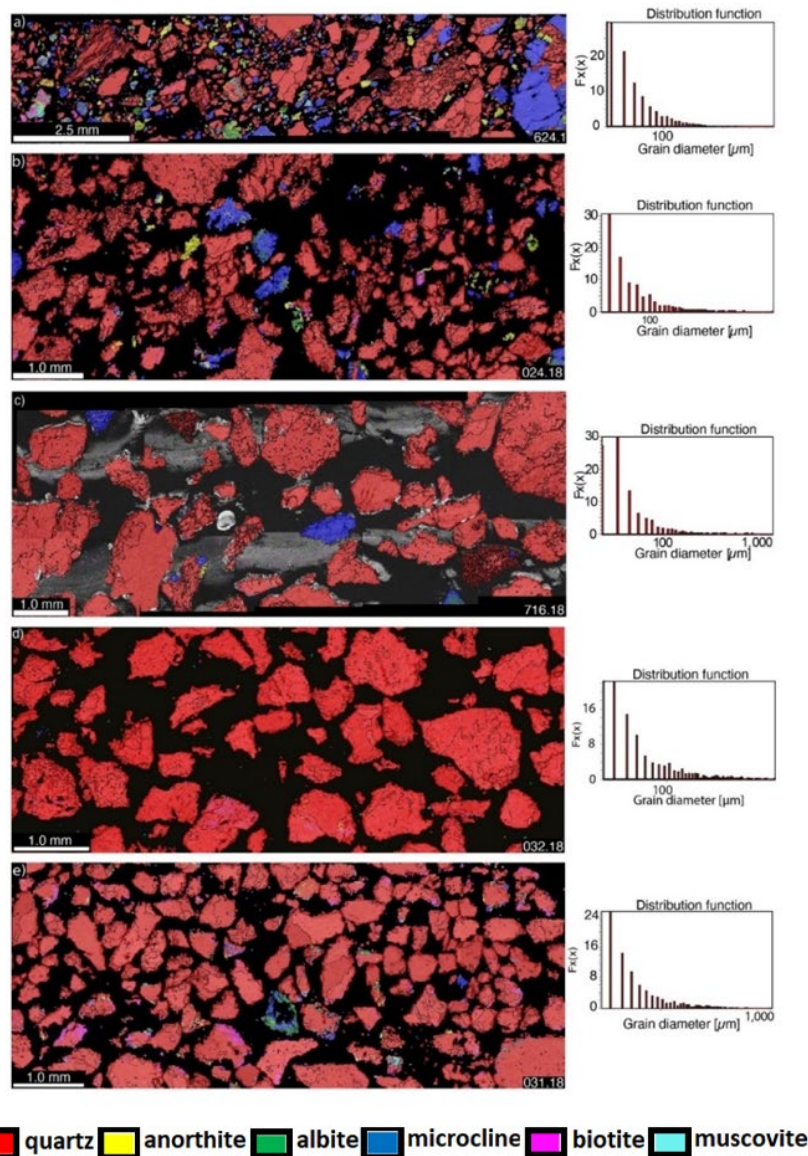


**Figure 3.** FEG-SEM/EBSD micrographic images representing the mineral phase maps of the natural sand samples, tested for ASR expansion, and the histograms of each distribution function.

Figure 4 shows maps of local misorientation (KAM) for the analyzed samples. These maps had a gradation in colors starting from blue, where grains had the lowest misorientation angles to green, yellow, and red where misorientations

reach a user-defined limit ( $< 10^\circ$ ). The sample with the largest expansion rate (624.18) had the widest variation in misorientation angle for quartz grains and consequently was the most deformed. Conversely, samples 032.18 and 031.18 were those with the lowest density of the GND, which translates to less variation in color and therefore less variation in misorientation angles.

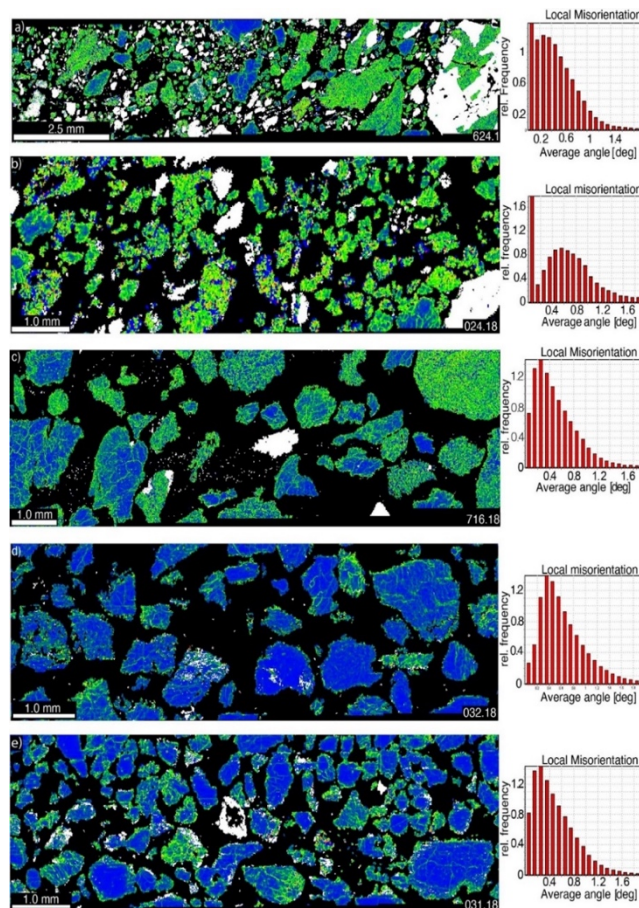


**Figure 4.** Local misorientation map (Kernel average misorientation, KAM) of quartz grains, based on local distortion of crystal lattice caused by geometrically necessary dislocations (GND) and the local misorientation histograms of each sand sample. Note: grains colored in blue have low dislocation densities contrasting with those in green, yellow, orange, and red, which have an increasing density of dislocations. Areas in white correspond to grains other than quartz.

A grain reference orientation deviation (GROD) angle map component is depicted in Figure 4. GROD angle maps help to visualize substructures inside the grain. The average misorientation is determined for each grain based on the user-defined grain detection. The deviation angle from this mean orientation was plotted for each pixel. This map is useful to highlight deformation in grains, even showing the smallest misorientation angle pixel by pixel in a deformed single crystal. On the maps of Figure 5 for grain detection, a critical misorientation value of  $10^\circ$  was set for the KAM maps.

Maps of grain boundaries were also plotted to help visualizing if the sands were composed by single or polycrystals. Most sands were presented single crystals where low angle boundaries (in red lines) predominate. All grains were white colored to highlight the grain boundaries. High angle boundaries are in black lines. The most deformed samples have high densities of subgrain boundaries, caused by the arrangement of necessary geometric dislocations. This can also be visualized under the polarized microscopes as undulatory extinction. The reactivity of the sand grains in relation to ASR is linked to the density of subgrain boundaries. Sample with the highest densities of subgrain boundaries (624.18) was the most reactive and samples with lowest densities (032.18 and 031.18) showed the lowest expansion rate, being the less reactive among the analyzed samples.

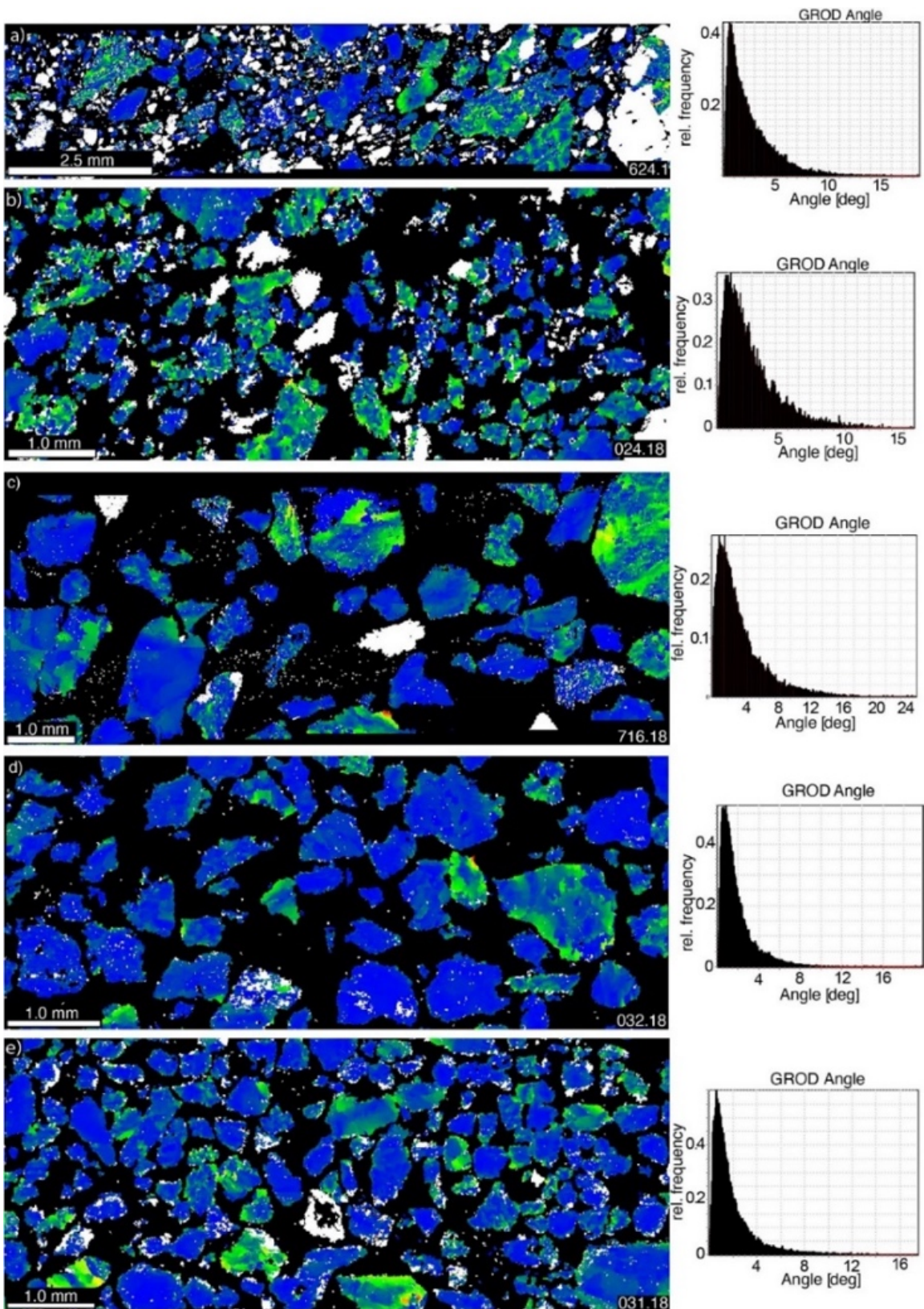


**Figure 5.** GROD angle map highlighting areas of deformation and the GROD angle histograms for each sample. Note: the less deformed grains are shown in blue and the most deformed ones in yellow to green. Minerals other than quartz are in white.

There was not a significant variation in the distribution of high boundaries between the samples that can be related to the rate of expansion observed. In general, sands are composed predominantly by polycrystalline quartz grains as seen in Figure 6. To test if the twin boundaries could play a role on the reactivity of the sand grains, Dauphiné twin boundaries for quartz grains were also plotted. There was no effective relationship between the density of twin boundaries in the samples and their degree of reactivity. In fact, the two less reactive samples, 032.18 and 031.18, with lowest expansion rates, were the ones with the highest frequency of twin boundaries in the quartz sands.

In the Dauphiné Twinning a characteristic peak of misorientation angle around  $60^\circ$  (in red colors) appears in the histogram of misorientation angle distribution showed in the same figure. The higher angles of the grain boundaries are presented in green colors. In the twinning relationship, the neighboring crystal lattices were separated by a rotation around the crystallographic axis *c*, leading to a superposition of the positives *a* axes of one crystal over the negatives *a* axes of the other crystal that makes up the twinned pair. For that reason, the twinned pairs of quartz crystals are indistinguishable under the optical microscope and can only be determined by diffraction methods (EBSD) [8]. These types of twinning can be generated either by growth or by deformation and, in the most cases, are not associated with the reactivity of sand crystals. However, as previously mentioned by Broekmans, 2004, working with Norwegian mylonites, there might be internal stresses or defects in the crystal that facilitate the accommodation of foreign ions into the silica network (as  $\text{Na}^+$  and  $\text{K}^+$ ), causing the rupture of its bonds, mainly in the regions of the crystals under high stress (deformed). Sites of high deformation in the crystal lattice, such as subgrains, might enhance the solubility of aqueous solutions rich in alkalis. This is due to the higher diffusivity ratio along the dislocation lines in highly deformed crystals when compared with undeformed quartz lattice with fewer dislocations.

The most reactive samples, 624.18 and 024.18 showed in Figure 3 share some characteristics that together make them prone to react in alkaline solutions. The most remarkable is the dislocation density, discussed earlier, the large proportions of reactive minerals, like feldspar, and the relatively fine size of sand grains for both samples, as shown in Tables 2 and 3 (powdery material: 3.1% and 3.0%; and fineness moduli: 2.84 and 2.38, respectively).

However, if only the content of potential reactive minerals were considered, the proportions of these minerals themselves could not be accountable for the differences in expansion rates as observed in the samples with expansion rates above the ABNT NBR limit of 0.19%, i.e., samples 716.18 (0.24%), 024.18 (0.29%) and 624.18 (0.36%). In these samples the bulk feldspar contents (the most reactive mineral in the system) are considerably different. Nevertheless, if samples 024.18 and 716.18 were compared to the less reactive 031.18, the difference in the feldspar content was not that much to justify the differences in reactivity between them. Therefore, other factors must be considered to explain how these samples have a contrasting behavior in terms of ASR reactivity. The only remarkable difference relies on the degree of deformation unveiled by the misorientation maps, where the most reactive samples correspond to those with widest variation in misorientation angles, while the samples with the shorter range of misorientation angles were the least reactive. The most deformed samples had larger numbers of subgrains. Subgrain walls, where necessary geometric dislocations are arranged, are sites of mismatch between adjacent sublattices. Therefore, this might act as a faster path for ion diffusivity, which could speed up the rate of reactions when compared to crystals with a lower density of GND. Crystal lattices with plenty of defects are prone to react when in contact with alkaline solutions.

Samples 716.18 and 032.18 with, respectively, 0.21% and 0.15% of expansions, above and below of the standardized limit of 0.19% (NBR 15577: 2008), possibly had a great contribution of intracrystalline defects in quartz, since their fineness moduli and powdery materials, as well as their proportions of potentially reactive minerals (aluminum silicates), were similar (Tables 2 and 3 for comparison as well as phase maps of Figure 3). Additionally, it was verified that in the studied samples there was no evidence of formation of new grains (dynamic recrystallization). Mostly subgrains were observed in the misorientation maps, in which the monocrystalline particles show substructures with angular deviation up to  $10^\circ$ , as well as Dauphiné twin boundaries with misorientation angles around  $60^\circ$ .

The FEG-SEM/EBSD/EDS techniques were decisive for the analyses of the samples, since they allowed a comprehensive investigation of all parameters involved in the reaction of minerals with alkaline aqueous solutions. All the parameters: i) identification and quantification of mineral composition in the mixture; ii) microstructural characteristics of the constituent particles of the aggregates; and iii) the semi-quantitative determination of the degree of deformation of the quartz grains, either acting combined or individually, were the ultimate cause of expansion found in this assessed.

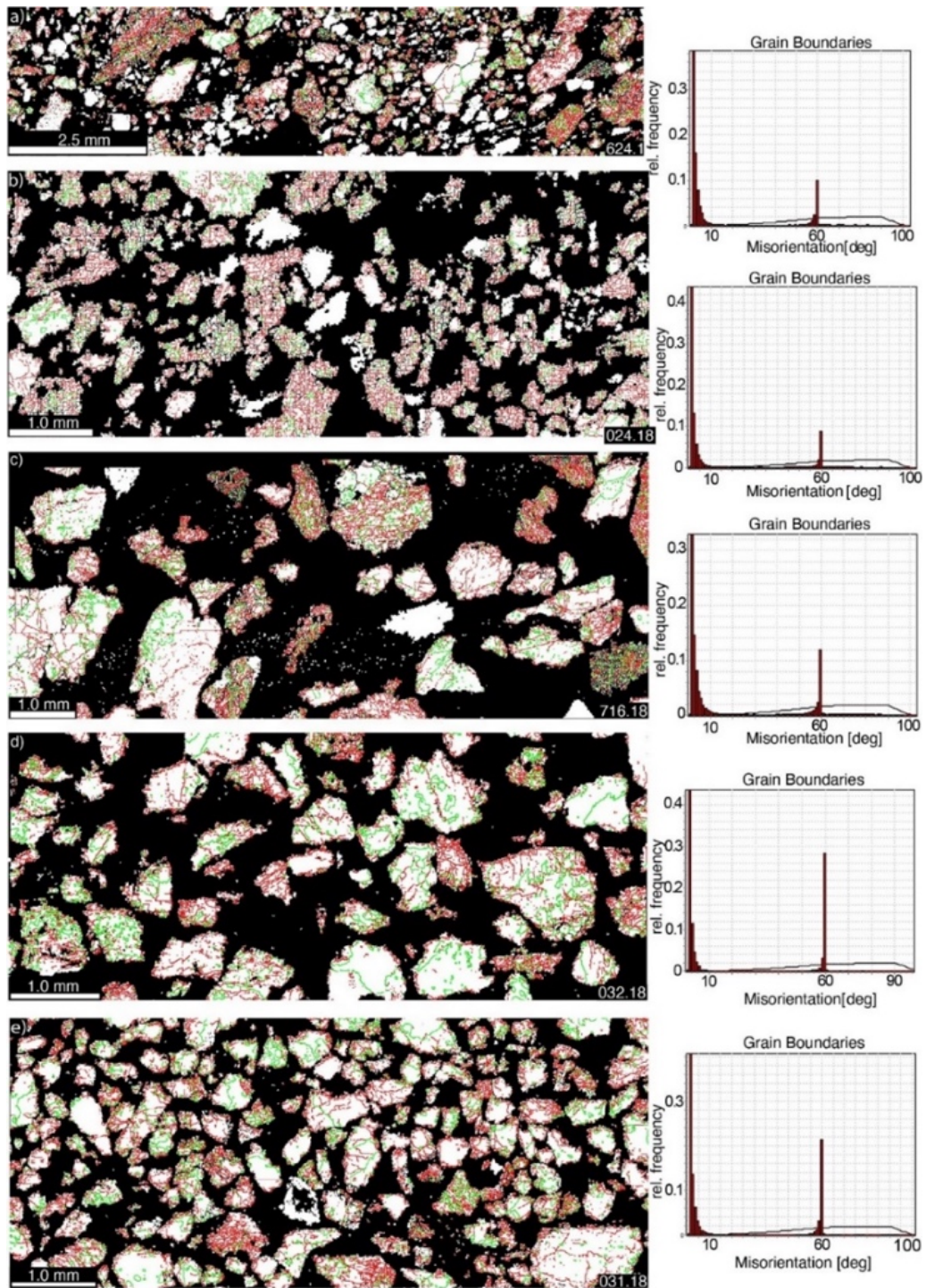


**Figure 6.** Images of the grain boundary maps of the sand samples and the histogram of misorientation angle distribution. Note: the color in red present the misorientation angle around 60° (Dauphiné Twinnin), and the green color, the higher angles of the grain boundaries or dislocations).

As investigated by Hasdemir et al. [9], and reported earlier, it was found in this research that the expansions by ASR were also a consequence of both the presence of silicate minerals and the deformed quartz grains in the natural sands. From the KAM images in Figure 4, it could be inferred that in samples with expansions greater than 0.19%, after 30 days, the degree of semi-quantitative deformation measured in the quartz was equal to 51.02% for sample 624.18

(0.36% expansion); 60.70%, for sample 030.18; and 67.90%, for sample 025.18, with about the same expansion of 0.30% in 30 days. For samples with expansion rates below the limit of 0.19%, after 30 days, the degree of deformation of quartz grains was around 30% or less, with 22.40% for sample 032.18 (0.15% expansion); 30.00% for sample 101.18; and 29.10% for sample 031.18, which had an average expansion of around 0.20% after 30 days.

In the case of sample 624.18, it was not easy to infer which factor contributed to the resulting expansion, since this sample has the highest proportion of aluminosilicates and fine particle sizes. Nevertheless, it is the sample with the largest proportion of deformed quartz grains, and with the highest distorted crystal lattices. However, other samples had lower content of feldspar minerals and similarities in density of crystal defects and, despite of that, they showed expansion rates closed to sample 624.18. Therefore, the arrangement of crystal defects as necessary geometric dislocation that cause local disorientation of the crystal seems to be the main cause of expansion measured in the natural sands analyzed.

## 5 CONCLUSIONS

The investigation of fine aggregates of natural sand by X-ray diffraction, accelerated potential reactivity test, elementary chemistry composition and, specially, backscattered electron diffraction technics, indicated that the primary causes of expansion or pathological manifestations by ASR resulted mainly by the presence of intracrystalline deformation in the quartz grains.

By the results obtained, it could be considered for the effectiveness of the use of the EBSD technique, complementing the elucidation of the potential reactivity of the aggregates used in Portland cement mortars and concretes. However, there were limitations observed and resolved by pre-treatment by polishing the samples to the mirrored surface, to reduce artifacts on the maps (reduction of the zero solution). The degree of quartz deformation assessed in the studied samples, obtained from misorientation data, was determinant to the evaluation of the potential reactivity of material used.

As additional advantages from EBSD analysis, it could be inferred by the shorter time of analysis and interpretation of a possible trend of expansion of the samples and their use for evaluating coarse aggregates, foreseeing their ASR reactivity in a less subjective way.

As a general alert to the public, 73% of the analyzed sands were considered to have potential reactivity for ASR from accelerated tests, with results above the limits recommended by Brazilian standard. Therefore, it is recommended, in addition to the current tests applied to the evaluation of reactivity of the geological materials used in civil construction, the implementation of a routine procedure for the analyses of deformation by means of EBSD.

## ACKNOWLEDGEMENTS

This work had financial and infrastructure support from Furnas Centrais Elétricas S.A./ANEEL/Lactec, P&D 0394-1504-2015; Lactec - Professional Master's; CNPq DT, process number 302672/2016. The authors would also like to thank Lactec; Professional Master course; UFPR PPGCEC; CNPq DT, process number 302672/2016//308777/2020-4, and law 8010/90; and COPEL, R&D 6491-0301/2013, LI 08/2468574-9 DI 09 / 0457074-0. L. Lagoeiro acknowledges the support from the National Council for Research and Development (CNPq) processes 425412/2018-0 and 305232/2018-5. Our thanks to Henrique Lagoeiro for the English review.

## REFERENCES

- [1] R. B. Figueira et al., "Alkali-silica reaction in concrete: mechanisms, mitigation and test methods," *Constr. Build. Mater.*, vol. 222, pp. 903–931, 2019.
- [2] R. G. Charlwood and Z. V. Solymar, "Long-term management of AAR-affected structures, an international perspective," in *Proc. 2nd Int. Conf., Alkali-Aggregate Reactions in Hydroelectric Plants and Dams*, Chattanooga, Tennessee, 1995, pp. 19–57.
- [3] L. S. Dent-Glasser and N. Kataoka, "The chemistry of "alkali-aggregate" reaction," *Cement Concr. Res.*, vol. 11, no. 1, pp. 1–9, 1981.
- [4] F. Rajabipour, E. Giannini, C. Dunant, J. H. Ideker, and M. D. A. Thomas, "Alkali – silica reaction: current understanding of the reaction mechanisms and the knowledge gaps," *Cement Concr. Res.*, vol. 76, pp. 130–146, 2015.
- [5] S. Multon, A. Sellier, and M. Cyr, "Chemo-mechanical modeling for prediction of alkali silica reaction (ASR) expansion," *Cement Concr. Res.*, vol. 39, no. 6, pp. 490–500, 2009., <http://dx.doi.org/10.1016/j.cemconres.2009.03.007>.
- [6] N. P. Hasparyk, P. J. M. Monteiro, and H. Casarek, "Effect of silica fume and rice husk ash on alkali-silica reaction," *ACI Mater. J.*, vol. 97-M57, pp. 486–492, 2000.



- [7] M. A. T. M. Broekmans, "Structural properties of quartz and their potential role for ASR," *Mater. Charact.*, vol. 53, no. 2, pp. 129–140, 2004.
- [8] F. Tiecher, M. E. B. Gomes, D. C. C. Dal Molin, N. P. Hasparyk, and P. J. M. Monteiro, "Relationship between degree of deformation in quartz and silica dissolution for the development of alkali-silica reaction in concrete," *Materials*, vol. 10, no. 9, pp. 1022, 2017, <http://dx.doi.org/10.3390/ma10091022>.
- [9] S. Hasdemir, A. Tugrul, and M. Yilmaz, "Evaluation of alkali reactivity of natural sands," *Constr. Build. Mater.*, vol. 29, pp. 378–385, 2012.
- [10] N. P. Hasparyk, "Investigação dos mecanismos de reação álcali-agregado: efeito da cinza de casca de arroz e da sílica ativa," M.S. thesis, Fac. Eng. Civ., Univ. Fed. Goiânia, Goiás, 1999.
- [11] American Society for Testing and Materials, *Potential Alkali Reactivity of Aggregates (Mortar-Bar Method)*, ASTM C1260, 2014.
- [12] Associação Brasileira de Normas Técnicas, *Aggregates – Alkali Reactivity of Aggregates. Parts 1-5: Petrographic Analysis for Evaluation of the Potential Reactivity of Aggregates with Alkali Compounds from Concrete*, NBR 15577, 2018.
- [13] Associação Brasileira de Normas Técnicas, *Agregado Miúdo – Determinação da Absorção de Água*, ABNT NBR NM 30, 2001.
- [14] Associação Brasileira de Normas Técnicas, *Agregados – Determinação do Material Fino que Passa Através da Peneira 75 µm, por Lavagem*, ABNT NBR NM 46, 2003.
- [15] Associação Brasileira de Normas Técnicas, *Agregado Miúdo – Determinação de Impurezas Orgânicas*, ABNT NBR NM 49, 2001.
- [16] Associação Brasileira de Normas Técnicas, *Agregado Miúdo – Determinação da Massa Específica e Massa Específica Aparente*, ABNT NBR NM 52, 2009.
- [17] Associação Brasileira de Normas Técnicas, *Agregados – Determinação da Composição Granulométrica*, ABNT NBR NM 248, 2003.
- [18] Associação Brasileira de Normas Técnicas, *Agregados para Concreto – Especificação*, ABNT NBR 7211, 2009.
- [19] Associação Brasileira de Normas Técnicas, *Agregados – Determinação do Teor de Argila em Torrões e Materiais Friáveis*, ABNT NBR 7218, 2010.
- [20] Associação Brasileira de Normas Técnicas, *Agregados – Índice de Desempenho de Agregado Miúdo Contendo Impurezas Orgânicas*, ABNT NBR 7221, 2012.
- [21] A. Wilkinson, "A new method for determination small misorientations from electron back scatter diffraction patterns," *Scr. Mater.*, vol. 44, no. 10, pp. 2379–2385, 2001.
- [22] P. S. Bate, R. D. Knutsen, I. Brough, and F. J. Humphreys, "The characterization of low-angle boundaries by EBSD," *J. Microsc.*, vol. 220, no. 1, pp. 36–46, 2005.
- [23] Caiuá. <http://www.aguasparana.pr.gov.br/pagina-60.html> (accessed Dec. 1, 2019).
- [24] Mineropar. "Geologia do Paraná. Parque Estadual de Vila Velha." [http://www.mineropar.pr.gov.br/arquivos/File/Paineis\\_geologicos/ParqueEstadualdeVilaVelha\\_portugues.pdf](http://www.mineropar.pr.gov.br/arquivos/File/Paineis_geologicos/ParqueEstadualdeVilaVelha_portugues.pdf) (accessed Dec. 1, 2019).
- [25] L. C. Weinschütz, "Estratigrafia de seqüências do grupo Itararé (neocarbonífero-eopermiano) na região de Rio Negro (PR) – Mafra (SC)," Ph.D. dissertation, Univ. Est. Paulista, Rio Claro, 2006.
- [26] Serviço Geológico do Brasil. "Geologia: Contexto Geológico Regional." [http://www.cprm.gov.br/publique/media/geologia\\_basica/plgb/curimata/curimata\\_geologia.pdf](http://www.cprm.gov.br/publique/media/geologia_basica/plgb/curimata/curimata_geologia.pdf) (accessed Dec. 1, 2019).
- [27] D. C. Miranda et al., "Avaliação do potencial de reatividade álcali-agregado de areias naturais do Estado do Paraná," in *An. 4º Simp. Parana. Patol. Constr.*, Curitiba, 2019.
- [28] S. Bauer, B. Cornell, D. Figurski, T. Ley, K. Folliard, *Alkali-Silica Reaction and Delayed Ettringite Formation in Concrete: A Literature Review*. Austin: University of Texas, 2006.
- [29] P. J. M. Monteiro, K. Shomglin, H. R. Wenk, and N. P. Hasparyk, "Effect of aggregate deformation on alkali-silica reaction," *ACI Mater. J.*, vol. 98, no. 2, pp. 179–183, 2001.

---

**Author contributions:** KFP: conceptualization, methodology, supervision, writing; LEL: conceptualization, supervision, writing; JLB: formal analysis, methodology, writing; DCM: formal analysis, methodology; MOGPB: conceptualization, methodology, supervision, writing; BGD: formal analysis, methodology, writing; NPH: conceptualization, funding acquisition, methodology, supervision, writing; SCK: conceptualization, methodology, supervision, writing.

**Editors:** Guilherme Aris Parsekian.



REVIEW

## Reaction mechanisms of alkali-activated materials

### *Mecanismos de reação de materiais álcali ativados*

Markssuel Teixeira Marvila<sup>a</sup> Afonso Rangel Garcez de Azevedo<sup>a</sup> Carlos Maurício Fontes Vieira<sup>a</sup> <sup>a</sup>Universidade Estadual do Norte Fluminense – UENF, Laboratório de Materiais Avançados – LAMAV, Campos dos Goytacazes, RJ, Brasil

Received 17 April 2020

Accepted 28 October 2020

**Abstract:** The Alkali-Activated Materials (AAM) are defined as materials obtained through the reaction between precursors and activators, and are separated into two classes depending on the products formed in the reaction, those rich in calcium, as the blast furnace slag, whose Ca/(Si+Al) ratio is higher than 1; and poor in calcium, which is the geopolymers subclass. In this review article, some bibliographical aspects were discussed regarding the discovery of these materials, through research conducted by Victor Glukhovskiy and through the characterization of historical monuments by Davidovits, which began in the 50s and 60s and persist to the present day. The main products obtained in the alkaline activation reaction were also addressed, using the definition of polysialates and zeolites, in the case of geopolymers, and the tobermorite structure, in the case of materials rich in calcium. The main steps of the alkali-activated reaction, such as dissolution, condensation, polycondensation, crystallization, and hardening, were discussed. Some techniques for characterizing the AA reaction products were also examined, such as X-ray diffraction (XRD), nuclear magnetic resonance spectrometry (NMR), Fourier transform infrared spectroscopy (FTIR), and scanning electron microscopy (SEM). Finally, the main factors that interfere in the kinetics of AA reactions were explored, in which the type of cure and the activating solution used in the alkali-activated materials production stands out.

**Keywords:** alkali-activated materials, geopolymers, precursors.

**Resumo:** Os materiais álcali ativados (MAA) são definidos como materiais obtidos por intermédio da reação entre precursores e ativadores, e são separados em duas classes dependendo dos produtos formados na reação, os ricos em cálcio, como é o caso da escória de alto forno, cuja relação Ca/(Si+Al) é maior do que 1; e pobres em cálcio, que constitui a subclasse dos geopolímeros. Nesse artigo de revisão foram discutidos alguns aspectos bibliográficos a respeito da descoberta desses materiais, por meio de pesquisas realizadas por Victor Glukhovskiy e por meio da caracterização de monumentos históricos por Davidovits, que se iniciaram nas décadas de 50 e 60 e persistem até os dias atuais. Também foram abordados os principais produtos obtidos na reação de ativação alcalina, utilizando a definição de polissialatos e zeólitas, no caso dos geopolímeros, e da estrutura da tobermorita, no caso dos materiais ricos em cálcio. As principais etapas da reação álcali ativadas, como dissolução, condensação, policondensação, cristalização e endurecimento, foram debatidas. Algumas técnicas para caracterização dos produtos da reação AA também foram examinadas, tais como difração de raios-X (DRX), espectrometria de ressonância magnética nuclear (RMN), espectroscopia no infravermelho com transformada de Fourier (FTIR) e microscopia eletrônica de varredura (MEV). Por fim, foram explorados os principais fatores que interferem na cinética das reações AA, onde destaca-se o tipo de cura e de solução ativadora utilizada na produção dos MAA.

**Palavras-chave:** materiais álcali ativados, geopolímeros, precursores.

**How to cite:** M. T. Marvila, A. R. G. Azevedo, and C. M. F. Vieira, “Reaction mechanisms of alkali-activated materials,” *Rev. IBRACON Estrut. Mater.*, vol. 14, no. 3, e14309, 2021, <https://doi.org/10.1590/S1983-41952021000300009>

Corresponding author: Markssuel Teixeira Marvila. E-mail: [markssuel@hotmail.com](mailto:markssuel@hotmail.com)

Financial support: CNPq, proc. nº 301634/2018.1; FAPERJ, proc. nº E-26/202.773/2017.

Conflict of interest: Nothing to declare.



This is an Open Access article distributed under the terms of the Creative Commons Attribution License, which permits unrestricted use, distribution, and reproduction in any medium, provided the original work is properly cited.

## 1 INTRODUCTION

### 1.1 Alkali -activated materials definition

Alkali-activated materials (AAM) are obtained from two basic components, the activator, and the precursor. The material used as a precursor is usually in powdered and mineralogically amorphous form. It can be composed of aluminum silicates, and they are named geopolymers, or present in its composition a predominance of calcium oxide [1], as occurs with blast furnace slag (BFS). The activating materials, in turn, are composed of alkali metals, in the form of hydroxide or silicates, dissolved in an aqueous solution. They are responsible for causing the hardening reactions due to high alkalinity, manifested by the high pH, above 14 [2]

### 1.2 Historical aspects

Historically alkali-activated materials were developed by Victor Glukhovsky in the 1950s and 1960s in the Soviet Union. The researcher developed systems activated in an alkaline manner by mixing materials from volcanic processes (rocks and ash) with activating solutions based on sodium hydroxide. In response, he obtained materials with a composition similar to Portland cement after hardening, that is, hydrated calcium silicate phases (C-S-H) [3]. These materials were named as soil silicates.

Around 1979, Davidovits, a French researcher and chemist, developed an Alkali-activated material using natural origin materials rich in silicon and aluminum, such as kaolin clay, activated by the solution of alkaline liquids [4]. The researcher patented his discovery by naming the materials obtained as geopolymers since they are obtained by a polymerization reaction similar to the one that gives rise to polymeric materials. However, unlike polymers, geopolymers have an inorganic composition. Because of this, another appropriate definition for these materials is that they are called inorganic polymers [5].

Although only the contributions of Victor Glukhovsky and Davidovits were highlighted, other researchers contributed considerably to the knowledge of AAM. Table 1 presents the main contributions of several researchers to the development of alkali activation reaction science. It is observed that initially, the researchers were concerned with characterizing building materials extracted from ancient monuments, such as the Roman aqueducts studied by Malinowski in 1979 and the Egyptian pyramids studied by Davidovits, and Sawyer in 1985 [6]. The authors proved that the materials used in these important monuments were obtained through alkaline activation processes. This fact motivated more researches in this area, and other alkaline activation studies carried out by Roy et al. (1991), Palomo and Glasser (1992) and Krivenko (1994), who, despite obtaining important results, still could not fully explain the mechanisms of alkali-activated reactions [6].

In 1994, Davidovits [7] presented a complex analysis on the microstructure of geopolymers through polysialate networks, and in 1995 Wang and Scrivener presented microstructural analyzes of alkali-activated materials rich in calcium [6]. These surveys improved the researchers' understanding of alkali-activated materials. In 2007, Provis and Van Deventer [8] presented a kinetic model of geopolymerization reactions using X-ray diffraction techniques that were able to explain the stages of this reaction by correlating them with the morphological structure of the gels formed.

In 2011, Habert et al. [9] carried out the environmental evaluation of the geopolymer concrete production by analyzing the life cycle, comparing it with the production cycle of Portland cement. The authors proved the environmental importance of the study of the alkali-activated material, which was shown as an ecological alternative to conventional Portland cement concrete.

After the consolidation of the main concepts related to the alkali-activated materials science, the material started to be used in larger constructions. As an example, we can mention the Australian constructions of the Victoria bridge in 2013 and the expansion of Brisbane West Wellcamp airport in 2014 with E-Creta, an alkali-activated concrete [10].

Recently, Davidovits developed research characterizing the material present in ancient monuments of pre-Columbian civilizations in South America, concluding that they were alkali-activated materials [11]. The studies carried out between 2016 and 2019 in the Tiahuanaco monuments (Tiwanaku/Pumapunku), Bolivia, and other monuments in Peru complement the studies carried out in the 70s and 80s and prove the durability of alkali-activated materials [12].

**Table 1.** Bibliographic history of some important discoveries about activated alkali materials. Source [6]–[12]:

Author	Year	Research
Feret	1939	Use of slag in cement
Purdon	1940	Combination of slag and alkaline solutions
Glukhovsky	1959	Theoretical basis and development of alkaline solutions in cement
Glukhovsky	1965	First material called alkaline cement
Davidovits	1979	Use of the term geopolymer
Malinowski	1979	Characterization of ancient Roman aqueducts
Forss	1983	Cement with alkaline slag and superplasticizers
Langton e Roy	1984	Characterization of old building materials
Davidovits e Sawyer	1985	Patent of a cement with chemical composition similar to the material that it believes to have been used in Egyptian pyramids
Krivenko	1986	Definition of $M_2O-MO-SiO_2-H_2O$
Malolepsy e Petri	1986	Activation of synthetic slags
Malek. et al.	1986	Application of radioactive waste in activated slag cements
Davidovits	1987	Comparison of old and modern cements
Deja e Malolepsy	1989	Proof of chloride resistance of AA materials
Kaushal et al.	1989	Incorporation of nuclear waste in AA materials
Roy e Langton	1989	Concrete production similar to the old ones
Majundar et al.	1989	$C_{12}A_7$ - slag activation
Talling e Brandstetr	1989	Alkaline slag activation
Wu et al.	1990	Alkaline activation of slag-based cement
Roy et al.	1991	Production of quick-setting alkaline cements
Roy e Silsbee	1992	Publication of the article “Alkaline activated cements: an overview”
Palomo e Glasser	1992	Activation of metakaolin
Krivenko	1994	Properties of alkaline cements
Davidovits	1994	Definition of the structure of geopolymers through polysialates
Wang e Scrivener	1995	Discovery of the microstructure of AA materials
Palomo	1999	Publication of the article “Alkaline activation of fly ash: the cement of the future”.
Krivenko, Roy e Shi	2006	Publication of the first book on alkaline activation
Provis e Deventer	2007	Definition of the kinetic modeling of the alkaline activation reaction
Habert et. al	2011	Environmental assessment of geopolymeric concrete production by life cycle
Australia	2013	Construction of the bridge in Victoria with E-Crete.
Australia	2014	Brisbane West Wellcamp airport expansion with E-Crete.
Davidovits	2016	Studies of deposits and monuments used by pre-Columbian civilizations in Bolivia and Peru
Davidovits	2019	Characterization of pre-Columbian monuments in Pumapunku-Tiwanaku, Bolivia

### 1.3 Advantages and disadvantages

As noted by the main invocations highlighted in the text and Table 1, research involving alkali-activated materials has gained considerable prominence in the construction materials scenario. Provis [2] highlights that this interest in the development of alkali-activated binders is motivated by economic advantages since the process allows the use of industrial by-products, such as slag and ash, to produce a material with considerable added value, which rivals with Portland cement. Another issue pointed out by Provis to explain why the increase in research is linked to sustainable development. It is known that the Portland cement production is very exploratory, besides emitting several tons of  $CO_2$  into the environment. This fact is not repeated in the cycle for the production of alkali-activated materials due to the

possibility of using by-products from other processes, which would be generated regardless of their application as a precursor to AAM.

In addition to those mentioned, different motivations for the development of more research on alkali-activated binders are related to the properties that these materials have. High chemical resistance to acids and high-temperature resistance is mentioned, due to the presence of alkaline aluminosilicate gels, with a highly reticulated nature, in addition to the low presence of water in their structure, when compared to hydrated Portland cement, which presents hydrated calcium silicate gels [13], [14]. AAM can also have good durability and high initial resistance, mainly in slag-based compounds [6]. They also have low shrinkage, low thermal conductivity, strong adhesion to metallic and non-metallic substrates [15], low permeability to ions and chlorides, low cost, a possibility to recover industrial waste, low CO<sub>2</sub> emissions, effective passivation of reinforcing steel, making it possible to be armed, if necessary [14].

Although the researchers do not deal much with the subject, the main disadvantages to be overcome for the application of AAM are related to the activating solution, due to two aspects: the difficulty of handling this material, which because it has a very high pH and it is very alkaline it can cause burns or respiratory problems when inhaling the hydroxides dust used in the solution; and the cost and availability of the silicates and hydroxides used in the solution. There are currently few studies on the use of waste as activators in AAM. The vast majority of researchers focus their studies on the development of new precursors. One of the major disadvantages of alkali-activated materials is linked to activators, which still use commercial materials, causing the exploitation of natural resources and making the price of the materials go up. It is noteworthy that the use of alternative activators tends to reduce these disadvantages, although in some cases there is a need for additional treatments, besides those carried out in commercial products, to make them suitable for use. This fact can cause an increase in the price of alternative activators, as highlighted by Azevedo et al. [16], who studied the application of glass waste in place of sodium silicate. The authors concluded that it is necessary to grind the residue for a long time, consuming a considerable amount of energy in the process.

#### 1.4 Alkali-activated materials classification

To organize the structure of this study, the explanation of the alkaline activation mechanisms, the principal objective of this article, will be divided into two groups, as suggested by some authors [17], [18]:

- a) Materials with precursors rich in aluminosilicates and without calcium oxide in their composition, such as metakaolin and ashes. These materials were the focus of Davidovits' study, and when they suffer the reaction, it becomes a mineralogical structure very similar to zeolites, as will be discussed below. They are known as geopolymers, geocements or polysialates [6].
- b) Materials with precursors rich in calcium oxide, which may have aluminum oxide or not. They are precursors that have a Ca/(Si+Al) ratio higher than 1 [1]. They were the focus of study by Victor Glukhovskiy, and when they harden, they present a composition similar to ordinary Portland cement, that is, they form C-S-H gels [19], [20].

## 2 ALKALI ACTIVATION REACTION OF LOW-CALCIUM PRECURSORS

### 2.1 Main low-calcium precursors

The main precursors used in alkaline activation for the geopolymers production, that is, the low-calcium precursors content are metakaolin and fly ash. Regarding metakaolin, it is worth noting that this compound has several studies carried out and it is considered by researchers as the principal material used as a precursor in AA reactions [21], [22]. The significant use of metakaolin can be attributed to its reactivity, which is quite high [23], and the way of obtaining the material, which is very simple.

This material is generated by calcining kaolin at temperatures ranging from 500 to 800°C, depending on the degree of crystallization and the purity of the material [24]. It is known that kaolinite, which is the main compound present in kaolin, undergoes a dehydroxylation reaction at around 550°C, transforming into metakaolinite. Figure 1 shows a scheme for the production of metakaolin from traditional kaolin [1], [20], [25]. It is observed that the burning at temperatures below 400°C is not suitable for the precursor production, as well as the burning of temperatures above 950°C, due to the mullite production that cannot be activated alkali due to its high crystallinity [15], [19].

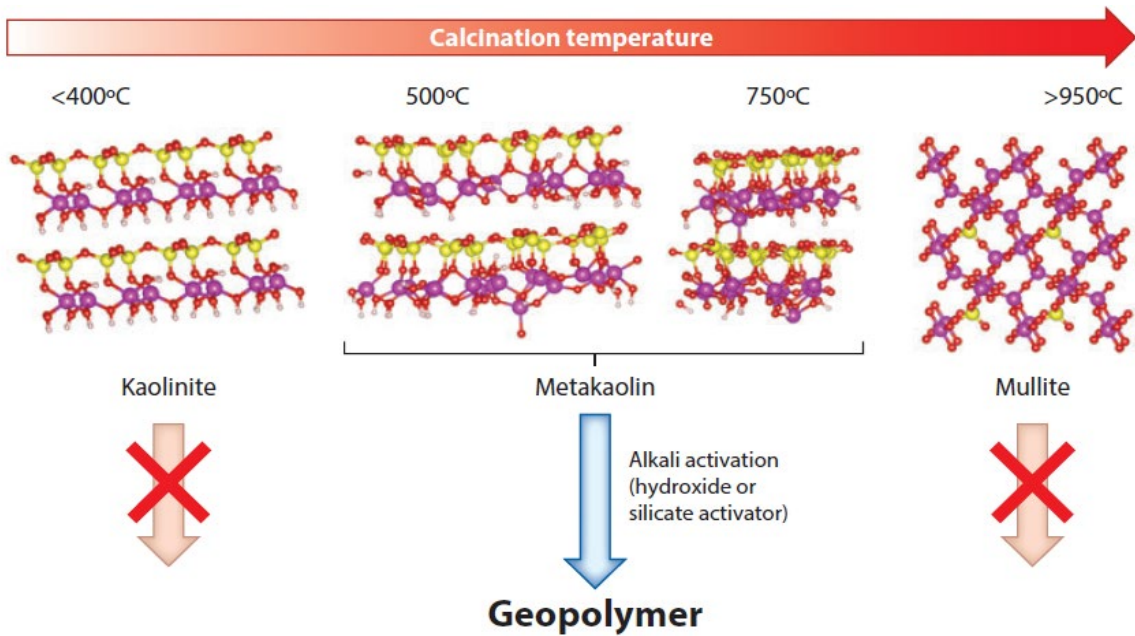


**Figure 1.** Calcination of kaolin for percussion production. Source: White et al. [20].

On environmental issues, it is interesting to note that there are some advantages in using metakaolin because its synthesis emits 5 to 6 times less  $\text{CO}_2$  than the Portland cement production process [26]. Besides, kaolin can be extracted not only from mineral sources but depending on the composition, it can be obtained through mine tailings or the paper industry [1]. The different sources will influence the reactivity of the obtained metakaolin, depending on, for example, the chemical and mineralogical composition of the clay used as raw material, but they are more ecologically viable solutions.

As for the disadvantages of the metakaolin use, we can mention a higher tendency of drying retraction presented by these materials when compared to fly ash [27]. This characteristic can be related to the chemical composition of these two precursors, which it is observed that metakaolin has a higher amount of aluminum oxide ( $\text{Al}_2\text{O}_3$ ) than fly ash. Overall, some research shows that metakaolin has about 55 to 62%  $\text{SiO}_2$  and between 35 to 42%  $\text{Al}_2\text{O}_3$ , while fly ash has between 50 to 55%  $\text{SiO}_2$  and approximately 20 to 25%  $\text{Al}_2\text{O}_3$  [24], [28]–[30]. The retraction is higher because the aluminum oxide dissolves faster than the silicon oxide, related to the two principal network makers in geopolymers [24]. That also explains the reactivity of metakaolin being higher than fly ash.

Another disadvantage is the price of metakaolin, which, because it is a commercial material, is usually higher than when using blast furnace slag, fly ash, or other industrial waste [15]. However, it is noteworthy that the price of metakaolin is extremely variable, depending on the location and specifications of the product, for example. Thus, even though there is a tendency for the price of metakaolin to be higher than in the other components used as precursors, commonly residues, this statement cannot be generalized. However, due to the high purity and reactivity, the products obtained by the alkaline reaction of metakaolin, in general, present a more well-defined gel microstructure [1].

On fly ash, it is worth noting that this material is a powdered by-product produced in thermoelectric plants during the coal burning, containing mainly aluminosilicate. They present fine spherical particles with the main chemical components of aluminum, silicon, calcium, iron, magnesium, and carbon wastes [31]. The particle size in the fly ash ranges from  $<1\ \mu\text{m}$  to more than  $100\ \mu\text{m}$ , and this by-product has an annual worldwide production of more than 900 million tons, according to the updated data from 2019 [15]. Therefore, the storage and fly ash disposal as industrial waste has become a serious environmental problem and a worldwide technical challenge. In Brazil, however, the energy matrix uses predominantly hydroelectric plants, which do not generate fly ash. For this reason, the study of this type of waste in Brazilian research is less practical, different from what occurs in other countries, such as China and the USA, which present easy availability of the waste [32].

Given its low price, good spherical structure, and a large amount of highly active amorphous aluminates and silicates, fly ash class F is the most recommended raw material for geopolymers synthesis [33]. The activity and solubility of Al

and Si can transform precursors into important geopolymeric products in an alkaline activator solution [34], [35]. According to the American Society of Test Materials classification [34], fly ash is defined as Class C ( $\text{CaO} > 20\%$ ) and Class F fly ash ( $\text{CaO} < 20\%$ ), respectively. Class C fly ash can be hydrated to form hydrated calcium silicate (CSH), has been widely used to partially replace cement in concrete, or as a calcium-rich precursor [31], [35], which will be discussed next in the explanation about AA of BFS. Class F fly ash is more suitable for geopolymers synthesis [36] because its amorphous content is higher than that one of class C fly ash [37].

The geopolymer products obtained with the use of Class F fly ash have excellent mechanical properties, as reported by the literature [35], [38]–[40]. The authors, however, report difficulty in the geopolymers synthesis with fly ash due to the curing of the material that must be done at high temperatures to increase the reactivity of the material, which is very low at ambient temperatures. This characteristic can be associated with the fly ash chemical composition, which, due to its higher levels of  $\text{Al}_2\text{O}_3$ , as reported [24], [28]–[30], and, in some specific cases, may have a high CaO content, around 12% [41], [42], justifying the need for thermal curing.

Besides metakaolin and fly ash, other types of precursors that have low amounts of calcium have reaction mechanisms typical of geopolymers. For example, other types of burnt clay can be cited as illite-smectites [43] or feldspars [44], [45]. There are also other precursors such as volcanic ash, natural pozzolans, and metallurgical slags with low amounts of calcium [46]–[49]. Recent research has proposed the application of industrial wastes, such as chamotte [50], from ceramics industries, and magnesium phosphate, from the chemical industry through ammonium production [51]. In both cases, there was a potential for the application of waste, but not in isolation. In the case of chamotte, the best results were obtained using 50% metakaolin and 50% waste [50], while in the case of magnesium phosphate, the most satisfactory results were obtained using 30% metakaolin and 70% waste, in which the authors obtained compressive strength of 30 MPa with only 7 hours of curing [51].

## 2.2 Stages of the alkaline activation reaction of geopolymers

According to Duxson et al. [52], in geopolymers, the alkaline activation reaction is divided, in general, into the following steps: dissolution, condensation, polycondensation, and crystallization of the gels. These steps constitute the Davidovits model, outlined by Duxson, and are briefly explained below, according to the scheme represented by Figure 2.

The first reaction process is the dissolution of the aluminosilicate materials and the release of the reactive monomers silicate and aluminate, represented respectively by  $[\text{Si}(\text{OH})_4]^-$  and  $[\text{Al}(\text{OH})_4]^-$ . Dissolution occurs by dropping the covalent bonds Si-O-Si and Al-O-Al that characterize aluminosilicates and is only possible in the presence of a strongly alkaline medium with a pH higher than 14, provided by the activating solution. More simply, it can be said that the alkaline solution breaks the bonds that hold aluminosilicates together, creating a colloidal phase [15], [52], [53].

The colloidal phase initiates a water elimination process, due to a nucleophilic substitution reaction, where the specimens  $[\text{Si}(\text{OH})_4]^-$  and  $[\text{Al}(\text{OH})_4]^-$ , which present an electric charge -1, are connected to the others due to the attraction among the OH groups of the silicate with the Al ions of the aluminates. The colloidal phases initiate the chemical equilibrium process, which is known as condensation, giving rise to intermediate compounds. In this stage, the formation of an unstable aluminosilicate species occurs, releasing water molecules in the process [14], [53].

This procedure continues, with more water release and the first gels formation. The search for balance continues, however, load balancing is not possible, because both aluminates and silicates have negative charges. Because of this, the presence of alkali metal ions, such as  $\text{Na}^+$  ou  $\text{K}^+$ , in the alkaline solution is so important. The positive charge of these ions provides a balance in the charges of the unstable gels that had been formed, causing a reorganization in the structure of the intermediate compounds, which initiate the formation of a more resistant final compound.

The polycondensation of the gels then occurs, which may or may not undergo crystallization and give rise to the stable gels present in the geopolymers final structure. Amorphous gels are called by some authors N-A-S-H (hydrated sodium aluminosilicate), while the crystalline or semi-crystalline phases are just called zeolites [54]. The material starts the hardening process, acquiring mechanical resistance and the other known properties of these activated alkali materials [15], [53]. Figure 3 shows the final structure of the 3D network formed in the composition of the geopolymers.

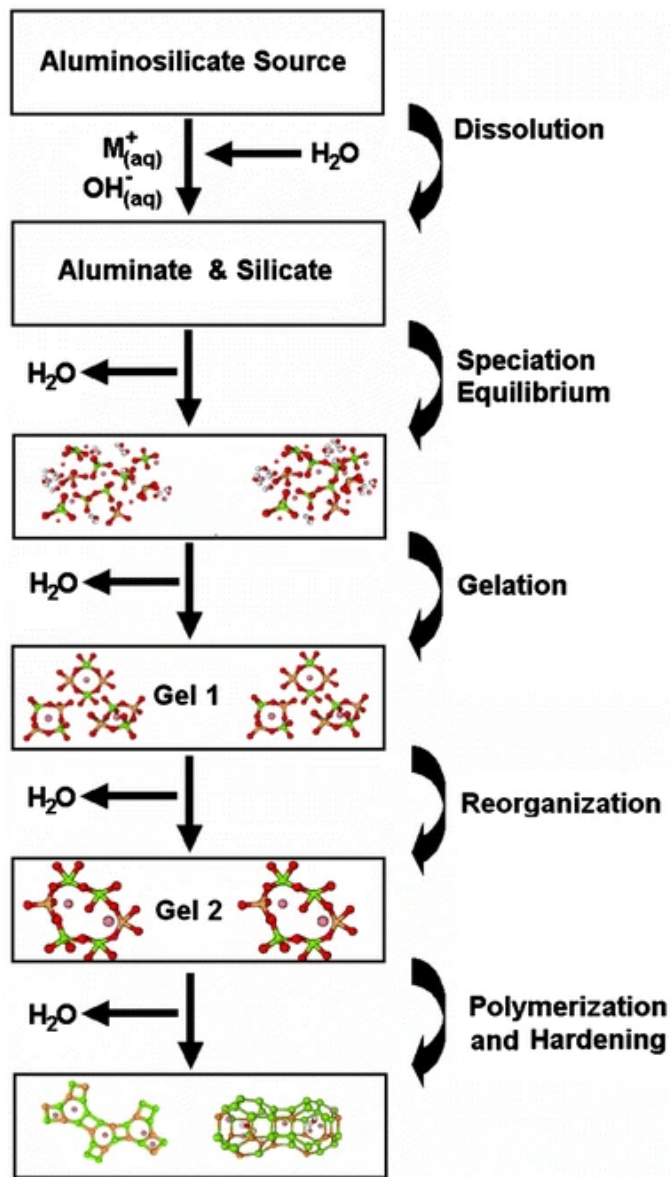


Figure 2. Duxson model of alkaline activation reaction of geopolymers (low in calcium). Source: Duxson et al. [53].

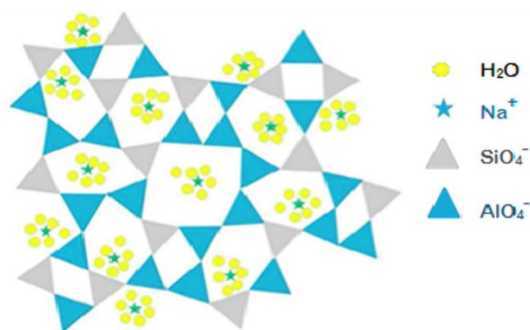


Figure 3. Illustration of the geopolymeric network in formation, amorphous N-A-S-H gels. Source: Lahoti et al. [14].



### 2.3 Compounds formed in the alkaline activation reaction of geopolymers

As mentioned above, some authors point out that the geopolymers formation follows a logic very similar to the zeolites formation, and this characteristic is addressed in the sequence of this text [14], [15], [52], [53]. What is worth noting is that the geopolymerization reactions give rise to polysialate compounds, which can have different configurations, depending on how the alkaline activation reaction is processed [7], [55].

The polysialate compounds correspond to three-dimensional networks of SiO<sub>4</sub> and AlO<sub>4</sub> tetrahedrons sharing the oxygen atoms, as shown in Figure 3. To maintain balance, the existence of positive Na<sup>+</sup>, K<sup>+</sup> e Ca<sup>2+</sup> ions is necessary, which must be present in the structure cavities to balance the negative charges of geopolymeric gels. Polysialates can also be defined as chain and ring polymers with Si<sup>4+</sup> and Al<sup>3+</sup> in coordination 4 times with oxygen, and their empirical formula is given by the equation below [3].

$$M_n \left[ - (Si - O_2)_z - Al - O \right]_n \cdot nH_2O \tag{1}$$

Where z=1, 2 or 3, represents the atomic relationship between Si/Al; M= monovalent cation as K<sup>+</sup> ou Na<sup>+</sup>; n= geopolymerization degree.

The types of polysialates distinguished by Davidovits are illustrated in Figure 4, being differentiated according to the atomic relationship between Si/Al [6] or between the molar ratio of SiO<sub>2</sub>/Al<sub>2</sub>O<sub>3</sub> [5], depending on the studied author. It is worth noting that the atomic relationship between Si/Al is half the molar ratio between SiO<sub>2</sub>/Al<sub>2</sub>O<sub>3</sub>. For example, when the atomic ratio is 1, the molar ratio is 2, and so on.

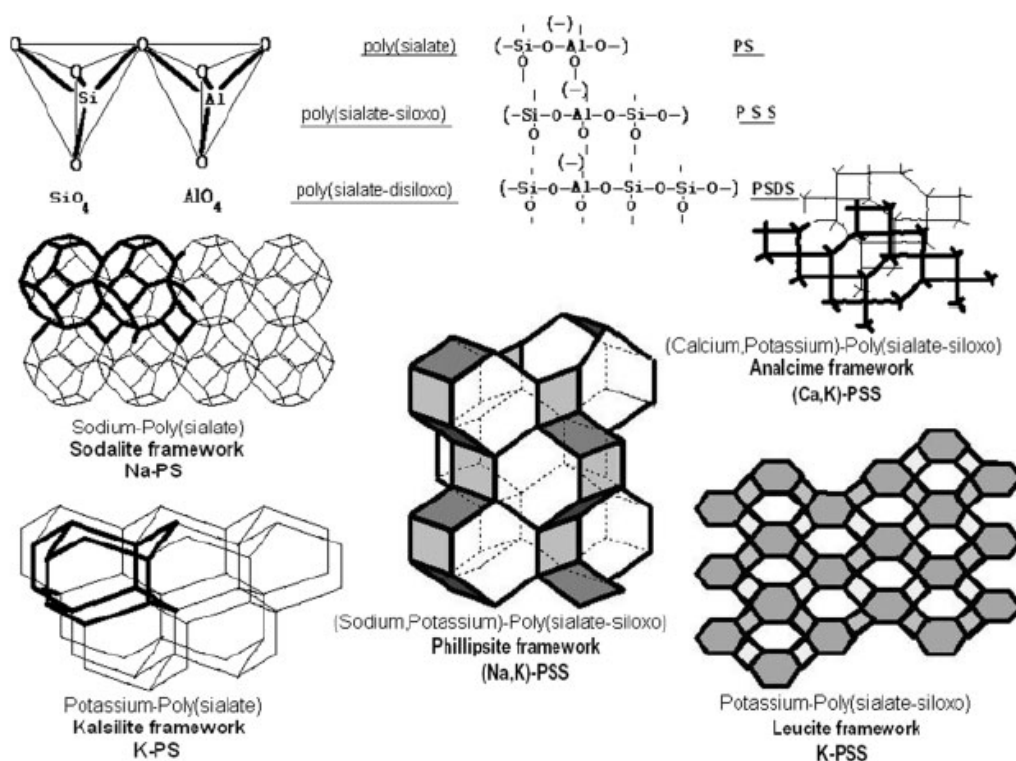


Figure 4. Geopolymer networks of Polysialates. Source: Majidi [5].

Taking the molar ratio as a base, we have the following classification: common polysialates (PS), where the SiO<sub>2</sub>/Al<sub>2</sub>O<sub>3</sub> ratio is 2, forming a type structure (Si - O - Al - O); polysialates-siloxo (PSS), with a SiO<sub>2</sub>/Al<sub>2</sub>O<sub>3</sub>ratio of approximately 4 and (Si - O - Al - O - Si - O) structure; and polysialates-disiloxo (PSDS), with a molar ratio of SiO<sub>2</sub>/Al<sub>2</sub>O<sub>3</sub> around 6 and chains of the type (Si - O - Al - O - Si - O - Si - O). This information can be seen in Figure 4,

where the networks of PS and PSS formed with the alkali metals sodium and potassium are visualized, such as the networks of kalsilite, leucilite, analcime, sodalite. The formation of these networks is directly related to the dosage of geopolymers in their production phase, either through molar relationships, solution molarity, or in the relationship between the activator and the precursor.

It is worth noting that, besides the model proposed by Davidovits for the geopolymerization reaction, there is another model that is very widespread and accepted in the study of this material, which is the Provis model [56]. In this model, detailed in Figure 5, it is defined that the precursor reaction rich in aluminosilicates and poor in calcium oxide, as in the case of metakaolin and fly ash, occurs initially with the formation of silicate and aluminate monomers, which grouped forming combined aluminosilicate oligomers. Thereafter, the reaction “separates” into two stages, in which part of the oligomers polymerizes in an amorphous and random manner, giving rise to geopolymeric gels. The other part undergoes the process of crystalline nucleation, forming nanocrystalline aluminosilicates nuclei, which subsequently originates crystalline zeolite phases. According to the Provis model, two distinct and simultaneous geopolymer formation reactions occur to a higher or lesser degree depending on different factors (such as temperature, cure time, solution’s molarity, and molar relationships of the precursors), originating an amorphous phase and another crystalline [8], [57].

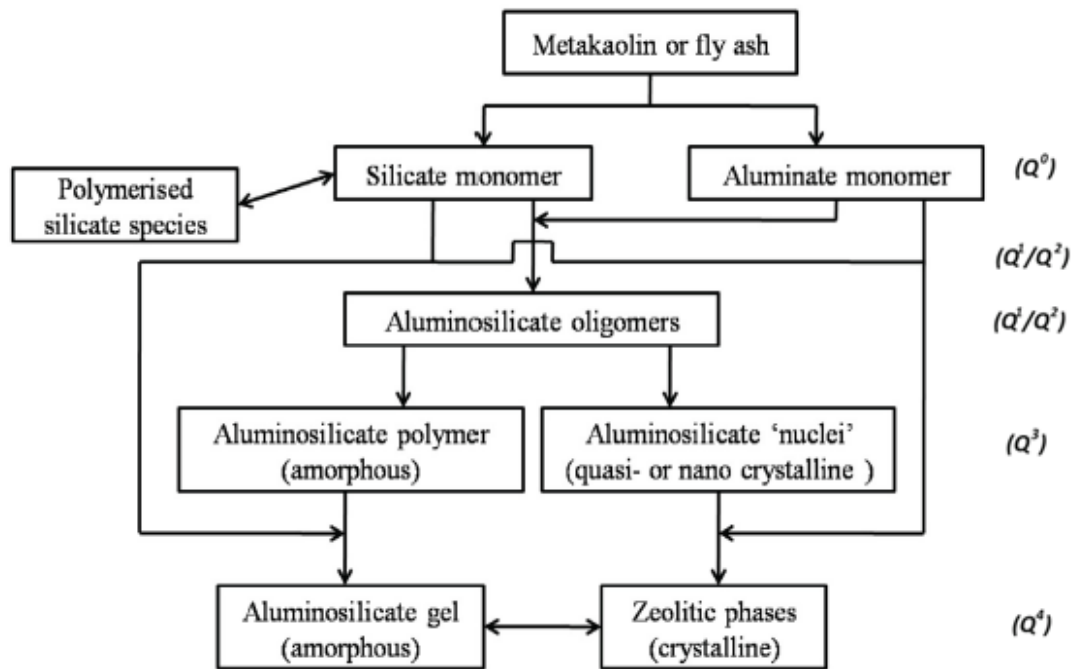


Figure 5. Provis model for the formation of geopolymers. Source: Wu [15].

The mechanism of polysialates formation, and also of the zeolite phases, is much more complex than was mentioned above. It is known, for example, that in the alkaline activation reaction of geopolymers, the polysialates formation formed mainly by iron oxide can occur, named as ferrosialates [58]. Iron can be present in three different forms in the ferrosialate chain: in  $Fe^{+3}$  species trapped in the main chain, in  $Fe^{+3}$  species acting for load balancing in interstitial sites or in the form of  $Fe_3O_4$  oxide linked to the chain through bonds secondary [59]. In general, iron forms a  $[Fe(OH)]^{2+}$  specimen that replaces  $[Al(OH)_4]^-$  specimens. In some cases it can also partially replace specimens  $[Si(OH)_4]^-$  in the geopolymer chain [58].

These compounds promote tensile strength in the geopolymer, which in general is low, but make the material conducive to the occurrence of corrosion, which in the case of use in conjunction with reinforced elements, may make the application of the material unfeasible [60]. Another property presented by ferrosialates is the of the geopolymer density reduction, due to its lamellar, tubular and spongy structure. This characteristic, however, increases the porosity of geopolymers with a high content of ferrosialates [59].

Although the formation of ferrosialates is benefited in precursors that have a high amount of iron oxide and whose cure is carried out at temperatures above 80°C, practically all geopolymers have low amounts of ferrosialates in their composition [61]. This fact illustrates and proves the complexity of the polysialate networks formation, which although simplified by several authors, presents mechanisms that are still little explored.

Figure 5 presents the information for  $Q^n$ , where  $n$  can take values from 1 to 4. This notation represents the silicon tetrahedral atom coordination, connected via oxygen to other silicon tetrahedral atoms [25]. It is possible to notice that as the geopolymerization reaction becomes more intense, larger amounts of chains are formed, the silicon tetrahedrons coordination increases, which bind and form gels. This analysis is performed by specific techniques such as nuclear magnetic resonance spectrometry, where it is possible to obtain the  $Q^n$  which means the silicon atoms quantity covalently linked.

It is noticed that the zeolites formation is a common characteristic and highlighted by different authors. That is why it will be explained what zeolites are and what their similarities are with geopolymers. Zeolites are hydrated, crystalline, or nanocrystalline aluminosilicates with a specific structure, composed of silica and alumina tetrahedra connected by shared oxygen atoms and containing well-defined channels and chambers, filled with ions and water molecules [54]. This structure makes its physical and chemical properties unique, which results in a wide range of practical applications [25]. The zeolites are based on the tetrahedron  $TO_4$ , where  $T$  is an aluminum or silicon atom, which can be considered as a basic building block. The connections between several  $TO_4$  tetrahedrons are called secondary units of construction (USF) [40].

The main difference between conventional zeolites and those formed in geopolymerization is that, in conventional production the molar ratios are much higher. For example, while in conventional production the molar ratio between  $H_2O/SiO_2$  is between 10 and 100 and the molar ratio between  $OH^-/SiO_2$  is between 2 and 20, in the case of geopolymers these relationships change to between 2 and 10 and between 0.1 and 0.5, respectively [62]. As an impact on the standard zeolites formation, a high crystallinity content is achieved, while in the formation of geopolymers zeolites are not formed separately, but they are mixed with amorphous gels of the N-A-S-H type, leading to more amorphous compounds [40]. In the case of geopolymers, a kind of composite material is formed and it has two distinct phases: a crystalline one formed by zeolites and an amorphous one, formed mainly by N-A-S-H gels.

Even if the geopolymerization reaction forms zeolites are not as pure as in the conventional process, which occurs by autoclave requiring a specific hydrothermal reactor, there is a great energy advantage in the geopolymerization process. The geopolymerization reaction, in addition to saving energy, provides time spent, contributing to sustainability in obtaining zeolites [54]. However, it is worth noting that zeolites are formed only in very specific situations within geopolymers, under predetermined temperatures (25 to 300°C) and pressure [63], [64].

The most commonly known zeolite species are analcime, zeolite A, zeolite X, sodalite, natrolite, among others [54], [65], highlighted in Table 2. As can be seen in Figure 4, some zeolite minerals are the same detailed in this figure as geopolymerization reaction products. The polysialates highlighted above are nothing more than zeolites with a lower degree of crystallinity due to the presence of amorphous N-A-S-H gels. Figure 6 presents an illustration of the sodalite-type zeolites (SOD), zeolite A (LTA), and zeolite X (FAU), which are formed by the arrangement of sodalite cages in different configurations. This fact illustrates that the most common zeolites obtained by the autoclave process are formed in geopolymers, but the simplest crystallographic arrangements, which favor the formation of larger amounts of sodalite as a result of zeolite A or X [65].

**Table 2.** Parameters of the main zeolites. Source: Rožek et al. [54]:

Abbreviation	Name	Chemical formula
ANA	analcime	$Na[AlSi_2O_6].H_2O$
CAN	hydroxycancrinite	$Na_8[AlSiO_4]_6(OH)_2.2H_2O$
CHA	chabazite (herschelite)	$Na[AlSi_2O_6].3H_2O$
FAU	Faujasite (Zeolite X)	$Na_2[Al_2Si_2.4O_{8.8}].6,7H_2O$
FAU	Faujasite (Zeolite Y)	$Na_{1.88}[Al_2Si_{4.8}O_{13.54}].9H_2O$
GIS	Zeolite Na-P1	$Na_{3.6}[Al_{3.6}Si_{12.4}O_{32}].12 H_2O$
LTA	Zeolite A	$Na_2[Al_2Si_{1.85}O_{7.7}].5 H_2O$
NAT	Natrolite	$Na_2[Al_2Si_3O_8].2 H_2O$
SOD	Sodalita	$Na_6[AlSiO_4]_6.8 H_2O$

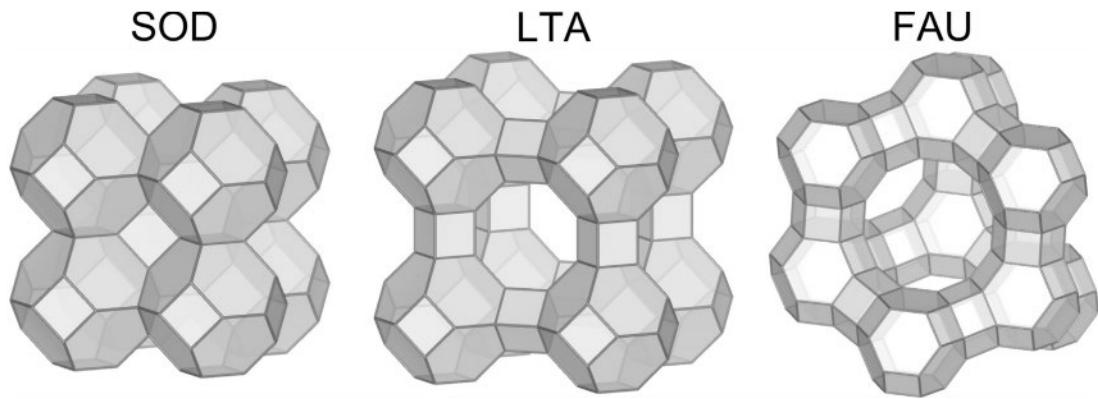


**Figure 6.** Illustration of the most common zeolites obtained by autoclave. Source: Rožek et al. [54].

### 3 ALKALI ACTIVATION REACTION OF OF CALCIUM-RICH PRECURSORS

After discussing the reaction of low-calcium precursors, it is valid to present the reaction mechanisms of AA materials formed from blast furnace slag, for example. It is known that in these cases, the precursor material is rich in calcium, and the products formed are different, being partly similar to the hydration products of Portland cement. As highlighted in the introduction, the calcium-rich precursor is defined as one with a  $\text{Ca}/(\text{Si}+\text{Al})$  ratio higher than 1 [1]. The first distinguishing feature, which deserves to be highlighted, of the systems formed by calcium-rich precursors concerning the geopolymers previously defined is that blast furnace slag, for example, is much more reactive at moderately alkaline pH than geopolymer materials [2]. This allows the use of several other materials as an activating solution, besides sodium and potassium hydroxides and silicates, such as alkali metal carbonate or sulfate solutions. That is because BFS reacts very slowly with water and the presence of alkaline compounds only accelerates the material's hardening reaction [53].

The alkali-activated reaction products of blast furnace slag in alkali metal silicate and hydroxide solutions are generally predominantly hydrated calcium silicate gels, similar to those obtained in the hydration of Portland cement [8], [66]. However, there is an important difference, because the gels have lower amounts of Ca and more amounts of Al in tetrahedral locations. That leads to a higher degree of polymerization and also to a significant degree of crosslinking between formed gel chains. While C-S-H compounds are formed in cement hydration, in BFS alkali-activated reaction, C-A-S-H gels are formed, giving rise to minerals known as tobermorites [8], [57].

Figure 7 shows an illustration of the tobermorite. As with Portland cement systems, the C-A-S-H gel includes layers of silicate chains coordinated tetrahedrally with a Dreierketten structure. The region between the coverslips contains  $\text{Ca}^{2+}$  cations, alkalis, and hydration water chemically incorporated into the gel structure. Some alkaline cations also balance the net negative charge generated when  $\text{Al}^{3+}$  replaces  $\text{Si}^{4+}$  at the tetrahedral chain locations [1].

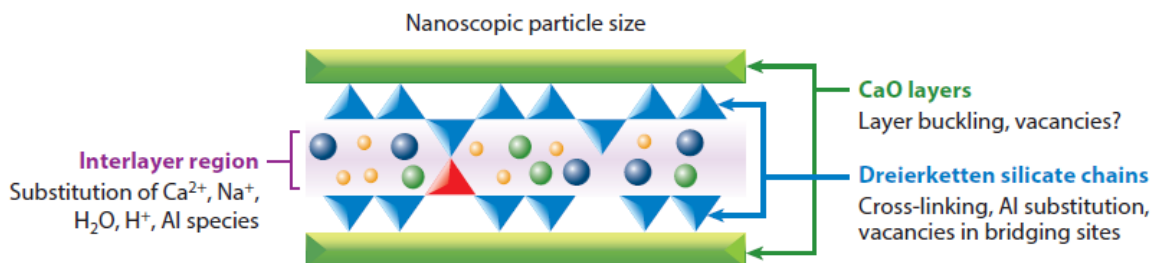


**Figure 7.** Tobermorite Structure. Source: Provis and Bernal [1].

However, as the amount of Al increases in the precursor's composition, Al precipitation begins to occur in the C-A-S-H chains, making it difficult for the chains to cross-link and become saturated. Thus, the precipitation of another

phase, rich in Al, occurs from the chains and impairing the formation of gels and sometimes changing the mechanical properties of the material [67].

The gels formation described is not as simple as mentioned in the previous paragraph. There is a wide formation of secondary phases that can be set up depending on the chemical composition of the studied precursors, as highlighted by Figure 8. That is because several factors, such as alkalinity, water/binder ratio, curing environment (duration, humidity, and temperature), besides the relationship among the components, the main ones being Ca, Mg, Si, Al, and Na, they affect the phases and compounds formed in the alkali-activated relationship [68], [69]. It is worth noting that the secondary phases formed are rich in Al since, as highlighted in the previous paragraph, the excess of Al causes the precipitation of other phases out of the principal C-A-S-H gels [2], [8], [57].

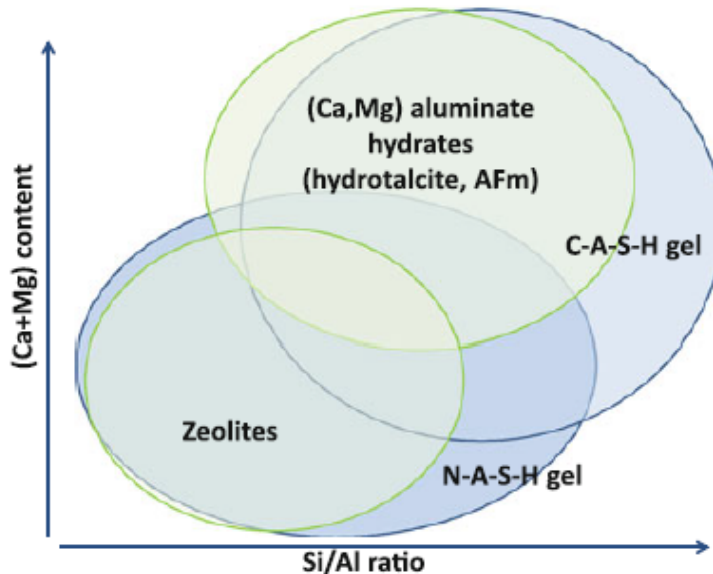


**Figure 8.** Formation of gels in the hydration of precursors with different calcium levels. Source: Provis [2].

Al may be substituted for Mg in C-A-S-H gels, but in very limited levels. If there is an excess of Al, and there is Mg in the material composition, another secondary compound called hydrotalcite is formed, which is often mixed with C-A-S-H gels [70]. The use of precursors with low Mg content, such as slag without this element, favors the formation of zeolites instead of hydrotalcite. Another important characteristic of secondary gels is the presence of alkali metals, such as Na, present in the activating solution. In general, alkali metals are located at the interstitial sites of the gels, producing a balance of electrical charges. However, an N-A-S-H phase can coexist as side products along with the predominant C-A-S-H phase in the alkaline activation of BFS [71]. It is known that N-A-S-H gels have a higher degree of amorphism than C-A-S-H gels and are favored in alkali activation with silicates. In the reaction with hydroxides, the formation of C-A-S-H gels is favored, presenting a high degree of crystallinity, driven by the presence of Na in the interstices of the gels [52].

The alkali activation mechanism of calcium-rich precursors is even more complex than the one of precursors low in this compound (geopolymers) and needs many studies. Besides the exemplary blast furnace slag, other materials such as steel, nickel, titanium, and phosphorous slag fit together in this group [39], [72], [73].

It is interesting to note that some researchers carried out the mixture of two different types of precursors to study the formation of alkali-activated reaction gels. The idea that reaction mechanisms occur separately for low and calcium-rich precursors is not always true in experimental research. Some studies, for example, carried out the mixture of blast furnace slag and fly ash in different proportions to study the alkaline activation of these materials together and how the gels are formed in this reaction [74], [75]. Figure 9, for example, presents a ternary diagram with the elements CaO, SiO<sub>2</sub> and Al<sub>2</sub>O<sub>3</sub>, and the gels formed in the AA reaction. The formation of gels types C-A-S-H and N-A-S-H is verified depending on the curing age studied or depending on the material composition evaluated.

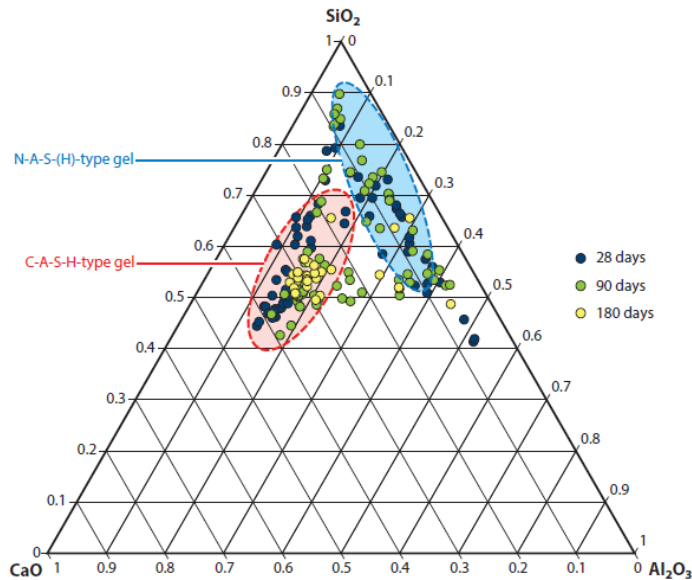


Figure 9. Ternary diagram of formation of alkaline activation gels. Source: Ismail et al. [74].

#### 4 CHARACTERIZATION OF GELS FORMED IN THE AA REACTION

A way to identify the formation of the gels in the alkali activation reaction and to prove the mechanisms presented in the previous paragraphs is through characterization tests. Some examples of this type of assay are X-ray diffraction (XRD), transmission electron microscopy (TEM), and/or scanning electron microscopy (SEM), nuclear magnetic resonance spectrometry (NMR), and Fourier transform infrared spectroscopy (FTIR).

For the determination of the crystalline structure, one of the main techniques employed is X-ray diffraction, and it is even possible to perform the quantitative determination of zeolite since a reliable database is available [76]. This technique is very widespread in the control of zeolites industrial production [77], for example, and some authors have sought to apply it to the study of alkali-activated materials [78], [79].

The creation of the database for quantitative analysis of the zeolite phases present in the alkali-activated materials is complex, and it is necessary to use information known from the international bibliography. For example, it is possible to associate the formation of zeolite X with peaks in the  $2\theta$  values of  $32^\circ$ ,  $43.5^\circ$  and  $50.5^\circ$ , obtained through the file of the International Center for Diffraction Data (ICDD) # 39-0218 [80]. Zeolite A, in turn, can be related to peaks in the  $2\theta$  values of  $7.5^\circ$ ,  $10.5^\circ$ ,  $30^\circ$  and  $34.9^\circ$  by ICDD file # 35-1009 [81], while zeolite K is detected at the peak with  $2\theta$  value of  $10^\circ$  by ICDD file # 22-0793 [82]. It is observed that the use of XRD for quantitative analysis of the crystalline phases formed by the alkali-activated mechanisms is not so simple, which is why several authors use a qualitative characterization, relating the appearance of the zeolitic phase peaks with the efficiency of the AA reaction.

More satisfactory results are obtained using XRD techniques in conjunction with others, such as FTIR [83], [84], or even thermogravimetric analysis (TGA) techniques [85]. In the case of the use of FTIR, it is possible to identify materials with a short-range structural order through the relation of the spectrometry obtained with standards known in the bibliography [86], [87]. That technique allows the analysis of amorphous and semi-crystalline bands within the material structure, complementing the XRD technique.

Figure 10, for example, shows the results of FTIR obtained in the geopolymers analysis based on metakaolin with partial replacement by palm oil in 5, 10, and 15% [86]. The authors found that the best resistance results were obtained with geopolymers containing 5% palm oil, attributed to the efficiency in geopolymerization. That fact was checked by the authors using FTIR, as illustrated by Figure 10, whose presence of bands in  $1659$ ,  $1408$ ,  $1000$ ,  $723$ ,  $589$ , and  $446\text{ cm}^{-1}$  is verified. The bands of  $1659$  and  $1408\text{ cm}^{-1}$  were attributed by the authors to the presence of NaOH and free water due to the activating solution, while the bands between  $800$  and  $400\text{ cm}^{-1}$  are related to the Si-O-Si bond. The most noticeable band in the figure is found at  $1000\text{ cm}^{-1}$ , related to the stretching of the Si-O-Al bond in the reaction products. The bands observed by the authors are compatible with other published works [18], [79], [80], [84]. The authors attributed the higher resistance obtained by geopolymers with 5% palm oil to the most noticeable bands observed by this composition, which proves the efficiency of the alkaline activation reaction [86].

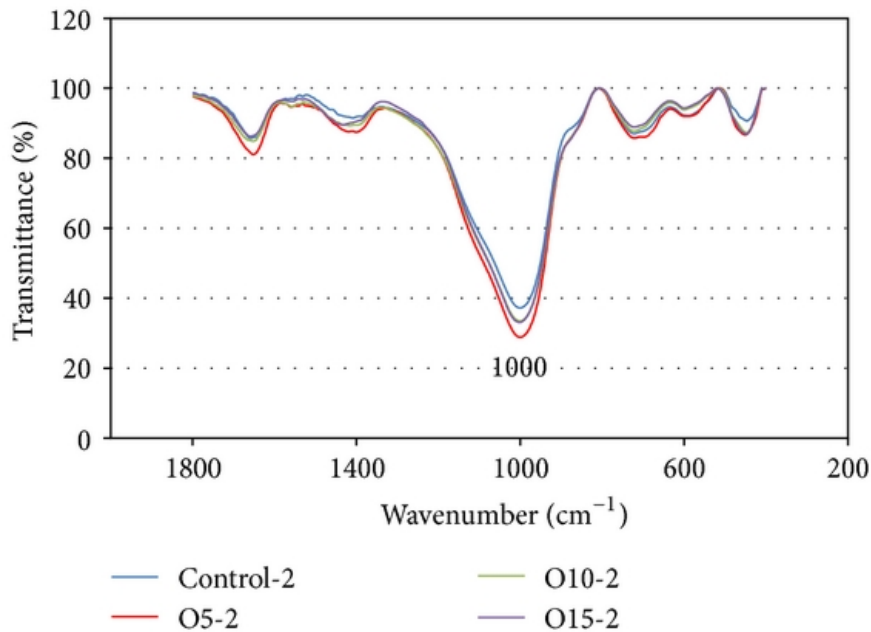


**Figure 10.** FTIR analysis for metakaolin geopolymers with partial incorporation of palm oil. Source: Hawa et al. [86].

Another way of characterizing the products of the AA reaction is by nuclear magnetic resonance (NMR) spectrometry, which in the case of the geopolymers study, for example, the resonance of two types of isotopes is carried out:  $Al^{27}$  e  $Si^{29}$  [39], [88], [89].

In the isotope  $Al^{27}$  resonance, analyzes are performed based on the frequency of 55 ppm, related to aluminum hydroxide, and the frequency of 76 ppm, related to sodium aluminate ( $Al^4$ ), where aluminum presents coordination 4, that is, it presents 4 covalent bonds [39], [84]. The analysis of the formation of geopolymeric networks is carried out by verifying the number of covalent bonds made by  $Al^{27}$ . For example, in the case of  $Al^4Q^0$ , aluminum has 4 covalent bonds, but none of them are made with silicon, that is, it is still sodium aluminate whose frequency is 76 ppm. In the case of do  $Al^4Q^1$ , aluminum has 4 covalent bonds, but one of them is with silicon, represented by a change in the resonance frequency for an interval between 71 to 75 ppm. The same pattern occurs in  $Al^4Q^2$ , change in the resonance frequency to a value between 65 to 70 ppm, and  $Al^4Q^3$ , between 60 to 65 ppm. When aluminum makes four covalent bonds with silicon, the symbol used is  $Al^4Q^4$ , forming a three-dimensional network with a frequency between 52 to 58 ppm [90], [91]. In this way, it is possible to check the progress or the alkaline activation reaction efficiency.

In the isotope  $Si^{29}$  resonance, the reference is made using tetramethylsilane, whose frequency is -94 ppm [88]. The analysis is carried out in the same way as for the  $Al^{27}$  isotope, with the difference that the connections between silicon and aluminum, or between silicon and silicon can be studied [89]. Unlike aluminum, which can be tetravalent, pentavalent, or hexavalent, silicon has tetracoordination, which is why the  $Si^4Q^n$  symbology is not widely used. In general, only  $Q^n$  is used to represent the bonds of this type of isotope [18], [92], [93]. Knowing all the frequency patterns for the isotopes of  $Al^{27}$  and  $Si^{29}$ , it is possible to create a database and correlate these values with, for example, what is observed in the main zeolites. It is known that zeolite A has a value of -88.9 ppm and sodalite of -88.4 ppm, with  $Si^4Al^4$  coordination [18], [94]. Thus, it is possible to identify the types of products obtained by the alkaline activation process using resonance techniques.

The morphological analysis of the alkali-activated reaction products can be observed by TEM or SEM, for example. Although some studies use the TEM technique [95], the vast majority of articles published in the AA materials area use SEM analysis, which will be presented in Figures 11-13. Figure 11 shows the SEM results obtained by the alkali-activated reaction of fly ash [10]. It is possible to identify N-A-S-H gels of amorphous and random nature, as well as crystalline gels, which correspond to zeolite P and analcime, two distinct types of zeolites.

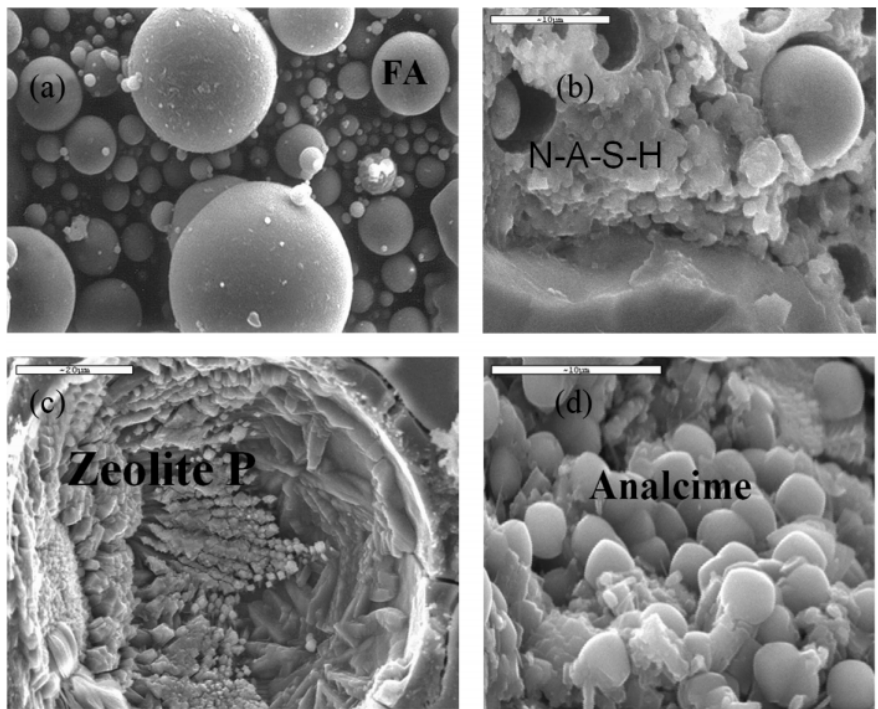


**Figure 11.** SEM of the activated alkali reaction of fly ash: (a) fly ash before the reaction; (b) N-A-S-H gels; (c) P zeolite gels; (d) analcime gels. Source: Palomo et al. [10].

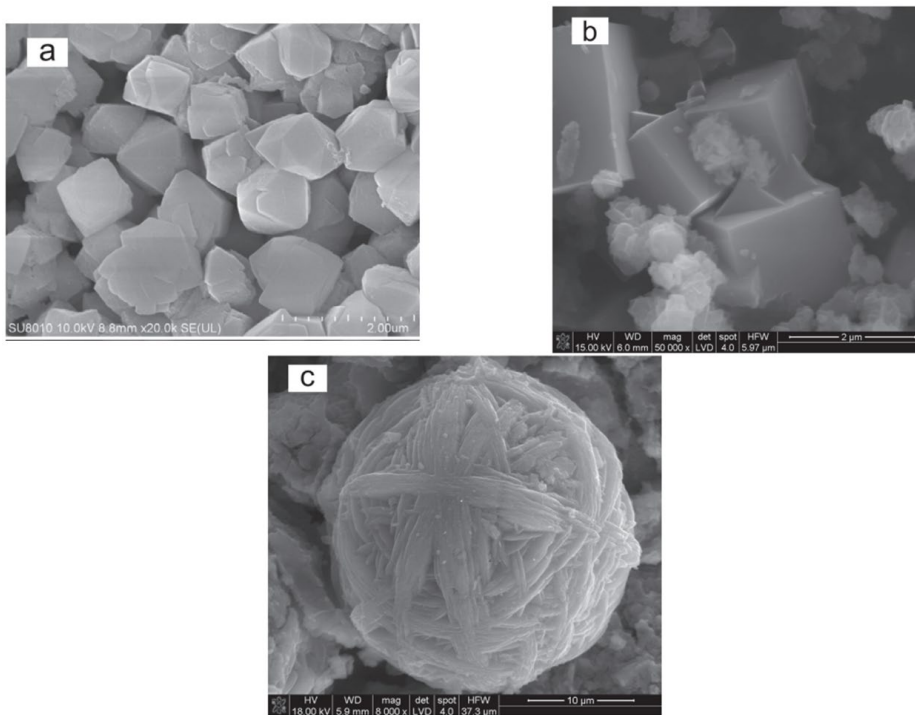


**Figure 12.** SEM of zeolites formed in the production of geopolymers: (a) faujasite; (b) zeolite A; (c) sodalite. Source: Rožek et al. [54].



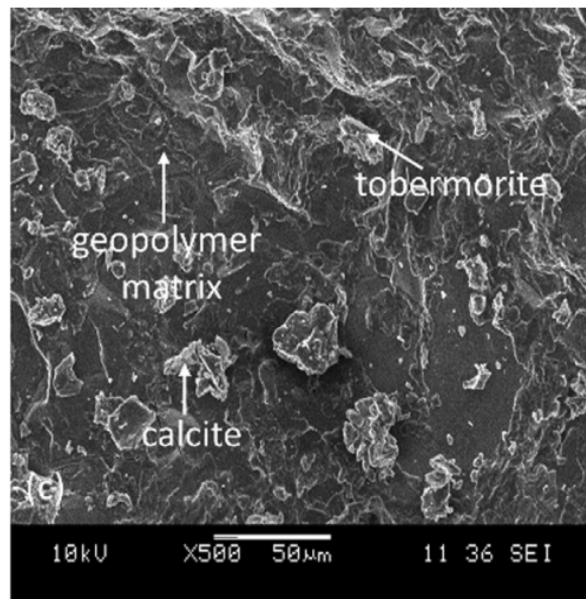


**Figure 13.** Morphology of tobermorite obtained in the alkaline activation of BFS. Source: Aziz et al. [99].

Figure 12 shows different zeolite gels formed in the alkali activation reaction of fly ash and metakaolin [54]. It is possible to identify faujasite, zeolite A, and sodalite gels, through the microstructural analysis of the products and the performance of additional characterization techniques mentioned above, such as XRD, FTIR and NMR [54]. These gels are very common in the formation of geopolymers. They are responsible for important properties in this material. Sodalite, for example, contributes to the crystalline structure stability and has hydrophilic properties, allowing cation exchange and the formation of stable and resistant products [96], [97].

It is considered the geopolymers' basic forming unit, and it is present even in other zeolite gels [97]. Faujasite and zeolite A gels have a more porous structure as their principal property due to their microscopy that is derived from the overlap of several sodalite cages [54], [98], as seen in Figure 6. The overlap of several sodalite cages groups makes it possible to obtain more complex and more crystalline zeolites, which have better mechanical properties, further reducing the density of the material obtained [96], [98].

On the morphological aspects formed in calcium-rich precursors, such as blast furnace slag, Figure 13 is analyzed, which shows the SEM of an BFS activated by sodium hydroxide, and silicate. The figure shows the presence of tobermorite gels (C-A-S-H), which do not have an aspect as visible as that of zeolites formed in geopolymers [99]. It is possible to prove the similarities of the formed material with those found in cementitious materials, where the C-S-H phase is verified. In addition, the Figure illustrates the presence of calcite particles mixed with tobermorite particles, making the difference between the two almost undetectable.

## 5 REACTION KINETICS OF ALKALI-ACTIVED

### 5.1 Influence of activators on the reaction kinetics of AA.

After explaining in detail the alkali-activated reactions mechanisms, it is interesting to present the factors that interfere with the reaction kinetics, that is, the factors that make these reactions faster or more efficient. One of the most important factors is related to the types of activators used in the process, as well as their viscosity and pH. Other factors are the influence of the cure type and the precursor granulometry, which modifies the reactivity of this material.

Regarding the activators, these materials are defined as hydroxides, silicates, sulfates, or carbonates of alkali metals, which, when diluted in water in a determined proportion can make the precursor harden [6]. Initially, it is necessary to highlight that the types of activators most used in research are hydroxides and silicates and that the two cause different kinetics in the AA reaction. Besides, it is usually common to use only sodium or potassium hydroxide, or even a combined solution of sodium hydroxide and silicate [13].

When using only hydroxides, there is no increase in the amount of silica in the system, while when using silicates the amount of silica in the system reaches higher levels [58]. It is known that in the AA reaction, the precursor's alumina is more reactive than silica, it is released first and available for the geopolymerization reaction in a shorter time than the silica present in the precursor [52]. Thus, the use of silicate-based activators promotes an acceleration in the reaction of geopolymerization or alkaline activation, due to the fact that the silica present in the silicate reacts more quickly with the alumina released by the precursors. The use of silicate favors the AA reaction process, leading to more resistant products than with the use of hydroxide alone [100].

It is necessary to highlight that the precursors' properties are unique and individual within each research due to issues related to granulometry and oxide composition. That makes it impossible to define an optimal amount of silica. Even so, some researchers report that the use of mixed actives containing hydroxide and sodium silicate allowed to obtain a resistance of 60 MPa at 7 days. The same authors had obtained resistance of 30 MPa at 28 days using only sodium hydroxide in alkaline activation [101]. In this research, a more resistant product was obtained in a much shorter curing time using a mixed solution composed of sodium hydroxide and silicate. The same pattern was found in other studies [30], [50], [102]. That indicates the benefits of applying silicate on the mechanical properties of alkali-activated materials.

Also, other negative factors can be cited by using only hydroxide in the solutions. When used alone, these materials are used in high molar concentrations to increase the precursor reactivity. It is noteworthy that each precursor presents exclusive parameters of reactivity, making it difficult to compare different studies. However, some authors highlight and prove this fact with experimental results [21], [51].

That high concentration can lead to significant occupational health and safety considerations in a large production facility, as these solutions are classified as corrosive under the workplace legislation in force in almost all countries in the world [1]. Also, the need for thermal curing is common when only hydroxides are used, as occurs when fly ash is used as a precursor, at temperatures of about 60°C [55], [103]. This fact is acceptable for pre-molded parts, but it makes the molded parts on site unfeasible.

Hydroxide-activated binders, whether based on fly ash or BFS, also tend to show higher permeability than their silicate-activated equivalents and tendency to efflorescence [104]. That is because the reaction extent reached by the binder before curing is generally low, which leads to an open microstructure and higher material porosity [105]. Efflorescence and other visible effects of alkali mobility are undesirable. However, they can be overcome to some extent by appropriate control of curing conditions or by the addition of secondary aluminum sources. That ensures that a sufficient extent of reaction is achieved before the material is put into service [106], [107].

One of the disadvantages of using mixed solutions is the silicate cost, which is higher than that of hydroxides, making the alkali-activated materials production more expensive, especially when compared to Portland cement-based materials [2]. Also, the use of silicate solutions in alkaline activation impairs the viscosity of the activating solution, making it difficult to work with the paste, mortar or alkali-activated concrete used [108]. Thus, although it presents a potential to increase the mechanical resistance, problems during the structures molding due to the low workability can cause defects or pathologies in the parts and reduce its resistance and durability parameters. Another important factor in the reactions kinetics is the of the solution's molarity, in the case of the hydroxide type activator using, or of the silica modulus ( $M_s$  or  $s$ ) in the case of the use together of silicates and hydroxides. These parameters are defined by Equations 2 and 3, respectively, and have simple definitions. The molarity represents the amount of of alkali metal hydroxide moles contained in a volume of solvent, usually water. The silica modulus represents the molar relationship between  $SiO_2$  and  $M_2O$  of a system formed by silicates and hydroxides, where M represents an alkali metal, such as sodium or potassium [1], [2], [57].

$$M = \frac{[NaOH]}{V} \tag{2}$$

where M= molarity (in moles/l); [NaOH]= number of moles of sodium, calculated by dividing the mass used in the solution by the molar mass worth 40g /mol, in moles; V= volume of the solution, in l.

$$M_s = \frac{[SiO_2]}{[Na_2O]} \tag{3}$$

where  $M_s$ = silica module, dimensionless;  $[SiO_2]$ = number of moles of silicon oxide, calculated by dividing the mass used in the solution by the molar mass that is worth 60g / mol, in moles;  $[Na_2O]$ = number of moles of sodium oxide, calculated by dividing the mass used in the solution by the molar mass worth 62g / mol, in moles.

On molarity, Figure 14 presents a graph that illustrates the rate of alkali-activated reaction as a function of different molarity values obtained by the calorimetry technique (5M, 10M, 12M, 15M, and 18M). It appears that, for the precursor used by the authors, the higher the molarity, the longer the reaction takes to reach its peak. The 10 M molarity has practically the same reactivity as 12 M, while the same thing happens for 15 M and 18 M. This study's authors concluded that the use of molarity of 5M is inefficient in the alkali-activated reaction and that the most recommended values of molarity are between 10 to 18M [109].

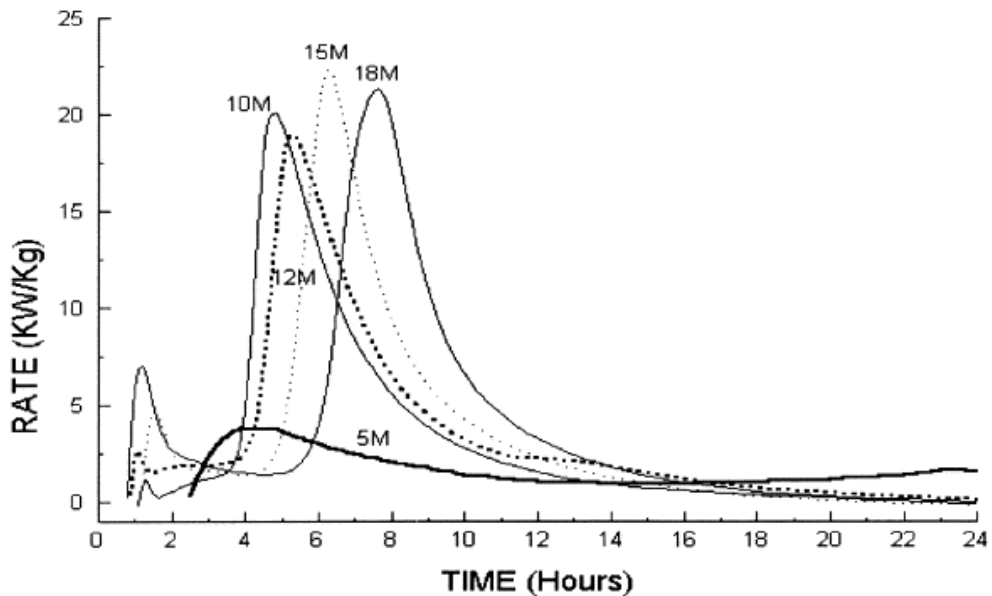


Figure 14. Calorimetry test as a function of molarity. Source: Alonso and Palomo [109].

On the silica modulus, Figure 15 shows the rates of alkali-activated reaction as a function of different values of  $M_s$  obtained by the calorimetry technique (0.6, 0.9, and 1.2) using blast furnace slag as a precursor. It appears that the higher the silica module, the higher the rate of energy released, and the higher the reactions kinetics, proving that the increase in the silica modulus accelerates and increases the reaction rates [110].

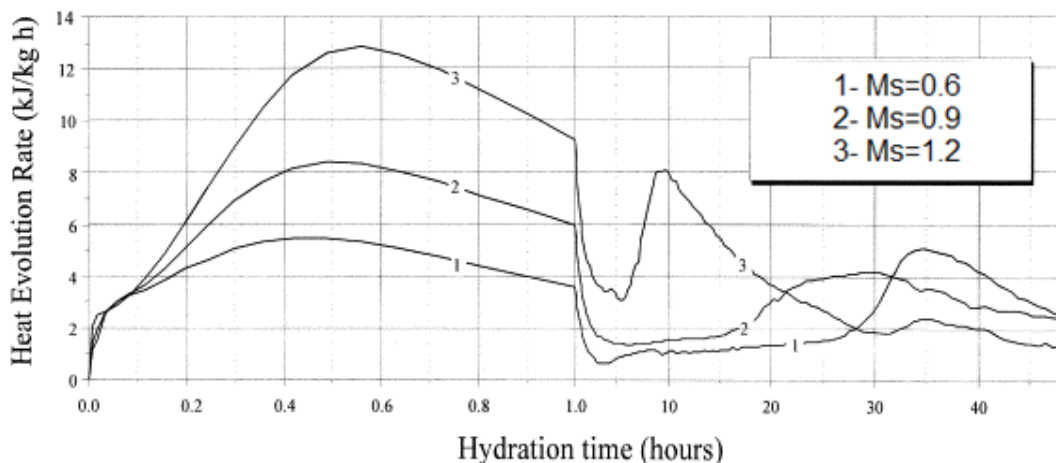


Figure 15. Calorimetry test as a function of  $M_s$ . Source: Krizan and Zivanovic [110].

There are few studies using sodium sulphate or sodium carbonate as alkaline activators, primarily because these compounds have low efficiency when compared to the hydroxides and silicates mentioned above, due to the influence of pH [111], [112]. Most research uses sulfates and carbonates together with sodium or potassium hydroxide, for example [113], in an attempt to correct the pH to values close to 14. Besides, there is a problem with using sulfate or carbonate solutions in reinforced structures because these materials can cause attack or degradation of armor [114] and can cause pathologies.

Regarding the types of alkali metals used in research, those with the highest applications are sodium and potassium. Comparing the efficiency of these two types of metals, it appears that the size of the cation is directly linked to the kinetics of the geopolymerization reactions. As  $\text{Na}^+$  is smaller than  $\text{K}^+$ , a smaller amount of silicate oligomers is formed [115]. Therefore, it is observed that the larger the cation, the higher the reaction kinetics of the AA because the more favored is the formation of larger silicate oligomers in which  $\text{Al}(\text{OH})_4^-$  prefers to bind. Thus, precursors activated with KOH have higher compressive strength compared to geopolymers synthesized from NaOH solutions [116]. Also, since  $\text{K}^+$  is more basic, higher silicate dissolution rates are possible, allowing for denser and more efficient polycondensation reactions, which increase the final mechanical strength of the matrix [115].

Although there is research with other alkali metals, such as lithium and cesium, the availability of these materials is much less than that of sodium and potassium and makes research related to these materials much less frequent [117], [118]. In any case, the cation size scale is as follows:  $\text{Cs} > \text{K} > \text{Na} > \text{Li}$ . That is why it is believed that that is also the efficiency scale of the reactions kinetics of alkaline activation, that is, that cesium is the most reactive and lithium the least, comparing these four alkali metals. The results found in the bibliography confirm this pattern of reaction kinetics [118], [119].

## 5.2 Cure type Influence

Another very important factor in the reactions kinetics of AA is the type of cure performed in the research. Even though each precursor has its peculiarities, due to the difference in chemical composition, reactivity, and particle size, there are reports of researchers studying the alkaline activation of fly ash, metakaolin, and blast furnace slag at room temperatures (25 to 30°C) and in a greenhouse environment (60 to 90°C). It was found that curing performed at a temperature of 60°C considerably increases the compressive strength of the materials [28], [120], [121]. This increase in the cure temperature favors resistance because it increases the dissolution of reactive species, such as silica and alumina, increasing the reactions kinetics [122]. However, oven curing deserves special attention since prolonged curing times distort the reactions, causing partial water evaporation with the formation of microcavities that lead to cracking of the samples, weakening the structure of the formed gels, suggesting that small amounts of structural water they need to be maintained in order to reduce cracks and maintain the integrity of the material [123], [124].

Curing at very high temperatures, above 100°C, also impairs the alkaline activation reaction because when curing occurs at very high temperatures, the samples do not have sufficient moisture [124]. The loss of water in an accelerated and precocious way accelerates carbonation, lowers pH levels, and results in a delay in the precursors activation, resulting in a high aluminum content in the formed gels. Under these conditions, the final product is granular, porous, and characterized by low mechanical resistance [125], [126]. It appears that the most appropriate is to perform thermal curing in milder temperatures and use a not too long curing period. To illustrate this information, Table 3 presents data from several studies with different precursors cured at different temperatures, also showing the compression strength obtained.

**Table 3.** Interference of the curing temperature in the kinetics of the AA reaction.

Precursor Type	Temperature (°C)	Time (days)	Compressive strength (MPa)
Fly ash Source [120].	60	7	5.12
	80	7	7.54
	120	7	7.90
Blast furnace slag Source [120].	60	28	12.53
	80	28	15.21
	120	28	11.63
Blast furnace slag Source [120].	60	7	35.11
	80	7	30.78

Table 3. Continue...

Precursor Type	Temperature (°C)	Time (days)	Compressive strength (MPa)
	120	7	40.20
	60	28	35.44
	80	28	35.80
	120	28	36.19
Fly ash	30	7	21.20
Source [123].	90	7	40.53
	30	28	24.98
	90	28	42.84
Blast furnace slag	25	7	25.16
Source [121].	60	7	40.99
	95	7	29.98
	25	28	43.52
	60	28	45.23
	95	28	31.06
Metakaolin	25	7	34.78
Source [28].	50	7	59.28
	80	7	55.72
	25	28	50.41
	50	28	60.14
	80	28	58.42
Metakaolin	30	7	7.03
Source [122].	60	7	17.87
	90	7	13.13

## 6 FINAL CONSIDERATIONS

This study aims to present an extensive and detailed review on the reaction mechanisms of alkali-activated materials, dividing them into two large groups, depending on the amount of calcium oxide contained in its chemical composition. Materials with reduced amounts of calcium ( $Ca / (Si + Al) < 1$ ) are defined as precursors of low calcium content, also named as geopolymers, and are therefore predominantly aluminum silicates. Upon undergoing geopolymeric reaction it forms compounds similar to zeolites, which are highly crystalline or nanocrystalline, but also have amorphous gels named N-A-S-H, both of which are based on polysialates. The main characteristics of these gels were discussed in the text, being approached the most studied types of precursors that fit in this class of materials, such as fly ash and metakaolin. The steps of the typical alkaline activation reaction of these materials were established, through the phases of dissolution, condensation, reorganization, polycondensation, with or without crystallization, and finally hardening.

Materials with significant amounts of calcium ( $Ca/(Si+Al) > 1$ ) present an alkali-activated reaction similar to Portland cement, however forming gels called C-A-S-H (tobermorite). Also, some secondary products are formed in this reaction, as is the case with N-A-S-H and hydrotalcite. The main example of a precursor that follows this reaction pattern is blast furnace slag. The characteristics of mixed gels and techniques for identifying formed gels were addressed, using X-ray diffraction (XRD), nuclear magnetic resonance spectrometry (NMR), Fourier transform infrared spectroscopy (FTIR), and scanning electronic microstructure (SEM).

Finally, a study of the reaction kinetics of alkali-activated was carried out and it was found that the type of activator solution used, such as the hydroxide-only base or the silicate and hydroxide base, modify the efficiency and speed of these reactions. Other factors, such as the type of alkali metal used (sodium, potassium), the molarity, or the silicon modulus of the solution, also affect the kinetics of the reactions. Curing factors, such as age and temperature conditions, can act as catalysts for alkali-activated reactions, and cures performed during excessive exposure times and at elevated temperatures (above 100°C) in general impair the mechanical properties obtained from alkali-activated materials.

As suggestions for future work to improve the understanding of the reaction mechanisms of alkali-activated materials, the development of standards and procedures with exclusive application to this class of materials stands out since currently technical standards of other construction components are adopted. Other important contributions are the

development of activators with less impact than conventional silicates and hydroxides and the understanding of how these activators modify the steps and kinetics of the alkaline activation reaction.

On precursors, additional studies are needed on the interference of other oxides in the mechanisms of alkali-activated reaction. It is known that some types of industrial waste contain iron oxide, magnesium, nickel, chromium, among others. The technology of alkali-activated materials is a great contribution to the evaluation of the interferences that these compounds cause in the formation of gels and the kinetics of the alkali-activated reaction, although there is already recent research that deals with this subject in an appropriate way. However, there are still relevant issues that need further understanding and discussion regarding the influence of these metal oxides on the alkali-activated reaction. It also stands out as a suggestion the need for the development of tools that can accurately measure the degree of activation of alkali-activated binders, as well as the rheological parameters of the material, enabling the development of even more efficient materials.

Another relevant contribution is the evaluation of the production of alkali-activated materials in large scale and real size, not only through simulations in laboratories with specimens, but using beams in reduced size, for example. This type of study allows the assessment of logistics and the understanding of how the reaction mechanisms of alkali-activated materials in a proportion closer to the real one is.

## ACKNOWLEDGEMENTS

The authors would like to thank FAPERJ and CNPq for their support.

## REFERENCES

- [1] J. L. Provis and S. A. Bernal, "Geopolymers and related alkali-activated materials," *Annu. Rev. Mater. Res.*, vol. 44, no. 1, pp. 299–327, 2014, <http://dx.doi.org/10.1146/annurev-matsci-070813-113515>.
- [2] J. L. Provis, "Geopolymers and other alkali activated materials: why, how, and what," *Mater. Struct. Constr.*, vol. 47, no. 1-2, pp. 11–25, 2014, <http://dx.doi.org/10.1617/s11527-013-0211-5>.
- [3] K. Komnitsas and D. Zaharaki, "Geopolymerisation: a review and prospects for the minerals industry," *Miner. Eng.*, vol. 20, no. 14, pp. 1261–1277, 2007, <http://dx.doi.org/10.1016/j.mineng.2007.07.011>.
- [4] C. G. S. Severo, "Características, particularidades e princípios científicos dos materiais ativados alcalinamente, Rev.," *Eletronica Mater. Process*, vol. 8, pp. 55–67, 2013.
- [5] B. Majidi, "Geopolymer technology, from fundamentals to advanced applications: A review," *Mater. Technol.*, vol. 24, no. 2, pp. 79–87, 2009, <http://dx.doi.org/10.1179/175355509X449355>.
- [6] F. Pacheco-Torgal, J. Castro-Gomes, and S. Jalali, "Alkali-activated binders: a review. Part 1. Historical background, terminology, reaction mechanisms and hydration products," *Constr. Build. Mater.*, vol. 22, no. 7, pp. 1305–1314, 2008, <http://dx.doi.org/10.1016/j.conbuildmat.2007.10.015>.
- [7] J. Davidovits, "Properties of geopolymer cements," in *1st Int. Conf. Alkaline Cem. Concr.*, 1994, pp. 131–149.
- [8] J. L. Provis and J. S. J. Van Deventer, "Geopolymerisation kinetics. 1. In situ energy-dispersive X-ray diffractometry," *Chem. Eng. Sci.*, vol. 62, no. 9, pp. 2309–2317, 2007, <http://dx.doi.org/10.1016/j.ces.2007.01.027>.
- [9] G. Habert, J. B. d'Espinose de Lacaillerie, and N. Roussel, "An environmental evaluation of geopolymer based concrete production: reviewing current research trends," *J. Clean. Prod.*, vol. 19, no. 11, pp. 1229–1238, 2011, <http://dx.doi.org/10.1016/j.jclepro.2011.03.012>.
- [10] A. Palomo, P. Krivenko, I. Garcia-Lodeiro, E. Kavalerova, O. Maltseva, and A. Fernández-Jiménez, "A review on alkaline activation: new analytical perspectives," *Mater. Constr.*, vol. 64, no. 315, e022, 2014, <http://dx.doi.org/10.3989/mc.2014.00314>.
- [11] J. Davidovits, L. Huaman, and R. Davidovits, "Ancient organo-mineral geopolymer in South-American Monuments: Organic matter in andesite stone. SEM and petrographic evidence," *Ceram. Int.*, vol. 45, no. 6, pp. 7385–7389, 2019, <http://dx.doi.org/10.1016/j.ceramint.2019.01.024>.
- [12] J. Davidovits, L. Huaman, and R. Davidovits, "Ancient geopolymer in south-American monument: SEM and petrographic evidence," *Mater. Lett.*, vol. 235, pp. 120–124, 2019, <http://dx.doi.org/10.1016/j.matlet.2018.10.033>.
- [13] F. Pacheco-Torgal, J. Castro-Gomes, and S. Jalali, "Alkali-activated binders: a review. Part 2. About materials and binders manufacture," *Constr. Build. Mater.*, vol. 22, no. 7, pp. 1315–1322, 2008, <http://dx.doi.org/10.1016/j.conbuildmat.2007.03.019>.
- [14] M. Lahoti, K. H. Tan, and E. H. Yang, "A critical review of geopolymer properties for structural fire-resistance applications," *Constr. Build. Mater.*, vol. 221, pp. 514–526, 2019, <http://dx.doi.org/10.1016/j.conbuildmat.2019.06.076>.
- [15] Y. Wu et al., "Geopolymer, green alkali activated cementitious material: Synthesis, applications and challenges," *Constr. Build. Mater.*, vol. 224, pp. 930–949, 2019, <http://dx.doi.org/10.1016/j.conbuildmat.2019.07.112>.

- [16] A. R. G. Azevedo, M. T. Marvila, H. A. Rocha, L. R. Cruz, and C. M. F. Vieira, "Use of glass polishing waste in the development of ecological ceramic roof tiles by the geopolymerization process," *Int. J. Appl. Ceram. Technol.*, vol. 17, no. 6, pp. 2649–2658, 2020., <http://dx.doi.org/10.1111/ijac.13585>.
- [17] N. R. Rakhimova and R. Z. Rakhimov, "Reaction products, structure and properties of alkali-activated metakaolin cements incorporated with supplementary materials – a review," *J. Mater. Res. Technol.*, vol. 8, no. 1, pp. 1522–1531, 2019, <http://dx.doi.org/10.1016/j.jmrt.2018.07.006>.
- [18] R. K. Preethi and B. V. Venkatarama Reddy, "Experimental investigations on geopolymer stabilised compressed earth products," *Constr. Build. Mater.*, vol. 257, 119563, 2020, <http://dx.doi.org/10.1016/j.conbuildmat.2020.119563>.
- [19] Z. Zhang, H. Wang, J. L. Provis, F. Bullen, A. Reid, and Y. Zhu, "Quantitative kinetic and structural analysis of geopolymers. Part 1. The activation of metakaolin with sodium hydroxide," *Thermochim. Acta*, vol. 539, pp. 23–33, 2012, <http://dx.doi.org/10.1016/j.tca.2012.03.021>.
- [20] C. E. White, J. L. Provis, T. Proffen, D. P. Riley, and J. S. J. Van Deventer, "Density functional modeling of the local structure of kaolinite subjected to thermal dehydroxylation," *J. Phys. Chem. A*, vol. 114, no. 14, pp. 4988–4996, 2010, <http://dx.doi.org/10.1021/jp911108d>.
- [21] T. Kovářik et al., "Thermomechanical properties of particle-reinforced geopolymer composite with various aggregate gradation of fine ceramic filler," *Constr. Build. Mater.*, vol. 143, pp. 599–606, 2017, <http://dx.doi.org/10.1016/j.conbuildmat.2017.03.134>.
- [22] E. Kamseu, V. Catania, C. Djangang, V. M. Sglavo, and C. Leonelli, "Correlation between microstructural evolution and mechanical properties of  $\alpha$ -quartz and alumina reinforced K-geopolymers during high temperature treatments," *Adv. Appl. Ceramics*, vol. 111, no. 3, pp. 120–128, 2012, <http://dx.doi.org/10.1179/1743676111Y.0000000013>.
- [23] A. Elimbi, H. K. Tchakoute, and D. Njopwouo, "Effects of calcination temperature of kaolinite clays on the properties of geopolymer cements," *Constr. Build. Mater.*, vol. 25, no. 6, pp. 2805–2812, 2011, <http://dx.doi.org/10.1016/j.conbuildmat.2010.12.055>.
- [24] A. Fernández-Jiménez, M. Monzó, M. Vicent, A. Barba, and A. Palomo, "Alkaline activation of metakaolin–fly ash mixtures: obtain of zeoceramics and zeocements," *Microporous Mesoporous Mater.*, vol. 108, no. 1-3, pp. 41–49, 2008, <http://dx.doi.org/10.1016/j.micromeso.2007.03.024>.
- [25] R. San Nicolas, S. A. Bernal, R. Mejía De Gutiérrez, J. S. J. Van Deventer, and J. L. Provis, "Distinctive microstructural features of aged sodium silicate-activated slag concretes," *Cement Concr. Res.*, vol. 65, pp. 41–51, 2014, <http://dx.doi.org/10.1016/j.cemconres.2014.07.008>.
- [26] J. S. J. Sindhunata, J. S. J. Van Deventer, G. C. Lukey, and H. Xu, "effect of curing temperature and silicate concentration on fly-ash-based geopolymerization," *Ind. Eng. Chem. Res.*, vol. 45, no. 10, pp. 3559–3568, 2006, <http://dx.doi.org/10.1021/ie051251p>.
- [27] C. Kuenzel, L. J. Vandeperre, S. Donatello, A. R. Boccaccini, and C. Cheeseman, "Ambient temperature drying shrinkage and cracking in metakaolin-based geopolymers," *J. Am. Ceram. Soc.*, vol. 95, no. 10, pp. 3270–3277, 2012, <http://dx.doi.org/10.1111/j.1551-2916.2012.05380.x>.
- [28] J. Cai, X. Li, J. Tan, and B. Vandevyvere, "Thermal and compressive behaviors of fly ash and metakaolin-based geopolymer," *J. Build. Eng.*, vol. 30, 101307, 2020, <http://dx.doi.org/10.1016/j.jobbe.2020.101307>.
- [29] Z. Sun, A. Vollpracht, and H. A. Van der Sloot, "pH dependent leaching characterization of major and trace elements from fly ash and metakaolin geopolymers," *Cement Concr. Res.*, vol. 125, 105889, 2019, <http://dx.doi.org/10.1016/j.cemconres.2019.105889>.
- [30] J. Cai, J. Pan, X. Li, J. Tan, and J. Li, "Electrical resistivity of fly ash and metakaolin based geopolymers," *Constr. Build. Mater.*, vol. 234, 117868, 2020, <http://dx.doi.org/10.1016/j.conbuildmat.2019.117868>.
- [31] M. Ahmaruzzaman, "A review on the utilization of fly ash," *Pror. Energy Combust. Sci.*, vol. 36, no. 3, pp. 327–363, 2010, <http://dx.doi.org/10.1016/j.pecs.2009.11.003>.
- [32] X. F. Wu and G. Q. Chen, "Coal use embodied in globalized world economy: from source to sink through supply chain," *Renew. Sustain. Energy Rev.*, vol. 81, pp. 978–993, 2018, <http://dx.doi.org/10.1016/j.rser.2017.08.018>.
- [33] İ. İ. Atabey, O. Karahan, C. Bilim, and C. D. Atiş, "The influence of activator type and quantity on the transport properties of class F fly ash geopolymer," *Constr. Build. Mater.*, vol. 264, 120268, 2020, <http://dx.doi.org/10.1016/j.conbuildmat.2020.120268>.
- [34] A. M. Rashad, "A brief on high-volume Class F fly ash as cement replacement: a guide for Civil Engineer," *Int. J. Sustain. Built Environ.*, vol. 4, no. 2, pp. 278–306, 2015, <http://dx.doi.org/10.1016/j.ijse.2015.10.002>.
- [35] R. Gupta, P. Bhardwaj, D. Mishra, M. Prasad, and S. S. Amritphale, "Formulation of mechanochemically evolved fly ash based hybrid inorganic-organic geopolymers with multilevel characterization," *J. Inorg. Organomet. Polym. Mater.*, vol. 27, no. 2, pp. 385–398, 2017, <http://dx.doi.org/10.1007/s10904-016-0461-0>.
- [36] American Society for Testing and Materials, *Standard Specification for Coal Fly Ash and Raw or Calcined Natural Pozzolan for Use in Concrete*, ASTM C618-17a, 2017.
- [37] F. Winnefeld, A. Leemann, M. Lucuk, P. Svoboda, and M. Neuroth, "Assessment of phase formation in alkali activated low and high calcium fly ashes in building materials," *Constr. Build. Mater.*, vol. 24, no. 6, pp. 1086–1093, 2010, <http://dx.doi.org/10.1016/j.conbuildmat.2009.11.007>.

- [38] M. Komljenović, Z. Baščarević, and V. Bradić, "Mechanical and microstructural properties of alkali-activated fly ash geopolymers," *J. Hazard. Mater.*, vol. 181, no. 1-3, pp. 35–42, 2010, <http://dx.doi.org/10.1016/j.jhazmat.2010.04.064>.
- [39] N. K. Lee, G. H. An, K. T. Koh, and G. S. Ryu, "Improved reactivity of fly ash-slag geopolymer by the addition of silica fume," *Adv. Mater. Sci. Eng.*, vol. 2016, pp. 1–11, 2016, <http://dx.doi.org/10.1155/2016/2192053>.
- [40] T. Bakharev, "Geopolymeric materials prepared using Class F fly ash and elevated temperature curing," *Cement Concr. Res.*, vol. 35, no. 6, pp. 1224–1232, 2005, <http://dx.doi.org/10.1016/j.cemconres.2004.06.031>.
- [41] N. Saboo, S. Shivhare, K. K. Kori, and A. K. Chandrappa, "Effect of fly ash and metakaolin on pervious concrete properties," *Constr. Build. Mater.*, vol. 223, pp. 322–328, 2019, <http://dx.doi.org/10.1016/j.conbuildmat.2019.06.185>.
- [42] S. D. Khadka, P. W. Jayawickrama, S. Senadheera, and B. Segvic, "Stabilization of highly expansive soils containing sulfate using metakaolin and fly ash based geopolymer modified with lime and gypsum," *Transp. Geotechnics*, vol. 23, 100327, 2020, <http://dx.doi.org/10.1016/j.trgeo.2020.100327>.
- [43] A. Buchwald, M. Hohmann, K. Posern, and E. Brendler, "The suitability of thermally activated illite/smectite clay as raw material for geopolymer binders," *Appl. Clay Sci.*, vol. 46, no. 3, pp. 300–304, 2009, <http://dx.doi.org/10.1016/j.clay.2009.08.026>.
- [44] D. M. González-García, L. Téllez-Jurado, F. J. Jiménez-Álvarez, and H. Balmori-Ramírez, "Structural study of geopolymers obtained from alkali-activated natural pozzolan feldspars," *Ceram. Int.*, vol. 43, no. 2, pp. 2606–2613, 2017, <http://dx.doi.org/10.1016/j.ceramint.2016.11.070>.
- [45] L. Tian, W. Feng, H. Ma, S. Zhang, and H. Shi, "Investigation on the microstructure and mechanism of geopolymer with different proportion of quartz and K-feldspar," *Constr. Build. Mater.*, vol. 147, pp. 543–549, 2017, <http://dx.doi.org/10.1016/j.conbuildmat.2017.04.102>.
- [46] J. N. Yankwa Djobo, A. Elimbi, H. K. Tchakouté, and S. Kumar, "Mechanical activation of volcanic ash for geopolymer synthesis: effect on reaction kinetics, gel characteristics, physical and mechanical properties," *RSC Advances*, vol. 6, no. 45, pp. 39106–39117, 2016, <http://dx.doi.org/10.1039/C6RA03667H>.
- [47] H. Xu and J. S. J. Van Deventer, "Factors affecting the geopolymerization of alkali-feldspars, Mining," *Metall. Explor.*, vol. 19, pp. 209–214, 2002, <http://dx.doi.org/10.1007/BF03403271>.
- [48] Y. J. N. Djobo, A. Elimbi, J. Dika Manga, and I. B. Djon Li Ndjock, "Partial replacement of volcanic ash by bauxite and calcined oyster shell in the synthesis of volcanic ash-based geopolymers," *Constr. Build. Mater.*, vol. 113, pp. 673–681, 2016, <http://dx.doi.org/10.1016/j.conbuildmat.2016.03.104>.
- [49] J. N. Y. Djobo, A. Elimbi, H. K. Tchakouté, and S. Kumar, "Volcanic ash-based geopolymer cements/concretes: the current state of the art and perspectives," *Environ. Sci. Pollut. Res. Int.*, vol. 24, no. 5, pp. 4433–4446, 2017, <http://dx.doi.org/10.1007/s11356-016-8230-8>.
- [50] A. R. G. Azevedo, C. M. F. Vieira, W. M. Ferreira, K. C. P. Faria, L. G. Pedroti, and B. C. Mendes, "Potential use of ceramic waste as precursor in the geopolymerization reaction for the production of ceramic roof tiles," *J. Build. Eng.*, vol. 29, 101156, 2020, <http://dx.doi.org/10.1016/j.jobbe.2019.101156>.
- [51] L. Mo, L. Lv, M. Deng, and J. Qian, "Influence of fly ash and metakaolin on the microstructure and compressive strength of magnesium potassium phosphate cement paste," *Cement Concr. Res.*, vol. 111, pp. 116–129, 2018, <http://dx.doi.org/10.1016/j.cemconres.2018.06.003>.
- [52] P. Duxson, S. W. Mallicoat, G. C. Lukey, W. M. Kriven, and J. S. J. Van Deventer, "The effect of alkali and Si/Al ratio on the development of mechanical properties of metakaolin-based geopolymers," *Colloids Surf. A Physicochem. Eng. Asp.*, vol. 292, no. 1, pp. 8–20, 2007, <http://dx.doi.org/10.1016/j.colsurfa.2006.05.044>.
- [53] P. Duxson, A. Fernández-Jiménez, J. L. Provis, G. C. Lukey, A. Palomo, and J. S. J. Van Deventer, "Geopolymer technology: the current state of the art," *J. Mater. Sci.*, vol. 42, no. 9, pp. 2917–2933, 2007, <http://dx.doi.org/10.1007/s10853-006-0637-z>.
- [54] P. Rožek, M. Król, and W. Mozgawa, "Geopolymer-zeolite composites: a review," *J. Clean. Prod.*, vol. 230, pp. 557–579, 2019, <http://dx.doi.org/10.1016/j.jclepro.2019.05.152>.
- [55] E. Najafi Kani, A. Allahverdi, and J. L. Provis, "Calorimetric study of geopolymer binders based on natural pozzolan," *J. Therm. Anal. Calorim.*, vol. 127, no. 3, pp. 2181–2190, 2017, <http://dx.doi.org/10.1007/s10973-016-5850-7>.
- [56] D. Van Gucht, O. Van den Bergh, T. Beckers, and D. Vansteenwegen, "Smoking behavior in context: where and when do people smoke," *J. Behav. Ther. Exp. Psychiatry*, vol. 41, no. 2, pp. 172–177, 2010, <http://dx.doi.org/10.1016/j.jbtep.2009.12.004>.
- [57] J. L. Provis and J. S. J. Van Deventer, "Geopolymerisation kinetics. 2. Reaction kinetic modelling," *Chem. Eng. Sci.*, vol. 62, no. 9, pp. 2318–2329, 2007, <http://dx.doi.org/10.1016/j.ces.2007.01.028>.
- [58] M. Nakai et al., "Synthesis of high silica \*BEA type ferrisilicate (Fe-Beta) by dry gel conversion method using dealuminated zeolites and its catalytic performance on acetone to olefins (ATO) reaction," *Microporous Mesoporous Mater.*, vol. 273, pp. 189–195, 2019, <http://dx.doi.org/10.1016/j.micromeso.2018.06.008>.
- [59] E. Kamsu, C. R. Kaze, J. N. N. Fekoua, U. C. Melo, S. Rossignol, and C. Leonelli, "Ferrisilicates formation during the geopolymerization of natural Fe-rich aluminosilicate precursors," *Mater. Chem. Phys.*, vol. 240, 122062, 2020, <http://dx.doi.org/10.1016/j.matchemphys.2019.122062>.



- [60] R. C. Kaze et al., "Microstructure and engineering properties of Fe<sub>2</sub>O<sub>3</sub>(FeO)-Al<sub>2</sub>O<sub>3</sub>-SiO<sub>2</sub> based geopolymer composites," *J. Clean Prod.*, vol. 199, pp. 849–859, 2018, <http://dx.doi.org/10.1016/j.jclepro.2018.07.171>.
- [61] M. Khatamian, A. A. Khandar, M. Haghghi, M. Ghadiri, and M. Darbandi, "Synthesis, characterization and acidic properties of nanopowder ZSM-5 type ferrisilicates in the Na<sup>+</sup>/K<sup>+</sup> alkali system," *Powder Technol.*, vol. 203, no. 3, pp. 503–509, 2010, <http://dx.doi.org/10.1016/j.powtec.2010.06.012>.
- [62] M. Król, P. Rożek, D. Chlebda, and W. Mozgawa, "Influence of alkali metal cations/type of activator on the structure of alkali-activated fly ash – ATR-FTIR studies, Spectrochim. Acta Part A Mol," *Biomol. Spectrosc.*, vol. 198, pp. 33–37, 2018, <http://dx.doi.org/10.1016/j.saa.2018.02.067>.
- [63] A. Nikolov, H. Nugteren, and I. Rostovsky, "Optimization of geopolymers based on natural zeolite clinoptilolite by calcination and use of aluminate activators," *Constr. Build. Mater.*, vol. 243, 118257, 2020, <http://dx.doi.org/10.1016/j.conbuildmat.2020.118257>.
- [64] P. Y. He, Y. J. Zhang, H. Chen, Z. C. Han, and L. C. Liu, "Low-cost and facile synthesis of geopolymer-zeolite composite membrane for chromium(VI) separation from aqueous solution," *J. Hazard. Mater.*, vol. 392, 122359, 2020, <http://dx.doi.org/10.1016/j.jhazmat.2020.122359>.
- [65] C. A. Rees, J. L. Provis, G. C. Lukey, and J. S. J. Van Deventer, "Attenuated total reflectance fourier transform infrared analysis of fly ash geopolymer gel aging," *Langmuir*, vol. 23, no. 15, pp. 8170–8179, 2007, <http://dx.doi.org/10.1021/la700713g>.
- [66] J. L. Provis, P. A. Walls, and J. S. J. Van Deventer, "Geopolymerisation kinetics. 3. Effects of Cs and Sr salts," *Chem. Eng. Sci.*, vol. 63, no. 18, pp. 4480–4489, 2008, <http://dx.doi.org/10.1016/j.ces.2008.06.008>.
- [67] J. F. Rivera, N. Cristelo, A. Fernández-Jiménez, and R. Mejía de Gutiérrez, "Synthesis of alkaline cements based on fly ash and metallurgic slag: Optimisation of the SiO<sub>2</sub>/Al<sub>2</sub>O<sub>3</sub> and Na<sub>2</sub>O/SiO<sub>2</sub> molar ratios using the response surface methodology," *Constr. Build. Mater.*, vol. 213, pp. 424–433, 2019, <http://dx.doi.org/10.1016/j.conbuildmat.2019.04.097>.
- [68] I. Perná and T. Hanzlíček, "The setting time of a clay-slag geopolymer matrix: the influence of blast-furnace-slag addition and the mixing method," *J. Clean. Prod.*, vol. 112, pp. 1150–1155, 2016, <http://dx.doi.org/10.1016/j.jclepro.2015.05.069>.
- [69] H. M. Khater, "Development and characterization of sustainable lightweight geopolymer composites," *Ceramica*, vol. 65, no. 373, pp. 153–161, 2019, <http://dx.doi.org/10.1590/0366-69132019653732551>.
- [70] T. Yang, Q. Wu, H. Zhu, and Z. Zhang, "Geopolymer with improved thermal stability by incorporating high-magnesium nickel slag," *Constr. Build. Mater.*, vol. 155, pp. 475–484, 2017, <http://dx.doi.org/10.1016/j.conbuildmat.2017.08.081>.
- [71] S. Jena and R. Panigrahi, "Performance assessment of geopolymer concrete with partial replacement of ferrochrome slag as coarse aggregate," *Constr. Build. Mater.*, vol. 220, pp. 525–537, 2019, <http://dx.doi.org/10.1016/j.conbuildmat.2019.06.045>.
- [72] J. Qiu, Y. Zhao, J. Xing, and X. Sun, "Fly ash/blast furnace slag-based geopolymer as a potential binder for mine backfilling: effect of binder type and activator concentration," *Adv. Mater. Sci. Eng.*, vol. 2019, pp. 1–12, 2019, <http://dx.doi.org/10.1155/2019/2028109>.
- [73] T. Bai, Z.-G. Song, Y.-G. Wu, X.-D. Hu, and H. Bai, "Influence of steel slag on the mechanical properties and curing time of metakaolin geopolymer," *Ceram. Int.*, vol. 44, no. 13, pp. 15706–15713, 2018, <http://dx.doi.org/10.1016/j.ceramint.2018.05.243>.
- [74] I. Ismail, S. A. Bernal, J. L. Provis, R. San Nicolas, S. Hamdan, and J. S. J. Van Deventer, "Modification of phase evolution in alkali-activated blast furnace slag by the incorporation of fly ash," *Cement Concr. Compos.*, vol. 45, pp. 125–135, 2014, <http://dx.doi.org/10.1016/j.cemconcomp.2013.09.006>.
- [75] I. Garcia-Lodeiro, A. Palomo, A. Fernández-Jiménez, and D. E. MacPhee, "Compatibility studies between N-A-S-H and C-A-S-H gels. Study in the ternary diagram Na<sub>2</sub>O-CaO-Al<sub>2</sub>O<sub>3</sub>-SiO<sub>2</sub>-H<sub>2</sub>O," *Cement Concr. Res.*, vol. 41, no. 9, pp. 923–931, 2011, <http://dx.doi.org/10.1016/j.cemconres.2011.05.006>.
- [76] M. Javed et al., "A facile solvent-free synthesis strategy for Co-embedded zeolite-based Fischer-Tropsch catalysts for direct gasoline production," *Chin. J. Catal.*, vol. 41, no. 4, pp. 604–612, 2020, [http://dx.doi.org/10.1016/S1872-2067\(19\)63436-4](http://dx.doi.org/10.1016/S1872-2067(19)63436-4).
- [77] S. Shahsavari and S. M. Sadrameli, "Production of renewable aromatics and heterocycles by catalytic pyrolysis of biomass resources using rhenium and tin promoted ZSM-5 zeolite catalysts," *Process Saf. Environ. Prot.*, vol. 141, pp. 305–320, 2020, <http://dx.doi.org/10.1016/j.psep.2020.04.023>.
- [78] J. Mishra, S. Kumar Das, R. S. Krishna, B. Nanda, S. Kumar Patro, and S. Mohammed Mustakim, "Synthesis and characterization of a new class of geopolymer binder utilizing ferrochrome ash (FCA) for sustainable industrial waste management," *Mater. Today Proc.*, vol. 33, pp. 5001–5006, 2020., <http://dx.doi.org/10.1016/j.matpr.2020.02.832>.
- [79] B. B. Jindal and R. Sharma, "The effect of nanomaterials on properties of geopolymers derived from industrial by-products: A state-of-the-art review," *Constr. Build. Mater.*, vol. 252, 119028, 2020, <http://dx.doi.org/10.1016/j.conbuildmat.2020.119028>.
- [80] C.-L. Hwang and T.-P. Huynh, "Effect of alkali-activator and rice husk ash content on strength development of fly ash and residual rice husk ash-based geopolymers," *Constr. Build. Mater.*, vol. 101, pp. 1–9, 2015, <http://dx.doi.org/10.1016/j.conbuildmat.2015.10.025>.
- [81] N.-E.-H. Fardjaoui, F. Z. El Berrichi, and F. Ayari, "Kaolin-issued zeolite A as efficient adsorbent for Bezanyl Yellow and Nylomine Green anionic dyes," *Microporous Mesoporous Mater.*, vol. 243, pp. 91–101, 2017, <http://dx.doi.org/10.1016/j.micromeso.2017.01.008>.

- [82] D. Sha, B. Pan, and Y. Sun, "Investigation on mechanical properties and microstructure of coal-based synthetic natural gas slag (CSNGS) geopolymer," *Constr. Build. Mater.*, vol. 259, 119793, 2020, <http://dx.doi.org/10.1016/j.conbuildmat.2020.119793>.
- [83] H. M. Khater, "Effect of silica fume on the characterization of the geopolymer materials," *Int. J. Adv. Struct. Eng.*, vol. 5, no. 1, pp. 12, 2013, <http://dx.doi.org/10.1186/2008-6695-5-12>.
- [84] M. A. Pereira, D. C. L. Vasconcelos, and W. L. Vasconcelos, "Synthetic aluminosilicates for geopolymer production," *Mater. Res.*, vol. 22, no. 2, e20180508, 2019, <http://dx.doi.org/10.1590/1980-5373-mr-2018-0508>.
- [85] T. S. Osholana, M. K. Dlodlu, B. Oboirien, and R. Sadiku, "Enhanced reactivity of geopolymers produced from fluidized bed combustion bottom ash," *S. Afr. J. Chem. Eng.*, vol. 34, pp. 72–77, 2020., <http://dx.doi.org/10.1016/j.sajce.2020.06.006>.
- [86] A. Hawa, D. Tonnayopas, and W. Prachasaree, "Performance evaluation and microstructure characterization of metakaolin-based geopolymer containing oil palm ash," *Scientific World Journal*, vol. 2013, pp. 1–9, 2013, <http://dx.doi.org/10.1155/2013/857586>.
- [87] S. Hu et al., "Synthesis of rare earth tailing-based geopolymer for efficiently immobilizing heavy metals," *Constr. Build. Mater.*, vol. 254, 119273, 2020, <http://dx.doi.org/10.1016/j.conbuildmat.2020.119273>.
- [88] H. Celerier et al., "Relation between working properties and structural properties from  $^{27}\text{Al}$ ,  $^{29}\text{Si}$  and  $^{31}\text{P}$  NMR and XRD of acid-based geopolymers from 25 to 1000°C," *Mater. Chem. Phys.*, vol. 228, pp. 293–302, 2019, <http://dx.doi.org/10.1016/j.matchemphys.2019.02.049>.
- [89] C. Dupuy, A. Gharzouni, I. Sobrados, N. Texier-Mandoki, X. Bourbon, and S. Rossignol, " $^{29}\text{Si}$ ,  $^{27}\text{Al}$ ,  $^{31}\text{P}$  and  $^{11}\text{B}$  magic angle spinning nuclear magnetic resonance study of the structural evolutions induced by the use of phosphor- and boron-based additives in geopolymer mixtures," *J. Non-Cryst. Solids*, vol. 521, 119541, 2019, <http://dx.doi.org/10.1016/j.jnoncrysol.2019.119541>.
- [90] Q. Wan, Y. Zhang, and R. Zhang, "Using mechanical activation of quartz to enhance the compressive strength of metakaolin based geopolymers," *Cement Concr. Compos.*, vol. 111, 103635, 2020, <http://dx.doi.org/10.1016/j.cemconcomp.2020.103635>.
- [91] Q. Tian, B. Guo, and K. Sasaki, "Immobilization mechanism of Se oxyanions in geopolymer: Effects of alkaline activators and calcined hydrotalcite additive," *J. Hazard. Mater.*, vol. 387, 121994, 2020, <http://dx.doi.org/10.1016/j.jhazmat.2019.121994>.
- [92] X. Tian, W. Xu, S. Song, F. Rao, and L. Xia, "Effects of curing temperature on the compressive strength and microstructure of copper tailing-based geopolymers," *Chemosphere*, vol. 253, 126754, 2020, <http://dx.doi.org/10.1016/j.chemosphere.2020.126754>.
- [93] Y.-L. Tsai, J. V. Hanna, Y.-L. Lee, M. E. Smith, and J. C. C. Chan, "Solid-state NMR study of geopolymer prepared by sol-gel chemistry," *J. Solid State Chem.*, vol. 183, no. 12, pp. 3017–3022, 2010, <http://dx.doi.org/10.1016/j.jssc.2010.10.008>.
- [94] S. Greiser, P. Sturm, G. J. G. Gluth, M. Hunger, and C. Jäger, "Differentiation of the solid-state NMR signals of gel, zeolite phases and water species in geopolymer-zeolite composites," *Ceram. Int.*, vol. 43, no. 2, pp. 2202–2208, 2017, <http://dx.doi.org/10.1016/j.ceramint.2016.11.004>.
- [95] M. Falah and K. J. D. MacKenzie, "Synthesis and properties of novel photoactive composites of P25 titanium dioxide and copper (I) oxide with inorganic polymers," *Ceram. Int.*, vol. 41, no. 10, pp. 13702–13708, 2015, <http://dx.doi.org/10.1016/j.ceramint.2015.07.198>.
- [96] H. Baykara, M. H. Cornejo, R. Murillo, A. Gavilanes, C. Paredes, and J. Elsen, "Preparation, characterization and reaction kinetics of green cement: ecuadorian natural mordenite-based geopolymers," *Mater. Struct.*, vol. 50, no. 3, 188, 2017, <http://dx.doi.org/10.1617/s11527-017-1057-z>.
- [97] T. Bakharev, "Thermal behaviour of geopolymers prepared using class F fly ash and elevated temperature curing," *Cement Concr. Res.*, vol. 36, no. 6, pp. 1134–1147, 2006, <http://dx.doi.org/10.1016/j.cemconres.2006.03.022>.
- [98] A. Buchwald, H.-D. Zellmann, and C. Kaps, "Condensation of aluminosilicate gels-model system for geopolymer binders," *J. Non-Cryst. Solids*, vol. 357, no. 5, pp. 1376–1382, 2011, <http://dx.doi.org/10.1016/j.jnoncrysol.2010.12.036>.
- [99] I. H. Aziz, M. M. A. B. Abdullah, M. A. A. Mohd Salleh, E. A. Azimi, J. Chairapa, and A. V. Sandu, "Strength development of solely ground granulated blast furnace slag geopolymers," *Constr. Build. Mater.*, vol. 250, 118720, 2020, <http://dx.doi.org/10.1016/j.conbuildmat.2020.118720>.
- [100] K. Sagoe-Crentsil and L. Weng, "Dissolution processes, hydrolysis and condensation reactions during geopolymer synthesis: part II. High Si/Al ratio systems," *J. Mater. Sci.*, vol. 42, no. 9, pp. 3007–3014, 2007, <http://dx.doi.org/10.1007/s10853-006-0818-9>.
- [101] E. Altan and S. T. Erdoğan, "Alkali activation of a slag at ambient and elevated temperatures," *Cement Concr. Compos.*, vol. 34, no. 2, pp. 131–139, 2012, <http://dx.doi.org/10.1016/j.cemconcomp.2011.08.003>.
- [102] M. A. Villaquirán-Cacedo and R. M. de Gutiérrez, "Synthesis of ceramic materials from ecofriendly geopolymer precursors," *Mater. Lett.*, vol. 230, pp. 300–304, 2018, <http://dx.doi.org/10.1016/j.matlet.2018.07.128>.
- [103] A. Fernández-Jiménez, A. Palomo, and M. Criado, "Microstructure development of alkali-activated fly ash cement: a descriptive model," *Cement Concr. Res.*, vol. 35, no. 6, pp. 1204–1209, 2005, <http://dx.doi.org/10.1016/j.cemconres.2004.08.021>.
- [104] Y. Wang et al., "Effects of Si/Al ratio on the efflorescence and properties of fly ash based geopolymer," *J. Clean. Prod.*, vol. 244, 118852, 2020, <http://dx.doi.org/10.1016/j.jclepro.2019.118852>.
- [105] Z. Zhang, J. L. Provis, X. Ma, A. Reid, and H. Wang, "Efflorescence and subflorescence induced microstructural and mechanical evolution in fly ash-based geopolymers," *Cement Concr. Compos.*, vol. 92, pp. 165–177, 2018, <http://dx.doi.org/10.1016/j.cemconcomp.2018.06.010>.

- [106] X. Xue, Y.-L. Liu, J.-G. Dai, C.-S. Poon, W.-D. Zhang, and P. Zhang, "Inhibiting efflorescence formation on fly ash-based geopolymer via silane surface modification," *Cement Concr. Compos.*, vol. 94, pp. 43–52, 2018, <http://dx.doi.org/10.1016/j.cemconcomp.2018.08.013>.
- [107] M. A. Longhi, E. D. Rodríguez, B. Walkley, Z. Zhang, and A. P. Kirchheim, "Metakaolin-based geopolymers: Relation between formulation, physicochemical properties and efflorescence formation," *Compos., Part B Eng.*, vol. 182, 107671, 2020, <http://dx.doi.org/10.1016/j.compositesb.2019.107671>.
- [108] A. J. Allen, J. J. Thomas, and H. M. Jennings, "Composition and density of nanoscale calcium-silicate-hydrate in cement," *Nat. Mater.*, vol. 6, no. 4, pp. 311–316, 2007, <http://dx.doi.org/10.1038/nmat1871>.
- [109] S. Alonso and A. Palomo, "Calorimetric study of alkaline activation of calcium hydroxide–metakaolin solid mixtures," *Cement Concr. Res.*, vol. 31, no. 1, pp. 25–30, 2001, [http://dx.doi.org/10.1016/S0008-8846\(00\)00435-X](http://dx.doi.org/10.1016/S0008-8846(00)00435-X).
- [110] D. Krizan and B. Zivanovic, "Effects of dosage and modulus of water glass on early hydration of alkali–slag cements," *Cement Concr. Res.*, vol. 32, no. 8, pp. 1181–1188, 2002, [http://dx.doi.org/10.1016/S0008-8846\(01\)00717-7](http://dx.doi.org/10.1016/S0008-8846(01)00717-7).
- [111] H. Alghamdi and N. Neithalath, "Novel synthesis of lightweight geopolymer matrices from fly ash through carbonate-based activation," *Mater. Today Commun.*, vol. 17, pp. 266–277, 2018, <http://dx.doi.org/10.1016/j.mtcomm.2018.09.014>.
- [112] J. Ahn, W.-S. Kim, and W. Um, "Development of metakaolin-based geopolymer for solidification of sulfate-rich HyBRID sludge waste," *J. Nucl. Mater.*, vol. 518, pp. 247–255, 2019, <http://dx.doi.org/10.1016/j.jnucmat.2019.03.008>.
- [113] Q. Lv, L. Jiang, B. Ma, B. Zhao, and Z. Huo, "A study on the effect of the salt content on the solidification of sulfate saline soil solidified with an alkali-activated geopolymer," *Constr. Build. Mater.*, vol. 176, pp. 68–74, 2018, <http://dx.doi.org/10.1016/j.conbuildmat.2018.05.013>.
- [114] A. Aboulayt, M. Riahi, M. Ouazzani Touhami, H. Hannache, M. Gomina, and R. Moussa, "Properties of metakaolin based geopolymer incorporating calcium carbonate," *Adv. Powder Technol.*, vol. 28, no. 9, pp. 2393–2401, 2017, <http://dx.doi.org/10.1016/j.apt.2017.06.022>.
- [115] A. Hosan, S. Haque, and F. Shaikh, "Compressive behaviour of sodium and potassium activators synthesized fly ash geopolymer at elevated temperatures: a comparative study," *J. Build. Eng.*, vol. 8, pp. 123–130, 2016, <http://dx.doi.org/10.1016/j.jobe.2016.10.005>.
- [116] T. da S. Rocha, D. P. Dias, F. C. C. França, R. R. S. Guerra, and L. R. C. O. Marques, "Metakaolin-based geopolymer mortars with different alkaline activators (Na + and K +)," *Constr. Build. Mater.*, vol. 178, pp. 453–461, 2018, <http://dx.doi.org/10.1016/j.conbuildmat.2018.05.172>.
- [117] J. Yuan et al., "Thermal evolution of lithium ion substituted cesium-based geopolymer under high temperature treatment, Part I: Effects of holding temperature," *Ceram. Int.*, vol. 44, no. 9, pp. 10047–10054, 2018, <http://dx.doi.org/10.1016/j.ceramint.2018.02.179>.
- [118] J. Wang, L. Han, Z. Liu, and D. Wang, "Setting controlling of lithium slag-based geopolymer by activator and sodium tetraborate as a retarder and its effects on mortar properties," *Cement Concr. Compos.*, vol. 110, 103598, 2020, <http://dx.doi.org/10.1016/j.cemconcomp.2020.103598>.
- [119] J. L. Bell, P. E. Driemeyer, and W. M. Kriven, "Formation of ceramics from metakaolin-based geopolymers: Part I-Cs-based geopolymer," *J. Am. Ceram. Soc.*, vol. 92, no. 1, pp. 1–8, 2009, <http://dx.doi.org/10.1111/j.1551-2916.2008.02790.x>.
- [120] G. Kastiukas, S. Ruan, S. Liang, and X. Zhou, "Development of precast geopolymer concrete via oven and microwave radiation curing with an environmental assessment," *J. Clean. Prod.*, vol. 255, 120290, 2020, <http://dx.doi.org/10.1016/j.jclepro.2020.120290>.
- [121] M. Nasir, M. A. M. Johari, M. Maslehuudin, M. O. Yusuf, and M. A. Al-Harhi, "Influence of heat curing period and temperature on the strength of silico-manganese fume-blast furnace slag-based alkali-activated mortar," *Constr. Build. Mater.*, vol. 251, 118961, 2020, <http://dx.doi.org/10.1016/j.conbuildmat.2020.118961>.
- [122] M. S. Muñoz-Villarreal et al., "The effect of temperature on the geopolymerization process of a metakaolin-based geopolymer," *Mater. Lett.*, vol. 65, no. 6, pp. 995–998, 2011, <http://dx.doi.org/10.1016/j.matlet.2010.12.049>.
- [123] W. I. Wan Mastura, H. Kamarudin, I. Khairul Nizar, M. M. Al Bakri Abdullah, and H. Mohammed, "The effect of curing time on the properties of fly ash-based geopolymer bricks," *Adv. Mat. Res.*, vol. 626, pp. 937–941, 2012., <http://dx.doi.org/10.4028/www.scientific.net/AMR.626.937>.
- [124] G. Kovalchuk, A. Fernández-Jiménez, and A. Palomo, "Alkali-activated fly ash: effect of thermal curing conditions on mechanical and microstructural development – Part II," *Fuel*, vol. 86, no. 3, pp. 315–322, 2007, <http://dx.doi.org/10.1016/j.fuel.2006.07.010>.
- [125] M. Criado, A. Fernández-Jiménez, and A. Palomo, "Alkali activation of fly ash. Part III: effect of curing conditions on reaction and its graphical description," *Fuel*, vol. 89, no. 11, pp. 3185–3192, 2010, <http://dx.doi.org/10.1016/j.fuel.2010.03.051>.
- [126] M. Criado, A. Fernández Jiménez, I. Sobrados, A. Palomo, and J. Sanz, "Effect of relative humidity on the reaction products of alkali activated fly ash," *J. Eur. Ceram. Soc.*, vol. 32, no. 11, pp. 2799–2807, 2012, <http://dx.doi.org/10.1016/j.jeurceramsoc.2011.11.036>.

---

**Author contributions:** MTM: conceptualization, writing, formal analysis, revision. ARG, CMFV: funding acquisition, supervision, formal analysis.

**Editors:** José Marcio Calixto, Guilherme Aris Parsekian.



ORIGINAL ARTICLE

# Numerical modeling and design of precast prestressed UHPFRC I beams

*Modelagem numérica e projeto de vigas I protendidas de UHPFRC*

Gustavo de Miranda Saleme Gidrão<sup>a</sup> Pablo Augusto Krahl<sup>b</sup> Ricardo Carrazedo<sup>c</sup> <sup>a</sup>Universidade Tecnológica Federal do Paraná – UTFPR, Departamento de Engenharia Civil, Guarapuava, PR, Brasil<sup>b</sup>Universidade de Campinas – UNICAMP, Faculdade de Engenharia Civil, Arquitetura e Urbanismo, Campinas, SP, Brasil<sup>c</sup>Universidade de São Paulo – USP, Escola de Engenharia de São Carlos – EESC, Departamento de Estruturas, São Carlos, SP, BrasilReceived 30 September 2018  
Accepted 16 August 2020

**Abstract:** Ultra-high-performance fiber reinforced concrete (UHPFRC) is a new material developed to present superior properties, as high compressive strength (higher than 130 MPa), high durability, and satisfactory ductile behavior. This paper reports the procedure to design precast UHPFRC beams, subject to flexural loads. First, an I-girder AASHTO Type II was designed, and simulated. Next, I-beams with diverse depths and steel ratios were designed, and simulated considering a four-point bending load test. It was found that the classical design equations used to predict the strength bending moment ( $M_{rd}$ ) showed good accuracy with the simulated models with a 4.5% error.

**Keywords:** UHPFRC, design, precast, flexural failure.

**Resumo:** O Concreto de ultra alto desempenho reforçado por fibras (CUADRF ou Ultra-high performance fiber reinforced concrete - UHPFRC) é um novo material desenvolvido para apresentar propriedades superiores, tais como altas resistências à compressão (superior a 130 MPa), grande durabilidade, além de comportamento dúctil satisfatório em situações de flexão. Atualmente, nota-se a crescente tendência de aplicação deste material na indústria de pré-moldados, sendo necessário o entendimento sobre o procedimento básico que rege o dimensionamento destas peças. O presente artigo reporta sobre o procedimento de cálculo para dimensionamento de uma viga pré-moldada protendida constituído de UHPFRC, sob condições de Estado Limite Último flexional. A viga estudada é do tipo “I” AASHTO Tipo II, com 26 cabos protendidos. Esta viga é simulada numericamente via software de elementos finitos e comparada com um resultado experimental reportado na literatura, verificando-se os mecanismos de falha para o elemento estrutural, e assim validando o modelo numérico proposto. Em seguida, são simuladas vigas I com altura e armaduras ativas variáveis. Após as simulações, equações clássicas de dimensionamento são utilizadas para previsão de momento resistente ( $M_{Rd}$ ), apresentando grande precisão com erro relativo menor que 4,5%.

**Palavras-chave:** UHPFRC, dimensionamento, pré moldados, estado limite último de flexão.

**How to cite:** G. M. S. Gidrão, P. A. Krahl, and R. Carrazedo, “Numerical modeling and design of precast prestressed UHPFRC I beams,” *Rev. IBRACON Estrut. Mater.*, vol. 14, no. 3, e14310, 2021, <https://doi.org/10.1590/S1983-41952021000300010>

## 1 INTRODUCTION

In 1993, Richard and Cherezy developed the Reactive Powder Concrete (RPC), using fine particles, mineral additions, and thermal treatment [1], [2]. RPC presented high durability levels and high strength, characteristics obtained due to the rigorous material selection, grain packing, and standard proceeding mixture [3], [4]. In this way, RPC presented compression strength around 150 – 200 MPa [1], [2], [5] and porosity levels below 4% [6].

Corresponding author: Gustavo de Miranda Saleme Gidrão. E-mail: [gustavo.gidrao@gmail.com](mailto:gustavo.gidrao@gmail.com)

Financial support: The authors gratefully acknowledge the financial support (grant ID – 141993/2014-6) provided by National Counsel of Technological and Scientific Development (CNPq) from Brazil.

Conflict of interest: Nothing to declare.



This is an Open Access article distributed under the terms of the Creative Commons Attribution License, which permits unrestricted use, distribution, and reproduction in any medium, provided the original work is properly cited.

The notable advances of superplasticizers and mineral additions allowed the production of concretes with high volumetric amounts of fine particles, perfectly packed and with low water-cement ratios allowing the development of the precursor Ultra-High-Performance Concrete (UHPC) [6]–[8]. UHPC presents (i) high mechanical properties in the long term, (ii) low permeability, and (iii) long life cycle under aggressive environments [6], [9].

Therefore, UHPC must present a water-cement ratio of around 0.2 and a minimum compressive strength of 130 MPa at 28 days [10], [11]. However, the matrix densification and decrease of microstructure imperfections may induce brittle failure of the elements that present low ductility due to its reduced tensile strength. The mitigation of brittle failures, metallic microfibers are added to the mixture, improving the ductile behavior, and then UHPC is named UHPFRC [7].

Considering its elevated properties, durability, and appropriated workability, UHPFRC is an emergent material with notable applications in the precast industry [7], [12]–[14]. Given this context, this paper describes a procedure for designing UHPFRC elements subjected to bending loads. The analytical results obtained with the proposed equations are compared to numerical simulation results of beams constituted of UHPFRC, presenting good accuracy.

## 2 BENDING DESIGN

Fehling et al. [7], [15] proposed basic assumptions and analytical equations to design UHPC and UHPFRC elements subjected to flexural loads. Figure 1 presents the stress-strain distribution of the rectangular beam studied by Fehling et al. [7], [15] considering axial force ( $N_{sd}$ ) and bending moment ( $M_{sd}$ ):

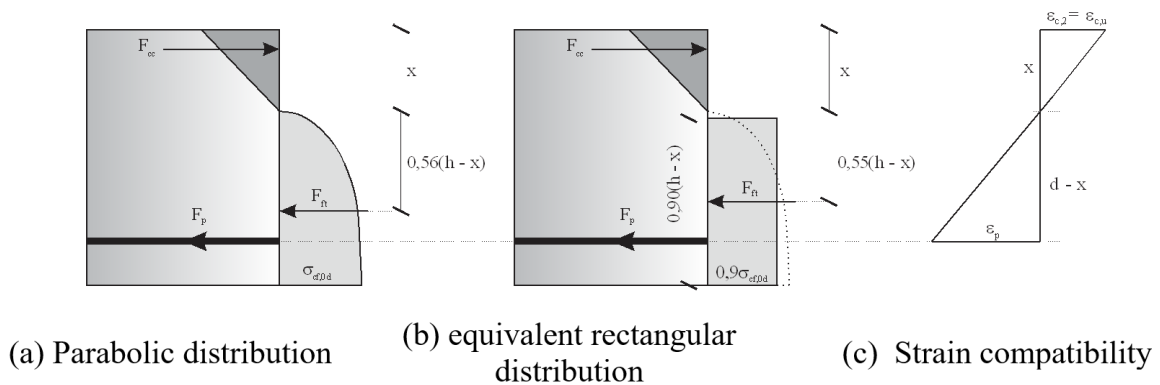


**Figure 1.** Stress distribution (a and b) and strain (c) for a rectangular cross-section (Fehling et al. [7])

In Figure 1,  $x$  is the neutral axis position;  $F_{cc}$  is the concrete compressive resultant force located at a distance equal to  $x/3$  from the top;  $F_{ft}$  is the concrete tensile force located at the centroid of the parabolic area representing the stress distribution; and  $F_{st}$  is the resultant steel force.

The herein presented assumptions are considered to develop the design equations:

- Bernoulli hypothesis: plane sections remain plane, and the deformed beam angles are small.
- Triangular compressive stress distribution is considered with a linear stress-strain compressive response for the concrete until the failure (see e.g., Figure 1).
- Tensile stress cannot be disregarded for UHPFRC, and its distribution can be considered parabolic (Figure 1a) or rectangular (Figure 1b)

The concrete tensile resultant force can be calculated by integrating the area of the stress distribution. Equation 1 indicates the resultant force considering a parabolic stress distribution. The resultant force is located at the centroid of the parabolic area from a distance equal to  $0.56(h - x)$  to the neutral axis [7], [15]. Equation 2 indicates the concrete tensile force considering a rectangular distribution. Comparing Equations 1 and 2, it can be observed an error smaller than 2.5%. Hence, for simplicity, this paper considers the rectangular distribution for concrete tensile stresses, according to Equation 2.

$$F_{ft} = 0.83 \cdot (h - x) \cdot b \cdot \sigma_{cf0d} \tag{1}$$

$$F_{ft} = 0.8I \cdot (h - x) \cdot b \cdot \sigma_{cf0d} \tag{2}$$

In Equation 2,  $h$  is the beam height,  $x$  is the depth of the neutral axis,  $b$  is the beam width,  $\sigma_{cf,0d}$  is the direct tensile strength.

Equation 3 gives the resultant compressive force ( $F_{cc}$ ), and Equation 4 presents the resultant force applied to the prestressed cables ( $F_{st}$ ) calculates using the stress-strain diagram of the steel cables.

$$F_{cc} = 0.50 \cdot b \cdot x \cdot f_{cd} \tag{3}$$

$$F_{st} = A_{st} \cdot \sigma_{st} \tag{4}$$

The equilibrium equations in terms of the axial forces and bending moments are given by Equations 5 and 6, respectively,

$$\Sigma F = 0 = N_{Sd} + F_{cc} - F_{ft} - F_{st} \tag{5}$$

$$\Sigma M = 0 = M_{Sd} - F_{cc} \cdot (d - x / 3) + F_{ft} \cdot (d - 0,45 \cdot x - 0,55 \cdot h) \tag{6}$$

Finally, it is necessary to impose a strain compatibility relationship for the cross-section (Equation 7). Figure 1c shows the strain response along with the height of the section, considering the cables embedded in the concrete.

$$\frac{\epsilon_c}{x} = \frac{\epsilon_{st}}{d - x} \tag{7}$$

In Equation 7, ( $\epsilon_{st}$ ) is the tensile strain at the reinforcement and ( $\epsilon_c$ ) the compressive strain of the concrete.

Finally, following the above-suggested steps, it is possible to design a beam with arbitrary dimensions (Figure 2),

1. Calculate the resultant axial forces:  $F_{ft}$ ,  $F_{cc}$ ,  $F_{sc}$  e  $F_{st}$ ;
2. Define the depth of the neutral axis ( $x$ ) using an iterative algorithm to promote the equilibrium of bending moments in the cross-section;
3. Update resultant forces at concrete and steel cables  $F_{cc}$  and  $F_{ft}$ ;
4. Impose the compatibility relationship to calculate the strains along with the cross-section height;
5. Determine the stress in the reinforcements  $\sigma_{s,t}$  using the constitutive stress-strain relation;
6. Calculate the required reinforcement area ( $A_{st}$ );

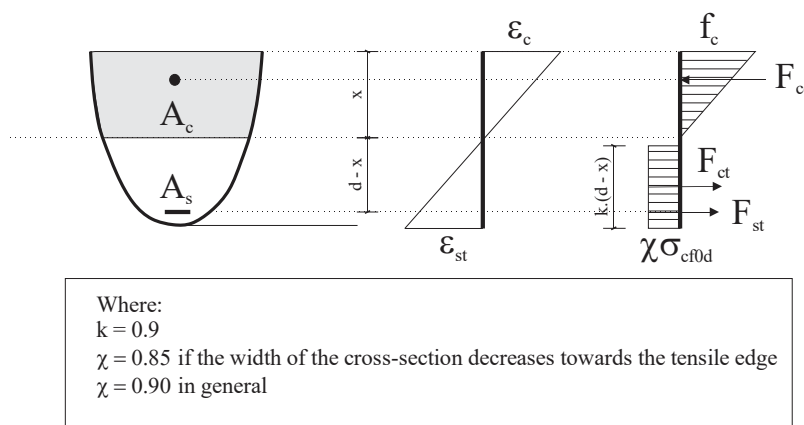


**Figure 2.** Design model to an arbitrary cross-section

### 3 CASES OF STUDY

In this section, the numerical and experimental results showed by Graybeal [16] are used to validate the proposed method for designing UHPFRC elements (section 2). The example consists of an I-beam PCI AASHTO II constituted by UHPFRC with 26 prestressed steel reinforcements and subjected to a bending test, according to Figure 3a and 3b. This section is commonly applied to bridge structures using C70 concrete. The Graybeal’s experimental results were used to calibrate a Finite Elements Model (FEM) using Concrete Damage Plasticity (CDP) to describe the non-linear behavior of the material, presented in Section 5.1.

Moreover, aiming to test the capability of the analytical equations proposed by Fehling et al. [7], [15], the strength of prestressed sections are predicted using a numerical FEM model and analytical model. These beams present heights  $h = 500$  mm,  $400$  mm and  $300$  mm, two reinforcement strands ( $\phi = 12,5$  mm) placed in the inferior flange, constant width  $b = 300$  mm and constant thickness  $e = 50$  mm, according to Figure 3c. The spans of the beams are 3 meters, and the point load application and boundary conditions are described in Figure 3d. The UHPFRC characteristics used in this analytical-numerical model were adopted, according to Krahl et al. [17], [18].

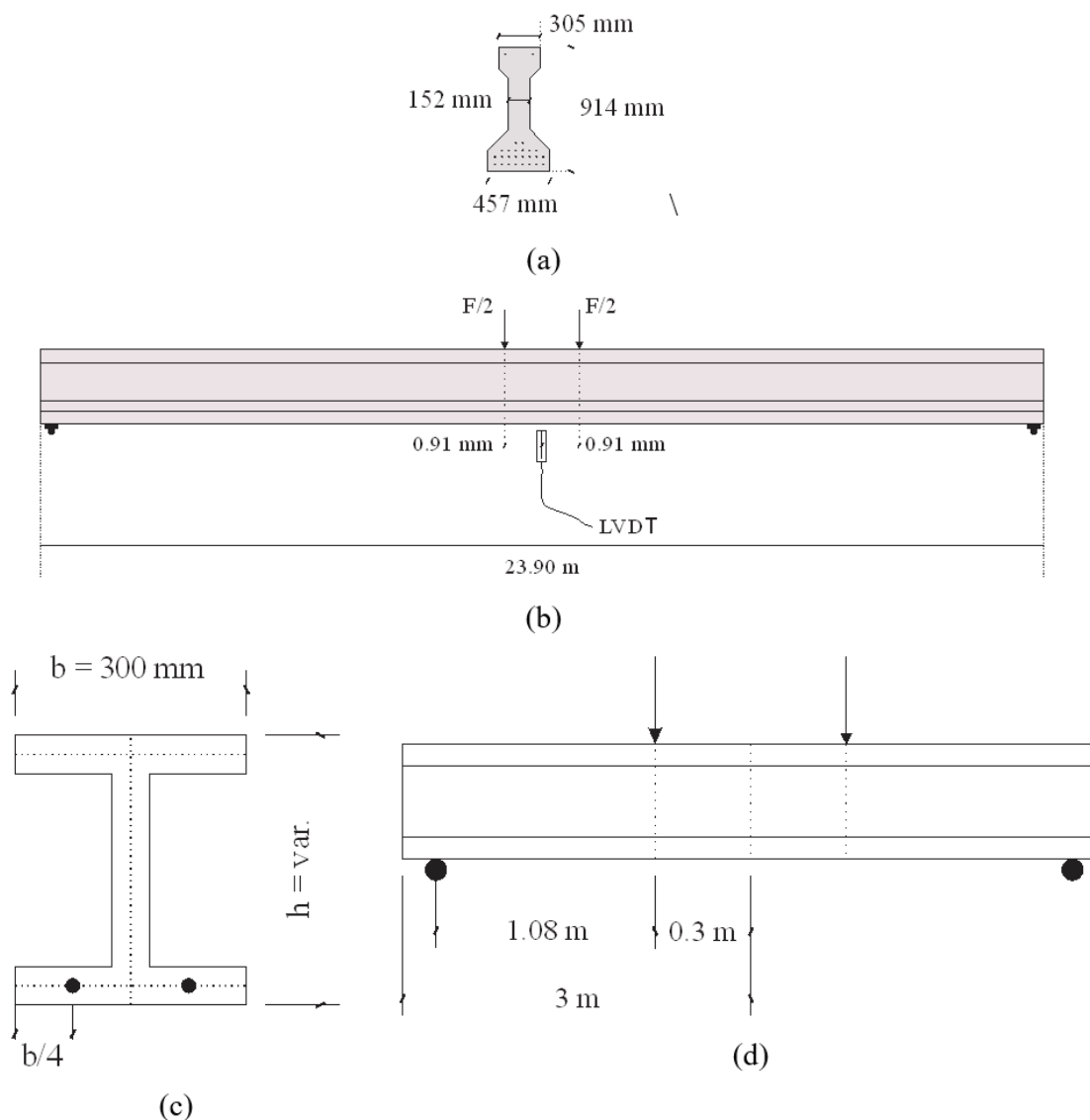


**Figure 3.** Studied girders: PCI AASHTO Type II: (a) cross-section, (b) Scheme test [15]. I-sections: (c) cross-section e (d) Scheme test.

Table 1 presents the different material characteristics for UHPFRC produced by Krahl and Graybeal. It is relevant the fact of the Graybeal’s concrete presents divergency in uniaxial tensile behavior, i.e.,: the value of 9MPa was presented by the author as the direct tensile strength, performed in dog bone samples [16]; and the value of 15.9MPa was presented as the calibrated uniaxial response of numerical model [16]. In this paper, we are showing the results obtained, considering these two different tensile strengths to analyze. Hence, the first girder “Complete Graybeal model” was simulated using the tensile strength of 15.9 MPa and considering the tensile and compressive uniaxial behaviors; and “Simplified Graybeal model” was modeled using the tensile strength of 9 MPa and a simplified uniaxial tensile law based in the direct tensile tests.

**Table 1.** Design parameters

Parameter	Graybeal	Krahl
Compressive Strength (MPa) - $f_c$	193	145
Direct tensile strength (MPa)	9** e 15.9***	6.9
Steel strength (MPa) – $f_{p,u}$	1860	1860
Prestress (MPa) – $f_{p,i}$	885	850
Prestresses strands diameter (mm) - $\phi$	12.7	12.7
Total area of the girder (m <sup>2</sup> )	0.23	Var.
* $d'_{bot}$ (mm)	102	25
* $d'_{top}$ (mm)	51	-
Steel Young Modulus - $E_s$ (GPa)	198	198
Concrete Young Modulus – $E_{ci}$ (GPa)	55	55
Moment of Inertia (m <sup>4</sup> )	0.02	Var.
Girder Height (mm)	914	Var.

\* $d'$  is the distance of the top and bottom face until steel strands gravity center. \*\* The value of 9 MPa is obtained by direct tensile test [16]. \*\*\*The value of 15.9 Mpa is obtained by numerical-experimental calibration [16]

## 4 NUMERICAL SIMULATION

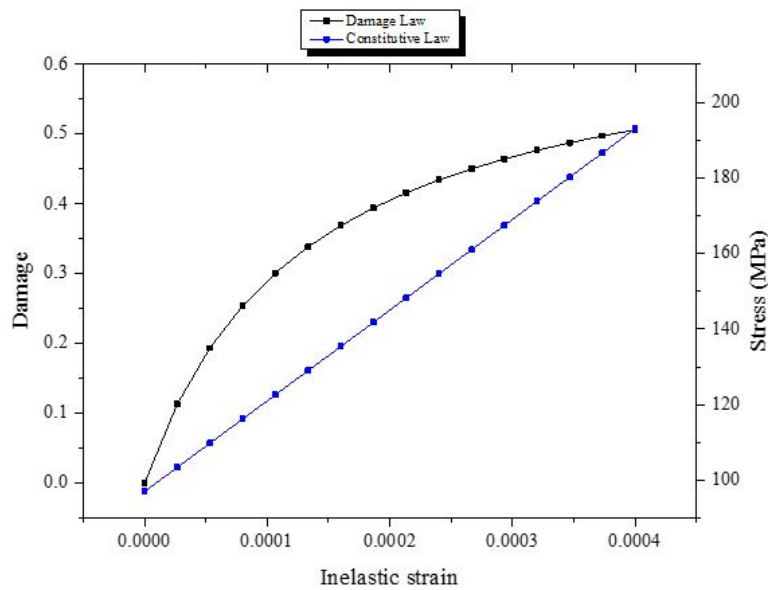
### 4.1 Graybeal’s girder constitutive model

The constitutive tensile law based on the calibrated tensile and compressive uniaxial behaviors given by Graybeal [16] is according to Figure 4a and b, with 15.9 MPa tensile strength. The second girder, “Simplified Graybeal model”, was modeled using the tensile strength of 9 MPa and a simplified uniaxial tensile law based on direct tensile tests; see Figure 4b simplified model. The constitutive model of Concrete Damage Plasticity (implemented in ABAQUS CAE Simulia) was applied to simulate both girders. The compressive and tensile damage evolution (i.e.,  $d_t$  and  $d_c$ ) are obtained by the methodology proposed by Birtel and Mark [19], through Equations 8 and 9:

$$d_t = 1 - \frac{\sigma_t E_c^{-1}}{\varepsilon_t^{pl} \left( \frac{1}{b_t} - 1 \right) + \sigma_t E_c^{-1}} \tag{8}$$

$$d_c = 1 - \frac{\sigma_c E_c^{-1}}{\varepsilon_c^{pl} \left( \frac{1}{b_c} - 1 \right) + \sigma_c E_c^{-1}} \tag{9}$$





(a) Compressive uniaxial response

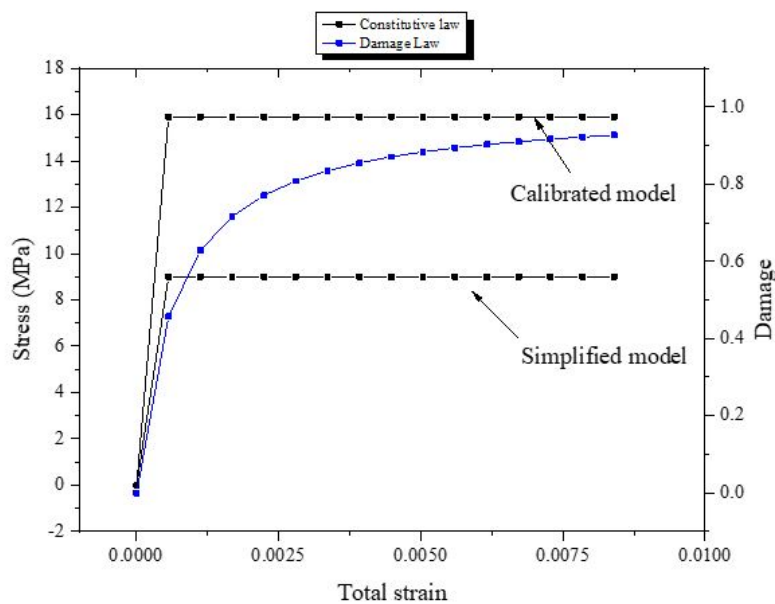


Figure 4. (a) e (b) UHPFRC Constitutive model - Graybeal [16]

In Equations 8 and 9 is the tensile stress of the concrete;  $\sigma_c$  is the compressive stress of the concrete;  $E_c$  is the elastic modulus of the intact material;  $b_c = 0.7$  and  $b_t = 0.57$  are empirical parameters related to damage evolution [19]; and are plastic strains, defined as  $\varepsilon^{pl} = b_c \varepsilon^{in}$ , and  $\varepsilon^{in}$  is given by the difference between total and elastic deformation ( $\sigma/E_c$ ). Table 2 presents the elasticity and plasticity parameters adopted.

ASTM 270-ksi steel was used in prestressed strands, with the constitutive law given by Figure 5 [20]. A prestress load of 885 MPa was adopted. The prestressed strands were considered totally embedded into the concrete. The steel elastic modulus is  $E_s = 197$  GPa.

**Table 2.** Plasticity and Elasticity parameters

Parameter	Value
Young Modulus ( $E_{ci}$ ), GPa	52.4
Dilatation angle (degree)	54
Eccentricity	0.1
K	0.666
$f_{b0}/f_{c0}$	1.07
Viscosity parameter	0.0

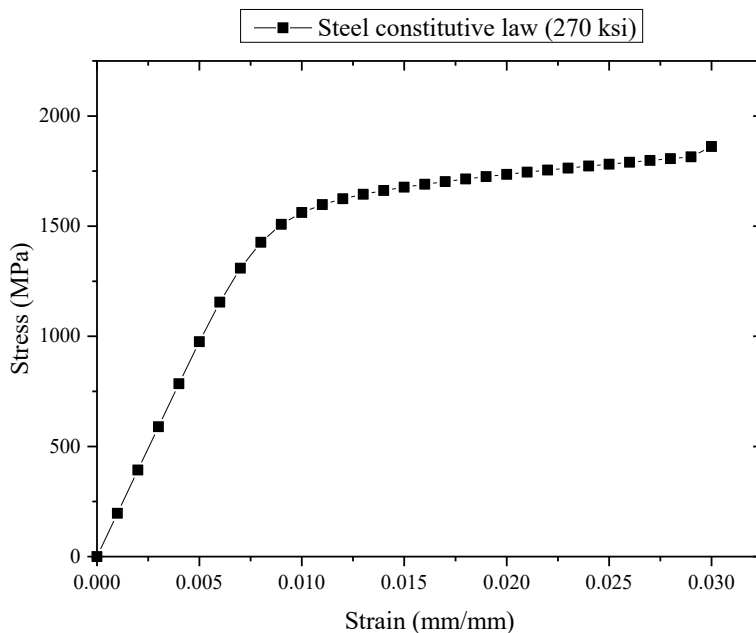


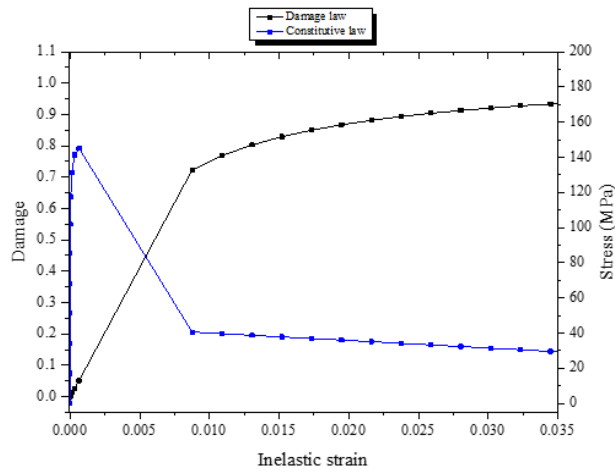
**Figure 5.** Steel bar constitutive law - ASTM 270

#### 4.2 Constitutive model (I-beams)

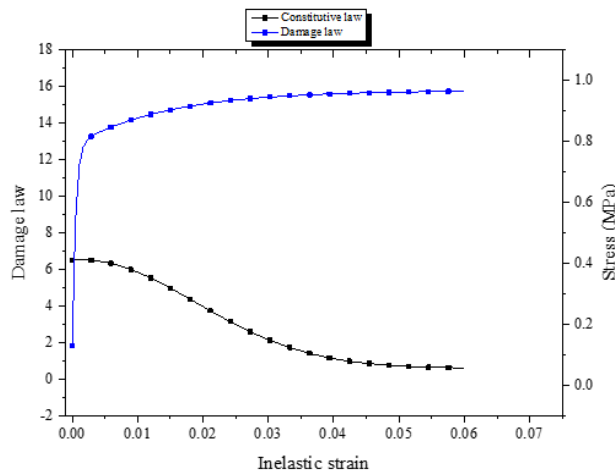
For the three simulated I-beams (Figure 3c and 3d), the UHPFRC constitutive law written in terms of the inelastic strain is applied according to Figures 6a and 6b, and Krahl et al. [17], [18]. Plasticity and elasticity parameters are given in Table 2; the design parameters and prestress load are presented in Table 1.

#### 4.3 Boundary conditions, mesh, and load

All beams were considered simply supported, and a 3D 8-nodes solid elements mesh was applied (C3D8R) to represent UHPFRC, with 3 degrees of freedom each node. Graybeal’s girders were modeled with a 50 mm mesh size for transversal direction and 150 mm for longitudinal axis. I-beams were modeled using a 40 mm mesh size for longitudinal direction, and 20 mm mesh size for transversal discretization. 3D truss finite elements were used to represent the prestressed strands with a 100 mm mesh size. The gravity load was considered as  $-9.81 \text{ m/s}^2$ , and concrete density equals to  $2500 \text{ kg/m}^3$ .



(a) Compressive uniaxial response



(d) Tensile uniaxial response

Figure 6. (a) e (d) UHPFRC constitutive model - Krahl et al. [17], [18]

A displacement control test was used for the three studied I-beams and for the Simplified Graybeal model. For the Complete Graybeal model, the same experimental methodology given in Graybeal [16] was performed, i.e., initial force control until 18 kN, and posterior displacements control until failure.

Therefore, the following cases were studied in this paper:

- (I) Complete Graybeal model: force and displacements control, with constitutive law calibrated according to experimental results of Graybeal [16];
- (II) Simplified Graybeal model: displacements control and simplified constitutive law based in the direct tensile tests;
- (III) I-beams: displacement control and constitutive law was given by Krahl et al. [17], [18].

## 5 RESULTS

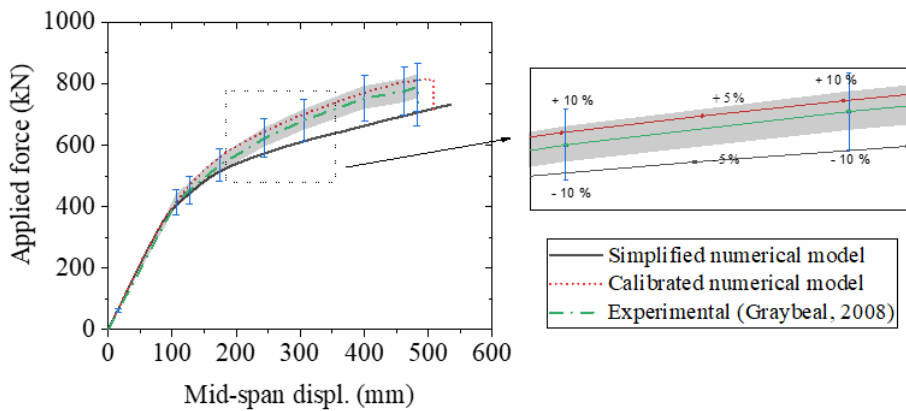
### 5.1 Garybeal's girders – Numerical Validation

Figure 7a presents the comparison between the numerical results and experimental behavior given by Graybeal [16]. The force-displacement curve obtained by the complete Graybeal model presented a 5% maximum error (gray area in

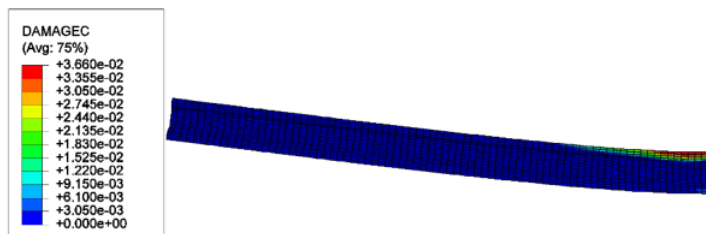
the graph). The estimated maximum force was 3.17% higher in the numerical model. The displacements prediction was 5.6% higher in the numerical model. For the Simplified Graybeal model, a maximum error of 10% was achieved in the force x displacement curve comparing the numerical and experimental results.

The experimental maximum bending moment was  $M_{rd} = 4318 \text{ kN} \cdot \text{m}$  [16]; the estimated values using the numerical approach were  $M_{rd} = 4455 \text{ kN} \cdot \text{m}$  (Complete Graybeal model) and  $M_{rd} = 4000.4 \text{ kN} \cdot \text{m}$  (Simplified Graybeal model).

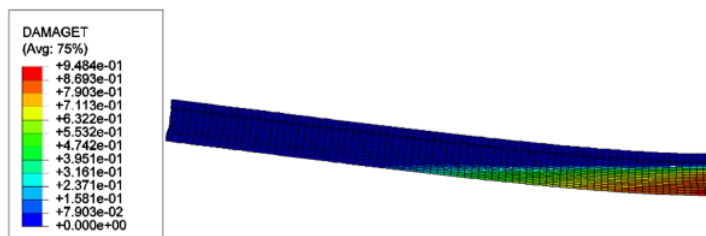
Relevant parameters are the tensile and compressive damage indexes (Figure 7b and 7c) over the load evolution. Yang et al. [21] showed that damage indexes are used to predict the cracking zones, which can be useful for the identification of the failure modes. For the Graybeal’s girders bending failures were observed, presenting predominant tensile damage indexes in the middle of the spans. When the peak force is reached, both models presented tensile damage indexes of 90% (Figure 7c), with excessive strains in the reinforcements, characterizing the flexural failure.



(a) Force-displacement



(b) Compressive damage (1/2 span)



(c) Tensile damage (1/2 span)

Figure 7 – Damage behavior of AASHTO PCI SII

## 5.2 Analytical design of Graybeal's girder

The analytical equations showed in section 2 are used to estimate the maximum bending moment of Graybeal's girders. Table 1 presents the material characteristics applied to prestress force and section parameters. Figure 8 presents a geometrical law in terms of the depth of the neutral axis and the compressed area, used in Equations 13 to 16. For the analytical design, better results were obtained with the tensile strength of 9 MPa.

The maximum strain in the compressive behavior is given by Equation 10, following the French Association of Civil Engineering (AFGC) [22]:

$$\varepsilon_{cud} = 1 + 14 \cdot \left( \frac{f_{ctm}}{f_{cm}} \right) \cdot \varepsilon_{c0d} = 5.8 \cdot 10^{-3} \quad (10)$$

In Equation 10,  $f_{ctm}$  is the tensile strength, which could be higher than cracking stress when UHPFRC presents strain-hardening behavior;  $f_{cm}$  is the average compressive strength;  $\varepsilon_{c0d}$  is the strain written in terms of the elastic limit ( $f_{cm}/E_{ci}$ ), and  $E_c$  is the young modulus initial tangent.

The calculus of  $\varepsilon_{cud}$  allows the determination of the limit between strain domains 2 and 3 of the Brazilian code ABNT NBR 6118:2014 (i.e., concrete with a strain of 5.8 ‰ and steel strands with 10 ‰). The determination of the neutral axis between dominium 2 and 3 (i.e.,  $x_{lim}$ ) is given by Equation 11:

$$x_{lim} = \frac{\varepsilon_{cc} (h - d'_{inf})}{\varepsilon_{cc} + \varepsilon_{st}} = 0.297m \quad (11)$$

The transversal section was divided into strips of 0.01 m heigh to account for the cumulative areas. Through the geometrical law, the geometrical law, it was possible to determine the values of  $A_c = 0.076 \text{ m}^2$  (compressed area), and  $A_t = 0.154 \text{ m}^2$  (tensile area) for the strain domain limit 2 and 3 ( $x_{lim}$ ); the force components for this configuration are expressed by Equation 12 to 15:

$$F_{cc} = 0.5 \cdot A_{cc} \cdot f_c \quad (12)$$

$$F_{sc} = n_{bar,top} \frac{\pi \phi^2}{4} f_p (\varepsilon_{prev} + \varepsilon_c) \quad (13)$$

$$F_{st} = n_{bar,bot} \frac{\pi \phi^2}{4} f_p (\varepsilon_{prev} + 10\text{‰}) \quad (14)$$

$$F_{ct} = 0.9 \cdot (A_{tot} - A_{cc}) \cdot 0.9 \cdot f_{ct} \quad (15)$$

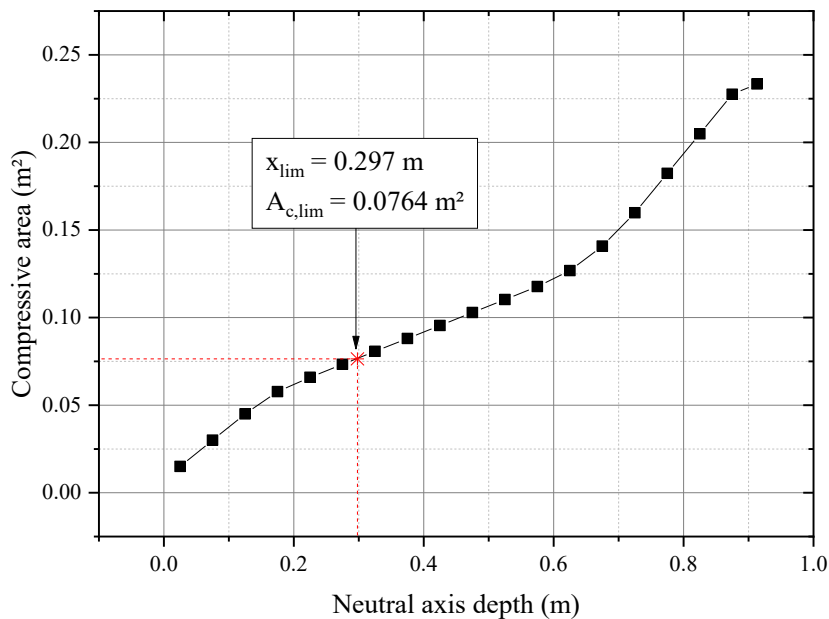


**Figure 8.** Geometrical law – Compressive area vs. Neutral axis depth (PCI AASHTO type SII)

In Equations 12-15,  $A_{cc}$  is the concrete compressed area,  $n_{bar}$  is the total number of strands,  $A_{tot}$  is the total area of the cross-section,  $f_p$  is the stress considering the total stress at strands,  $f_c$  is the compressive strength;  $f_{ct}$  is the direct tensile strength;  $\epsilon_{prev}$  is the previous strain in the prestressed strands, equals to 4.5 ‰ (for  $f_{pi} = 885$  MPa),  $f_p$  is the stress in the strands.

Table 3 presents the initial parameters obtained with Equations 13-16 using  $x = x_{lim}$ , establishing the equilibrium of forces in the cross-section, it is possible to determine the imbalanced vector  $\Delta R$  that governates the position of the neutral axis to ensure the balance until  $\Delta R$  approaches zero.

**Table 3.** Design data for Graybeal beam

Forces	[kN]
Rcc (lim)	14796
Rsc (lim)	274
Rst (lim)	4939
Rct (lim)	1979
$\Delta R$ (initial)	9328
Rcc (final)	5669
Rsc (final)	411
Rst (final)	4939
Rct (final)	1141
$\Delta R$ (final)	0.09

In this way, for each iteration of  $\Delta R$ ,  $A_{cc}$ ,  $A_{st}$ ,  $\varepsilon_c$ , and  $\varepsilon_{st}$  are updated. The values of  $R_{cc}$  (force in concrete),  $R_{sc}$  (force in compressed reinforcements),  $R_{st}$  (force in tensile reinforcement), and  $R_{ct}$  (force in tensile concrete) for the initial and final  $\Delta R$  are presented in Table 3. Evaluating the neutral axis final position, it was possible to verify that the prestressed strands are working with strains equals to  $\varepsilon_{st} = \varepsilon_{pnd} + 10 \text{ ‰} = 15.02 \text{ ‰}$ , following the hypothesis of domain 2. The resistant bending moment of cross-section is obtained by Equation 16:

$$M_{rd} = A_{cc} \cdot f_{cd} \cdot \left(\frac{2}{3}\right) \cdot x + R_{sc}(x - d') + A_{ct} 0.9 \cdot \eta \cdot f_{ct} 0.9 (h - x) + \dots + \sum_{n=1}^{26 \text{ bars}} \frac{\pi \phi^2}{4} f_p \cdot Y_i \quad (16)$$

In Equation 16,  $Y_i$  are the distances of gravity center of prestressed steel strands to the neutral axis of the beam;

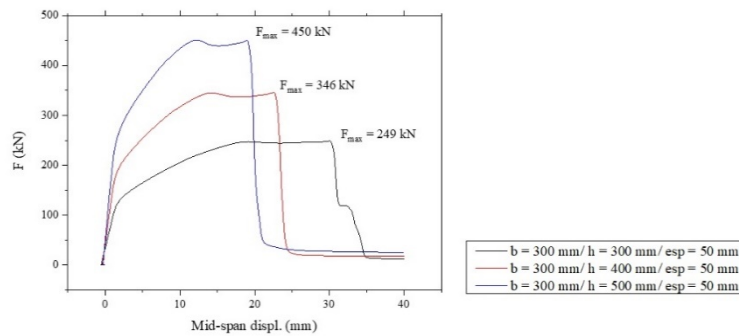
Finally, the strength bending moment of 4527 kN·m was obtained through the analytical design equations. This value is very close to the experimental value obtained by Graybeal [16] and the numerical simulation developed in this paper (4318 kN·m), with a 4.7% error.

### 5.3 I-beams

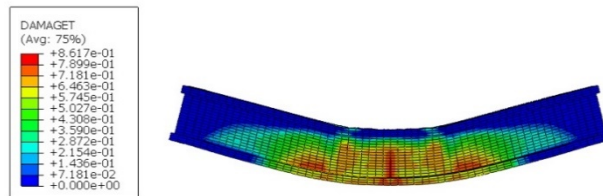
Figure 9 presents the force-displacement of I-beams (see the simulation condition in Figure 3c and 3d). It is possible to verify the high ductile behavior of the beams, showing high displaceable capacity until the total loss of strength.

Figures 9b and 9c show the tensile and compressive damage distribution for the I-beam section with  $h = 400$  mm and  $b = 300$  mm. It can be noted a high level of tensile damage in the inferior zone at the center of the span, characterizing the bending failure mode. Nevertheless, it is also possible to detect the presence of tensile damage at the diagonals around the supports, showing the influence of the bending-shear composed failure mode, probably due to the minor span/height relation ( $L/h$ ) in comparison with Graybeal's girder.

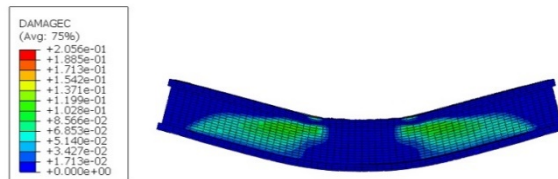
Equations presented in Section 2 were used to predict the maximum bending moment of the designed sections. Figure 9d presents the comparison of analytical bending moments and the values obtained through the numerical simulation. There is a correspondence between the numerical and analytical results that can be achieved, showing the accuracy of the proposed model given by Fehling et al. [7], [15] and adapted by this paper.



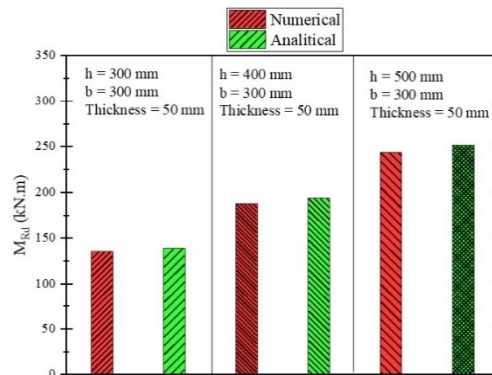
(a)



(b)



(c)



(d)

**Figure 9.** Prestressed I-Girder – Parametrical analysis: (a) Force-displacement, (b) tensile damage, (c) Compressive damage, (d) Comparison of bending moments

## 6 CONCLUDING AND REMARKS

This paper approaches the numerical modeling and design of prestressed UHPFRC I-beams subjected to flexural tests. The main aspects can be highlighted:

- The potential of concrete damage plasticity constitutive model was demonstrated to application in UHPFRC prestressed beams, presenting correspondence with the experimental results of Graybeal [16] for the PCI AASHTO SII beams;



- The strength bending moments obtained by the analytical design equations showed to be accurate to predict the experimental and numerical results, with 5% error;
- A qualitative analysis shows the high strength and satisfactory ductile behavior of beams, with high energy dissipation before the failure;
- Due to the high span/height relation, the Graybeal's girders presented a typical flexural failure. For the I-beams studied, with reduced L/h coefficient, it was possible to observe a composed bending-shear failure mode;
- The numerical simulation developed in this paper presented high accuracy, showing an error of 5% in the prediction of strength for Graybeal's girders and I-beams.
- The simplified Graybeal model presented an error of 10%, estimating the maximum force strength. This difference evidences the latent influence of experimental variability between uniaxial sample tests and real structure behavior.

The Brazilian code ABNT NBR 6118:2014 does not present the prescriptions for to design of prestressed and non-prestressed UHPFRC sections. In this way, this paper proposes a simple procedure to be applied at the design of prestressed beams subjected to bending loads.

## REFERENCES

- [1] P. Richard and M. Cheyrezy, "Composition of reactive powder concretes," *Cement Concr. Res.*, vol. 25, no. 7, pp. 1501–1511, 1995, [http://dx.doi.org/10.1016/0008-8846\(95\)00144-2](http://dx.doi.org/10.1016/0008-8846(95)00144-2).
- [2] P. Cheyrezy, "Richard, reactive powder concretes with high ductility and 200-800 Mpa compressive strength," *Spec. Publ. ACI.*, vol. 144, 1994, <http://dx.doi.org/10.14359/4536>.
- [3] A. Ali, *Behaviour of Prestressed Ultra-High Performance Concrete I-Beams Subjected to Shear and Flexure*. Ottawa: University of Ottawa 2013.
- [4] K. Habel and P. Gauvreau, "Response of ultra-high performance fiber reinforced concrete (UHPFRC) to impact and static loading," *Cement Concr. Compos.*, vol. 30, no. 10, pp. 938–946, 2008, <http://dx.doi.org/10.1016/j.cemconcomp.2008.09.001>.
- [5] P. Richard, M. Cheyrezy, S. D. Bouygues, and S. Quentin, "Composition of reactive powder concretes," *Cement Concr. Res.*, vol. 25, no. 7, pp. 1501–1511, 1995, [http://dx.doi.org/10.1016/0008-8846\(95\)00144-2](http://dx.doi.org/10.1016/0008-8846(95)00144-2).
- [6] T. Zdeb, "Ultra-high performance concrete – properties and technology," *Bull. Polish Acad. Sci.*, vol. 61, pp. 183–193, 2013, <http://dx.doi.org/10.2478/bpasts-2013-0017>.
- [7] E. Fehling, M. Schmidt, J. Walraven, T. Leutbecher, and S. Fröhlich, *Ultra-High Performance Concrete UHPC*. Berlin: Ernst and Sohn, 2014.
- [8] F. Larrard and T. Sedran, "Optimization of ultra-high-performance concrete by the use of a packing model," *Cement Concr. Res.*, vol. 24, no. 6, pp. 997–1009, 1994, [http://dx.doi.org/10.1016/0008-8846\(94\)90022-1](http://dx.doi.org/10.1016/0008-8846(94)90022-1).
- [9] K. Hanna, G. Morcous, and M. Tadros, "Effect of supplementary cementitious materials on the performance of concrete pavement," *J. Mater. Civ. Eng.*, vol. 26, no. 4, pp. 789–793, 2014, [http://dx.doi.org/10.1061/\(ASCE\)MT.1943-5533.0000862](http://dx.doi.org/10.1061/(ASCE)MT.1943-5533.0000862).
- [10] H. G. Russell and B. A. Graybeal, *Ultra-High Performance Concrete: A State-of-the-Art Report for the Bridge Community*. McLean, VA: U.S. Department of Transportation, 2013.
- [11] D. Wang, C. Shi, Z. Wu, J. Xiao, Z. Huang, and Z. Fang, "A review on ultra high performance concrete: Part II. Hydration, microstructure and properties," *Constr. Build. Mater.*, vol. 96, pp. 368–377, 2015, <http://dx.doi.org/10.1016/j.conbuildmat.2015.08.095>.
- [12] A. Spasojević, "Structural implications of ultra-high performance fibre-reinforced concrete in bridge design," M.S. thesis, Ec. Polytech. Fed. Lausanne, Suisse, 2008.
- [13] T. M. Ahlborn, E. J. Puese, and D. L. Misson, *Ultra-High Performance Concrete for Michigan Bridges: Material Performance-Phase I*. Michigan: Michigan Dept. Transp., 2008.
- [14] M. Rebstroff and G. Wight, "Experience and applications of ultra high performance concrete in Asia," in *Proc. 2nd Int. Symp. Ultra High Perform. Concr.*, 2008, pp. 19–30.
- [15] T. Leutbecher and E. Fehling, "A simple design approach for UHPFRC in bending," in *RILEM-fib-AFGC Int. Symp. Ultra-High Perform. Fibre-Reinf. Concr.*, 2013, pp. 509–518.
- [16] B. Graybeal, "Flexural behavior of an ultrahigh-performance concrete I-girder," *J. Bridge Eng.*, vol. 13, no. 6, pp. 602–610, 2008, [http://dx.doi.org/10.1061/\(ASCE\)1084-0702\(2008\)13:6\(602\)](http://dx.doi.org/10.1061/(ASCE)1084-0702(2008)13:6(602)).
- [17] P. A. Krahl, G. M. S. Gidrão, and R. Carrazedo, "Compressive behavior of UHPFRC under quasi-static and seismic strain rates considering the effect of fiber content," *Constr. Build. Mater.*, vol. 188, pp. 633–644, 2018., <http://dx.doi.org/10.1016/j.conbuildmat.2018.08.121>.
- [18] P. A. Krahl, R. Carrazedo, and M. K. El Debs, "Mechanical damage evolution in UHPFRC: Experimental and numerical investigation," *Eng. Struct.*, vol. 170, pp. 63–77, 2018, <http://dx.doi.org/10.1016/j.engstruct.2018.05.064>.

- [19] V. Birtel and P. Mark, "Parameterised finite element modelling of RC beam shear failure," in *Abaqus User's Conf.*, 2006, pp. 95–108.
- [20] R. K. Devalapura and M. K. Tadros, "Stress-strain modeling of 270 ksi low-relaxation prestressing strands," *PCI J.*, vol. 37, no. 2, pp. 100–106, 1992, <http://dx.doi.org/10.15554/pci.03011992.100.106>.
- [21] I. H. Yang, C. Joh, and B.-S. Kim, "Structural behavior of ultra high performance concrete beams subjected to bending," *Eng. Struct.*, vol. 32, no. 11, pp. 3478–3487, 2010, <http://dx.doi.org/10.1016/j.engstruct.2010.07.017>.
- [22] AFGC, "Ultra high performance fibre-reinforced concretes recommendations," in *AFGC*, 2013.

---

**Author contributions:** Contribution description of each co-author for the study. [GSMG: conceptualization, writing, methodology, investigation, review & editing; PAK: conceptualization, writing, methodology, investigation, review & editing; RC: supervision, conceptualization, writing, methodology, investigation, review & editing.]

**Editors:** Bernardo Horowitz, José Luiz Antunes de Oliveira e Sousa, Guilherme Aris Parsekian.



ORIGINAL ARTICLE

# Residual strength of reinforced concrete stub columns subject to moderate temperatures

*Resistência residual de colunas curtas de concreto armado submetidas a temperaturas moderadas*

Eduardo Henrique Barros Lima<sup>a</sup>

Daniel Carlos Taissum Cardoso<sup>a</sup>

<sup>a</sup>Pontifícia Universidade Católica do Rio de Janeiro – PUC-Rio, Departamento de Engenharia Civil e Ambiental, Rio de Janeiro, RJ, Brasil

Received 24 January 2020

Accepted 21 August 2020

**Abstract:** This work aims to evaluate the residual strength of reinforced concrete stub columns subjected to moderate temperatures. To accomplish this task, an experimental program was carried out including compression tests on plain concrete specimens exposed to temperatures up to 600 °C and on reinforced concrete stub columns with two different tie configurations heated at a constant rate for up to 120 min. The results show a loss of residual compressive strength with temperature and the beneficial influence of ties to prevent the spalling phenomenon, although samples with more ties exhibited lower capacity. Finally, the results were compared to the analytical prediction using a cross-sectional approach with idealized stress-strain relations, showing a good correlation. The applicability of the Isotherm 500 °C method is discussed for moderate temperatures.

**Keywords:** residual strength, columns, reinforced concrete, moderate temperatures.

**Resumo:** O presente trabalho tem como objetivo avaliar a resistência residual de colunas curtas de concreto armado submetidas a temperaturas moderadas. Para isso, foi realizado um programa experimental incluindo ensaios de compressão em corpos-de-prova cilíndricos de concreto simples de 5x10 cm submetidos a temperaturas de até 600 °C e de colunas curtas de concreto armado de 15x30 cm com duas diferentes configurações de estribos e submetidos a distintos tempos de exposição de até 120 min sob uma taxa de aquecimento constante. Os resultados comprovam a perda de resistência residual à compressão com a temperatura e a influência benéfica dos estribos na prevenção do fenômeno de spalling, embora amostras com mais estribos tenham apresentado menor resistência. Por fim, os resultados foram comparados a previsão analítica utilizando abordagem seccional com diagramas tensão-deformação idealizados, tendo apresentado boa correlação. A aplicabilidade do método da isoterma 500 °C é discutida para temperaturas moderadas.

**Palavras-chave:** resistência residual, colunas, concreto armado, temperaturas moderadas.

**How to cite:** E. H. B. Lima and D. C. T. Cardoso, “Residual strength of reinforced concrete stub columns subject to moderate temperatures,” *Rev. IBRACON Estrut. Mater.*, vol. 14, no. 3, e14311, 2021, <https://doi.org/10.1590/S1983-41952021000300011>

## 1 INTRODUCTION

Concrete is known for its good fire performance due its low thermal conductivity and due to the fact that is incombustible and does not exhale toxic gases when exposed to high temperatures [1]. However, the heterogeneous nature of the concrete and the uncertainties associated with the nature of the fire and its corresponding thermal loading make the interaction between material and loading very complex [2]. Despite this, it is known that the exposure to high temperatures can lead to physical-chemical transformations in the cement paste such as the decomposition of ettringite, evaporation of free water, lamellar and adsorbed water, detachment of water chemically linked to CSH crystals (dehydration), as well as crystal dehydration and differential expansion

Corresponding author: Daniel Carlos Taissum Cardoso. E-mail: [dctcardoso@puc-rio.br](mailto:dctcardoso@puc-rio.br)

Financial support: This study was financed in part by the Coordenação de Aperfeiçoamento de Pessoal de Nível Superior (CAPES) – Finance code 001 – and by Brazilian agencies FAPERJ and CNPq.

Conflict of interest: Nothing to declare.



This is an Open Access article distributed under the terms of the Creative Commons Attribution License, which permits unrestricted use, distribution, and reproduction in any medium, provided the original work is properly cited.

of non-hydrated components. In addition, the aggregates can also undergo changes due to their state of humidity, permeability and nature and the paste-aggregate interface can degrade due to incompatibility between the thermal properties of the two constituents, forming micro cracks [1], [3]–[5]. As a consequence of these transformations, concrete may experience changes in its physical-chemical-mechanical properties, which include reduction of density, variation of specific heat and thermal conductivity and reduction of compression strength and modulus of elasticity. These changes are influenced by the time of exposure to fire, the maximum temperature reached, the heating/cooling speed and the concrete mix. However, the porosity and initial humidity also play an important role in the behavior, since the water trapped in the pores can lead to the development of pore-pressure, with the consequent appearance of tensile stresses that cause the detachment (or debonding) of the concrete – spalling. This phenomenon may also occur as a consequence of the introduction of thermal stresses associated in restrained structural members or in structures subjected to high thermal gradients [6]. Spalling is more severe in high-strength concretes, which are characterized by a lower porosity and permeability, and the use of fibers has been seen as an interesting alternative to mitigate the problem [7]–[9].

The steel used for reinforcement can also undergo significant loss of strength when heated. Although the behavior depends on the type of steel used and the heating conditions, the original performance can be recovered after cooling if the maximum temperature reached is less than 450 °C for cold rolled steel and 600 °C for hot rolled steel. There is a consensus in the literature that the properties of steel used as passive reinforcement are almost completely recovered after a heating cycle at 500 °C. At higher temperatures, the strength of the steel should be properly assessed [10], [11].

In reinforced concrete structures, the behavior in a fire situation is controlled by the history of multiaxial stress states, by the temperature distribution and by the moisture content in the structure [12]. A first significant effect on the behavior is the loss of bond between steel and concrete for temperatures above 150 °C, affecting the material's composite behavior [13]–[15]. For higher temperatures, the coefficient of thermal expansion of concrete - initially similar to that of steel - undergoes variations, leading to differential expansions that further affect the bond between materials and produce stresses that cause the concrete to breakdown, crack and delaminate, exposing the reinforcement to fire [12]. These cracks can ultimately contribute to the heating of steel bars, which can increase differential thermal expansion and, consequently, cracking. According to Chung and Consolazio [16], the presence of steel bars influences the transport of water inside the heated concrete, creating clogging areas that can increase the risk of spalling. However, the water retention around the bars alters the heat transmission, tending to reduce the temperature inside the concrete. The spalling effect on reinforced concrete members can be mitigated through the use of ties [6], [17]. The ties also contribute to increase the compressive strength and deformation capacity of concrete in the confined region [17]–[19].

Several tests on reinforced concrete columns with different geometries have been reported in the literature [17], [18], [20]–[25]. In general, tests are performed using standard ISO 834 fire curves [26] and losses in strength and stiffness and failure modes are usually presented. There is also a wide range of methods to predict the performance of structural members, including numerical [26]–[33] and those recommended by Eurocode 2, Part 1-2 [34], which include, for example, the simplified zone and 500 °C isotherm methods. It is worth mentioning that the latter considers that the strength of the structural element can be determined considering the original properties of the concrete for the regions subjected to temperatures below 500 °C. Finally, in addition to obtaining the constitutive laws, one of the biggest challenges for obtaining analytical solutions is the prediction of the temperature profile in the cross section. In this regard, different advanced and simplified heat transfer models are also described in the literature [35]–[37].

In some fire situations, the structures do not always reach severe temperatures, such as those in the range of 1000 to 1200 °C specified in the standard fire curves of ISO 834 [26], and there may be cases in which the fire load/ventilation is low, with a much softer heating ramp. In this regard, it is worth highlighting the following points

- a) the temperature reached by the gas and the heating rate depend on a series of parameters, such as the thermo-physical properties of the compartment surface, ventilation characteristics (openings), protection measures and specific fire load. The parametric standard fire curve of Eurocode 1, Part 1-2 [38] offers the possibility of considering these parameters for design;
- b) in the case of localized fires, the gas temperature decreases with distance to the focus (far field), depending on the size of the fire [39]–[41];
- c) the results of fire tests carried out in the literature vary considerably in the results [40], [41]. The Tisova test with mobile fire, for example, points out that columns reached temperatures below 200 °C and a heating rate of 1 °C / min [42].

Results of recent simulations in concrete frames in different fire conditions also point out that the temperatures in the reinforcements were below 500 °C [43].

Even so, once the fire has ceased, it is necessary to evaluate the residual strength of the structural members, so that it can be decided for its strengthening or demolition of the structure. However, standards, design recommendations and studies in the literature usually address verification in high temperatures, where the impacts on the structure are undeniable. The decisions to be made by the engineer require rigorous evaluation, taking into account aspects of cost and safety and, therefore, the consideration of conservative scenarios in terms of safety will result in interventions with higher costs. In this context, it is noteworthy that there are few experimental results on short reinforced concrete columns subjected to moderate temperatures and, although the beneficial effects of using ties to increase ductility, residual capacity and spalling prevention have been reported in the literature, the results are still limited to specific cases of temperature or to higher concrete strength classes [44]–[46].

This work aims to evaluate the behavior and residual strength of reinforced concrete columns subjected to moderate temperatures, based on an experimental program focused on structural members fabricated with low mechanical strength concrete, with two different tie configurations. The columns are subjected to moderate thermal loading rates, seeking to reproduce mild fire conditions, as previously mentioned. The consideration of low-strength concretes aims to simulate the material of historic and old buildings, which usually exhibit a greater risk of fire [47]. In fact, at the same time that these buildings are more prone to fire, low-strength concretes have a better behavior with respect to spalling. Finally, the experimental results are compared with analytical predictions using the residual constitutive relationships of the materials and, further, discussed in the light of the 500 °C isotherm method.

## 2 MATERIALS AND METHODS

The experimental program adopted in this research aims to evaluate the residual compressive strength of reinforced concrete exposed to moderate temperatures. To accomplish this task, the experimental program was divided into two stages:

- Stage I: residual characterization tests of simple concrete and steel bars for different temperatures (control);
- Stage II: compression tests on reinforced concrete cylindrical members with two different tie configurations and subjected to slow thermal loading, considering different exposure times.

The materials used for the casting of concrete specimens consist of siliceous aggregates (coarse and fine), cement and water. The coarse aggregate used was gravel #0 (9.5 mm) while the fine aggregate came from dry river sand. The cement used was of the Brazilian CII-E-32 type and the water used to manufacture the concretes was obtained from the local supply system. The proportions used for making the concrete specimens, in mass, were 1:3.05:2.86:0.83 (cement:sand:gravel:water) in both stages. The anticipated compressive strength was 20 MPa, with the purpose to study a relatively low strength concrete. The specimens for the different tests were prepared in the laboratory, demoulded after 24 hours and stored under a humid blanket for 28 days, before testing. For steel, 10 mm diameter Brazilian CA-50 steel ribbed bars were used, with yield strength of 500 MPa and elastic modulus of approximately 200 GPa.

### 2.1 Stage I

In this stage, eight plain concrete cylindrical specimens of 5 cm in diameter and 10 cm in height were tested, divided into four groups, according to the peak temperature considered: ambient (20 °C, for control), 200 °C, 400 °C and 600 °C. The equipment used for heating the specimens was an electric furnace with a maximum capacity of 1000 °C from the SP Labor - SP1200 brand, as shown in Figure 1a. The specimens were thermally loaded at an average rate of 10 °C / min to the desired temperature, being exposed for an additional 30 minutes at constant temperature. After heating, the specimens were removed from the oven and cooled to room temperature. This procedure was adopted to avoid thermal gradients associated with sudden cooling. Table 1 presents a summary of the tests with the appropriate nomenclatures adopted in this stage to identify the specimens. The parameters related to the results, also presented in the table, will be described in Section 3.1.



**Figure 1.** Electric furnaces used in the experimental program: a) Stage I; b) Stage II.

**Table 1.** Identification (ID) of specimens for Stage I and summary of results.

ID	Temperature	$f_{c0}$	$f_{c0,mean}$	$(f_{c20} - f_{c0})/f_{c20}$	$\epsilon_{c1,\theta}$	$E_{cs\theta}$	$E_{cs\theta,mean}$	$(E_{cs20} - E_{cs\theta})/E_{cs20}$
	(°C)	(MPa)	(MPa)	-	-	(GPa)	(GPa)	-
CP1_20	Ambient	19.2	19.1	-	0.0033	19.5	19.4	-
CP2_20		19.0				19.4		
CP1_200	200	17.1	16.1	16%	0.0032	11.9	11.1	43.0%
CP2_200		15.2				10.2		
CP1_400	400	13.8	13.8	28%	0.0071	2.35	2.65	86.3%
CP2_400		13.7				2.95		
CP1_600	600	8.3	7.8	59%	0.0146	0.53	0.48	97.5%
CP2_600		7.4				0.43		

It is worth mentioning that, given the small dimensions of the specimens, it was assumed that the total heating time was sufficient to obtain homogenization of the temperature in the specimen. This hypothesis can be easily proved through theoretical analysis. In addition, it is worth mentioning the work of Chang et al. [48], where the authors adopted a constant external temperature for 1.5 to 2.5 hours for complete temperature homogenization in 15x30 cm specimens. In the present study, the volume of the specimen is approximately 15% of that used by Chang et al. [48] and, therefore, a period of 30 min would be more than enough for this homogenization, justifying the hypothesis assumed.

After heating and properly cooled, the specimens were tested in compression. The tests were performed with a loading rate of 0.05 mm/min up to rupture, using a servo-hydraulic actuator MTS model 204.63 with a load capacity of 100 kN. A pair of displacement transducers coupled to the specimen with the aid of acrylic rings was used to determine the strains. All information was collected automatically throughout the test. The objective of this step was to obtain the concrete stress-strain diagrams for specific temperatures.

The behavior of steel bars after being subjected to moderate temperatures was also investigated, following a procedure similar to that adopted for concrete. Six samples of 150 mm from the bars were tested in tension for ambient condition and after exposure to 250 °C and 500 °C for 30 min (same furnace used for the concrete specimens), with two samples for each condition. No special preparation was made for the samples, which were tested under displacement control at a rate of 5 mm/min on a universal testing machine model MTS 311 with a capacity of 1000 kN. The test was carried out without any additional external instrumentation and the measurements were only the total displacement of the actuator and the applied force. This strategy proved to be sufficient for a simple comparison between the different conditions.

## 2.2 Stage II

In Stage II, cylindrical reinforced concrete specimens with 15 cm in diameter, 30 cm in height and with 3 cm of cover were tested, divided into 5 groups according to the thermal loading time: 0 (room temperature, for control), 30, 60, 90 and 120 min. Despite the milder fire consideration in the present work, the times were chosen in order to

follow those observed in normative recommendations for a standard fire. The longitudinal reinforcement adopted for all samples was the same, comprised of four 10 mm diameter CA-50 ribbed bars, distributed uniformly in the perimeter. For each of the thermal loading groups from 0 to 90 min, two specimens were made with only two ties spaced 20 cm and two others with three stirrups spaced 10 cm, as shown in Figure 2a. Due to the occurrence of explosive spalling during heating for the configuration with two ties and high thermal loading times, the 120 min group had only two specimens with three ties tested. It is worth noting that the ties were used in an attempt to simulate the usual conditions i) with absence or few ties and ii) with usual spacing. The study of ties spacing that could provide greater gains in strength and ductility due to confinement is not scope of the work. For the thermal loading, an approximately linear heating rate was adopted, with a ramp between 4 and 5 °C / min, aiming to reproduce a milder loading condition, normally experienced in cases with low ventilation and low fire load. As pointed out by Chang et al. [48], results of fire tests on concrete columns [49] indicate heating rates of 2 to 4 °C / min for temperatures in the range of 250 to 750 °C. The use of constant rates represents a simplification, also adopted by Chang et al. [48]. The equipment used for heating was an Brasimet electric muffle with a maximum capacity of 1200 °C, as shown in Figure 1b. Seeking to reduce the heat exchange between the ends of the specimens and, thus, approach the problem to an one-dimensional heat flow condition during thermal loading, the ends of the specimens were thermally insulated with the aid of a 5 cm-thick stone wool insulation, as shown in Figure 2b. After heating, the specimens were removed from the oven and cooled naturally at room temperature, in the same fashion as in Stage I. It is important to highlight that specimens were free to expand and retract during heating and cooling processes, in an attempt to minimize associated thermal stresses. Table 2 presents a summary of the tests performed in Stage II, with the appropriate nomenclatures and test conditions. The parameters related to the results, also presented in the table, will be described in Section 3.2.

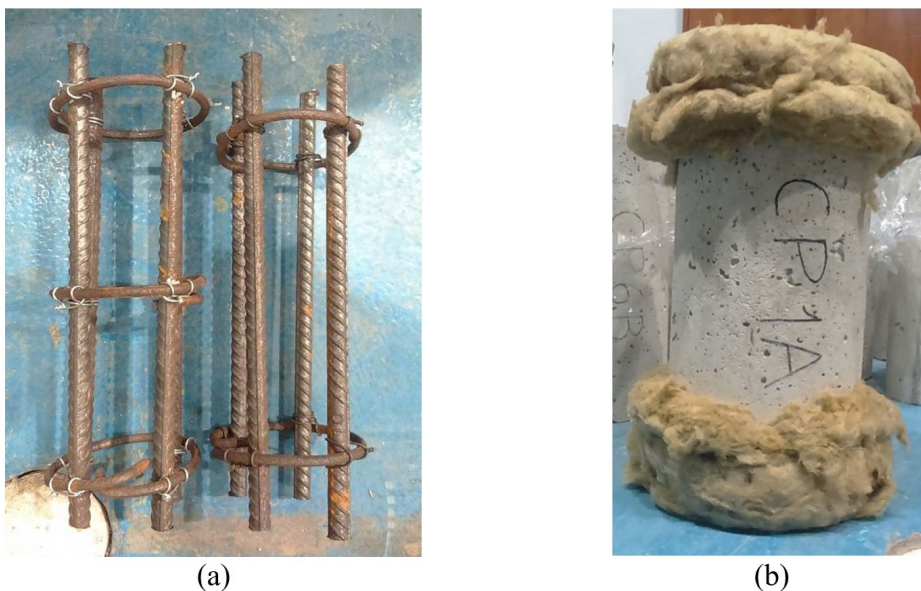


**Figure 2.** Preparation of Stage II specimens: a) reinforcement configuration with two and three ties; b) stone wool thermal insulation applied at the ends.

The compression tests were performed on a Controls model 50-C46Z00 testing machine, with a load capacity of 2000 kN up to rupture at a mechanical loading rate of 0.1 mm/min. As in Stage I, displacement transducers coupled to the specimen with acrylic rings were used to determine the strains during the test. Once again, all test information was automatically recorded by the data acquisition system. The objective of Stage II was to simulate a mild fire with a constant thermal load rate and considering typical fire duration times. The stress-strain relations obtained in Stage I were used for the theoretical analysis of the results of Stage II, where the cross-sectional temperature distribution is non-uniform and, therefore, the mechanical response varies along the radius.

**Table 2.** Identification (ID) of stub columns of Stage II and summary of results.

ID	Time of exposure	Number of ties	Maximum Temperature	Spalling ?	$\sigma_u$	$\sigma_{u,mean}$	$(\sigma_{u20} - \sigma_u) / \sigma_{u20}$
	(min)	-	(°C)	(Yes/No)	(MPa)	(MPa)	-
CP1_0_2	0	2	20	No	23.55	22.09	-
CP2_0_2	0	2	20	No	20.63		
CP1_0_3	0	3	20	No	20.04	19.80	-
CP2_0_3	0	3	20	No	19.55		
CP1_30_2	30	2	170	No	22.04	20.38	7.8%
CP2_30_2	30	2	169	No	18.71		
CP1_30_3	30	3	169	No	16.83	18.34	7.4%
CP2_30_3	30	3	185	No	19.85		
CP1_60_2	60	2	315	No	18.45	18.19	17.7%
CP2_60_2	60	2	318	No	17.92		
CP1_60_3	60	3	315	No	15.21	15.30	22.7%
CP2_60_3	60	3	313	No	15.39		
CP1_90_2	90	2	408	Yes	-	-	-
CP2_90_2	90	2	400	Yes	-	-	-
CP1_90_3	90	3	422	No	17.86	16.41	17.1%
CP2_90_3	90	3	423	No	14.96		
CP1_120_3	120	3	422	Yes	-	15.92	19.6%
CP2_120_3	120	3	496	No	15.92		

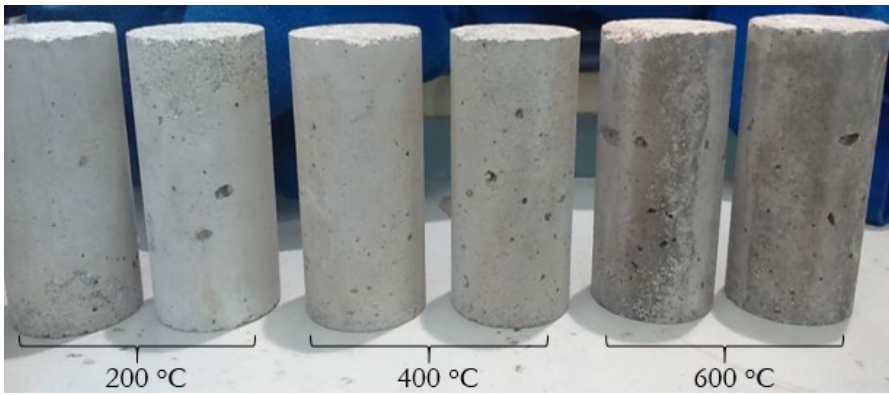
### 3 RESULTS AND DISCUSSIONS

#### 3.1 Stage I

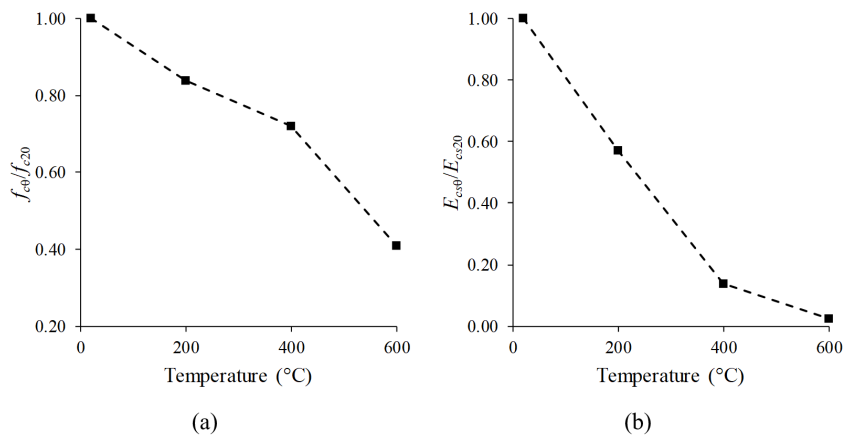
Regarding the color of the concrete, the specimens heated to 200 °C did not present any change, remaining with their original gray color. For the samples submitted to 400 °C, the color remained gray, but with pink points. Finally, the specimens heated to 600 °C showed a color change to a darker gray with reddish streaks, which indicates friability - liable to crumble or disintegrate - and high water suction [50]. Figure 3 illustrates the changes in the color of the plain concrete.

Table 1 shows the values of compressive strength and modulus of elasticity obtained in the tests for the concrete specimens and Figures 4a and 4b show, respectively, the variation of  $f_{c\theta}/f_{c20}$  and  $E_{cs\theta}/E_{cs20}$  with temperature, where  $f_{c\theta}$  is the compressive strength for a temperature  $\theta$ ,  $f_{c20}$  is strength at room temperature,  $E_{cs\theta}$  is the secant module at a temperature  $\theta$  and  $E_{cs20}$  is the secant module at room temperature – obtained as the slope of the secant line between 0 to 40% of the strength. As expected, it is observed that both the residual compressive strength and the modulus are reduced as the temperature of exposure increases, while the peak deformations increased. With respect to the strength, there was a reduction of approximately 15% for a temperature of 200 °C, 30% for 400 °C and 60% for 600 °C with respect to the control specimens. These retentions of residual strength are in accordance with the values found by Chan et al. [51] for normal strength concretes, as well as the values presented in Eurocode 2 [34].





**Figure 3.** Changes of color of plain concrete specimens exposed to temperatures of 200, 400 and 600 °C.



**Figure 4.** Retention of properties with temperature of exposure: a) compressive strength; b) secant modulus of elasticity.

Figure 5a illustrates the stress-strain relations obtained from the compression tests for the concrete specimens of Stage I. The curves for each temperature showed good consistency, and it is possible to observe, in addition to the erosion of strength already reported, reductions in modulus of elasticity and increases in the peak and ultimate strains with increasing temperatures. The stress-strain curves obtained in this stage will be used in Section 3.3, to perform theoretical correlation with the results obtained in the short columns of Stage II. Figure 5b shows the force vs actuator displacement results for the steel bars tested in tension. From the similarity between the responses, it is possible to observe that the behavior of the steel is not affected after exposure to temperatures up to 500 °C.

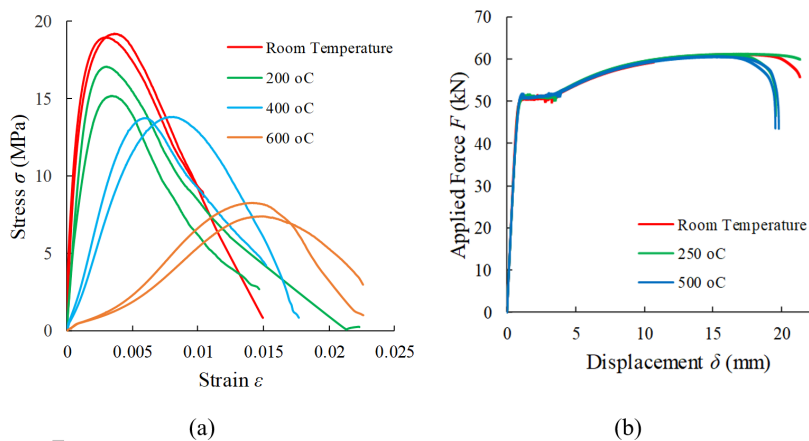


**Figure 5.** Response of materials after exposure to different temperatures: a) stress-strain relations for plain concrete; b) force-displacement curves for steel.

### 3.2 Stage II

During thermal loading, some specimens showed spalling from temperatures over 400 °C, as shown in Table 2. They had their cross section reduced and, therefore, were not subjected to compression tests, resulting in a reduction in the number of samples tested. The phenomenon occurred, consistently, for specimens with 2 ties. On the other hand, confirming expectations, samples containing 3 ties showed better control against spalling, associated with the confinement provided by the transverse reinforcement. Figure 6 illustrates the samples after explosive spalling.

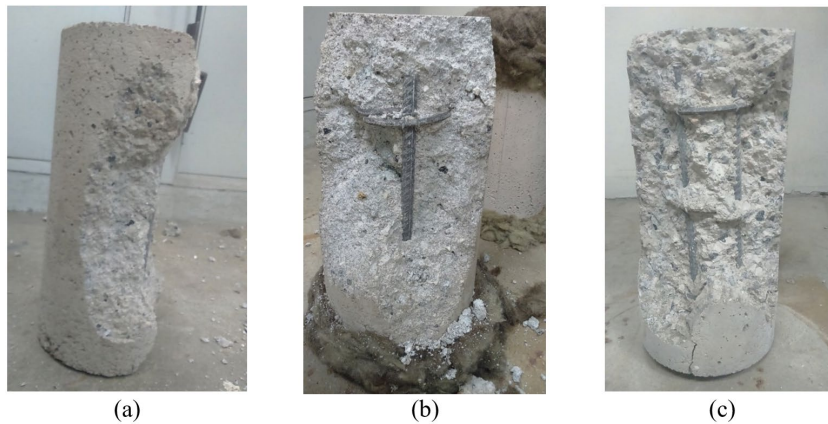


**Figure 6.** Spalling of specimens: a) CP1\_90\_2 (408 °C); b) CP2\_90\_2 (400 °C); c) CP1\_120\_3 (422 °C).

Figure 7 shows the failure modes of some of the short columns tested, where it is possible to observe the formation of surface cracks and the diagonal rupture pattern that occurred in some cases. Figure 8a and 8b show the curves for average stress  $\sigma_c$  vs strain  $\varepsilon$  of the short columns tested for conditions with two and three ties, respectively, where the average stress was obtained by dividing the applied force by the total area of the cross section. It can be noted some variability in the strengths of the two groups for similar exposure temperatures, as well as in the peaks of strain. However, in general, samples with 2 ties failed in a fragile manner with greater strength, expect for one of the specimens exposed for 30 min. Despite contributing to the confinement of the central portion of concrete and to a more ductile rupture at higher temperatures, it is known that the steel reinforcement introduces porous interfaces between steel and concrete, which can locally reduce the strength and influence the transport of water inside the heated concrete, increasing the risk of spalling [16]. In addition, the intermediate tie may have restricted the free expansion of concrete during heating, introducing thermal-induced damage. However, only analysis by microscopy or tomography could reveal in greater detail the extent of the resulting damage and the presence of the porous area. Figure 9 presents a comparison between the strengths of specimens with 2 and 3 ties for different exposure times, from where it is possible to observe more clearly the trend of columns with three stirrups to exhibit lower capacity than those with 2 ties. From Table 2 and Figure 9, it is worth noting that the reduction in strength in relation to the original condition reaches the order of 20% for exposure times of 60 min, with apparent stabilization for longer periods of time. It is also important to note the variation in the results, which may be associated with the material's own variability in terms of mechanical properties and imperfections.

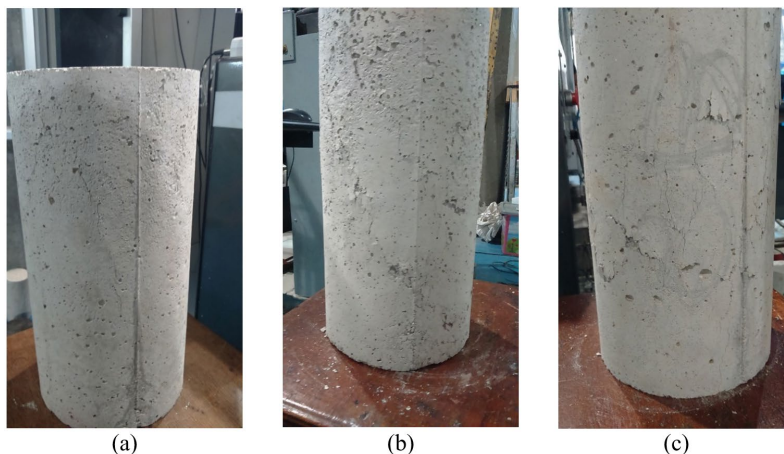


**Figure 7.** Examples of failure modes of reinforced concrete stub columns: a) CP1\_30\_2; b) CP1\_90\_3; c) CP2\_120\_3.

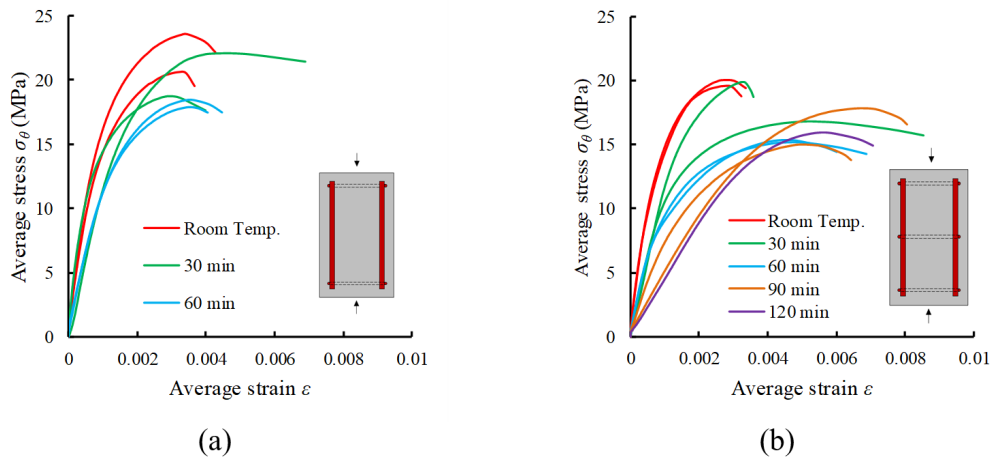


Figure 8. Average stress vs stress curves for reinforced concrete stub columns: a) two ties; b) three ties.

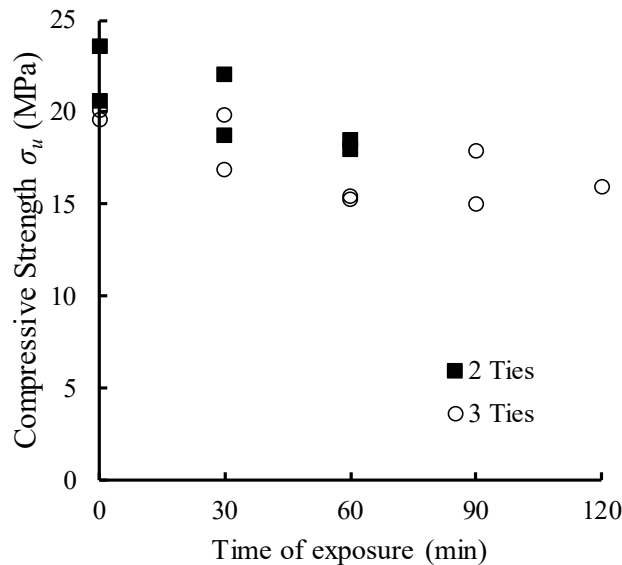
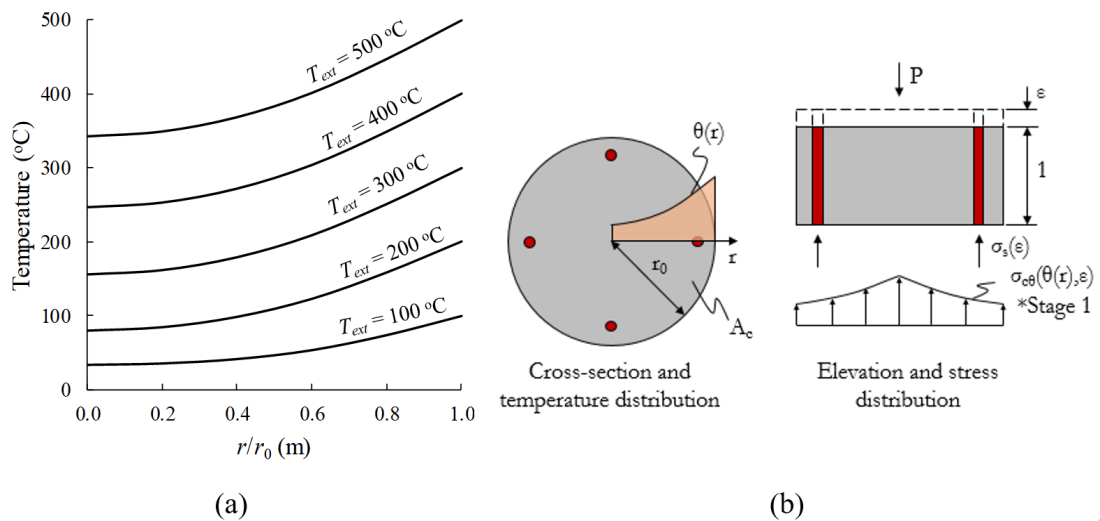


Figure 9. Strength of stub columns with two or three lateral ties for different times of exposure.

### 3.3 Comparison with Theoretical Model

For the theoretical prediction, the first step is to determine the cross-sectional temperature distribution with time. For this, a one-dimensional heat transfer analytical model was used (long cylinders without internal heat generation) and considering the problem of imposing a temperature at the outer surface. Thus, the solution can be obtained using the variable separation technique for a given initial temperature distribution in the cylinder [52]. As the temperature in the case in question is variable, an incremental solution was adopted where, for each increment of 20 °C applied to the surface, the profile obtained in the previous step was considered. In a simplified way, it was assumed that the thermal conductivity coefficient of the concrete,  $k$ , the specific heat,  $c_p$ , and the specific mass,  $\rho$ , remained constant throughout the test, with values  $k = 1.3 \text{ W/(m °C)}$ ,  $c_p = 1000 \text{ J/(kg °C)}$  and  $\rho = 2400 \text{ kg / m}^3$ , respectively. It was also admitted that the initial temperature in the cylinder was uniform and equal to 20 °C, the heating rate was 4 °C/min and that the temperature in the air inside the muffle was equal to the temperature on the outer surface of the concrete cylinder. With these data, it was possible to obtain the temperature distribution shown in Figure 10a.



**Figure 10.** Theoretical model: a) temperature distribution with the relative distance between center and outer face ( $r/r_0$ ); b) stress distribution as a function of specific strain and temperature profile.

With the profile determined, the next step is to determine the average stress vs. strain curve for the column. In this case, for each imposed strain value, the stresses at each point of the concrete cross section were estimated from the interpolation of the stress-strain curves ( $\sigma_{c\theta}-\varepsilon$ ) idealized for each temperature, according to the Equation 1 recommended in the Model Code 2010 [53].

$$\sigma_{c\theta}(\theta, \varepsilon) = f_{c\theta} \frac{k_c \cdot \left( \frac{\varepsilon}{\varepsilon_{c1\theta}} \right) - \left( \frac{\varepsilon}{\varepsilon_{c1\theta}} \right)^2}{1 + (k_c - 2) \left( \frac{\varepsilon}{\varepsilon_{c1\theta}} \right)} \tag{1}$$

where  $f_{c\theta}$  and  $\varepsilon_{c1\theta}$  are respectively the compressive strength and strain for the peak of stress for a given temperature  $\theta$ ,  $k_c$  is a plasticity number defined as the ratio between the initial tangent module,  $E_{ci}$ , and  $E_{c1} = f_{c\theta}/\varepsilon_{c1\theta}$ . In the present work, the parameters adopted in the idealized curves were adjusted to the experimental results obtained in Stage I (see Table 1), with an additional reduction factor multiplied to the concrete compressive strength  $k_{esc} = 0.8$  to incorporate the scale effect [54] and possible changes in the sample's collapse mechanisms by the introduction of the metallic reinforcement. On the other hand, the stiffness and the strain at peak were maintained according to Table 1, with  $k_c$  values equal to 5.40, 3.98, 1.93 and 1.83, respectively, for temperatures of 20 °C, 200 °C, 400 °C and 600 °C. In the case of intermediate temperatures, the parameters were interpolated. Moreover, it was verified through tests carried out with steel that the residual properties were not affected for temperatures up to 500 °C. Therefore, the ideal model is bilinear, with elastic modulus  $E_s = 200$  GPa and yield strength  $f_y = 500$  MPa. Finally, the force mobilized  $P$  as a function of an imposed strain can be obtained as shown in Figure 10b and the average stress  $\sigma_c$  is calculated according to the sectional analysis defined in Equation 2 below:

$$\sigma_c(\varepsilon) = \frac{P(\varepsilon)}{A_c} = \frac{k_{esc} \int_0^{r_0} 2\pi \sigma_{c\theta}(\theta(r), \varepsilon) dr + A_s \sigma_s(\varepsilon)}{A_c} \tag{2}$$

where  $r_0$  is the cylinder radius,  $\theta$  is the temperature inside the cylinder (function of radius),  $A_s = 4 \times 78.5 \text{ mm}^2$  is the total reinforcing steel area,  $A_c$  is the concrete area and  $\sigma_s = \varepsilon E_s < f_y$  is the stress at steel. In the calculation, thermal stresses associated with gradients or eventual restraints were not considered.

Figures 11a-e present the comparisons between the theoretical and experimental predictions for the various conditions investigated. Comparing the results, it is possible to conclude that, taking into account the simplicity of the analysis, the correlation between experiment and theoretical model is good, although in some cases the predictions were above the experimental values, especially for longer exposure times. Figure 11f shows the ratio between the strengths obtained experimentally and using the theoretical model, indicating a mean of 0.916 and a coefficient of variation (CoV) of 9.31%. The differences for longer exposure times are explained by a weakening of the outer layers in direct contact with the hot air and by the presence of thermal stresses and damage – effects not captured in sectional analysis. Nevertheless, it is important to note that none of the samples reached a surface temperature of 500 °C and the use of

the established method of the 500 °C isotherm would be extremely against safety, as it would lead to the false conclusion that no strength loss would be experienced by the columns with respect to the original condition. Therefore, questions can be raised regarding its applicability at moderate temperatures.

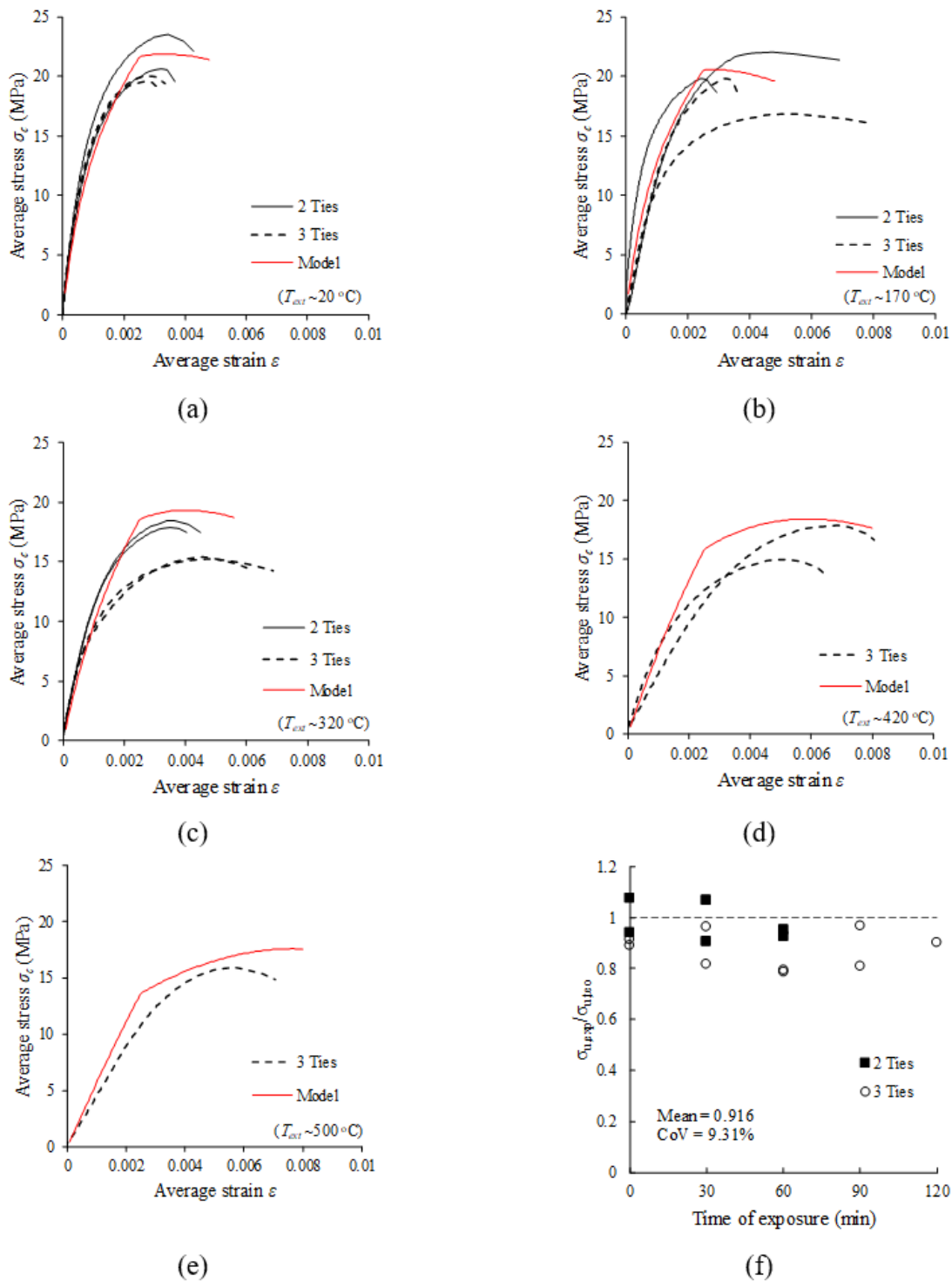


**Figure 11.** Comparison between experimental and analytical results: a) room temperature; b) 30 min of exposure; c) 60 min of exposure; d) 90 min of exposure; e) 120 min of exposure; f) ratio between experimental and theoretical strengths ( $\sigma_{u,exp}/\sigma_{u,teo}$ ).

## 4 CONCLUSIONS

The conclusions obtained from the following work are:

- The experimental results showed that the residual strength of the concrete investigated in the study (low mechanical strength) is affected by temperature and that the reductions are in good agreement with those recommended in the Eurocode 2 [34]. The reductions reached 60% for concretes subjected to 600 °C for 30 min, in relation to the ambient condition;
- The spalling phenomenon was observed during thermal loading, even at temperatures of around 400 °C, which may result in a reduction in the cross-sectional area of the structural element and direct exposure of reinforcing steel to fire. The adoption of intermediate ties proved to be adequate in preventing the phenomenon, as pointed out in the literature [44]–[46];
- Short columns with intermediate ties presented lower strength, but, in general, greater ductility. This difference was observed for exposure times of 30 and 60 min and must be associated with the appearance of thermal-induced stresses and damage caused by the restraints to expansion associated to the introduction of the intermediate tie. This result contrasts with the observations in the literature for concretes with higher mechanical strengths, which indicate an increase in residual strength due to the action of confinement. It is noteworthy that the transverse reinforcement rate adopted in the present work is low (compatible with spacing and diameters used in practice) and, therefore, a reduced confinement action would also be expected;
- The theoretical model, although simple, proved to be adequate for theoretical prediction of behavior. Differences can be explained by the influence of thermal stresses and imperfections generated by the introduction of metallic reinforcement (not covered in the analysis). A mean of 0.916 was obtained for the ratios between experimental and theoretical strengths;
- Taking into account that none of the tested stub columns reached a surface temperature of 500 °C, but that strength reductions of up to 20% were obtained in relation to the ambient condition, the application of the 500 °C isotherm method would lead to a strength estimate against safety and, therefore, its applicability for moderate temperatures must be better evaluated.

## ACKNOWLEDGEMENTS

All tests were performed at the Structures and Materials Laboratory of the Pontifical Catholic University of Rio de Janeiro. This study was partially funded by the Coordenação de Aperfeiçoamento de Pessoal de Nível Superior - CAPES, finance code 001 - and by the Brazilian agencies FAPERJ and CNPq.

## REFERENCES

- [1] P. K. Mehta and P. J. Monteiro, *Concrete: Microstructure, Properties and Materials*. New York: McGraw-Hill Education, 2017.
- [2] I. A. Fletcher, S. Welch, J. L. Torero, R. O. Carvel, and A. Usmani, "Behaviour of concrete structures in fire," *Therm. Sci.*, vol. 11, no. 2, pp. 37–52, 2007.
- [3] W. M. Lin, T. D. Lin, & L. J, "Microstructures of fire-damaged concrete", *Mater. J.*, vol. 93, no. 3, pp. 199–205, 1996.
- [4] B. Fernandes, A. M. Gil, F. L. Bolina, and B. F. Tutikian, "Microestrutura do concreto submetido a altas temperaturas: alterações físico-químicas e técnicas de análise," *Rev. IBRACON Estrut. Mater.*, vol. 10, no. 4, pp. 838–863, 2017.
- [5] E. Annerel and L. Taerwe, "Revealing the temperature history in concrete after fire exposure by microscopic analysis," *Cement Concr. Res.*, vol. 39, no. 12, pp. 1239–1249, 2009.
- [6] J. C. Liu, K. H. Tan, and Y. Yao, "A new perspective on nature of fire-induced spalling in concrete," *Constr. Build. Mater.*, vol. 184, pp. 581–590, 2018.
- [7] C. G. Han, Y. S. Hwang, S. H. Yang, and N. Gowripalan, "Performance of spalling resistance of high performance concrete with polypropylene fiber contents and lateral confinement," *Cement Concr. Res.*, vol. 35, no. 9, pp. 1747–1753, 2005.
- [8] M. Zeiml, D. Leithner, R. Lackner, and H. A. Mang, "How do polypropylene fibers improve the spalling behavior of in-situ concrete," *Cement Concr. Res.*, vol. 36, no. 5, pp. 929–942, 2006.
- [9] Y. S. Heo, J. G. Sanjayan, C. G. Han, and M. C. Han, "Synergistic effect of combined fibers for spalling protection of concrete in fire," *Cement Concr. Res.*, vol. 40, no. 10, pp. 1547–1554, 2010.
- [10] I. B. Topçu and C. Karakurt, "Properties of reinforced concrete steel rebars exposed to high temperatures," *Res. Lett. Mater. Sci.*, vol. 2008, pp. 1–4, 2008.
- [11] R. Chijiwa, Y. Yoshida, R. Uemori, H. Tamehiro, K. Funato, & Y. Horii, "Development and practical application of fire-resistant steel for buildings", Nippon Steel Technical Report, pp. 47-55, 199.

- [12] G. A. Khoury, "Effect of fire on concrete and concrete structures," *Prog. Struct. Eng. Mater.*, vol. 2, no. 4, pp. 429–447, 2000.
- [13] P. D. Morley and R. Royles, "Response of the bond in reinforced concrete to high temperatures," *Mag. Concr. Res.*, vol. 35, no. 123, pp. 67–74, 1983.
- [14] C. H. Chiang and C. L. Tsai, "Time-temperature analysis of bond strength of a rebar after fire exposure," *Cement Concr. Res.*, vol. 33, no. 10, pp. 1651–1654, 2003.
- [15] A. F. Bingöl and R. Gül, "Residual bond strength between steel bars and concrete after elevated temperatures," *Fire Saf. J.*, vol. 44, no. 6, pp. 854–859, 2009.
- [16] J. H. Chung and G. R. Consolazio, "Numerical modeling of transport phenomena in reinforced concrete exposed to elevated temperatures," *Cement Concr. Res.*, vol. 35, no. 3, pp. 597–608, 2005.
- [17] A. H. Shah and U. K. Sharma, "Fire resistance and spalling performance of confined concrete columns," *Constr. Build. Mater.*, vol. 156, pp. 161–174, 2017.
- [18] K. A. Zaidi, U. K. Sharma, and N. M. Bhandari, "Effect of temperature on uni-axial compressive behavior of confined concrete," *Fire Saf. J.*, vol. 48, pp. 58–68, 2012.
- [19] V. Kodur and R. McGrath, "Fire endurance of high strength concrete columns," *Fire Technol.*, vol. 39, no. 1, pp. 73–87, 2003.
- [20] K. H. Tan and Y. Yao, "Fire resistance of four-face heated reinforced concrete columns," *J. Struct. Eng.*, vol. 129, no. 9, pp. 1220–1229, 2003.
- [21] V. K. R. Kodur, F. P. Cheng, T. C. Wang, and M. A. Sultan, "Effect of strength and fiber reinforcement on fire resistance of high-strength concrete columns," *J. Struct. Eng.*, vol. 129, no. 2, pp. 253–259, 2003.
- [22] J. M. Franssen, B. Zhao, and T. Gernay, "Experimental tests and numerical modelling on slender steel columns at high temperatures," *J. Struct. Fire Eng.*, vol. 7, no. 1, pp. 30–40, 2016.
- [23] Y. H. Chen, Y. F. Chang, G. C. Yao, and M. S. Sheu, "Experimental research on post-fire behaviour of reinforced concrete columns," *Fire Saf. J.*, vol. 44, no. 5, pp. 741–748, 2009.
- [24] J. M. Franssen and J. C. Dotreppe, "Fire tests and calculation methods for circular concrete columns," *Fire Technol.*, vol. 39, no. 1, pp. 89–97, 2003.
- [25] F. Ali, A. Nadjai, and S. Choi, "S., "Numerical and experimental investigation of the behavior of high strength concrete columns in fire," *Eng. Struct.*, vol. 32, no. 5, pp. 1236–1243, 2010.
- [26] International Organization for Standardization, *Fire Resistance Tests – Elements of Building Construction*, ISO-834, 1975.
- [27] M. J. Terro, "Numerical modeling of the behavior of concrete structures in fire," *ACI Struct. J.*, vol. 95, pp. 183–193, 1998.
- [28] R. B. Caldas, J. B. M. Sousa Jr., and R. H. Fakury, "Interaction diagrams for reinforced concrete sections subjected to fire," *Eng. Struct.*, vol. 32, no. 9, pp. 2832–2838, 2010.
- [29] J. C. Dotreppe, J. M. Franssen, and Y. Vanderzeipen, "Calculation method for design of reinforced concrete columns under fire conditions," *ACI Struct. J.*, vol. 96, no. 1, pp. 9–18, 1999.
- [30] V. K. R. Kodur, T. C. Wang, and F. P. Cheng, "Predicting the fire resistance behaviour of high strength concrete columns," *Cement Concr. Compos.*, vol. 26, no. 2, pp. 141–153, 2004.
- [31] S. Bratina, B. Čas, M. Saje, and I. Planinc, "Numerical modelling of behaviour of reinforced concrete columns in fire and comparison with Eurocode 2," *Int. J. Solids Struct.*, vol. 42, no. 21-22, pp. 5715–5733, 2005.
- [32] D. Di Capua and A. R. Mari, "Nonlinear analysis of reinforced concrete cross-sections exposed to fire," *Fire Saf. J.*, vol. 42, no. 2, pp. 139–149, 2007.
- [33] S. F. El-Fitiyany and M. A. Youssef, "Assessing the flexural and axial behaviour of reinforced concrete members at elevated temperatures using sectional analysis," *Fire Saf. J.*, vol. 44, no. 5, pp. 691–703, 2009.
- [34] European Committee for Standardization, *Design of Concrete Structures, Part 1–2: Structural Fire Design*, Eurocode 2, 2004.
- [35] V. K. R. Kodur, B. Yu, and M. M. S. Dwaikat, "A simplified approach for predicting temperature in reinforced concrete members exposed to standard fire," *Fire Saf. J.*, vol. 56, pp. 39–51, 2013.
- [36] T. T. Lie, *Structural Fire Protection* (ASCE Manuals and Reports on Engineering Practice, 78). New York: American Society of Civil Engineers, 1992.
- [37] U. Wickström, *A Very Simple Method for Estimating Temperature in Fire Exposed Concrete Structures* (Fire Technology Technical Report SP-RAPP, 46). Swedish National Testing Institute, 1986, pp. 186–194.
- [38] European Committee for Standardization, *Actions on Structures – Part 1-2: General Actions – Actions on Structures Exposed to Fire*, Eurocode 1, 2002.
- [39] A. Law, J. Stern-Gottfried, M. Gillie, and G. Rein, "The influence of travelling fires on a concrete frame," *Eng. Struct.*, vol. 33, no. 5, pp. 1635–1642, 2011.
- [40] X. Dai, S. Welch, and A. Usmani, "A critical review of "travelling fire" scenarios for performance-based structural engineering," *Fire Saf. J.*, vol. 91, pp. 568–578, 2017.

- [41] J. Stern-Gottfried and G. Rein, "Travelling fires for structural design—Part I: literature review," *Fire Saf. J.*, vol. 54, pp. 74–85, 2012.
- [42] D. Rush and D. Lange, "Towards a fragility assessment of a concrete column exposed to a real fire—Tisova Fire Test," *Eng. Struct.*, vol. 150, pp. 537–549, 2017.
- [43] A. Law, J. Stern-Gottfried, M. Gillie, and G. Rein, "The influence of travelling fires on a concrete frame," *Eng. Struct.*, vol. 33, no. 5, pp. 1635–1642, 2011.
- [44] M. J. Terro and S. A. Hamoush, "Effect of confinement on siliceous aggregate concrete subjected to elevated temperatures and cyclic heating," *Mater. J.*, vol. 94, no. 2, pp. 83–89, 1997.
- [45] B. Wu, X. P. Su, H. Li, and J. Yuan, "Effect of high temperature on residual mechanical properties of confined and unconfined high-strength concrete," *Mater. J.*, vol. 99, no. 4, pp. 399–407, 2002.
- [46] K. A. Zaidi, U. K. Sharma, and N. M. Bhandari, "Effect of temperature on uni-axial compressive behavior of confined concrete," *Fire Saf. J.*, vol. 48, pp. 58–68, 2012.
- [47] J. M. Watts Jr. and M. E. Kaplan, "Fire risk index for historic buildings," *Fire Technol.*, vol. 37, no. 2, pp. 167–180, 2001.
- [48] Y. F. Chang, Y. H. Chen, M. S. Sheu, and G. C. Yao, "Residual stress–strain relationship for concrete after exposure to high temperatures," *Cement Concr. Res.*, vol. 36, no. 10, pp. 1999–2005, 2006.
- [49] M. S. Sheu, Y. H. Chen, Y. F. Chang, and M. D. Yeh, *Seismic Resistance of Fired-Damaged Interior RC Columns, Project No. 092-301070000-G1020*. Taipei, Taiwan: ABRI, Ministry of Interior, 2004.
- [50] N. R. Short, J. A. Purkiss, and S. E. Guise, "Assessment of fire damaged concrete using colour image analysis," *Constr. Build. Mater.*, vol. 15, no. 1, pp. 9–15, 2001.
- [51] Y. N. Chan, G. F. Peng, and M. Anson, "Residual strength and pore structure of high-strength concrete and normal strength concrete after exposure to high temperatures," *Cement Concr. Compos.*, vol. 21, no. 1, pp. 23–27, 1999.
- [52] Y. Cengel, *Heat and Mass Transfer: Fundamentals and Applications*. New York: McGraw-Hill Higher Education, 2014.
- [53] Fédération Internationale du Béton, *Fib Model Code for Concrete Structures 2010*, 2013.
- [54] A. Carpinteri, G. Ferro, and I. Monetto, "Scale effects in uniaxially compressed concrete specimens," *Mag. Concr. Res.*, vol. 51, no. 3, pp. 217–225, 1999.

---

**Author contributions:** EHBL: conceptualization, data analysis, writing; DCTC: conceptualization, writing, funding acquisition, supervision.

**Editors:** Ricardo Carrazedo, José Luiz Antunes de Oliveira e Sousa, Guilherme Aris Parsekian.





ORIGINAL ARTICLE

# Strain, natural frequency, damping coefficient and elastic modulus of mortar beams determined by fiber Bragg grating (FBG) sensors

*Deformação específica, frequência natural, coeficiente de amortecimento e módulo elástico de vigas de argamassa determinados por sensores em fibra ótica com rede de Bragg (FBG)*

Gustavo Macioski<sup>a</sup>

Valmir de Oliveira<sup>b</sup>

Marcelo Henrique Farias de Medeiros<sup>a</sup>

<sup>a</sup>Universidade Federal do Paraná – UFPR, Programa de Pós-graduação em Engenharia Civil – PPGEC, Curitiba, PR, Brasil

<sup>b</sup>Universidade Tecnológica Federal do Paraná – UTFPR, Programa de Pós-graduação em Engenharia Elétrica e Informática Industrial - CPGEI, Curitiba, PR, Brasil

Received 17 June 2020

Accepted 11 September 2020

**Abstract:** Structural health monitoring can detect anomalies in time, allowing the implementation of more efficient maintenance and repair actions in special engineering structures. An alternative in the monitoring and evaluation of structures in civil engineering is the use of optical fibers inscribed with Bragg gratings (FBG or Fiber Bragg Grating). This paper aims to compare available techniques to estimate the elastic modulus of cementitious composites, as well as contribute to the application of optical fiber sensors in the monitoring of strain, natural vibration frequency, damping coefficient and elastic modulus of mortar beams. The FBG sensors manufactured and calibrated by the authors presented a good precision for measuring those parameters in mortar samples. The results show that FBG sensors and strain gauge sensors present a similar result for strain and estimation of the elastic module (static and dynamic), therefore, bare FBGs could be further investigated for non-destructive testing.

**Keywords:** modulus of elasticity, structural analysis, impulse excitation of vibration, non-destructive testing, optical fiber sensors.

**Resumo:** O monitoramento estrutural pode detectar anomalias no tempo, permitindo a implementação de ações de manutenção e reparação mais eficientes em estruturas de obras de arte. Uma alternativa no monitoramento e avaliação de estruturas em engenharia civil é a utilização de fibras óticas inscritas com redes de Bragg (FBG ou *Fiber Bragg Grating*). Este trabalho visa comparar as técnicas disponíveis para estimar o módulo elástico de compósitos cimentícios, bem como contribuir para a aplicação de sensores de fibra ótica na avaliação da tensão, frequência natural de vibração, coeficiente de amortecimento e módulo elástico de vigas de argamassa. Os sensores FBG fabricados e calibrados pelos autores apresentaram uma boa precisão na medição destes parâmetros em amostras de argamassa. Os resultados mostram que os sensores FBG e strain gauges apresentam resultados semelhantes para a deformação específica e estimativa do módulo elástico (estático e dinâmico), portanto, FBGs nuas poderiam ser investigadas mais detalhadamente em testes não-destrutivos.

**Palavras-chave:** módulo de elasticidade, análise estrutural, impulso de excitação de vibração, ensaio não destrutivo, sensores em fibra ótica.

**How to cite:** G. Macioski, V. Oliveira, and M. H. F. Medeiros, “Strain, natural frequency, damping coefficient and elastic modulus of mortar beams determined by fiber Bragg grating (FBG) sensors”, *Rev. IBRACON Estrut. Mater.*, vol. 14, no. 3, e14312, 2021, <https://doi.org/10.1590/S1983-41952021000300012>

Corresponding author: Gustavo Macioski. E-mail: [gmacioski@gmail.com](mailto:gmacioski@gmail.com)

Financial support: This study was financed in part by the “Coordenação de Aperfeiçoamento de Pessoal de Nível Superior - Brasil (CAPES)” - Finance Code 001.

Conflict of interest: Nothing to declare.



This is an Open Access article distributed under the terms of the Creative Commons Attribution License, which permits unrestricted use, distribution, and reproduction in any medium, provided the original work is properly cited.

## INTRODUCTION

Young's modulus, elastic modulus or modulus of elasticity is a mechanical parameter that represents the stiffness of a solid material that can be affected by the material chemical composition, microstructure, and defects [1]–[5]. It can be obtained by the ratio of the requested normal stress to the specific deformation suffered by the material [6].

Determining this parameter is essential for the calculation of the serviceability requirements of structures defined by ACI 318 Building Code for concrete structure design [7] and other international structural standards. Mindess et al. [8] emphasize that from the elastic modulus it is possible to estimate the time of support removal during construction, check excessive deformation of beams and estimate decompression limits, crack opening and vibration frequency in structures. Thus, all structural analysis depends directly on the elastic modulus of materials. Although this parameter can be estimated from the compressive strength, the elastic modulus can also be obtained experimentally by quasi-static or dynamic tests.

In quasi-static tests, a load is uniformly applied over a section and the strain related to the load is measured during the destructive test [9]. This methodology is the most used for the characterization of elastic modulus in concrete and it is standardized by ASTM C469 [10].

The strain measurement during the static test is usually performed by strain gauges or displacement transducers during the test, such as LVDTs (inductive transducers) and dial indicators (mechanical transducers) [11]–[15]. Similarly, during compression testing, some authors have already used fiber Bragg grating sensors (FBGs) to monitor concrete strain to calculate static elastic modulus [16], [17]. FBGs are optical fiber-based sensors able to measure strain and temperature due to its light reflection properties [18], its inscribing process and measuring principle will be further explained.

For Mobley [19], in the dynamic tests, the aim is to evaluate the performance of the structures, thus enabling the safety evaluation and the elaboration or confirmation of existing mathematical models. In dynamic tests, the elastic modulus is determined from the wave ability to propagate within the material. Since this is a parameter that can be obtained in the same sample (nondestructive testing) over a certain period, the evaluation of the dynamic elastic modulus of concrete is widely used in the evaluation of concrete durability (diagnosis of infrastructure).

It is noteworthy that dynamic tests are not affected by creep since the vibration levels applied to the samples imply very low stresses [20]. For this reason, Mehta and Monteiro [21] consider the dynamic elastic modulus in concrete and mortars approximately equal to the tangent modulus at the origin of the stress-strain curve determined in the static test and, therefore, up to 30% higher than the static modulus obtained in compression tests. In dynamic methods, the determination of the elastic modulus depends directly on the isotropy of the material, the support conditions and the position of the actuators and receivers.

For dynamic testing in concrete, ASTM C597 [22] standardizes the pulse velocity method for obtaining its dynamic elastic modulus [15], [23]. While ASTM C215 [24] describes the determination of the dynamic modulus in cylindrical samples by forced excitation using accelerometers [11], [14].

Similarly, ASTM E1875 [25] and ASTM E1876 [26] standards describe a similar vibration test (for different geometries and materials) by forced excitation and resonance techniques, respectively. While the first method evaluates the damped frequency of the material after an impact, the second method detects the resonance phenomenon when the material is continuously excited at different frequencies [13], [27]. In ASTM E1875 [25] and ASTM E1876 [26] standards, the type of sensor to be used is not described. However, the frequency response shall be measured within 1 Hz precision.

Indentation techniques can also be applied to estimate the elastic modulus of materials due to a probe penetration on the surface of a sample. This test is usually performed on a small scale (nano and micro indentation); hence, it does not allow the evaluation of the elastic modulus of heterogeneous materials. However, the method has already been used in the evaluation of the elastic modulus of crystalline phases of Portland cement, for example [28]–[31].

Using FBG, some authors have already evaluated the deformation of structural elements [32]–[39], the stress distribution within the concrete [40] and corrosion processes [41]. Dynamic and vibration tests were already performed by FBG sensors [42]–[44]. However, no research was found in the literature to estimate the static modulus of concretes and mortars by non-destructive simple bending tests using FBG. Also, it was not possible to find researches that have used optical sensors to determine the dynamic elastic modulus of materials since those researches are focused on measuring only deformations and vibration frequencies.

Given the different testing methods available for determining the elastic modulus of a material, and the different types of sensors available, a study is required to verify the possibility of performing these tests using fiber Bragg gratings sensors (FBG). Also, there is a need to understand how different sensors such as the FBG can influence the final results for strain,

natural frequency, damping coefficient and elastic modulus of materials. Table 1 shows the main contributions of this study and the methods and sensors already used by other authors [14], [17], [27], [33]–[37], [40], [45]–[55].

**Table 1.** Sensors applied to mortar and concrete monitoring.

	Dial indicator/ LVDT	Strain gauge	FBG	Microphone	Accelerometer
Displacement	□●				
Strain		□●	□●		
Frequency of vibration		□●	□●	□●	□●
Damping coefficient		□●	●	□●	●
Static modulus by bending	●	□●	●		
Dynamic modulus		●	●	□●	□●

□ Literature review ● This study

Thus, this paper aims to present the structural evaluation of mortar beams instrumented with different sensors, including FBG, for the determination of elastic modulus (static and dynamic). This research aims to contribute to the comparison of existing methods and validate the use of FBG as a sensor in the determination of parameters used in the characterization of materials and validation of structural designs, as well as in the diagnosis of existing structures.

### FIBER BRAGG GRATING (FBG)

Optical fiber is a flexible and transparent filament made from extruded glass or plastic. Standard optical fiber has a diameter of a few micrometers (125µm), slightly larger than human hair, and it is often used as a conductor of coded light [56].

Optical fiber is made up of two main components: core and cladding. The cladding reflects the diffused light into the core, ensuring that light transmission through it has a minimal loss. Thus, light is maintained in the core through total internal reflection effect [57]. This makes the fiber act as a waveguide, transmitting light between the two ends.

Due to the diffraction phenomenon, it is possible to change the refractive index of the glass in specific sections periodically, creating an optical filter inside the fiber. This modification is possible due to the photosensitivity of the optical fiber, which allows a permanent change in the refractive index in the fiber core when exposed to ultraviolet (UV) light [53]. Although not fully understood, this phenomenon occurs due to the existence of defects related to the incorporation of germanium atoms in the glassy structure of optical fibers during their manufacture, which when exposed to UV radiation break their bonds and generate light absorption bands [58].

Some techniques allow the improvement of fiber photosensitivity such as increasing germanium concentration in the fiber core and the use of co-dopants as boron during their manufacture. Another technique also used is hydrogenation, which consists of exposing the fiber to hydrogen in a high-pressure chamber [18], [59].

After inscribing a Bragg grating in the optical fiber core, the material will develop the ability to reflect a specific wavelength as a function of the grating spacing created. The process of acquiring or interrogating an FBG is performed by connecting a broadband light into the fiber to monitor the optical spectrum of light transmitted or reflected by the FBG [60], as it can be seen in Figure 1.

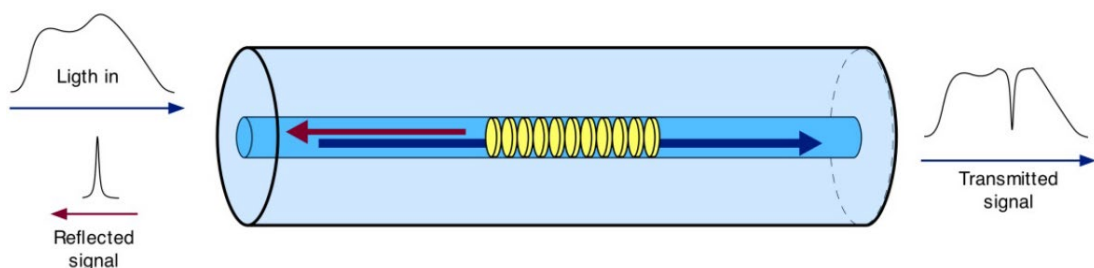


**Figure 1.** Transmitted and reflected signals during the interrogation of an FBG sensor [61]

The peak wavelength that arises after the fabrication of an FBG sensor is described by Equation 1, where  $\lambda_B$  is the Bragg wavelength (nm),  $n_{ef}$  is the effective fiber core refractive index, and  $A$  is half the spacing between phase mask grids (nm) used during the inscribing process, known as the phase mask period [58].

$$\lambda_B = 2 \cdot n_{ef} \cdot A \tag{1}$$

From this light reflection property, the reflected signal can be calibrated for changes in the sensor. When the fiber undergoes axial deformations or temperature changes, there is a change in the microstructure spacing and, consequently, in the Bragg wavelength. There is also some variation in the refractive index from the photoelastic effect. These effects are independent for each existing FBG in a fiber optic segment. The strain  $\Delta\varepsilon$  ( $\mu\text{m}/\text{m}$ ) and temperature  $\Delta T$  ( $^\circ\text{C}$ ) sensitivity of an FBG sensor can be determined by the change in the wavelength spectrum  $\Delta\lambda_b$  (nm), as described by Equation 2 [62].

$$\frac{\Delta\lambda_B}{\lambda_B} = (1 + p_e) \cdot \Delta\varepsilon + (\alpha_A + \alpha_n) \cdot \Delta T \tag{2}$$

With  $p_e$  being the photoelastic constant (-0.212),  $\alpha_A$  is the thermo-optical coefficient ( $8.3 \cdot 10^{-6}/^\circ\text{C}$ ) and  $\alpha_n$  the coefficient of thermal expansion of the fiber ( $0.55 \cdot 10^{-6}/^\circ\text{C}$ ) [63], [64].

## MATERIALS AND EXPERIMENTAL PROGRAM

### FBG manufacturing

For the manufacture of optical sensors, single-mode standard optical fiber (Draktel, SSMF G.652.D) with an effective refractive index of 1.468 was used. The inscribing was performed at a wavelength of 1540.9 nm using direct illumination by an ArF excimer laser (Coherent, Xantos XS model) operating at 193 nm with a frequency of 250 Hz and 1.5 mJ/pulse energy. The sensor manufacture is based on the diffraction of a UV beam emitted by a pulsed LASER using a phase mask (diffraction grating) to create a Bragg grating into the fiber core. During the inscribing process, a couple of mirrors are used to adjust the beam height and a cylindrical lens is used to focus the beam into the fiber core. Details on the manufacturing setup and inscribing process can be observed in Figure 2.

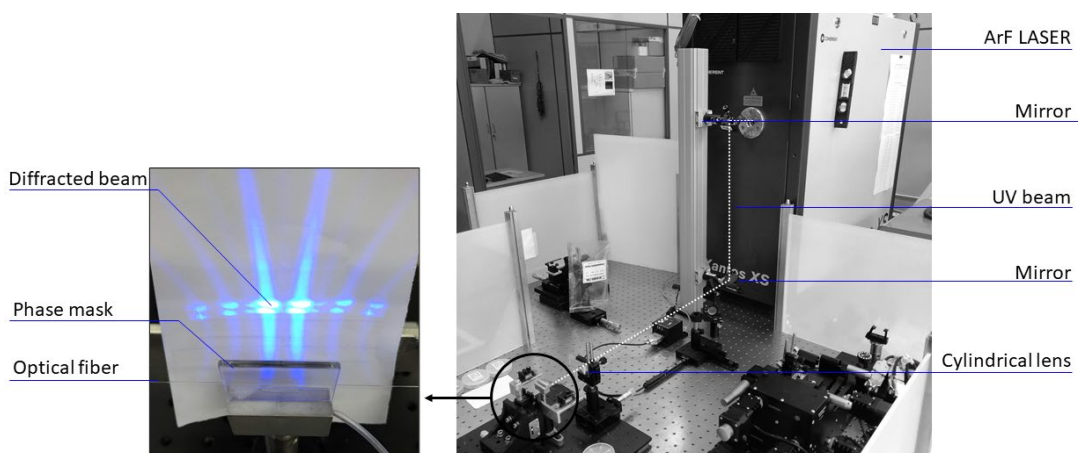


Figure 2. FBG inscribing process

After the FBG inscribing process, the FBG was calibrated according to its response to strain. A digital dial indicator (Mitutoyo, S1012M) was used in a servomotor apparatus for that purpose. The fibers were fixed to the metal ends of

the apparatus using an epoxy glue with a drying period of 24 hours. For the calibration, ten wavelength measurements were made for each fiber deformation in three stretching cycles. The measurements were performed with the aid of an optical interrogator (MicronOptics, model SM-125).

### Specimen preparation

For the evaluation of the structural elements, mortar prisms were molded using Portland cement type III according to ASTM C150 [65] classification and natural fine aggregate. The aggregate had a specific mass of  $2.73 \pm 0.17 \text{ g/cm}^3$  according to ASTM C128 [66] and a fineness modulus of 2.36 according to ASTM C136 [67].

The mix design used was 1:2.75 by mass with water/cement ratio (w/c) of 0.485; the same composition used for Portland cement compressive strength characterization according to ASTM C109 [68]. Mortars were made using the procedures described by ASTM C305 [69] in a mechanical mixer. Three prismatic samples (25x25x285) mm were molded, demolded at 24h and subjected to submerged cure in lime-saturated water at room temperature (22 °C) until the test age (28 days). Cylindrical specimens (5x10) cm were also produced which presented, according to ASTM C39 [70], at 28 days, the mechanical compressive strength of 51.2 MPa. The test was performed in a hydraulic testing machine (EMIC, DL30000) after gridding the surface of the samples.

### Instrumentation and calculations

To determine the static and dynamic elastic modulus of the mortar beams, different sensors and techniques were employed. For this, at 28 days, the beams were crimped to allow a span length of 250 mm. The cantilevered boundary condition was adopted because it can be used for all techniques and would produce equivalent results. Also, higher displacements and lower frequencies are obtained from this condition, allowing a higher precision on the measurements. Figure 3 shows the positioning of all sensors used in the mortar beam, although each sensor was used separately. For the static tests, five consecutive sample loads (1, 2, 3, 4 and 5 kg) were performed, and for each specimen, the tests were repeated 3 times.

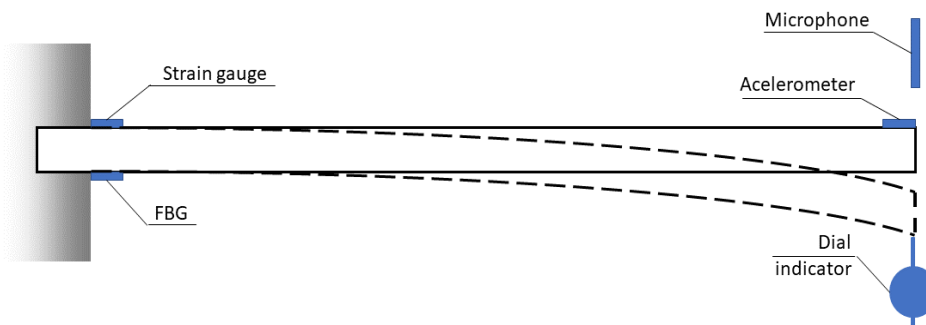


Figure 3. Cantilevered mortar beam and sensors

At the end of the beam, a digital dial indicator (Mitutoyo, S1012M) with a  $0.01 \mu\text{m}$  precision was positioned with the aid of a magnetic rod. By reading the beam vertical displacement  $\delta$  (m) in the digital dial indicator it was possible to determine the static modulus  $E$  (Pa) by Equation 3 [71]. Where  $P$  is the load (N),  $L$  the span length (m) and  $I$  the moment of inertia of the beam section ( $\text{m}^4$ ).

$$E = \frac{P \cdot L^3}{3 \cdot \delta \cdot I} \tag{3}$$

Near to the beam support, strain gauge and FBG sensors were fixed. For the FBG sensor, initially, the acrylate layer from the fiber optic region was removed to ensure the adhesion between the fiber cladding and the resin. The optical fiber had to be placed slightly tensioned, allowing tensile and compression measurements in the sample. Therefore, one extremity of the sensor was glue, then the other end of the fiber was manually pulled (generating 2 nm displacements

in the reflected spectrum) and the other end of the sensor was fixed. For this, a short drying period light-curable resin (Opallis Flow, FMG) was used. The FBG sensor installation and static loading can be seen in Figure 4. The acquisition of the FBG (reflected signal spectrum evaluation) data was performed by an optical interrogator (Microoptics, model SM-130). For the test, a sampling frequency of 1 kHz was used.

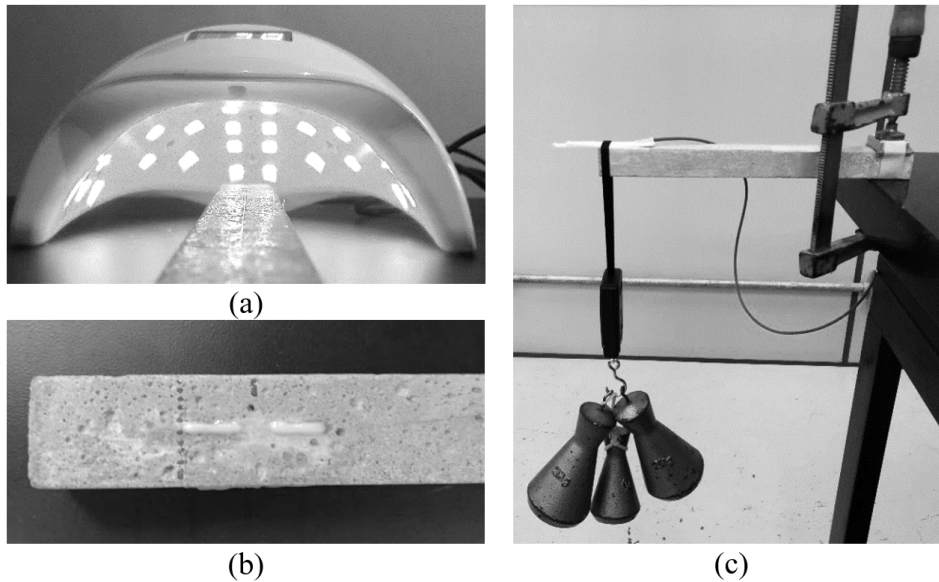


**Figure 4.** FBG instrumentation details: (a) resin UV curing, (b) final instrumentation and (c) cantilevered beam during static loadings

The linear grid strain gauge (Omega, model SGD-10/120-LY11), with 120  $\Omega$  electrical resistance and a 10 mm grid, was fixed using cyanoacrylate glue all over its surface with a 24-hour drying time. The acquisition of its signal was performed in a data acquirer (Lynx, model ADS2000) with a sampling frequency of 1kHz that used a quarter-bridge circuit for signal balancing.

From the strain values obtained by the FBG and the strain gauge, it was possible to calculate the equivalent static elastic modulus  $E$  (Pa) from Equation 4 [71]. This equation was also used to estimate the specific strain equivalent to the vertical displacement recorded by the dial indicator. In Equation 4,  $P$  is the applied load (N),  $L$  the span length (m),  $b$  the section width (m),  $h$  the section height (m) and  $\varepsilon$  the measured strain (m/m). Since the strain ( $\varepsilon$ ) was measured a few millimeters from the crimp, the measured value at the center of the sensor was adjusted to the crimped point based on triangle similarity.

$$E = \frac{6 \cdot P \cdot L}{b \cdot h^2 \cdot \varepsilon} \quad (4)$$

In addition to the strain gauge and FBG, the dynamic modulus was calculated using a high-precision accelerometer with a capacity up to 5 gravities (Kyowa, AS-5GB) connected to a data acquirer on a full-bridge circuit (Lynx, model ADS2000).

During the dynamic test, the beam was excited by a light tap its extremity using a 200 g metal bar according to ASTM E1875 [25], allowing it to go into dampened vibration with a temporal signal acquisition. It is noteworthy that the intensity of the excitation does not interfere with the frequency of vibration, material damping and the calculated elastic modulus. For each beam, the tests were also repeated 3 times.

After the acquisition, a Fast Fourier Transform (FFT) was performed, which converts the signal from the time domain to a representation in the frequency domain, allowing the natural vibration frequency of the material to be obtained.

Using Equation 5, it was possible to calculate the dynamic elastic modulus. Where  $E$  is the elastic modulus (Pa),  $f_1$  is the natural vibration frequency for the first vibrational mode (Hz),  $\lambda_1$  is the constant of the first vibrational mode ( $\lambda_1^2 = 1.875^2$ ),  $L$  is span length (m),  $I$  the moment of inertia (m<sup>4</sup>) and  $M$  the mass per meter or linear mass of the beam (kg/m).

$$E = \frac{M}{I} \left( 2 \cdot \pi \cdot f_1 \cdot \left( \frac{L}{\lambda_1} \right)^2 \right)^2 \quad (5)$$

The dynamic test was also performed on the SONELASTIC apparatus (ATCP Brand) following the requirements of ASTM E1876 [26] and ASTM C215 [24]. In the test, a directional microphone (CA-DP) is used to capture the acoustic pickup from the excited beam.

In this case, the intensity of a mechanical wave passing through the solid is acquired, and the dynamic modulus calculation follows Equation 6, described by ASTM E1876 [26]. In which,  $E$  is the elastic modulus (Pa),  $m$  the mass of the beam (kg),  $f_1$  the natural vibration frequency for the first vibration mode (Hz),  $b$  the section width (m),  $L$  the span length (m),  $h$  the height of the section (m),  $T_1$  the correction factor for prismatic geometry (-).

$$E = 0.9465 \cdot \left( \frac{m \cdot f_1^2}{b} \right) \cdot \left( \frac{L^3}{h^3} \right) \cdot T_1 \quad (6)$$

From the vibration tests, it was possible to calculate the damping coefficient of the mortar. The damping coefficient  $\xi$  (-) was estimated by the logarithmic decrement method, according to Equation 7 [72]. In the equation,  $A_0$  represents the initial amplitude and  $A_n$  represents the amplitude (in the sensor measurement unit) after  $n$  vibration cycles. For the calculation, the reading was always performed on the tenth oscillation of the damped wave.

$$\xi = \frac{1}{2 \cdot \pi \cdot n} \cdot \ln \left( \frac{A_0}{A_n} \right) \quad (7)$$

Finally, numerical modeling of the beam was performed to determine the theoretical strain near the support and the natural vibration frequency via finite element methods (FEM). This method was only used as a comparison basis to verify how experimental results would deviate from the theoretical model. For this, a finite shell element was used in a mesh with dimensions of 2 mm and the elastic modulus adopted was the one estimated by ACI 318 [7]. Usually, this method is used to estimate serviceability criteria in structure design and can be calculated by Equation 8, where  $f_{ck}$  is the characteristic compressive strength of concrete at 28 days (Pa). Although there are several models for the estimation of the elastic modulus based on the concrete mechanical strength [27], the American building code requirements for structural concrete was adopted since this is the most widely used for structural design analysis. This model considers the compressive strength measured in cylindrical specimens for the estimation of the elastic module of the whole structure, including any slender beams.

$$E = 4700 \cdot \sqrt{f_{ck}} \quad (8)$$

From the numerical simulation (FEM) it was possible to estimate in the cantilevered beam the theoretical strain near the support and vertical displacement at the end, as well as the theoretical natural frequency. Figure 5 presents a flowchart summarizing the tests and simulations performed and the parameters obtained for the calculation of the static and dynamic elastic modulus in this paper.

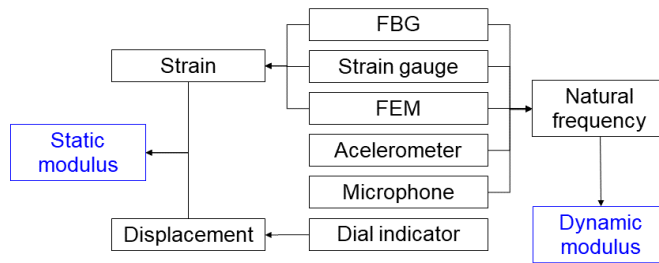


Figure 5. Evaluated techniques flowchart

## RESULTS AND DISCUSSION

### FBG sensor calibration

During the FBG calibration, the optical fiber was pulled on a metal apparatus and the strain was monitored by a dial indicator. Figure 6a shows the loading cycles and Figure 6b shows the calibration of the FBG sensor.

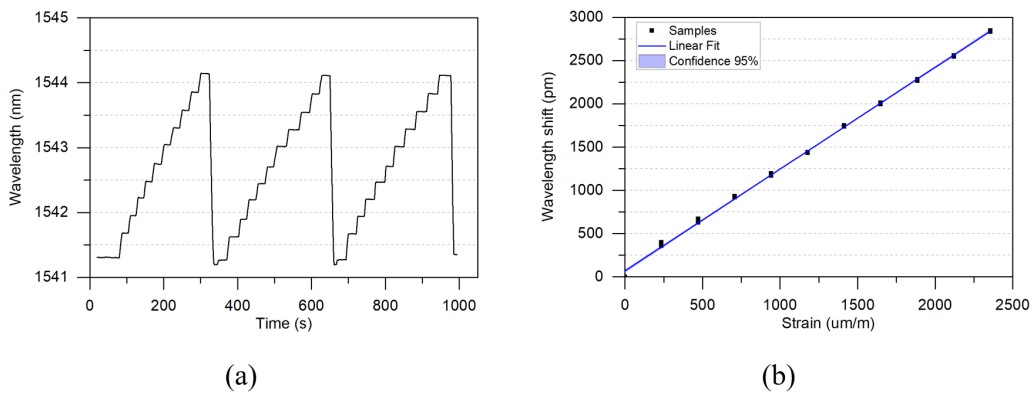


Figure 6. Sensor calibration: (a) Strain cycles during calibration and (b) FBG linear calibration

It is observed that during loading cycles there was no hysteresis (conservation of deformation after unloading) and no nonlinear variations in wavelength during calibration. After a linear adjustment, the FBG sensor had a sensitivity of  $1.2180 \text{ pm}/\mu\text{m}/\text{m}$ , or  $1.2180 \text{ pm}/\varepsilon$ , with an adjusted  $R^2$  of 0.9989. Figure 6b still shows the confidence interval of 95%, which remained close to the linear adjustment.

From Equation 2, it is possible to estimate the theoretical calibration of the sensor. Therefore, considering the photoelastic fiber constant as  $-0.212$  (the default value for single-mode fibers) and the recording length as  $1540.9 \text{ nm}$ , the theoretical value of the wavelength variation as a function of the strain is  $1.2142 \text{ pm}/\varepsilon$ , result 0.31% lower than the experimental data obtained.

This variation is permissible and may be related to differences in fiber photoelastic properties or variations in effective fiber wavelength after the inscribing process. The value found for the strain sensitivity obtained for FBG is also close to values obtained or indicated by other authors [57], [58], [73]–[75]. Thus, the sensor presented a linear elastic behavior with low variation (mean error of 5 pm) in the readings, thus indicating a good precision for strain measurements in structural elements.

### Static modulus

For the determination of the static elastic modulus, the mortar cantilevered beams were loaded at its end so that the sensor measurements could be performed. For the FBG test, it was possible to identify the displacement of the reflected spectrum by the optical sensor as a function of the loads applied, as shown in Figure 7.



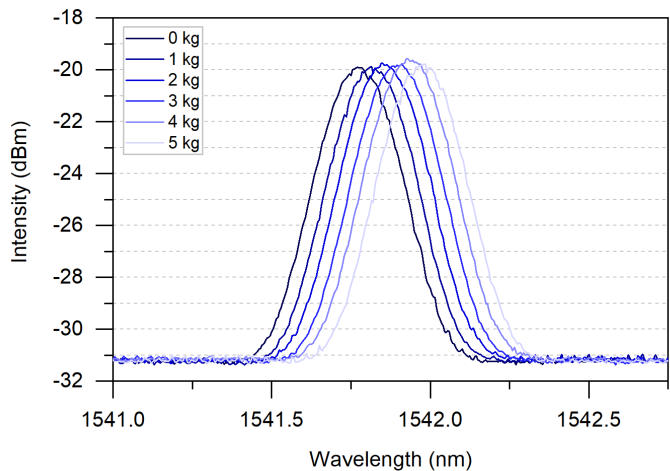


**Figure 7.** FBG reflected peak during loadings

As the load increased, the wavelength increased, as expected, due to the distancing of the Bragg grating. During the loading, there was no change in the spectrum shape, which averaged a full width at half maximum (FWHM) of  $0.3205 \text{ nm} \pm 0.0012 \text{ nm}$  and reflected peak intensity of  $11.702 \pm 0.035 \text{ dBm}$ . In the FEM simulation, it was possible to verify the stress distribution along the beam length (Figure 8).

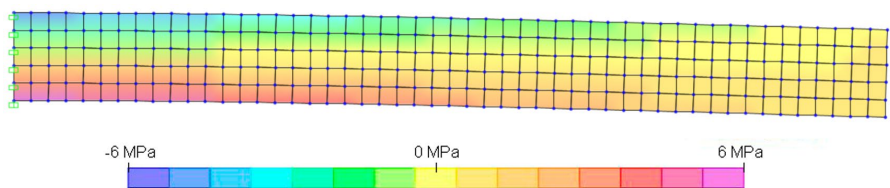


**Figure 8.** Beam stress distribution via FEM

In Figure 8, it is observed that there was an increase in the stress concentration near the beam support, with negative values (tensile) on the upper face and positive values (compression) on the lower face, symmetrically. From the results, it is noted that the mesh used to verify the stress distribution and beam deformations was adequate since the simulation presents a good stress distribution and it is possible to verify at different points the geometric properties of the element. With the measurements obtained by the dial indicator, FBG, strain gauge and FEM simulation, it was possible to compare the values of the strain obtained near the support, Figure 9.

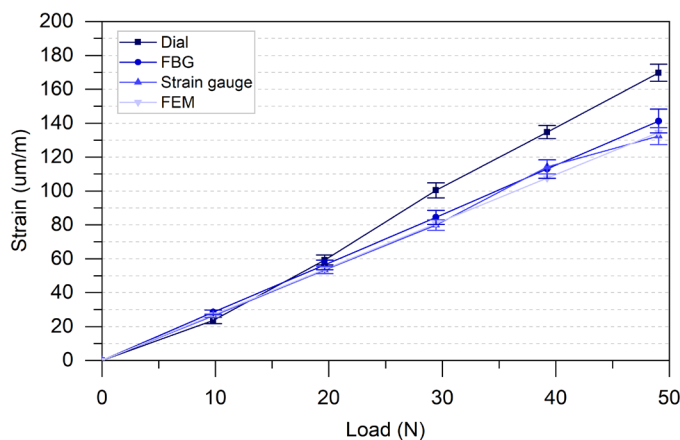


**Figure 9.** Strain measured by sensors

During loading, only the dial indicator readings showed a slight deviation when compared to the other readings. It is noteworthy that the test performed with the dial indicator was the only methodology that evaluated the vertical displacement of the beam, while the others measured the strain itself. The dial indicator was also the only sensor that relied on the visual record of the readings. Although the sensor was positioned ensuring the perpendicularity between the beam and the sensor, Montija [76] states that readings with displacement transducers may vary due to the difficulty of guaranteeing the perpendicularity of the measuring rod to the monitored element, as well as that part of the sensor deforms during the readings. The comparison of the results obtained for the static elastic modulus of the mortar beams is presented in Figure 10.

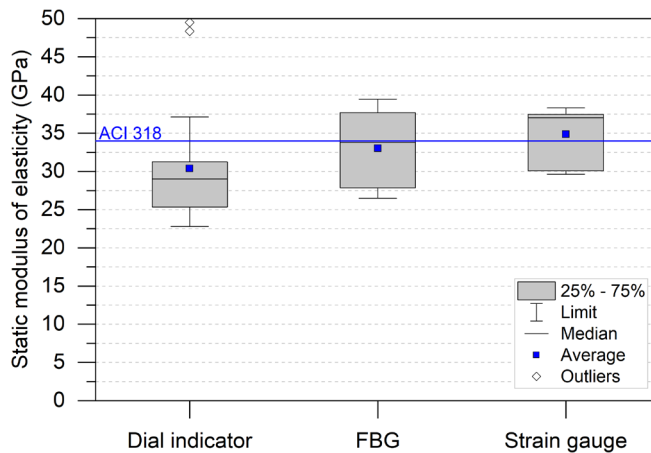


Figure 10. Static elastic modulus of the mortar beam

After performing an analysis of variance (ANOVA), at a significance level of 0.05, it was possible to prove that the methods used influenced the elastic modulus values obtained. It was also observed, after means comparison by Tukey at a significance level of 0.05, that there were no significant differences between the elastic modulus obtained by the FBG and the strain gauge. Thus, it can be stated that the dial indicator underestimated the elastic modulus by 10% when compared to the theoretical value estimated by ACI 318 [7] of 34.06 GPa.

The average value obtained by the FBG and the strain gauge was  $33.95 \pm 0.59$  GPa, a result 2% lower than that obtained by the ACI building code. Thus, it is possible to state that the optical fiber sensor made it possible to determine the elastic modulus with good precision and similar to the electric strain gauge - the most used method to evaluate strain in structures. The FBG was the methodology that presented the median of the data distribution closest to its theoretical value, indicating good reliability. It is not known which measurement yields the correct results since all techniques adopted are an estimation of the measured parameter. Therefore, authors must state the method adopted in their research and take into consideration the influence of the boundary condition and sensor used.

Although there is a variation in the aggregate and cement properties, it was possible to find in the literature a 35 GPa static modulus of mortars with the same mix design used in this paper [13], [77], [78].

## Dynamic modulus

To calculate the dynamic elastic modulus, the mortar beams were excited and the damped vibration signal was recorded over time. This signal, after processed (fast Fourier transform - FFT), allowed the verification of the dominant frequencies, referring to how many oscillations the beam suffered in the interval equivalent to one second. The damped vibration spectrum over time and the frequency domain spectrum of the performed tests are shown in Figure 11 to Figure 14.

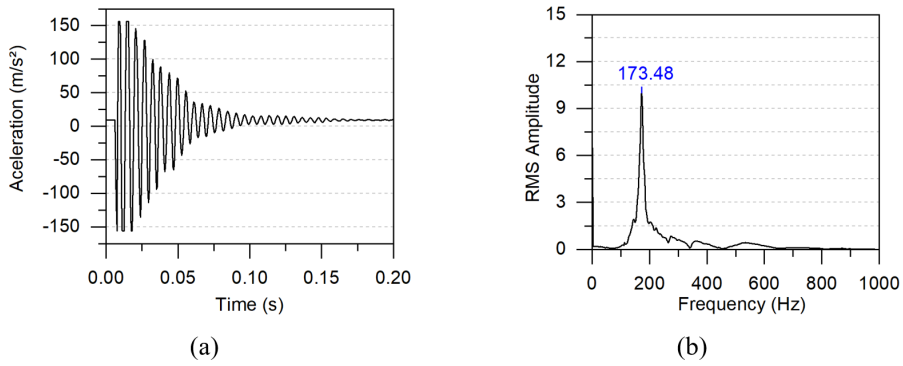


Figure 11. Accelerometer signal in (a) time and (b) frequency domain

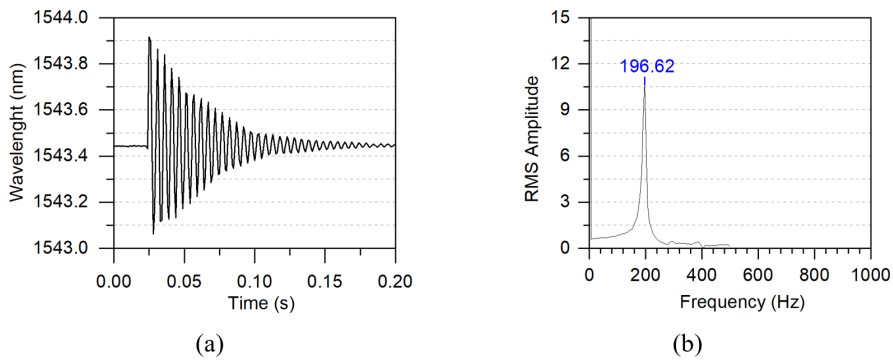


Figure 12. FBG signal in (a) time and (b) frequency domain

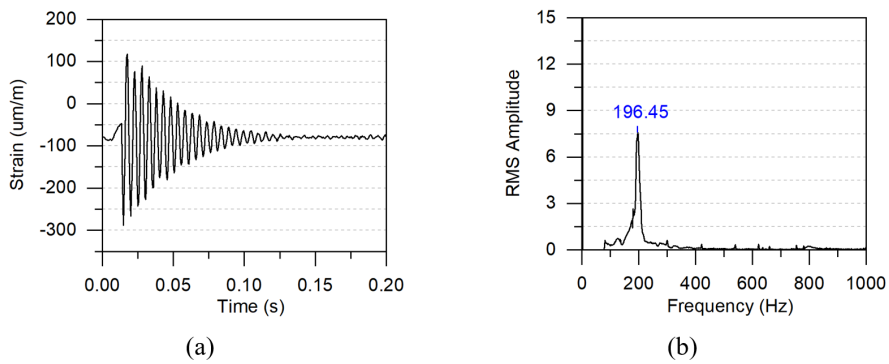


Figure 13. Strain gauge signal in (a) time and (b) frequency domain

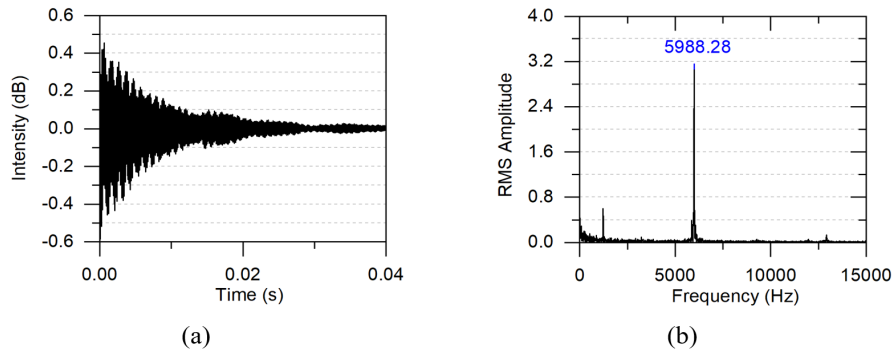


Figure 14. Microphone signal in (a) time and (b) frequency domain

The obtained frequency is presented as a function of the root mean square (RMS) amplitude - a statistical measure of the magnitude of the sensor. From the results, it was possible to verify that all sensors allowed the acquisition of beam vibration with good precision (well-defined damping coefficient and frequency peak). For the microphone, a high frequency is observed since the sensor registered a sound wave and not strain measurements like the other sensors. Figure 15 shows the average values of the natural frequencies.

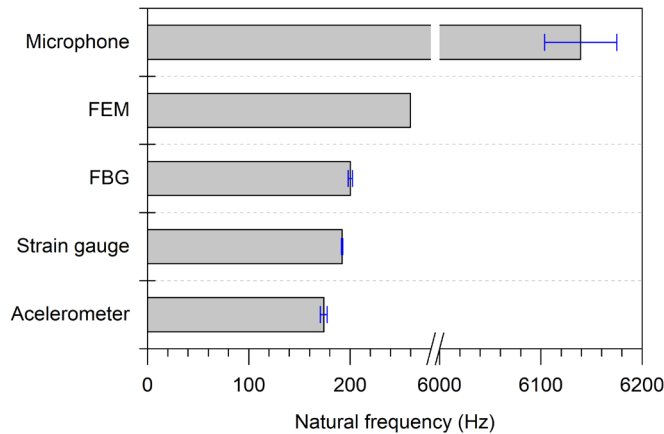


Figure 15. Natural resonant vibration frequencies

It is observed in Figure 15 that each sensor presented a distinct natural frequency of vibration. In the statistical analysis, the results obtained by the microphone were disregarded, since the obtained frequencies are in another order of magnitude (kHz). After the ANOVA test, it was proved that the means are statistically different from each other and, therefore, the method/sensor used to measure the vibration influenced the frequencies obtained. It was also observed that only the FBG and strain gauge methods did not present statistically significant differences (Tukey with a 95% confidence level).

Thus, it is possible to state that the estimated theoretical frequency via FEM was the highest among the techniques used, due to the use of the elastic modulus estimated by ACI 318 [7]. The result obtained by the accelerometer was 33% lower than the estimated theoretical value via FEM. The average frequency value obtained by the FBG and the strain gauge were on average 25% lower than the theoretical value. Silva et al. [53], during dynamic tests, also verified no statistically significant differences between vibration frequencies in concrete and wood beams using strain gauge and FBG. Since the natural vibration frequency depends on the geometry, it is not possible to compare the values obtained in this research with other works in the literature. By applying the logarithmic decrement method, according to Equation 7, it was possible to estimate the damping coefficient of the beam by the sensors (Figure 16).

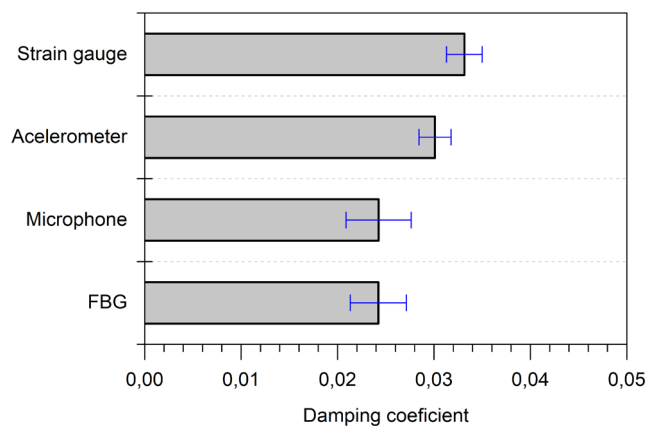


Figure 16. Sample damping coefficient

After the ANOVA test at a significance level of 0.05, no significant differences were found between the means obtained. Therefore, the type of sensor used did not influence the material damping coefficient measurement, which presented an average of 0.0279.

Since the damping coefficient is an intrinsic property of the material, as it is the elastic modulus, and does not depend on the geometry of the structural element, it can be verified that the obtained value is similar to what was found by other authors. In mortar specimens, Gidrão [13] observed damping coefficients from 0.02 to 0.14 and Swamy and Rigby [79] between 0.02 and 0.15. After signal acquisition and processing, the dynamic elastic modulus of the beams was calculated. Figure 17 presents the obtained values for the dynamic elastic modulus.

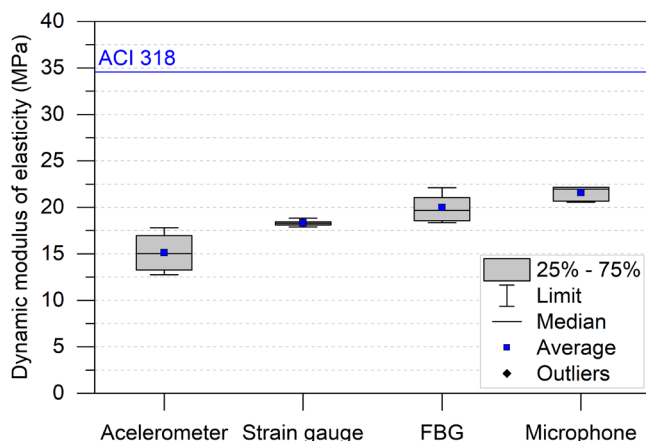


Figure 17. Dynamic elastic modulus of the mortar beam

From the results of the statistical analysis (ANOVA) it is possible to conclude that, at a confidence level of 0.05, there are significant differences between the means of the used methods. In the Tukey test, the results obtained by the FBG and the strain gauge are not statistically different. This finding highlights the accuracy in detecting the natural vibration frequency and the elastic modulus obtained by the optical fiber sensor (FBG) and proves the feasibility of its use in the monitoring of concrete structures.

The dynamic elastic modulus for the same mortar beams ranged from 15.12 to 23.42 GPa, and all results were below the estimated value by ACI 318 [7] of 34.06 GPa. When compared with the static modulus obtained by FBG, the same method for the dynamic test showed an average reduction of 40% in the values. The pulse velocity tends to reduce slightly as the length decreases due to the increased attenuation of higher frequency components [80]. Therefore, the lower values for the dynamic elastic module could be explained by the length of the specimen which did not affect the static measurements. So, this behavior must be considered during inspections of slender or long members since low elastic module values could be obtained due to the sample geometry.

## CONCLUSIONS

Different methods are used in this paper to obtain the same properties of a material. The research presents a state of the art on methods and sensors for structural experimental analysis. From the results obtained in the study of the static and dynamic modulus of mortar beams by different methods, it can be concluded that:

- The results show how the sensor and technique adopted can influence the final results, Thence, it is essential that published papers state the details on their experiment and take the sensor and boundary conditions into consideration during their analysis.
- FBG sensor had a sensitivity of 1.2180 pm/ $\mu\text{m}/\text{m}$ , with an adjusted  $R^2$  of 0.9989, result 0.31% higher than the theoretical adjustment. Overall, the optical fiber sensor (FBG) presented a good precision for measuring strain, natural vibration frequency, damping coefficient and elastic modulus (static and dynamic) of the mortar.
- There is a nonlinear behavior of the vertical displacement of the beam acquired by the dial indicator in the static test, which underestimated 10% the elastic modulus values of the material. And it was proved that the theoretical model proposed by the American Concrete Institute (ACI) to calculate the static elastic modulus of concrete is reliable

- The type of sensor/method did not influence the material damping coefficient measurement, which presented an average of 0.0279. Although the results are consistent, further investigations are required to evaluate how this property can be influenced by the material and its geometry.
- There were no significant differences between the static and dynamic elastic modulus obtained by the FBG and the strain gauge. Therefore, the optical fiber sensor (FBG) presented a high accuracy in the detection of the strain, natural vibration frequency, damping coefficient and elastic modulus of the mortar beams and could be used for structural instrumentation.
- When compared with the static modulus obtained by FBG, the same method for the dynamic test showed an average reduction of 40% in the values due to the length of the specimen which only affected the dynamic measurements.

## ACKNOWLEDGMENTS

The authors thank PPGECC and CESEC at UFPR, as well as the Multi-User Photonics Facility at UTFPR-CT, for the provided equipment.

## REFERENCES

- [1] B. Zech and M. J. Setzer, "The dynamic modulus of hardened cement paste. Part 2: ice formation, drying and pore size distribution," *Mater. Struct.*, vol. 22, no. 2, pp. 125–132, Mar 1989.
- [2] B. Zech and M. J. Setzer, "The dynamic elastic modulus of hardened cement paste. Part I: a new statistical model-water and ice filled pores," *Mater. Struct.*, vol. 21, no. 5, pp. 323–328, Sep 1988.
- [3] A. Alsalman, C. N. Dang, G. S. Prinz, and W. M. Hale, "Evaluation of modulus of elasticity of ultra-high performance concrete," *Constr. Build. Mater.*, vol. 153, pp. 918–928, Oct 2017.
- [4] M. Alves, G. L. Andreatta, G. Macioski, and A. Medeiros, "Efeito da substituição da água de amassamento por gelo nas propriedades de concretos C30 e C70," in *An. 59º Cong. Bras. Concr.*, 2017.
- [5] A. Behnood, J. Olek, and M. A. Glinicki, "Predicting modulus elasticity of recycled aggregate concrete using M5' model tree algorithm," *Constr. Build. Mater.*, vol. 94, pp. 137–147, Sep 2015.
- [6] P. C. C. Hewlett, *Lea's Chemistry of Cement and Concrete*, 5th ed. Oxford: Butterworth-Heinemann Elsevier, 2003.
- [7] American Concrete Institute, *Building Code Requirements for Structural Concrete*, ACI 318, 2014, p. 524.
- [8] S. Mindess, J. F. Young, and D. Darwin, *Concrete*, 2nd ed. Upper Saddle River: Prentice Hall, 2003.
- [9] K. J. Bastgen and V. Hermann, "Experience made in determining the static modulus of elasticity of concrete," *Materiaux Constructions*, vol. 10, no. 6, pp. 357–364, Nov 1977.
- [10] American Society for Testing Materials, *Standard Test Method for Static Modulus of Elasticity and Poisson's Ratio of Concrete in Compression*, ASTM C469, 2014, p. 5.
- [11] S. Han and J. Kim, "Effect of temperature and age on the relationship between dynamic and static elastic modulus of concrete," *Cement Concr. Res.*, vol. 34, no. 7, pp. 1219–1227, 2004.
- [12] B. D. Liu, W. J. Lv, L. Li, and P. F. Li, "Effect of moisture content on static compressive elasticity modulus of concrete," *Constr. Build. Mater.*, vol. 69, pp. 133–142, 2014.
- [13] G. M. S. Gidrão, "Propriedades dinâmicas do concreto e relações com sua microestrutura," M.S. thesis, Esc. Eng. São Carlos, Univ. São Paulo, 2015.
- [14] Y. Zhou, J. Gao, Z. Sun, and W. Qu, "A fundamental study on compressive strength, static and dynamic elastic moduli of young concrete," *Constr. Build. Mater.*, vol. 98, pp. 137–145, 2015.
- [15] D. Kocab, B. Kucharczykova, P. Misak, P. Zitt, and M. Kralikova, "Development of the Elastic Modulus of Concrete under Different Curing Conditions," *Procedia Eng.*, vol. 195, pp. 96–101, 2017.
- [16] J. M. L. Reis, L. C. S. Nunes, A. L. C. Triques, L. C. G. Valente, and A. M. B. Bragaa, "Mechanical characterization using optical fiber sensors of polyester polymer concrete made with recycled aggregates," *Mater. Res.*, vol. 12, no. 3, pp. 269–271, 2009.
- [17] A. Castro-Caicedo, P. Toores, and R. Lain, "Packaging and testing of fiber Bragg gratings for use as strain sensor in rock specimens," in *Proc. 8th Iberoam Opt Meeting and 11th Latin Am. Meeting Opt, Lasers Appl.*, vol. 8785, no. 1, p. 7, 2013.
- [18] A. Othonos, "Fiber Bragg gratings," *Rev. Sci. Instrum.*, vol. 68, no. 12, pp. 4309, 1998.
- [19] R. K. Mobley, *An Introduction to Predictive Maintenance*. Amsterdam: Butterworth-Heinemann, 2002.
- [20] P. J. M. Monteiro, P. R. L. Helene, and S. H. Kang, "Designing concrete mixtures for strength, elastic modulus and fracture energy," *Mater. Struct.*, vol. 26, no. 8, pp. 443–452, Oct 1993.

- [21] P. K. Mehta and P. J. M. Monteiro, *Concrete - Microstructure, Properties, and Materials*, 4th ed. Berkeley: McGraw-Hill Education, 2013.
- [22] American Society for Testing Materials, *Standard Test Method for Pulse Velocity Through Concrete*, ASTM C597, 2009, p. 4.
- [23] N. G. Silva and C. C. Campiteli, "Correlação entre módulo de elasticidade dinâmico e resistências mecânicas de argamassas de cimento, cal e areia," *Ambient. Constr.*, vol. 8, no. 4, pp. 21–35, 2008.
- [24] American Society for Testing Materials, *Fundamental Transverse, Longitudinal, and Torsional Resonant Frequencies of Concrete Specimens*, ASTM C215, 2014, p. 7.
- [25] American Society for Testing Materials, *Standard Test Method for Dynamic Young's Modulus, Shear Modulus, and Poisson's Ratio by Sonic Resonance*, ASTM E1875, 2008, p. 9.
- [26] American Society for Testing Materials, *Standard Test Method for Dynamic Young's Modulus, Shear Modulus, and Poisson's Ratio by Impulse Excitation of Vibration*, ASTM E1876, 2015, p. 17.
- [27] H. J. F. Diógenes, L. C. Cossolino, A. H. A. Pereira, M. K. El Debs, and A. L. H. C. El Debs, "Determination of modulus of elasticity of concrete from the acoustic response," *Rev. IBRACON Estrut. Mater.*, vol. 4, no. 5, pp. 11, Oct 2011.
- [28] J. Han, G. Pan, and W. Sun, "Elastic modulus change investigation of cement paste before and after carbonation using nanoindentation technique," *Procedia Eng.*, vol. 27, pp. 341–347, 2012.
- [29] W. Li, S. Kawashima, J. Xiao, D. J. Corr, C. Shi, and S. P. Shah, "Comparative investigation on nanomechanical properties of hardened cement paste," *Mater. Struct.*, vol. 49, no. 5, pp. 1591–1604, 2016.
- [30] D. C. S. Garcia, M. M. N. S. Soares, A. C. S. Bezerra, M. T. P. Aguilar, and R. B. Figueiredo, "Microstructure and hardness of cement pastes with mineral admixture," *Materia*, vol. 22, no. 2, 2017.
- [31] E. Mousavi, A. Cheshomi, and M. Ashtari, "Estimating elasticity modulus and uniaxial compressive strength of sandstone using indentation test," *J. Petrol. Sci. Eng.*, vol. 169, pp. 157–166, 2018.
- [32] Y. Wang et al., "Determination of load-strain characteristics of concrete slabs by using embedded fiber Bragg grating sensors," in *Proc. Fifth Eur. Conf. Smart Struct. Mater.*, 2000, vol. 4073, pp. 297–304.
- [33] A. Quintela, C. Jauregui, J. Echevarra, and J. M. Lopez-Higuera, "Embedded temperature strain fibre Bragg grating sensor system validation for concrete structures," *J. Opt. A, Pure Appl. Opt.*, vol. 4, no. 6, pp. S387–S390, Nov 2002.
- [34] M. Majumder, T. K. Gangopadhyay, A. K. Chakraborty, K. Dasgupta, and D. K. Bhattacharya, "Fibre Bragg gratings in structural health monitoring: present status and applications," *Sens. Actuators A Phys.*, vol. 147, no. 1, pp. 150–164, Sep 2008.
- [35] C. Rodrigues, C. Félix, A. Lage, and J. Figueiras, "Development of a long-term monitoring system based on FBG sensors applied to concrete bridges," *Eng. Struct.*, vol. 32, no. 8, pp. 1993–2002, 2010.
- [36] M. Fajkus, J. Nedoma, P. Mec, M. Pinka, M. Novak, and S. Zabka, "Deformation sensor composed of fiber Bragg grating and the strain gauge for use in civil engineering," in *Proc. Electro-Optical Remote Sens. XII*, 2018, vol. 10796, pp. 34.
- [37] P. Mec, M. Stolarik, S. Zabka, and M. Novak, "Application of FBG in the experimental measurements of structural elements deformation from cement composites," in *Proc. Electro-Optical Remote Sens. XII*, 2018, vol. 10796, pp. 29.
- [38] V. Saouma and L. Perotti, "Constitutive model for alkali-aggregate reactions," *ACI Mater. J.*, vol. 103, no. 3, pp. 194–202, 2006.
- [39] V. E. Saouma, D. Z. Anderson, K. Ostrander, B. Lee, and V. Slowik, "Application of fiber Bragg grating in local and remote infrastructure health monitoring," *Mater. Struct.*, vol. 31, no. 4, pp. 259–266, 1998.
- [40] G. Kaklauskas, A. Sokolov, R. Ramanauskas, and R. Jakubovskis, "Reinforcement strains in reinforced concrete tensile members recorded by strain gauges and FBG sensors: experimental and numerical analysis," *Sensors*, vol. 19, no. 1, 2019.
- [41] J. Gao, J. Wu, J. Li, and X. Zhao, "Monitoring of corrosion in reinforced concrete structure using Bragg grating sensing," *NDT Int.*, vol. 44, no. 2, pp. 202–205, Mar 2011.
- [42] J. S. Leng and A. Asundi, "NDE of smart structures using multimode fiber optic vibration sensor," *NDT Int.*, vol. 35, no. 1, pp. 45–51, 2002.
- [43] J. R. Lee, H. Tsuda, and N. Toyama, "Impact wave and damage detections using a strain-free fiber Bragg grating ultrasonic receiver," *NDT Int.*, vol. 40, no. 1, pp. 85–93, 2007.
- [44] C. C. Chen, W. H. Wu, F. Shih, and S. W. Wang, "Scour evaluation for foundation of a cable-stayed bridge based on ambient vibration measurements of superstructure," *NDT Int.*, vol. 66, pp. 16–27, 2014.
- [45] A. Carrión, V. Genovés, J. Gosálbez, R. Miralles, and J. Payá, "Ultrasonic signal modality: a novel approach for concrete damage evaluation," *Cement Concr. Res.*, vol. 101, pp. 25–32, Nov 2017.
- [46] P. C. Chang, A. Flatau, and S. C. Liu, "Review paper: health monitoring of civil infrastructure," *Struct. Health Monit. An Int. J.*, vol. 2, no. 3, pp. 257–267, Sep 2003.
- [47] U. Dahlen, N. Ryden, and A. Jakobsson, "Damage identification in concrete using impact non-linear reverberation spectroscopy," *NDT Int.*, vol. 75, pp. 15–25, Oct 2015.

- [48] Y. Farnam, M. R. Geiker, D. Bentz, and J. Weiss, "Acoustic emission waveform characterization of crack origin and mode in fractured and ASR damaged concrete," *Cement Concr. Compos.*, vol. 60, pp. 135–145, Jul 2015.
- [49] B. Glisic and D. Inaudi, *Fibre Optic Methods for Structural Health Monitoring*. Newport Beach: John Wiley & Sons, 2007.
- [50] G. Karaiskos, A. Deraemaeker, D. G. Aggelis, and D. V. Hemelrijck, "Monitoring of concrete structures using the ultrasonic pulse velocity method," *Smart Mater. Struct.*, vol. 24, no. 11, pp. 113001, 2015.
- [51] A. Khadour and J. Waeytens, "Monitoring of concrete structures with optical fiber sensors" in F. P. Torgal et al., Eds., *Eco-Efficient Repair and Rehabilitation of Concrete Infrastructures*. Duxford: Woodhead Publishing, Jan. 2018, pp. 97–121.
- [52] E. Penner, "Avaliação de desempenho de sistemas estruturais de pontes de concreto," Ph.D. dissertation, Esc. Politéc., Univ. São Paulo, 2001.
- [53] J. C. C. Silva, C. Martelli, H. J. Kalinowski, E. Penner, J. Canning, and N. Groothoff, "Dynamic analysis and temperature measurements of concrete cantilever beam using fibre Bragg gratings," *Opt. Lasers Eng.*, vol. 45, no. 1, pp. 88–92, Jan 2007.
- [54] C. Frotté, C. S. A. di Nubila, A. Nagalli, W. Mazer, G. Macioski, and L. O. S. Oliveira, "Study of physical and mechanical concrete properties with partial replacement of natural aggregate by recycled aggregate from CDW," *Rev. Materia*, vol. 22, no. 2, e11811, 2017.
- [55] M. Abdelrahman, M. K. ElBatanouny, P. Ziehl, J. Fasl, C. J. Larosche, and J. Fraczek, "Classification of alkali-silica reaction damage using acoustic emission: A proof-of-concept study," *Constr. Build. Mater.*, vol. 95, pp. 406–413, Oct 2015.
- [56] F. Mitschke, *Fiber Optics: Physics and Technology*, 2nd ed. Berlin: Springer, 2016.
- [57] A. N. Chester, S. Martellucci, and A. M. V. Scheggi, *Optical Fiber Sensors*, 1st ed. California: Springer, 1987.
- [58] R. Kashyap, *Fiber Bragg Gratings*, 2nd ed. Oxford: Academic Press, 2010.
- [59] K. O. Hill, Y. Fujii, D. C. Johnson, and B. S. Kawasaki, "Photosensitivity in optical fiber waveguides: application to reflection filter fabrication," *Appl. Phys. Lett.*, vol. 32, no. 10, pp. 647–649, May 1978.
- [60] S. Yin, P. B. Ruffin, and F. T. S. Yu, *Fiber Optic Sensors*, 2nd ed. New Hampshire: CRC Press, 2008.
- [61] C. A. J. Gouveia, J. M. Batista, and A. S. P. Jorge, "Refractometric optical fiber platforms for label free sensing," in *Current Developments in Optical Fiber Technology*, 1st ed., Rijeka: IntechOpen, 2013, p. 30.
- [62] C. K. Y. Leung et al., "Review: optical fiber sensors for civil engineering applications," *Mater. Struct.*, vol. 48, no. 4, pp. 871–906, Nov 2015.
- [63] K. T. V. Grattan and B. T. Meggitt, *Optical Fiber Sensor Technology: Devices and Technology*, 1st ed. London: Springer US, 1998.
- [64] S. Daud and J. Ali, *Fibre Bragg Grating and No-Core Fibre Sensors*, 1st ed. Switzerland: Springer, 2018.
- [65] American Society for Testing Materials, *Standard Specification for Portland Cement*, ASTM C150, 2018, p. 9.
- [66] American Society for Testing Materials *Standard Test Method for Relative Density (Specific Gravity) and Absorption of Fine Aggregate*, ASTM C128, 2015, p. 6.
- [67] American Society for Testing Materials, *Standard Test Method for Sieve Analysis of Fine and Coarse Aggregates*, ASTM C136, 2019, p. 5.
- [68] American Society for Testing Materials, *Standard Test Method for Compressive Strength of Hydraulic Cement Mortars*, ASTM C109, 2018, p. 9.
- [69] American Society for Testing Materials, *Standard Practice for Mechanical Mixing of Hydraulic Cement Pastes and Mortars of Plastic Consistency*, ASTM C305, 2014, p. 3.
- [70] American Society for Testing Materials, *Standard Test Method for Compressive Strength of Cylindrical Concrete Specimens*, ASTM C39, 2018.
- [71] R. C. Hibbeler, *Resistência dos Materiais*, 7th ed. São Paulo: Pearson Universidades, 2009.
- [72] L. C. Cossolino and A. H. A. Pereira, *Relatório Técnico-Científico ITC04 Amortecimento: Classificação e Métodos de Determinação*. São Paulo: ATCP, 2010, p. 14.
- [73] W. Chen and X. Dong, "Modification of the wavelength-strain coefficient of FBG for the prediction of steel bar corrosion embedded in concrete," *Opt. Fiber Technol.*, vol. 18, no. 1, pp. 47–50, Jan 2012.
- [74] C. Li, H. Sun, and L. Li, "A review: the comparison between alkali-activated slag (Si + Ca) and metakaolin (Si + Al) cements," *Cement Concr. Res.*, vol. 40, no. 9, pp. 1341–1349, 2010.
- [75] A. Othonos and K. Kalli, *Fiber Bragg Gratings - Fundamentals and Applications in Telecommunications and Sensing*, 1st ed. Norwood: Artech House Print on Demand, 1999.
- [76] F. C. Montija, "Aspectos da variabilidade experimental do ensaio de módulo de deformação do concreto," M.S. thesis, Univ. São Paulo, São Paulo, 2007.
- [77] M. R. G. Pena, "Estudo da fissuração associada à retração em argamassas para reparo em estruturas de concreto," M.S. thesis, Esc. Politéc., Univ. São Paulo, 2004.



- [78] G. Macioski, L. A. Martins, T. Mueller, and A. Matoski, "Avaliação das propriedades de argamassas com adição de fibra de Curauá (*Ananas Erectifolius*)," *Rev. Eng. Constr. Civ.*, vol. 3, no. 2, pp. 52–62, 2014.
- [79] N. Swamy and G. Rigby, "Dynamic properties of hardened paste, mortar and concrete," *Materiaux Constructions*, vol. 4, no. 1, pp. 13–40, 1971.
- [80] IAEA, *Guidebook on Non-Destructive Testing of Concrete Structures*, 2002.

---

**Author contributions:** GM: conceptualization, methodology, data acquisition, analysis, writing; VO: data acquisition, writing; MHFM: supervision, writing.

**Editors:** Vladimir Guilherme Haach, Guilherme Aris Parsekian.



## ORIGINAL ARTICLE

## Behavior of CFA and H-section steel piles in lateral loading: experimental and numerical analysis

### *Comportamento de estacas escavadas em hélice contínua (CFA) e de estacas metálicas em seção H sob carregamento lateral: análise experimental e numérica*

Alex Micael Dantas de Sousa<sup>a</sup> Yuri Daniel Jatobá Costa<sup>b</sup> Arthur Gomes Dantas de Araujo<sup>c</sup> Carina Maia Lins Costa<sup>b</sup> <sup>a</sup>Universidade de São Paulo – USP, Escola de Engenharia de São Carlos, Departamento de Engenharia de Estruturas, São Carlos, SP, Brasil<sup>b</sup>Universidade Federal do Rio Grande do Norte – UFRN, Departamento de Engenharia Civil, Natal, RN, Brasil<sup>c</sup>Universidade Federal Rural do Semi-Árido – UFERSA, Departamento de Engenharia Civil, Angicos, RN, BrasilReceived 16 June 2020  
Accepted 26 September 2020

**Abstract:** The behavior of continuous flight auger (CFA) piles and steel H-section piles to lateral loading is investigated using numerical analyses supported by field tests. A three-dimensional finite element numerical model to lateral load is presented. The numerical model was validated with the results of twelve lateral load tests performed on CFA and steel H-section piles installed in two deposits of sandy soils. The three-dimensional approach proposed in this study is in good agreement with the response observed with the field tests, and thus represents a reliable soil-pile interaction for laterally loaded piles in sandy soil. Parametric analyses were used to assess the influence of relevant variables to lateral soil-pile interaction. Major findings of this paper indicate that the ultimate lateral load of short rigid piles is considerably more influenced by changes in soil-pile relative stiffness than that of long flexible units. Pile diameter and soil-pile interface friction are found to exert a marked effect on the lateral load of CFA piles, while soil dilatancy is found to play a minor influence on the response of CFA piles.

**Keywords:** laterally loaded pile, soil-pile interaction, three-dimensional finite element method, field test, p-y curve.

**Resumo:** O comportamento de estacas escavadas com trado em hélice contínua (CFA) e estacas metálicas de seção H sujeitas à cargas horizontais é investigado através de análises numéricas baseadas em resultados experimentais. O modelo numérico foi validado com os resultados de 12 ensaios de carregamento lateral de estacas realizados em estacas CFA e estacas metálicas de seção H instaladas em duas regiões de solos arenosos. A abordagem tridimensional proposta neste estudo está de acordo com a resposta observada nos ensaios de campo e, portanto, representa uma interação solo-estaca confiável para estacas carregadas lateralmente em solo arenoso. Análises paramétricas foram utilizadas para avaliar a influência de variáveis relevantes para a interação lateral solo-estaca. As principais descobertas deste trabalho indicam que a capacidade de carga lateral última de estacas rígidas curtas é consideravelmente mais influenciada por mudanças na rigidez relativa do solo-estaca do que no caso de estacas flexíveis longas. O diâmetro da estaca e o atrito da interface solo-estaca tem efeito significativo na capacidade de carga lateral das estacas CFA, enquanto a dilatação do solo exerce uma menor influência na resposta destas.

**Palavras-chave:** estacas carregadas lateralmente, interação solo-estaca, método dos elementos finitos tridimensional, ensaios de campo, curva p-y.

**How to cite:** A. M. D. Sousa, Y. D. J. Costa, A. G. D. Araujo, and C. M. L. Costa, “Behavior of CFA and H-section steel piles in lateral loading: experimental and numerical analysis,” *Rev. IBRACON Estrut. Mater.*, vol. 14, no. 3, e14313, 2021, <https://doi.org/10.1590/S1983-41952021000300013>

Corresponding author: Alex Micael Dantas de Sousa. E-mail: alex\_dantas@usp.br

Financial support: Fundação de Amparo à Pesquisa do Estado de São Paulo, Grant/Award Number: FAPESP - 2018/21573-2; Conselho Nacional de Desenvolvimento Científico e Tecnológico.

Conflict of interest: Nothing to declare.



This is an Open Access article distributed under the terms of the Creative Commons Attribution License, which permits unrestricted use, distribution, and reproduction in any medium, provided the original work is properly cited.

## 1 INTRODUCTION

Soil-structure interaction has been extensively investigated regarding axial vertical loads in deep foundations [1]–[3]. At the same time, in several circumstances, piles need to be designed to support major lateral loads, as a result of the action of wind, water flow, horizontal earth pressure [4], earthquakes, and traffic movement. Bridges [5], tall buildings, transmission lines, retaining walls [4], offshore structures [6]–[8], wharfs [9], are a few examples of structures in which lateral loads assume primary significance.

Among existing methods for the analysis of laterally loaded single piles,  $p$ - $y$  curve methods are largely employed in current design practice. In the  $p$ - $y$  curve approach, a laterally loaded pile is treated as a beam on an elastic foundation with independent springs. The soil resistance per unit length ( $p$ ) is assumed to hold a non-linear relationship with the pile lateral displacement ( $y$ ). The relationship between  $p$  and  $y$  is known as the subgrade reaction modulus  $k_h$  ( $k_h = p/y$ ). The soil-pile system is assumed to reach the ultimate lateral resistance at a particular pile deflection level. The non-linearity between soil resistance and pile displacement has been substantiated by numerous full-scale tests [5], [10]–[14].

Although versatile and practical for structural design purposes, the  $p$ - $y$  curve approach has several shortcomings, such as: (1) continuity of the soil is not accounted for, since the springs are uncoupled; (2) shearing forces in the pile-soil contact and pile toe are neglected; (3) pile diameter and bending stiffness are only considered indirectly; (4) soil dilatancy is neglected, even though experimental evidence reveals that pile-soil resistance can significantly increase with increasing soil dilatancy [12], [15]; (5) the soil-pile ultimate resistance ( $p_u$ ) is calculated according to Rankine's theory, which assumes full slippage conditions between the soil and the structure [16], [17], even though perfectly smooth conditions are not found in the field; (6) the coefficient of horizontal earth pressure ( $K$ ) is considered equal to the at-rest earth pressure coefficient ( $K_0$ ) rather than the post-installation earth pressure coefficient, which may result in underestimated ultimate soil resistances for piles [12], [18], [19].

An alternative to the  $p$ - $y$  curve approach is the three-dimensional finite element method (3-D FEM) analysis. Although comparatively more complex to implement, 3-D FEM can reliably simulate several aspects of the problem involving a laterally loaded pile that are unable to be accomplished in  $p$ - $y$  curve methods. 3-D FEM methods should be preferred over  $p$ - $y$  curve methods because they are more rigorous in their analytical methodology.

Many numerical studies have been extensively conducted to assess the behavior of piles under lateral loading. Although several studies used 3-D FEM analysis supported by field data [5], [12], [15], [20]–[22], some relevant aspects of the problem involving laterally loaded pile behavior have not been well understood.

For instance, while the effect of the pile bending stiffness on pile response has been widely investigated in the literature [12], [23], [24], very little importance has been granted to the soil-pile relative stiffness, even though this variable is comparatively more suitable for describing the soil-pile interaction. Moreover, different studies present contradictory conclusions on the influence of pile diameter on the lateral behavior of piles, which warrants further research. Terzaghi [25] and Vesic [26] postulated that the pile diameter did not influence the subgrade reaction modulus ( $k_h$ ). Using numerical and large-scale tests, Ashford and Juirnarongrit [27] and Fan and Long [12] verified that the pile diameter has an insignificant influence on  $k_h$ . However, other investigations involving experimental and analytical components found that  $k_h$  and the ultimate lateral capacity ( $H_u$ ) increase linearly with the pile diameter [5], [23], [28].

Another parameter of interest for the soil-pile interaction that needs further examination is the soil-pile interface property (interface friction for granular soils or interface adhesion for non-granular soils). From a FEM analysis validated against field tests, Choi et al. [15] found that the soil-pile interface friction coefficient had a great impact on the lateral load capacity of bored piles embedded in weathered granite soil. On the other hand, the computational results presented by Kim and Jeong [5] indicated that the interface adhesion exerts an insignificant influence on the subgrade reaction modulus obtained with large diameter piles in clay.

Perceived gaps and conflicting results in the literature support the need for additional research using reliable 3-D FE models. The purpose of this study is to present the results of a 3-D FE model developed to represent the lateral load behavior of concrete flight auger (CFA) piles and steel H-section piles installed in two profiles of sandy soils. Accuracy of the proposed model was checked against the results of a total of 12 lateral load tests performed in the field with both CFA piles and steel H-section piles. Parametric analyses were carried out to investigate the influence of (i) soil-pile relative stiffness, (ii) pile diameter, (iii) interface friction between the pile and the soil and (iv) soil dilatancy. Therefore, this study brings together experimental and numerical results that provide important background for the future preliminary design of piles under lateral loading in similar soil conditions.

## 2 SITE CHARACTERISTICS

The experimental component of this investigation was carried out at a site located in the City of Natal (05°47'42"S, 35°12'34"W), in the Northeast region of Brazil (Figure 1a). Tertiary and quaternary sediments compose the subsoil of Natal, which is typical of vast extensions of the upper Brazilian northeast region. The tertiary deposits comprise a continuous sequence of clastic sediments, ranging from clay to conglomerate, which presents lateritic features with iron oxides bonding the soil particles together [29]. Overlying the tertiary deposits are quaternary deposits of eolian (dune) and alluvial sediments, composed of quartz sands with sub-rounded fine to coarse grains. Specifically, the experimental site is in a deflation zone composed of sandy soils of eolian origin, with grain size distribution containing less than 20% of finer sediments.

The field tests were conducted in two different locations within the experimental site, which are labeled in this study as testing Area A and testing Area B. The distance between both locations within the experimental site is approximately 300 m. The experimental site was characterized by field and laboratory tests. The field survey included four standard penetration tests (SPT) and one piezocone (CPT<sub>u</sub>) test in each area of investigation. Subsoil profiles of Areas A and B are schematically shown in Figure 1b and Figure 1c, respectively, which include the variation with depth of the mean SPT blow count corrected for 60% efficiency ( $N_{60}$ ), the cone tip resistance ( $q_c$ ), and the friction ratio ( $R_f$ ). Groundwater level was not detected during borehole logging. The water table is usually encountered at great depths below the ground surface (> 50 m). Surveying in Area B was performed before the placement of the surficial backfill layer.

In both areas, the surficial soil layer is composed of a 3-m-thick pure sand backfill, collected from a neighboring cut sector within site. Below the backfill sand lay natural layers of dune sediments, composed of sand and silty sand. The backfill is a medium uniformly graded quartz silica sand of eolian origin that classifies as SP, according to the Unified Soil Classification System. The grain size distribution of the backfill sand is shown in Figure 2a. The sand has an average particle size of 0.35 mm, a coefficient of uniformity of 2.2, and a coefficient of curvature of 1.07. The sand has less than 2% of the particles finer than 0.075 mm and more than 98% finer than 2 mm. Its specific gravity is 2.59, and maximum and minimum void ratios are 0.83 and 0.60, respectively. The top sand layer was compacted with relative density ( $D_r$ ) of 45% in Area A, and 70% in Area B. Controlled compaction in the field was carried out using vibrating drum rollers.

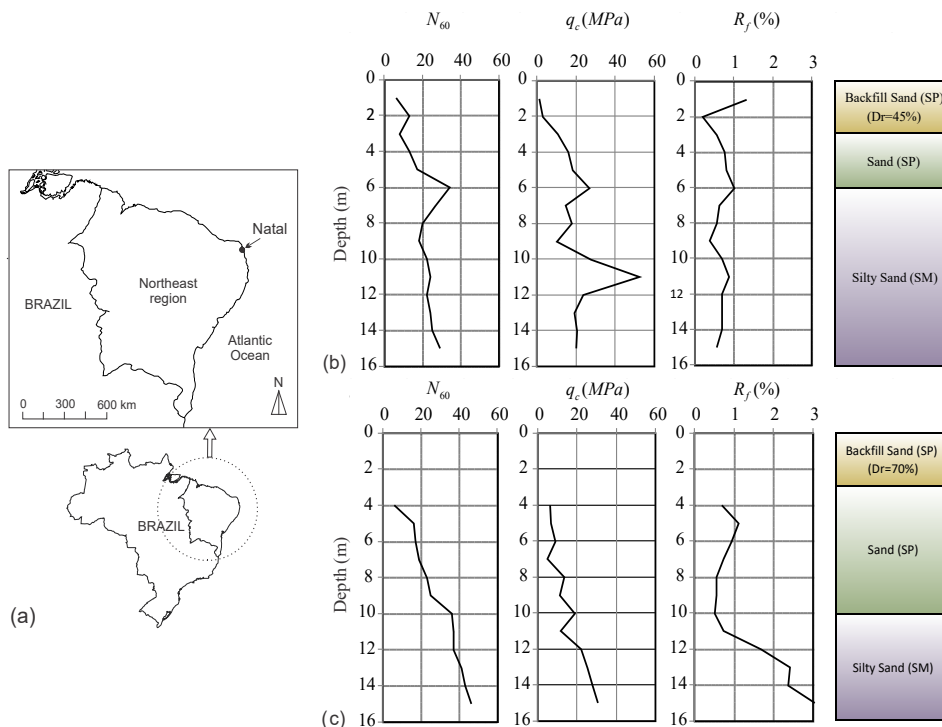
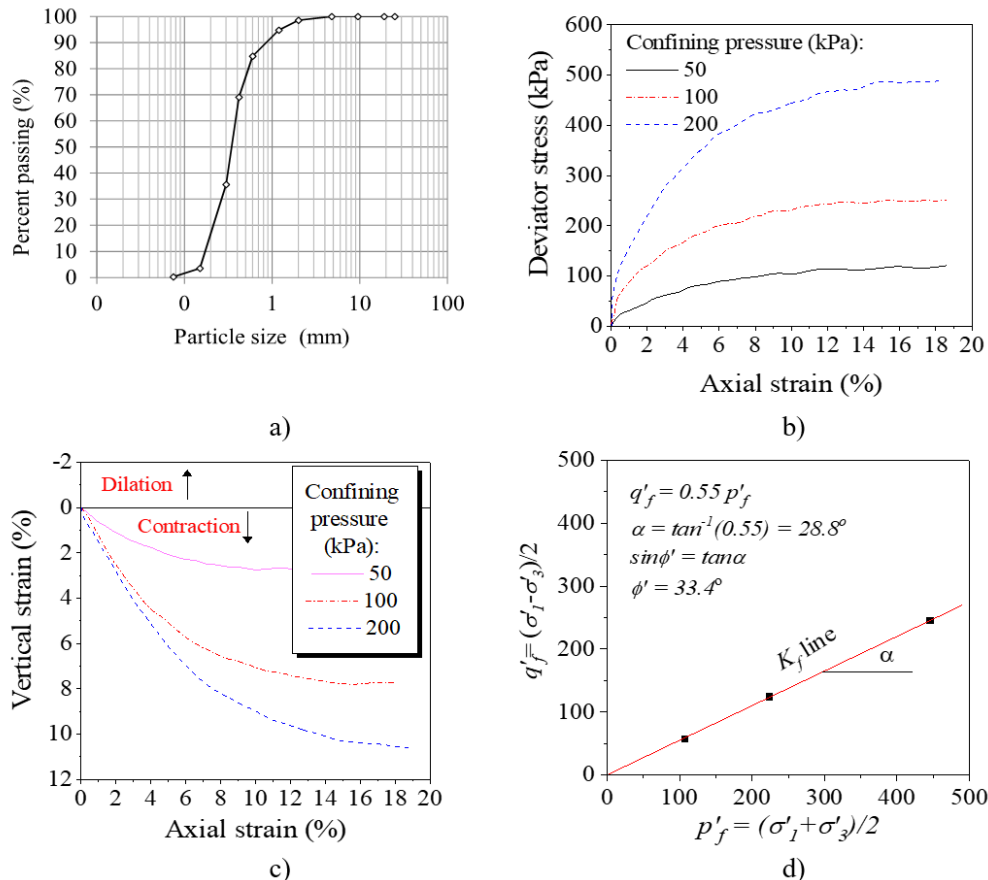


Figure 1. (a) Location of test site; (b) Site investigation results in Area A; (c) Site investigation results in Area B.

Shear strength parameters of the backfill sand were obtained from two series of conventional CID triaxial compression tests carried out with confining effective stresses ( $\sigma'_3$ ) of 50 kPa, 100 kPa, and 200 kPa. One series of tests was prepared with target relative density ( $D_r$ ) of 45%, and another series was prepared with  $D_r = 70\%$ , which are the same densities used in the field. Peak friction angle ( $\phi'_p$ ) was calculated from the  $K_f$  line of  $p$ - $q$  diagrams of the tested soil. Values of  $\phi'_p$  equals  $33.6^\circ$  and  $38.1^\circ$  for  $D_r = 45\%$  and  $70\%$ , respectively. Deviator stress-axial strain and volume change behavior for the soil at the relative density of 45% are presented in Figure 2b and Figure 2c, respectively, and the corresponding  $K_f$  line is indicated in Figure 2d.



**Figure 2.** Properties of the backfill sand: (a) grain-size distribution; (b-c) results of CID triaxial tests performed on sand samples prepared with a relative density of 45%; (d)  $p$ - $q$  diagram of the tested sand.

### 3 FIELD TESTING PROGRAM AND INSTRUMENTATION

A total of 12 field load tests were carried out to investigate the lateral behavior of single piles in the two sandy soil profiles. Continuous flight auger (CFA) and steel H-section model piles were installed in Areas A and B, as indicated in Figure 3. The tests were performed simultaneously on two piles with identical lengths and cross-sections, which reacted against each other. As shown in Figure 3, piles CFA-i and CFA-ii were tested together, and so did piles HS1-i and HS1-ii, and HS2-i and HS2-ii. A summary of the testing sequence is presented in Table 1, which indicates the pile type, the area where the test was carried out, and the test designation.

The CFA piles were cast with a diameter ( $D$ ) of 0.6 m and length ( $L$ ) of 10 m. The integrity of the CFA piles was verified by a low-strain integrity test that uses the pulse-echo method, commonly named as pile integrity test (PIT). The reinforcement of the CFA piles consists of 10 longitudinal steel bars with 20 mm in diameter enveloped by a steel spiral with 8.0 mm in diameter and 200 mm in spacing. Concrete with characteristic compressive strength of 35 MPa at 28 days was used for the CFA piles. The initial flexural stiffness ( $E_p I_p$ ) of the CFA pile cross-section is 220 MN m<sup>2</sup>.

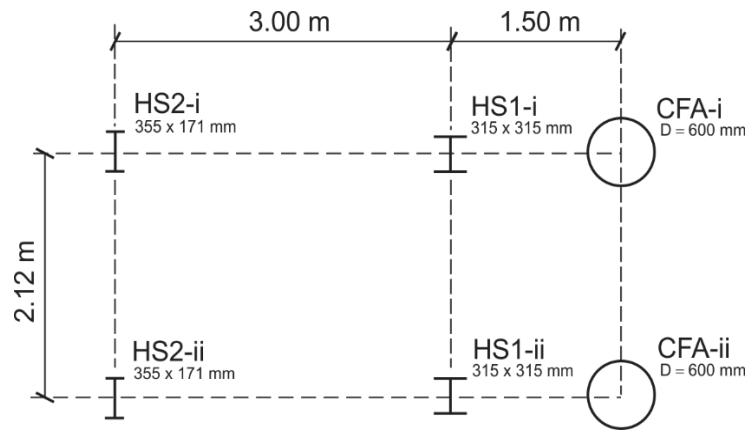


Figure 3. Elevation view showing the position of model piles.

Table 1. Testing program summary

Test N°	Pile type	Testing Area	Backfill relative density, $D_r$ (%)	Designation
1	CFA	B	70	CFA-B-70-i
2	CFA	B	70	CFA-B-70-ii
3	CFA	A	45	CFA-A-45-i
4	CFA	A	45	CFA-A-45-ii
5	HS1	A	45	HS1-A-45-i
6	HS1	A	45	HS1-A-45-ii
7	HS2	A	45	HS2-A-45-i
8	HS2	A	45	HS2-A-45-ii
9	HS2	B	70	HS2-B-70-i
10	HS2	B	70	HS2-B-70-ii
11	HS1	B	70	HS1-B-70-i
12	HS1	B	70	HS1-B-70-ii

Two different steel H-section piles were used, as shown in Figure 3. One pair of steel piles had cross-section with width = 315 mm, height = 315 mm, flange thickness = 17.4 mm and web thickness = 17.4 mm (HS1-i and HS1-ii). The other pair of steel piles had cross-section with width = 171 mm, height = 355 mm, flange thickness = 11.6 mm and web thickness = 7.2 mm (HS2-i and HS2-ii). All steel piles had a total length of 6 m and embedded length in the ground of 4.5 m. The initial bending stiffness ( $E_p I_p$ ) of the cross-section of piles HS1 and HS2 are 56 MN.m<sup>2</sup> and 29 MN.m<sup>2</sup>, respectively.

In both testing areas, HS1 and HS2 piles were tested before the casting of the CFA piles. Spacing between the CFA and the HS1 pairs of piles (Figure 3) was defined to accommodate the use of these piles as a reaction for a vertical load test performed in another pile installed after completion of the lateral load tests, which is not included in the present study. The distance between HS1 and CFA piles was assumed sufficient to minimize cross-interference. Based on experimental results from physical model tests, Davisson [30] concluded there is essentially no influence of one pile on another, providing the spacing normal to the direction of loading is at least 2.5  $D$  from the pile axis. According to results from instrumented tests on small-scale models of laterally loaded piles, at a depth of 3.45  $D$  below the soil surface, horizontal stress changes extend to a maximum distance of 2.5  $D$  beside the pile [31].

The layout of the installation and instrumentation of the CFA model piles is depicted in Figure 4a. A shallow pit with a depth of 0.5 m was excavated between the piles to accommodate the loading system. The load was applied in cumulative equal increments using a hydraulic cylinder with a maximum nominal capacity of 500 kN. The cylinder was positioned as close as possible to the pile head. Load measurements were obtained by a calibrated load cell with a maximum nominal capacity of 500 kN. Horizontal pile displacements ( $y_i$ ) were recorded at the ground surface level

using dial gages with a resolution of 0.01 mm and a maximum stroke of 50 mm. The dial gauges were mounted in magnetic-articulated bases set on two steel reference beams.

Similar instrumentation, as described above, was used in the tests with the steel piles, and a general scheme of its setup is illustrated in Figure 4b. The loading system was mounted directly on the ground surface, and the horizontal displacements of the pile ( $y_i$ ) were recorded at 0.5 m and 1.2 m above the ground surface.

All lateral loading tests were performed with static quick maintained load (QML) [32] and followed the Brazilian code ABNT NBR 12131:2006 [33]. Each load increment was held constant for 5 min, and displacement readings were taken at every minute. The unloading phase was carried out with four 5-minute-long decrements. The unloading stages were not recorded in Test 5 due to the sudden disassembling of the loading system during the last stage.

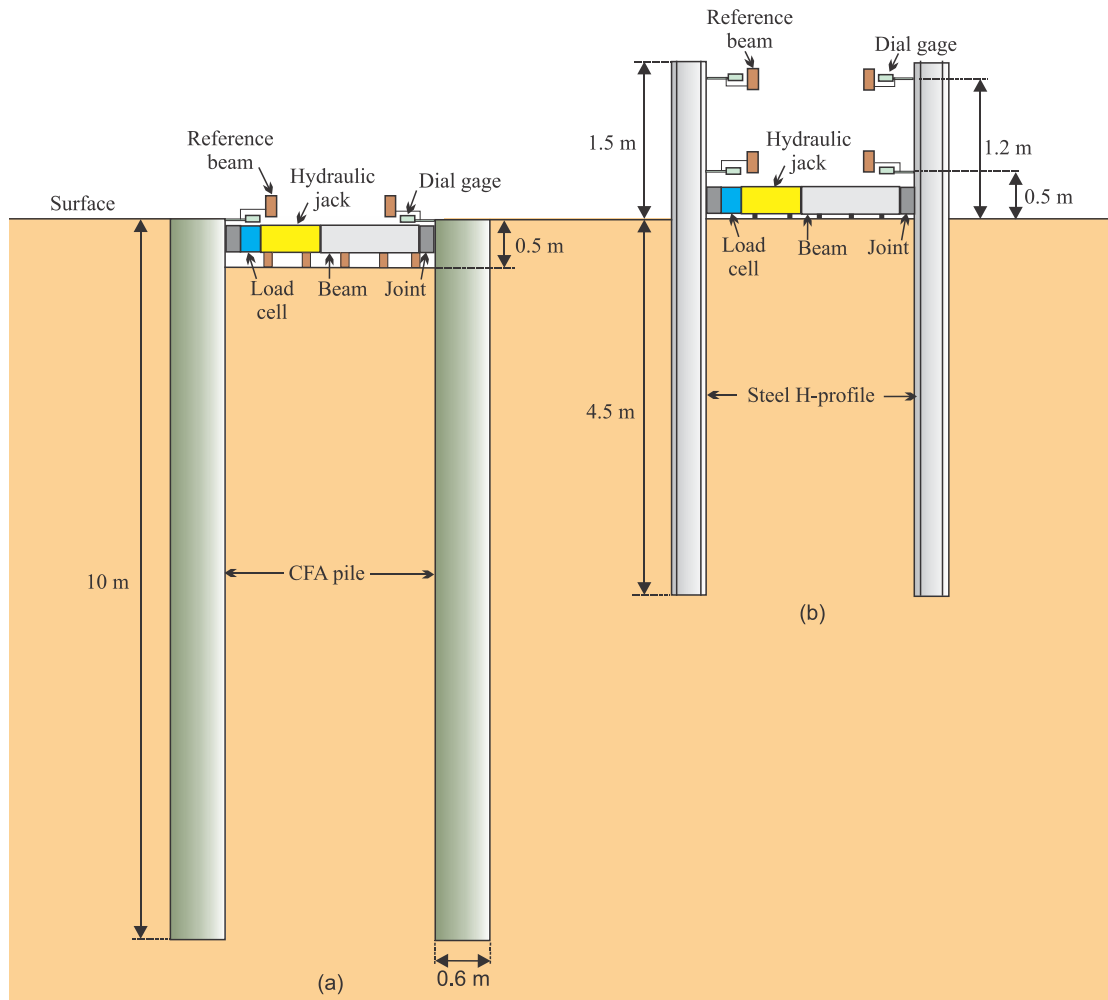


**Figure 4.** General scheme of testing assemblage and used apparatus: (a) CFA piles; (b) steel H-section piles.

#### 4 FIELD TEST RESULTS

Figure 5 shows the lateral applied load ( $H$ ) versus measured lateral displacement ( $y_i$ ) curves of each individual pile, obtained from the field tests performed in Areas A and B. The displacements ( $y_i$ ) recorded with the upper dial gages in the tests with the steel H-section profiles are omitted from Figure 5 for clarity. By comparing the results of the same pair of piles, it is possible to notice that the curves of the steel H-section piles situate within a narrower range than those of the CFA piles. Imperfections in the shaft of the CFA piles associated with the construction process may partially explain the poorer repeatability of the tests with this pile type since no cast-in-place pile is exactly equal to another.

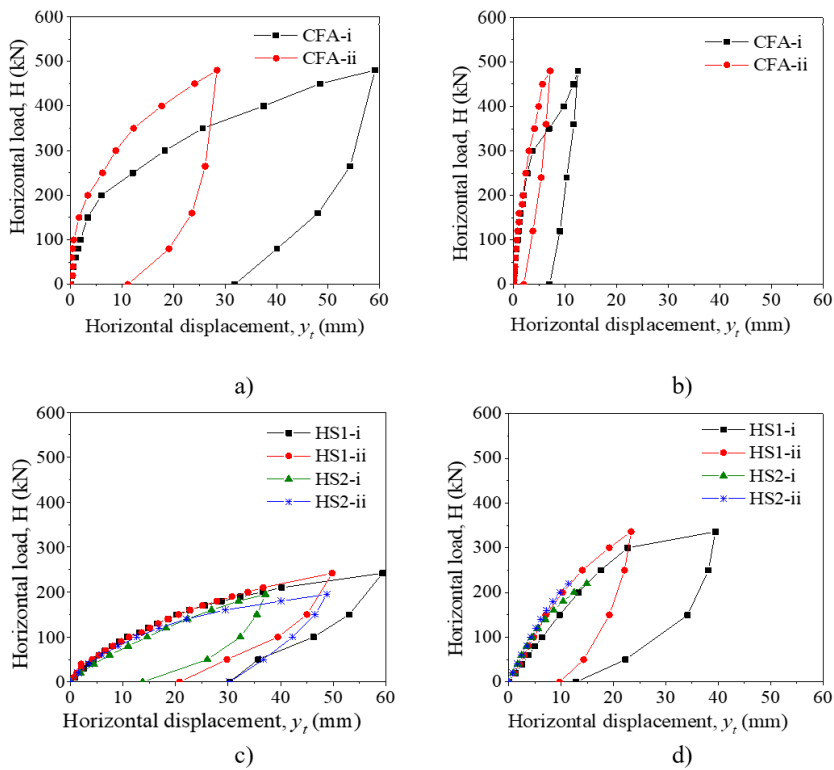


**Figure 5.** Results of the lateral tests: (a) CFA piles in Area A; (b) CFA piles in Area B; (c) steel H-section piles in Area A; (d) steel H-section piles in Area B.

The CFA piles reached larger maximum lateral loads in comparison to the steel piles. The average value of the maximum horizontal load with the CFA piles was 480 kN in both testing areas, which is close to the limit load of 500 kN of the loading system. In Area A, the average value of the maximum horizontal load of pair HS1 was 242 kN, and of the pair HS2 was 195 kN. Slightly higher maximum lateral loads were obtained with the steel piles installed in Area B due to the greater relative density of the sand backfill: 334 kN with pair HS1 and 220 kN with pair HS2. The unloading portion of the curves reveals that the horizontal displacement recovered after unloading is significant and is larger with the steel piles than the CFA piles, due to the resilient feature of the steel.

In both testing areas, the results of the HS1 and HS2 piles were close. As expected, the curves of the HS1 piles showed slightly larger horizontal loads for a specific displacement, due to the higher cross-section flexural stiffness of that pile type.

The constant of horizontal subgrade reaction ( $n_h$ ) was back calculated from the load test results of the CFA piles using the following equation [22]:

$$y_0 = 2,435H \frac{T^3}{E_p I_p} + 1,623(He) \frac{T^2}{E_p I_p} \tag{1}$$

where:  $y_0$  = horizontal displacement of the pile at the ground surface;  $H$  = horizontal applied load;  $e$  = position of the axis of application of  $H$  above the ground surface;  $E_p$  = Young’s modulus of pile material;  $I_p$  = moment of inertia of pile cross-section;  $T$  = pile characteristic length, given as:

$$T = \sqrt[5]{\frac{E_p I_p}{n_h}} \tag{2}$$



Since the displacements of the CFA piles were recorded at the level of the terrain, Equation 1 was solved assuming  $y_0 = y_t$ . The characteristic length  $T$  was obtained from Equation 1 assuming the distance from the ground surface to the point of application of the load ( $e$ ) equals zero. After finding the characteristic length,  $n_h$  was calculated from Equation 2.

The constant of horizontal subgrade reaction of the steel H-section piles was calculated by solving a system composed of Equations 1 and 3, which gives  $T$ ,  $E_p I_p$ , and  $y_0$  for each applied load  $H$ .

$$y_0 = y_t + S_0(e + e') - \frac{He^3}{3E_p I_p} - \frac{He^2 e'}{2E_p I_p} \tag{3}$$

where:  $y_t$  = mean horizontal displacement of piles tested simultaneously against each other;  $S_0$  = rotation of the pile head at the ground surface;  $e'$  = vertical distance from the axis of application of  $H$  to the position of measurement of  $y_t$ . In the assemblage of the tests with the steel H-section piles,  $e = 0.2$  m, and  $e' = 0.3$  m or 1 m (see Figure 4).

The rotation of the pile head at the ground surface was calculated from Matlock and Reese [34]:

$$S_0 = -1.623H \frac{T^2}{E_p I_p} - 1.750He \frac{T}{E_p I_p} \tag{4}$$

This approach for the computation of  $n_h$  assumes that the modulus of subgrade reaction, obtained for the soil near the surface of the terrain, varies linearly with depth and is representative of the entire ground along the pile length. However, potential inaccuracies produced by this assumption are not supposed to be significant, since it is well established that the response of a pile to lateral loading is essentially controlled by the stiffness of the soil at shallow depth [13], [35]. Zhang et al. [36] reported depths of influence between 3 and 4 times the pile diameter. Considering the soil profile of the present study, such depth of influence is within the surficial sand layer, which suggests that the pile response is ruled by this layer.

Figure 6a and Figure 6b show the relationship between  $n_h$  and the horizontal displacement  $y_0$  obtained for Areas A and B, respectively. The horizontal displacement  $y_0$  is normalized by dimension  $B$ , which is the diameter of the CFA pile or the width of the steel pile. The constant of horizontal subgrade reaction follows a steep decrease at small horizontal displacements and tends to stabilize with increasing displacements. Values of  $n_h$  were significantly larger with the denser backfill sand of Area B. As pointed out by Prakash and Kumar [37] the modulus of horizontal reaction depends strongly on the relative density of sands.

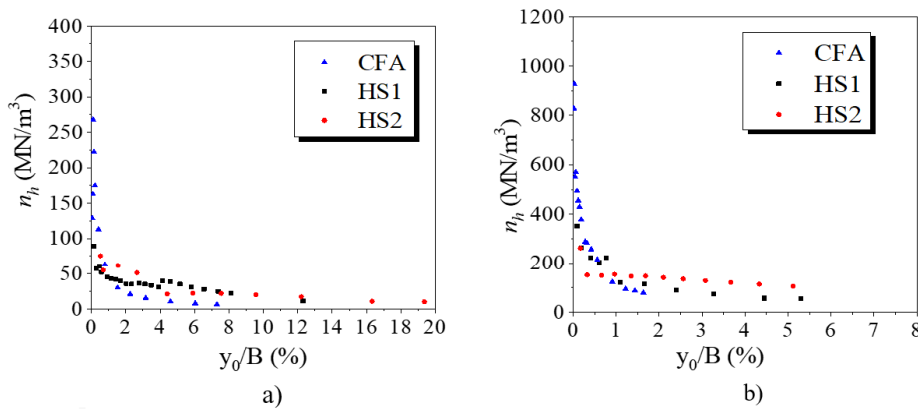


**Figure 6.** Relationship between the constant of subgrade reaction  $n_h$  and the horizontal pile displacement at ground level: (a) Area A; (b) Area B.

### 5 THREE-DIMENSIONAL NUMERICAL MODELING OF Laterally LOADED CFA AND STEEL H-SECTION PILES

The finite-element program Plaxis3D was used to simulate the response of a single pile under lateral load in the studied soil profiles. Figure 7a and Figure 7b show the typical undeformed 3-D FE mesh used in the analyses of the CFA piles. The model boundaries extended to a width of 10 m from the pile center and to a depth equal to 20 m (*i.e.*,

the pile length plus 10 m below the pile-toe level). These dimensions were considered sufficient to exclude boundary effects in previous investigations. The outer vertical boundary of the mesh is fixed in the horizontal direction and free in the vertical direction. The base of the soil model is constrained in both vertical and horizontal directions. The mesh consists of 15-node wedge elements, which were applied to simulate both the soil and the CFA pile. The meshing discretization used in this study followed the approach proposed by Kim and Jeong [5]. For the proposed numerical model, the mesh was manually refined close to the pile. Although one dimension of the elements in the vicinity of the pile is considerably smaller than the other two (i.e., elements with large aspect ratio, as shown in Figure 7c), the use of wedge elements with quadratic approximation (15 nodes) reduced potential numerical problems of convergence. Moreover, since the mean size of the element cannot be freely defined in the software, refinement of the mesh close to the pile was necessary to ensure a higher number of elements and nodes in the loading direction.

All numerical simulations were carried out under drained conditions. The soil behavior was modeled by the hardening soil (HS) constitutive model developed under the framework of the theory of plasticity, in which a stress-strain relationship, due to the primary loading, is assumed to be a hyperbolic curve [38]. Soil failure takes place according to the Mohr-Coulomb failure criterion. The CFA pile was considered as an isotropic linear-elastic material. The material properties of soils and piles used in this analysis are depicted in Table 2.

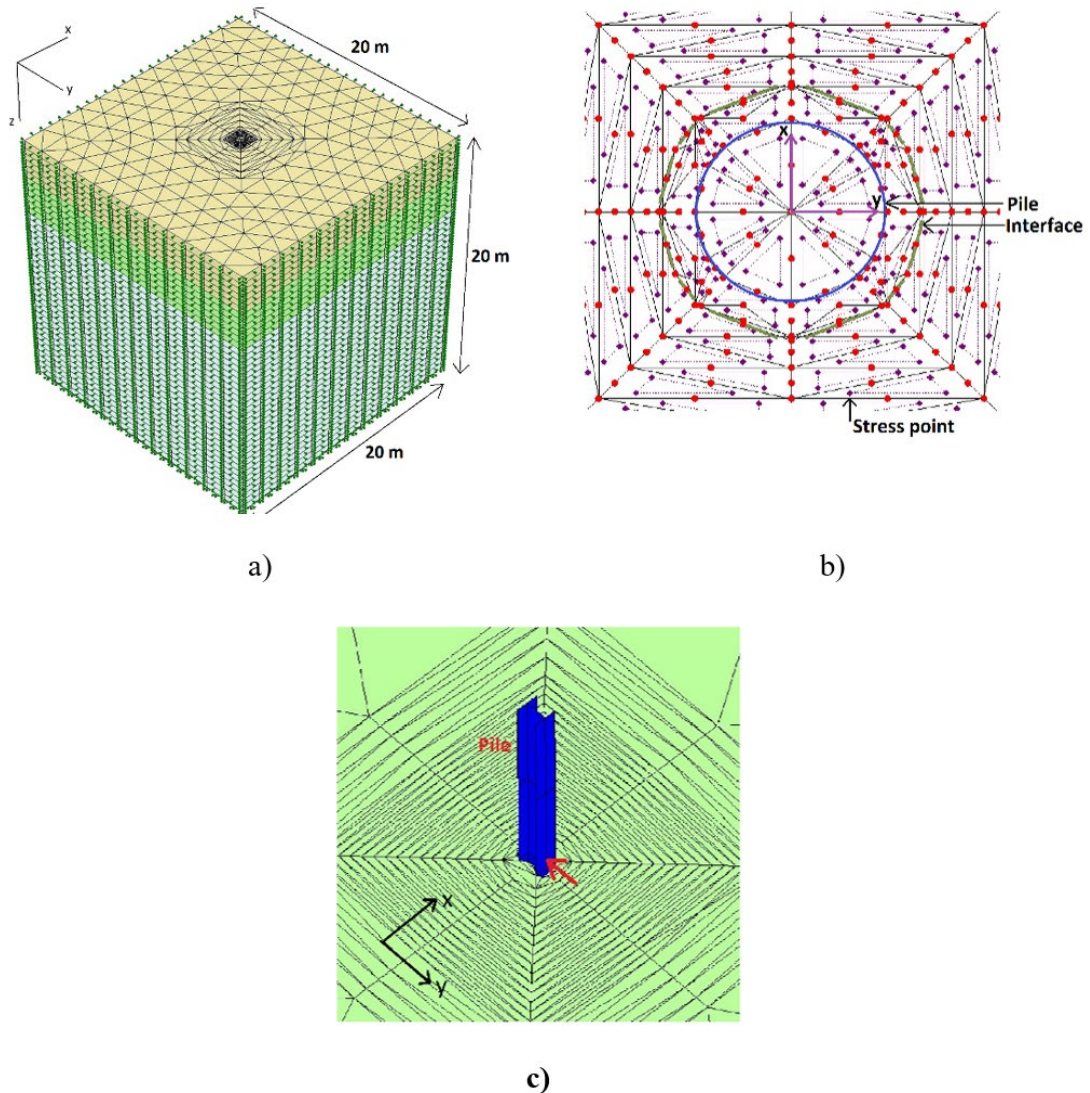


**Figure 7.** Three-dimensional finite-element mesh: (a) 3D view of CFA pile model; (b) cross-section in x-y plane of CFA pile model; (c) surface view of steel H-section HS1 pile model.

**Table 2** - Material properties used in the FE analysis

Material		Parameter		
CFA pile	Concrete unit weight, $\gamma$ (kN/m <sup>3</sup> )	25		
	Pile Young's modulus, $E_p$ (MPa)	35,000		
	Pile coefficient of Poisson, $\nu_p$	0.2		
H-Steel pile	Pile Young's modulus, $E_p$ (MPa)	207,000		
Soil		Backfill	Sand	Silty Sand
Area A ( $D_r = 45\%$ )	Soil unit weight, $\gamma$ (kN/m <sup>3</sup> )	16	17.5	17
	Soil Young's modulus, $E_s$ (MPa)	50	100	100
	Soil coefficient of Poisson, $\nu_s$	0.30	0.35	0.35
	Peak friction angle, $\phi'_p$ (°)	31.6	38	36.4
	Soil-pile interface friction angle, $\delta$ (°)	22.3	27.5	26.2
	Effective cohesion, $c'$ (kPa)	5	5	10
	Dilatancy angle, $\psi$ (°)	0	5	10
Area B ( $D_r = 70\%$ )	Soil unit weight, $\gamma$ (kN/m <sup>3</sup> )	18	17	18
	Soil Young's modulus, $E_s$ (MPa)	100	100	100
	Soil coefficient of Poisson, $\nu_s$	0.35	0.35	0.35
	Peak friction angle, $\phi'_p$ (°)	35.1	37	40.6
	Soil-pile interface friction angle, $\delta$ (°)	25.1	26.7	29.7
	Effective cohesion, $c'$ (kPa)	5	5	10
	Dilatancy angle, $\psi$ (°)	10	5	10

The main parameter governing the soil-pile interface properties in Plaxis software is the strength reduction factor ( $R_{inter}$ ), which is the ratio between interface friction coefficient ( $\mu_{inter} = \tan\delta$ ) and soil friction coefficient ( $\mu = \tan\phi'$ ) or the ratio between interface cohesion ( $c_{inter}$ ) and soil cohesion ( $c'$ ).  $R_{inter}$  varies between 0 and 1. The baseline  $R_{inter}$  value used in the present study is 0.7.

The steel H-section piles were modeled using plate elements with prescribed flexural and axial rigidities. The models with the steel piles were built with the same dimensions of the models with the CFA pile. A three-dimensional surface view of the model with steel profile HS1, showing the shape of the undeformed mesh around the pile, is presented in Figure 7c.

Figure 8 compares the experimental and numerical results in terms of horizontal load ( $H$ ) versus horizontal displacement ( $y_0$ ) relationships. The lateral load capacities obtained from the field tests are compared with those predicted from the different methods in Table 3.

FHWA [39] proposes tolerable horizontal movements of a single pile of less than 38 mm from a serviceability standpoint. According to AASHTO [40], tolerable displacements of a pile shall be limited to 50 mm or less where vertical displacements are small or to 25 mm or less where combined vertical and horizontal displacements are possible. The ultimate lateral load capacity obtained from the load tests is shown in Table 3 assuming an allowable horizontal displacement  $y_0 = 20$  mm as a serviceability limit for the foundation. Since the displacement level of 20 mm was not reached in the tests performed in Area B, the corresponding experimental ultimate loading capacity was obtained from the extrapolation of the curves using the method of Mazurkiewicz [41].

The three-dimensional finite element model closely matched the ultimate lateral capacities to the experimental data (Table 3). The computed ultimate lateral capacity for testing Area A approached the field results closely. The largest discrepancy between numerical and measured results was 21% for H-section pile HS1 embedded in the soil of testing Area B. The 3-D FEM analysis also closely matches the general trend of the experimental curves of CFA and steel H-section piles (Figure 8). Small differences between the three-dimensional numerical simulations and the field results were expected and may be attributed to the variability of soil properties and pile characteristics.

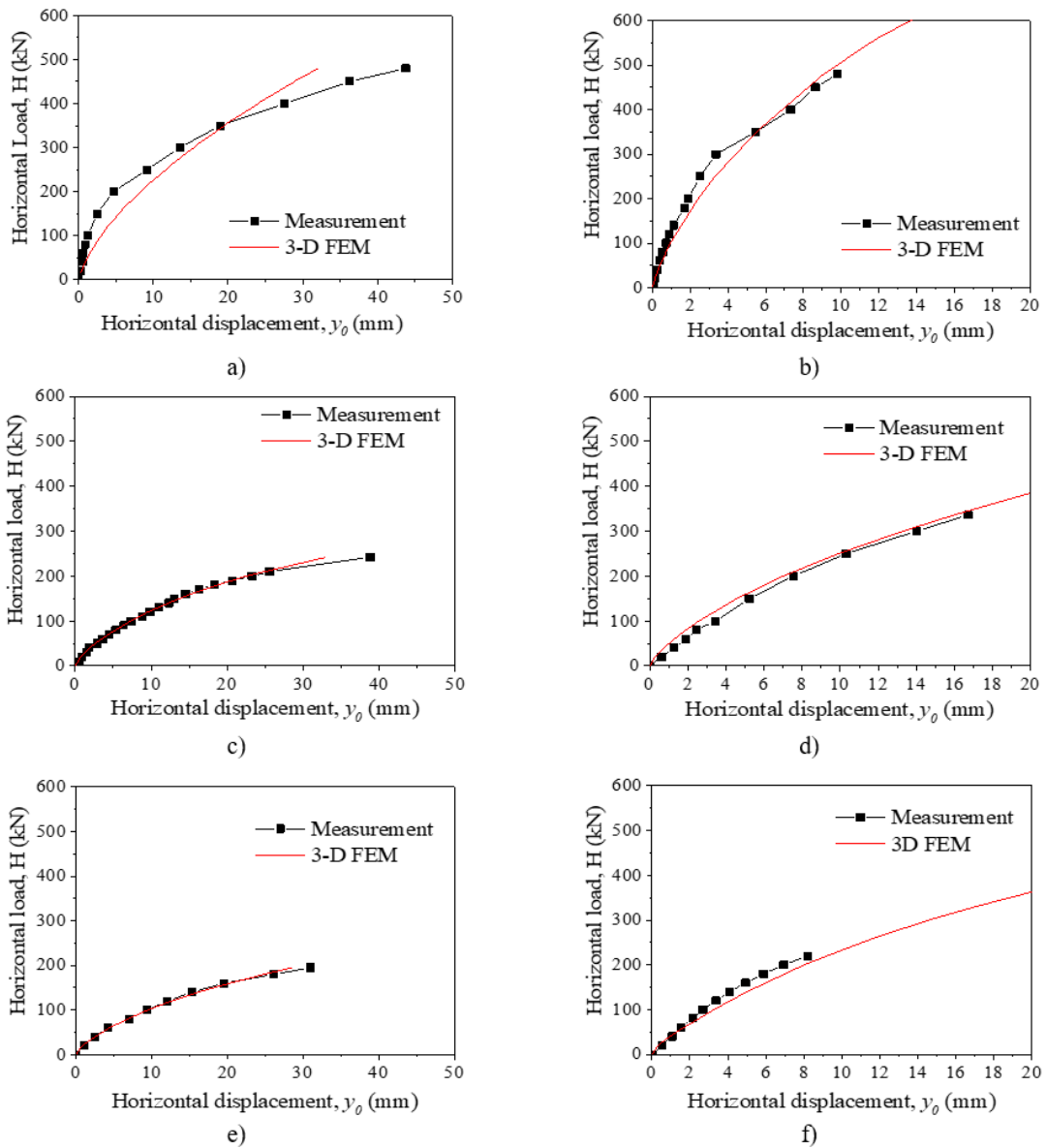


**Figure 8.** Comparison of the response of laterally loaded piles obtained from field tests and by numerical modelling: (a) CFA pile in Area A; (b) CFA pile in Area B; (c) steel pile HS1 in Area A; (d) steel pile HS1 in Area B; (e) steel pile HS2 in area A; (f) steel pile HS2 in Area B.

**Table 3.** Comparison of lateral load capacity of CFA and steel H-section piles obtained from the field tests and the numerical simulations.

Testing Area	Ultimate lateral capacity (kN)		
	Pile type	Field	FEM
A ( $D_r = 45\%$ )	CFA	355	355
	HS1	188	187
	HS2	162	157
B ( $D_r = 70\%$ )	CFA	690 <sup>1</sup>	716
	HS1	490 <sup>1</sup>	385
	HS2	312 <sup>1</sup>	362

Note: <sup>1</sup>Values extrapolated according to Mazurkiewicz [41].

Parametric studies were performed to analyze the influence of (i) the soil-pile relative stiffness, (ii) the pile diameter, (iii) the interface friction between pile and soil, (iv) and soil dilatancy (the volume change characteristics of the soil). The analysis of soil-pile relative stiffness was carried out for CFA piles and steel HS1 piles in Areas A and B. Analysis of pile diameter, soil-pile interface friction and soil dilation were developed considering CFA piles only.

Figure 9 shows the response of the steel HS1 pile in Area A for different bending stiffness values ( $E_p I_p$ ), which were varied by changing the Young's modulus of the pile ( $E_p$ ) while keeping the second moment of inertia ( $I_p$ ) constant. In Figure 9,  $E_p I_p$  is the baseline bending stiffness of profile HS1, which is equal to 56 MNm<sup>2</sup>. Results show that variations in pile stiffness drastically affects the behavior of the pile under lateral loading. Similar trends were also obtained from the parametric analysis carried out with the other pile types embedded in Areas A and B. The results are in accordance with the findings reported by Norris et al. [11], which used the strain wedge (SW) model to predict the behavior of cast-in-place and steel piles in cohesive and cohesionless soils.

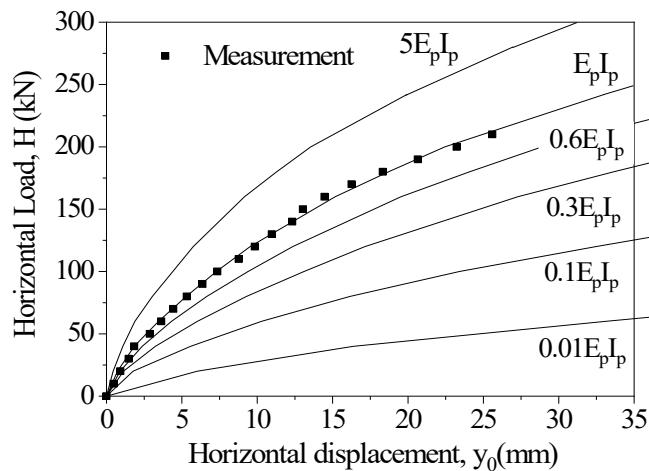


Figure 9. Response of steel H-section pile HS1 embedded in Area A, for various bending stiffness values.

Deeper insight into the effect of pile stiffness can be attained under the framework of soil-pile relative stiffness. Within this concept, the pile and the surrounding soil behave as a single system. The characteristic pile length,  $T$ , defined by Equation 2, can be used to determine whether the soil-pile system behaves as a rigid or a flexible member [13], [42].  $T$  is also called relative stiffness factor and expresses a relation between the stiffness of the soil, *i.e.*, the constant of horizontal subgrade reaction ( $n_h$ ), and the flexural stiffness of the pile ( $E_p I_p$ ). Figure 10 shows the normalized ultimate lateral capacity ( $H_u^*$ ) as a function of the nondimensional length, given by the ratio between the pile length and the characteristic pile length ( $L/T$ ). The nondimensional length is another way of quantifying the soil-pile relative stiffness and has the advantage of incorporating the pile length. The larger the nondimensional length, the more flexible the soil-pile system. Data points shown in Figure 10 belong to CFA pile and steel pile HS1 in Areas A and B and were computed for a constant lateral displacement  $y_0 = 20$  mm. A trend line fitting the data points is also shown in Figure 10, along with the corresponding empirical equation.  $H_u^*$  is expressed as:

$$H_u^* = \frac{H_u}{I_R B^3} \tag{5}$$

where:  $H_u$  = ultimate lateral load at a 20-mm lateral displacement, as previously defined;  $B$  = pile diameter or width;  $\gamma$  = effective unit weight of the surficial sand layer;  $I_R$  = rigidity index of the surficial sand layer, given as [43]:

$$I_R = \frac{G_s}{p' \tan'} \tag{6}$$

where:  $G_s = E_s/2(1+\nu_s)$  = shear modulus of the soil;  $p'$  = reference pressure, assumed = 100 kPa.

Figure 10 shows that the normalized ultimate lateral capacity  $H_u^*$  decreases with increasing soil-pile relative stiffness. At low  $L/T$  ratios, a small variation in relative stiffness causes a dramatic variation in  $H_u^*$ . Short rigid piles are, therefore, much more influenced by changes in relative stiffness than long flexible members. The effect of soil-pile stiffness becomes much less significant for  $L/T$  ratios above 10.  $L/T = 4$  has been commonly accepted as the limit beyond which the pile behaves like a long flexible unit [30], [44]. Information presented in Figure 10 can be used in the design of laterally loaded piles in similar local soils for a preliminary estimation of the ultimate lateral capacity.

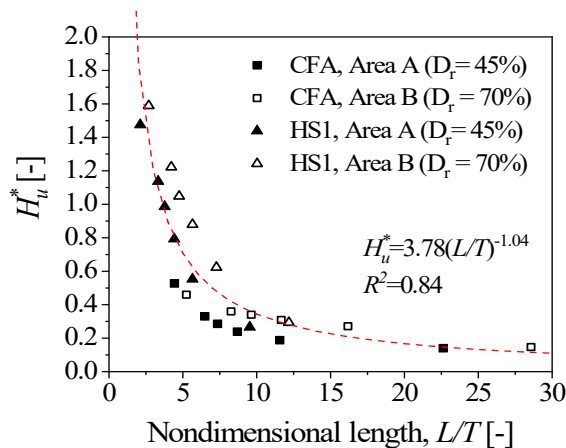


Figure 10. Normalized ultimate lateral capacity of piles  $H_u^*$  as a function of the nondimensional length  $L/T$ .

The influence of the pile diameter on pile behavior was investigated in the light of the soil-pile relative stiffness concept. The study included the modeling of CFA piles with diameters of 0.3, 0.6, 0.9, and 1.2 m, embedded in Area A. The non-dimensional length ratio ( $L/T$ ) was maintained unchanged while the pile diameter was varied. Figure 11 shows the effect of the diameter of the pile on the horizontal load ( $H$ ) for various non-dimensional length ratios ( $L/T$ ). Linear trend lines were fitted to the data points in Figure 11. Appropriate values of horizontal load were obtained from the calculated  $H-y_0$  curve of each corresponding pile and using Equation 1 with the selected characteristic length  $T$ . The computational results shown in Figure 11 indicate that the effect exerted by the diameter was significant and became more evident with smaller non-dimensional length ratios. In addition, the relationship between the horizontal load and the pile diameter appears to be nearly linear for the range of examined diameters and non-dimensional length ratios, which agrees with the findings reported by Carter [28], Guo [23], and Kim and Jeong [5].

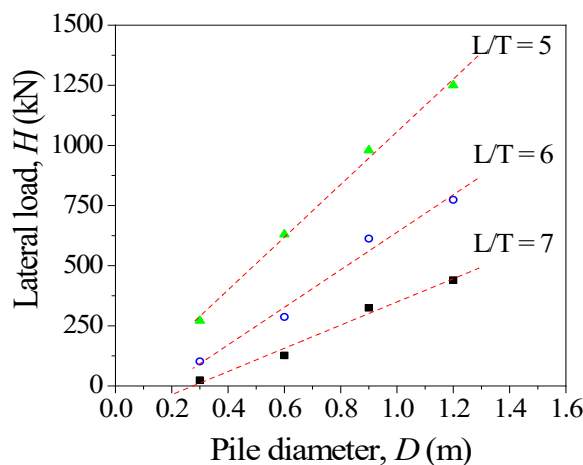


Figure 11. Relationship between lateral load and diameter of CFA piles for various non-dimensional length ratios.

The effect of soil-pile interface friction on the CFA pile response was evaluated by varying the interface strength reduction factor ( $R_{inter}$ ) within the backfill sand layer. As mentioned previously,  $R_{inter}$  is the main controlling parameter of the soil-pile interface in PLAXIS 3D software. The change of the ultimate lateral capacity ( $H_u$ ) was investigated for strength reduction factors ranging from 0.1 to 0.9, as presented in Figure 12. The computed results reveal that the ultimate lateral capacity presents a non-linear increase with increasing interface property. The influence of  $R_{inter}$  on  $H_u$  is more relevant between  $R_{inter} = 0.1$  to 0.3. Moreover, changes in interface property were comparatively more prominent in Area B, which has the denser surficial backfill sand.

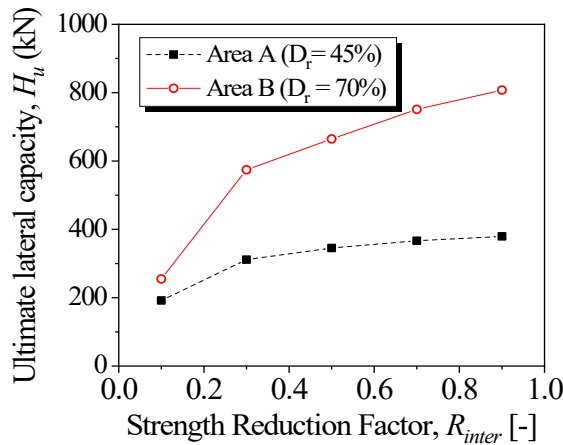


Figure 12. Change of ultimate lateral capacity of CFA piles with interface property.

Shear strength of dense cohesionless soils is largely dependent on volume change properties of the material [45]. The effect of soil dilatancy on soil-pile interaction was assessed by assigning dilatancy angles from  $0^\circ$  to  $15^\circ$  to the backfill sand of both testing areas. Figure 13 shows the variation of the ultimate lateral capacity ( $H_u$ ) at 20-mm lateral displacement with dilatancy angle ( $\psi$ ), obtained with the computed data of the CFA pile. The figure shows that soil dilatancy has an influence on pile performance. An increment in the angle of dilatancy from  $0^\circ$  to  $15^\circ$  caused an average 9% increase in the lateral load capacity of the CFA pile. In addition, influence on ultimate lateral capacity is slightly more evident in Area B, which has the denser backfill sand. Comparatively, Choi et al. [15] obtained an increase of 20% in the lateral load capacity of bored piles in weathered granite soil, at a 20-mm lateral displacement, as  $\psi$  increased from  $0^\circ$  to  $15^\circ$ .

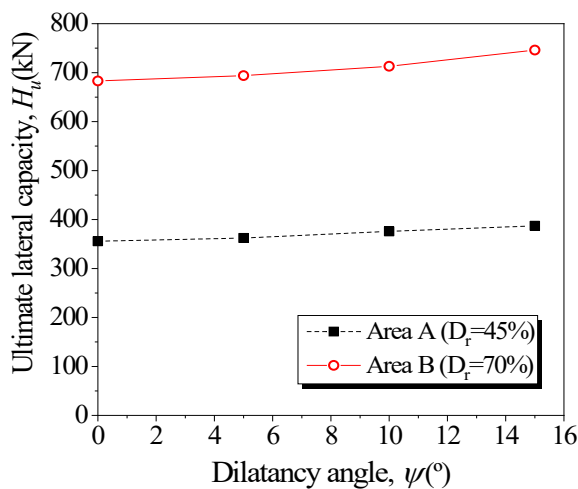


Figure 13. Ultimate lateral capacity of the CFA pile as a function of soil dilatancy.

## 6 SUMMARY AND CONCLUSIONS

The response of continuous flight auger (CFA) bored piles and steel H-section driven piles to lateral loading was evaluated in this study by field tests and via a three-dimensional finite element (3-D FE) model. The proposed numerical model was substantiated with field tests performed on four CFA piles and eight steel H-section piles in two distinct sandy soil profiles. The three-dimensional finite element approach closely matched the response of CFA and steel H-section piles in terms of the relationships between the applied horizontal load and the horizontal pile displacement recorded from the field tests. A series of parametric analyses was carried out to investigate the role of relevant variables on lateral soil-pile interaction. The main findings of the study can be summarized as follows:

- (1) The pile ultimate lateral load is drastically affected by soil-pile system relative stiffness. Short rigid piles are much more influenced by changes in relative stiffness than long flexible units. The effect of soil-pile stiffness becomes significant for nondimensional length ratios ( $L/T$ ) below 4.
- (2) Pile diameter exerts a marked effect on pile lateral load, which is more prominent with stiffer soil-pile systems. Moreover, the relationship between horizontal load and pile diameter appears to be nearly linear for the range of examined diameters and nondimensional length ratios.
- (3) The ultimate lateral load capacity of CFA piles significantly increases with increasing soil-pile interface friction coefficient. Soil-pile interface friction affects more the ultimate lateral capacity of piles embedded in denser soils. In addition, variations in ultimate lateral capacity appear to be more significant with lower interface friction coefficients.
- (4) Soil dilatancy causes a slight increase in the ultimate lateral capacity of the CFA piles in the sandy soil deposits. An increment in the angle of dilatancy from  $0^\circ$  to  $15^\circ$  in the surficial sand layer caused an increase of about 9% in the lateral load capacity of the CFA pile for both tested relative densities of 45% and 70%.

## ACKNOWLEDGEMENTS

The authors gratefully acknowledge the financial support provided by the National Council for Scientific and Technological Development (CNPq) and the São Paulo Research Foundation (FAPESP - 2018/21573-2). The authors also acknowledge the contributions from João Paulo Costa and Avelino Lourenço on conducting the static lateral loading tests in the field.

## REFERENCES

- [1] M. G. Ritter, M. L. Menegotto, M. F. Costella, R. C. Pavan, and S. E. Pilz, "Analysis of soil-structure interaction in buildings with deep foundation," *IBRACON Struct. Mater. J.*, vol. 13, no. 2, pp. 248–260, 2020, <http://dx.doi.org/10.1590/s1983-41952020000200005>.
- [2] L. M. P. Rosa, B. R. Danziger, and E. M. L. Carvalho, "Soil-structure interaction analysis considering concrete creep and shrinkage," *IBRACON Struct. Mater. J.*, vol. 11, no. 3, pp. 564–585, May 2018, <http://dx.doi.org/10.1590/s1983-41952018000300008>.
- [3] E. C. Alves and L. A. Feitosa, "Analysis of the global tall buildings stability in flat slabs considering the soil structure interaction," *IBRACON Struct. Mater. J.*, vol. 13, no. 1, pp. 183–199, Feb 2020, <http://dx.doi.org/10.1590/s1983-41952020000100013>.
- [4] L. M. Gil-Martín, J. F. Carbonell-Márquez, M. A. Fernández-Ruiz, and E. Hernández-Montes, "Theoretical and experimental short-term behavior of non-symmetrical wall pile retaining systems," *Eng. Struct.*, vol. 112, pp. 172–183, Apr 2016, <http://dx.doi.org/10.1016/j.engstruct.2016.01.019>.
- [5] Y. Kim and S. Jeong, "Analysis of soil resistance on laterally loaded piles based on 3D soil-pile interaction," *Comput. Geotech.*, vol. 38, no. 2, pp. 248–257, Mar 2011, <http://dx.doi.org/10.1016/j.compgeo.2010.12.001>.
- [6] P. Michel, C. Butenweg, and S. Klinkel, "Pile-grid foundations of onshore wind turbines considering soil-structure-interaction under seismic loading," *Soil. Dyn. Earthquake Eng.*, vol. 109, pp. 299–311, Jun 2018, <http://dx.doi.org/10.1016/j.soildyn.2018.03.009>.
- [7] A. Nardelli, "The shaft friction degradation of piles under cyclic axial loading in wind turbine foundations," M.S. thesis, Dept. Geotech. Eng., Sch. Eng. Univ. São Paulo, São Paulo, 2019.
- [8] L. Arany, S. Bhattacharya, J. Macdonald, and S. J. Hogan, "Design of monopiles for offshore wind turbines in 10 steps," *Soil. Dyn. Earthquake Eng.*, vol. 92, pp. 126–152, Jan 2017, <http://dx.doi.org/10.1016/j.soildyn.2016.09.024>.
- [9] E. Zacchei, P. H. C. Lyra, and F. R. Stucchi, "Nonlinear static analysis of a pile-supported wharf," *IBRACON Struct. Mater. J.*, vol. 12, no. 5, pp. 998–1009, Oct 2019, <http://dx.doi.org/10.1590/s1983-41952019000500003>.
- [10] L. C. Reese and R. C. Welch, "Lateral loading of deep foundations in stiff clay," *J. Geotech. Eng. Div. ASCE*, vol. 101, no. GT7, pp. 633–649, 1975.
- [11] G. Norris, M. Ashour, and A. Shamsabadi, "Effect of the non-linear behavior of pile material on the response of laterally loaded piles," in *Int. Conf. Recent Adv. Geotech. Earthq. Eng. Soil Dyn.*, 2001, pp. 1–8.



- [12] C. C. Fan and J. H. Long, "Assessment of existing methods for predicting soil response of laterally loaded piles in sand," *Comput. Geotech.*, vol. 32, no. 4, pp. 274–289, Jun 2005, <http://dx.doi.org/10.1016/j.compgeo.2005.02.004>.
- [13] L. C. Reese and W. F. Van Impe, *Single Piles and Pile Groups Under Lateral Loading*, 2nd ed. London: CRC Press, 2011.
- [14] M. A. Almeida, M. G. Miguel, and S. H. C. Teixeira, "Horizontal bearing capacity of piles in a lateritic soil," *J. Geotech. Geoenviron. Eng.*, vol. 137, no. 1, pp. 59–69, Jan 2011., [http://dx.doi.org/10.1061/\(ASCE\)GT.1943-5606.0000410](http://dx.doi.org/10.1061/(ASCE)GT.1943-5606.0000410).
- [15] H.-Y. Choi, S.-R. Lee, H.-I. Park, and D.-H. Kim, "Evaluation of lateral load capacity of bored piles in weathered granite soil," *J. Geotech. Geoenviron. Eng.*, vol. 139, no. 9, pp. 1477–1489, Sep 2013., [http://dx.doi.org/10.1061/\(ASCE\)GT.1943-5606.0000831](http://dx.doi.org/10.1061/(ASCE)GT.1943-5606.0000831).
- [16] L. C. Reese, W. R. Cox, and F. D. Koop, "Analysis of laterally loaded piles in sand," in *Proc. 6th Annu. Offshore Technol. Conf.*, 1974, pp. 473–485.
- [17] American Petroleum Institute, *Recommended Practice 2A-WSD: Planning, Designing and Constructing Fixed Offshore Platforms: Working Stress Design*, 22nd ed. Washington, D.C., 2014.
- [18] H. M. Coyle and R. R. Castello, "New design correlations for piles in sand," *J. Geotech. Eng. Div.*, vol. 107, no. 7, pp. 965–986, 1981.
- [19] K. M. Rollins, R. J. Clayton, R. C. Mikesell, and B. C. Blaise, "Drilled shaft side friction in gravelly soils," *J. Geotech. Geoenviron. Eng.*, vol. 131, no. 8, pp. 987–1003, Aug 2005, [http://dx.doi.org/10.1061/\(ASCE\)1090-0241\(2005\)131:8\(987\)](http://dx.doi.org/10.1061/(ASCE)1090-0241(2005)131:8(987)).
- [20] J. R. Peng, M. Rouainia, and B. G. Clarke, "Finite element analysis of laterally loaded fin piles," *Comput. Struct.*, vol. 88, no. 21–22, pp. 1239–1247, Nov 2010, <http://dx.doi.org/10.1016/j.compstruc.2010.07.002>.
- [21] V. P. Faro, "Carregamento lateral em fundações profundas associadas a solos tratados : concepção, provas de carga e diretrizes de projeto," Ph.D. dissertation, Progr. Pós-grad. Eng. Civ., UFRGS, Porto Alegre, 2014.
- [22] C. E. R. Lautenschläger, "Modelagem numérica do comportamento de fundações profundas submetidas a carregamento lateral," M.S. thesis, Progr. Pós-grad. Eng. Civ., UFRGS, Porto Alegre, 2010.
- [23] W. D. Guo, "Subgrade modulus for laterally loaded piles," in *Proc. Eight Int. Conf. Civ. Struct. Eng. Comput.*, 2001, pp. 273–274, <http://dx.doi.org/10.4203/ccp.73.112>.
- [24] M. Ashour and G. Norris, "Modeling lateral soil-pile response based on soil-pile interaction," *J. Geotech. Geoenviron. Eng.*, vol. 126, no. 5, pp. 420–428, May 2000, [http://dx.doi.org/10.1061/\(ASCE\)1090-0241\(2000\)126:5\(420\)](http://dx.doi.org/10.1061/(ASCE)1090-0241(2000)126:5(420)).
- [25] K. Terzaghi, "Evaluation of coefficients of subgrade reaction," *Geotechnique*, vol. 5, no. 4, pp. 297–326, Dec 1955, <http://dx.doi.org/10.1680/geot.1955.5.4.297>.
- [26] A. B. Vesic, "Beams on elastic subgrade and Winkler's hypothesis," in *Proc. 5th Int. Conf. Soil Mech. Found. Eng.*, 1961, pp. 845–850.
- [27] S. A. Ashford and T. Juirnarongrit, "Evaluation of pile diameter effect on initial modulus of subgrade reaction," *J. Geotech. Geoenviron. Eng.*, vol. 129, no. 3, pp. 234–242, Mar 2003, [http://dx.doi.org/10.1061/\(ASCE\)1090-0241\(2003\)129:3\(234\)](http://dx.doi.org/10.1061/(ASCE)1090-0241(2003)129:3(234)).
- [28] D. P. Carter, "A non-linear soil model for predicting lateral pile response," M.S. thesis, Dept. Civ. Eng., Univ. Auckland, Auckland, New Zealand, 1984.
- [29] J. M. Mabesoone and J. C. Silva, "Geomorphological aspects – sedimentary coastal strip of Pernambuco, Paraíba and part of Rio Grande do Norte," *Geol. Stud.*, vol. Ser. B, no. 10, pp. 117–132, 1991.
- [30] M. T. Davisson, "Lateral load capacity of piles," in *Proc. 49th Ann. Meeting Highw. Res. Board*, 1970, no. 333, pp. 104–112.
- [31] H. Lin, L. Ni, M. T. Suleiman, and A. Raich, "Interaction between laterally loaded pile and surrounding soil," *J. Geotech. Geoenviron. Eng.*, vol. 141, no. 4, 04014119, Apr 2015, [http://dx.doi.org/10.1061/\(ASCE\)GT.1943-5606.0001259](http://dx.doi.org/10.1061/(ASCE)GT.1943-5606.0001259).
- [32] B. H. Fellenius, "Test loading of piles and new proof testing procedure," *J. Geotech. Eng. Div.*, vol. 101, no. GT9, pp. 855–869, 1975.
- [33] Associação Brasileira de Normas Técnicas, *Estacas – Prova de Carga Estática – Método de Ensaio*, ABNT NBR 12131, 2006.
- [34] H. Matlock and L. C. Reese, "Foundation analysis of offshore pile supported structures," in *Proc. 5th Int. Conf. Soil Mech. Found. Eng.*, 1961, pp. 91–97.
- [35] H. G. Poulos and E. H. Davis, *Pile Foundation Analysis and Design*. New York: Wiley, 1980.
- [36] L. Zhang, M. Zhao, and X. Zou, "Behavior of laterally loaded piles in multilayered soils," *Int. J. Geomech.*, vol. 15, no. 2, pp. 06014017, Apr 2015, [http://dx.doi.org/10.1061/\(ASCE\)GM.1943-5622.0000319](http://dx.doi.org/10.1061/(ASCE)GM.1943-5622.0000319).
- [37] S. Prakash and S. Kumar, "Nonlinear lateral pile deflection prediction in sands," *J. Geotech. Eng.*, vol. 122, no. 2, pp. 130–138, Feb 1996, [http://dx.doi.org/10.1061/\(ASCE\)0733-9410\(1996\)122:2\(130\)](http://dx.doi.org/10.1061/(ASCE)0733-9410(1996)122:2(130)).
- [38] T. Schanz, P. A. Vermeer, and P. G. Bonnier, "The hardening soil model: formulation and verification," in *Beyond 2000 in Computational Geotechnics*, R. B. J. Brinkgreve, Ed., Boca Raton: Taylor & Francis, 1999.
- [39] Federal Highway Administration, *Design, Analysis, and Testing of Laterally Loaded Deep Foundations that Support Transportation Facilities*. Washington, D.C.: Fed. Highw. Adm. (Rep. FHWA-HIF-18-031), 2018.

- [40] American Association of State Highway and Transportation Officials, *Standard Specifications for Highway Bridges*, 17th ed. Washington, D.C., 2002.
- [41] B. K. Mazurkiewicz, *Test Loading of Piles According to Polish Regulations* (Prel. Rep. 35). Stockholm: Swedish Academy of Eng. Sciences, 1972.
- [42] B. B. Broms, "Lateral resistance of piles in cohesionless soils," *J. Soil Mech. Found. Div.*, vol. 90, no. 3, pp. 123–156, 1964.
- [43] A. S. Vesic, "Bearing capacity of shallow foundations," in *Foundation Engineering Handbook*, 1st ed., H. F. Winterkorn and H. Y. Fang, Eds., New York, NY: Van Nostrand Reinhold, 1975, pp. 121–147.
- [44] M. J. Tomlinson, *Pile Design and Construction Practice*, 4th ed. London: E & FN Spon., 1994.
- [45] M. D. Bolton, "The strength and dilatancy of sands," *Geotechnique*, vol. 36, no. 1, pp. 65–78, Mar 1986, <http://dx.doi.org/10.1680/geot.1986.36.1.65>.

---

**Author contributions:** AMDS: numerical analyses, manuscript editing and review; YDJC: conceptualization, funding acquisition, supervision, analysis of results and writing; AGDA: experimental analyses; CMLC: supervision and manuscript review.

**Editors:** Mark Alexander, Guilherme Aris Parsekian.



ORIGINAL ARTICLE

# Influence of hydraulic jiggling of construction and demolition waste recycled aggregate on hardened concrete properties

*Influência da jigagem hidráulica de agregados reciclados de resíduos de construção e demolição nas propriedades no estado endurecido dos concretos*

Iago Lopes dos Santos<sup>a</sup>

Luciana Vanni Frantz<sup>b</sup>

Angela Borges Masuero<sup>a</sup>

<sup>a</sup>Universidade Federal do Rio Grande do Sul – UFRGS, Departamento de Engenharia Civil, Programa de Pós-graduação em Engenharia Civil: Construção e Infraestrutura – PPGCI, Núcleo Orientado para a Inovação da Edificação, Porto Alegre, RS, Brasil

<sup>b</sup>Universidade Federal do Rio Grande do Sul – UFRGS, Departamento de Engenharia Civil, Porto Alegre, RS, Brasil

Received 10 June 2020  
Accepted 18 September 2020

**Abstract:** Concern with the maintenance of natural resources has increased research about recycled aggregates for concrete production. However, the heterogeneity of recycled aggregates is one of the main constraints for their use in practice, because it can generate variability in concrete properties, hence reducing their final quality. Then, the jiggling has been seen as a promising way of improving recycled aggregate quality. This paper aimed to evaluate its use for better application in concrete. A modified jig was used to sort recycled coarse aggregates. Concrete were produced with water/cement ratio from 0.5 and 100% of recycled coarse aggregate. The recycled aggregate properties upgrade were achieved and the results of compressive strength and modulus of elasticity of recycled concrete made with aggregate which were submitted to jiggling were increased, indicating a potential application in wide scale.

**Keywords:** construction and demolition waste, aggregate, variability and hydraulic jiggling.

**Resumo:** A preocupação com a manutenção dos recursos naturais tem elevado a quantidade de pesquisas sobre agregados reciclados para a produção de concretos. Contudo, a heterogeneidade desses agregados é uma das principais restrições para sua utilização na prática, pois pode gerar variabilidade nas propriedades do concreto, reduzindo assim sua qualidade final. Assim, a jigagem tem sido vista como um instrumento promissor de melhoria dos agregados reciclados. Esse artigo teve como objetivo avaliar o uso da jigagem de agregados reciclados visando sua melhor aplicação em concreto. Um jigge modificado para separar agregados graúdos reciclados foi utilizado. Os concretos foram produzidos com relação água/cimento de 0,5 e com 100% de agregado graúdo reciclado. O incremento das propriedades dos agregados graúdos reciclados foi alcançado e os resultados de resistência à compressão e módulo de elasticidade do concreto produzido com agregados que foram submetidos a jigagem foram mais elevados, indicando ter uma aplicação potencial em larga escala.

**Palavras-chave:** resíduos de construção e demolição, agregados, variabilidade e jigagem hidráulica.

**How to cite:** I. L. Santos, L. V. Frantz, and A. B. Masuero, “Influence of hydraulic jiggling of construction and demolition waste recycled aggregate on hardened concrete properties,” *Rev. IBRACON Estrut. Mater.*, vol. 14, no. 3, e14314, 2021, <https://doi.org/10.1590/S1983-41952021000300014>

## INTRODUCTION

In recent decades, the recycling of construction and demolition waste (CDW) has been studied as a sustainable alternative for the minimization of consumption and exploitation of natural resources and also the waste generation in construction sector. The construction industry is considered the world’s largest solid waste generator with an estimated amount of more than 10 billion tons and a growth perspective to coming years [1]–[3] For the Brazilian scenario, it is

Corresponding author: Iago Lopes dos Santos. E-mail: [iago.lopes.santos@gmail.com](mailto:iago.lopes.santos@gmail.com)

Financial support: None.

Conflict of interest: Nothing to declare.



This is an Open Access article distributed under the terms of the Creative Commons Attribution License, which permits unrestricted use, distribution, and reproduction in any medium, provided the original work is properly cited.

estimated that the production of these residues although variable and correlated with the Human Development Index (HDI) is higher than 70 million tons per year (about 500 kg/inhabitants/year), configuring more than 50% of all urban solid waste in the country [4].

The waste generated by the construction industry is usually disposed in landfills and usually it is dumped in improper area becoming a major environmental problem. On the other hand, studies have been carried out over the last decades aiming at a nobler destination for this waste, such as its use as aggregates in the concrete production. However, CDW have a wide variety of materials, such as bricks, tiles, plaster, concrete and mortar resulting from the use of different construction techniques and systems present in the sector itself which characterizes great variability of aggregates [5], [6]. This variability in the composition and the origin of recycled materials, consequently in the recycled aggregates properties may jeopardize their application, so there is increasing concern about the quality of CDW aggregates which must exhibit high densities and homogeneity for use in structural concretes which [7], [8].

The quality of recycled aggregates from construction and demolition waste is directly related to pores and low resistance of these aggregates [5]. In order to reduce this variability, several processing, separation and classification techniques are applied to improve the materials used, such as: x-ray, infrared, water and air jigging, among others [9]–[12].

Among these techniques, jigging is a beneficiation process which by applying expansion and contraction pulsatile blows of water or air in a particle bed, it performs the density separation of the mixture material on layers with increasing order of magnitude from top to bottom [13]–[15]. Jigs are widely used equipment in the mining industry due to the ease and low cost operation. They are one of the oldest known processes for concentrating minerals which is based exclusively on the differences in density of the particles [13]. Recently, their use is expanding to other sectors, such as civil construction aiming to reduce variability and to improve the quality of aggregates for concrete production [5], [16], [17]. Sampaio et al. [10] and Ambrós et al. [12] showed the stratification of concrete/brick/gypsum particles in a air jigging system to separate recycled CDW aggregates was efficient. Also, Cazacliu et al. [18] have observed that it is possible to drastically improve the quality of recycled concrete aggregates.

However, as a viable alternative, this research proposes to evaluate the use of the technique of jigging of recycled aggregates aiming at its better application in concrete. Thus, the study was divided into two distinct phases: the characterization of recycled construction and demolition waste aggregate before and after jigging and the evaluation of the hardened properties of concrete produced with recycled aggregates after density separation.

## MATERIALS AND EXPERIMENTAL PROGRAM

### Materials

In this study, a Brazilian Portland cement CPV-ARI according to NBR 16697 [19], which is equivalent to cement Type III specified by ASTM C150/C150M-19a [20], were used for all concrete mixes. It was chosen because it is the purest cement in the local market. Due the minimum of the mineral additions presents on this cement, it is the best used for effectiveness of results of research. The Tables 1 and 2 show the main properties of this cement.

**Table 1.** Chemical characterization of cement CPV-ARI

Oxides	(%)	Oxides	(%)
CaO	77.01	SiO <sub>2</sub>	1.27
SO <sub>3</sub>	5.29	SrO	0.51
MgO	5.14	TiO <sub>2</sub>	0.23
Al <sub>2</sub> O <sub>3</sub>	4.50	Na <sub>2</sub> O	0.20
Fe <sub>2</sub> O <sub>3</sub>	4.15	P <sub>2</sub> O <sub>5</sub>	0.19
K <sub>2</sub> O	1.37	MnO	0.09

A quartz natural river fine aggregate whose particle size distribution is within the usable zone of NBR 7211 [27], with a fineness modulus of 2.16 determined according to NBR NM 248 [28], with specific density of 2.50 g/cm<sup>3</sup> and bulk density of 1.59 g/cm<sup>3</sup> in accordance with NBR NM 52 [29] was used in this study.

**Table 2.** Physical and mechanical characterization of cement CPV-ARI

Tests	CPV- ARI	Units	Standard	limits
Specific density	3.14	g/cm <sup>3</sup>	NBR 16605 [21]	-
Fineness (Blaine)	4628	cm <sup>2</sup> /g	NBR 16372 [22]	≥ 3000
#200	0.3	%	-	≤ 6
#325	1.7	%	-	-
Expansibility	0.0	mm	NBR 11582 [23]	-
Loss on ignition (1000° C)	3.6	%	NBR NM 18 [24]	≤ 4,5
Initial setting time	249	min	NBR 16607 [25]	≥ 60
Final setting time	323	min	NBR 16607 [25]	≤ 600
Compressive strength – day 1	21.1	MPa	NBR 7215 [26]	≥ 14
Compressive strength – day 3	37.6	MPa	NBR 7215 [26]	≥ 24
Compressive strength – day 7	42.5	MPa	NBR 7215 [26]	≥ 34
Compressive strength – day 28	47.9	MPa	NBR 7215 [26]	-

The coarse aggregate used was a recycled aggregate of construction and demolition waste from a landfill located in the city of Porto Alegre/RS, Brazil, which collects rubbles from different constructions, demolitions and refurbishments in the city. For its characterization, the specific density of 2.49 g/cm<sup>3</sup> was based on the method proposed by Leite [30], the bulk density of 1.14 g/cm<sup>3</sup> in accordance with NBR NM 45 [31], fineness modulus of 6.62 according to NBR NM 248 [28] and water absorption of 10.11% proposed by Leite [32]. The water used in this study is provided from the public supply network.

## Experimental program

### Preparation of recycled aggregates

The coarse aggregates were collected from landfill in particle size range of 4.8 to 25 mm, regularly available for concrete production. They were washed to remove the large amount of impurities presents on their surface and then dried in an oven at 100°C. The CDW aggregates were sieved with the aid of a mechanical siever using particles in size range between 4.8 mm and 19 mm, because it is within the hydraulic jig operational range. The homogenization and quarrying were performed following the prescription of NBR NM 27 [33], until it was obtained aliquots of 25 kg, in order to all samples were representative and minimize the variability of the concrete produced. The characterization of recycled aggregates subjected to water jiggling will be shown in section 3.1, as it is part of the study results.

### Jiggling process

This research aims to evaluate the influence of the water jiggling process on the main properties of CDW recycled aggregates and its effects on the compressive strength and modulus of elasticity of concrete. Therefore, the sorting of CDW recycled aggregates was carried out in a batch pilot-scale hydraulic jig model AllJig S-400 (Figure 1a) from Allmineral with a capacity of approximately 25 kg per batch and an operating size range of 1 to 19 mm. This equipment is U-shaped with two sections, being one responsible for air pulsation and the other one for a separation chamber with stratification layers (Figure 1b). Both sections are filled with water and through the air injection into a tank containing water, the sample is moved in the separation plates of the other section. A centrifugal blower model SCL 30DH MOR of 1.32 kW which provides an air flow rate of up to 1.1 m<sup>3</sup>/min and generates pressures in the order of 30 kPa is used for air injection into a closed air chamber located on top of the jig. The jiggling chamber is assembled with three acrylic boxes with square section dimensions of 430 x 430 x 50 mm and six smaller boxes with dimensions of 430 x 430 x 25 mm fitted one over the other. The aggregate density separation is achieved as a result of the air flow through the particles bed that are supported on a perforated plate with a diameter equal to 1 mm inside the separation chamber (Figure 1c). During this process, two distinct upward air flows pass simultaneously through the bed, and therefore a continuous flow keeps the bed in a pre-expanded state and a pulsatile flow promotes successive blows of expansion and compression of

the bed, segregating particles of different densities due to the vertical movement of the particles in reply to the combined action of the drag force (upward movement) and the gravity force (downward movement).

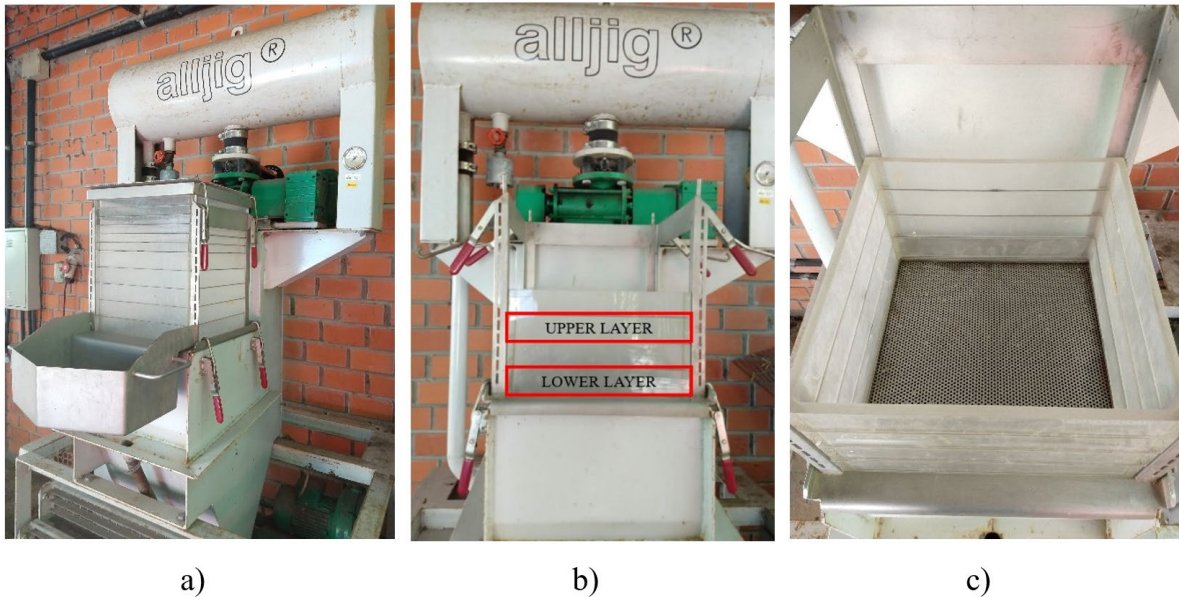


Figure 1. a) hydraulic jig b) stratification layer; c) perforated plate  $\phi$  1 mm

For jiggling, an amount of 25 kg of aggregates was defined in accordance with the maximum capacity of the equipment. These were added inside the jig and the separation chamber was filled with water so that the sample remained submerged and then the pulsation mechanism was activated. Some jiggling control parameters were previously defined, such as: jiggling time of 2 min, pulse frequency of 80 RPM (revolutions per minute) and bed expansion of 5 cm. The jig was fed through the full volume of three vertical layers of 5 cm and two smaller layer of 2.5 cm. At the end of each test, the boxes containing the stratified material were removed separately by a collector attached to the top of the jig, so that the horizontal drag of the boxes deposited all its contents inside each layer. For this research, only the denser aggregate disposed in lower layer and the less dense aggregate belonging to upper layer were used (Figure 1b).

### Concrete production and test methods

Previously the concrete production, the coarse recycled aggregates have passed through the pre-saturation stage, in order these materials do not absorb the mixing water. Due to the high water absorption potential of these aggregates, the water in the mixture would be absorbed by them and would influence the performance and the concrete properties, and therefore, this research stage is essential. The pre-saturation rate of the coarse recycled aggregate was set at 80%, the same used by Cordeiro [34] and recommended by NBR 15116 [35]. For this procedure, the aggregates were submerged for 24 hours in order to achieve total saturation, so that subsequently they were dried until they got the condition of 80% saturation, measured through the loss of mass. The aggregate was saturated inside and its surface kept dry, allowing a better adherence with the mortar. Afterward, concretes were prepared following the methodology used by Malysz [36] with water/binder ratio of 0.50 and the mixture proportioning was defined by using weight proportioning in the ratio of 1:4 for the components cement: aggregates. A liquid superplasticizer admixture with a rate of 0.26% in relation to the mass of cement, pH of 6.58, density equal to  $1.061 \text{ g/cm}^3$  and solid percentage of 31.58% was added in the mixture. Three groups of concrete were prepared: (a) concrete with recycled aggregates submitted to jiggling process and disposed in lower layer; (b) concrete with CDW aggregates submitted to jiggling and disposed in upper layer; and (c) a control concrete with aggregates that are not submitted to jiggling.

The concretes were molded in cylinders  $\phi 100 \text{ mm} \times 200 \text{ mm}$  and filled in two stage; in the first stage, a layer of concrete was poured into the mold and compacted on a shaking table for 15 seconds; after that in second stage, more concrete was added until the mold was full and compacted on shaking table for 15 seconds. After 24 hours, the samples

were demolded and cured in a climate chamber (relative humidity > 95% and temperature of  $(23 \pm 2)$  °C) until the ages set by experiments.

In order to evaluate the compressive strength, the concretes were ruptured at 28 days according to NBR 5739 [37]. A hydraulic testing machine, model DL20000, with a compression load rate of  $0.45 \pm 0.15$  MPa/s was used to rupture the samples. The modulus of elasticity test of the concrete was also performed at 28 days, as prescribed by NBR 8522 [38].

## RESULTS AND DISCUSSIONS

### Recycled aggregates properties

Construction and demolition waste is residue generated from refurbishment, excavation or demolition and usually includes inert materials (concrete, ceramics, bricks, tiles, etc.) with lower amounts of other components such as wood, glass, gypsum, bituminous mixtures, among others [39]. The main obstacle to the use of recycled aggregate of construction and demolition in concrete is the great heterogeneity of its composition, since the construction sector includes several types of systems, avoiding the development of precise models to control and predict the properties of recycled aggregates [40]. Figure 2 shows the stratification results, in percentage of mass in each layer analyzed, of the composition of recycled aggregates before and after they are submitted to jiggling. Concrete aggregates, mortars, ceramic materials and residues present in lower layer and upper layer of the equipment were quantified in relation to the total mass of CDW aggregates.

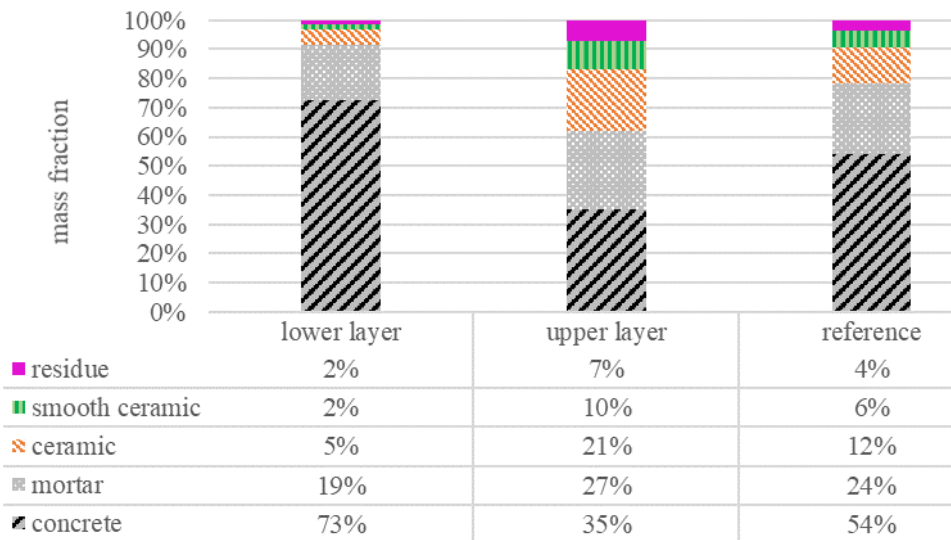


Figure 2. CDW aggregates composition of each layer

It is noted that CDW aggregate components separation took place when were subjected to the jiggling process, with a greater fraction of higher density aggregates present in the lower layer and the less density aggregates disposed in the upper layer, following a trend line of the results and proving the jiggling efficiency, in accordance with described by Sampaio and Tavares [13]. At first, it is possible to observe that the most part of concrete aggregate tended to concentrate in lower layer (73% mass) due the higher density in relation to other materials. The amount of ceramic aggregate before jiggling was 18% and after the sort operation it was set at only 7%. On the other hand, the mortar has an intermediate density then the jiggling process was less efficient, but no least important, reducing from 24% to 19% in lower layer. These results corroborate those found by Sampaio et al. [10] and Ambrós et al. [41] although they differ from those found by Corrêa [42] Malysz [36] and Mondini [43] who did not consider the CDW separation satisfactory in pneumatic jig, because they found different density materials in all stratification layers of jig. In fact, this study shows the hydraulic jiggling efficiency to separate CDW particles, indicating as an alternative to obtain nobler aggregates for concrete production.

Figure 3 shows the results of the characterization of all recycled aggregates used in the research. It can be seen that the specific density of CDW coarse aggregate was 2.53 g/cm<sup>3</sup> in lower jig layer, 2.46 g/cm<sup>3</sup> in upper layer and 2.49 g/cm<sup>3</sup> for those aggregates that did not go through the jiggling process. As shown in the results of CDW composition, the greater presence of concrete aggregate and lower amount of ceramic materials in lower layer can be a positive factor in increasing the specific density of aggregates. Due the mixed aggregates present on upper layer resulted in a less specific density in relation to aggregates that were not jiggling submitted. Thus, it can be concluded that the jiggling procedure has an influence on the specific density of CDW aggregate. In contrast to the specific density, the jiggling process did not have as much influence on the bulk density, with a slight decrease in value for the aggregates who were jiggling submitted. However, it cannot be assumed that it is influenced by gravimetric improvement process.

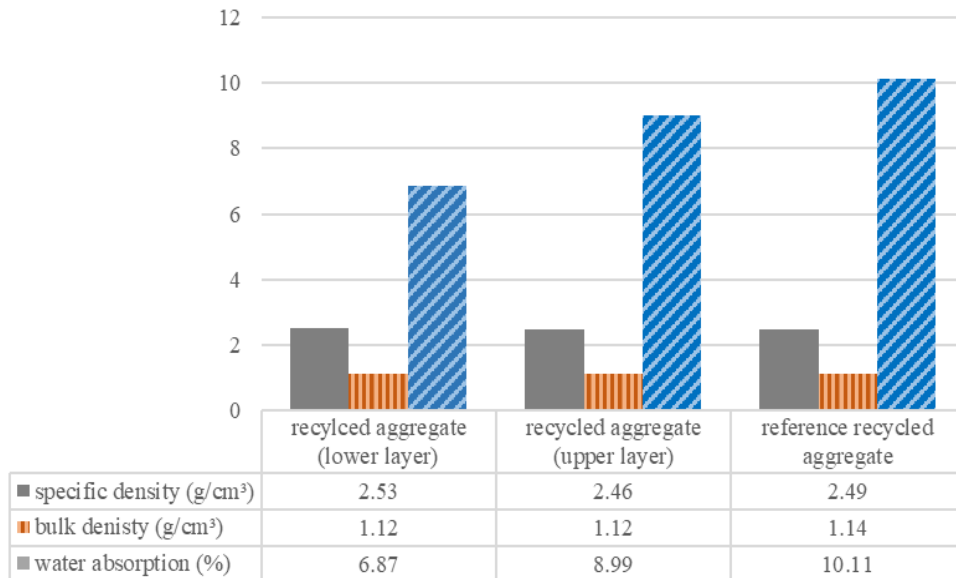


Figure 3. Characterization of CDW recycled aggregates

Recycled aggregates have a higher porosity when compared to natural aggregates, which results in a greater capacity to absorb water and may affect some concrete properties in the fresh and hardened state [34]. Therefore, the determination of the water absorption rate of CDW aggregates is necessary in order to avoid future problems for concrete. Figure 4 shows the results of water absorption rate of the CDW aggregates that were submitted to jiggling process and compares it with those that did not go through jiggling.

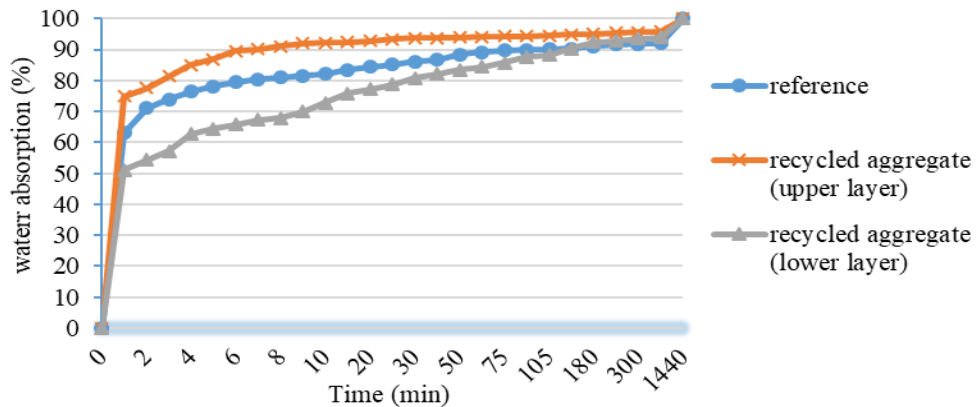


Figure 4. Water absorption rate of recycled aggregates



Figure 4 shows that recycled RCD aggregates absorb a large amount of water in the first minute, up to 54% for aggregate in lower layer, 63% for aggregate in upper layer and 74% for aggregates that were not jigging, due the high porosity of its structure. With the results obtained, it was found that jigging process provided an improvement in CDW aggregates properties in terms of water absorption. For that, a decrease of 32.04% in water absorption of aggregate on lower layer and 11.07% for aggregate on upper layer was noted when comparison is made with those that did not go through jigging. The aggregates of lower layer are basically constituted of concrete aggregate with a higher specific density, which is less porous than ceramic aggregate which may be a determining factor in this result.

### Compressive Strength of recycled concrete

The compressive strength of all recycled concrete is shown in Figure 5. The average, standard deviation and coefficient of variation were obtained by six samples at 28 days of age. It was observed that the compressive strength of concrete made with aggregates set in lower layer of jig showed a slight increase of 13.17% compared to reference concrete. When the comparison is with aggregates from both stratification layers was carried out, the results obtained were those expected, which those concrete made with aggregates from lower layer showed an increase in compressive strength compared to concrete made with aggregates from upper layer.

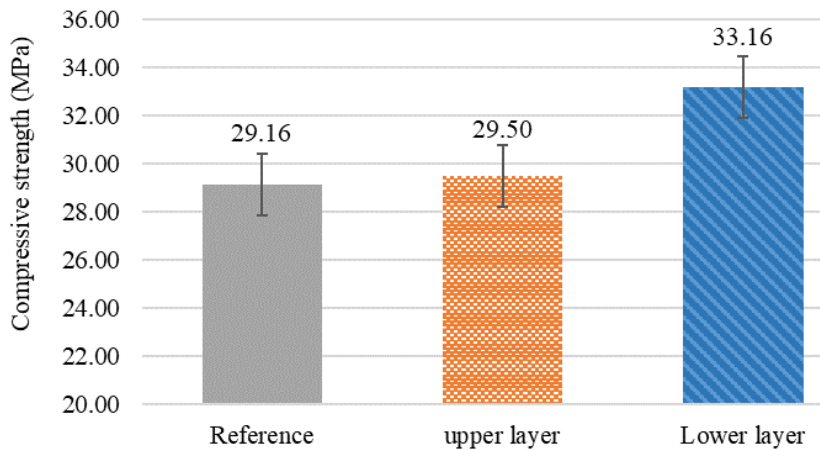


Figure 5. Compressive strength of recycled concrete at 28 days

Table 3 shows the analysis of variance (ANOVA) applied to the study in order to verify the influence of the stratification layer in results of this research. According to this analysis of variance and taking a significance level of 5% as a decision criterion, it was observed that the stratification layers of jig were not statistically significant influence on the compressive strength of concretes.

Table 3. Analysis of variance (ANOVA) - compressive strength of recycled concrete

Source of variation	SQ	gl	MQ	F	P	Sig.
stratification layers	1407.825	2	703.9126	2.403571	13%	non
residue	4100.057	14	292.8612			
Total	5507.882	16				

SQ: Quadratic sum; GL: Degrees of freedom (n-1); SQF: quadratic average; F: test F (calculated Value); P: Significance level; If p < 5% = significant impact; p > 5% = non-significant

### Modulus of elasticity of recycled concrete

Concrete is a heterogeneous material, so the factors that determine its elastic performance are the volumetric fraction, the density and the modulus of elasticity of their components as well as the characteristics of the interface transition zone of concrete. The modulus of elasticity of concrete is influenced by the porosity of their components, being the density

inversely proportional to the porosity, this is an important factor in determining the elastic performance of concrete. According to some researchers, the coarse aggregate has a significant effect on the modulus of elasticity of concrete [44]–[46]. Ho et al. [47] emphasized that the more porous aggregates in mixture results in a lower modulus of elasticity values for concrete. The results of the modulus of elasticity test for concrete are present in Figure 6. The average, standard deviation and coefficient of variation were obtained by testing four samples at 28 days of age.

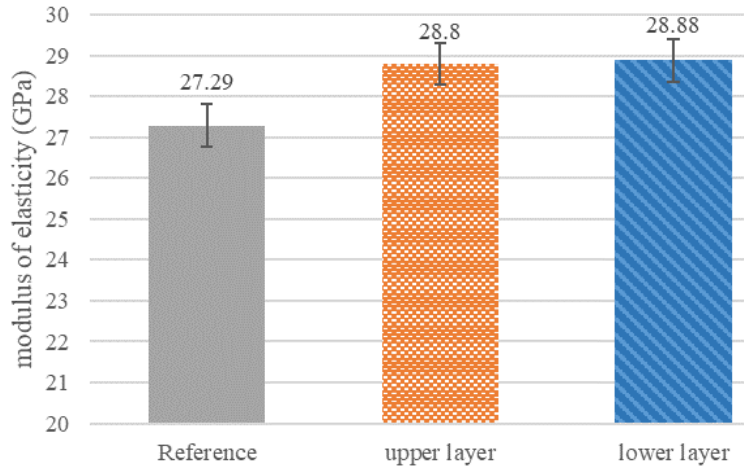


Figure 6. Modulus of elasticity of concrete at 28 days

The results shown a slight increase of 5.82% in value of the modulus of elasticity of concrete made with aggregates on lower layer compared to reference concrete. However, for concrete with less dense aggregates whose arrangement took place in upper layer of the equipment an increase of 5.53% in value of modulus of elasticity compared to reference concrete can be observed.

Table 4 shows the analysis of variance applied to the study in order to verify the influence of the stratification layer in the results of the modulus of elasticity of concrete. According to this analysis of variance and taking a significance level of 5% as a decision criterion, it was observed that the stratification layers of the jig were statistically significant influence on the modulus of elasticity of the concrete.

Table 4. Analysis of variance (ANOVA) – modulus of elasticity of the concrete

Source of variation	SQ	gl	MQ	F	P	Sig.
stratification layers	4.856022222	2	2.428011	7.527939	2.3138%	yes
residue	1.9352000000	6	0.322533			
Total	6.791222222	8				

SQ: Quadratic sum; GL: Degrees of freedom (n-1); SQF: quadratic average; F: test F (calculated Value); P: Significance level; If p < 5% = significant impact; p > 5% = non-significant

Although the stratification layer effects on the modulus of elasticity was considered statistically significant by Fisher’s test, a comparative average analysis was done and it was observed that the modulus of elasticity of concrete are equal to each other.

## CONCLUSIONS

This research presents the processing of CDW recycled coarse aggregates through hydraulic jiggling aiming reduce the inherent variability of this material and to favor its use in concrete and in order to improve its properties in the hardened state. The main conclusions of the study are presented below:

- hydraulic jiggling proved to be an efficient technique for processing recycled aggregates, as the particles were separated by density in different stratification layers of jig. In general, the separation of the CDW components is

noticeable, in which higher density aggregates were accommodated on lower layer and less dense ones on upper layer, following a trend line of the results;

- after jiggling, an improvement in specific density values and water absorption rates was obtained due the high presence of concrete aggregate in the lower layer which has a higher specific density and it is less porous than ceramic aggregates;
- the concrete produced with CDW recycled coarse aggregates that were submitted to jiggling process showed increased values of compressive strength and modulus of elasticity compared to the reference concrete.

## ACKNOWLEDGEMENTS

The authors of this research thank the Mineral Processing Laboratory (LAPROM) for the availability of the hydraulic Jig, the Laboratory of Materials and Built Environment Technology (LAMTAC) of the Nucleus Oriented for Innovation in Building (NORIE) for the support in carrying out the experiments and to CAPES for financing this work.

## REFERENCES

- [1] C. Ulsen, H. Kahn, G. Hawlitschek, E. A. Masini, and S. C. Angulo, "Separability studies of construction and demolition waste recycled sand," *Waste Manag.*, vol. 33, no. 3, pp. 656–662, 2013.
- [2] A. Akhtar and A. K. Sarmah, "Construction and demolition waste generation and properties of recycled aggregate concrete: a global perspective," *J. Clean. Prod.*, vol. 186, pp. 262–281, 2018.
- [3] J. Wang, H. Wu, V. W. Y. Tam, and J. Zuo, "Considering life-cycle environmental impacts and society's willingness for optimizing construction and demolition waste management fee: an empirical study of China," *J. Clean. Prod.*, vol. 206, pp. 1004–1014, 2019.
- [4] M. Contreras et al., "Recycling of construction and demolition waste for producing new construction material (Brazil case-study)," *Constr. Build. Mater.*, vol. 123, pp. 594–600, 2016.
- [5] K. Hu, Y. Chen, F. Naz, C. Zeng, and S. Cao, "Separation studies of concrete and brick from construction and demolition waste," *Waste Manag.*, vol. 85, pp. 396–404, 2019.
- [6] Z. Wu, A. T. W. Yu, L. Shen, and G. Liu, "Quantifying construction and demolition waste: an analytical review," *Waste Manag.*, vol. 34, no. 9, pp. 1683–1692, 2014.
- [7] P. S. Lovato, "Verificação dos parâmetros de controle de agregados reciclados de resíduos de construção e demolição para utilização em concreto," M.S. thesis, Prog. Pós-grad. Eng. Civ., Esc. Eng., Univ. Fed. Rio Grande do Sul, Porto Alegre, 2007.
- [8] M. Behera, S. K. Bhattacharyya, A. K. Minocha, R. Deoliya, and S. Maiti, "Recycled aggregate from C&D waste & its use in concrete: a breakthrough towards sustainability in construction sector: a review," *Constr. Build. Mater.*, vol. 68, pp. 501–516, 2014., <http://dx.doi.org/10.1016/j.conbuildmat.2014.07.003>.
- [9] I. Vegas, K. Broos, P. Nielsen, O. Lambertz, and A. Lisbona, "Upgrading the quality of mixed recycled aggregates from construction and demolition waste by using near-infrared sorting technology," *Constr. Build. Mater.*, vol. 75, pp. 121–128, 2015.
- [10] C. H. Sampaio et al., "Stratification in air jigs of concrete/brick/gypsum particles," *Constr. Build. Mater.*, vol. 109, pp. 63–72, 2016.
- [11] F. Di Maria, F. Bianconi, C. Micale, S. Baglioni, and M. Marionni, "Quality assessment for recycling aggregates from construction and demolition waste: an image-based approach for particle size estimation," *Waste Manag.*, vol. 48, pp. 344–352, 2016.
- [12] W. M. Ambrós, C. H. Sampaio, B. G. Cazacliu, G. L. Miltzarek, and L. R. Miranda, "Usage of air jiggling for multi-component separation of construction and demolition waste," *Waste Manag.*, vol. 60, pp. 75–83, 2017.
- [13] C. H. Sampaio and L. M. M. Tavares, *Beneficiamento Gravimétrico: uma Introdução aos Processos de Concentração Mineral e Reciclagem de Materiais por Densidade*. Porto Alegre: Ed. UFRGS, 2005.
- [14] F. Boylu et al., "Effect of coal moisture on the treatment of a lignitic coal through a semi-pilot-scale pneumatic stratification jig," *Int. J. Coal Prep. Util.*, vol. 35, no. 3, pp. 143–153, 2015.
- [15] D. Kowol and P. Matusiak, "Badania skuteczności osadzarkowego oczyszczania kruszywa z ziaren węglanowych," *Min. Sci.*, vol. 22, pp. 83–92, 2015.
- [16] R. S. Paranhos, B. G. Cazacliu, C. H. Sampaio, C. O. Petter, and F. Huchet, "A sorting method to value recycled concrete," *J. Clean. Prod.*, vol. 112, no. 4, pp. 2249–2258, 2016.
- [17] E. Khoury, W. Ambrós, B. Cazacliu, C. H. Sampaio, and S. Remond, "Heterogeneity of recycled concrete aggregates, an intrinsic variability," *Constr. Build. Mater.*, vol. 175, pp. 705–713, 2018.
- [18] B. Cazacliu et al., "The potential of using air jiggling to sort recycled aggregates," *J. Clean. Prod.*, vol. 66, pp. 46–53, 2014., <http://dx.doi.org/10.1016/j.jclepro.2013.11.057>.
- [19] Associação Brasileira de Normas Técnicas, *Cimento Portland – Requisitos*, NBR 16697, 2018.
- [20] ASTM International, *Standard Specification for Portland Cement*, ASTM C150/C150M-19a, 2019.
- [21] Associação Brasileira de Normas Técnicas, *Cimento Portland e Outros Materiais em Pó – Determinação da Massa Específica*, NBR 16605, 2017.

- [22] Associação Brasileira de Normas Técnicas, *Cimento Portland e Outros Materiais em Pó – Determinação da Finura pelo Método de Permeabilidade ao Ar (Método de Blaine)*, NBR 16372, 2015.
- [23] Associação Brasileira de Normas Técnicas, *Cimento Portland – Determinação da Expansibilidade Le Chatelier*, NBR 11582, 2016.
- [24] Associação Brasileira de Normas Técnicas, *Cimento Portland – Análise Química – Determinação de Perda ao Fogo*, NBR NM 18, 2012.
- [25] Associação Brasileira de Normas Técnicas, *Cimento Portland – Determinação dos Tempos de Pega*, NBR 16607, 2018.
- [26] Associação Brasileira de Normas Técnicas, *Cimento Portland – Determinação da Resistência à Compressão de Corpos de Prova Cilíndricos*, NBR 7215, 2019.
- [27] Associação Brasileira de Normas Técnicas, *Agregado para Concreto – Especificação*, NBR 7211, 2009.
- [28] Associação Brasileira de Normas Técnicas, *Agregados – Determinação da Composição Granulométrica*, NBR NM 248, 2003.
- [29] Associação Brasileira de Normas Técnicas, *Agregado Miúdo – Determinação da Massa Específica e Massa Específica Aparente*, NBR NM 52, 2009.
- [30] M. B. Leite, “Avaliação de propriedades mecânicas de concretos produzidos com agregados reciclados de resíduos de construção e demolição,” Ph.D. dissertation, Esc. Eng., Univ. Fed. Rio Grande do Sul, Porto Alegre, 2001.
- [31] Associação Brasileira de Normas Técnicas, *Agregados – Determinação da Massa Unitária e do Volume de Vazios*, NBR NM 45, 2006.
- [32] M. B. Leite et al., “Proposta de adaptação do procedimento proposto por Leite (2001) para determinação da absorção de agregados reciclados de resíduo de construção demolição,” in *An. 7º Cong. Int. sobre Patol. Reabil. Estrut.*, 2011.
- [33] Associação Brasileira de Normas Técnicas, *Agregados – Redução da Amostra de Campo para Ensaio de Laboratório*, NBR NM 27, 2001.
- [34] L. N. P. Cordeiro, “Análise dos parâmetros principais que regem a variabilidade dos concretos produzidos com agregados graúdos reciclados de concreto,” Ph.D. dissertation, Progr. Pós-Grad. Eng. Civ., Univ. Fed. Rio Grande do Sul, Porto Alegre, 2013.
- [35] Associação Brasileira de Normas Técnicas, *Agregados Reciclados de Resíduos Sólidos da Construção Civil – Utilização em Pavimentação e Preparo de Concreto Sem Função Estrutural – Requisitos*, NBR 15116, 2004.
- [36] G. N. Malysz, “Estudo da influência da jigagem nas propriedades do concreto com agregado graúdo reciclado,” M.S. thesis, Progr. Pós-grad. Eng. Civ. Const. Infraestrut., Univ. Fed. Rio Grande do Sul, Porto Alegre, 2018.
- [37] Associação Brasileira de Normas Técnicas, *Concreto – Ensaio de Compressão de Corpos de Prova Cilíndricos*, NBR 5739, 2018.
- [38] Associação Brasileira de Normas Técnicas, *Concreto – Determinação dos Módulos Estáticos de Elasticidade e de Deformação à Compressão*, NBR 8522, 2017.
- [39] European Commission Joint Research Centre, *Supporting Environmentally Sound Decisions for Construction and Demolition (C&D) Waste Management – A Practical Guide to Life Cycle Thinking (LCT) and Life Cycle Assessment (LCA)*, JRC Report EUR 24918 EN 2011, 2011.
- [40] L. A. C. Viana Jr., A. T. C. Sales, and L. C. Sales, “Efeitos da variabilidade de agregados de RCD sobre o desempenho mecânico do concreto de cimento Portland,” *Rev. Materia*, vol. 23, no. 1, pp. e11958, 2018.
- [41] W. M. Ambrós, C. H. Sampaio, B. G. Cazacliu, P. N. Conceição, and G. S. Reis, “Some observations on the influence of particle size and size distribution on stratification in pneumatic jigs,” *Powder Technol.*, vol. 342, pp. 594–606, 2019.
- [42] A. A. B. Corrêa, “Propriedades mecânicas de concretos com agregados reciclados: estudo de redução da variabilidade em concretos utilizando agregados submetidos à separação por jigagem a seco,” Trabalho de conclusão de graduação, Univ. Fed. Rio Grande do Sul, Porto Alegre, 2014.
- [43] B. G. Mondini, “Avaliação da variabilidade de concretos utilizando resíduos de construção e demolição submetidos ao processo de separação por jigagem a seco,” Trabalho de conclusão de graduação, Univ. Fed. Rio Grande do Sul, Porto Alegre, 2018.
- [44] P. C. Aitcin and P. K. Metha, “Effect of coarse-aggregate characteristics on mechanical properties of high-strength concrete,” *ACI Mater. J.*, vol. 87, no. 2, pp. 103–107, 1990.
- [45] W. Baalbaki et al., “Influence of coarse aggregate on elastic properties of high performance concrete,” *ACI Mater. J.*, vol. 88, no. 5, pp. 499–503, 1991.
- [46] J. L. Marriaga and L. G. L. Yépez, “Effect of sedimentary and metamorphic aggregate on the static modulus of elasticity of high-strength concrete,” *Dyna*, vol. 78, no. 170, pp. 235–242, 2011.
- [47] N. Y. Ho et al., “Efficient utilization of recycled concrete aggregate in structural concrete,” *J. Mater. Civ. Eng.*, vol. 25, no. 3, pp. 318–327, 2013.

---

**Author contributions:** ILS: conceptualization, writing, data curation, formal analysis, methodology; LVF: conceptualization, writing, data curation, formal analysis; ABM: funding acquisition, supervision, data curation, formal analysis, methodology.

**Editors:** Edna Possan, Guilherme Aris Parsekian.



## ORIGINAL ARTICLE

# Seismic analysis of reinforced concrete buildings with participating masonry infills

## *Análise sísmica de edifícios de concreto armado com alvenarias participantes*

Gerson Moacyr Sisniegas Alva<sup>a</sup> Alessandro Onofre Rigão<sup>b</sup> João Kaminski Junior<sup>c</sup> Marco Antônio Silva Pinheiro<sup>c</sup> <sup>a</sup>Universidade Federal de Uberlândia – UFU, Faculdade de Engenharia Civil, Uberlândia, MG, Brasil<sup>b</sup>Universidade Federal de Santa Maria – UFSM, Coordenadoria Acadêmica, Cachoeira do Sul, RS, Brasil<sup>c</sup>Universidade Federal de Santa Maria – UFSM, Departamento de Estruturas e Construção Civil, Santa Maria, RS, Brasil

Received 18 June 2020

Accepted 22 October 2020

**Abstract:** In this paper, seismic analyses are performed of a reinforced concrete frame building with participating masonry walls are carried out. The spectral method of the Brazilian code – ABNT 15421:2006 – was used to obtain the lateral seismic loads. The equivalent diagonal-strut model was employed to simulate the axial stiffness of the masonry walls in the frames, according to different formulations founded in literature. The main purpose is to evaluate the differences implemented by the different formulations for the equivalent strut on the seismic response. This paper also aims at comparing results obtained when the masonry stiffness is not considered under seismic loads. The results obtained are analyzed with the purpose of providing contributions for structural engineers in the design of framed structure buildings with participating masonry walls subjected to seismic loads.

**Keywords:** participating masonry, infilled frames, dynamic analysis; structural analysis.

**Resumo:** Neste trabalho são realizadas análises sísmicas em edifício de concreto armado com sistema estrutural de pórticos preenchidos com alvenarias participantes. Para a determinação das forças sísmicas, utiliza-se o método espectral da ABNT NBR 15421:2006. Para a simulação da rigidez axial das alvenarias nos pórticos emprega-se o modelo de diagonal equivalente, segundo diversas expressões encontradas na literatura. O principal objetivo é avaliar as diferenças entre essas expressões da literatura para a diagonal equivalente na resposta sísmica. Outro objetivo é de comparar resultados ao se desconsiderar a rigidez das alvenarias sob a ação sísmica. Os resultados são comentados e fornecem contribuições a engenheiros estruturais para o projeto de estruturas aporricadas de edifícios com alvenarias participantes submetidos a ações sísmicas.

**Palavras-chave:** alvenarias participantes, pórticos preenchidos, análise dinâmica, análise estrutural.

**How to cite:** G. M. S. Alva, A. O. Rigão, J. Kaminski Junior, and M. A. S. Pinheiro, “Seismic analysis of reinforced concrete buildings with participating masonry infills,” *Rev. IBRACON Estrut. Mater.*, vol. 14, no. 3, e14315, 2021, <https://doi.org/10.1590/S1983-41952021000300015>

## 1 INTRODUCTION

The infill masonry walls in framed structures are always present in multi-story concrete buildings, especially for use in sealing functions. Masonry walls that have only a sealing function are not considered as participating elements in the design of the structure and, for this reason, are not included in the structural model. However, the presence of these masonry walls influences static and dynamic behavior of structural systems subjected to lateral loads (wind and seismic forces). In seismic regions, infill walls affect strength, stiffness and ductility in framed structures and may lead to harmful failure modes, as seen with shear hinges in the columns due to the short column effect. Consequently, infilled frames have been the subject of a lot of research over the last four decades.

Corresponding author: Gerson Moacyr Sisniegas Alva. E-mail: [alva\\_gerson@yahoo.com.br](mailto:alva_gerson@yahoo.com.br)

Financial support: CNPq (Process: 308720/2018-0).

Conflict of interest: Nothing to declare.



This is an Open Access article distributed under the terms of the Creative Commons Attribution License, which permits unrestricted use, distribution, and reproduction in any medium, provided the original work is properly cited.

In Brazil, structural designs usually disregard infill masonry walls in the structural model, although their inclusion may provide important information regarding the cracking states of walls due to excessive lateral deflection of buildings – Alva et al. [1], Silva [2], Alva and Montandon [3] – and better accuracy in assessments of human comfort and wind dynamic effects in tall buildings. Noteworthy here is that in Brazil there is currently no code in force dealing with infill masonry walls with a structural function in frame buildings. In the building codes of various countries, there are several codes that deal with such masonry, including the American codes ATC FEMA 306 [4] and MSJC TMS 402-16 [5], the Canadian code CSA S304 [6] and the New Zealand code NZS 4230 [7].

In 2017, the Structural Masonry Study Commission (CE-002: 123.010) of the Brazilian Civil Construction Committee (ABNT/CB-002) was installed to update and unify the codes for structural masonry of clay blocks - ABNT NBR 15812 [8] - and concrete blocks - ABNT NBR 15961 [9]. The new code for design - ABNT NBR 16868-1 [10] - was approved and published in 2020. Annex D of this code presents a proposal (informative) for the consideration of infill masonry walls as part of the bracing system, known as participating masonry. The code defines participating masonry as structural masonry built inside a frame intentionally designed and built as part of the bracing system. The code uses the Canadian code CSA S304 [6] as a basis and recommends the equivalent diagonal model for the consideration of participating masonry. It is possible that the future approval of the Brazilian code for updated and unified structural masonry will encourage the use of participating masonry in the country. This could be introduced as another option for increasing stiffness and strength under lateral loads at Ultimate and Service Limit States checks of the entire structural system.

In terms of seismic events, Rodrigues et al. [11] highlight that South America has distinct regions in terms of seismic activity. The western border has high seismic activity, due to its location on the boundary between tectonic plates, which justifies the fact that the countries located in this region have had codes for seismic design for decades. On the other hand, the eastern border is inside an internal tectonic plate, which ensures greater stability and reduced seismic activities. In Brazil, it was only in 2006 that the first code for seismic design was approved - ABNT NBR 15421 [12]. However, Rodrigues et al. [11] warn that more recent studies developed by the University of São Paulo point to the need to update seismic mapping in Brazil. The study by Nóbrega et al. [13] indicates that although seismic activity in Brazil is less frequent with low magnitudes, it should not be overlooked and highlight the fact that ABNT NBR 15421 [12] presents a seismic acceleration map, based on a worldwide study carried out in the 1990's. However, new studies have been proposed changes to this map, noting that it does not correspond well to the actual situation, with an underestimation of seismic actions in some regions. For these reasons, it is expected that the consideration of seismic actions in structural projects will be more frequent, as a consequence of the growth in research on the subject in Brazil, followed by the updating of seismic records in the country.

This paper presents numerical simulations of a multistory reinforced concrete frame building with participating masonry walls submitted to lateral seismic loads. The main objective of this paper is the quantitative comparison of results provided by several formulations proposed in the literature to obtain the axial stiffness of the equivalent diagonal-struts, which simulate the presence of the masonry under lateral loads. This paper also aims at comparing results in the case when the presence of masonry is overlooked concerning the structural behavior under seismic loads.

## 2 PREVIOUS STUDIES IN LITERATURE

In international literature, there are many publications on research involving experimental investigations based on masonry infilled frames. As key examples, emphasis is placed on studies from Mehrabi et al. [14], Durrani and Haider [15], Flanagan and Bennett [16], Al-Chaar et al. [17], Asteris et al. [18], Tasnimi and Mohebkah [19], Liu and Manesh [20], Mansouri et al. [21], Basha and Kaushik [22] and Morandi et al. [23]. Experimental investigations cover both concrete and steel frames, which are strongly motivated toward behavior experienced under seismic loads. The analysis of the failure modes, the influence of the presence of openings on the walls, the simulation of old structures designed for gravity loads only, the absence or deficiency of the seismic detailing of the concrete structure and the study of the damage limitation (seismic performance levels) due to the relative displacements between stories are the object of study in most experimental investigations.

Numerical modelling with the aid of the Finite Element Method (FEM) is an effective tool for studying the behavior of masonry infilled frames, mainly due to the costs and operational difficulties for carrying out experimental tests. Among the various studies related to the use of the FEM for numerical analysis of infilled frames over the last two decades, one finds Doudoumis [24], Mondal and Jain [25], Asteris [26], Gosh and Amde [27], Mohyeddin et al. [28], Stavridis and Shing [29], Baloevic et al. [30] and Mohammadi and Motovali Emami [31]. In most of these studies, the numerical simulations consider the material nonlinearity, the failure criterion/plastification of the materials and aim at generating the analysis of the behavior of infilled frames in terms of stiffness, strength and failure modes. The influence of the presence of openings is also an object of study, also included in linear analysis [25].

Simplified models that simulate the infill walls by equivalent diagonal-struts are quite attractive in the analysis of infilled frames subjected to lateral loads, particularly in structural design, due to their simplicity. The models with a single diagonal-strut are very well established and provide satisfactory results, as long as a suitable formulation is chosen to obtain the axial stiffness of the equivalent diagonal-strut (or for the equivalent diagonal width, according to Section 3). The limitations of single diagonal models and the application of models with multiple-strut models are discussed in Crisafulli et al. [32], El-Dakhakhni et al. [33], Asteris et al. [34], Fiore et al. [35], Uva et al. [36] and Sattar and Liel [37].

Infilled masonry walls have great influence on obtaining the fundamental period of vibration of the structure, an essential parameter in the design of structures subjected to seismic loads. According to Asteris et al. [38], although there are several analytical formulations in the literature and in design codes for estimating the fundamental period of the structure, most of these do not take into account the presence of masonry nor the presence of openings on the walls, factors that evidently influence the structure stiffness. In addition, such expressions, by not considering the presence of filling masonry, are unable to capture the effects of irregularities in the arrangement of masonry along the height or across the spans on the fundamental period of the building. Research conducted by Amanat and Hoque [39] points out that conventional modal analysis by FEM, which does not include the presence of infill masonry walls, generally provides fundamental periods longer than those measured in buildings. For this reason, design codes impose an upper limit on the fundamental period obtained from modal analysis. The effect of infill masonry walls on the fundamental period of vibration of buildings subjected to seismic loads can be found in Asteris et al. [38], Amanat and Hoque [39], Kose [40], Ricci et al. [41], Perrone et al. [42] and Asteris et al. [43].

In Brazil, research on infill masonry walls in frame structural systems began two decades ago. From such research, the following studies are noted: Alvarenga [44], Santos [45], Tanaka [46], Madia [47], Silva [2], Sousa [48], Pitanga [49], Montandon [50], Medeiros [51], Grandi [52]. The studies conducted by Alvarenga [44] and Grandi [52] brought pioneering national contributions on the experimental behavior of masonry infilled steel frames. The cited studies were generally dedicated to numerical modeling by FEM [2], [45], [46], [48]–[51], using equivalent strut modelling [2], [44], [45], [47], [48], [50]–[52] and analysis of the influence felt from the presence of openings [2], [46]. In the analysis of buildings carried out in the referred studies, only wind loading was considered. There is a lack of national investigations involving seismic analysis in buildings with participating masonry walls.

In the investigations by Silva [2] and Montandon [50], several numerical simulations of infilled frames were carried out to analyze the Limit States of cracking (in service) of the masonry infills caused by the excessive lateral deflections of the structure subjected to wind loading. In these two studies, the results provided by different expressions proposed in the literature were also compared to obtain the equivalent diagonal width, concluding that the Durrani and Luo [53] expression is the one that provides results closest to those provided with 2D modelling including the contact problem between masonry-frame, with the aid of the ANSYS program.

### 3 MODELLING OF MASONRY INFILLED FRAMES

The lateral loads (seismic and wind forces) acting on the structural systems of masonry tend to produce the deformed shape illustrated in Figure 1a, with separation between the frame structural members and the infill masonry walls in the tensile corners and the formation of a compressive stress field across the diagonal of the wall.

The simplest and most used model in structural design for considering the interaction between frame and masonry under lateral loads is the equivalent diagonal-strut model, which is covered by several codes. In this model, the wall is represented by a pinned diagonal member, whose section is defined by the thickness of the wall and the so-called equivalent diagonal-strut width ( $a$ ), as shown in Figure 1b.

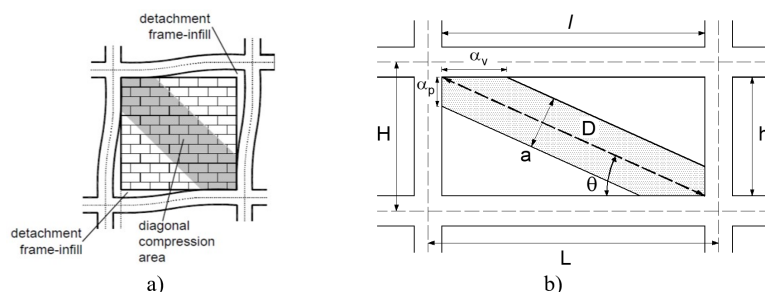


**Figure 1.** a) Effects of lateral loads on masonry infilled frames – Asteris et al. [18]. b) Dimensions used for calculating the equivalent diagonal-strut width - Silva [2]

There are several expressions proposed in specialized literature for calculating the equivalent diagonal width, such as those contained in Table 1. Other expressions, in addition to these, are presented in Table 1 and can be found in Asteris et al. [34] and in Morandi et al. [23]. All parameters in Table 1 are explained in Montandon [50].

The expression proposed by Mainstone [54] is the best known in the literature and is used, for example, in codes such as ATC FEMA [4]. The Canadian standard CSA S304 [6] adopts the expression as proposed by Hendry [55], taking as an upper limit the equivalent width value proposed by Paulay and Priestley [58]. The Brazilian code ABNT NBR 16868-1 [10] proposes the same expression as the Canadian standard.

The various expressions found in the literature lead to quite different results. In many cases, the ratio between the largest and the smallest width provided by the expressions can reach differences of up to three times one from another. The expression presented in Mainstone [54] is known to provide the lowest values of equivalent diagonal width. The results provided by several expressions proposed in the literature for the equivalent diagonal width were recently published in Alva and Montandon [3] for different geometric characteristics of frames and masonry.

**Table 1.** Analytical equations for calculation of the equivalent strut width

Authors	Expression
Mainstone [54]	$a = 0.175(\lambda_H)^{-0.4} D$
Hendry [55]	$a = \frac{\sqrt{\alpha_p^2 + \alpha_v^2}}{2} D$ $\alpha_v = \frac{\pi}{\lambda_p} \leq l$ $\alpha_p = \frac{\pi}{2\lambda_p} \leq h$
Liauw and Kwan [56]	$a = \frac{0.95 \text{sen}(2\theta)}{2\sqrt{\lambda_H}} D$
Decanini and Fantin [57]: cracked	$\lambda_H \leq 7.85$ $a = \left(0.010 + \frac{0.707}{\lambda_H}\right) D$
	$\lambda_H > 7.85$ $a = \left(0.040 + \frac{0.470}{\lambda_H}\right) D$
Paulay and Priestley [58]	$a = \frac{D}{4}$ $a = \gamma \text{sen}(2\theta) D$
Durrani and Luo [53]	$\gamma = 0.32 \sqrt{\text{sen}(2\theta)} \left(\frac{H^4 E_t}{m E_p I_p h}\right)^{-0.1}$ $m = 6 \left(\frac{I + 6 E_V I_V H}{\pi E_p I_p L}\right)$
Chrysostomou and Asteris [59]	$a = 0.27(\lambda_H)^{-0.4} D$

The modeling of masonry infilled frames can also be performed using FEM with 2D or 3D finite elements, considering the separation and sliding between the two surfaces (masonry-frame) and, when necessary, the material nonlinearity. Research by Asteris et al. [60] presents a complete overview (state of the art) on the different strategies for this type of modeling, with comments on the advantages and disadvantages of each.

In turn, as demonstrated in Doudoumis [24] and Asteris et al. [60], the modeling via FEM with finite elements for plane stress and material linear analysis can be useful in different situations, such as the verification of more simplified models, also serving to measure the expressions proposed for determining the equivalent diagonal width. This type of modeling was used more recently in investigations by Silva [2], Alva et al. [1], Montandon [50], Alva and Montandon [3], and will be touched upon in Section 4.2.3.

#### 4 NUMERICAL SIMULATIONS: MULTISTORY BUILDING

In order to achieve the main objectives of this paper, numerical simulations were carried out on a multistory reinforced concrete building with participating masonry walls. The case of the absence of masonry was also included



for comparative purposes. All information regarding the building can be found in Section 4.1, including that necessary for the determination of seismic forces.

As previously mentioned, the central focus of the analysis is the comparison of results ascertained through the use of different expressions proposed in the literature for the equivalent diagonal width in frame structural models.

The modal analysis was performed with different hierarchical models (Section 4.2), for the purpose of comparison and validation of results of the model used in the determination of the seismic loads.

For the seismic analysis, the spectral method of ABNT NBR 15421 [12] was used, the data from this method, used for determining the design response spectrum, can be found in Section 4.3. The spectral method was chosen due to it demonstrating sufficient accuracy for structural design applications, as well as being simpler than method based on response history analysis.

### 4.1 Investigated Building

This numerical example consists of a 12-story (hypothetical) commercial building of reinforced concrete (including a roof) with a structural system that consists of frames in both orthogonal directions. The structural plan view is shown in Figure 2. The building was investigated by Alva et al. [61], who assumed seismic zone 0 (city of São Carlos-SP), thus neglecting seismic actions. This figure also indicates the frame chosen in the analysis of this paper.

A floor to floor height of 3.0 m is specified. Beams and columns were designed according to ABNT NBR 6118 [62] and the participating masonry walls, were in accordance with code ABNT NBR 16868-1 [10]. For this paper, the building under consideration is located in the city of Rio Branco-AC, supported on soil that exhibits an average number of blows from SPT test equal to 25 for the 30 m below the ground surface. In terms of reinforcement detailing, a concrete frame designed with standard detailing will be employed, which corresponds to the criteria established in ABNT NBR 6118 [62]. In turn, the gravity loads are the same as those adopted by Alva et al. [61]. In order to obtain gravity loads, the following values were assumed: 25 kN/m<sup>3</sup> for the self-weight of reinforced concrete, walls in all beams (2.5 kN/m<sup>2</sup> of masonry wall) and 2.0 kN/m<sup>2</sup> for the live load.

Flexural stiffness reductions were applied for beams and columns, in order to take into account material nonlinearity (in an approximate approach) according to ABNT NBR 6118 [62].

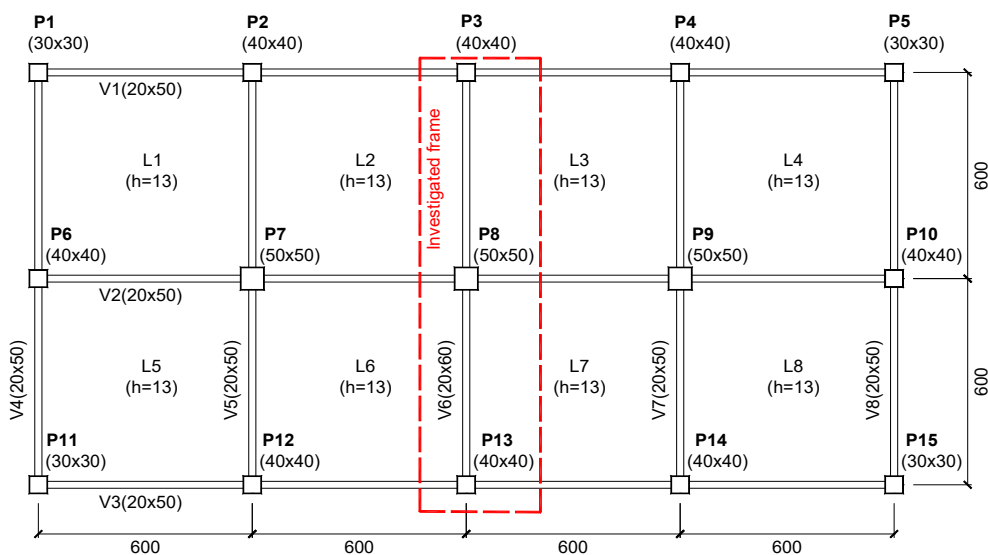


Figure 2. Structural plan view of the analyzed building

For pre-assessment purposes, seismic loads were calculated using the Equivalent Lateral Force Method, which were applied to the frame without the presence of participating masonry walls. The design of beams and columns in this situation indicated that the sections and the concrete strength of these elements could be kept the same as the building investigated in Alva et al. [61].

Thus, the specification of the materials is:

Reinforced concrete structure:

- Compressive strength of concrete (beams and columns): C40 for the first two stories and C25 for the other stories;
- Modulus of elasticity of concrete (beams and columns):  $E_c = 35GPa$  for the first two stories and  $E_c = 28GPa$  for the other stories;
- Longitudinal steel reinforcement of beams and columns: CA-50.

As for the criterion of durability, environmental aggressiveness class II was assumed, with concrete cover of beams and columns equal to 3.0 cm.

Participating masonry:

- Hollow clay blocks with solid wall
- Participating masonry thickness (without covering):  $t = 19cm$
- Thickness of longitudinal block walls:  $2.2cm$
- Characteristic compressive strength of block unit:  $f_{bk} = 10.0MPa$
- Average compressive strength of mortar:  $f_a = 8.0MPa$
- Characteristic compressive strength of prism:  $f_{pk} = 6.0MPa$
- Height of participating masonry walls:  $h = 240cm$
- Length of participating masonry walls:  $l = 555cm$
- Modulus of elasticity of participating masonry:  $E_a = 3.6GPa$

## 4.2 Modal Analysis: applied structural models

The modal analysis was carried out using three different hierarchical models: one simple (shear building models, according to Section 4.2.1), a model with intermediary hierarchical order (plane frame model with equivalent diagonals, according to Section 4.2.2) and a higher hierarchical model (according to Section 4.2.3 with 2D finite elements) useful as a reference and for the validation of the simplest models.

The use of the three different hierarchical models in modal analysis is also useful for comparing results in the simulation of the first vibration modes of the structure - these are usually the most important in seismic analysis. Noteworthy here are the comparisons made on the fundamental period of vibration provided by the different models, since this parameter is of great importance in determining seismic forces with the Equivalent Lateral Force Method, present in several design codes.

The modal analysis of the models presented in Section 4.2.1 were performed using the MATHCAD program. The models presented in 4.2.2 and 4.2.3 were performed using the ANSYS (R18) program.

### 4.2.1 Shear Building Models

Shear building models (S.B.) are widely used in seismic analysis of multistory buildings and may provide good estimates of seismic behavior in buildings with rectangular and symmetric plans when compared to more refined models (such as 3D frames or FEM models). In these models, the masses are lumped at the level of each floor and the lateral stiffness of each floor is obtained from the equivalent single-degree-of-freedom oscillator.

The traditional shear building models assume the hypothesis that beams/slabs are non-deformable (have infinite axial and flexural stiffnesses) and columns are axially inextensible. In this case, each story has a degree of freedom only in the horizontal direction. The lateral stiffness of the story is obtained by the sum:

$$k_p = \sum_{i=1}^{n_{col}} 12 \frac{EI_i}{h^3} \quad (1)$$

where

$I_i$  is the second moment of area (inertia) of column  $i$  of the story;

$E$  is the longitudinal modulus of elasticity of the columns;

$h$  is the distance between consecutive stories;

$n_{col}$  is the number of columns per story.

However, the calculation of the lateral stiffness of the story considering the flexibility of beams and slabs allows for a more accurate assessment of the same and, consequently, of the seismic acting forces. The study by Caterino et al. [63] addresses some methods proposed in the literature to estimate the lateral stiffness of the stories and which consider the stiffness of beams and columns. In turn, the authors propose that lateral stiffness be calculated similarly to that mentioned in Equation 1:

$$k_p = \sum_{i=1}^{n_{col}} \alpha_i 12 \frac{EI_i}{h^3} \tag{2}$$

where  $\alpha_i$  is a dimensionless coefficient which varies between 0.25 and 1 and depends on the degree of rotational restraint imposed by the beams on the adjacent column. The  $\alpha_i$  coefficient is calculated using expressions that depend on the flexural stiffness of beams, columns and the estimated position of the points of contraflexure (zero bending moment), these are found in Caterino et al. [63]. The method proposed by the authors provided good results when compared to those provided by simulations of entire buildings modeled in a commercial program that uses FEM.

The presence of infill masonry walls increases the lateral stiffness of the stories. Their contribution to the lateral stiffness of the story can be obtained from the axial stiffness of the equivalent diagonal:

$$k_a = \sum_{i=1}^{n_{par}} \frac{E_a a t}{L} \cos \theta \tag{3}$$

where

- $E_a$  is the longitudinal modulus of elasticity of masonry;
- $a$  is the equivalent diagonal width, which depends on the adopted expression (see Table 1);
- $t$  is the wall thickness;
- $L$  is the equivalent diagonal length in the structural model;
- $\theta$  is the equivalent diagonal angle in relation to the horizontal;
- $n_{par}$  is the number of walls per story.

Similar to that performed by Gaetani d’Aragona et al. [64], the lateral stiffness of the story can be obtained by the sum of the contributions of the frame members (beam and column) and the masonry infill walls:

$$k = k_p + k_a \tag{4}$$

In this paper, the lateral stiffness of the story was obtained from the application of a unit lateral displacement in the single-story frame, as shown in Figure 3, with the axial inextensible simulation of beam and columns.

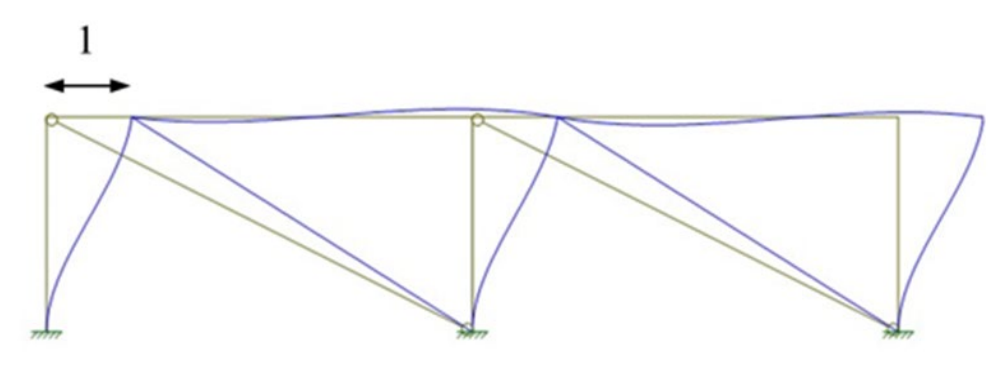


**Figure 3.** Lateral stiffness of each story due to unit displacement for shear building models

The participating masonry walls are simulated by the pinned diagonal members (equivalent diagonals). On the subject of the estimation of the moment of inertia to the bending of the beams, the contribution of slabs (effective width) - as recommended by Saatcioglu and Humar [65] – as well as the eccentricity of the beam axis in relation to the median plane of the slab, as recommended by Araújo [66] have all been considered. The effective width of the slabs was obtained from the criteria of ABNT NBR 6118 [62].

The values of the equivalent diagonal width according to the expressions in Table 1 are shown in Table 2, which also shows the values of the lateral stiffness of each story with the described procedure. The lateral stiffness values of the stories were remarkably close to those calculated using Equation 4, with maximum differences of about 5%.

**Table 2.** Values of the equivalent strut width and lateral stiffness (S.B. models)

Authors (EQUIVALENT STRUT WIDTH)	Equivalent strut width (cm)		Lateral stiffness (S.B.) (N/m)	
	Stories	Stories	Stories	Stories
	1-2	3-12	1-2	3-12
Without infill walls	-	-	$0.9506 \times 10^8$	$0.7610 \times 10^8$
CSA S304 [6]	151.17	151.17	$2.184 \times 10^8$	$1.994 \times 10^8$
Mainstone [54]	78.25	76.52	$1.589 \times 10^8$	$1.385 \times 10^8$
Durrani and Luo [53]	101.52	99.28	$1.779 \times 10^8$	$1.571 \times 10^8$
Liauw and Kwan [56]	143.50	139.56	$2.121 \times 10^8$	$1.889 \times 10^8$
Decanini and Fantin [57]	207.06	196.16	$2.640 \times 10^8$	$2.361 \times 10^8$
Paulay and Priestley [58]	151.17	151.17	$2.184 \times 10^8$	$1.994 \times 10^8$
Chrysostomou and Asteris [59]	120.73	118.06	$1.936 \times 10^8$	$1.724 \times 10^8$

#### 4.2.2 Plane Frame Models

For the modeling of the chosen plane frame (see Figure 2), the contribution of slabs (effective width) and the effect of the eccentricity of the beam axis in relation to the median plane of the slab were considered concerning the calculation of the second moment of area (inertia) of beams, in line with the concepts of Section 4.2.1.

Regarding the finite elements of the ANSYS program, the BEAM3 element was used for beams and columns, which consists of a 2D plane frame member with three degrees of freedom per node. For the simulation of the equivalent diagonals, the LINK10 element was used, which consists of a truss member with the possibility of activating only uniaxial tension or compression. For the problem at issue, only axial compression was activated. In this case, for the correct modeling of the masonry participation according to the different vibration modes, two LINK10 elements were defined per wall. Thus, the plane frame model with participating masonry presented a configuration of the diagonals in “X”.

#### 4.2.3 FEM-PS/Contact Models

For a more refined modeling, numerical simulations with two-dimensional finite elements were performed, considering a plane stress (FEM-PS), including the contact problem between participating masonry and concrete frame. The numerical modeling described in this Section is demonstrated with more details in Silva [2], Alva et al. [1], Montandon [50] and Alva and Montandon [3].

PLANE182 element from the ANSYS program was used to model both concrete and masonry structures. This finite element is applicable in the case of plane stresses and has four nodes. Each node has two degrees of freedom, which are the translations in the X and Y directions. These directions form the XY plane along which the infilled frame is located. Regarding discretization, finite elements of dimensions 5 cm x 5 cm were defined, both for the reinforced concrete frame and for the masonry wall. The adopted discretization was based on a mesh refinement study and by Silva [2] investigations.

The CONTA172/TARGE169 elements were used for the contact pair, allowing for the simulation of sliding and separation between the surfaces of the reinforced concrete frame and the masonry wall. In the ANSYS program, the normal contact stiffness factor FKN was calibrated in order to obtain the lowest possible penetration between surfaces, but with the guarantee of numerical convergence.

Other parameters defined in the contact problem are the friction coefficient ( $\mu$ ) between the masonry-frame surfaces, the maximum shear strength stress between the surfaces ( $f_{v,max}$ ) and the cohesion ( $\tau_0$ ). The following values were adopted:  $\mu=0.5$ ;  $\tau_0 = 0.35$  MPa e  $f_{v,max} = 0.365$  MPa. These values were estimated based on current Brazilian structural masonry codes, assuming that the maximum possible stress at the wall-frame interface is the masonry shear strength.

Figure 4a illustrates one of the models investigated by Alva et al. [1] for a single-story infilled frame, with details of the discretization used, the deformed shape and the field of compressive principal strains. Figure 4b illustrates the model used in this paper for the 12-story frame. In order to simulate slab contribution, the modulus of elasticity of the beam was increased proportionally to the gain of second moment of area (inertia) obtained considering the effective widths and the eccentricity of the beam axis in relation to the slab average plane.

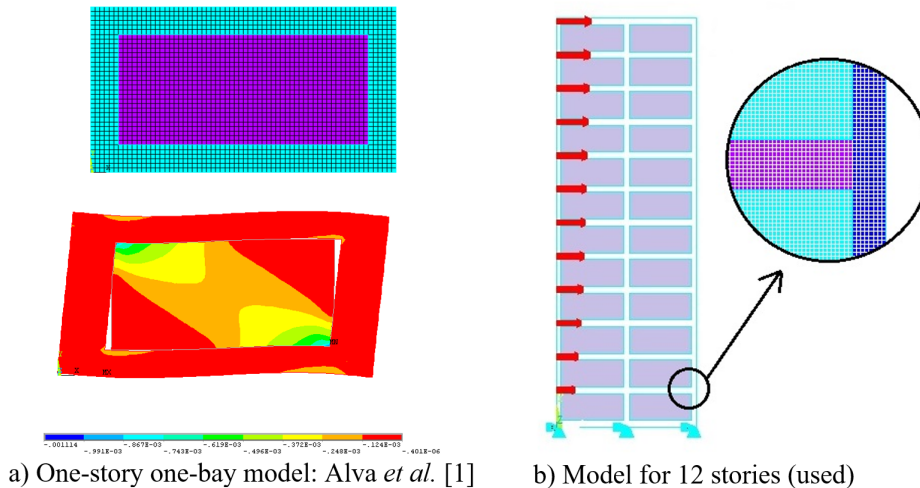


Figure 4. Examples of FEM-PS/Contact model

#### 4.2.4 Summary of applied structural models and nomenclature

Figure 5 shows the scheme for the three structural models used in the modal analysis of this paper. The nomenclature of the shear building models and the plane frame models follow the expression used to determine the equivalent diagonal width.

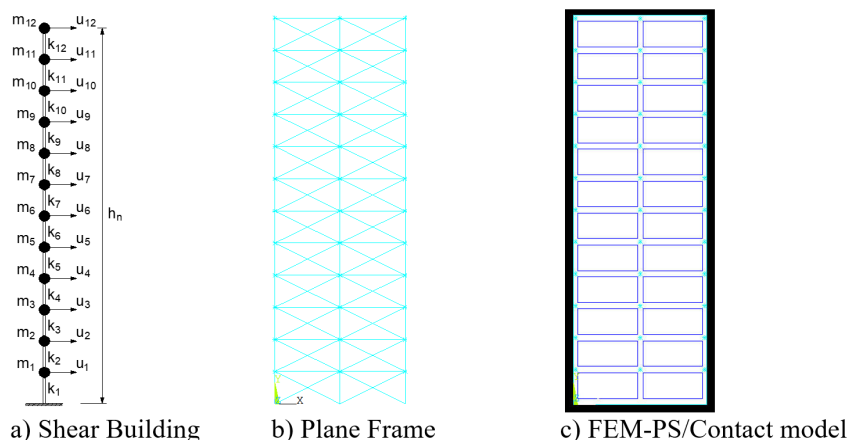


Figure 5. Structural models used in the modal analysis

### 4.3 Seismic analysis using the spectral method: ABNT NBR 15421 [12]

The building is located in seismic zone 3 (Rio Branco-AC), for which the normalized horizontal (seismic) acceleration for soils class B (rock) is  $0.10g$ , where  $g$  is the gravitational acceleration.

The design response spectrum in ABNT NBR 15421 [12] for horizontal accelerations, which assumes a damping ratio equal to 5%, is defined for three ranges of periods (in s) by:

$$S_a(T) = a_{gs0} \left( 18.75T \frac{C_a}{C_v} + 1.0 \right) \text{ for } 0 \leq T \leq 0.08 \frac{C_v}{C_a} \tag{5}$$

$$S_a(T) = 2.5a_{gs0} \text{ for } 0.08 \frac{C_v}{C_a} \leq T \leq 0.4 \frac{C_v}{C_a} \tag{6}$$

$$S_a(T) = \frac{a_{gs1}}{T} \text{ for } T \geq 0.4 \frac{C_v}{C_a} \tag{7}$$

where

$T$  is the natural period (in seconds) for the vibration mode considered;

$a_{gs0}$  and  $a_{gs1}$  are the spectral accelerations for the 0.0s and 1.0s periods, respectively, with prior consideration of the soil seismic amplification effect:

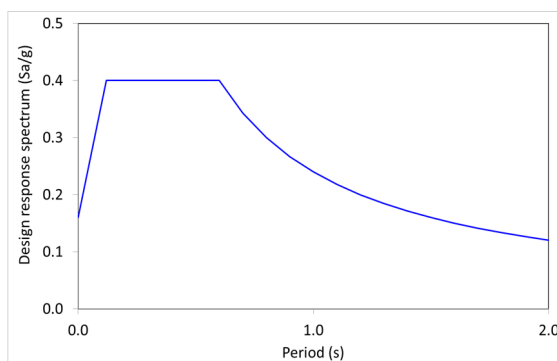
$$a_{gs0} = C_a a_g \tag{8}$$

$$a_{gs1} = C_v a_g \tag{9}$$

$C_v$  and  $C_a$  are the soil seismic amplification factors, for the 0.0s and 1.0s periods, respectively (Table 3 from ABNT NBR 15421 [12]);

$a_g$  is the characteristic horizontal (seismic) acceleration.

Based on the data of the location and soil characteristics, the following values of the necessary parameters for the construction of the design spectrum were obtained, which is shown in Figure 6:



$$a_g = 0.10g \quad (\text{Seismic zone: 3})$$

$$C_a = 1.6 \quad \text{and} \quad C_v = 2.4$$

(Site class: D)

**Figure 6.** Design response spectrum for the analyzed building: ABNT NBR 15421 [12]

Based on the nature of the building occupation and the seismic-resistant detailing chosen for the concrete structural system (frames), the coefficients applied to the modal responses (forces and displacements) in the seismic analysis are reached by the spectral method:

Importance factor  $I = 1.0$  (occupancy category I)

Response-modification coefficient:  $R = 3.0$

Displacement amplification coefficient:  $C_d = 2.5$  (concrete frame with usual detailing)

Modal responses in terms of forces, moments and support reactions must be multiplied by  $I/R$ . In turn, the modal responses in terms of absolute and relative displacements must be multiplied by the  $C_d/R$  factor.

## 5 ANALYSIS OF THE RESULTS AND DISCUSSION

### 5.1 Modal analysis

Figure 7 illustrates the configuration of the first three vibration modes according to the structural models mentioned in Section 4.2.

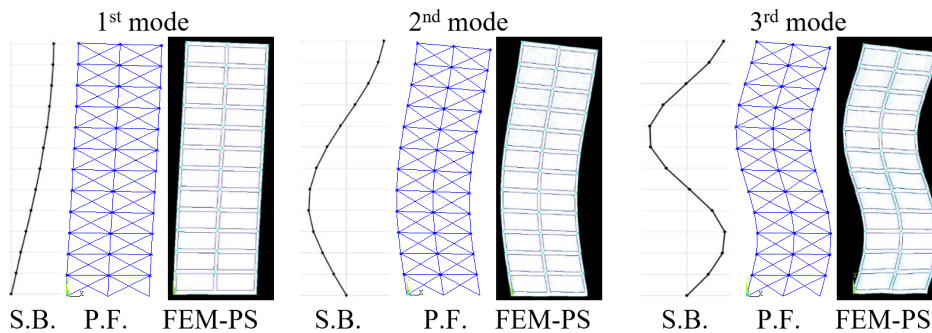


Figure 7. First three mode shapes of vibration according to the applied structural models

Emphasis is here placed on the fact that the first modes contribute more significantly to the seismic response of buildings [67]. In many practical cases, consideration of the first three modes only is sufficient for most short to medium-rise buildings. For high-rise buildings, it may be necessary to consider more than three modes [65]. Table 3 shows the values of the respective natural frequencies for shear building and plane frame models. FEM-PS/Contact model led to following values for natural frequencies: 1.129 Hz (1<sup>st</sup> mode), 3.633 Hz (2<sup>nd</sup> mode) and 6.964 Hz (3<sup>rd</sup> mode). Noteworthy here is that the first three already capture more than 94% of the total mass, for all simulated models (with and without masonry).

Table 3. Natural frequencies (Hz): models without and with masonry walls

Authors (EQUIVALENT STRUT WIDTH)	Shear Building			Plane Frame		
	1 <sup>st</sup> mode	2 <sup>nd</sup> mode	3 <sup>rd</sup> mode	1 <sup>st</sup> mode	2 <sup>nd</sup> mode	3 <sup>rd</sup> mode
Without infill walls	0.745	2.214	3.630	0.580	1.762	3.042
CSA S304 [6]	1.183	3.525	5.728	1.138	3.600	6.832
Mainstone [54]	0.993	2.956	4.855	0.960	2.958	5.938
Durrani and Luo [53]	1.052	3.138	5.164	1.026	3.185	5.892
Liau and Kwan [56]	1.156	3.442	5.657	1.117	3.521	6.645
Decanini and Fantin [57]	1.292	3.846	6.322	1.212	3.910	7.536
Paulay and Priestley [58]	1.183	3.525	5.728	1.138	3.600	6.832
Chrysostomou and Asteris [59]	1.104	3.289	5.405	1.072	3.350	6.258

It is evident that the presence of the participating masonry walls increases the frequency of the vibration modes. For the first mode, this increase was between 33.3% (Mainstone) and 73.4% (Decanini and Fantin) for the shear building models, and it was between 65.5% (Mainstone) and 108.9% (Decanini and Fantin) for the plane frame models.

Regarding the models with participating masonry, the frequency of the first mode obtained with the FEM-PS/Contact model - taken as a reference - was 1.129 Hz. In the shear building models, the frequencies of the first mode

were between 0.993 Hz (Mainstone) and 1.292 Hz (Decanini and Fantin), thus observing maximum differences of 13.7% regarding the reference model. Likewise, in the plane frame models, a maximum difference of 15.0% was observed concerning the reference model, with the frequencies of the first mode ranging between 0.960Hz (Mainstone) and 1.212 Hz (Decanini and Fantin). Noted here was that, for the same expression used in the equivalent diagonal width, the shear building models provided results remarkably close to the plane frame models.

Based on the results from Table 3, one notes that the expressions of Liauw and Kwan [56] and CSA S304 [6] used, respectively, in the shear building and plane frame models, are those that came closest to the frequency of the first vibration mode of the reference model, with maximum differences around 2%.

From the values of the cumulative modal effective mass fraction, it becomes evident that the first three vibration modes already capture more than 94% of the total mass for all models approached - shear building and plane frames (with and without masonry) - including for FEM-PS/Contact model.

Table 4 contains the values of the fundamental periods provided by each structural model. Worthy of mention here is that the increase in stiffness promoted by the participating masonry causes a significant decrease in the fundamental period of the structure when compared to the model without masonry. This decrease was between 25.4% and 42.3% by analyzing the shear building models. When analyzing the plane frame models, this decrease was between 39.6% and 52.1%.

**Table 4.** Fundamental periods: models without and with masonry walls

Authors (EQUIVALENT STRUT WIDTH)	Shear Building T (s)	Plane Frame T (s)
Without infill walls	1.342	1.724
CSA S304 [6]	0.845	0.879
Mainstone [54]	1.001	1.042
Durrani and Luo [53]	0.951	0.975
Liauw and Kwan [56]	0.865	0.895
Decanini and Fantin [57]	0.774	0.825
Paulay and Priestley [58]	0.845	0.879
Chrysostomou and Asteris [59]	0.906	0.933

Comparing only the models with participating masonry, the expression proposed by Mainstone [54] provides the largest fundamental period, which expresses maximum differences with the other expressions of around 23% for the shear building models and 26% for the plane frame models.

The FEM-PS/Contact model (reference) presented a fundamental period equal to 0.886s. In the shear building models, the fundamental periods were between 0.774s (Decanini and Fantin) and 1.001s (Mainstone); in this case, the maximum difference is 13.7% in relation to the reference model. In the plane frame models, the fundamental periods were between 0.825s (Decanini and Fantin) and 1.042s (Mainstone), thus observing a maximum difference of 15.0% regarding the reference model.

ABNT 15421 [12] presents the following expression for the approximate calculation of the fundamental period of the structure:

$$T_a = C_T h_n^x \quad (10)$$

where

$C_T = 0.0466$ ,  $x = 0.9$  for the case in question (seismic forces are fully resisted by concrete frames) and  $h_n$  is the height of the building in meters.

The approximate expression of ABNT 15421 [12] provided a fundamental period  $T_a = 1.172s$ . Moreover, according to the same code, the fundamental period based on modal analysis should not exceed the value of  $C_{up} T_a$ , with  $C_{up} = 1.6$  for the case at hand (Seismic Zone 3). Thus, there is an upper limit of  $C_{up} T_a = 1.876s$ .

The approximate period of ABNT NBR 15421 [12] was longer than those provided by modal analysis for all models with participating masonry walls. Actually, Equation 10 does not take into account the distribution of the infill walls nor geometrical-mechanical properties that these hold. Compared to the shear building and plane frame models, this



increase was between 12.4% and 51.4%. Regarding the modal analysis with the reference model (FEM-PS/Contact), the approximate period of ABNT 15421 [12] provided a value 32.3% higher. In this case, for the analysis with the Equivalent Horizontal Forces Method, the use of the approximate fundamental period would lead to smaller seismic forces than those obtained with the periods extracted from the modal analysis of the models with participating masonry walls (see the design response spectrum of Figure 6).

The focus of attention is here directed to several empirical expressions that are found in the specialized literature, especially in design codes for estimating the fundamental period, based on the monitoring of buildings under earthquakes, given as a function of the total height and/or the base of the building. However, as highlighted by Asteris et al. [43], many of these expressions may or may not consider the presence of infill masonry and, therefore, provide quite variable results among them. The authors also emphasize that the height of the building and the presence of infill masonry walls are the most critical parameters that affect the fundamental period. For this reason, it is important to evaluate the fundamental period with an adequate structural model that includes masonry.

The model of plane frame without masonry, even considering the contribution of the slab and the eccentricity of the beam axis in relation to the median plane of the slab, presented a fundamental period (1.724s) close to the upper limit of ABNT 15421 [12] (1.826s) and significantly higher than the approximate value of 1.172s of the same code. This overestimation of the fundamental period tends to occur in numerical models that disregard any contribution of stiffness from non-structural elements (such as infill masonry walls) in modal analysis, as previously mentioned in Amanat and Hoque [39].

### 5.2 Calculation of the seismic forces: spectral method

The procedure for calculating seismic forces using the spectral method, through applying shear building models, was implemented in the MATHCAD program. The step-by-step procedure presented in Chopra [67] was used.

The peak response of the story shear forces was obtained by combining the peak modal values according to the SRSS rule (Square Root of Square Sum).

According to ABNT NBR 15421 [12], the number of modes considered must be sufficient in order to capture 90% of the total mass. In all analyses, six vibration modes were considered, which resulted in the capture of approximately 99% of the total mass.

### 5.3 Comparative analyses: spectral method

#### 5.3.1 Lateral seismic loads on stories and total shear force at the base

Table 5 contains a comparison of the values of the lateral seismic loads on each story as a function of the expression used for the equivalent width. The expression in Mainstone [54] leads to the lowest values of seismic forces between the analyzed expressions, whereas that of Decanini and Fantin [57] leads to the highest values.

**Table 5.** Lateral seismic loads at each story (kN)

Floor	Without infill walls	CSA S304 [6]	Mainstone [54]	Durrani and Luo [53]	Liauw and Kwan [56]	Decanini and Fantin [57]	Chrysostomou and Asteris [59]
12	60.23	79.80	70.84	73.47	78.59	85.36	76.05
11	51.12	73.40	63.43	66.39	71.99	79.25	69.25
10	42.25	66.25	55.76	58.93	64.71	72.19	61.88
9	35.51	59.99	49.47	52.76	58.42	65.79	55.62
8	30.26	54.21	44.00	47.25	52.68	59.73	49.97
7	26.50	48.75	39.31	42.34	47.32	53.82	44.83
6	23.87	43.45	35.12	37.81	42.17	47.89	39.98
5	21.99	38.15	31.16	33.44	37.04	41.81	35.22
4	20.15	32.47	27.02	28.82	31.55	35.26	30.15
3	17.61	26.12	22.21	23.55	25.38	28.00	24.41
2	13.40	18.66	16.14	16.70	18.07	19.64	17.50
1	8.32	10.38	9.32	9.53	10.11	10.77	9.87
Base	0	0	0	0	0	0	0

Table 6 contains the values of the total seismic horizontal force at the base of the structure  $H_t$  for the different expressions used for the equivalent width. The expression in Mainstone [54] provided the lowest value (463.77 kN) and with the expression in Decanini and Fantin [57], the highest value (599.51 kN). Thus, the maximum difference between the expressions for the total horizontal force at the base was 29.2%.

**Table 6.** Total shear force at the base of the structure

Expression	Total shear force (kN)
Without infill walls	351.20
CSA 304 [6]	551.61
Mainstone [54]	463.77
Durrani and Luo [53]	490.98
Liauw and Kwan [56]	538.01
Decanini and Fantin [57]	599.51
Paulay and Priestley [58]	551.61
Chrysostomou and Asteris [59]	514.74

The Brazilian code ABNT NBR 15421 [12] specifies a minimum value for the total horizontal seismic force at the base of the structure obtained with the spectral method - called  $H_t$ . This value must not be less than 85% of the value obtained with the equivalent lateral force method - called  $H$ . Using the approximate fundamental period  $T_a$ ,  $H$  equal to 469.63 kN was obtained. From Table 6, for all models with masonry, the spectral method led to total base forces greater than  $0.85H$ , which is equivalent to 399.19 kN. The same did not happen for the model without masonry. In turn, when using the fundamental period extracted from modal analysis in the method of equivalent horizontal forces, the spectral method provided values very close to  $0.85H$  for models with masonry.

### 5.3.2 Absolute and relative lateral displacements of the stories

Figure 8a shows the absolute lateral displacements of the stories for the model without masonry and for models with masonry according to the expression used for the equivalent diagonal. Similarly, Figure 8b shows the relative lateral displacements divided by the distance between consecutive stories (interstory drifts). Absolute and relative displacements were obtained by Plane Frame model (see Figure 5b).

Figure 8a shows that, with the exception of Mainstone [54], the expressions of equivalent diagonal width provided results reasonably close to each other for absolute lateral displacements, with maximum differences around 10%. On the other hand, the expression in Mainstone [54] provided values from 39.2% to 54.3% higher than the other expressions, when considering the horizontal displacement at the top of the building.

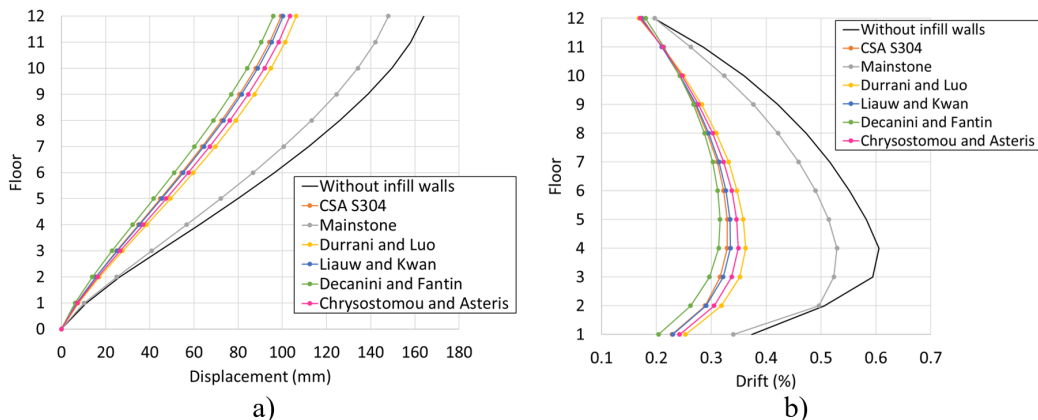


**Figure 8.** Lateral displacement of each floor and Interstory Drifts

Regarding interstory drifts, the maximum values occurred between stories 4 and 5 for Decanini and Fantin [57] and CSA S304 [6] expressions and between stories 3 and 4 for the other expressions. With the exception of the Mainstone expression [54], the maximum values of interstory drifts provided by the other expressions of equivalent width produced values between 0.316% and 0.363% (maximum differences around 15%). The expression in Mainstone [54] led to a maximum interstory drift value of 0.529%, i.e., it provided values 46.0% to 67.5% higher than those of other expressions. For the model without participating masonry walls, the maximum value was 0.606%.

According to ABNT 15421 [12], for occupancy category I, the maximum interstory drift should be limited to 2%. Therefore, in all models, including the case without participating masonry, this limit is not exceeded.

However, the referred code does not provide specific information about displacement limits for reducing damage in elements, such as infilled walls. Recent studies, such as those by Morandi et al. [23] and those by Hak et al. [68] associate drift values with the levels of damage caused to infill masonry. According to Morandi et al. [23], drifts below 0.30% cause minor damage to masonry, with superficial cracking mainly concentrated in the mortar joints. For drifts between 0.30% and 0.50%, the masonry is damaged, with bi-diagonal cracking and the sliding in the mortar bed joints; however, the repairing of masonry is technically and financially viable. For 1.75% drifts, the masonry walls are severely damaged and their recovery is economically questionable, but without threat to human lives. Thus, through the values of interstory drifts in Figure 8, there is a prevision of moderate damage to the masonry due to the seismic action, but with technical and economic feasibility of repair.

### 5.3.3 Second order effects (P-Δ)

For the assessment of global second-order effects, the stability coefficient  $\theta$  presented in ABNT NBR 15421 [12] was used. For all models (with and without participating masonry), the stability coefficients  $\theta$  were less than 0.1. Therefore, it was unnecessary to consider the global second order effects in the structural analysis. The maximum value obtained for  $\theta$  was equal to 0.0579 in models without masonry walls and equal to 0.0385 in models with masonry infill walls (Mainstone [54] expression).

### 5.3.4 Internal forces in the structural members

In order to compare results, the bending moments in columns and the compressive stress in the equivalent diagonals obtained with the different expressions from Table 1 are shown, referring only to the characteristic seismic loads. The internal forces in members were obtained through the Plane Frame model (see Figure 5b).

Figures 9a and 9b show the maximum bending moment (absolute value)  $M_A$  of the story, for the interior and exterior columns, respectively, along the height of the building. Noteworthy is that the  $M_A$  bending moment is used in the approximate methods of ABNT NBR 6118 [62] for the design of members subjected to combined bending and compressive axial forces (local second-order effects).

Between the base (foundation) section and the first story, for the interior column, the bending moments were 1.34 to 1.73 times lower due to the presence of the participating masonry walls, for which the Mainstone [54] expression provided the highest values. For the exterior columns, the results were similar: values from 1.28 to 1.63 times lower than in the case without masonry, and the Mainstone [54] expression was the most conservative. By comparing all the expressions for the equivalent diagonal width, one notes that the maximum differences in columns bending moments between the base and the first story were of 27% to 30%.

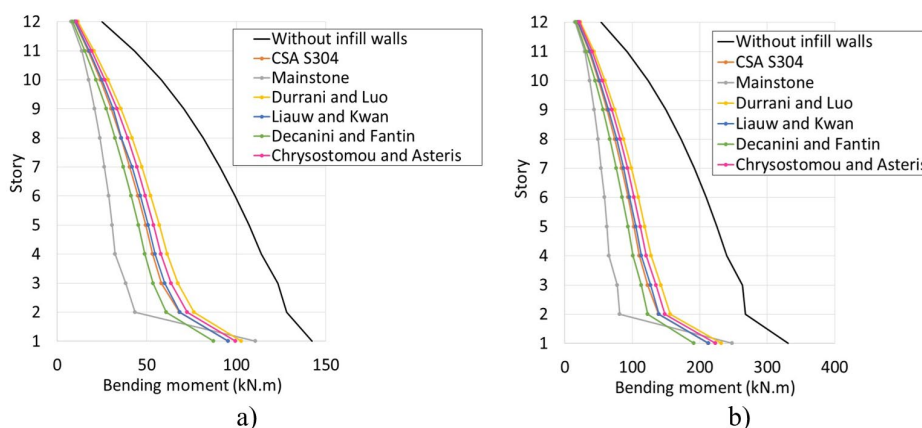


Figure 9.  $M_A$  bending moment of each story: a) exterior columns; b) interior column

From the second story, analyzing both the internal and the exterior columns, Mainstone [54] is the expression that provided the lowest values of  $M_A$  and Durrani and Luo [53], that which provided the highest values.

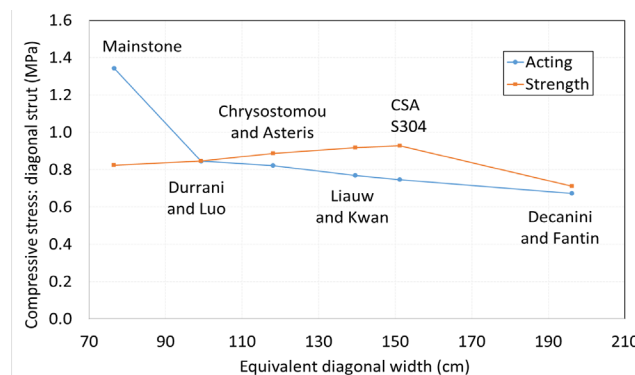
Between the second and fourth stories, one notes that when compared to the values obtained using the Mainstone [54] expression, the other expressions led to values of 50% to 95% higher for  $M_A$ , however, with maximum differences between these around 26%. Along this same stretch of the building (along the height), there are signs that the presence of the participating masonry reduced the  $M_A$  moments between 1.84 to 3.47 times for the internal column and between 1.77 to 3.23 times for the exterior columns, when compared to the case without participating masonry.

Table 7 contains the maximum values of acting compressive stress  $\sigma$  in the equivalent diagonals. The stress is obtained by the ratio between the acting axial load in the diagonal-strut  $N$  and the cross-sectional area, which consists of the product between the wall thickness and the diagonal equivalent width  $a$ . In all models from Table 7, the maximum stress value occurred between the second and third stories. The Mainstone [54] expression led to higher axial loads (maximum) in the equivalent diagonals; values 59% to 100% higher in relation to the other expressions. Apart from the Mainstone [54] expression, the maximum difference observed among the other expressions was 26%.

**Table 7.** Acting compressive stresses in equivalent diagonal struts: seismic loads

Expression	N(kN)	a (cm)	$\sigma$ (MPa)
CSA S304 [6]	214.46	151.17	0.747
Mainstone [54]	195.37	76.52	1.344
Durrani and Luo [53]	159.53	99.28	0.846
Liauw and Kwan [56]	203.91	139.56	0.769
Decanini and Fantin [57]	250.58	196.16	0.672
Paulay and Priestley [58]	214.46	151.17	0.747
Chrysostomou and Asteris [59]	184.40	118.06	0.822

In Figure 10, a comparative graph is presented for the analysis of the maximum acting stress and the strength stresses, depending on the variation along the equivalent diagonal width. The strength stresses were calculated according to the code ABNT NBR 16868-1 [10], with the strength reduction factors for masonry applicable in Exceptional load combinations, in accordance with ABNT 15812 [8].



**Figure 10.** Compressive stresses in the diagonal strut: acting and strength values

Figure 10 shows that the increase in the equivalent diagonal width led to a decrease in internal forces in the masonry walls, although it caused an increase in the total horizontal seismic forces at the base (due to the increase in stiffness of the structure). Apart from the Mainstone [54] expression, all other expressions led to higher strength stresses than the acting stresses, demonstrating as such, a more favorable situation for the CSA S304 [6] expression, where its application resulted in a acting stress/strength stress ratio equal to 0.805. The Mainstone [54] expression was the most conservative, with a relation between acting stress/strength stress ratio equal to 1.633.

## 6 CONCLUSIONS

This paper dealt with the seismic analysis of buildings with a reinforced concrete frame system and participating masonry walls. The spectral method of ABNT NBR 15421 [12] was used for determining the seismic forces. The infill walls in the structural system were simulated by the equivalent diagonal model.

Seven expressions proposed in the literature were used in the analysis performed in this paper to obtain the equivalent diagonal width. The differences provided by such expressions reached approximately 165%, with the Mainstone [54] expression being the most conservative, i.e., the one that provided the lowest value for the equivalent diagonal width. This pronounced difference motivated the analysis concerning results that such expressions would lead to in terms of seismic forces in the building, internal forces in members and horizontal displacements.

Regarding the obtaining of the seismic forces, shear building models were used, in which the lateral stiffness of the stories was obtained considering the presence of the participating masonry walls, the contribution of the slabs and the eccentricity of the beam in relation to their average plane. Through modal analysis, the shear building models were compared and validated with two models: i) plane frame model with equivalent diagonals activated only for compression; ii) model with finite elements of plane stress with simulation of the problem of contact between wall and frame (reference model). The results from the modal analysis indicated the suitability of the procedure used to determine lateral stiffness in the shear building models, which provided results that were relatively close to the other two models of higher hierarchy.

As expected, the presence of the participating masonry walls promoted an increase in the lateral stiffness of the structure when compared to the case without masonry, leading to smaller fundamental vibration periods. In the numerical example analyzed in this paper, this reduction arrived at 52%, depending on the structural model adopted. Among the models with participating masonry simulated with the various expressions of equivalent diagonal, the maximum difference between the fundamental periods was 26%, which is, however, around 15% when compared to the reference model. Naturally, models with greater widths of equivalent diagonal had lower fundamental vibration periods. By analyzing the approximate fundamental period of ABNT NBR 15421 [12], the Brazilian code was noted as providing values up to 51% higher than the models that used equivalent diagonals (shear building and plane frames) and 32% higher in relation to the reference model. Such conclusions pertaining to the fundamental period of vibration are important especially when making decisions on the employment of the Equivalent Lateral Force Method in the determination of seismic loads.

In the seismic analysis of the numerical example, using the different expressions for the equivalent diagonal, differences of up to 29% were obtained regarding the total horizontal seismic force at the base of the structure and Mainstone [54] expression provided the lower value. However, this expression was that which provided the highest values of compression stress in the equivalent diagonals when compared to the other expressions. The Mainstone [54] expression was also the one that provided the highest values of bending moment in the columns between the foundation and the first story - a stretch where the highest bending moments were encountered in the building.

Finally, the conclusion was drawn that the differences in results observed in the structural analysis and in checks on masonry strength when applying different expressions for the equivalent diagonal width justify the need for further studies that contribute to Brazilian design codes and allow for the introduction of recommendations specific to the case of buildings with participating masonry, especially in structures resistant to seismic loads.

## ACKNOWLEDGMENTS

To CNPq for financial support to the first author (Process: 308720/2018-0).

## REFERENCES

- [1] G. Alva, J. Kaminski Jr., G. Mohamad, and L. Silva, "Serviceability limit state related to excessive lateral deformations to account for infill walls in the structural model," *Ibracon Struct. Mater. J.*, vol. 8, no. 3, pp. 390–426, 2015, <http://dx.doi.org/10.1590/S1983-41952015000300008>.
- [2] L. Silva, "Modelagem de pórticos de concreto armado preenchidos com a consideração de aberturas nos painéis de alvenaria," M.S. thesis, Univ. Fed. Santa Maria, Santa Maria, 2014. [Online]. Available: <https://www.ufsm.br/cursos/pos-graduacao/santa-maria/ppgec/>
- [3] G. Alva and G. Montandon, "Modelos estruturais para a análise de pórticos preenchidos com alvenaria em edifícios de concreto armado," *Ibracon Struct. Mater. J.*, vol. 12, no. 5, pp. 1058–1085, 2019, <http://dx.doi.org/10.1590/s1983-41952019000500006>.
- [4] Applied Technology Council, *Evaluation of Earthquake Damaged Concrete and Masonry Wall Buildings*, FEMA 306, 1998.
- [5] Masonry Standards Joint Committee, *Building Code Requirements for Masonry Structures*, TMS 402-16, 2016.

- [6] Canadian Standards Association, *Design of Masonry Structures*, S304-14, 2014.
- [7] New Zealand Standard, *Design of Reinforced Concrete Masonry Structures*, NZS 4230, 2004.
- [8] Associação Brasileira de Normas Técnicas, *Alvenaria Estrutural – Blocos Cerâmicos – Parte 1: Projetos*, NBR 15812, 2010.
- [9] Associação Brasileira de Normas Técnicas, *Alvenaria Estrutural – Blocos de Concreto – Parte 1: Projetos*, NBR 15961, 2011.
- [10] Associação Brasileira de Normas Técnicas, *Alvenaria Estrutural – Parte 1: Projeto*, NBR 16868, 2020.
- [11] R. Rodrigues, C. Mazzilli, and T. Bittencourt, "Comparative analysis of normative provisions for seismic design and detailing of reinforced concrete structures," *Ibracon Struct. Mater. J.*, vol. 12, no. 5, pp. 1220–1247, 2019, <http://dx.doi.org/10.1590/s1983-41952019000500013>.
- [12] Associação Brasileira de Normas Técnicas, *Projeto de Estruturas Resistentes a Sismos – Procedimento*, NBR 15421, 2006.
- [13] P. Nóbrega, B. Souza, M. Felipe, and S. Nóbrega, "Sobre os mapas de perigo sísmico para o projeto de estruturas," in *An. 61º Cong. Bras. Concr.*, 2019, pp. 1–16.
- [14] A. Mehrabi, P. Shing, M. Schuller, and J. Noland, "Experimental evaluation of Masonry-Infilled RC frames," *J. Struct. Eng.*, vol. 122, no. 3, pp. 228–237, 1996, [http://dx.doi.org/10.1061/\(ASCE\)0733-9445\(1996\)122:3\(228\)](http://dx.doi.org/10.1061/(ASCE)0733-9445(1996)122:3(228)).
- [15] A. Durrani and S. Haider, "Seismic response of R/C frames with unreinforced masonry infills," in *Proc. 11th World Conf. Earthquake Eng., Acapulco*, 1996, pp. 1–8.
- [16] R. Flanagan and R. Bennett, "In-plane behavior of structural clay tile infilled frames," *J. Struct. Eng.*, vol. 125, no. 6, pp. 590–599, 1999, [http://dx.doi.org/10.1061/\(ASCE\)0733-9445\(1999\)125:6\(590\)](http://dx.doi.org/10.1061/(ASCE)0733-9445(1999)125:6(590)).
- [17] G. Al-Chaar, M. Issa, and S. Sweeney, "Behavior of masonry-infilled nonductile reinforced concrete frames," *J. Struct. Eng.*, vol. 128, no. 8, pp. 1055–1063, 2002, [http://dx.doi.org/10.1061/\(ASCE\)0733-9445\(2002\)128:8\(1055\)](http://dx.doi.org/10.1061/(ASCE)0733-9445(2002)128:8(1055)).
- [18] P. Asteris, D. Kakaletsis, C. Chrysostomou, and E. Smyrou, "Failure modes of in-filled frames," *Electron. J. Struct. Eng.*, vol. 11, no. 1, pp. 11–20, 2011.
- [19] A. Tasnimi and A. Mohebbkhal, "Investigation on the behavior of brick-infilled steel frames with openings, experimental and analytical approaches," *Eng. Struct.*, vol. 33, no. 3, pp. 968–980, 2011, <http://dx.doi.org/10.1016/j.engstruct.2010.12.018>.
- [20] H. Liu and P. Manesh, "Concrete masonry infilled steel frames subjected to combined in-plane lateral and axial loading – an experimental study," *Eng. Struct.*, vol. 52, pp. 331–339, 2013, <http://dx.doi.org/10.1016/j.engstruct.2013.02.038>.
- [21] A. Mansouri, M. Marefat, and M. Khanmohammadi, "Experimental evaluation of seismic performance of low-shear strength masonry infills with openings in reinforced concrete frames with deficient seismic details," *Struct. Des. Tall Spec. Build.*, vol. 23, no. 15, pp. 1190–1210, 2014, <http://dx.doi.org/10.1002/tal.1115>.
- [22] S. Basha and H. Kaushik, "Behavior and failure mechanisms of masonry-infilled RC frames (in low-rise buildings) subject to lateral loading," *Eng. Struct.*, vol. 111, pp. 233–245, 2016, <http://dx.doi.org/10.1016/j.engstruct.2015.12.034>.
- [23] P. Morandi, S. Hak, and G. Magenes, "Performance-based interpretation of in-plane cyclic tests on RC frames with strong masonry infills," *Eng. Struct.*, vol. 156, pp. 503–521, 2018, <http://dx.doi.org/10.1016/j.engstruct.2017.11.058>.
- [24] I. Doudoumis, "Finite element modelling and investigation of the behaviour of elastic infilled frame under monotonic loading," *Eng. Struct.*, vol. 29, no. 6, pp. 1004–1024, 2007, <http://dx.doi.org/10.1016/j.engstruct.2006.07.011>.
- [25] G. Mondal and S. Jain, "Lateral stiffness of masonry infilled reinforced concrete (RC) frames with central opening," *Earthq. Spectra*, vol. 24, no. 3, pp. 701–723, 2008, <http://dx.doi.org/10.1193/1.2942376>.
- [26] P. Asteris, "Lateral stiffness of brick masonry infilled plane frames," *J. Struct. Eng.*, vol. 129, no. 8, pp. 1071–1079, 2003, [http://dx.doi.org/10.1061/\(ASCE\)0733-9445\(2003\)129:8\(1071\)](http://dx.doi.org/10.1061/(ASCE)0733-9445(2003)129:8(1071)).
- [27] A. Gosh and A. Amde, "Finite element analysis of infilled frames," *J. Struct. Eng.*, vol. 128, no. 7, pp. 881–889, 2002, [http://dx.doi.org/10.1061/\(ASCE\)0733-9445\(2002\)128:7\(881\)](http://dx.doi.org/10.1061/(ASCE)0733-9445(2002)128:7(881)).
- [28] A. Mohyeddin, H. Goldsworthy, and E. Gad, "FE modelling of RC frames with masonry infill panels under in-plane and out-of-plane loading," *Eng. Struct.*, vol. 51, pp. 73–87, 2013, <http://dx.doi.org/10.1016/j.engstruct.2013.01.012>.
- [29] A. Stavridis and P. Shing, "Finite-element modeling of nonlinear behavior of masonry-infilled RC frames," *J. Struct. Eng.*, vol. 136, no. 3, pp. 285–296, 2010, [http://dx.doi.org/10.1061/\(ASCE\)ST.1943-541X.116](http://dx.doi.org/10.1061/(ASCE)ST.1943-541X.116).
- [30] G. Baloevic, J. Radnic, and A. Harapin, "Numerical dynamic tests of masonry-infilled RC frames," *Eng. Struct.*, vol. 50, pp. 43–55, 2013, <http://dx.doi.org/10.1016/j.engstruct.2012.11.034>.
- [31] M. Mohammadi and S. M. Motovali Emami, "Multi-bay and pinned connection steel infilled frames; an experimental and numerical study," *Eng. Struct.*, vol. 188, pp. 43–59, 2019, <http://dx.doi.org/10.1016/j.engstruct.2019.03.028>.
- [32] F. Crisafulli, A. Carr, and R. Park, "Analytical modelling of infilled frame structures – a general review," *Bull. N. Z. Soc. Earthq. Eng.*, vol. 33, no. 1, pp. 30–47, 2000.
- [33] W. El-Dakhkhni, M. Elgaaly, and A. Hamid, "Three-strut model for concrete masonry-infilled steel frames," *J. Struct. Eng.*, vol. 129, no. 2, pp. 177–185, 2003, [http://dx.doi.org/10.1061/\(ASCE\)0733-9445\(2003\)129:2\(177\)](http://dx.doi.org/10.1061/(ASCE)0733-9445(2003)129:2(177)).

- [34] P. Asteris, S. Antoniou, D. Sophianopoulos, and C. Chrysostomou, "Mathematical macromodeling of infilled frames: state of the art," *J. Struct. Eng.*, vol. 137, no. 12, pp. 1508–1517, 2011, [http://dx.doi.org/10.1061/\(ASCE\)ST.1943-541X.0000384](http://dx.doi.org/10.1061/(ASCE)ST.1943-541X.0000384).
- [35] A. Fiore, A. Netti, and P. Monaco, "The influence of masonry infill on the seismic behaviour of RC frame buildings," *Eng. Struct.*, vol. 44, pp. 133–145, 2012, <http://dx.doi.org/10.1016/j.engstruct.2012.05.023>.
- [36] G. Uva, D. Raffaele, F. Porco, and A. Fiore, "On the role of equivalent strut models in the seismic assessment of infilled RC buildings," *Eng. Struct.*, vol. 42, pp. 83–94, 2012, <http://dx.doi.org/10.1016/j.engstruct.2012.04.005>.
- [37] S. Sattar and A. Liel, "Seismic performance of non-ductile reinforced concrete frames with masonry infill walls -I: development of a finite element enhanced strut modeling approach," *Earthq. Spectra*, vol. 32, no. 2, pp. 795–818, 2016, <http://dx.doi.org/10.1193/90914eqs139m>.
- [38] P. Asteris, C. Repapis, F. Foskolos, A. Fotos, and A. Tsaris, "Fundamental period of infilled RC frame structures with vertical irregularity," *Struct. Eng. Mech.*, vol. 61, no. 5, pp. 663–674, 2017, <http://dx.doi.org/10.12989/sem.2017.61.5.663>.
- [39] K. Amanat and E. Hoque, "A rationale for determining the natural period of RC building frames having infill," *Eng. Struct.*, vol. 28, no. 4, pp. 495–502, 2006, <http://dx.doi.org/10.1016/j.engstruct.2005.09.004>.
- [40] M. Kose, "Parameters affecting the fundamental period of RC building with infill walls," *Eng. Struct.*, vol. 31, no. 1, pp. 93–102, 2009, <http://dx.doi.org/10.1016/j.engstruct.2008.07.017>.
- [41] P. Ricci, G. Verderame, and G. Manfredi, "Analytical investigation of elastic period of infilled RC MRF buildings," *Eng. Struct.*, vol. 33, no. 2, pp. 308–319, 2011, <http://dx.doi.org/10.1016/j.engstruct.2010.10.009>.
- [42] D. Perrone, M. Leone, and M. Aiello, "Evaluation of the infill influence on the elastic period of existing frames," *Eng. Struct.*, vol. 123, pp. 419–433, 2016, <http://dx.doi.org/10.1016/j.engstruct.2016.05.050>.
- [43] P. Asteris, C. Repapis, E. Repapi, and L. Cavaleri, "Fundamental period of infilled reinforced concrete frame structures," *Struct. Infrastruct. Eng.*, vol. 13, no. 7, pp. 929–941, 2016, <http://dx.doi.org/10.1080/15732479.2016.1227341>.
- [44] R. Alvarenga, "Análise teórico-experimental de estruturas compostas de pórticos de aço preenchidos com alvenaria de concreto celular autoclavado," Ph.D. dissertation, Univ. São Paulo, São Carlos, 2002. [Online]. Available: <http://www.set.eesc.usp.br/producao/>
- [45] E. Santos, "Influência da alvenaria no comportamento estrutural de edifícios altos de concreto armado," M.S. thesis, Univ. Cat. Pernambuco, Recife, 2007.
- [46] E. Tanaka, "Influência da alvenaria dotada de aberturas na rigidez global de um edifício," M.S. thesis, Univ. Est. Campinas, Campinas, 2011.
- [47] F. Madia, "Estudo de pórticos preenchidos com alvenaria," M.S. thesis, Univ. Fed. São Carlos, São Carlos, 2012.
- [48] P. Sousa, "Efeito dos painéis de vedação nas características dinâmicas de edificações de concreto armado," M.S. thesis, Univ. Fed. Rio de Janeiro, 2014.
- [49] M. Pitanga, "Contribuição ao estudo de pórticos de concreto armado preenchidos com alvenaria de blocos cerâmicos," Ph.D. dissertation, Univ. Fed. Pernambuco, Recife, 2016.
- [50] G. Montandon, "Modelos estruturais para a análise de pórticos preenchidos com blocos cerâmicos em edifícios de concreto armado," M.S. thesis, Univ. Fed. Uberlândia, Uberlândia, 2018. [Online]. Available: <http://www.ppgec.feciv.ufu.br/>
- [51] W. Medeiros, "Pórticos em concreto pré-moldado preenchidos com alvenaria participante," M.S. thesis, Univ. Fed. São Carlos, São Carlos, 2018.
- [52] A. Grandi, "Avaliação experimental por meio de ensaios cíclicos de pórtico de aço preenchido com alvenaria participante," M.S. thesis, Univ. Fed. Viçosa, Viçosa, 2018.
- [53] A. Durrani and Y. Luo, "Seismic retrofit of flat-slab buildings with masonry infills," in *Proc. NCEER Workshop on Seismic Response Mas. Infills*, Buffalo, N.Y., 1994, pp. 1–8.
- [54] R. Mainstone, *Supplementary Note on the Stiffness and Strengths of Infilled Frames*. Garston: Building Research Station, 1974.
- [55] A. Hendry, *Structural Brickwork*. London: MacMillan, 1981. <http://dx.doi.org/10.1007/978-1-349-81439-8>.
- [56] T. Liauw and K. Kwan, "Nonlinear behavior of non-integral infilled frames," *Comp. and Struct.*, vol. 18, no. 3, pp. 551–560, 1984, [http://dx.doi.org/10.1016/0045-7949\(84\)90070-1](http://dx.doi.org/10.1016/0045-7949(84)90070-1).
- [57] L. Decanini and G. Fantin, "Modelos simplificados de la mampostería incluida en porticos: características de rigidez y resistencia lateral en estado limite," in *J. Argentinas Ing. Estructural*, vol. 2, Buenos Aires, Argentina, 1986, pp. 817–836.
- [58] T. Paulay and M. Priestley, *Seismic Design of Reinforced Concrete and Masonry Buildings*. New York: Wiley, 1992. <http://dx.doi.org/10.1002/9780470172841>.
- [59] C. Chrysostomou and P. Asteris, "On the in-plane properties and capacities of infilled frames," *Eng. Struct.*, vol. 41, pp. 385–402, 2012, <http://dx.doi.org/10.1016/j.engstruct.2012.03.057>.
- [60] P. Asteris, D. Cotsovos, C. Chrysostomou, A. Mohebhah, and G. Al-Chaar, "Mathematical micromodeling of infilled frames: state of the art," *Eng. Struct.*, vol. 56, pp. 1905–1921, 2013, <http://dx.doi.org/10.1016/j.engstruct.2013.08.010>.

- [61] G. Alva, J. Kaminski Jr., A. Rigão, and M. Pinheiro, "Consideração das alvenarias participantes na rigidez lateral de edifícios de concreto armado," in *An. 61º Congr. Bras. Concr.*, Fortaleza, 2019, pp. 1–16.
- [62] Associação Brasileira de Normas Técnicas, *Projeto de Estruturas de Concreto – Procedimento*, NBR 6118, 2014.
- [63] N. Caterino, E. Cosenza, and B. Azmoodeh, "Approximate methods to evaluate storey stiffness and interstorey drift of RC buildings in seismic areas," *Struct. Eng. Mech.*, vol. 46, no. 2, pp. 245–267, 2013, <http://dx.doi.org/10.12989/sem.2013.46.2.245>.
- [64] M. Gaetani d’Aragona, M. Polese, E. Cosenza, and A. Prota, "Simplified assessment of maximum interstorey drift for RC buildings with irregular infills distribution along the height," *Bull. Earthquake Eng.*, vol. 17, no. 2, pp. 707–736, 2019, <http://dx.doi.org/10.1007/s10518-018-0473-y>.
- [65] M. Saatcioglu and J. Humar, "Dynamic analysis of buildings for earthquake-resistant design," *Can. J. Civ. Eng.*, vol. 30, no. 2, pp. 338–359, 2003, <http://dx.doi.org/10.1139/102-108>.
- [66] J. Araújo, "Avaliação dos métodos simplificados para o cálculo de lajes maciças apoiadas em vigas flexíveis," *Teor. Prat. Eng. Civ.*, no. 12, pp. 1–11, 2008.
- [67] A. Chopra, *Dynamic of Structures: Theory and Applications to Earthquake Engineering*, 4th ed. Upper Saddle River: Prentice Hall, 2012.
- [68] S. Hak, P. Morandi, G. Magenes, and T. Sullivan, "Damage control for clay masonry infills in the design of RC frame structures," *J. Earthquake Eng.*, vol. 16, no. S1, pp. 1–35, 2012, <http://dx.doi.org/10.1080/13632469.2012.670575>.

---

**Author contributions:** GMSA: conceptualization, data curation, formal analysis, investigation, methodology, validation, writing. AOR: investigation, methodology, writing. JKJ and MASP: supervision.

**Editors:** Sérgio Hampshire de Carvalho Santos, Guilherme Aris Parsekian.